Cranfield University

Department of Aerospace and Guidance Systems

School of Engineering and Applied Science

Royal Military College of Science

Shrivenham

Experimental and Computational tudies of Factors Affecting Impinging Jet Flowfields

PhD Thesis

June 1997

By Mr. M. Myszko

Supervised by Dr. K. Knowles

Summary

An experimental and computational study was made of a single circular jet impinging onto a flat ground board. A ½" nozzle running at a fixed nozzle pressure ratio of 1.05 was used in the experimental phase (giving an nozzle exit Reynolds number of $90x10^3$), the nozzle to ground plane separation being varied between 2 and 10 nozzle diameters. Measurements were performed in the free and wall jets using single and cross-wire hot-wire anemometry techniques and pitot pressure probes in order to detemine mean velocity and normal and shear stress distributions. Some analysis is also presented of earlier measurements on high pressure ratio impinging jets.

Nozzle height was found to effect the initial thickness of the wall jet leaving the impingement region, increasing nozzle to ground plane separation increasing the wall jet thickness, although this separation distance did not seem to affect the rate at which the wall jet grew. Nozzle height was also found to have a large effect on the peak level of turbulence found in the wall jet up to a radial distance from the jet axial centre line of 4.5 nozzle diameters, after which the profiles become self-similar. Lowering the nozzle tended to increase the peak level measured in all the turbulent stresses within this development region. The production of turbulent kinetic energy in the wall jet, which is an indication of the amount of work done against the mean flow by the turbulent flow was found to increase dramatically with decreasing nozzle height. This was attributed to greater shearing of the flow at lower nozzle heights due to a thinner wall jet leaving the impingement region. A moving impingement surface was found to cause separation of the wall jet inner boundary layer on the 'approach' side leading to very rapid decay of peak velocity. The point of separation was found to occur at radial positions in the region of 7.0 to 8.0 nozzle diameters, this reducing slightly for lower nozzle heights.

A parametric investigation was performed using the k-ε turbulence model and the PHOENICS CFD code. It was found that due to inadequacies in the model, it failed to predict accurately the growth of the wall jet, both in terms of its initial thickness and the rate of growth. It did, however, predict an increase in wall jet thickness with both

increasing nozzle height and exit turbulence intensity and decreasing nozzle pressure ratio. Modifications were made to the constants in the model to try and improve the predictions, with a limited degree of success. The low Reynolds number k-ε turbulence model was shown to give a slightly improved non-dimensional wall jet profile, although this did not improve the predicted rate of growth of the wall jet.

Acknowledgements

The author wishes to express his sincere thanks to Dr. K. Knowles for encouraging him to continue this research, his limitless advice and suggestions during the research phase and his continual badgering during writing up. Acknowledgement must also go to Professor A. Brown (Head of S.E.A.S.) for finding the funding to support the author during this work and for permission to use the experimental equipment.

A special thanks must go to Dr. M. V. Finnis for his expert guidance in the use of the experimental equipment and in the software development. Thanks also to Alan Norris and Mark Eyles (A.L. 5 Laboratory Managers) and Mark Wilson and Alistair Saddington (Post Graduate Students) for their general assistance. Mr C. Prowting (Computer Services, Cranfield) and Dr. M. Malin (CHAM) also require acknowledgement for their help during the computational phases.

And lastly, thanks go to Louise for her patience, understanding and wealth of encouragement, especially during the last year of this project.

Declaration

No portion of the work presented in this thesis has been submitted in support of an application for another degree or qualification at this or any other University or Institution of Learning.

Publications

Included below is a list of publications in journals, books and conferences (refereed and non-refereed) that have resulted from this study.

Refereed Publications

M Myszko and K Knowles, "Turbulence Measurements in Radial Wall Jets", accepted by *International Journal of Experimental Thermal and Fluid Sciences*, 1997. **(Invited paper)**

M Myszko and K Knowles, "Radial Wall Jets - Turbulence Measurements", in: *Engineering Turbulence Modelling and Experiments 3*, eds. W. Rodi and G. Bergeles, pp 453-462. Published by Elsevier Science B.V., Amsterdam, 1996. [ISBN 0 444 82463 4]

K Knowles and M Myszko, "Complex Three-Dimensional Jet Flows: Computation and Experimental Validation", in: *Computation of Three-Dimensional Complex Flows*, Notes on Numerical Fluid Mechanics Vol. 53, eds. M. Deville, S. Gavrilakis and I.L. Rhyming, pp 123-129, Published by Vieweg Verlag, Braunschweig/Weisbaden, 1996. [ISBN 3-528-07653-4; ISSN 0179-9614]

Also Presented at *IMACS-COST Conference on Computational Fluid Dynamics*, Three-Dimensional Complex Flows, EPFL, Lausanne, 13-15 September 1995.

K Knowles and M Myszko, "Studies of Impinging Jet Flows and Radial Wall Jets", in: *Turbulence, Heat and Mass Transfer 1*, eds. K. Hanjalic and J.C.F. Pereira, pp 250-257. Published by Begell House Inc., New York, 1995. **(Invited paper)** [ISBN 1-56700-040-1]

Also Presented at *ICHMT International Symposium on Turbulence, Heat and Mass Transfer*, Lisbon, Portugal, 9-12 August 1994.

Non-refereed Publications

M Myszko and K Knowles, "Numerical Modelling of a Single Impinging Jet and Experimental Validation", *The PHOENICS Journal of Computational Fluid Dynamics and its Applications*, 9, 1, pp 51-60, April 1996. [ISSN 0969-8248]

Also Presented at *PHOENICS User Conference, Trento*, Italy, 8-10 November 1995.

M Myszko and K Knowles, "Turbulence Measurements and Modelling of a Radial Wall Jet Formed by the Impingement of a Single Jet", *RAeS Aerodynamics Research Forum*, London, 4-5 January 1996. (No written paper)

K Knowles and M Myszko, "Radial Wall Jets Formed by High Speed Impinging Jets", *ASME/JSME Forum on High Speed Jet Flows*, Hilton Head, S Carolina, 13-18 August 1995. ASME FED Vol. 214, eds. Raman, Kaji and Freitas, pp 53-58. [ISBN 0-7918-1469-6]

K Knowles and M Myszko, "The turbulent, radial wall jet - effect of impinging jet conditions", *Advances in Turbulence V* , Fluid Mechanics and its Applications Vol. 24, ed. R. Benzi, pp 271-275, pub. Kluwer Academic Publishers, Dordrecht, 1995. [ISBN 0-7923-3032-3]

Also Presented at *5th European Turbulence Conference*, Siena, Italy, 5-8 July 1994.

M Myszko and K Knowles, "Development of the wall jet from an impinging, round, turbulent, compressible jet", *AIAA 25th Fluid Dynamics Conference*; Colorado Springs, Colorado, 20-23 June 1994. AIAA-94-2327.

M Myszko and K Knowles, "Turbulent impinging jet flowfields" , *COST Action F1 Workshop I*, "Complex Three-Dimensional Viscous Flows: Prediction, Modelling, Manipulation, Control, Experiment", EPFL Lausanne, Switzerland, 4-6 October 1993. (No written paper)

Nomenclature

A	Constant
A_n	Area of Cell Face
a	Hot-wire Overheat Ratio
a	King's Law Constant
a_n	Diffusion Coefficient
B	Constant
b	Jet Thickness (to 10% of U_m)
b	King's Law Constant
C_υ, C_D, $C_{2\varepsilon}$	Constants used in the k-ε Turbulence Model
C_m	Nozzle Discharge Coefficient
C_p	Constant Pressure Specific Heat
c	King's Law Constant
D_n	Diameter of Nozzle Exit (½" unless stated otherwise)
E	Wall Roughness Parameter
f	Mean Flow Retardation Parameter
f_υ, f_1, f_2	Constants in Low-Reynolds Number k-ε Turbulence Model
F_υ, F_2	Constants used in Two-Layer Turbulence Model
H_n	Distance Between Nozzle Exit and Ground Board
H_p	Distance Between Probe Centre and Ground Board
h	Heat Transfer Coefficient
K	Constant of Proportionality for Wall Jet Correlation
k	Temperature Correction for Kings Law
k	Turbulent Kinetic Energy
k	Thermal Conductivity
k_{nozzle}	Initial Nozzle Exit Value of k
k	Yaw Factor for a Hot-wire (=0.21)
$l_{1\rightarrow 9}$	Cosine Factor
l_m	Length Scale
NPR	Nozzle Pressure Ratio (p_n/p_∞)
Nu	Nusselt Number
NY	Number of Cells in the Y Direction in the Grid Co-ordinate System
NZ	Number of Cells in the Z Direction on the Grid Co-ordinate System
n	King's Law Exponent
n	Total number of Experimental Samples
Prt ()	Prandtl Number
P_k	Production of Turbulent Kinetic Energy
p_n	Total Pressure at Nozzle Exit
p	Pressure
p_∞	Ambient Air Pressure
Q	Rate of Heat Loss
R	Specific Gas Constant
Re_n	Reynolds Number (Based upon Nozzle Diameter and Nozzle Exit Velocity)
R_{20}	Resistance of Probe Wire at 20°C (Ω)
R_c	Resistance of Probe Cable (Ω)
R_p	Resistance of Probe Prongs (Ω)
R_T	Total Resistance of Probe System (Ω)

R_{wc}	Resistance of Probe Wire when Cold (Ω)
R_{wh}	Resistance of Probe Wire when Hot (Ω)
r	Radial Distance from Jet Axial Centre Line
$r_{½}$	Half Thickness of the Free Jet (to 50% U_m)
St	Strouhal Number
S_ϕ	Volumetric Source Term (i.e. Heat Generated)
T	Temperature (^{0}K)
T_c	Calibration Temperature of Probe (^{0}K)
T_o	Stagnation Temperature (^{0}K)
T_w	Temperature of Probe Wire (^{0}K)
T_u	Turbulence Intensity
t_1, t_2	Time at Intervals 1, 2, etc.
U	Mean Velocity Normal to Ground Board
U_{eff}	Effective Velocity Measured by the Hot-wire
U_m	Local Maximum Mean Velocity Normal to Ground Board
U_n	Maximum Mean Velocity at Nozzle Exit
u	Turbulence Fluctuation Normal to Ground Board
uv	Product of Instantaneous Turbulent Fluctuations
V	Hot-wire Voltage
V	Mean Velocity Parallel to Ground Board
V_g	Mean Surface Speed
V_m	Local Maximum Mean Velocity Parallel to Ground Board
v	Turbulent Fluctuation Parallel to Ground Board
Y_n	Distance to Nearest Wall
$Y_{½}$	Half Thickness of the Wall Jet (to 50% of V_m)
Y^+	Non-dimensional Distance from Wall
x	Exponent in Wall Jet Correlation

Greek Symbols

α	Angle Made by the Intercept of the Cross-wires
α_{20}	Temperature Coefficient of Resistivity
γ	Ratio of Specific Heats (=1.4 for Air)
δ_{ij}	Kronecker Delta (=1 if i=j, otherwise =0)
ε	Dissipation of Turbulent Kinetic Energy
ε_{nozzle}	Initial Nozzle Exit Value of ε
θ	Angle of Flow with Respect to the Normal of the Hot-wire
θ_1, θ_2	Angle of Hot-wire with Respect to Prongs on Probe
κ	von Kármán Constant (=0.41)
λ	Ratio of Measured Velocities from the Cross-wires
μ	Laminar Viscosity
ν	Kinematic Viscosity
ν_t	Eddy (Turbulent) Viscosity
π	Total Production of Turbulent Kinetic Energy ($\pi = \pi_1 + \pi_2$)
π_1	Production of Turbulent Kinetic Energy due to Work done by the Normal Stresses
π_2	Production of Turbulent Kinetic Energy due to Work done by the Shear Stresses
π_m	Local Maximum for the Production of Turbulent Kinetic Energy
ρ	Density
σ_k, σ_ε	k-ε Turbulence Model Constants
τ_w	Wall Shear Stress
υ_τ	Resultant Friction Velocity

ϕ	Scalar Quantity (i.e. Temperature, Etc.)

Subscripts

P, E, W	Cell Positions in Domain
n	Neighbouring Cell in Domain (i.e. w=west, e=east, s=south, n=north, h=high & s=south)

Superscripts

*	Imperfect Variables Based on Estimated Pressure Field
'	Correction Required to Obtain Result from Estimated Result
^	Pseudovelocity Correction

Abbreviations

A/DC	Analogue to Digital Converter
CFD	Computational Fluid Dynamics
CTA	Constant Temperature Anemometer
FSD	Full Scale Deflection
HGI	Hot Gas Ingestion
JIR	Jet Impingement Rig
LDA	Laser Doppler Anemometery
OJWT	Open Jet Wind Tunnel
RMCS	Royal Military College of Science
STOVL	Short Takeoff and Vertical landing
V/STOL	Vertical / Short Takeoff and Landing

Contents

Chapter 1 : Introduction and Review

This chapter is subdivided into four basic sections. Firstly, an introduction discussing the importance and need for this work and introducing some of the problems connected with impinging jets. There then follows a description of the flow field created by impinging jets and some of the features associated with then, followed by a review of previously published work, both experimentally and computationally. Finally, there is a brief discussion concerning the scope of the work presented in this thesis.

1.1 Background

Impinging jets occur in a wide variety of practical engineering circumstances, from the fabric industries where they are used to aid drying, to the aerospace industries where they are formed underneath V/STOL aircraft hovering in ground effect. For such reasons, these flows have received considerable attention in the past, both experimentally and numerically. Due to the rapid growth in the power of economical computational facilities, renewed attention has been paid to impinging jets over the last few years as a test case for turbulence models and solution codes.

Impinging jets are widely used in the field of heat and mass transfer because of their ease of control, relative effectiveness and inexpensive running costs. Specific applications have included the cooling of turbine blades, the cooling of electrical equipment, the annealing of metal and plastic sheets and the heating and drying of textiles, veneer, paper and film materials (Kataoka 1985, Polat 1993). To these ends, a wide range of configurations have been used from single impinging jets to multiple arrays of round and slotted jets in confined and unconfined conditions. As the drying of materials off production lines can be a time-consuming and expensive process, the optimisation of jet configurations has become increasingly critical and achieving the greatest heat and mass transfer for a given energy input is important. Much attention has recently been given to the prediction of heat transfer beneath impinging jets using Computational Fluid Dynamics (CFD) techniques with some success, although there

still remains serious shortfalls in these predictions. It is the greatly increased use of such techniques on a seemingly simple-to-model flowfield that has lead to a far greater understanding of the problems associated with obtaining this optimum configuration.

In the field of V/STOL or STOVL aircraft, a primary design consideration is the flow environment created by the propulsion system during hover or low-speed operation in ground proximity. The behaviour of these aircraft in such conditions can be the limiting factor in the overall design. With the increase in thrust required for advanced supersonic STOVL jet-lift aircraft, problems associated with flowfield development will become more and more important (see Knowles and Bray (1991) for a summary of these problems).

A range of issues can occur with STOVL aircraft in ground proximity. Firstly, conditions can occur when spent exhaust gases from the engine can be re-ingested through the engine air-intakes (known as Hot Gas Ingestion, HGI, see Figure 1.1). Since the output thrust is sensitive to the density, and hence the temperature of the inlet air, ingestion of a small part of the exhaust gases can lead to large and very sudden losses in thrust level. Of even greater significance, if ingestion is linked with large temperature distortions, compressor stall or surge can occur. These problems are greatest when hovering or moving forward into a head-wind, the cross-wind stagnating the wall jet formed by the exhaust plume's radial spread over the ground (see Figure 1.2), causing it to roll up upon itself. This is commonly referred to as the ground vortex and is a region of highly unsteady, re-circulating, separated flow. This separated flow is prone to aperiodic breakdown and growth cycles (Cimbala et al. 1987 & 1991), the breakdown leading to higher levels of HGI (see Figure 1.3).

Induced pressures on the airframe caused by the entrainment of ambient air into the fast moving jets (due to viscous shear forces) can significantly influence the lifting performance of the aircraft (known as suckdown, see Figure 1.4). These jets can extend up to 30m below the fuselage, at which point the entrainment process has reduced the jet velocity to such an extent that their own buoyancy becomes important. While in ground effect, the radial wall jet formed by jet impingement will also entrain ambient air

into its free boundary. As the wall jet surface area is far larger than that of the free jet, the problem of suckdown is greatly increased, leading to a 2-3% reduction in effective installed thrust (Williams and Wood, 1966). Jet impingement can create other problems such as ground surface erosion and severe acoustic and thermal environments for operating ground crews.

In an attempt to understand these problems, much theoretical and experimental work has been performed on the impinging jet flowfield. This research has lead to many predictive techniques being generated, from simple engineering correlations for the flowfield to detailed numerical models to predict complex flow features such as the self-sustaining oscillations of a jet (commonly known as screech) which are sometimes found at a certain of Reynolds numbers.

The use of this flowfield for validation of CFD models has grown due to the relatively simple computational domain needed, especially at low nozzle to ground plane separations (H_n/D_n). The choice of an impinging jet as a test case for the *IAHR Working Group on Refined Flow Modelling* (Brison and Brun, 1991) is one example of the increased interest placed on this subject. Although much work has been performed on general flow features and on local heat transfer beneath jets, there is still a lack of good detailed experimental flowfield data (Cooper et al. 1993) giving concise information on the experimental boundary conditions required for accurate computational modelling. There are also several parametric effects associated with flowfields involving impinging jets which require explanation, some of which are described below.

1.2 The Impinging Jet Flow Field

Described below are the main features of the flowfield created by an impinging jet that are of interest this project.

1.2.1 The Free Jet

A subsonic free jet has two main flow characteristics: a region called the potential core where the jet is unaffected by the ambient conditions around it. The potential core remains at a constant velocity with varying downstream position forming a "top hat" velocity profile (see Figure 1.5(a)). Around this core, there is a region of viscous mixing between the jet and the ambient fluid, being unstable and consisting of large scale eddies. It is this turbulent shear layer which is responsible of the entrainment of the ambient fluid surrounding it and the consequent spread of the jet. This mixing region gradually spreads inwards until the potential core no longer exists (see Figure 1.5(a)) at which point, typically 5-6 D_n downstream of the nozzle exit, the velocity profile no longer exhibits the central constant-velocity feature. The jet continues to grow in width as it moves downstream due to entrainment of the ambient fluid into the jet causing further decay of the peak centreline velocity. The flow in this region develops until velocities reach the self-similar profile (profiles collapsing into the same shape when non-dimensionalised with a velocity and thickness) of a fully-developed jet. Turbulence intensity profiles develop in a similar manner, although self-similar profiles do not occur until much further downstream. As the nozzle pressure ratio is increased up to the sonic jet case, it has been shown (Curtis 1987) that the spreading rate of the free jet decreases and this will be discussed in more detail later.

Subsonic air jets described above exist until the Nozzle Pressure Ratio (NPR), the ratio of nozzle stagnation pressure to ambient pressure, reaches a value of 1.893 (critical pressure ratio for isentropic flow), above which a weak shock wave forms across the nozzle exit dropping the flow to subsonic values. This flow pattern changes rapidly with further increases in NPR and when the static pressure at the nozzle lip becomes around 10% higher than the ambient pressure, a pattern of 'diamonds' or 'cells' form composed of intersecting expansion and compression shock waves, the jet now being called 'underexpanded' (see Figure 1.5(b)). These shock waves gradually drop the flow to subsonic conditions, after which the jet can be described as a subsonic jet with an offset in its origin. Underexpanded jets spread at a slightly faster rate than subsonic jets

thought to be due to the increased turbulence generated by the interaction of the shock waves with the edge of the shear layer.

Under certain conditions and mainly at low Reynolds numbers (based on nozzle conditions), jets have shown a tendency to form periodic coherent structures within the jet mixing region. These structures occur at a range of Reynolds numbers and at the range of present interest (90,000 based on nozzle exit) tend to generate axisymmetric ring vortices for a circular jet. The ring vortices increase the level of turbulent mixing in this shear layer, consequently increasing jet spreading rate and jet peak velocity decay.

1.2.2 The Impingement (Deflection) Region

As a free jet flow approaches an impingement surface, the flow is rapidly decelerated to rest in the quasi-perpendictular direction with respect to the plate. At the point of intersection of the jet centreline and the impingement plate, a stagnation bubble forms due to the rapid increase in the flow's static pressure up to the jet's total pressure before impingement. The jet is deflected through 90^0 and forms a flow which is quasi-parallel to the plate, this being known as the wall jet. The flow is rapidly accelerated away from the impingement point due to this favourable pressure gradient.

Heat transfer between the impingement surface and the fluid can be very high in this region. When the nozzle height, non-dimensionalised with nozzle exit diameter (H_n/D_n), is large ($H_n/D_n > 8.0$) and a fully developed free jet impinges, the heat transfer described by the Nusselt (Nu) number peaks at the stagnation point. This peak value has been shown to be dependent on the turbulence intensity of the flow at impingement and for low speed jets, peak Nu occurs when the outer shear layer of the free jet has just decayed the potential core. Increased Nu can occur with artificially induced turbulence levels, increased initial nozzle exit turbulence intensity, Tu, causing increased Nu. For low nozzle heights where the potential core impinges on the surface, two peaks occur surrounding the stagnation point, the inner peak being explained by the radial acceleration of the fluid away from the stagnation point and the outer peak corresponding to the impingement of the free jet mixing region with the surface.

1.2.3 The Wall Jet

The radially spreading jet formed by the impingement of a jet on a surface is termed the wall jet. After a short development region, the wall jet exhibits a self-similar velocity profile (as described by Glauert 1956), characterised by the action of surface friction forming an inner boundary layer and a shear layer with the ambient surrounding fluid forming a mixing region similar to that of the free jet. The wall jet decays with increasing radial distance from the impingement point (r/D_n) due to the action of turbulent mixing with the entrained fluid, this also causing the jet to grow in vertical height, usually characterised by the wall jet half-thickness, $Y_{½}$ (height in profile to half the local peak velocity).

Heat transfer between the wall jet flow and the surface is higher than that for similar parallel flow over the surface, believed to be due to the outer shear layer causing increased turbulence generation, which penetrates to the inner boundary. As radial distance from the stagnation point increases, peak wall jet velocity falls due to turbulent decay and radial growth of the wall jet. This leads to a rapid decrease in the heat transfer and by $r/D_n > 5.0$, Nu becomes independent of impingement conditions .

1.2.4 Wall Jet Separation

Where a cross-flow and/or moving surface are present, the wall jet can stagnate and separate, a cross-flow forming a region of recirculating flow commonly referred to as the ground vortex (see Figure 1.6). Viewed from above, the flow feature is elliptical in shape, resembling a horseshoe with the vortex being folded back downstream by the action of the cross-flow. This vortex causes a reduction in static pressure beneath it, this pressure profile (see Figure 1.7) being used to identify the penetration of the vortex up-stream (Bray 1992, Wilson 1995).

1.3 Review of Experimental Work

A large amount of experimental work has been conducted on impinging jets over the last 40 years, considering a wide range of parametric and flowfield features. The optimisation of flow conditions for heat and mass transfer has lead to numerous publications, many of then reviewed by Martin (1977), Goldstein and Franchett (1988) and Jambunathan et al. (1992). A literature survey by Gauntner (1970) covers much of the early work on the flowfield features relevant to V/STOL aircraft, while a recent review by Margason (1993) discusses the research into jets in cross-flow covering the last fifty years. It is not the author's intention to repeat these reviews, but some work needs further explanation as it is of direct relevance to this research.

1.2.1 Free Jet

Donaldson and Snedeker (1971) undertook an investigation in subsonic and supersonic jets, with velocity profiles being calculated from pitot/static measurements. They concluded that for a subsonic jet, the mean velocity profiles become fully developed with self-similar profiles after $(H_n-H_p)/D_n = 7.32$ (where (H_n-H_p) is used to represent downstream distance in the jet from the nozzle exit[1]). After further development of the turbulent profile ($(H_n-H_p)/D_n \approx 11$), the mean velocity decay was shown to be approximately hyperbolic in shape, following well the $1/(H_n-H_p)$ relationship suggested by many including Squire (1950). Squire also looked at the length of the potential core formed by subsonic jets which showed a consistent length of around $5D_n$, a figure which has also been supported by more recent work (Mathieu and Charnay 1981).

A study of free jets with relevance to V/STOL applications was conducted by Curtis (1987). He used a traversing pitot/static probe to measure free jet profiles formed by a 1" round nozzle at NPRs ranging from 1.04 - 3.00. He found that the length of the potential core increased with NPR up to the sonic jet case, and the jet boundary spreading rate decreased. His mass flow calculations also showed a decrease in free jet

[1] This notation is adopted here to be consistent with that used for the later impinging jet studies.

entrainment rates with increasing NPR up to sonic conditions, these effects being explained by a decrease in the turbulence intensity in the mixing region, due to a lengthening of the turbulent length scale with dynamic head. It has more recently been suggested that the "suppressed mixing behaviour of compressible shear layers" (Strykowski et al. 1996) may account for this reduced turbulence intensity. Curtis states that the turbulence produced by the nozzle design affects the rate of spread of the jet, lower initial turbulence causing lower spreading, but does not affect the rate of decay of peak velocity and that this is more pronounced at lower NPRs. He also states that initial nozzle exit conditions (NPR, Tu, etc.) have no appreciable effect on the wall jet and although nozzle height effect was not looked at, cites Cox and Abbot (1964), suggesting it to be negligible for a subsonic jet.

1.2.2 The Impingement Region

Bradshaw and Love (1959) made velocity and static pressure measurements in impingement and wall jet regions formed by a circular turbulent jet impinging on a flat surface. They concluded that the impingement region was small in size, only being slightly larger than the thickness of the jet entering the region. They also showed that the shear stress reached a maximum at the edge of the static pressure bubble, with radial velocity reaching a maximum under the influence of this pressure gradient and viscous forces then dissipating the flow.

Colin and Olivari (1969) showed that the size of the stagnation bubble with respect to its half-thickness changed very little with nozzle-to-plate separation as long as the free jet had reached a similar profile before impingement. If the potential core impinged, the bubble was smaller, with a larger pressure gradient in the radial direction. Bradbury (1972) took pitot pressure measurements in the free jet and static pressure measurements on the ground board for a subsonic, round, impinging jet. He suggested that the flow in the impingement region acts as a nearly inviscid fluid up to $r = 1.5r_{½}$ as long as the entry flow is similar in profile, pointing out that away from the impingement region, turbulent mixing reduces the peak dynamic head.

Experimental work by Gutmark et al. (1978) revealed the large changes that occur to the inflowing jet's turbulence, especially in its spectral content. They detected a spectral frequency range in which turbulent energy is unchanged by the deflection; at higher frequencies, they argued that the turbulence was attenuated due to viscous dissipation while at low frequencies, the turbulence was augmented due to the lateral stretching of the ring vortices surrounding the free jet. Flow-visualization photographs obtained by Yokobori et al. (1979) show these vortices coalesce on impact, and for $H_n/D_n > 4.0$, these large-scale structures appear to breakdown to small-scale random turbulence. Popiel and Trass (1982) showed, using flow-visualization, that for $H_n/D_n = 2.0$, the peak in Nusselt number at around $r/D_n = 2.0$ coincided with the impact of these ring vortices on the surface.

Cooper et al. (1993) made detailed mean and turbulence measurements in the impingement region after identifying a need for flowfield data to complement Nusselt number measurements made by Baughn and Shimizu (1989) for CFD validation. Single and cross-wire readings were taken at small r/D_n (up to $r/D_n = 6.0$) for differing nozzle heights at two flow Reynolds numbers ($2.3x10^4$ & $7.0x10^4$, based on nozzle exit). These were achieved by the use of two nozzles (D_n = 26mm and 101.6mm) with a supply pipe length-to-diameter ratio of 80:1, giving the nozzle exit flow the characteristic of fully developed pipe flow. Dantec hot wire probes (55P11 single-wire & 55P61 cross-wire) were sampled using a 12-bit ADC for 51.2 seconds at 100Hz in batches of 512 samples.

This set of data showed a linear radial wall jet growth away from the stagnation point with an increase in the slope with increasing nozzle discharge height, this was explained as being due to increased free jet mixing before impingement at increased heights. The streamwise (wall-normal) turbulence intensity was shown to increase smoothly on the jet axial centre line unto $0.3D_n$ above the ground where there was a sudden fall, believed to be due to a wall dampening effect on the turbulent fluctuations. Although there was shown to be quantitative differences in the radial development of the turbulent profiles for differing nozzle heights, an increase in height causing increased fluctuations, the qualitative behaviour was similar, the differences being attributed to differing levels of free jet fluctuating velocity before impingement.

With differing Reynolds number, the profiles at r/D_n=1.5 were shown to be practically identical, but at r/D_n=3.0, the mean velocity was some 10% higher for the higher Reynolds number case with a corresponding higher level of turbulence intensity, thought to be due to the larger mean velocity gradient. Cross-wire results showed turbulence intensities normal to the wall being around 60% of the streamwise values.

1.2.3 Wall jet

Glauert (1956) performed the first theoretical study into what one of his colleagues termed the "wall jet". He considered the wall jet as consisting of two sections, the inner boundary layer governed by Blasius's (1913) formula for flow in a pipe using the 1/7 power law and the outer section following Prandtl's (1942) hypothesis for free turbulent shear flow. The two approaches were merged at a point were the rate of change of shear stress was zero (point of peak velocity). Although this allowed him to derive a solution, it meant that complete similarity of the wall jet was no longer theoretically possible.

He concluded that the exact relationship for the rate of growth of the wall jet varied with Reynolds number, but was of the form:

$$\frac{Y_{\frac{1}{2}}}{D_n} = K\left(\frac{r}{D_n}\right)^x$$

Equation 1.1.

where the exponent, x, ranged between 1.005 and 1.038.

Bakke (1957) made an experimental investigation of a turbulent low-speed jet of air impinging on and spreading out over a flat, smooth plate. The aim of this work was to determine the mean velocity distribution and rate of growth of the flow and to compare these with the theoretical predictions of Glauert (1956). A simple experimental apparatus was used to produce a single normal impinging jet with a peak nozzle exit speed set to $34ms^{-1}$ (NPR approximately equal to 1.008). The height of the nozzle remained constant at a value H_n/D_n=0.53 with a nozzle diameter of 28.4mm. The

velocity distribution along the plate was measured by means of a 1mm external diameter total pressure tube connected to a 'Casella' U-tube manometer. No account was taken of the static pressure distribution and its effect on velocity profiles.

From the profiles obtained, the height to half peak velocity, $Y_{½}$, was found to be proportional to the radial distance from the jet axial centre raised to the power 0.94, contrasting with Glauert's theoretical value above. No attempt was made to deduce the value of the constant of proportionality as the nozzle height and pressure ratio remained constant; no other factors were considered.

The work of Poreh et al. (1967) was inspired by the differences found between the theoretical analyses of Glauert and the empirical work of Bakke. A variety of initial jet conditions were studied, with H_n fixed at 24" (0.61m) throughout and the peak nozzle exit velocity ranging from 53 to 113m/s. A variety of nozzle diameters were used varying from 1" to 3" (0.0254 to 0.0762m) so causing H_n/D_n to vary between 8 and 24.

The experimental work also used the results of Bradshaw and Love (1959) in the correlation of the data. The results contained very little scatter and showed that the flowfield was virtually independent of Re_n. The spreading rate of the wall jet could adequately be described by:

$$\frac{Y_{\frac{1}{2}}}{H_n} = 0.098\left[\frac{r}{H_n}\right]^{0.9}$$

Equation 1.2.

This shows that the wall jet thickness depends on the power 0.9 rather than 1.025 (for these conditions) suggested by Glauert and 0.94 as measured by Bakke. Poreh et al. also concluded that the wall jet flowfield produced by a circular jet was dependent on H_n/D_n but this was not included in the correlation. They stated that the flow field of the wall jet depended on the initial conditions, even at large distances from the stagnation point.

Hrycak et al. (1970) performed an experimental study of the flow characteristics of a circular air jet formed from a circular nozzle impinging on a smooth flat plate with varying heights of 2 - 30 diameters and Reynolds numbers (based on nozzle exit) between 600 - 100,000. Their results indicated that "the nozzle-to-plate spacing has more influence on the static pressure distribution along the impingement plate in the deflection region than either the nozzle diameter or the nozzle exit Reynolds number" and this lead to an H_n/D_n term in their correlation for the wall jet half-thickness:

$$\frac{Y_{\frac{1}{2}}}{D_n} = \left[0.00081 \times \frac{H_n}{D_n} + 0.0864\right]\left[\frac{r}{D_n}\right]^{0.95}$$

Equation 1.3.

Extensive data was presented by Schwantes (1973) on impinging jets in cross-flow. He investigated the effect of different nozzle temperatures, nozzle to cross-flow velocities and nozzle heights for an impinging jet of nozzle diameter D_n=50mm on a fixed ground plane using pitot/static probes.

He found that in a cross flow, penetration of a ground vortex decreased markedly as the height of the nozzle was decreased, this being attributed to a lower wall jet momentum at lower nozzle heights due to a less efficient turning process. Due to low-frequency turbulent fluctuations in the measurements, he was unable to establish unambiguously whether greater distance from the nozzle to the ground produced thicker wall jets.

Miller and Wilson (1993) undertook a major study of the impingement process for high-pressure ratio (NPR = 2.7 - 4.7) single and twin round nozzle (D_n=25mm) flows impinging on a flat plate for a range of nozzle heights. Wall jet velocity profiles were recorded using pitot/static rakes and a correlation for the wall jet half velocity height, $Y_{½}$ was given by:

$$\frac{Y_{\frac{1}{2}}}{D_n} = \left[0.0005 \times \frac{H_n}{D_n} + 0.0864\right]\left[\frac{r}{D_n}\right]^{1.01}$$

Equation 1.4.

This includes a term to compensate for the height effect that was measured. A nozzle pressure ratio effect was also noted, increasing NPR tending to decrease the rate of spread of the wall jet. No attempt was made to correlate this factor. A correlation for the decay of peak wall jet velocity was also deduced :

$$\frac{V_m}{U_n} = 0.565 \times J^* \times \sqrt{C_m} \times \left[2.016 \times \frac{Y_{1/2}}{D_n}\right]^{-0.5} \times \left[\frac{H_n}{D_n}\right]^{-0.088} \times \left[\frac{r}{D_n}\right]^{-0.555}$$

Equation 1.5.

where J^* is a momentum term defined by :

$$J^* = NPR^{0.143} \times \left(1 + 0.318[NPR - 1.893]^{0.748}\right)$$

Equation 1.6.

and C_m is the nozzle discharge coefficient.

Myszko (1993) investigated the effect of nozzle height and NPR on the development of a wall jet produced by a single round nozzle. Pitot and static pressure profiles were taken for a H_n/D_n range of 2 - 30 and radial positions up to r/D_n=30 for NPRs = 1.05 - 4.0. He found that increasing nozzle to ground plane separation caused a thicker wall jet to result with an increase in wall jet momentum flux at a fixed radial location. The data also suggested that increased NPR caused a reduction in the wall jet thickness, although there was a lot of scatter in the data due to poor pressure control.

An extensive investigation of the mean and turbulent characteristics of three-dimensional planer wall jets was undertaken by Padmanabham and Lakshmana Gowda (1991), normal and shear stress results being published. One of the aims of the work was to continue the investigation of Palmer and Keffer (1972) who had looked at the production of turbulent kinetic energy in the wall jet and in common with Eskinazi and Erian (1969) had argued that there might be a transfer of energy from the turbulent flow to the mean flow (re-laminarization) in certain regions of the flow.

The production of turbulent kinetic energy (π) is given by:

$$\pi = -\rho\left(\overline{v^2} - \overline{u^2}\right)\frac{\partial V}{\partial r} + \left(-\rho\overline{uv}\left(\frac{\partial V}{\partial y} + \frac{\partial U}{\partial r}\right)\right)$$

Equation 1.7.

and is an indication of the work done against the mean flow by the turbulent fluctuations in that flow.

For the wall jet, the radial gradient of U is at least an order of magnitude smaller than the gradient of V, and so π can be expressed as:

$$\pi = -\rho\left(\overline{v^2} - \overline{u^2}\right)\frac{\partial V}{\partial r} + \left(-\rho\overline{uv}\frac{\partial V}{\partial y}\right)$$

Equation 1.8.

or:

$$\pi = \pi_1 + \pi_2$$

Equation 1.9.

where :

$$\pi_1 = \rho\left(\overline{v^2} - \overline{u^2}\right)\frac{\partial V}{\partial r}$$

Equation 1.10.

and

$$\pi_2 = -\rho\overline{uv}\frac{\partial V}{\partial y}$$

Equation 1.11.

It was argued that for wall jets (or asymmetric velocity profiles), π could become negative if π_2 became large and negative (in this case π_1 would always be positive as the gradient term was always negative and $\overline{v^2}$ was greater than $\overline{u^2}$). This condition was called energy reversal and, if it occurred, it would imply that the turbulence was feeding the mean flow. Padmanabham and Lakshmana Gowda (1991) found that π did not go negative at any point in the flow, the value of π_1 was always able to compensate for the negative value of π_2.

Overall, changes in the value of π for the same flow conditions would mean changes in the level of energy stored in the mean flow (and corresponding turbulent flow), a higher value of π for one condition meaning there was less energy in the mean flow and more in the turbulent. If the level of π in the wall jet following impingement were to reduce for higher values of H_n/D_n, then there would be less energy moved from the mean flow to the turbulent flow, implying that the turning process was more efficient (for the mean flow).

1.2.4 Separation of the Wall Jet

Bray (1992) undertook a parametric investigation into high NPR impinging jets in cross-flows using the experimental apparatus at RMCS. Ground vortex separation position was located from measured static pressure profiles for various NPR, nozzle height, ratio of nozzle exit speed to cross-flow speed and surface velocity parameters. The data showed a variation in the wall jet separation with nozzle height, reduced H_n/D_n causing a reduced separation distance (i.e. wall jet separation position moved closer to the impingement point at low nozzle heights). The addition of a moving ground plane, with velocities equal to and half the magnitude of the cross- flow was shown to further reduce the separation distance. Bray was unable to deduce from the data whether this was primarily due to increased surface shear stress under the wall jet with the moving ground plane, or due to a lack of cross-flow momentum deficit because of the removal of the cross-flow boundary layer build. Its is most likely due to a combination of both

effects but it is important to know their relative contributions when considering modelling a STOVL aircraft in ground effect.

Local heat transfer was reported by Polat and Douglas (1990) and Polat et al. (1991) for a single impinging slot jet (Reynolds numbers up to 35,000) on a moving surface (up to 9 ms^{-1}) at $H_n/D_n = 2.5$. A large effect on local heat transfer was noticed on the side with surface motion towards the jet centre line, with a skewing of the Nussett number profiles. This was attributed to cooler temperature ambient fluid being "dragged" in to the jet region by the motion of the surface, having the effect of reducing the overall heat transfer. It was later reported by Polat (1993) that similar work conducted with round jets had shown local heat transfer was "not appreciably affected" for surface-to-jet bulk velocity ratios twice that tested for with slot jets. It was cited that this was most likely due to the spent fluid having a higher degree of freedom to spread around the ground jet on the surface.

1.3 Review of Computational Work

There are many numerical models that have been used for the prediction of impinging jets ranging from very simple zero-equation turbulence models to Direct Numerical Simulations (DNS), all of which have been used with differing degrees of success in the past. With the dramatic increase in the performance of computing power over the last decade, the two-equation, eddy viscosity turbulence model has become the standard predictive tool for many turbulent flow simulations. The turbulence models detailed below are explained in greater depth in Appendix B.

The k-ε turbulence model has been widely used (Jones and McGuirk 1980, Childs and Nixon 1987, Barata at al. 1989, Hwang and Liu 1989, Bray 1992, Craft et al 1993) to predict impinging jet flow fields ranging from single impinging jets to the latest ideas on three-jet lifting configurations for the next generation of STOVL aircraft (Barata, Durão and McGuirk 1989). This model has the benefit of being widely and easily used and understood, leading to most of the computational validations being for this model. This has meant that shortcomings in the model have become well known and although

the model correctly predicts the trends expected and observed in the experimental work, the accuracy of the results is generally poor for this flowfield.

The k-ε model fails in the three major regions of an impinging jet flow field: the axisymmetric free jet, the impingement region (because of the stagnation point and streamline curvature) and the radial wall jet. The constants used in the model were originally tuned for free turbulent flows and wall-bounded shear flows and this may account for problems faced with strong free shear flows. A study conducted by Rodi (1980) showed that a 5% change in the values of the constants used in the ε equation can result in a 20% change of the spreading rate of a free jet.

It has been well reported that the standard k-ε model tends to over-predict the rate of spread of a round free jet by around 25% (Rodi 1980), Malin (1988) attributing this to deficiencies in the ε-transport equation. Rodi (1980) proposed a correction for this with the addition of an algebraic stress correction to two of the empirical constants. If this correction is applied to axisymmetric free jets, the rate of spread is reduced to give better agreement with experimental data, although there still exists a slight over-prediction (Knowles et al. 1993).

This turbulence model seems to be sensitive to the adverse pressure gradient caused by the stagnation of the free jet on the ground plane and to the curvature in streamlines during impingement. It is well reported that eddy viscosity models have an inability to predict the effect of streamline curvature properly, rotational strains and other body-forces on the flow (Speziale 1991). Work reported by Craft et al. (1993) covering the performance of various k-ε models in the impingement region of a round turbulent jet indicates that it is the use of the eddy-viscosity stress-strain law, used to represent the normal stresses in the flow, that causes a major problem. Comparisons with the experimental data of Cooper et al. (1993) showed that it was the excessive turbulent energies (values of normal velocity turbulence, u, up to 4 times as large as experimental results) that was leading to excessive mixing in the impingement region, this being indicated by too low a peak velocity and too high a wall jet half thickness at r/D_n=2.5. Barata et al. (1986, 1987 & 1989) undertook a large comparison of results

using the k-ε model and their own Laser Doppler Anemometry (LDA) experimental data. Although comparisons with far flowfield mean flow measurements were relatively good, difficulties still existed in the impingement region, the incorrect prediction of the Reynolds shear stress sign being a particular example. Childs and Patel (1990) attributed this to the assumption of isotropic turbulent eddy viscosity which is inherent in all eddy-viscosity turbulence models due to the use of the Boussinesq Eddy Viscosity hypothesis (Boussinesq 1877).

For wall jets, it is somewhat surprising to find that the standard k-ε model tends to under-predict the spreading rate of radial wall jets, whilst over-predicting the growth of plane wall jets by up to 30% (Launder and Rodi 1983). Malin (1988) argued that the reason was that a radial wall jet suffers from lateral divergence, causing the numerically calculated increase in length scale between plane and radial wall jets to be underestimated. This suggests that the level of ε is too low for the radial case, causing the prediction of the turbulent energy and shear stress to be too low. This is consistent with Barata et al. (1989) who accounted for differences from experimental data as due to incorrectly predicted shear stress distributions. A further problem arises in the use of the Boussinesq Eddy Viscosity hypothesis (Boussinesq 1877) for eddy-viscosity turbulence models (including k-ε) which implies zero shear stress occurs at the point of zero velocity gradient. For a radial wall jet, it has been shown that this is not the case, zero shear stress occurs below peak velocity (and hence below zero velocity gradient) (Launder and Rodi 1983), this being ascribed to outer shear layer turbulent fluctuations penetrating the inner layer (Schwarz and Cosart 1961, Bedìì-Özdemìr and Whitelaw 1992). On a practical note, it is often the shear stress profile that is correctly predicted in this respect, the position of the peak velocity being calculated too low (Launder and Rodi 1983). This is of importance, as it is the shear stress profile which dictates the rate of wall jet growth.

Malin originally proposed (Glynn and Jal 1987) corrections for the constants of the k-ε model for use in the radial wall jet based on the principle used by Rodi (1980). He went on to use a more theoretical technique (Malin 1988) to increase the value of ε

in a radial wall jet, so increasing the rate of spread. The corrections of Rodi and Malin were tried by Glynn and Jal (1987) and later by Knowles et al. (1993) in an effort to predict correctly the spread of a wall jet formed from an impinging jet. Both found that the Rodi correction gave good agreement for the free jet case and that both corrections used together gave an improved answer over the standard model, although the wall jet thickness was still under-predicted by a considerable amount. It was suggested by Glynn and Jal (1987) that further work on the constants in the correction would lead to better answers but that there was a fundamental problem with this turbulence model when used on these flows. Knowles et al. (1993) went on to use the Malin correction on both the free and wall jet portions and found that the wall jet thickness was now correctly predicted, at the expense of the free jet which was vastly over-predicted. An error was later found in the coding (Knowles 1996), so questioning this result.

The final problem with the use of the k-ε model lies in its requirement for wall functions when solid boundaries are faced. Wall functions are used to avoid the problems of modelling the direct influences of viscosity near a boundary and can dramatically influence the success of the model (Patel et al. 1985). The validity of this procedure is restricted to domains in the flow where the Reynolds number is high enough for viscous forces to be insignificant, and there are a number of cases where this approach has to be abandoned. Several investigators have shown that simple wall functions based on the logarithmic law and the equilibrium turbulence assumption are not appropriate for turbulent boundary layers (Cousteix and Houdeville 1983, Mankbadi and Mobark 1991, Justesen and Spalart 1990) and Michelassi et al. (1993) commented that this was also true for unsteady and separated flows. It is believed that the use of these functions in impinging jet flowfields has a marked effect on the simulation.

To counter the problems of the logarithmic law-of-the-wall function, often used with the k-ε model, low Reynolds number k-ε models were developed (Launder and Sharma 1974, Hoffmann 1975, Reynolds 1976, Hassid and Poreh 1978, Wilcox and Rubesin 1980, Dutoya and Michard 1981, Lam and Bremhorst 1981 and Chien 1982). Their performance was tested and reported on for a number of test cases in a review by Patel et al. (1985). The basic difference from the standard k-ε model is the addition of

extra functions in the ε equation which modify the standard empirical constants and the addition of viscous diffusion terms. The conclusions of the review of Patel et al. were that only the models of Launder and Sharma (1975) and Wilcox and Rubesin (1980) yield results comparable with experimental data and that still further fine tuning of the functions was required.

The major problem with low Reynolds number models is their requirement for the first cell to be within the laminar sublayer of the boundary layer. This leads to the need for very thin cells, causing a large number of cells in the domain if low cell aspect ratios are to be retained. Although this gives increased accuracy, it is at the expense of increased computational time.

To counter this problem, Rodi (1991) suggested the two-layer model. This works on the principle that k-ε is fine for the fully-turbulent portion of the flow, so the standard model is used down towards the boundary until the local Reynolds number (based upon the minimum distance to the ground and local velocity) reaches around 350. After this, in the viscosity-affected region, a single-equation turbulence model suggested by Norris and Reynolds (1975) is used. This fixes the dissipation rate (ε) and uses a transport equation to determine k. No indication of how well this model would perform with impinging jets is available, but the improvement over the standard logarithmic law of the wall for turbulent boundary layer flows and the reduction in computing time (as there is no longer the need for such a fine grid at the boundary) means this model is worthy of further examination.

Computational work has been carried out on impinging jets using the second order Reynolds Shear Stress closure model (RSM). An ERCOFTAC-IAHR meeting held at Lyons (Brison and Brun 1991) and later at Manchester (Leschziner and Launder 1993) tested a number of different k-ε (with standard and low Reynolds number wall functions) and RSM predictions and found that neither gave good agreement with reported experimental results over the entire flow-field. At the meeting, it was argued that the RSM failed to improve the prediction dramatically because of the use of the

standard wall function. They recommended that the standard wall sub-model should be replaced with a low-Reynolds number version.

Declercq and Dutré (1994) also reported poor agreement with experimental data for the RSM, indicating shortcomings in the sub-model for the wall-reflection process. They recommended that a low-Reynolds number second order model should be used in the wall boundary-affected areas, and that such a model was under development.

In summary, previous computational studies have shown shortcomings in the ability of the standard k-ε model to predict the details of flowfields generated by impinging jets, the impingement process and the logarithmic law of the wall both accounting for the poor predictions. More advanced second order closure models (e.g. RSM) have been shown to be little better, again the treatment of conditions at the boundary being isolated as problematic. The use of low-Reynolds number corrections for this region has been suggested, but their requirement for thin cells at the boundary interface and the consequent cell aspect ratio problem that follows makes their use problematic unless computing power is not a problem (although it has recently been suggested that this model can be implemented for only 30% extra cost (Leschziner 1996)).

1.4 Scope of this Thesis

This thesis discusses both experimental and computational work performed by the author at Cranfield University's Shrivenham campus at RMCS, on the normal impingement of a single, round, turbulent jet. The primary aim was to continue the work of Bray (1992) by concentrating on one of the unanswered aspects of his work. As has been discussed, the nozzle to ground plane separation and impingement surface velocity relative to the nozzle were shown to affect ground vortex penetration. A more detailed investigation into the mean and turbulent flow properties of a developing wall jet was thought to be helpful in isolating and explaining some of these findings. An experimental test programme was devised to measure wall jet properties for a number of differing parametric conditions on both a fixed and moving impingement surface.

A computational investigation using the k-ε turbulence model and PHOENICS CFD software was performed, running in parallel with the experimental work. The aim was to investigate the performance of this relatively simple, cheap and increasingly used turbulence model for the impinging jet case and to see whether it could predict the parametric effects seen in the experimental data. Such parametric studies have not been widely reported in the literature.

This thesis treats the two components (experimental and computational) of this work in parallel, with separate chapters on the methods used for each component (Chapter 2 and Chapter 3 respectively) and separate discussions of their results (Chapter 4 and Chapter 5 respectively). The two strands are tied together in Chapter 6 with a discussion of the overall conclusions from both the experimental and computational work.

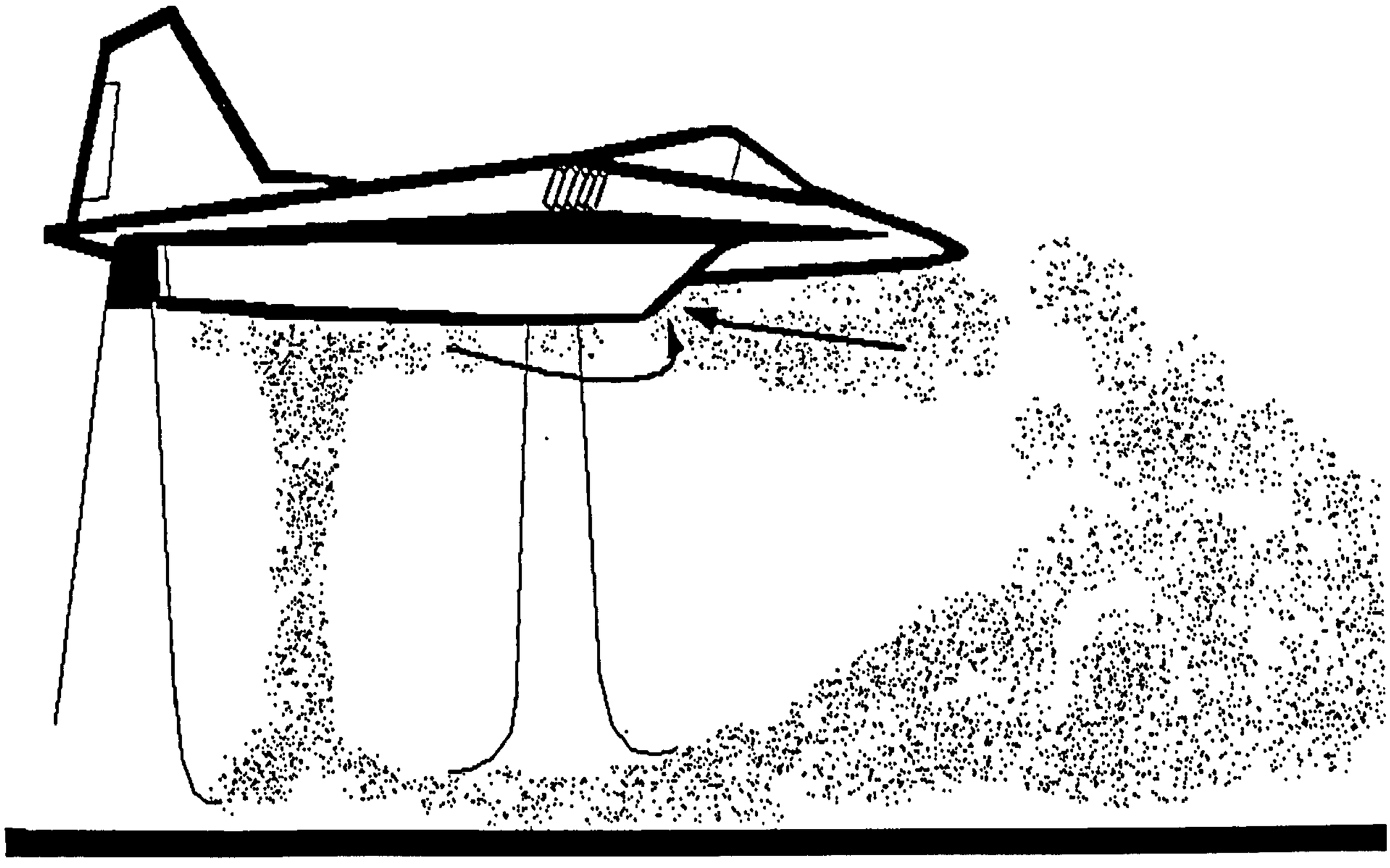

Figure 1.1 : Hot Gas Ingestion

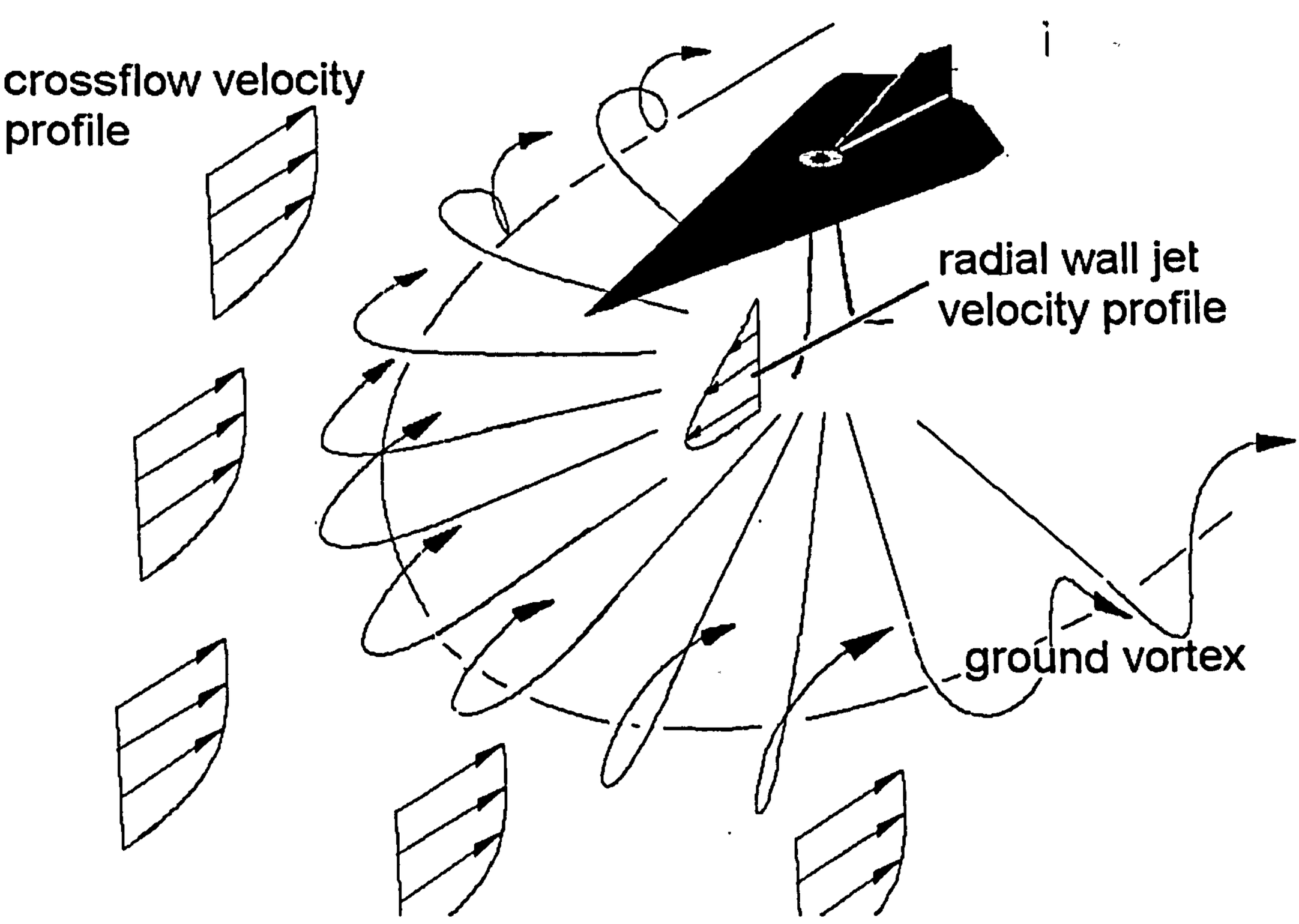

Figure 1.2 : Stagnation of a Wall Jet by the Crossflow

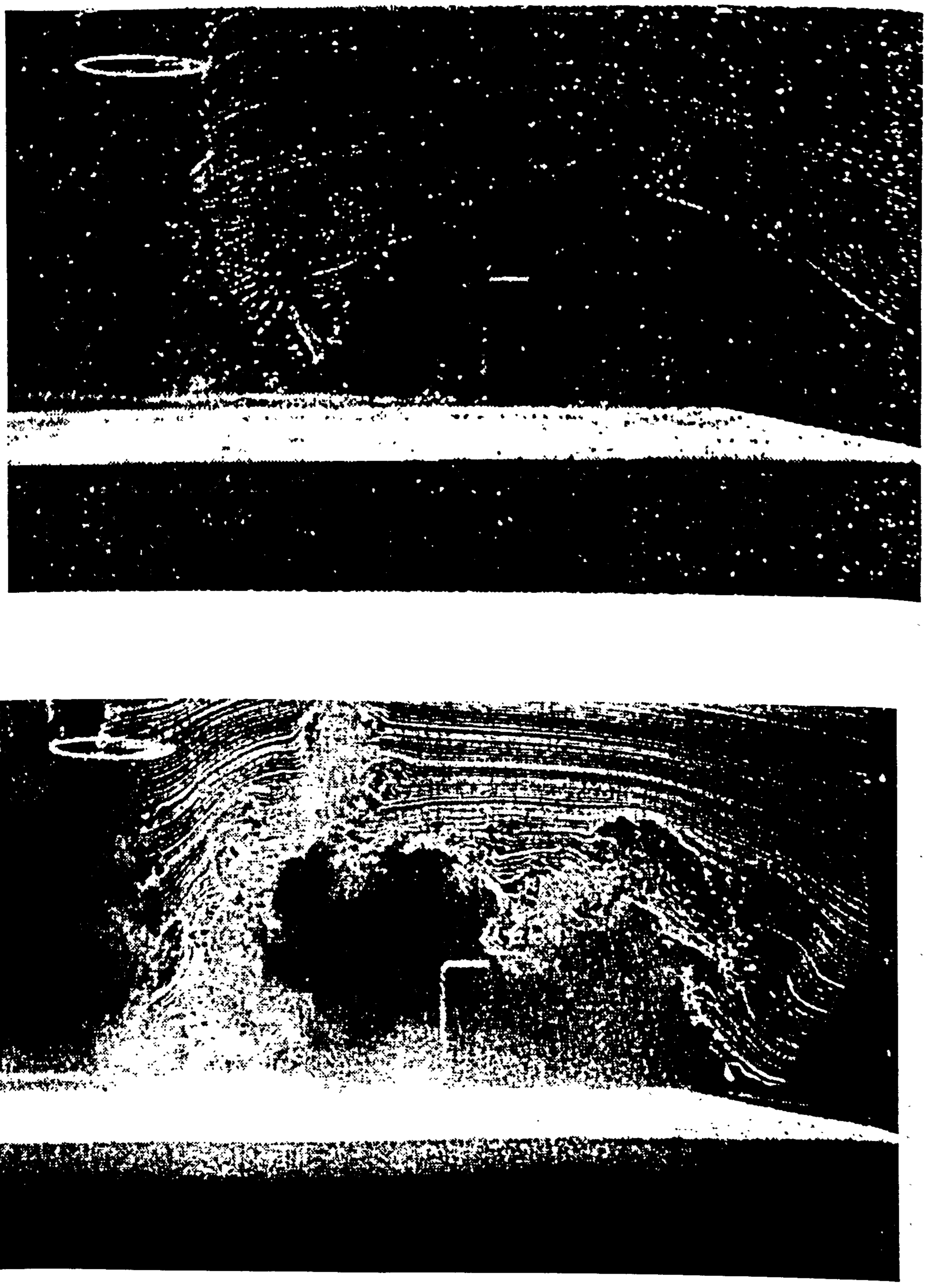

Figure 1.3 : Aperiodic Break-down of Ground Vortex Leading to Higher Levels of Hot Gas Ingestion (Cimbala et al. 1991)

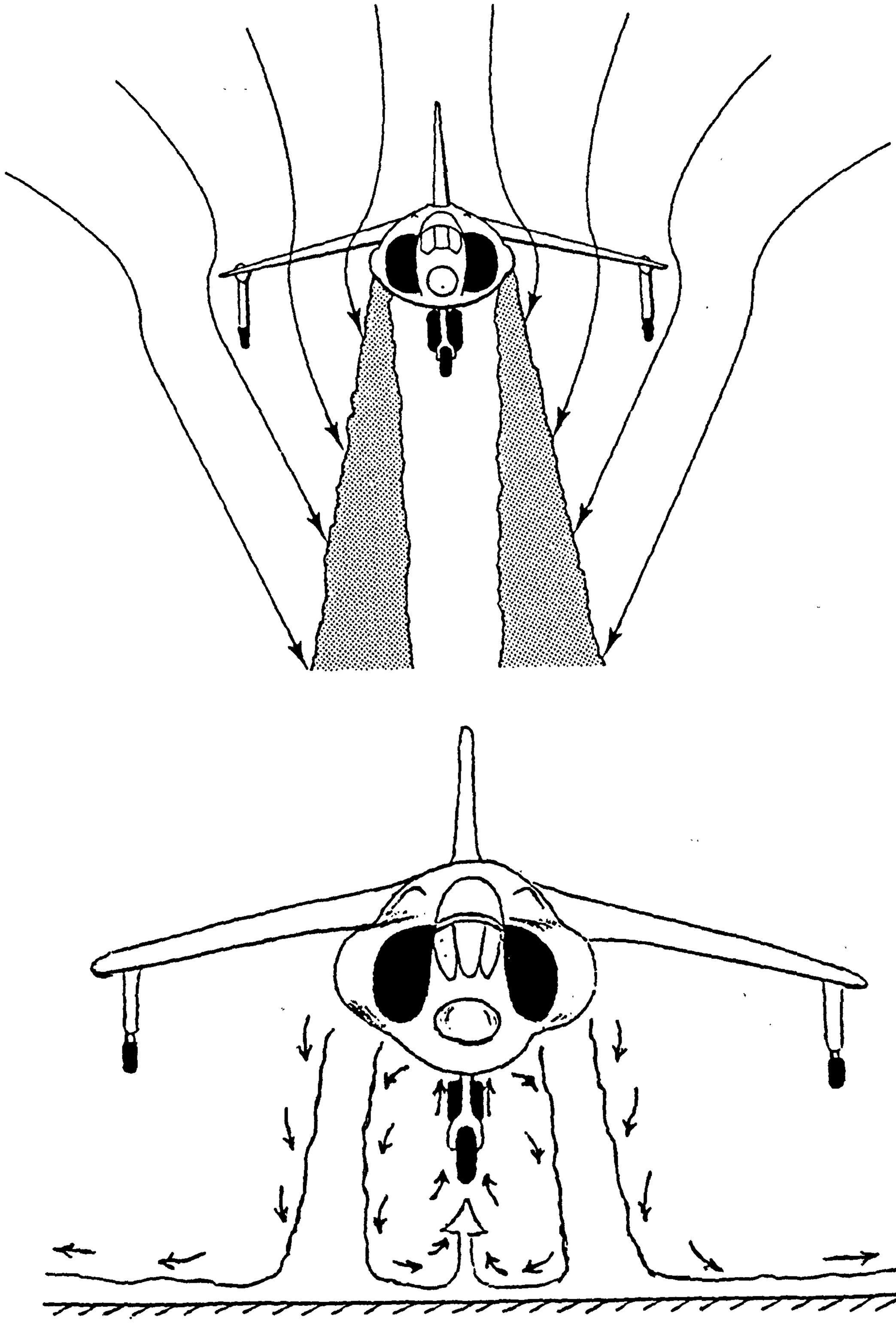

Figure 1.4 : Induced Pressures due to Entrainment causing Suckdown

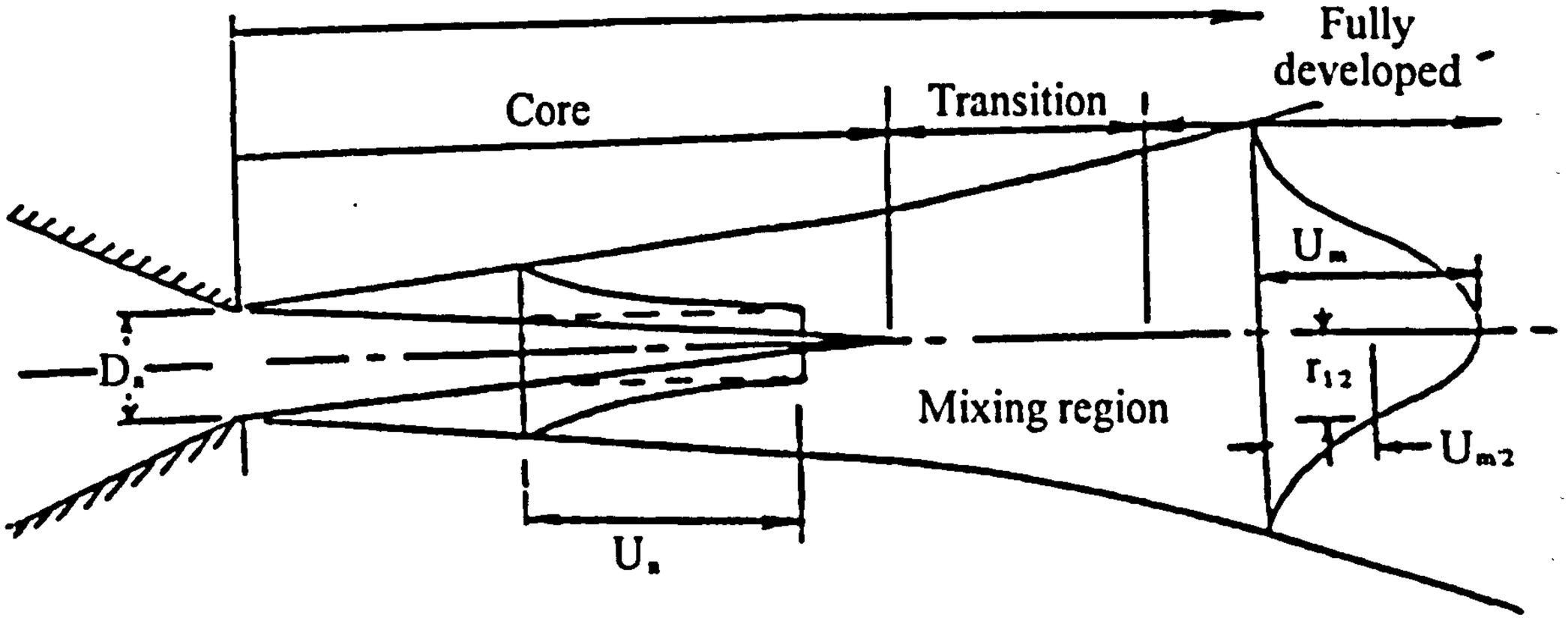

(a) : Subsonic Free Jet

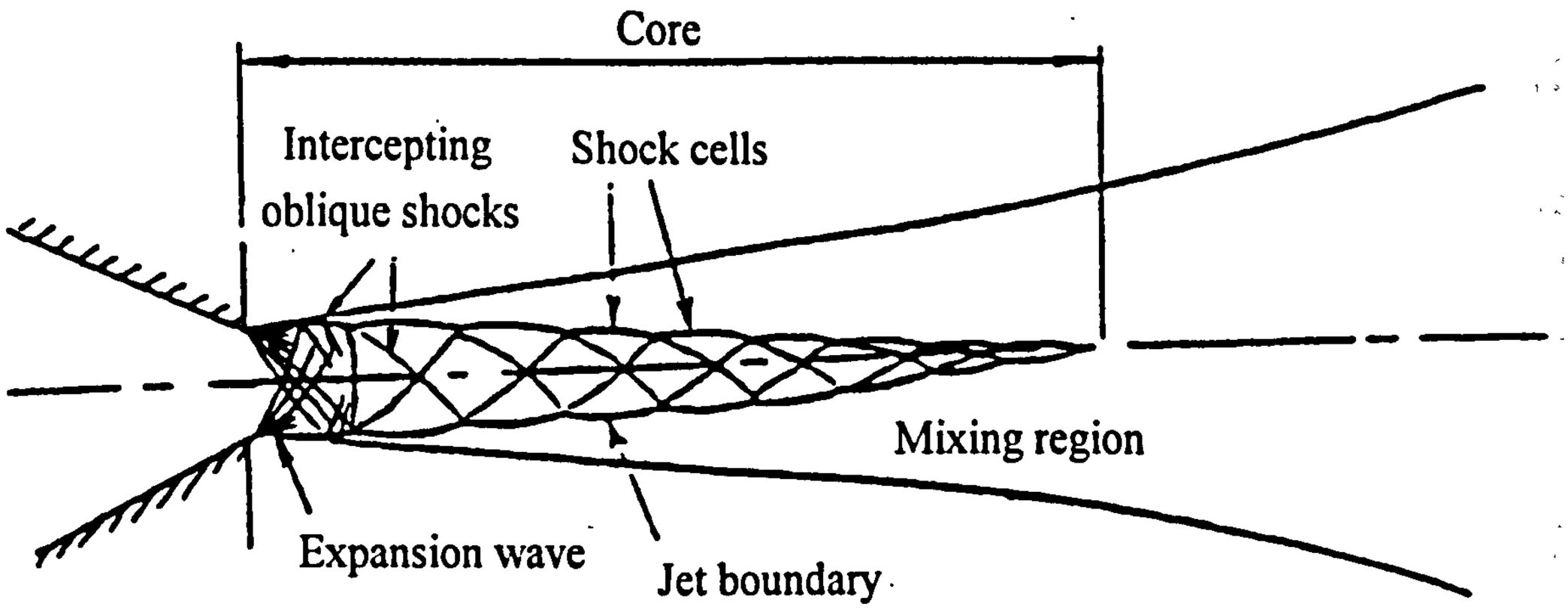

(b) : Supersonic Free Jet

Figure 1.5 : Free Jet Flow Structure (Bray 1992)

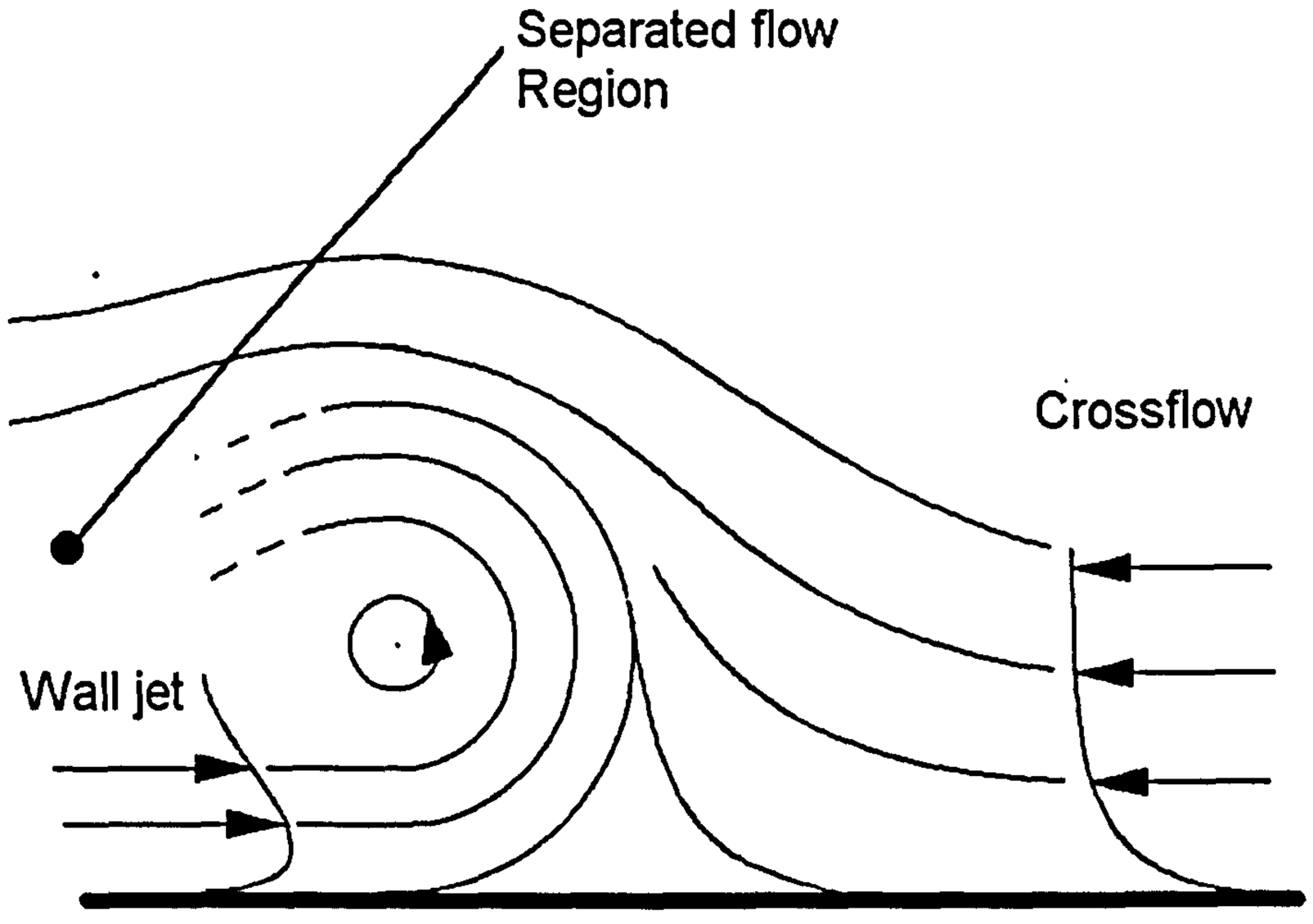

Figure 1.6 : Formation of a Ground Vortex by the Stagnation of a Wark Jet due to a Cross-flow (Wilson 1995)

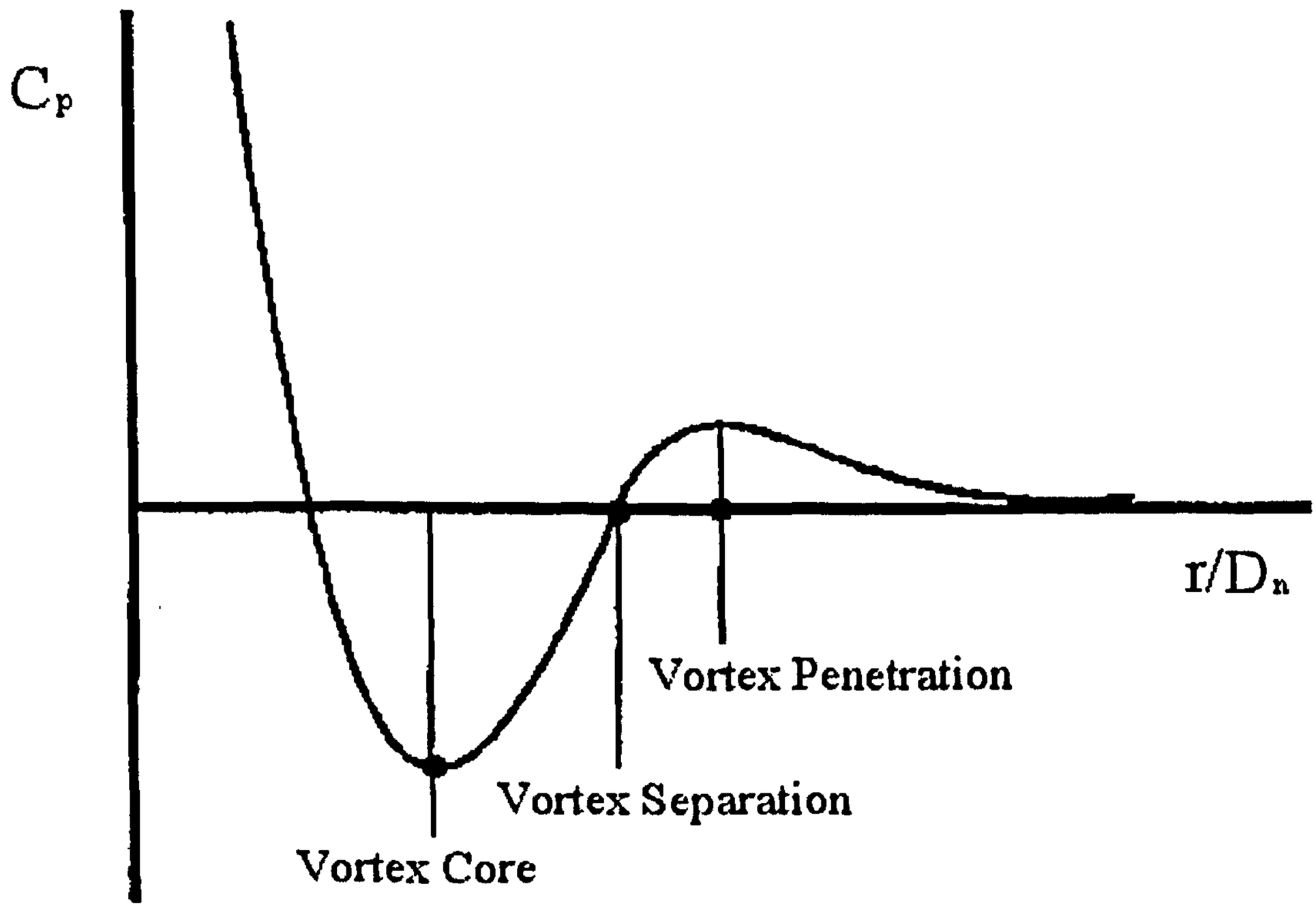

Figure 1.7 : Surface Static Pressure Beneath a Ground Vortex (Wilson 1995)

BLANK IN ORIGINAL

Chapter 2 : Experimental Method

The experimental work was conducted in four phases which are described in detail below. Phase Zero was a continuation of the reduction of data collected in the author's Bachelor of Engineering final year project, while Phases One, Two and Three required the collection of new data with the corresponding development of the existing equipment and techniques. The co-ordinate system used in all phases of the work is given in Figure 2.1.

2.1 Phase Zero

This phase consisted of further reduction of pitot and static pressure measurements taken as part of the final year project for the author's Bachelor of Engineering degree. The experimental apparatus used to collect the data analysed in Phase Zero is described in Myszko (1993), but as this forms the basis for development work conducted in subsequent phases, it will be described in detail here. The author wishes to make clear that the following section describes the experimental equipment already in existence at the outset of this research and the tests which had previously been conducted.

2.1.1 Experimental Apparatus

The experimental apparatus was positioned in the Open Jet Wind Tunnel (OJWT) (see Figure 2.2) where there was a conveniently positioned supply of compressed air from the Howden compressors, the wind tunnel not being used during these tests. The Howdens, two screw type compressors driven by electric motors (483.0 kW total), are capable of being run in parallel (1.8kgs^{-1} at 4 bar(g)) or series (0.9kgs^{-1} at 7 bar(g)) as in all these tests. The air was dried by passing it through a 4.5 m^3 storage / drying tank containing silica gel beads which were routinely dried by passing heated air back through the tank and then to atmosphere. The drying system was semi-automatic and was run on average every other third day of testing. If runs were made involving particularly high mass flow rates, the drier was run more frequently. After drying, the compressed air was

then passed to a 34m^3 storage tank which was half filled with scrap metal to act as a heat sink to provide a relatively constant air temperature. The compressors ran with a fully automatic control system which kept the pressure in the storage tank between 6.2 bar(g) and 7.4 bar(g), and incorporated a number of safety trips (oil pressure, oil temperature, water coolant temperature, etc.) to ensure safe running. The air was then passed to the rig via a 5" diameter supply pipe which terminated at the working section of the OJWT.

This air passed to a settling chamber via a section of 2½" steel pipe in which was positioned a variable pressure regulator which reduced the supply pressure from the storage tank to that required in the chamber. The output of this main regulator was set using a reference pressure supplied via a control system (see below).

The settling chamber was that used by Bray (1992) and later Wilson (1995) and was approximately 340mm wide, 140mm deep and 150mm high (externally), being split into three horizontal sections (see Figure 2.3) held together by M8 bolts. The chamber was designed to support up to two 1" nozzles, both normal and inclined to the vertical. Inclination was obtained by replacement of the lower section with a suitably angled plate. In these tests, only one nozzle (similar to that used in tests by Bray (1992) - see Figure 2.4) was used, having an exit diameter D_n = 12.7mm and a length of $10D_n$. As the chamber was designed to accept two nozzles, a single nozzle was not on the centre-point of the chamber, being $^1/_3$ of the width in from one edge. The chamber had four static pressure tappings, one per side on the middle section which enabled plenum static pressure to be measured via a Bourdon pressure gauge. One of these tappings was used to mount a K-type thermocouple to monitor chamber temperature, the output of the thermocouple being amplified using an RS Thermocouple amplifier and then digitised using a Hewlett Packard 3497A 14 bit A/D converter. The inside of the chamber was fitted with a filter system to remove any dirt / rust particles in the supply which might damage the equipment. The filter material used was Multivee 99, supplied by Vokes, and was easily capable of removing the particles in the air supply without causing a noticeable pressure loss. To account for any possible pressure loss, the pressure tapping for the settling chamber pressure gauge was moved to the lower section below the filter material. The settling chamber was mounted to the frame-work around the working

section of the OJWT, the 2½“ steel supply pipe supporting the weight of the chamber. The chamber was prevented, to a degree, from moving or vibrating by two adjustable support rods connected between the chamber and the support frame. Location and alignment of the chamber was difficult due to the nature of this support system.

The pressure control system for this phase of the work had previously been used on work conducted at Shrivenham for Miller and Wilson (1993) and is shown in Figure 2.5. It used a small manual hand-regulator to provide a reference pressure to the main regulator. The settling chamber pressure was displayed on a Bourdon gauge connected to the plenum via the lower static pressure tapping, as described above. This system was capable of setting a settling chamber pressure to ±2.0% for an NPR range 1.3 - 4.0, but was much less accurate for lower NPRs, such as 1.05, due to the lack of sensitivity of the Bourdon pressure gauges at these low pressures. The control pressure supplied to the hand regulator passed through a solenoid valve (240V(AC)) that vented to atmosphere once activated and which was operated by an emergency stop button. This meant that loss of mains power or activation of the button would cut the reference pressure and hence close the main regulator

The impingement surface was a 3m by 2m table, the surface being varnished and sanded to a smooth finish, placed in the working section of the OJWT. This allowed measurements to be made up to $140D_n$ (using a ½” nozzle, the probe and stand extending a further $20D_n$ behind the measuring point) from the jet axial centre line, with the impingement point not in the centre of the table.

2.1.2 Data Collection

The pitot and static pressure data were collected using separate total and static pressure rakes and processed on a 286-based PC (see Figure 2.6). The pitot rake consisted of 32 probes of 1.1mm outside diameter (0.685 mm ID) spanning a height of 200mm with the spacing being concentrated to give finer resolution in the lower half of the rake. The static rake consisted of 12 probes of 1.65mm OD evenly spaced over a span of 170mm. Both of the rakes had a multi-port coupling at the end of the length of

2.0mm OD tubing connected to the rake to enable quick changes. Both the pitot and static pressure rakes were uncalibrated.

The pressures from the rakes were fed into a scanning valve which allowed a single pressure output to be selected from numerous incoming pressures. This was controlled by the computer, being able to step through the pressures in numerical order. The single output was then fed into a Furness Controls Micromanometer, which gave a FSD of ±5.0V for a selectable range of 1000mm, 100mm, 10mm or 1mm $H_2O(g)$. This range was required to read the possible high total pressures encountered close to the impingement point while still being able to resolve accurately the relatively low static pressures. The analogue voltage output was connected to an AC-10 8-bit A/D converter on the PC enabling sample rates of 500Hz for a period of 15 seconds. As the AC-10 could only digitise 0-5V, a sub-ambient pressure giving a negative reading on the micromamometer would be reported as zero volts by the AC-10. This was overcome by swapping the pressure tube on the micromamometer to the negative input (reference input) so giving a positive voltage. The computer program was then set so that any voltages were multiplied by -1.0, so returning the sign of the pressure.

2.1.3 Experimental Procedure

As the settling chamber had previously been used (Bray (1992), Wilson (1995)), an initial assumption of symmetrical flow from the nozzle was made. This meant the rake could be positioned at any azimuthal position around the nozzle.

The settling chamber was set level and to the correct height with respect to the impingement surface using a height gauge. The nozzle height was set first, the chamber then being checked for levelness. This was an iterative cycle, taking a great deal of time. Radial distances were then marked out on the table in nozzle diameters from the point of intersection of the nozzle centre line on the table, found using a template which matched up to the edge of the settling chamber. The rake was positioned at the required r/D_n and the settling chamber NPR set using the manual regulator. At the end of the computer run, the pressure was turned off and the rake positioned at the next r/D_n. This was repeated

until all profiles were taken using both rakes for that value of H_n/D_n and all required NPRs, the nozzle height then being reset.

2.1.4 Tests Performed

Pitot and static profiles were taken normal to the impingement surface under the following conditions.

Pitot / Static Pressures								
Hn/D_n NPR	2.0	4.0	8.0	10.0	15.0	20.0	25.0	30.0
2.0	x	x	x	x				
2.5	x	x	x	x				
3.0	x	x	x	x	x	x	x	x
4.0	x	x	x	x				

All the above tests were taken at r/D_n = 8.0, 9.0, 10.0, 15.0, 20.0, 25.0 & 30.0

2.1.5 Error Analysis

It is estimated that the user could read the atmospheric pressure on the mercury column to ±0.1mm, which leads to an error of 0.15% in atmospheric pressure. This does not take into account changes in the value of atmospheric pressure during the run, but as the length of the run was short (approximately 20 minutes) and the error in setting the nozzle NPR was ±2.0%, this was considered to be a small error.

Positioning errors were estimated to be small compared with the pressure control error, with the probe positioned to within ±1.0mm of the required position. This translates to a maximum error of ±1% at r/D_n=8.0 reducing to ±0.26% at r/D_n=30.0.

Since these tests have been performed, the error in the Furness Controls Micromamometer has been measured as 2.5%, this being exacerbated by the relatively low resolution of the AC-10 8 bit A/D. The A/D could only resolve to 0.0195V, which over the 0-5V range of the micromamometer, meant a resolution error of 0.4%. If we

assume the A/D to be in error in its digitisation by the last bit, the accuracy of the AC-10 would in fact be 0.8%. This gives a pressure reading error of around 3.3%.

Repeatability runs were performed using the pitot rake and pressure measuring system, 5 profiles taken at a fixed radial position and NPR. It was found that the pressure profiles were only repeatable to about 5% (calculated on the variation of peak total pressure in the profile), mainly due to the inaccuracies of the pressure control system.

2.2 Phase Zero Plus

This section describes development work performed on the impingement rig in the OJWT during the author's BEng project. Although no analysis of data collected using the experimental setup described below is included in this report, the information is relevant to further discussions in later phases.

2.2.1 Pressure Control Development

As the manual pressure control system was not accurate enough for runs at NPR = 1.05, the conditions under which hot-wire measurements were to be taken, a new system was developed to set the settling chamber pressure using computerised control (see Figure 2.7) developed by the author. A 0-3.5 bar(g) Druck pressure transducer was mounted on the lower static pressure tapping of the chamber, which gave a full-scale output of 100mV. This was amplified using a VIP-20 amplifier to give a FSD of 5.0V and filtered using a Kemo low pass filter set at 10Hz to remove electrical interference from the laboratory. This signal was then digitised using an AC-10 8-bit A/D converter so that the computer could record the plenum pressure.

The reference pressure fed to the main regulator in the supply pipe was provided by a Watson Smith current pressure convertor, which gave out 0-1.0 bar(g) for 0-20mA supplied. This current was supplied by a Marconi Instruments GPIB 6140 adapter which communicated to the computer via an IEEE interface. This enabled the computer to control the value of the reference pressure, the resolution being FSD in 1000 steps. The

control pressure supply to the reference regulator came from a tapping in the 5" Howden supply pipe before the main regulator.

A FORTRAN computer program was written by the author which worked on a simple feed back system (see Figure 2.8). The plenum pressure was compared with the required pressure, calculated from a given NPR and atmospheric pressure (manually read on a Mercury column) to give an error adjustment. This error was then used with a suitable gain to give an adjustment to the regulator and so make an adjustment to the plenum pressure. Adjustments to the reference pressure were made every second, data collection only being allowed when the plenum pressure was within a predefined tolerance of ±0.5 %.

2.2.2 Hot-wire Anemometry

During this phase, single wire hot-wire anemometry was used to take profiles in the free jet and wall jet of the impinging jet (see Figure 2.9). The hot-wire probe, a Dantec 55P01 single wire, was connected to a Dantec Constant Temperature Anemometer (CTA 56C17) via a 4m length of coaxial cable and a 1m straight probe support, 55H21, giving a total cable length of 5m. The voltage output of the anemometer was then passed to a Disa 55D10 lineariser and then to a mean and rms voltmeter whose outputs were then digitised using a 14 bit A/D converter. Once calibrated, this allowed the computer to record the mean and turbulent resultant velocity over the single wire probe.

The probe was manually traversed in the flow field using a travelling microscope stand which was suitably modified to hold the probe support securely. This allowed traverses of 150mm in the X direction and 100mm in the Y direction with step sizes down to 0.05mm when using the Vernier scale.

The bridge of the CTA was balanced for each probe used using the technique described in Appendix A. The hot-wire was calibrated using Disa 55D90 calibration equipment (see Appendix A), the compressed air supply coming from a 10 bar(g) Bristol compressor capable of $0.0081 kgs^{-1}$ which was piped to the OJWT working section via a

½" steel pipe ending in a variable-pressure regulator and a 240V (AC) solenoid valve. The air was filtered as it left the compressor but was not dried, a small water trap just before the filter being the only means of removing water from the air. This equipment supplied a flow rate of air which changed linearly with a change in the supply pressure. This flow of air was then passed through a nozzle with an accurately-known exit area which, once calibrated for changes in ambient temperature and pressure, gave a known exit velocity. This enabled a relationship of CTA output voltage against fluid velocity over that probe to be investigated.

The relationship between the velocity over the hot-wire and the voltage required to keep the wire at a constant temperature is derived in Appendix A and is given by King's law which states:

$$E^2 = a + bu^n$$

Equation 2.1

where E is the anemometer voltage, u is the fluid velocity and a, b and n are constants specific to each wire. These constants were found from the calibration data of E against u using a software routine written by Dr M. V. Finnis, details of which are given in Appendix A. The value of n was then set in the lineariser, the offset being that required for zero output voltage with no flow (theoretically the value of a) and the gain set to a suitable value. A number of considerations had to be taken into account when calibrating the hot-wire, all of which are discussed further in Appendix A. Temperature compensation of the hot-wire signal was not used as the variation in settling chamber fluid temperature was near ambient and the variation in calibration nozzle flow temperature from ambient was small (Myszko 1993).

No repeatability data for the calibration were obtained as only one calibration was performed which only went down to 20.0ms^{-1}. As the King's law curve is very sensitive to velocities lower than about 10.0ms^{-1}, it is expected that the repeatability was very low.

2.3 Phase One

This phase consisted of single- and cross-wire hot-wire anemometry profiles taken in the free and wall jets of an impinging jet at a fixed NPR of 1.05 using hot-wire techniques developed in Phase Zero Plus.

2.3.1 Experimental Apparatus

The experimental equipment used in this phase was a development of the Phase Zero Plus setup, the 286-based PC was replaced with a 486 DX2 66Mz PC. Modifications were made to the pressure control system (see Figure 2.10), firstly to improve the tolerance possible and the system's ability to remain within that tolerance during a sample, and secondly to decrease the time taken to reach the tolerance level. To achieve this a number of changes were made to the way the reference pressure was supplied to the main regulator valve. The Phase Zero Plus system obtained control pressure via a tapping in the 5" supply pipe before the main valve. This meant the control pressure varied between 6.2 bar(g) and 7.4 bar(g) as the storage tank pressure fluctuated, so complicating the situation for the computerised control software. This was altered so that the primary control pressure was supplied by the Bristol compressor (previously only used for hot-wire calibration) which, after a regulator, gave a more constant control pressure.

The pressure transducer A/D converter was changed for a CIL F-Block which is a high speed (up to 50kHz) 16 bit A/D converter. This A/D had four input channels with onboard memory of 64kB, so was capable of holding a total of 32768 individual voltages with sample intervals as low as 20μs. The improved resolution of the pressure signal enabled a more accurate measurement of the chamber pressure and the increased sample speed meant more samples could be taken to obtain a truer value for the mean chamber condition before an adjustment was made. The VIP-20 and Kemo filter were still used to amplify and filter the signal before digitisation. This, together with changes made in the way the computer algorithm operated and changes in the criteria for leaving the pressure control routine to take a sample meant that the tolerance on the pressure control system

could be reduced to 0.05% without a major increase in the length of time to take a velocity profile. The chamber pressure was also measured after the probe voltage was sampled, the probe voltage read back and accepted only if the chamber pressure was within the predefined tolerance at the end of the probe sample. Settling chamber and atmospheric temperature were also sampled using the F-Block A/Ds, the RS amplifier still being used to give a voltage proportional to the temperature, the values being recorded every time a sample was accepted.

The travelling microscope traverse used in Phase Zero Plus was modified so that two 400-step stepper motors driving 6mm diameter, 1mm pitch lead screws could operate the sliders. These stepper motors were driven by two Digiplan SD3 stepper motor drive units connected to a Digiplan IEEE controller (see Figure 2.11). A third (Z) axis was also added to the traverse, this being a small RS linear actuator driving a slider in a tube which was also controlled by the Digiplan IEEE interface. This enabled 150mm traverses in the X direction (parallel to the ground board) and 100mm traverses in the Y (normal to the ground board) and Z (parallel) directions. Backlash in each axis was calculated by repeated end-to-end traverses, the backlash adjustment required being the total position error from start to finish divided by the number of changes in direction. This adjustment was then automatically made by the computer whenever a change in direction occurred. This enabled repeatable end-to-end traverses to be made to within ±75μm. The drive system was fitted with an emergency stop button which deactivated the drives (stopping any motion) and which was also connected to limit switches at the start and end of travel of each axis.

2.3.2 Data Collection

Free jet and wall jet profiles were taken using both single- and cross-wire hot-wire anemometry. The single-wire technique was that used in Phase Zero Plus, although the probe was traversed using the new stepper motor traverse.

Because the calibrations in Phase Zero Plus were of dubious accuracy, the technique used to calibrate the hot-wires was modified so that the calibration range was

increased from 100 - 20 ms^{-1} to 100 - 5 ms^{-1}. This was achieved by using three different-sized nozzles to increase the speed range, the voltage against velocity data for the three nozzles then being combined and sorted into velocity order so that it could be solved to give the King's law coefficients as before. No temperature compensation of the hot-wire signal was used in this Phase for the reasons given in Section 2.2.2.

The calibration technique used gave the constants a, b and n so it was decided to abandon the mean and rms voltmeters as concerns were raised over the accuracies of their calibration in Myszko (1993). The output signal of the CTA was fed into a channel of the CIL F-Block (see Figure 2.12). This enabled a sample rate of up to 50kHz with a maximum number of samples being 32768. The individual voltages were then converted into velocities using King's law by an assembler routine written by Dr. M. V. Finnis, the routine being written in assembler language to reduce any time penalty.

For single-wire profiles, it was then a simple case of calculating the mean and variance of the sample, the mean velocity being defined as:

$$U = \frac{1}{n}\sum_{i=1}^{n} U_i$$

Equation 2.2

and the variance as:

$$u^2 = \frac{1}{n}\sum_{i=1}^{n}(U_i - U)^2$$

Equation 2.3

Where n is the number of samples and U_i is an instantaneous value.

As the single-wire was only used for free jet profiles, the previously-used straight support was replaced with a right-angled version (55H22). This meant that the probe measured with the main flow direction being normal to the table and the probe stem horizontal. The sample rate was set at 1kHz with the sample length at each point in the flow being fixed at 15s, the signal being passed through a low-pass filter set to 500Hz.

The cross-wire data were collected using the same rig as the single-wire phase (Dantec Straight Cross-wire Probe (55P61), Right-Angle Cross-wire Probe (55P63) and Straight Probe Support (55H25)), the two outputs from the CTA being fed into two channels on the F-Block (see Figure 2.12). This enabled the voltages on the two wires of the cross-wire to be sampled with a 20μs pause between each.

The two voltages were solved to give the flow magnitude and direction using the technique described in Appendix A. The individual wires on the cross-wire were calibrated using the single-wire method to give two sets of King's law coefficients. The above assembler routine was then used to give the instantaneous velocities over each of the two wires, the ratio of these, λ, being required for the solution procedure. The equations in Appendix A returned instantaneous streamwise and normal velocities, the mean and variance being found for each of these using equations 2.2 and 2.3. The value of k, the yaw coefficient, for each wire was taken as 0.21 as given by Lomas (1986, page 23) for the type of wire used.

For free jet profiles, as stated above, a right angled cross-wire (55P63) was used (see Figure 2.2) but due to the size of this probe the lowest probe height was $3.5D_n$. In the wall jet, a straight cross-wire was used (55P61) (see Figure 2.2), but to enable the probe to get as close to the table as possible, it was angled to the table. This angle was measured using a travelling microscope and used to correct the angle the wires made with the surface for the reduction process. The sample rate for the probe was set to 1kHz with a sample time of 15s and a low-pass filter frequency of 500Hz, the sample interval between the individual wires on the probe being 20μs. This sample interval was considered small enough to assume simultaneous measurement as it was far below the time scales of any fluctuation in the signal due to the 500Hz low-pass filter setting. Appendix A contains a discussion of the problems faced measuring turbulent flows using a cross-wire hot-wire probe.

2.3.3 Experimental Procedure

The traverse was set in position, located on special locking plates on the table surface to prevent movement, so that all required profiles could be taken at that H_n/D_n value without having to reposition it. The settling chamber and nozzle was set normal to the table (after adjustment so that it was level) and to the correct nozzle height using the method described in Phase Zero.

For the free jet profiles, with both single- and cross-wire, the probe support was attached to the Z axis on the traverse and set so that the probe was normal to the table. The probe was set on the jet centre-line in both axes using a travelling microscope. This microscope was also used to set the height of the probe above the impingement surface.

For wall jet profiles, the same method as above was used to set the X and Z axes on the jet axis centre line. For each profile, the probe was then moved to the correct radial position, its height above the impingement surface being reset for each position, with a small magnifying glass used to see when the bottom prongs of the cross wire just made contact with the surface.

It was found that the operation of the control system was greatly improved if the supply pressure from the Howdens fell below 4 bar (this being found accidentally when the compressors shut down on a safety trip, the storage tank pressure falling to below 4 bar). It was decided that to decrease the time a profile took, the Howden compressors would be operated manually, the storage tank being pumped up to 4 bar(g) and only re-pressurised once the supply pressure had reached 0.5 bar(g).

Repeat runs were performed on the hot-wire calibration equipment to assess its repeatability using the equation :

$$\frac{dU}{U} = -\frac{A}{n(V^2-A)}\frac{dA}{A} - \frac{1}{n}\frac{dB}{B} - \frac{\ln\left[\frac{(V^2-A)}{B}\right]}{n} + \frac{2V^2}{n(V^2-A)}\frac{dV}{V}$$

Equation 2.4

as given by Finnis (1993). The first three terms on the right hand side represent errors introduced due to inaccuracies in the calibration, whereas the fourth term accounts for any error in reading the voltage (signal conditioning, voltage resolution, etc.). As there was no signal conditioning of the output and as the hot-wire voltage was digitised using a 16-bit F-Block with a very low resolution error, the last term was ignored.

2.3.4 Tests Performed

Single- and cross-wire hot-wire profiles were taken in the free jet and wall jet under the following conditions:

Free Jet Profiles (C = Cross-wire, S = Single-wire)								
H_p/D_n H_n/D_n	9.0	8.0	7.0	6.0	5.0	4.0	3.0	2.0
10.0	C	C,S	C	S	C	C,S		S

Wall Jet Profiles (Cross-wire)														
r/D_n H_n/D_n	1.0	1.5	2.0	2.5	3.0	3.5	4.0	4.5	5.0	6.0	7.0	8.0	9.0	10.0
2.0	x	x	x	x	x	x	x	x	x	x	x	x	x	x
4.0	x	x	x	x	x	x	x	x	x	x	x	x	x	x
8.0	x	x	x	x	x	x	x	x	x	x	x	x	x	x
10.0	x	x	x	x	x	x	x	x	x	x	x	x	x	x

All tests were performed at an NPR of 1.05

2.3.5 Error Analysis

Although the control tolerance of the pressure system was set to 0.05%, there were two errors introduced in reading the settling chamber pressures. The first was the error associated with the pressure transducer which is stated at 0.06%, the second being the error associated with reading atmospheric pressure. As stated in Phase Zero, the user could read the mercury column to ±0.1mm to give an error of 0.015%, but as in this case the runs lasted for 2-3 hours, changes in atmospheric pressure over that time would

cause a larger error. It is estimated that atmospheric pressure could reasonably change by up to 3mmHg over 2-3 hours, this could be a lot larger if the weather was stormy or squally at the time of measurement. This change in mercury level could produce an error of up to 0.4% in the required settling chamber pressure, a lot higher if there were larger localised changes in atmospheric pressure. As the pressure transducer was now sampled using the 16-bit F-Block, resolution of the voltage was no longer a problem. If the accuracy of the A/D was given by an error in the last bit, the accuracy / resolution would be 0.0006%, far in excess of the accuracy of the transducer. This gives an error in setting the settling chamber pressure with respect to ambient conditions of ±0.51%, which in turn gives an NPR error of ±0.025% at NPR = 1.05.

The probe was traversed on the stepper motor-driven travelling microscope stand, which could make end-to-end traverses (100mm shortest) to within ±75μm giving a step positioning error of 0.075%. The initial datum was set using a travelling microscope for the X and Z axes for both sets of data, which had a Vernier scale to 0.05mm. This was also the error for the setting of the datum on the Y axis for the free jet profiles. As the probe distance above the surface for the wall jet profiles was set using operator judgement for when the prongs touched the surface, the estimate of error is difficult, but the author estimates the Y axis datum was set to within ±0.25mm.

As the F-Block A/Ds were also used for digitising the hot-wire voltages, the main error on the sample data came from the calibration of the King's law constants for the wires and from the measurement of the angle between the two wires and between the probe and the impingement surface. As a travelling microscope was used to measure the angles, the error is small and is estimated at $\pm 0.2^0$. The absolute accuracy of the calibration data is difficult to access, but 20 repeatability runs performed over a few days showed the error in the calibration of each constant of King's law to be around ±2.0%. This gave estimated errors due to calibration of 2.0% for the main stream-wise velocity component, 4.8% for the normal velocity component and around 9.0% for the shear stress. Appendix A contains a further discussion of errors associated with the use of hot-wires for turbulent flow measurement.

2.4 Phase Two

This phase consisted of cross-wire hot-wire anemometry profiles taken in the wall jet of an impinging jet at a fixed NPR of 1.05. Further development of the rig continued from Phase One, the accuracies for calibration and sample data were improved, as well as increases in performance of the pressure control software. The air supply source was also changed from the Howden compressors to a centrifugal fan.

2.4.1 Experimental Apparatus

The pressure control system was further developed to improve its speed and accuracy, with a particular interest in the operational safety of the system (see Figure 2.13). This was because experimental runs could take up to 7 hours to complete due to changes in the sampling routine, so requiring the rig to run without constant operator attendance.

The most important difference was a change from the Howdens as the compressed air supply for the rig. This was because safety protocol for the operation of these two large compressors required the attendance of at least two personnel during their operation, so limiting the rig to a maximum of one profile per day (the increase in profile time being due to sampling changes discussed later). A centrifugal fan driven by a 3.73kW electric motor was employed providing a pressure of 55 mbar(g), which was just capable of running the ½"(12.7mm) nozzle continuously at NPR=1.05. This was plumbed into the 2½" pipe line just before the main pressure regulator.

Observation of previous testing using the pressure control system of Phase One showed that the settling chamber pressure tended to "bounce along" either the top or bottom of the tolerance band, so increasing the number of data samples rejected. To solve this, the routine was modified so that the program only left the pressure control routine to take a hot-wire sample when the NPR was within an inner tolerance (defined by the normal tolerance multiplied by a factor set to 0.6 for all further tests), the hot-wire sample only being accepted if the NPR was within the normal tolerance at the end. This

meant that the vast majority of the samples were now accepted, decreasing the time to take a profile dramatically.

Two modes of failure of the pressure control system were identified: no supply pressure or no return signal from the settling chamber pressure transducer. To prevent these, 2 Furnell miniature pressure transducers were added to monitor the control system supply pressures. The first was a 0-10 bar(g) pressure transducer whose FSD output of 227.3mV was amplified by 20 using a CIL B-Block (a two channel variable amplifier / filter). The filter on the B-Block was set to low-pass at 10Hz, as frequency response was not important. This transducer was connected to the supply from the Bristol compressor to confirm that there was a enough pressure to control the system. If this pressure dropped below a specified value, the computer program would shut down the rig in a controlled and safe manner to enable a continuation of that run once the supply pressure had increased again.

The second transducer was connected to monitor the control reference pressure sent to the main regulator. This was to prevent an excessive control pressure to the main regulator, again if this went above a specified value (based on the required NPR), a safe shut down of the rig would occur. An excessive control pressure was most likely to occur due to one of two failures. Firstly, the main regulator sticking closed followed the sudden opening of the valve to a position much greater than that required for the given NPR. The second mode was a failure of the chamber pressure transducer, most likely to be the constant return of zero volts. The computer routine would continue increasing the control reference pressure and hence the chamber pressure. This would, of course, continue until the valve was fully open (NPR $\approx$ 5.0) unless the reference pressure was monitored. Both of these Furnell transducers were digitised using an F-Block, sampled for 100ms at 1kHz and averaged.

A second modification was the addition of a highly accurate barometric pressure transducer (800 - 1100 mbar for 0-5 V) which was digitised using a channel on an F-Block, sampling at 1kHz for 200ms. The control program monitored the atmospheric pressure every time the pressure control routine was accessed, so that continuous

adjustments to the chamber pressure could be made to account for variations in atmospheric conditions.

It was decided that a major limitation of the ability of the control system was the lack of resolution on the Marconi IEEE controller used to provide a voltage for the control regulator. This was replaced with a CIL O-Block, a two-channel 12-bit D/A converter giving ±5.0 V FSD. The current / pressure converter was suitably modified to give full output on the addition of 5.0V (by adjustment of the regulator range and zero offset), the use of the O-Block now giving FSD in 2024 steps. The output of each of the two O-Block channels was calibrated against an F-Block (see Figure 2.14) to improve performance.

The same Druck pressure transducer was used on the settling chamber as in Phase One, but this was connected to a B-Block and then to the F-Block. The B-Block was used to amplify the signal 50 times and filter the signal at low-pass 10Hz, as well as providing a regulated 10V power supply required for the transducer.

The mounting of the settling chamber to the OJWT framework was changed as the previous system had proved to be difficult to set up initially. Instead of the chamber weight being supported by the steel compressed air supply pipe, six struts were connected to the chamber, three to one corner locking that in space and the remainder to each of the other corners. The other ends of the struts were bolted to the surrounding framework using rose joints so that their overall length could be adjusted without having to disconnect them. Once the chamber was in position and at the right height, the struts were tensioned against each other so making a rigid structure. The air was supplied to the chamber via a length of 2½" flexible tubing capable of withstanding 20 bar(g).

The RS thermocouple amplifier was replaced by a CIL K-Block, a 6-channel, 12-bit K-type thermocouple reader with an internal cold junction compensator. This accepted the thermocouple used to measure the settling chamber temperature, as well as one for the ambient temperature and a second to monitor the wall jet flow temperature, recorded at the end of the impingement table (70 D_n from the nozzle axial centre-line).

The stepper motor-driven travelling microscope traverse was replaced with a bought-in system from Time and Precision Ltd. The traverse was of three axes, the Y and X having a span of 1.0m and the Z axis being 0.5m. The Y axis on the traverse was a parallel-coupled system (see Figure 2.15), i.e. two parallel sliders linked by a belt drive system driven by one motor. The stepper motors had a resolution of 400 steps with lead screws of 1mm pitch, giving the traverse a resolution of 400 steps/mm. Backlash was countered using the same technique as in Phase Zero Plus, the end-to-end traverse position error being reduced to 50μm over an included length of 1m. Limit switches were positioned on the traverse at the end of the slider span and linked to the emergency stop system of the Digiplan controller card to prevent excess travel. The traverse was mounted on a bought-in mounting frame (also from Time and Precision Ltd) made of lengths of 45x45mm extruded aluminium. This allowed the height of the bottom of the traverse to the floor to be adjusted from 0.25m to 1.25m.

The centrifugal fan used to supply the air for the nozzle was controlled by a manual on/off switch system on the main electric switch box. This was modified to accept a remote start/finish relay controlled by a CIL R-Block, a four channel relay block capable of switching 240V(AC). This enabled the computer to turn on the fan at the start of a run and turn the fan off at the end of a test or on the detection of a system error. An emergency stop system was also incorporated into the fan control system so that the power could be cut to the fan in an emergency.

As there now were three independent emergency stop systems in operation (traverse system, pressure supply from Bristol compressor and centrifugal fan), it was decided to combine these systems so that operation of one would activate the other two. A system was designed and built incorporating relays in the individual systems operated by any of the existing buttons. The individual systems could be taken out of the combined system at any time and operated separately. The computer also had the ability to operate the system by means of one of the channels on the R-Block, but once operated the system had to be reset manually. There was also a voltage output from the combined system so that the computer could register a manual operation of the system and reset the computer routines involved.

2.4.2. Data Collection

All data were collected in this phase using the Dantec 55P61 cross wire probe and the techniques described in Phase One.

The main change to the hot-wire technique was that the signal from the two wires underwent temperature compensation. The air leaving the centrifugal fan was heated to around 28-30^{0}C, much higher than the near-ambient temperature air from the Howden compressors and from the Bristol compressor used in the calibration. As discussed in Appendix A, the constants in the King's law equation are only valid for a fluid flow temperature which is the same as at the time of calibration. To account for this small error, the voltage from each wire was adjusted for temperature variations using the method discussed in Appendix A.

Two CTA 56N20 signal conditioners were used to condition and filter the CTA output voltage before digitisation, these had both high- and low-pass filters and an on-board amplifier. For these tests, the high pass filter was set to DC, allowing all signals to pass. The low pass filter was set to 1kHz, the conditioner removing fluctuations greater than 1kHz and the amplifier was set to a gain of 1.

To avoid any aliasing problems, the sample rate for the digitisation of the hot-wire voltages was increased to 2.5kHz, this reducing the maximum sample time to 6s. As this was not considered to be long enough, the computer routines were modified so that multiple samples could be taken for any point in the flow.

Individual means of the separate samples of 6s in length (consisting of equal number of points) were combined using:

$$V_s = \frac{1}{n}\sum_{i=1}^{n} V_{s_i}$$

Equation 2.5

whereas the variances were combined using:

$$v_s = \frac{1}{n}\sum_{i=1}^{n}\left(v_{s_i} + \left(V_{s_i} - V_s\right)^2\right)$$

Equation 2.6

where V_{si} is the mean of the individual sample and v_{si} is the variance.

The total number of samples (n) taken at a point was controlled by the computer routine, this being adjusted until the change in the present mean and variance (based on n samples) at a position compared with the mean and variance calculated from the n-1 samples was less than 0.5%. A criterion that at least a minimum of three samples (18s at a sample rate of 2.5kHz) and a maximum of 20 samples (120s) were placed on the routine. It was found that the greatest number of samples were required when the turbulence intensity was at its highest (eg. 30 - 32%), although in 76 profiles taken with 89 sample positions on each, the 120s maximum criterion was only reached twice.

2.4.3 Experimental Procedure

The settling chamber was levelled and set to the correct height using the same method as in Phase One, the new mounting structure making this job quicker and easier. The traverse stand was set level and positioned so that the X axis could cover all the positions without having to reposition it. The probe was positioned on the jet axis centre line using the travelling microscope as described in Phase One, the height above the ground plane being set by measuring the difference between the probe prongs and a block of known height. The height was reset at each radial location.

2.4.4 Tests Performed

Cross-wire hot-wire profiles were taken normal to the impingement surface under the following conditions.

r/D_n H_n/D_n	1.0	1.5	2.0	2.5	3.0	3.5	4.0	4.5	5.0	6.0	7.0	8.0	9.0	10.0	12.0	14.0	16.0	18.0	20.0
2.0	x	x	x	x	x	x	x	x	x	x	x	x	x	x	x	x	x	x	x
4.0	x	x	x	x	x	x	x	x	x	x	x	x	x	x	x	x	x	x	x
8.0	x	x	x	x	x	x	x	x	x	x	x	x	x	x	x	x	x	x	x
10.0	x	x	x	x	x	x	x	x	x	x	x	x	x	x	x	x	x	x	x

All tests were performed at an NPR of 1.05.

2.4.5 Error Analysis

The barometric pressure transducer had a quoted error of 0.03% on FSD and, as this was continually monitored during the run, this replaced the estimated error of 0.4% due to atmospheric changes. This meant the error in the chamber NPR was reduced to 0.01%.

The new traverse system was found to have an end-to-end position error of ±0.05mm, which in the shortest axis (Z) meant an error of 0.01% at full span decreasing to 0.005% for the X and Y axes. The same method as Phase One was used for setting the datum in X and Z with an estimated position error of ±0.05mm. The Y axis method was improved, the method used being similar to that for the other two axes, giving an initial position error of ±0.05mm.

All other errors as in Phase One.

2.5 Phase Three

This section details the experimental setup and data collected in the last phase of this project. Tests were performed with a jet of NPR = 1.05 impinging on a surface moving under the jet at $10ms^{-1}$, profiles being taken using both pitot pressure measurement at various radial locations and V_s = -10.0, 0.0 and 10.0 ms^{-1}.

2.5.1 Experimental Apparatus

The experimental rig was moved from the OJWT to a purpose-built Jet Impingement Rig (J.I.R.) positioned away from the tunnel (see Figure 2.16). The main reason for this move was to release the OJWT for other work. As the centrifugal fan now supplied the air for the nozzle there was no longer a need to be positioned near an outlet from the Howdens.

A framework 2m high by 3m square was constructed from 6"-square steel box section to support the chamber. A centre section was constructed to allow the settling chamber to be adjustable in height (1m span) with mounting holes every 0.0254m down its length, which was hollow to allow the compressed air supply pipe and associated data collection and control signal wiring to pass to down to the chamber. The chamber was mounted onto this structure using long M8 bolts (40mm in length) which allowed fine adjustment in height and angle.

The air was supplied by the same centrifugal fan and pressure control system as used in Phase Two with a few modifications. The pressure transducer was replaced with a Druck 0-5 psi(g) transducer as the fan was not able to supply pressure at the levels required to justify the previous transducer. This was powered and the signal amplified and filtered using the CIL B-Block as before.

The second modification was that the Bristol compressor, previously used for supply of a control pressure and hot-wire calibration, was replaced by a Clark rotary compressor, also capable of 10 bar(g) but with a mass flow rate of $0.0139 kgs^{-1}$. This had an air filter (removal of 40μm particles) straight after the outlet followed by a coalescing filter capable of removing water particles as small as 5μm from the flow. The compressor was then connected to the pressure control system and the hot-wire calibration equipment via ½" flexible tubing.

The motor and casing of the fan unit were fitted with surface temperature K-type thermocouples and connected to the CIL K-Block. This enabled the computer to monitor these temperatures and to shut the system down if an upper limit was reached. This was to enable safer unattended running of the rig.

The traverse was that used in Phase Two, a software modification being made so that a model-world co-ordinate system could be used instead of the X, Y and Z of the traverse. The benefit of this was that the traverse did not have to be set accurately to the table and it was not assumed that the X, Y and Z axes of the traverse were at 90^0 to each other. These three model axes, known to the system as U, V and W respectively, were defined by the direction cosines in the X, Y and Z directions, i.e.;

$$U = l_1X + l_2Y + l_3Z$$

$$V = l_4X + l_5Y + l_6Z$$

$$W = l_7X + l_8Y + l_9Z$$

Equation 2.7

where U, V and W are the model-world positions, X, Y and Z are the traverse positions and $l_1 \rightarrow l_9$ are the cosine coefficients. These were found by making a move along each of the defined U, V and W axes, the corrections required in X, Y and Z giving the values of l_x. The conversion between the two systems was performed using software written by Dr M. V. Finnis.

As a moving surface was required for these tests, the rolling road from the OJWT was used and modified so that it could be controlled by the computer. The road had a belt 48"(1.219m) wide which ran on a platen (table top) 60"(1.524m) long around drums of 271.0mm in diameter (see Figure 2.17). The drive drum was powered by a 20.0kW electric motor controlled by a control unit taking a feedback from a revolution counter on the motor. The platen had a suction box underneath to prevent the belt from lifting up from the platen surface under reduced static pressure conditions, the suction provided by a variable speed centrifugal fan. The level of suction could be adjusted in four areas of the platen (left side, right side, front, and middle and back) using butterfly valves. The effect of the suction from the sides of the belt on the flow field developed on the belt is though to be very small, and as all measurements were conducted on the centre-line of the belt, the effect on the measurements is believed to be negligible. Both of the motors where turned on/off by switches on the control console, their speed of rotation controlled by two rheostats which provided a voltage (0-5V) to the control unit. The measurement of the belt speed was by means of an optical switch on an 8-hole disc connected to a digital counter which displayed the speed in feet per second updated every second.

The first modification was to replace the optical counter with a revolution counter which had a resolution of 2500 pulses per rev (see Figure 2.18). The output, which was TTL-compatible, was fed to a new counter display set for ms^{-1} and a CIL C-Block, a

single channel frequency counter capable of up to 100kHz. The C-Block had three time periods (64.9μs, 1.05s and 16.6s) for which it returned the number of pulses received, this was multiplied by a factor based on the diameter of the drum and the pulses per revolution to give the belt speed. The new counter was mounted on to the end of the undriven drum to counter two possible failure modes of the system. Firstly, if too much suction were applied it would be possible to stall the belt, the driven drum rotating and slipping against the belt as the drive unit monitored motor RPM. Because the undriven drum rotates with the belt, the returned frequency would suddenly go to zero. The second potential failure was the breaking of the belt, again the drive drum would continue to rotate. Although this was unlikely to occur and if it did, would probably result in major damage to measuring equipment around it, the computer would be able to shut down the rig to prevent further damage.

The voltage provided to the control unit came from the second channel on the CIL O-Block (the first channel being used for the pressure control system). The voltage needed to run the belt at $10ms^{-1}$ with suction turned on was found, an upper limit then being set at 110% of this. If this upper limit were reached, the control routine would shut down the equipment to prevent excessive current demand from the electric motor driving the belt. To reduce demand on start up of the belt the suction was only turned on when the belt had reached 25% of the required speed, the suction being turned off once the belt had come to a halt to reduce the run down time of the system. This also prevented problems of the belt drifting from side to side on the rollers when not under load. The speed of the suction fan was set using the rheostat on the control panel, because there were no free O-Block outputs. The power to the main relay in the belt control system was linked to the emergency stop system described in Phase Two, activation of the system isolating the power to the rolling road.

During initial tests, a fault developed on the IEEE interface card for the traverse, causing the traverse to move in one axis without command and ignoring the activation of the emergency stop system. The traverse moved down onto the moving belt of the rolling road causing damage to the pitot probe, probe support and mounting system and to the belt itself. It was found that the emergency stop system on the traverse worked on

the assumption that this interface card was operating properly, and did not interrupt the power to the drive cards.

Following this incident, the IEEE interface card was replaced by an identical spare, the rolling road belt, the pressure probe and support were replaced with new items. To prevent a similar accident the emergency stop system, including the limit switches on the traverse axes, were rewired so that they operated a relay isolating the power supply to the traverse system. New limit switches on sliding mounts were also placed on each axis, confining the possible movement of the traverse to a given area. These were also included in the emergency stop system. The control routine was modified so that the computer checked the status of the traverse every time the status of the emergency stop system was checked (2-4 times a second). Previously, the traverse status was only checked when moving to make sure the move was completed correctly.

2.5.2 Data Collection

The data were collected in this phase using a single hole Pitot pressure tube connected to a Furness Controls Micromamometer (similar to that used in Phase Zero), the voltage output of which was digitised using CIL F-Blocks as used in the hot-wire phases.

The Pitot probe was constructed from a single length of 1.1mm (outer diameter) aluminium tube and bent through 90 degrees for ease of mounting. The measuring end of the tube was flatted (to approximately 0.5mm) to increase the profile resolution. The probe was connected to the micromanometer using a length (approximately 4m) of 2.0mm OD plastic tubing. Sample rates were fixed at 2500Hz for 15 seconds, the reduced number of sample points being a result of the extremely low frequency resolution of the micromanometer precluded any turbulent measurements (although a RMS value was calculated and stored as a feature of the sample routine). The pitot probe was not calibrated.

The Furness controls micromanometer used in this phase was calibrated by A. J. Saddington and was shown to be in error by +2.5% FSD. This was compensated for in the sampling program.

2.5.3 Experimental Procedure

The settling chamber was levelled and set to the correct height using the method described in Phase One, the new mounting structure on the J.I.R. dramatically reducing the time required to readjusted the H_n/D_n value.

The traverse was positioned so that the probe could be traversed over the fully range of r/D_n for each value of V_g. At each new H_n/D_n, the direction cosines used in the traverse software were reset. This consisted of making a probe move in each measurement axis, the number of steps made by each traverse stepper motor being recorded and later processed. The position on the probe on the axis and the height of the probe above the surface was set using a Vernier height gauge (as in Phase One).

2.5.4 Tests Performed

Pitot pressure profiles were measured normal to the table under the following conditions:

Tests Performed at V_g = 0.0 ms^{-1} and V_g = -10.0ms^{-1}																			
r/D_n / H_n/D_n		1.0	1.5	2.0	2.5	3.0	3.5	4.0	4.5	5.0	6.0	7.0	8.0	9.0	10.0	12.0	14.0	16.0	18.0	20.0
2.0	V_g=0.0																			
	V_g=10.0																			
4.0	V_g=0.0	x	x	x	x	x	x	x	x	x	x	x	x	x	x	x	x	x	x	x
	V_g=10.0	x	x	x	x	x	x	x	x	x	x	x	x	x	x	x	x	x	x	x
8.0	V_g=0.0	x	x	x	x	x	x	x	x	x	x	x	x	x	x	x	x	x	x	x
	V_g=10.0	x	x	x	x	x	x	x	x	x	x	x	x	x	x	x	x	x	x	x
10.0	V_g=0.0	x	x	x	x	x	x	x	x	x	x	x	x	x	x	x	x	x	x	x
	V_g=10.0	x	x	x	x	x	x	x	x	x	x	x	x	x	x	x	x	x	x	x

Tests Performed V_s=10.0 ms^{-1}																
r/D_n H_n/D_n	1.0	1.5	2.0	2.5	3.0	3.5	4.0	4.5	5.0	6.0	7.0	8.0	9.0	9.5	10.0	10.5
2.0																
4.0	x	x	x	x	x	x	x	x	x	x	x	x	x	x	x	x
8.0	x	x	x	x	x	x	x	x	x	x	x	x	x	x	x	x
10.0	x	x	x	x	x	x	x	x	x	x	x	x	x	x	x	x

All tests performed at an NPR of 1.05

2.5.5 Error Analysis

The accuracy of the pressure measurements reported in this phase is hard to estimate. The micromamometer was calibrated before its use against a newly acquired micromamometer of similar specification and there was found to be a difference of 2.5% at Full Scale Deflection (FSD). It was assumed that the difference was due to an error on the older model (the one used in these tests) and a correction for this was taken into account. The accuracy of the micromamometer is stated at 1.0% FSD. The atmospheric barometer used for the pressure control routines was also used, in conjunction with a K-type thermocouple, to calculate the air density, this value being used for the pressure to velocity conversion. The wall jet static pressure was assumed to be equal to ambient pressure. This gives an error in the velocity measurements of 2.0%.

The rolling road speed was monitored using a shaft encoder and a frequency counter. The encoder has a stated accuracy of ±5 steps per revolution and an resolution of 2500 steps per revolution. The frequency counter has a stated accuracy of 50 pulses per minute over its frequency range. This gives an error in the belt speed, at 10 ms^{-1}, of 0.25%.

Although modifications were made to the pressure control and traverse systems between Phase 2 and Phase 3, these were not expected to improve accuracy. Therefore, all remaining errors were as stated in Phase 2.

2.6 Summary

The following table is included as a summary of the different experimental configurations and measurements taken during the various phases of the experimental programme.

Phase	Air Supply	NPR Control		Traverse		Measurement	
		System	Accuracy	System	Accuracy	System	Accuracy
Zero	Howdens	Manual	±2.0%	Manual	±1.0mm	Pitot / Static (uncalibrated)	±3.3%
	Wall Jet Velocity Profiles, NPR=2.0 - 4.0, H_n/D_n=2.0 - 10.0, r/D_n=8.0 - 30.0 & V_g=0.0						
One	Howdens	Computer	±0.025%	Microscope Stand	±0.075mm	Single and Cross-wire (no Temp. Compensation)	2.0%, 4.8% & 9.0%
	Free and Wall Jet Velocity Profiles, NPR=1.05, H_n/D_n=2.0 - 10.0, r/D_n=1.0 - 10.0 & V_g=0.0						
Two	Fan	Computer	±0.01%	Traverse	±0.050mm	Cross-wire	2.0%, 4.8% & 9.0%
	Free and Wall Jet Velocity Profiles, NPR=1.05, H_n/D_n=2.0 - 10.0, r/D_n=1.0 - 20.0 & V_g=0.0						
Three	Fan	Computer	±0.01%	Traverse	±0.050mm	Pitot / Static (uncalibrated)	2.0%
	Free and Wall Jet Velocity Profiles, NPR=1.05, H_n/D_n=2.0 - 10.0, r/D_n=1.0 - 20.0 & V_g=-10.0, 0.0 & 10.0						

BLANK IN ORIGINAL

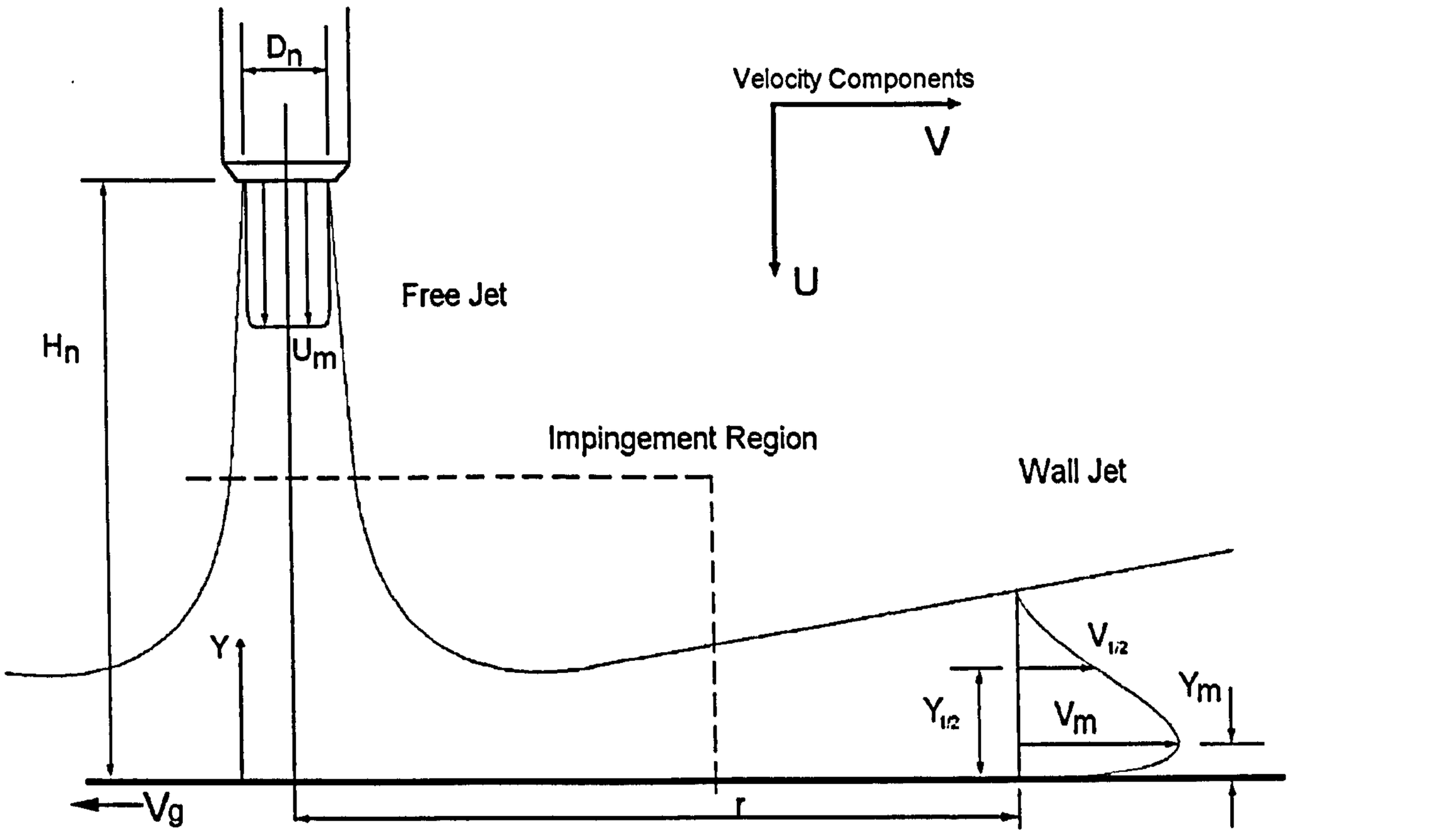

Figure 2.1 : Co-ordinate System used for Experimental Investigation

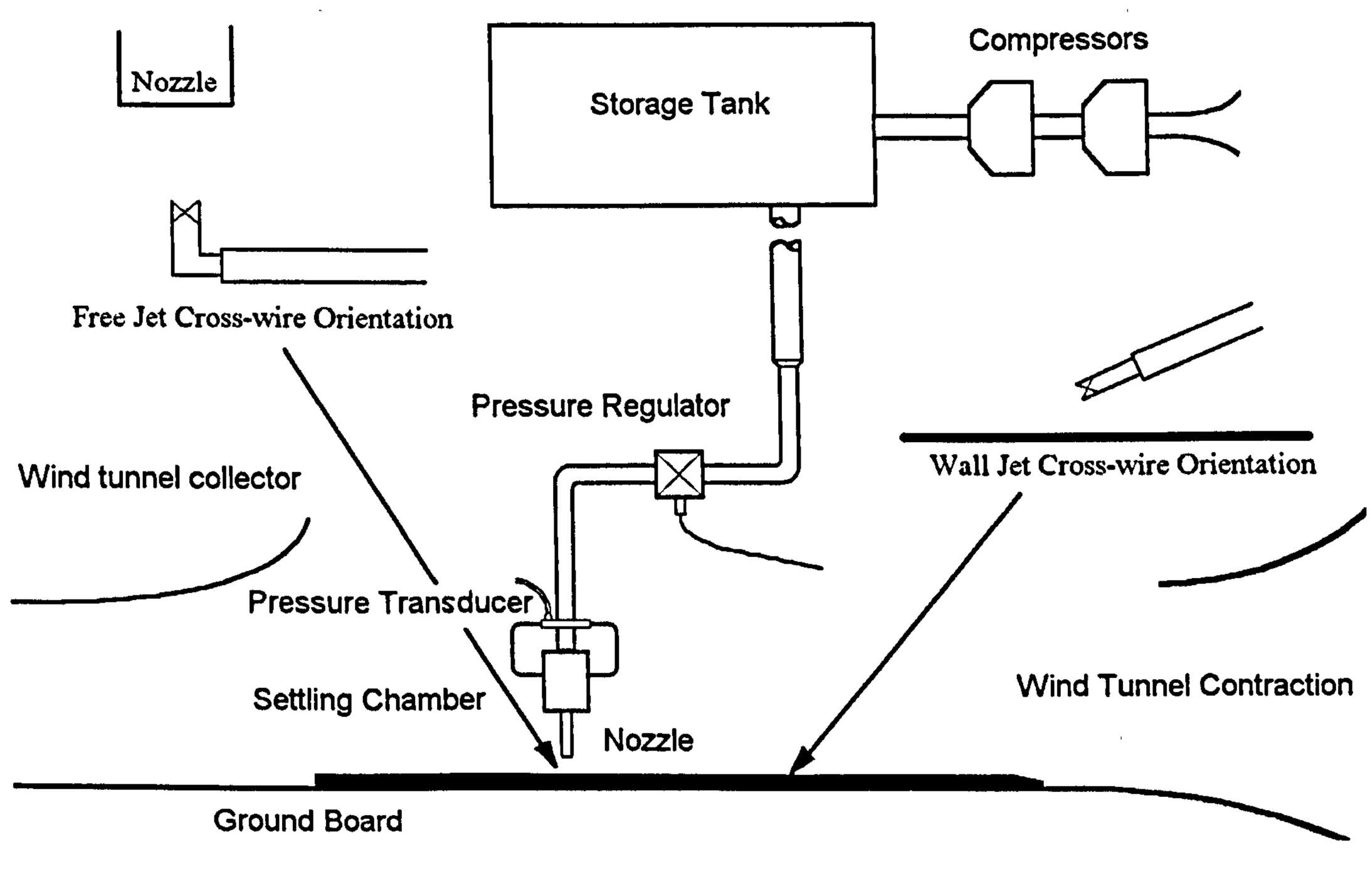

Figure 2.2 : Arrangement of Experimental Equipment used in Phase Zero

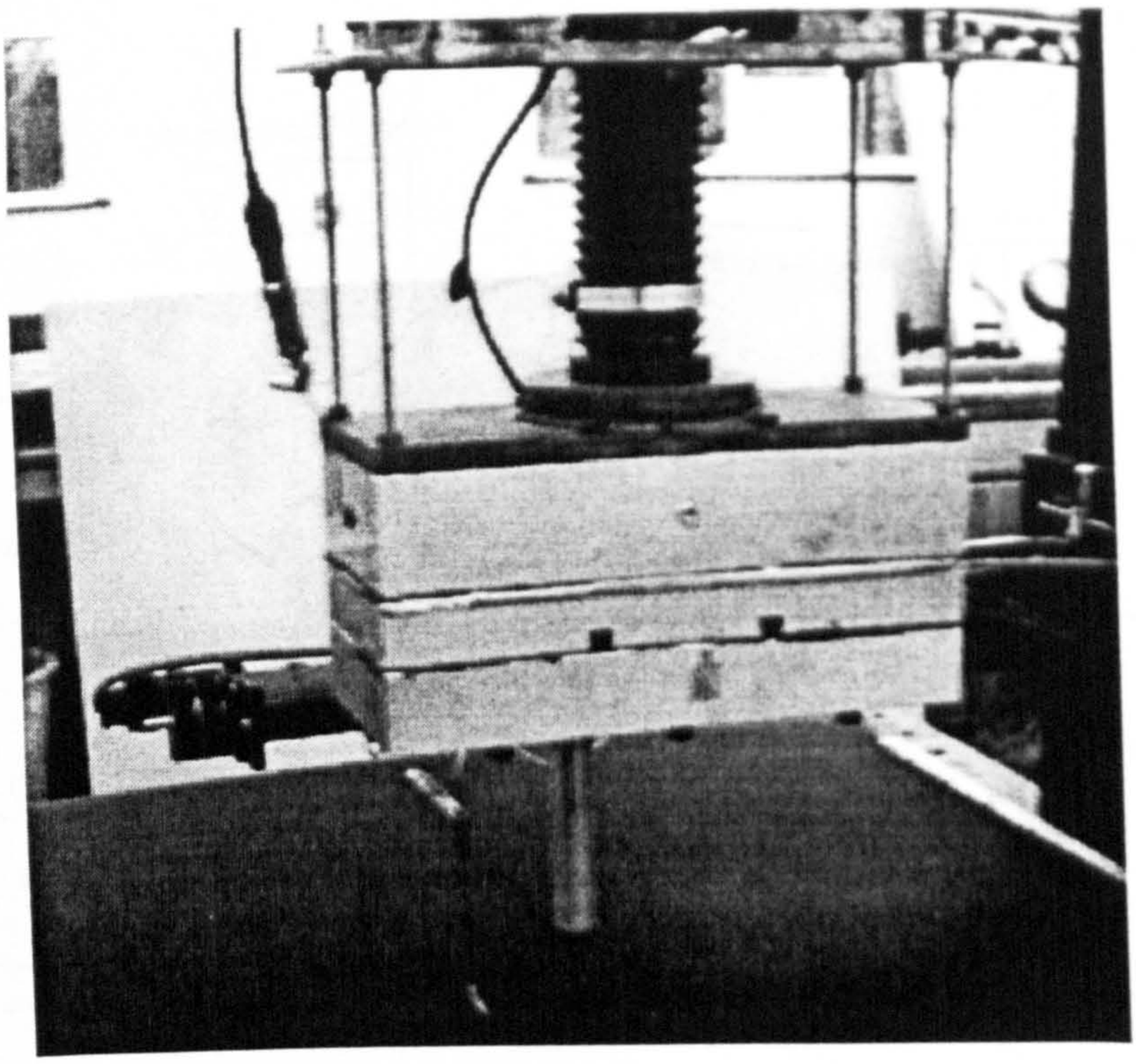

Figure 2.3 : Settling Chamber used in Experimental Investigation

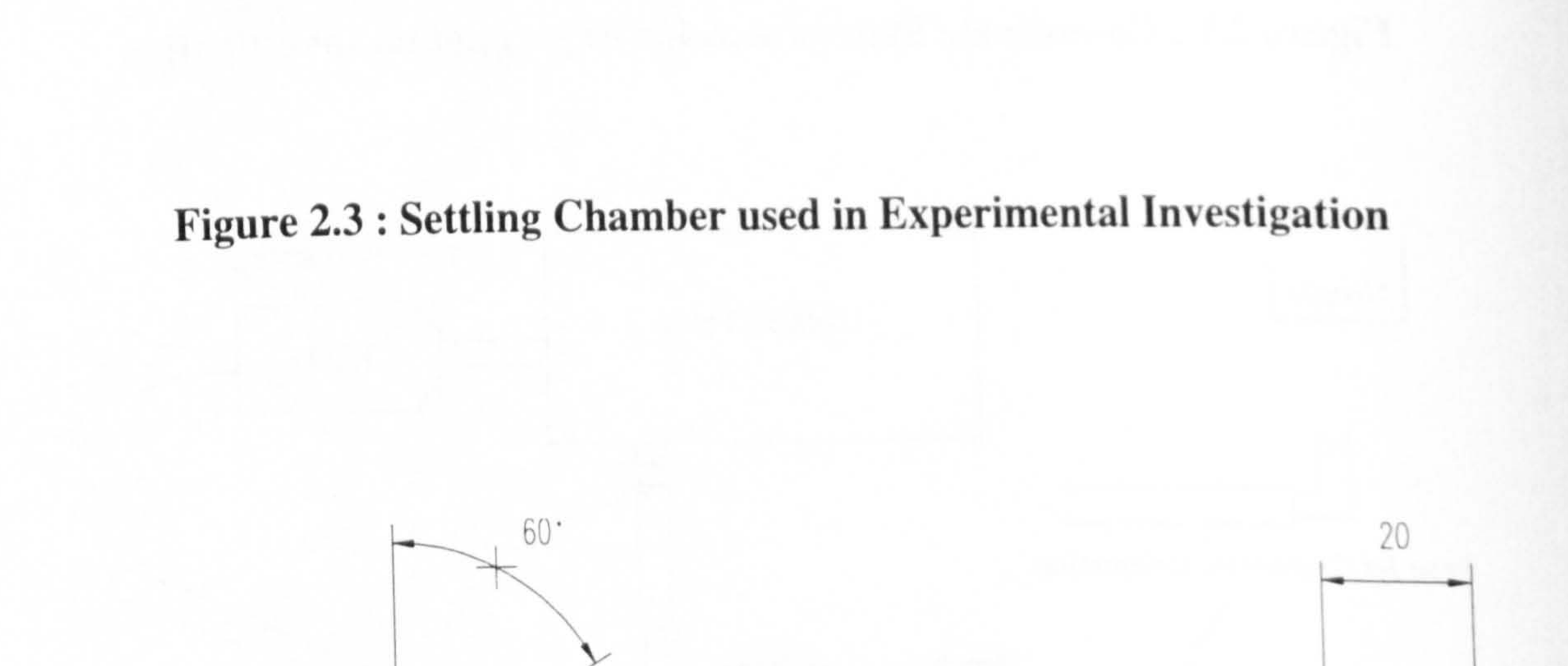

Figure 2.4 : Details of Half-inch "Kingston" Nozzle used in Experimental Investigation

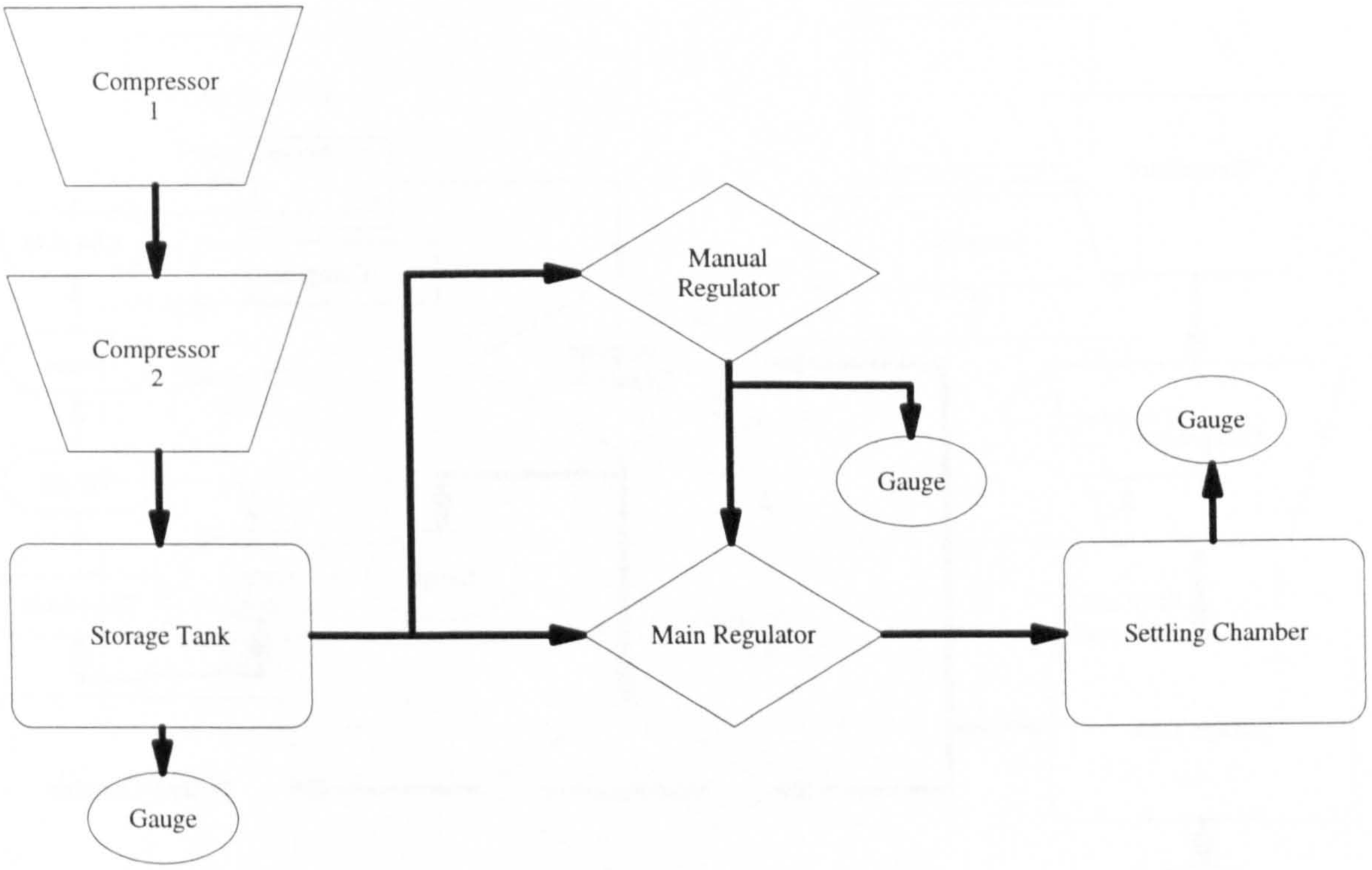

Figure 2.5 : Phase Zero Manual Pressure Control System

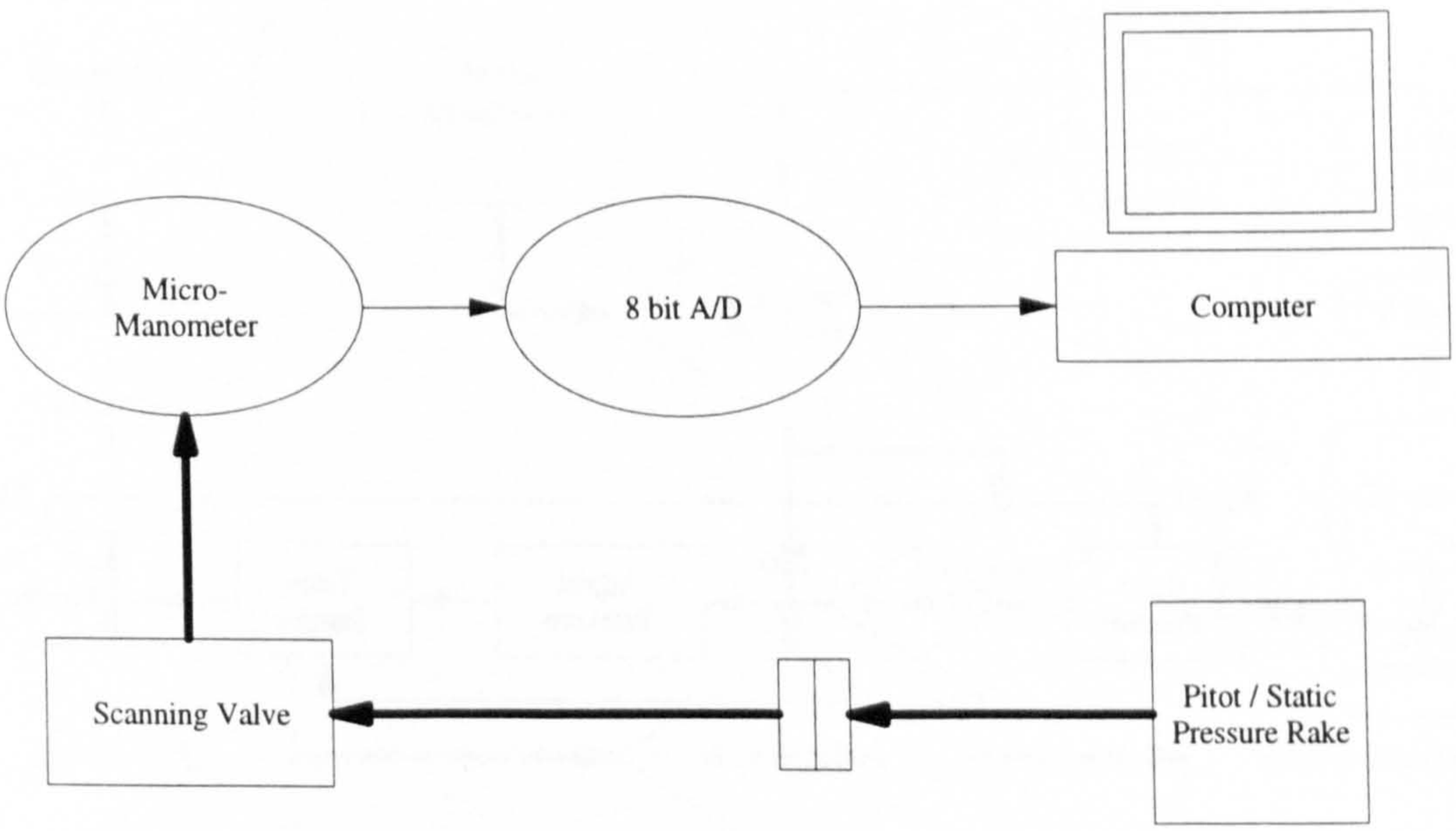

Figure 2.6 : Phase Zero Data Collection System

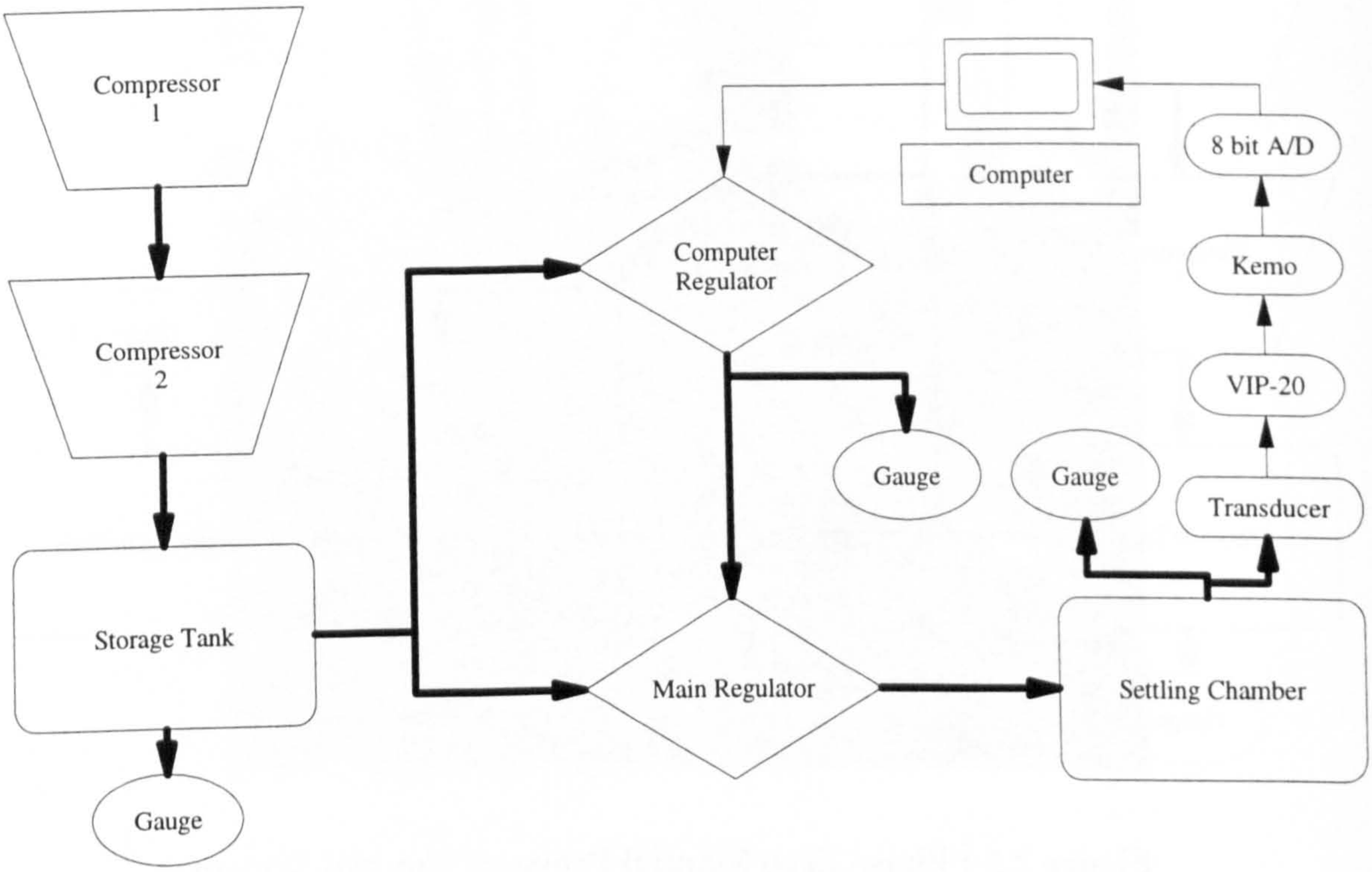

Figure 2.7 : Phase Zero Plus Computerised Pressure Control System

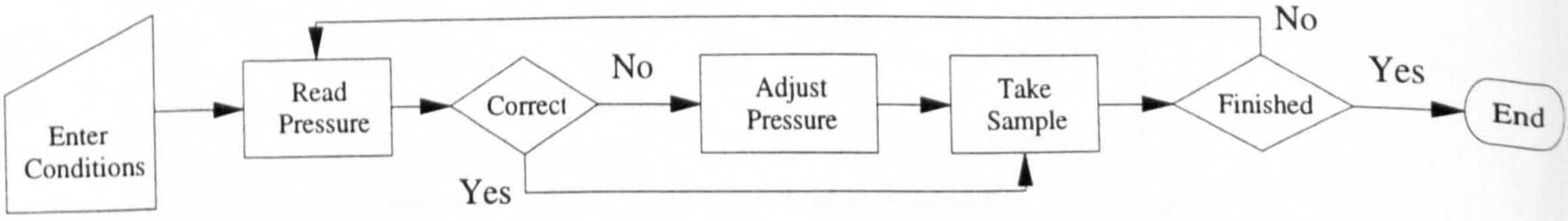

Figure 2.8 : Flow Chart of Pressure Control Routine

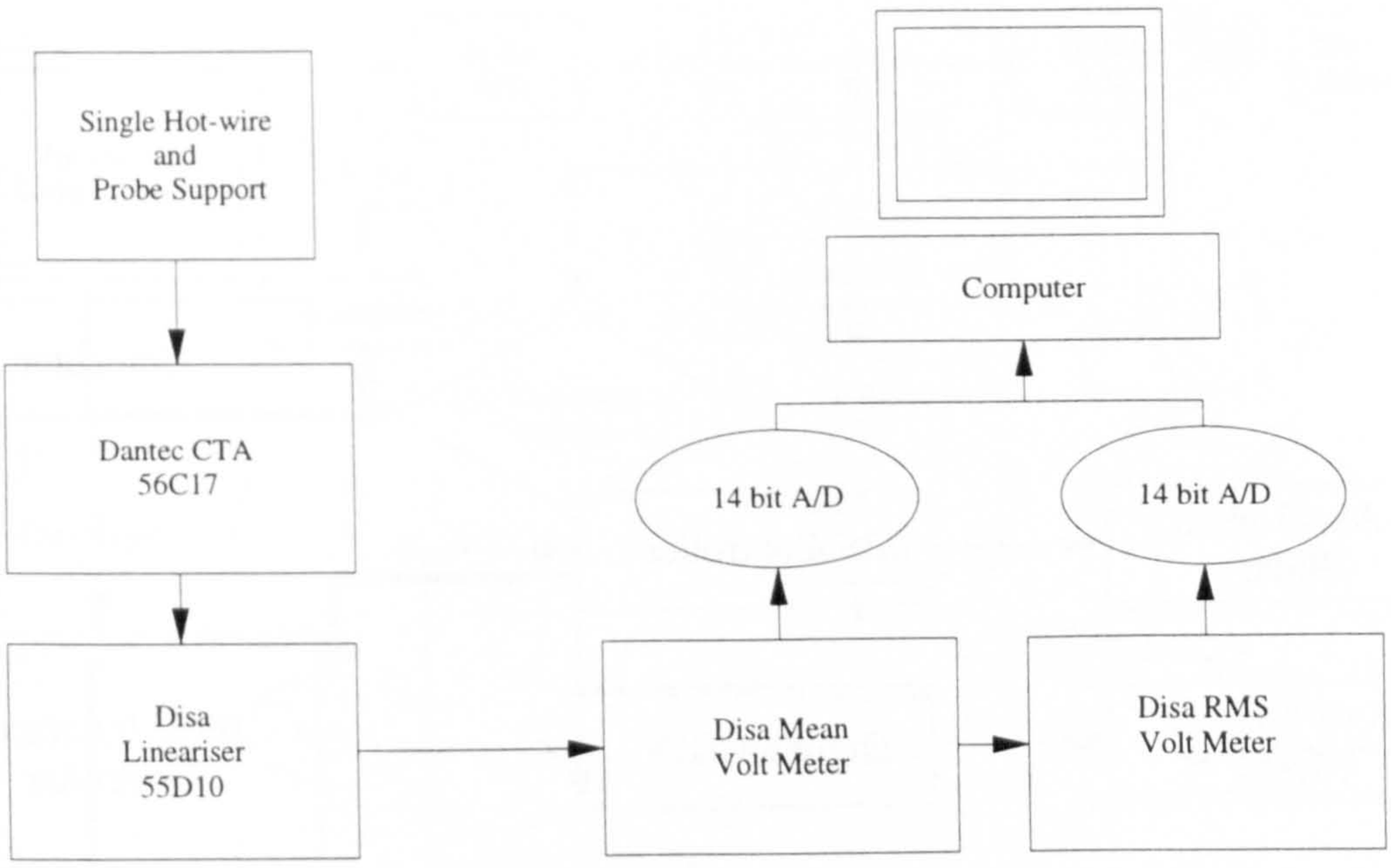

Figure 2.9 : Phase Zero Plus Data Collection

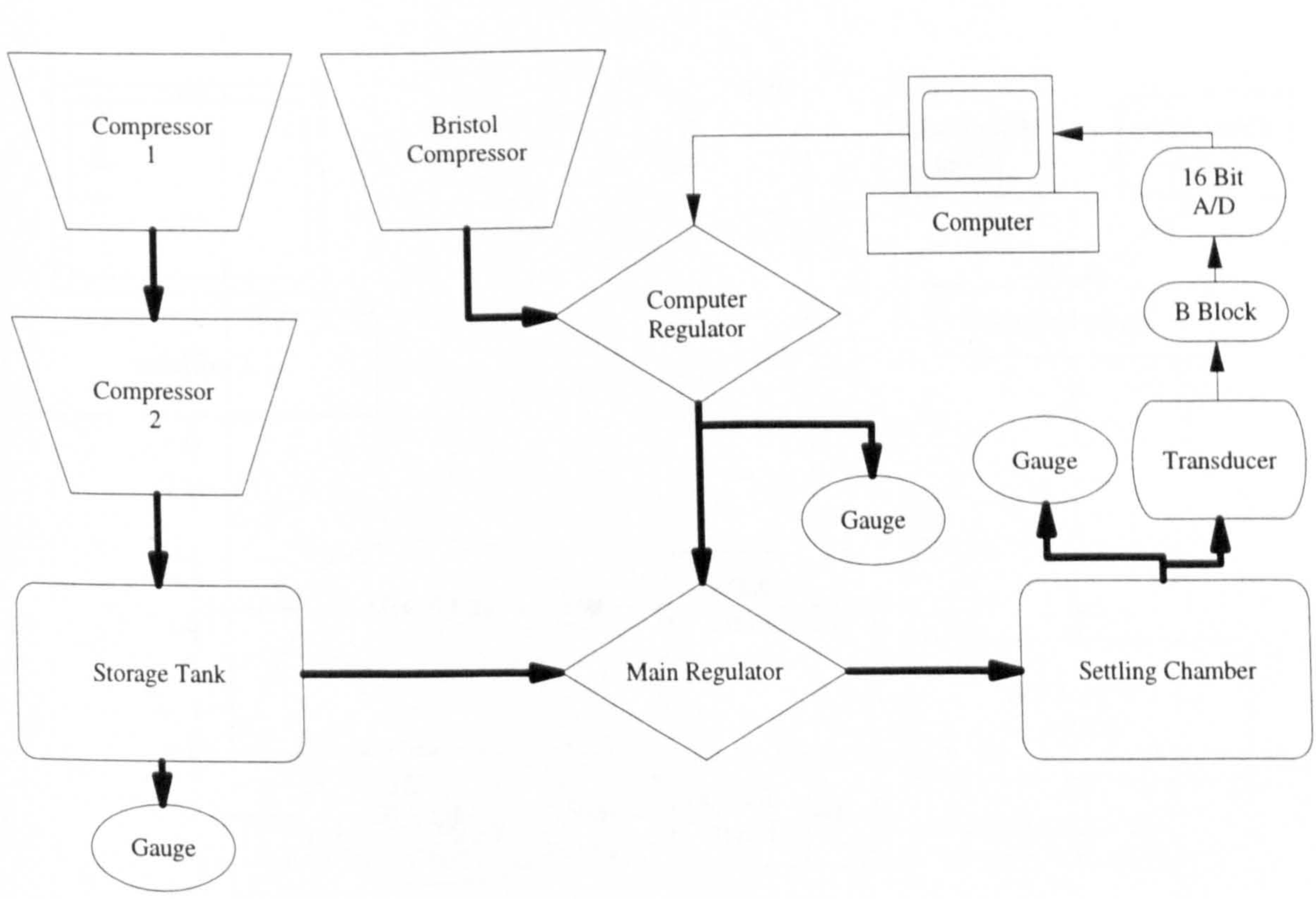

Figure 2.10 : Phase One Computerised Pressure Control System

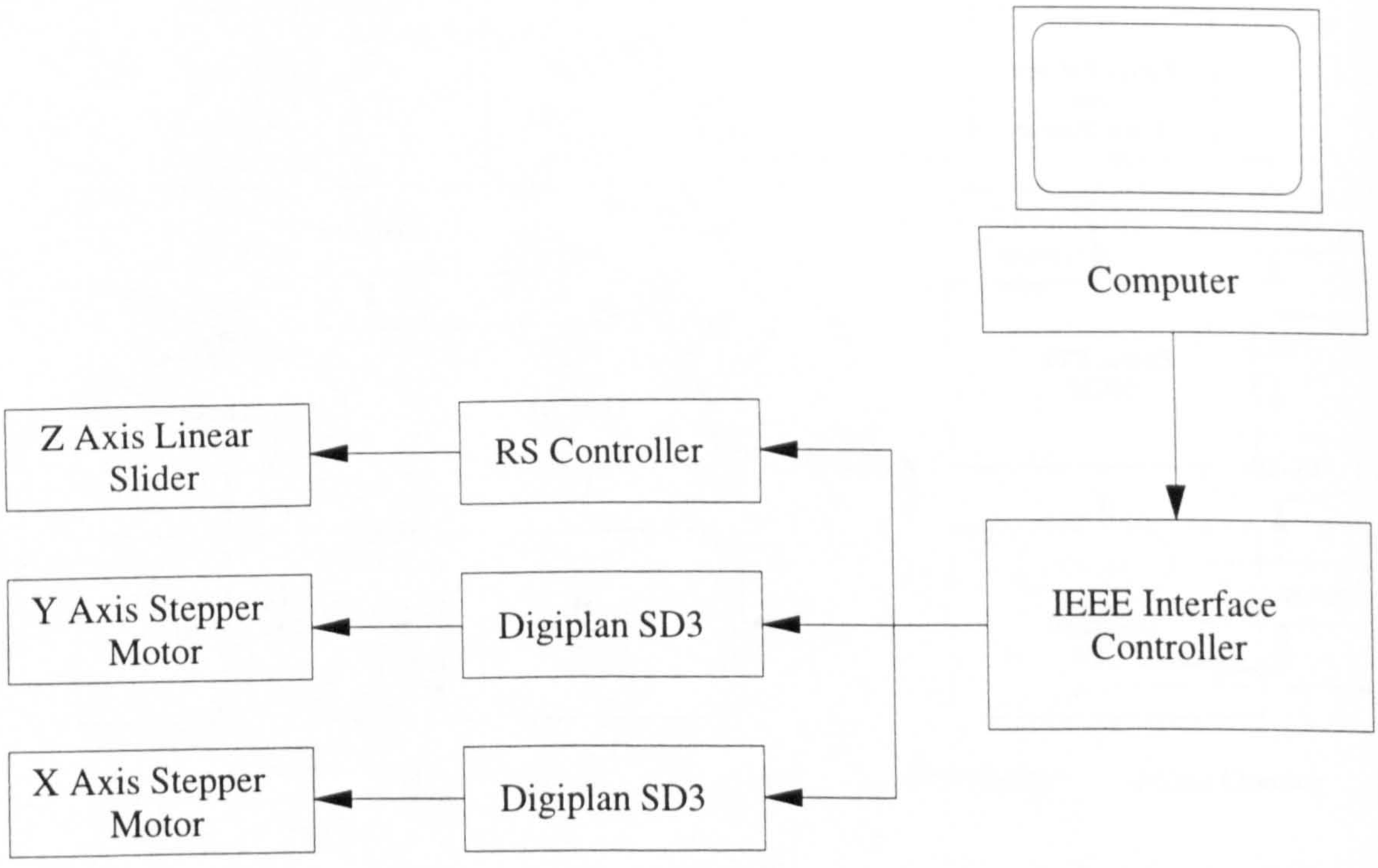

Figure 2.11 : Travelling Microscope Traverse

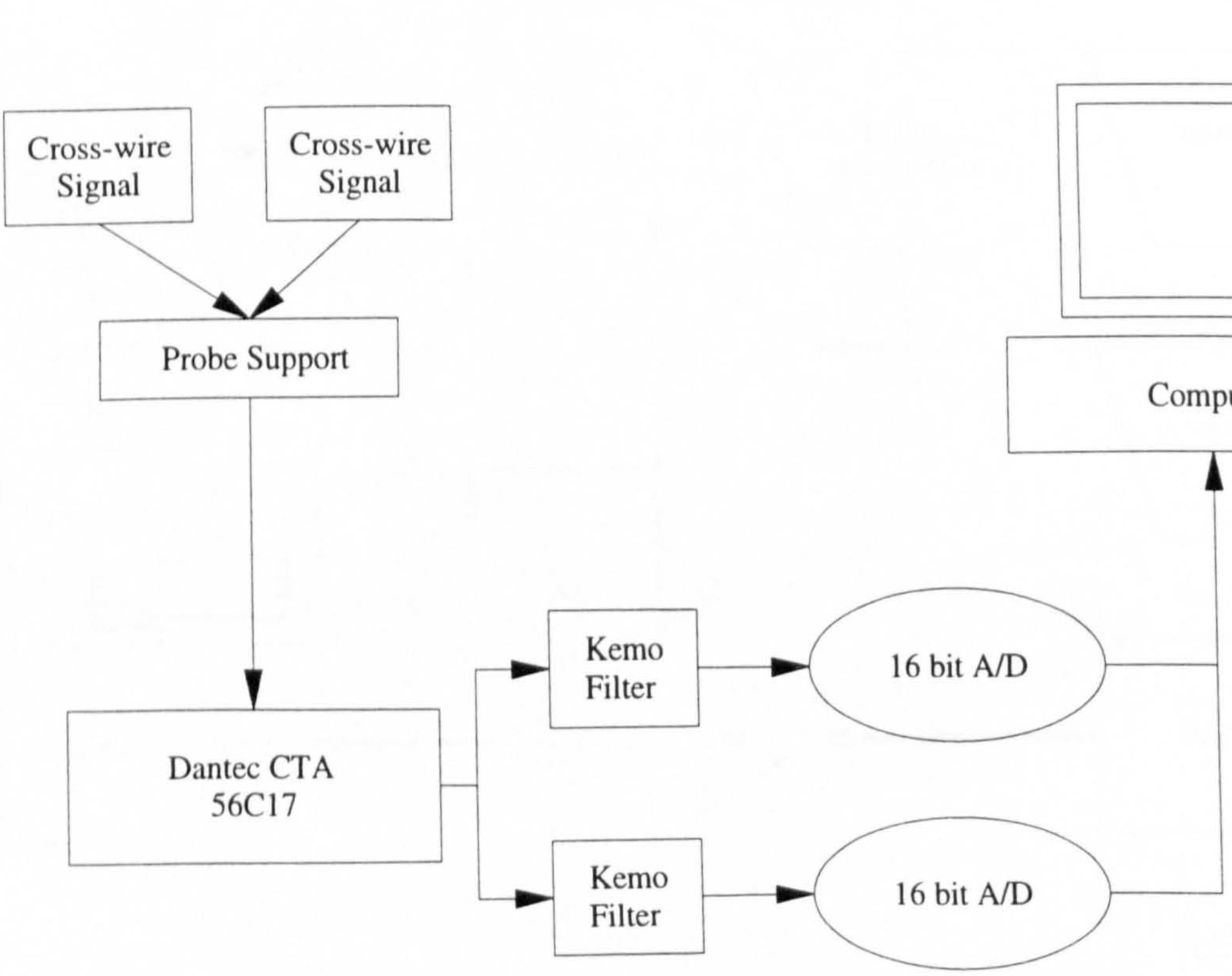

Figure 2.12 : Phase One Data Collection System

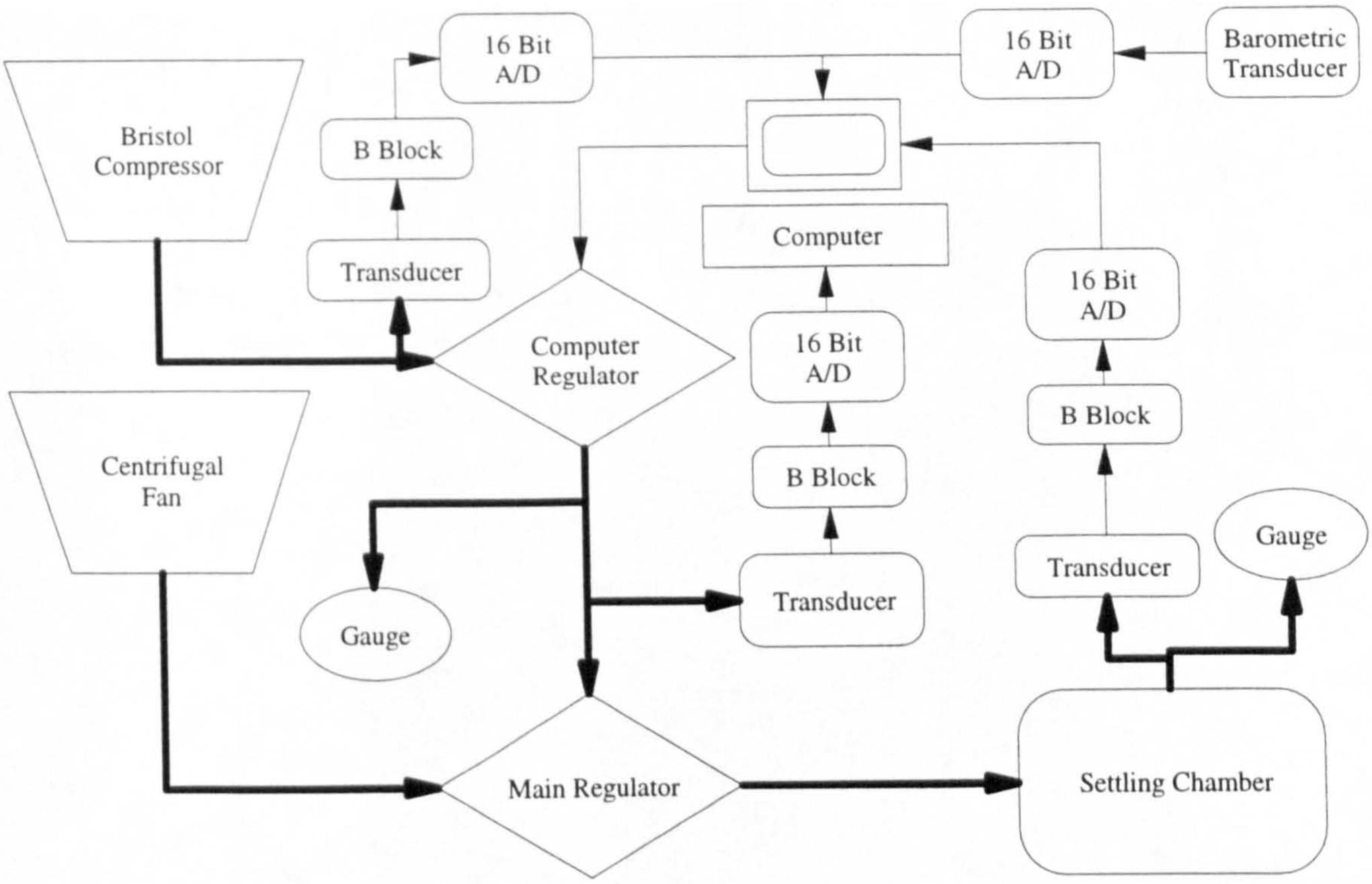

Figure 2.13 : Phase Two Computerised Pressure Control System

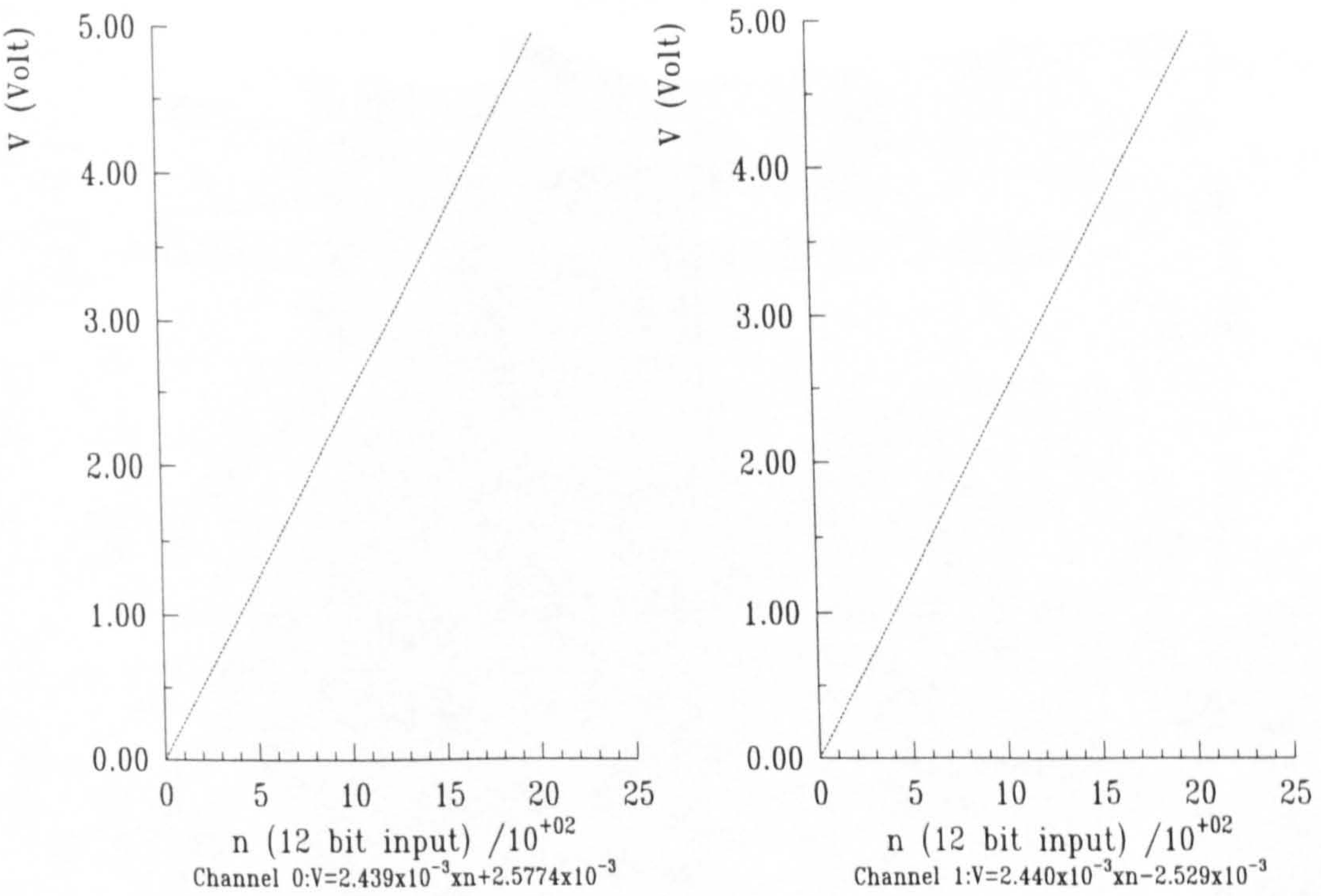

Figure 2.14 : 2 Channel O-Block Calibration

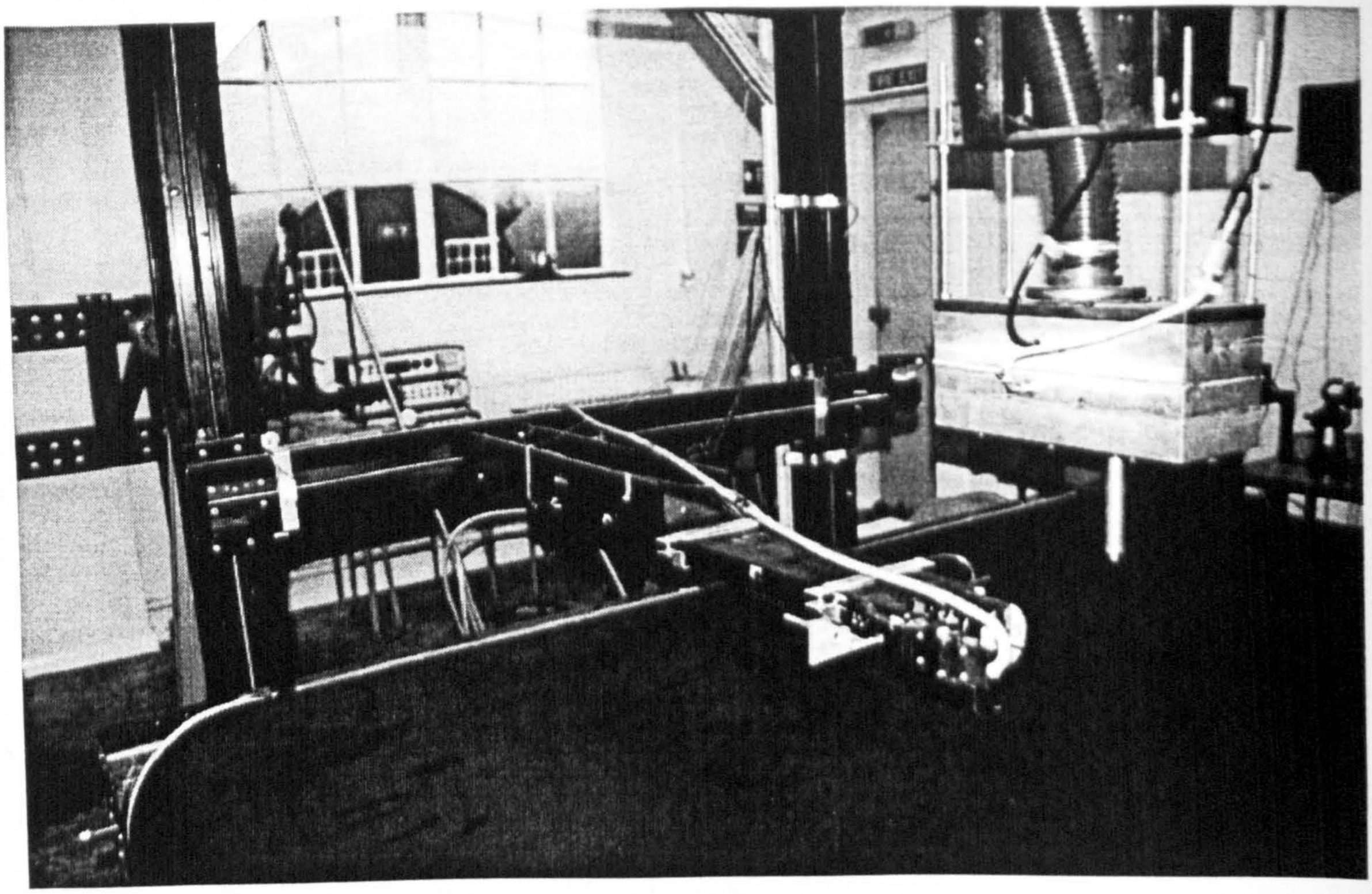

Figure 2.15 : Phase Two Traverse System

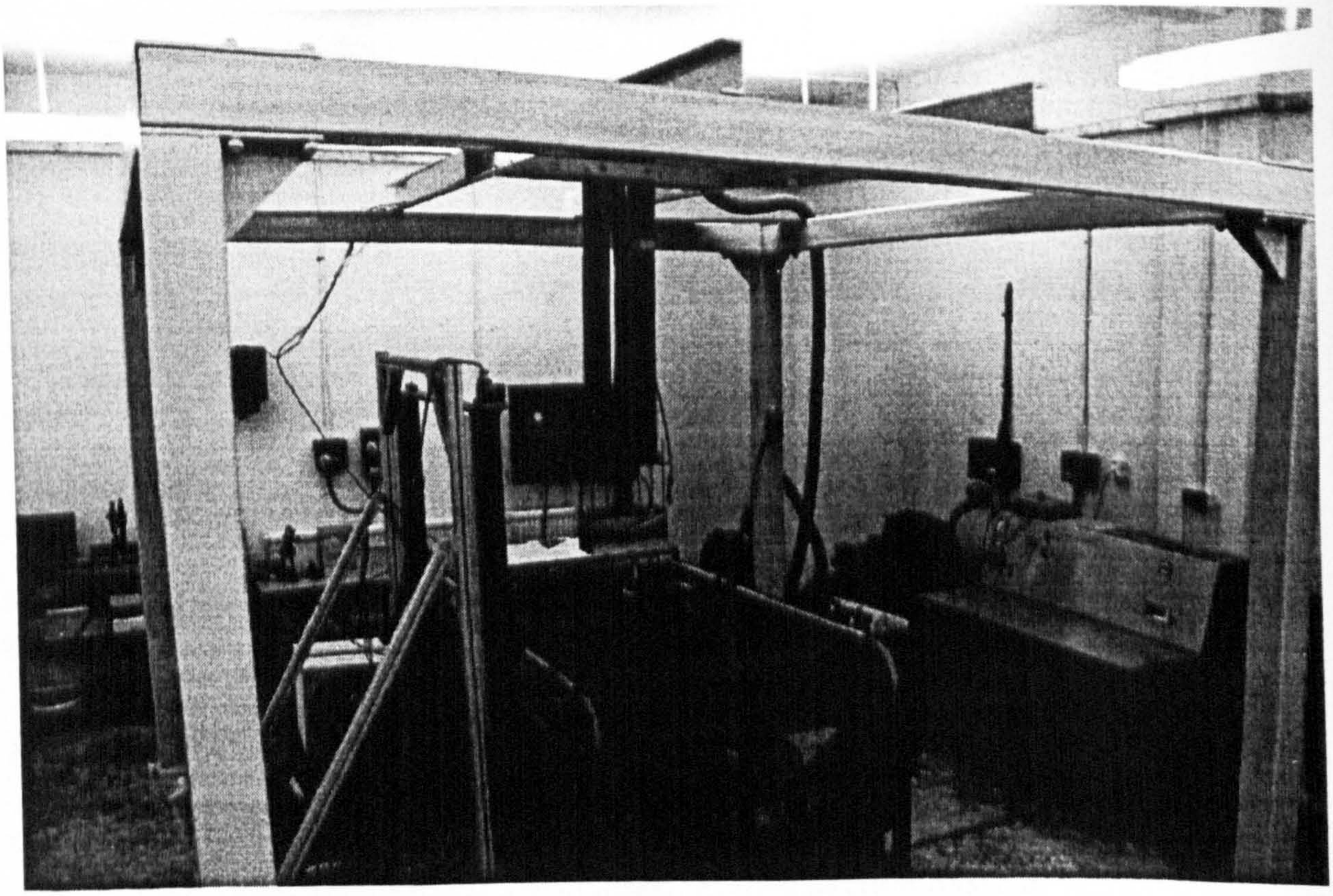

Figure 2.16 : Jet Impingement Rig (JIR)

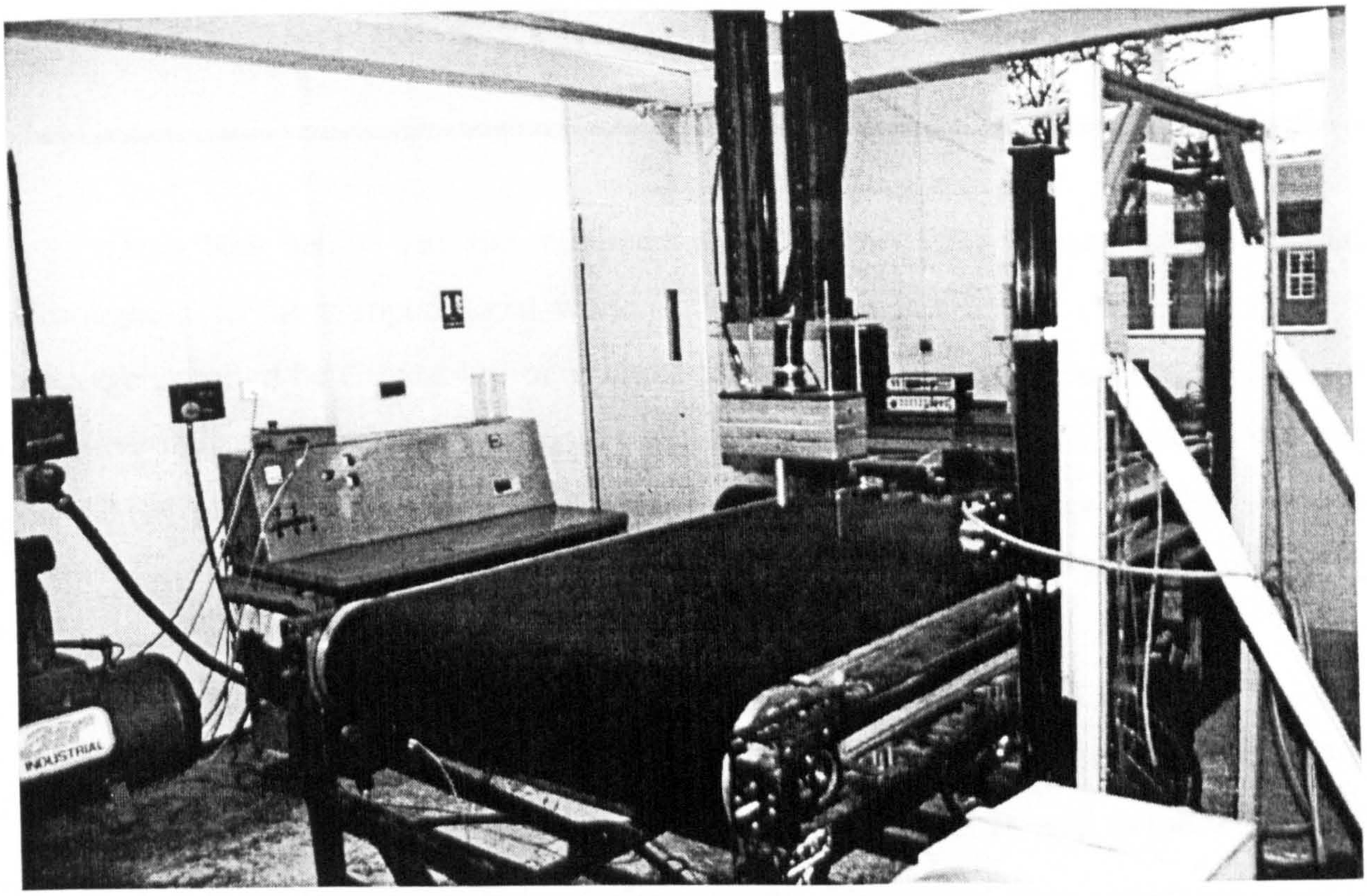

Figure 2.17 : Rolling Road and Control Console

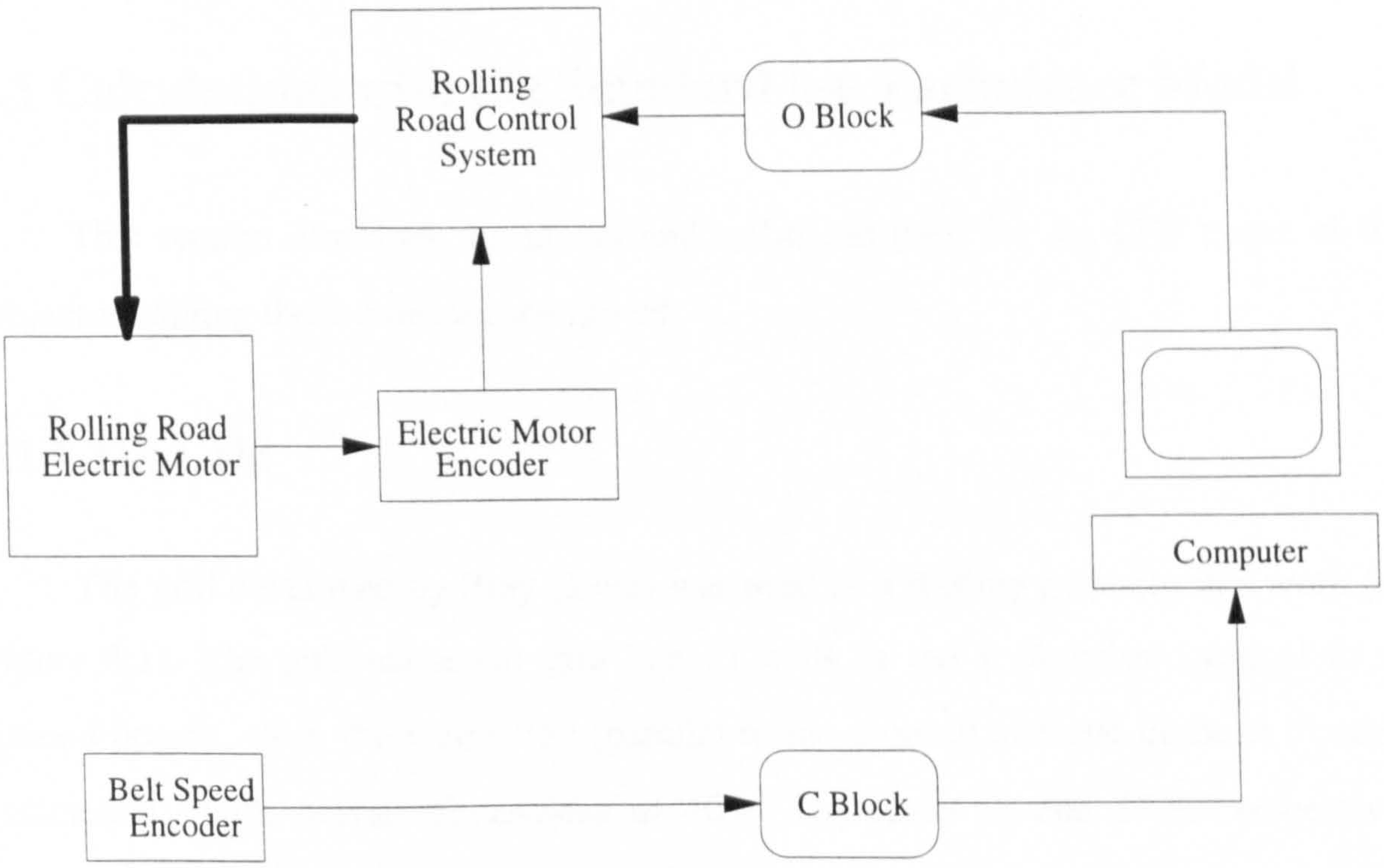

Figure 2.18 : Phase Three Computerised Rolling Road Control System

BLANK IN ORIGINAL

Chapter 3 : Computational Method

Described below are the methods used in the CFD phase of the project. Throughout all the computational work performed, the PHOENICS (Version 2.0) CFD package supplied by CHAM Ltd of Wimbledon, London was used (see Appendix B for the governing equations and Appendix C for the solution method). The package was run on a SUN network at the Cranfield University, Shrivenham, Computer Centre on an AXIL 420 (equivalent to a SUN SPARC 20) or on a stand-alone SUN SPARC 2 workstation. The FORTRAN compiler used throughout was F77.

This chapter details the model set-up, equations and variables solved and details the modifications applied to the standard k-ε turbulence model as well as the set-up used for the low Reynolds number k-ε turbulence model. The aim of these simulations was to gain an understanding concerning the level of accuracy obtainable for the prediction of an impinging jet. The results of these predictions are discussed in Chapter 5.

3.1 Calculations with the Standard k-ε Turbulence Model

This section describes the model and technique used for the CFD phase of this project involving the k-ε turbulence model.

3.1.1 The Grid

The grid developed by Bray (1992) was used as a starting point for this work (see Figure 3.1). The polar-cartesian grid had 51 cells in the y direction (normal to the ground board), 49 in the r direction (parallel to the ground) and one in the α direction (azimuthal), with overall dimensions of 40.07 D_n, 12.50 D_n and 57.30^0 respectively based on a 1" (25.4mm) nozzle.

Initially, the cell sizes were halved so that the grid could be used to model a ½" (12.7mm) nozzle as used in the experimental phases instead of the 1" (25.4mm) nozzle used by Bray. Runs performed indicated that the size of the first cell on the ground plane was too small, the Y^+ for the centre of the first cell being too low for the worst case of H_n/D_n=10.0. A number of different grids were tried with varying first cell thickness until an optimal grid was found, having a reduced number of cells in the y direction (49 instead of 51). The size of the grid in the α direction was also reduced to 2^0 as this was found to aid convergence.

3.1.2 General Domain

This section describes the general settings used with the model.

3.1.2.1 Compressibility

The density of the fluid at each cell was calculated using the ideal gas law equation:

$$\rho = \frac{p}{RT}$$

Equation 3.1

where R is the Specific Gas Constant defined in the initial conditions, p is the static pressure at that point calculated by PHOENICS and T is the temperature of the fluid in the cell.

For all cases discussed, the temperature of the fluid was calculated using:

$$T = \frac{\left(C_p \times T_o - 0.5 \times (u^2 + v^2 + w^2)\right)}{C_p}$$

Equation 3.2

where T_o is the stagnation temperature of the flow. For all these cases, T_o was taken as being the stagnation temperature of the jet.

3.1.2.2 Kinematic Viscosity

The kinematic viscosity of the flow was modelled using Sutherland's formula to account for the effect of temperature changes in the flow. Sutherland's formula states:

$$\upsilon = \frac{\left(a \times T^{1.5} \times \rho\right)}{b + T}$$

Equation 3.3

where, for air, a = 1.46 x 10^{-6} kg s^{-1} m^{-1} $K^{-½}$ and b = 110.0.

3.1.2.3 Turbulence Model

The k-ε model was activated using the PHOENICS TURMOD(KEMODL) command. This made the following settings

$$C_\mu C_D = 0.09,\ C_{1\varepsilon} = 1.44,\ C_{2\varepsilon} = 1.92,\ \mathrm{Prt}(k) = 1.0\ \&\ \mathrm{Prt}(\varepsilon) = 1.314$$

where Prt(x) is the relevant Prandtl number.

3.1.3 Boundary Conditions

Figure 3.2 shows the boundary breakdown used in this report. The domain boundaries were split into 6 main sections, the conditions which were used in the model are described below

3.1.3.1 Initial Conditions

The initial conditions set for the domain for all runs were as follows:

1. Atmospheric pressure set to 755 mmHg
2. Ambient temperature set to 290°K
3. Specific Gas Constant, R = 287.0 J kg^{-1} K^{-1}

4. Ratio of specific heats, $\gamma = 1.4$

5. Constant pressure specific heat, $C_p = 1005.0\ J\ kg^{-1}\ K^{-1}$

6. Fluid laminar viscosity, $\mu = 1.75 \times 10^{-5}\ kg\ m^{-1}\ s^{-1}$

Initial values of density and kinematic viscosity used were calculated from the above values, initial values for the velocities were set to $1.0 \times 10^{-5}\ ms^{-1}$ (not zero to prevent possible numerical problems). It was found that the best convergence times were achieved if initial domain values for k and ε were set to 1% of the nozzle exit value and the eddy viscosity, ν_t, set to 1.0×10^{-3}.

3.1.3.2 Nozzle Inflow

The nozzle and its exit were modelled in a similar way to that used by Bray (1992), a section of blocked-off cells representing the nozzle itself. The side of this nozzle facing the domain had the logarithmic-law-of-the-wall function applied to model more accurately the outer domain flow down the nozzle side (see Appendix B for more details of the wall function used).

The nozzle exit was modelled as the next row of cells below the blocked section, the mass flow rate per unit area and velocity from this row of cells entering the domain being fixed. The mass flow rate and velocity were calculated as follows:

1. Nozzle exit NPR and turbulence intensity, Tu , were defined by the user.

2. Nozzle exit velocity and density were calculated using isentropic flow equations.

3. Exit mass flow per unit area was the product of exit velocity and static density.

The turbulence characteristics at exit were defined as:

1. The initial value for k, the turbulent kinetic energy, was set using

$$k_{nozzle} = (U_m \times Tu)^2$$

Equation 3.4

2. The initial value for ε, the rate of dissipation of k, was set using

$$\varepsilon_{nozzle} = 0.015\left(\frac{k_{init}^{1.5}}{0.035D_n}\right)$$

Equation 3.5

The velocity and turbulent profiles of the jet were assumed to be uniform across the nozzle exit. The effect of non-uniform exit velocity on free jet mixing has been discussed by Knowles (1996).

3.1.3.3 Plane of Symmetry

The plane of symmetry at the jet axis centre-line was left undefined by the user. PHOENICS internally modelled this domain face as a smooth, frictionless wall.

3.1.3.4 Ground Plane

The impingement ground plane was modelled as a solid wall extending the full length of the grid in the r direction. The logarithmic law of the wall function was applied to this surface with the V velocity being set to zero on this face (no-slip condition).

3.1.3.5 Upper Flow Boundary

On the upper boundary, the pressure was fixed to that of ambient, the extent of the domain being such that any small error in the pressure at this boundary should not effect the areas of interest in the domain. The boundary was also set to allow mass flow to enter and leave the domain.

3.1.3.6 Outflow Boundary

The conditions on the outflow boundary were identical to those used for the upper flow boundary (see the previous section).

3.1.4 Convergence

Convergence was checked for by two means. Firstly, the values of all the solved-for variables were monitored at a point in the outer reaches of the wall jet, these being stored at uniform sweep intervals in the result file. At the end of the run, these were checked to confirm that the flow had reached a steady value at the point. Secondly, the residuals of the solved-for variables were monitored as the run progressed. The residuals were summed over the entire domain and then normalised by the appropriate net flux for that variable in the domain. For the pressure and velocities, convergence often meant the errors were less than 0.1%. The turbulence quantities (k especially) were considerably harder to converge, often errors in the region of 1 - 2% being the best obtainable for k.

3.2 Modifications to k-ε Model

The following section describes three modifications made to the standard k-ε model.

3.2.1 Rodi Correction

The free jet modification used is that described by Rodi (1980) in which the 25% over-prediction of the free jet growth is reduced by reducing the values of the coefficients C_μ and $C_{2\varepsilon}$ and hence the rate of dissipation ε. This is achieved by making the coefficients a function of the jet thickness and the mean velocity gradients at that point in space.

$$C_\mu C_D = 0.09 - 0.04f$$

Equation 3.4

$$C_{2\varepsilon} = 1.92 - 0.0667f$$

Equation 3.5

with:

$$f=\left[\frac{b}{U_m}\left|\frac{\partial U_m}{\partial y}\right|\right]^{0.2}$$

Equation 3.6

where U_m is the maximum mean velocity of the jet at a given axial position, b is the jet thickness (to 10% of U_m) and $\frac{\partial U_m}{\partial y}$ is the gradient of the maximum mean velocity at that slice of jet.

The correction was only applied to the free jet portion of the flow, the grid being separated into 2 regions (see Figure 3.3), the area using the new modified constants and the remaining using the standard k-ε. The equations were implemented in the PHOENICS ground coding, a section of the program which allows the operator to add additional FORTRAN code into the solution sequence. The velocity gradient, peak velocity and jet width were found at each slab (a slab being a row of cells in the Y plane) as the solution sequence worked its way down through the domain during each sweep. The new coefficients were calculated for that slab and used in the PHOENICS k-ε turbulence routine (GXTURB.F) to calculate the new values for the solved variables on that slab. To aid the initial start-up of the correction, the standard k-ε model was used for the first 250 sweeps so that an initial jet formed. Minimum values were placed on $C_\mu C_D$ and $C_{2\varepsilon}$ of 0.061 and 1.872 respectively.

3.2.2 Malin Correction

The wall jet correction used is that described by Glynn and Jal (1987) and credited to Malin (1988) which accounts for the under-prediction of the growth of the radial jet by increasing the value of the $C_{2\varepsilon}$ coefficient, using a function f similar to that described above and keeping the standard value for C_μ.

$$C_\mu C_D = 0.09$$

Equation 3.7

$$C_{2\varepsilon} = 1.92 + 0.16f$$

Equation 3.8

with:

$$f = \left[\frac{b}{V_m}\left|\frac{\partial V_m}{\partial r}\right|\right]^{0.2}$$

Equation 3.9

As with the Rodi correction, the grid was broken into two sections (see Figure 3.3), one where the correction was used and the rest where the unmodified model was retained, this again being coded in the PHOENICS ground section, similar to Section 3.2.1. The GXTURB.F routine was modified so that it accepted an array containing the new modified constants for each slab instead of the previous single value for each slab. As with the Rodi correction, the new coding was not activated until 250 sweeps had been completed with the standard k-ε model and a maximum value for $C_{2\varepsilon}$ of 2.05 was set throughout.

When the Rodi and Malin corrections were applied to the same model, the two grids were superimposed on each other, forming a domain with three regions, the free jet with the Rodi correction, the wall jet with the Malin correction and the impingement region (1.5 x 1.5 D_n) where the standard k-ε coefficients were used. The standard coefficients were also used in the area above the nozzle exit (see Figure 3.3).

3.2.3 Chen Correction

The standard k-ε model uses a single time scale (i.e. k/l_m where l_m represents the length scale of the production) to characterise the various dynamic processes occurring in a turbulent flow, and so fixes the rates at which the source terms (production and destruction) and the transport terms (convection and diffusion) can proceed at a value proportional to this time scale. However, as turbulent flow consist of fluctuations with a spectrum of time scales, this single-scale approach was considered not to be adequate under all circumstances, especially where the turbulence is removed from local

equilibrium, i.e. the rate of dissipation does not equal the rate of production. This is particularly true for turbulent boundary layers or separated flow (Michelassi et al. 1993). Chen and Kim (1987) proposed a modification which improved the dynamic response of the ε equation by introducing an additional time scale k/V_k, where V_k is the volumetric production rate of k. The model was then tuned by adjustment of several of the standard model coefficients to maintain good agreement with experimental data on classical turbulent shear layers.

The correction is described in further detail in Appendix B, and was activated by a PHOENICS command switch set in the Q1 file (TURMOD(KECHEN)) applying the correction to the entire flow domain.

Convergence of the model seemed to be unaffected by the addition of this correction compared to the standard model although the processing time was increased slightly. The same convergence criteria were applied to this model as were used for the previous runs.

3.3 Low Reynolds Number k-ε Model

It has been shown by several investigators that simple wall functions based on a logarithmic law and equilibrium turbulence assumptions are not appropriate for unsteady turbulent boundary layers (see Fan et al. 1993). It has been shown that the accuracy of the model deteriorates with increasing level of unsteadiness, due to its high Reynolds number dependence.

The low Reynolds number k-ε turbulence model used in these studies was that of Lam and Bremhorst (1981), the form described by Patel at al. (1985) being implemented in PHOENICS. The model is described in further detail in Appendix B, its use being activated in PHOENICS by the use of the Q1 command switch TURMOD(KEMODL-LOWRE).

3.3.1 The Grid

A requirement of the turbulence model used was that the value of Y^+ for the first cell should be below 4.5 and preferably the Y^+ of the first five cells should be below 11.0. To satisfy this requirement, the grid was refined in the wall region. This was performed on the grid used in the standard k-ε study by progressively reducing the cell height in the Y direction (leaving the cell density and size unchanged in the r direction) until the criteria were met. Table 3.1 shows grid densities used in this study.

3.3.2 General Domain

The general settings used in the low-Reynolds number model were the same as described above for the k-ε turbulence model.

3.3.3 Boundary Conditions

The boundary conditions used in the low-Reynolds number model were the same as described above for the k-ε turbulence model.

3.3.3 Convergence

Convergence for all low Reynolds number k-ε turbulence model runs was confirmed using methods similar to those used for the standard k-ε model (see section 3.1.4).

3.4 Summary

The CFD work could be considered as consisting of three phases. Firstly, the modelling of an impinging jet flow field using the standard k-ε model was assessed as a datum, this phase also including the prediction of parametric trends revealed in the experimental work. Secondly, the effectiveness of some published modifications to the standard coefficients used in the turbulence model and finally, the replacement of the

logarithmic wall function with the low Reynolds number k-ε model. The results discussed in Chapter 5 follow this basis.

Grid Designation	Nz	Ny	First Cell Thickness
Grid 1	49	49	1.270
Grid 2	50	49	0.953
Grid 3	51	49	0.635
Grid 4	52	49	0.476
Grid 5	53	49	0.318
Grid 6	54	49	0.238
Grid 7	55	49	0.159
Grid 8	56	49	0.119
Grid 9	57	49	0.080
Grid 10	58	49	0.060
Grid 11	59	49	0.040
Grid 12	60	49	0.030

Table 3.1 : First Cell Thickness (mm) for Low Reynolds Number k-ε Grids

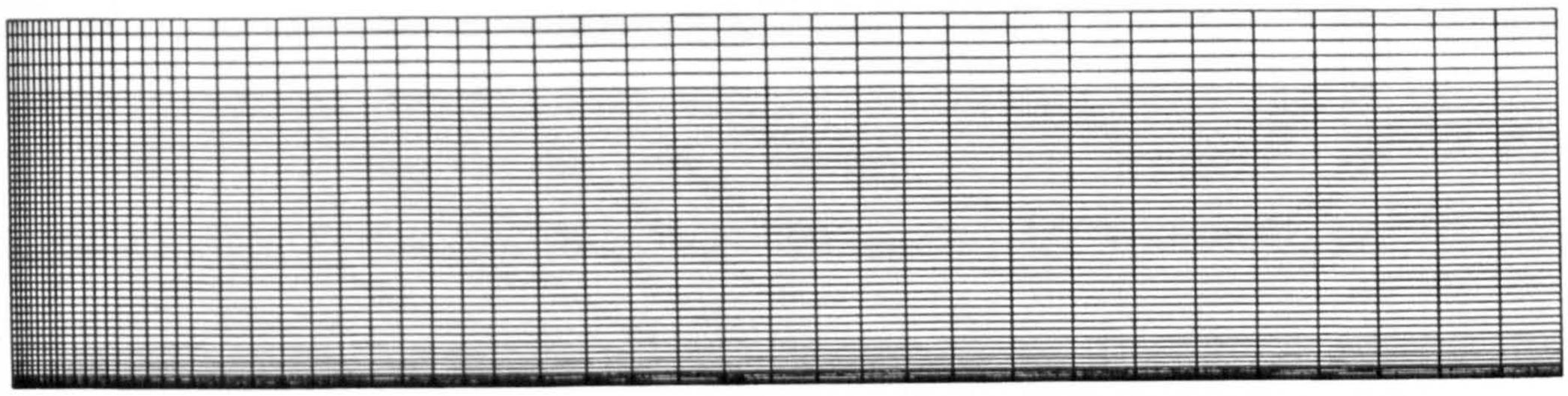

Figure 3.1 : Basic Grid Developed by Bray (1992)

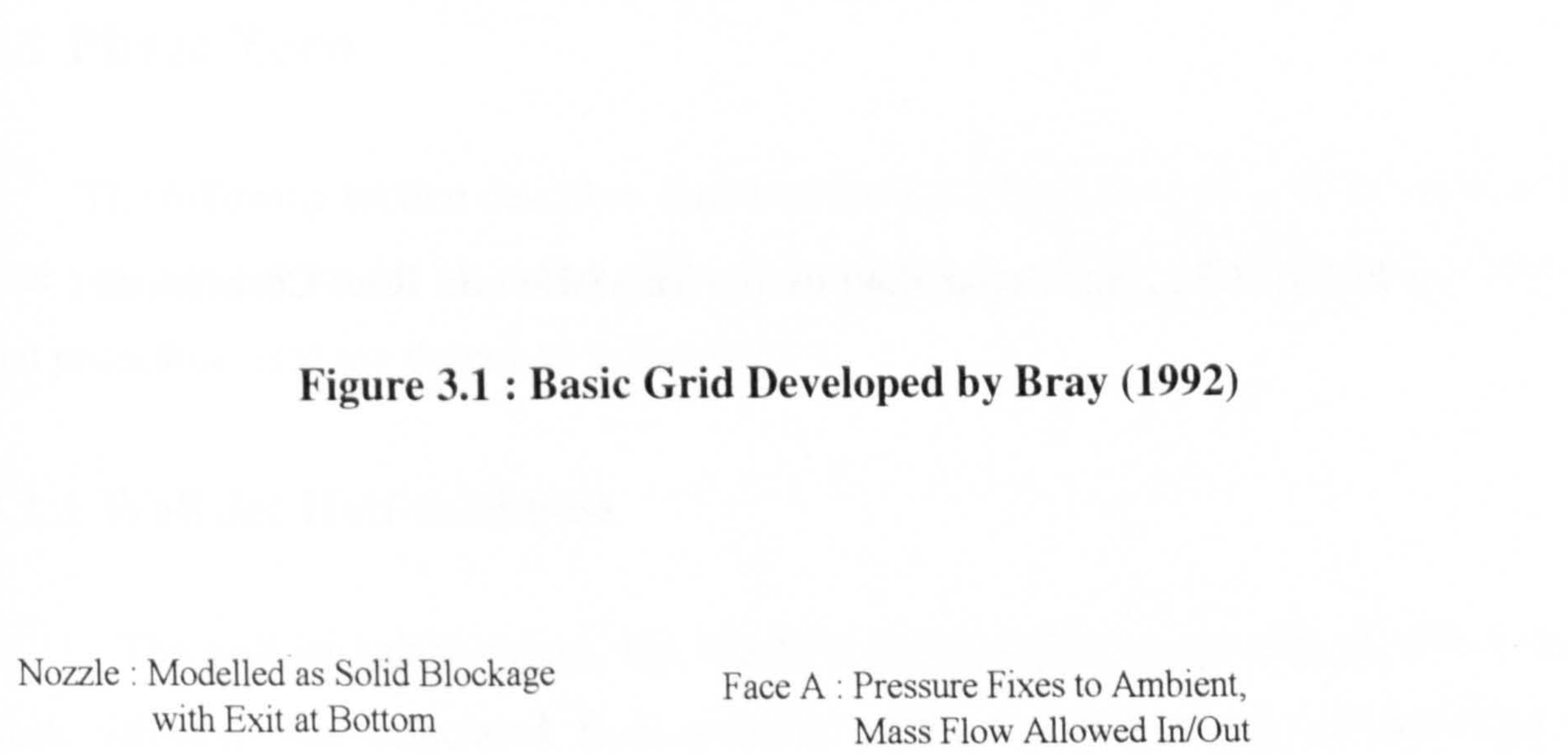

Figure 3.2 : Breakdown of Boundaries Used on k-ε Grid

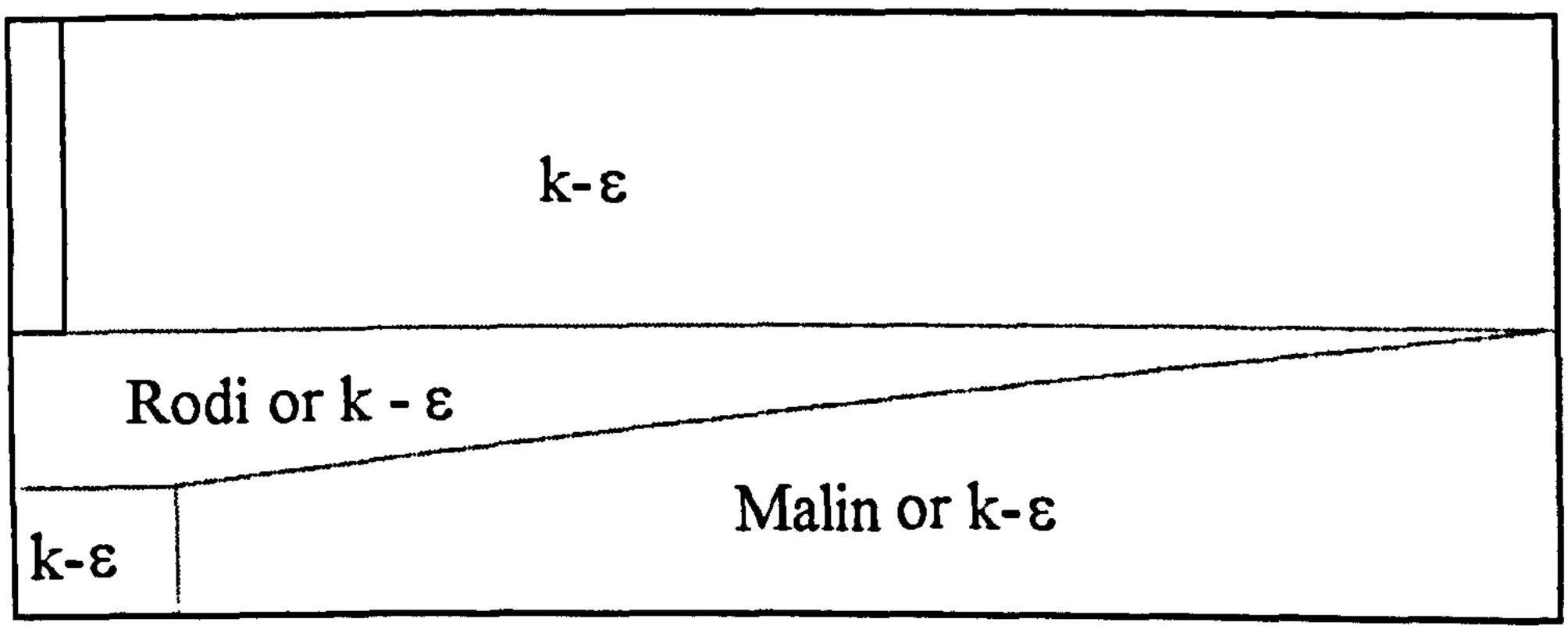

Figure 3.3 : Zone Separation used with Malin and Rodi Corrections

Chapter 4 : Experimental Results and Discussion

This chapter describes the results obtained in the experimental phases of this project together. Further discussion is included in Chapter 6 in light of the CFD results contained in Chapter 5.

4.1 Phase Zero

The following section describes further reduction of results obtained in the author's final year project for his Bachelor of Engineering degree. The experimental equipment and procedure used are described in Section 2.1.

4.1.1 Wall Jet Half-thickness

The wall jet half-thickness, the height in the profile from the ground to half the peak velocity, was calculated from velocity profiles deduced from the pitot/static pressure measurements taken using the equipment and apparatus described in Chapter 2 under Phase Zero. The wall jet thickness was calculated using a linear interpolation of data points about the $V_{½}$ value in order to return a more accurate answer.

When $Y_{½}/D_n$ was plotted against radial position, r/D_n (see Figure 4.1), it was found that it increased at a nearly-linear rate. This was not surprising as the previous correlations (see Section 1.2.3) had powers on the radial term ranging from 0.9 to 1.025. After further examination, it became clear that at r/D_n= 25.0, the value of $Y_{½}$ was consistently lower than the trend. As this appeared on all the plots, it was unlikely that it was due to an experimental error or a data processing error. A close examination of the apparatus and its surroundings did not give any apparent reason for this discrepancy, the position did not occur on any joint or in line with any obstruction. As the spreading rate

at this r/D_n position was consistently different, it was decided to remove this data point from any further calculations (although it will be plotted on figures).

Plots such as Figure 4.1 can be made for 4 NPR and 4 H_n/D_n combinations, and when these plots were compared for the different nozzle height settings at a given NPR and radial location (see Figure 4.2), it was found that increasing the H_n/D_n setting tended to increase the wall jet half-thickness slightly. This was not a linear increase with nozzle height, as predicted by Hrycak et al. (1970) and Miller and Wilson (1993), but seemed to die off for a $H_n/D_n > 15$, being nearly flat from there on. The above trend was found on all plots made.

For a given radial position and nozzle height, wall jet thickness can be plotted against NPR (see Figure 4.3). It was found that increasing the nozzle pressure ratio tended to decrease the thickness of the wall jet. This was also noted by Miller and Wilson (1993) but not incorporated into their correlation. It is noted that there is a large degree of scatter in the results (for all H_n/D_n and r/D_n values), this being attributed to the primitive nature of the pressure control system used to obtain these results (Myszko 1993). It is also noted that the work of Bray (1992) showed NPR effects on the flow field, these effects being described as non-linear.

4.1.2 Comparison of Results with Previous Correlations

When the data were compared with previous available correlations for a fixed H_n/D_n and NPR (see Figure 4.4), it became clear that the correlation of Miller and Wilson (1993) was a far closer fit than any of the earlier equations. The predictions of Poreh et al. (1967) and Hrycak et al. (1970) tended vastly to under-predict the rate of spread of the wall jet as did that of Miller and Wilson but to a far lesser degree. It is worth remembering that Miller and Wilson included the wall jet static pressure in their reduction process and this may account for their correlation agreeing closer with the current experimental data. As this seemed to be the best correlation, a graph of $Y_{½}/D_n$ against H_n/D_n was plotted to see how variations in nozzle height affected the prediction (see Figure 4.5). As can be seen, Miller and Wilson's correlation under-predicts the

spreading rate at around $H_n/D_n = 5.0$ to 18.0 and over-predicts at $H_n/D_n > 25.0$ but is a reasonable average over this range.

Figure 4.6 shows a plot of half-thickness against NPR for a fixed height and radial position. It can be seen that the correlation of Miller and Wilson under-predicts the wall jet thickness and depending upon the value of H_n/D_n, the error can be quite large.

4.1.3 Correlation

As the previous models tended to predict poorly the current values of $Y_{½}/D_n$, it was decided to try and fit a correlation to the current experimental data incorporating terms for the observed NPR and H_n/D_n effects.

The earlier correlations had been of the form:

$$\frac{Y_{\frac{1}{2}}}{D_n} = K \times \left[\frac{r}{D_n}\right]^x$$

Equation 4.1

where K is a constant incorporating any height effects and x is a power. It was decided to use this as a starting point.

If the log of both sides is taken, we get:

$$\log\left(\frac{Y_{\frac{1}{2}}}{D_n}\right) = \log K + x \times \log\left(\frac{r}{D_n}\right)$$

Equation 4.2

which, if Log $Y_{½}/D_n$ is plotted against Log r/D_n (see Figure 4.7), gives a straight line of gradient x and intercept Log K. This was performed for all the data available and the mean taken for the value of the growth power, x. This worked out to have a value of 0.97. This was consistent with previously published work, ranging from 0.9 to 1.025.

The intercept of these straight lines with the Y axis gave the value of K for each data set. It was assumed that the constant K would follow the same format as previous correlations, only being slightly modified to account for the NPR effect noted earlier. Therefore this gave us:

$$K = A \times \left(\frac{H_n}{D_n}\right) + B \times NPR + C$$

Equation 4.3

Using all the intercepts from the previous graphs, we had 28 equations and 3 unknowns.

From an examination of Figures 4.2 and 4.5, it was clear that one straight line would not be able to predict accurately $Y_{½}/D_n$ over the height range required. The two possible solutions to this problem were to fit a curve to the data or to have a number of straight lines. To fit a curve to a 3-dimensional surface seemed unnecessarily complicated and so it was decided that two straight lines, one for the range $0 < H_n/D_n < 10.0 \rightarrow 15.0$ and the second $10.0 \rightarrow 15.0 < H_n/D_n$ would give accurate enough predictions without the use of overly-complicated equations. As only height-effect data were recorded for $H_n/D_n > 10.0$ (these tests were only performed at NPR = 3.0), a solution to B (the NPR coefficient) was not obtainable for the second line. Therefore for this case, the value of B was taken to be zero.

The equations were solved and the answers averaged to give a general result for the prediction of the wall jet half-thickness. For the first line:

$$A = 0.00118$$

$$B = -0.0063$$

$$C = 0.1173$$

and for the second line:

$$A = 0.00005$$

$$C = 0.1095$$

The position where the two lines cross is definable by H_n/D_n and NPR and can be found by equating the two constants K for the lines. Thus, the point where one is used in preference to the other is given by the equation:

$$\frac{H_n}{D_n} = 5.575 \times NPR - 6.9$$

Equation 4.4

Therefore this gives the correlation for predicting the wall jet half-thickness as:

For $2.0 \leq \frac{H_n}{D_n} \leq 5.575 \times NPR - 6.9$

$$\frac{Y_{\frac{1}{2}}}{D_n} = \left[0.00118 \times \frac{H_n}{D_n} - 0.0063 \times NPR + 0.1173\right]\left[\frac{r}{D_n}\right]^{0.97}$$

Equation 4.5

and for $\frac{H_n}{D_n} > 5.575 \times NPR - 6.9$

$$\frac{Y_{\frac{1}{2}}}{D_n} = \left[0.00005 \times \frac{H_n}{D_n} + 0.1095\right]\left[\frac{r}{D_n}\right]^{0.97}$$

Equation 4.6

The lower height line forces a lower boundary condition on NPR, NPR > 1.435. As only supersonic jet conditions were used to calculate the above constants, the lower limit on NPR has to be set at 1.893. An upper limit of NPR=4.0 also has to be set as the variation in $Y_{½}$ with NPR has given indications of being non-linear, so the level of accuracy of the correlation beyond the levels of the test NPRs is unknown.

4.1.4 Evaluation

The model was evaluated by first comparing it to the raw data collected under the various conditions. Graphs of $Y_{½}/D_n$ against r/D_n were plotted (see Figure 4.9 where $H_n/D_n < [5.575 \times NPR - 6.9]$ and Figure 4.8 where $H_n/D_n > [5.575 \times NPR - 6.9]$) and as can be seen, both predict the rate of growth of the wall jet well. The model of Miller and Wilson (1993) is also included in Figure 4.8 and Figure 4.9 to compare with the current predictive model. There seemed to be relatively little difference between the two models on these plots, but when $Y_{½}/D_n$ was plotted against H_n/D_n (see Figure 4.10), the improvement of the latest model was readily evident. There is a far more accurate prediction of the effect of the single jet height whilst still being able to predict accurately the rate of growth with radial distance.

The second hoped-for improvement to the model was in its ability to predict the NPR effect noticed in the raw data. When the model was plotted on a graph of $Y_{½}/D_n$ against NPR (Figure 4.11), it was clear that the gradient of the line was far too steep (approximately twice as steep as required). This was put down to the large amount of scatter encountered in these readings due to the use of the manual pressure regulation system. The predictions of Miller and Wilson (1993) are also included on the plot and it can be seen that although the gradient of the present correlation is wrong, it still gives a better prediction of the NPR effect in the range tested. If a better NPR term is required in the model, the tests would have to be repeated using the computer controlled system described in Phase Zero Plus onwards, in order to maintain an accurate NPR during the recording of the results. It has been suggest by Bray (1993) that the NPR effect is non-linear, he found that the ground vortex separation point of a wall jet in a cross-flow had two local peaks with varying NPR, one at around 1.8 and the other at around 3.0. The plot (Figure 4.11) also seems to agree with this trend, wall jet thickness being consistently thicker at NPRs of 2.0 and 3.0. Although it would be easy to suggest that there is a double peak to the NPR variation, there is by no means enough data to say this with any degree of confidence.

4.1.5 Phase Zero Summary

The new correlation presented above incorporates terms for nozzle height and nozzle pressure ratio effects and is shown to predict accurately wall jet growth with radial distance and against height of the nozzle based on the pitot/static data collected by Myszko (1993). The prediction of the NPR effect did not give as good a result as hoped, the gradient of the decrease in wall jet half thickness with NPR being too great. The large amount of scatter in the NPR results was the main cause of the inaccuracy.

4.2 Phase One

The following section describes results taken using experimental equipment and procedures detailed in Section 2.3. The data presented in this section represents 60 hours of data collection, each profile taking around 45 minutes to collect.

4.2.1 Free Jet 3-Dimensional Profiles

Using a single hot-wire, profiles at varying radial positions were taken in the free jet (nozzle set to H_n/D_n=10.0) at four fixed probe heights (H_p/D_n=2, 4, 6 & 8, H_p being the distance of the probe above the ground board), to form 3-dimensional profiles of the axial velocity and turbulence intensity.

When the velocity results where plotted (see Figures 4.12, 4.13, 4.14 & 4.15), it became clear that there was a problem with the nozzle exit profiles. Although the decay of the potential core and maximum velocity is clearly visible, the plateau caused by the potential core is slanted to one side. This is also shown on the turbulence intensity (defined with respect to the peak velocity recorded at the nozzle exit) profiles (see Figures 4.16, 4.17, 4.18 & 4.19), where the peak value in the shear layer surrounding the potential core is not uniform around the jet.

4.2.2 Free Jet Symmetry Profiles

To investigate this lack of symmetry in the jet profiles, further single hot-wire traverses were taken through the jet axial centre line. The table below lists the test conditions, traverse directions and nozzle orientations used (see also Figure 4.20):

Figure	Direction	Comments
4.21	D-B	
4.22	C-A	
4.23	C-A	Nozzle rotated through 180^0
4.24	E-C	Nozzle moved to second position
4.25	C-A	Nozzle in original position, new baffle in plenum
4.26	C-A	Modifications made to baffle
4.27	C-A	Run as twin nozzle to check pressure distribution in plenum
4.28	D-B	Re-check velocity distribution

From direction D-B (Figure 4.21), the profile looks reasonably good, except for an unexplained jump in the turbulence level in the potential core, but from direction C-A (Figure 4.22), the plateau shows the slant seen in the 3-dimensional plots. The velocity was high in the direction of the centre of the settling chamber dropping as the probe moved outwards. The turbulence intensity also shows the lack of symmetry commented on earlier. To try and isolate the cause of the problem, a number of tests were run.

1. **Nozzle Rotated by 180^0 (Figure 4.23)**: This did not seem to affect the profile at all, the slant still occurring in the same direction. This indicated that the problem was one of flow distribution in the settling chamber itself.

2. **Nozzle Moved to Second Position (Figure 4.24)**: In this position, the same slant in the velocity profile was measured, the direction also remaining the same (high towards the centre of the chamber). This led to the conclusion that because there was no baffle in the plenum to disperse the flow, the supply flow was entering the chamber and exiting straight down the nozzle, the profile being higher on the inside due to its closeness to the centre of the inlet pipe.

3. **Baffle Added to Plenum (Figure 4.25)**: A simple baffle was added to the centre of the settling chamber to redistribute the flow. This comprised a single sheet of perforated steel with the holes underneath the inlet pipe being blocked. The pressure tapping for the transducer was moved to below the baffle to remove any inaccuracy due to pressure drops across the sheet. As can be seen, this had a marked effect on the exit profile, the slant being almost removed. The profile still did not represent the top hat profile expected for a potential core flow and the turbulence profile still showed signs of asymmetry.

4. **Modified Baffle (Figure 4.26)**: The baffle was modified by the addition of a second perforated steel sheet added below the first to further distribute the flow inside the plenum. Again this caused a marked improvement in the exit profile, the corners of the top hat became sharper and more defined. The turbulence profile also improved, becoming far more symmetrical.

5. **Twin Nozzle Run (Figure 4.27)**: The chamber was run with both nozzles attached to see whether this would affect the pressure distribution in the chamber and hence the exit velocity profiles. Little change was noticed.

6. **Re-check of Velocity Distribution at 90^0 (Figure 4.28)**: The original velocity profile (direction D-B) was re-checked to see whether the baffle had changed the profile shape. A slight improvement was noticed when compared with Figure 4.21.

4.2.3 Wall Jet Symmetry Profiles

Checks were made to ensure that the wall jet flow was symmetrical following the changes made to the settling chamber. These were done using the Pitot probe rake and the equipment used in Phase Zero, the pressure control system, however, was the computerised version of Phase One. Profiles were taken at four equally-spaced azimuthal

positions at a radial location of r/D_n=20.0 for H_n/D_n=4.0 and NPR=1.05. Five profiles were also taken at the same azimuthal position under similar conditions to confirm the repeatability of the pressure measuring system.

Pressure profiles of the repeatability runs are shown in Figure 4.29(b) and profiles from the four different azimuthal positions in Figure 4.29(a). It was found that the difference in pressures at the four different locations was close to the repeatability of the readings. With this in mind, it was decided that as long as care was taken in the initial set-up of the chamber, the wall jet flow produced was symmetrical to within the capability of the measuring system used.

4.2.4 Free Jet Cross-wire Profiles

Having established an acceptably symmetrical exit velocity profile, free jet profiles were taken using the cross-wire at various H_p/D_n for H_n/D_n=10.0. Only half-profiles were taken as it was found that if the probe was inserted through the jet to measure the other half, probe interference became noticeable as the cross-wire probe was approximately twice as large as the single-wire probe. This showed itself as an audible change in the noise generated by the free jet and as an asymmetric turbulence profile (the Reynolds shear stress being particularly sensitive to this interference).

Non-dimensional mean U velocity component (see Figure 2.1) profiles are shown on Figure 4.30(a). This shows the standard top hat profile close to the nozzle exit decaying to the standard self-similar profile at H_p/D_n=5.0 and onwards, inferring that the potential core of the jet has decayed after 5 D_n from the jet exit. This is consistent with the results of Kataoka (1985) who showed that the optimum H_n/D_n for maximum Nusselt number (and hence maximum heat transfer) was around 5-6 D_n. This was where the potential core had decayed and the turbulence level at the centre of the jet had begun to rise.

Figure 4.30(c) shows the V velocity component of the free jet. It is interesting to note that the value is not zero in the potential core region as would be expected if there were no mixing there. As the U velocity profiles do in fact show a potential core, there

are two likely explanations. The most feasible is that the calibration on one of the two cross-wires was slightly out, having the effect of giving an inaccurate velocity reading over that wire. The data reduction program would then use this false velocity measurement to indicate that there was a slight angle to the flow direction, hence giving the non-zero V velocity component. The second explanation is that there was a W (tangential) component to the flow (i.e., there was swirl in the free jet or a W component induced by the probe support). As the V component was small compared to the U component, the error that the W flow would make in the readings would show up larger on Figure 4.30(c).

Figures 4.30(b) and 4.30(d) show non-dimensional turbulence profiles for the u and v components respectively. These show the development of the shear layer in the free jet as the probe is moved downwards, its width and the value of the turbulence growing. The value of the turbulence in the potential core and hence at the nozzle exit is around 5.0% (based on nozzle exit velocity) for both components, this is higher than the previously quoted value of 1.5% for the same settling chamber set up (Myszko 1993), which was measured with a single wire. As the k-ε CFD model requires the setting of the turbulence value for the velocity component at nozzle exit, it is recommend that a value of 5.0% is used for comparison with data obtained from this experimental set-up. These two figures also indicate that the nozzle was not set perpendicular to the ground board for these tests as at a probe height of H_p/D_n=5.0 & 4.0, the minimum value of the turbulence intensity does not occur on the jet axial centre line as should theoretically happen. This point is further supported by Figure 4.30(e) which shows the Reynolds shear stress profiles for the free jet. The value of the shear stress on the axial centre should be zero for all H_p/D_n, but it can be seen to be offset at all probe heights. There seems to be a small shear stress uniformly across the potential core, possibly due to the entrance of the flow into the nozzle pipe and due to the build up of a boundary layer in the nozzle pipe. The V velocity component error may also affect the reading as well as non-axisymmetric entrainment into the jet, possibly due to non-axisymmetric surroundings.

Figure 4.31 the variation of centre-line and peak values of mean and turbulent velocities as the probe is moved down stream as well as the free jet half thickness ($r_{½}$). Plot (b) show the level of scatter in the measuring the peak U velocity component and as such, do not show the constant velocity feature of the potential core in which these measurements were taken. Plots (c) to (e) show how the peak fluctuating value (located in the outer shear layer) increases with downstream distance in the jet and how the centre line value remains reasonably constant for the first 4 D_n downstream, after which, decay of the potential core results in rising turbulence levels.

4.2.5 Wall Jet Cross-wire Profiles

Non-dimensional wall jet V velocity component profiles are shown in Figure 4.32. As can be seen, all of the data collapse well to the standard self-similar profile after a radial position of $r/D_n > 2.0$. Before this, the flow is still turning within the impingement region, and so self-similarity is not obtained. The point at which similarity occurs is far closer to the jet axial centre-line than previously mentioned (Myszko 1993), this probably being due to the greatly increased accuracy of the pressure control and flow measuring system.

Figure 4.33 shows the non-dimensional U velocity component profiles at the four different H_n/D_n settings. Obtaining self-similarity for this component is far more difficult than for the V component due to its comparatively small magnitude, the accuracy of the calibration having a great effect on the results. It shows that after the impingement region has been cleared ($r/D_n > 2.5$ for H_n/D_n=10.0), the trend of the results is towards a self-similar profile, although there is a lot of scatter. The velocity at the wall (i.e., $Y/Y_{½}$=0.0) should be zero and this is not the case. There seems to be a small offset in the values on all the graphs, unlikely to be due to random experimental error because of its repeatability. The most likely explanation is the sensitivity of the cross-wire to small errors in its angle or small errors in the wire's calibrations. As the U component is very small compared to the V component (5% at best), any small error would have a disproportionately large effect on the U readings.

Non-dimensional turbulence profiles for the v and u components are shown in Figures 4.34 and 4.35 respectively. The v component profiles show that the maximum turbulence intensity is reached very quickly in the Y direction and remains high, having a flat portion, for a lot longer than the u component. The maximum turbulence intensity is of the order of 28-30% (of local maximum V velocity) for the v component and in the order of 20-22% for the u component (the square root has to be taken of the results on the graph to obtain turbulence intensity), which is consistent with published work (Padmanabham and Lakshmana Gowda 1991, Cooper et al. (1993)). The main feature of these two sets of profiles is that, although the mean velocity profiles attain similarity as soon as they leave the impingement region (within $r/D_n<2.0$), the turbulence properties do not reach similarity until at least $r/D_n>4.5$. This may be the criterion for the definition of the impingement region.

The Reynolds stress profiles (Figure 4.36) confirm this point still further, self-similarity not occurring until $r/D_n>4.5$ (profiles at $H_n/D_n=10.0$ clearly showing the influence of the free jet). It is interesting to note that the full shear stress profile for the boundary layer formed on the ground board was not measured, as the values should go negative and then return to zero. The measurements are deemed to have occurred at the point where the two hot wires cross; the wires extend below this point to the prongs, so there was a minimum ground plane/probe separation distance. At small values of r/D_n the boundary layer formed would be small, growing in size as the radial distance increases so it is unsurprising that the full profile was not measured at these relatively small radial positions. The values of peak non-dimensional shear stress were on average 30% higher than those reported by Padmanabham et al. (1991) for a planar wall jet run under similar nozzle conditions ($D_n=19.1mm$, $U_n=80ms^{-1}$ & $Re_n=9.54x10^4$).

The radial variation of the peak non-dimensional values of the measured mean and turbulent quantities are given in Figure 4.37. As can be seen, the value of H_n/D_n has a large effect on the peak value in the wall jet up to $r/D_n>4.5$ and as mentioned earlier this is the position where the turbulence quantities become self-similar. This self similarity is clearly shown as the values for the four different H_n/D_n collapse onto the same line.

This fact is important in the optimisation of the value of H_n/D_n for maximum heat and mass transfer. The best transfer occurs when the flow is highly turbulent, so aiding the transfer of heat and mass from the wall into the main flow. As the majority of heat transfer occurs within and close to the impingement region, the flow at $r/D_n>5.0$ is insignificant to heat transfer and hence the use of multiple arrays of jets. Moving the jet closer to the surface will increase the local Nu in the region around the impingement point. As stated in Chapter 1, the highest peak Nu occurs at a $H_n/D_n=5$ to 6 where the potential core has decayed and the turbulence level on the axial centre line begins to increase, but lower H_n/D_n should give better Nu values surrounding this point.

4.2.6 Wall Jet Spreading Rate

Figure 4.38 shows the radial development of the wall jet thickness, $Y_{\frac{1}{2}}/D_n$, for the four nozzle heights tested. Except for $H_n/D_n=4.0$, which does not seem to follow the trend of the other three, the observation of a height effect seems true. The rate of spread of the radial jet (i.e. the gradient of the lines) seems not to be affected by H_n/D_n; it is the initial thickness of the wall jet leaving the impingement region that seems to increase with increasing H_n/D_n.

This means that previous correlations for the prediction of the wall jet thickness (Poreh 1969, Hyrcak et al. 1972, Miller and Wilson 1991) are introducing inaccuracies, even if a height effect term is included (Figure 4.38 includes a comparison with the correlation derived in Phase Zero at $H_n/D_n=10.0$). All these correlations use a height effect term to change the gradient of the line, whereas it now seems that the height effect term should be used to offset the correlation, the gradient of the line remaining constant.

4.2.7 Zero Reynolds Stress compared with Peak Wall Jet Velocity

Figure 4.39 shows how the height of the peak V, mean wall jet velocity, and the height of zero Reynolds shear stress above the surface normalised with wall jet half thickness varies with radial location. For V, it can be seen that this relative height tends to decrease slightly with increasing r/D_n. For the higher H_n/D_n there is some indication that this value increases first, reaching a peak at around $3\text{-}4D_n$ and then decreasing, that

the wall jet inner boundary layer growing faster than the outer shear layer in the area of the impingement point. The value of $Y_{½}$ may be affected by the thicker free jet at these small radial locations, causing a distorted result.

The position of zero Reynolds shear stress also seems to decrease with radial location, although the amount of data is lower due to difficulties measuring the thin boundary layers at lower values of r/D_n. It is worth noting that the height of zero Reynolds stress is consistently around 30% lower than that of peak wall jet velocity, and hence zero velocity gradient. This is important for CFD modelling of this flow as the turbulence models used in the CFD phase of this work was based upon the hypothesis of Boussinesq (1877) (see Appendix B) which states that zero Reynolds shear stress occurs at the point of zero velocity gradient, which in this case is the point of peak velocity.

4.2.8 Wall Jet Momentum Flux

Wall jet momentum flux against radial location, r/D_n, for the four differing nozzle heights is shown in Figure 4.40. The value of M_f was calculated by the integration of the velocity profile obtained from the cross-wire results using:

$$M_f = 2 \times \pi \times r \times \rho \times \int_{0.0}^{0.8 \times V_m} V^2 dy$$

Equation 4.7

where ρ is the flow density. Previous work (Myszko 1993, Miller and Wilson 1993) has shown that the static pressure of the flow quickly returns to ambient conditions following impingement. Therefore, the density used here was calculated using the ambient conditions recorded at the start of the run.

The figure shows that the peak momentum flux occurs around r/D_n = 2.0 - 3.5, after which the value falls away due to decay of the measured wall jet profiles. It has to be noted that this plot does not show the increase in peak momentum flux as well as that recorded using pitot / static pressure probes by Myszko (1993). The most likely cause is

the variation in hot-wire calibration from one set of readings to another, exaggerated by the square term in the momentum flux equation.

4.2.9 Production of Turbulent Kinetic Energy

The production of turbulent kinetic energy (π) is shown as ground normal profiles in Figure 4.41 non-dimensionalised by the peak value in the profile (π_m) for different nozzle heights. It is clear that there is a lot more scatter in the results at a nozzle height of 4 D_n, this being consistent with results discussed earlier in this Phase. Although the profiles seem to take the same shape at H_n/D_n=4.0 as at other heights, the normalising $Y_{½}$ seems to be too small causing a stretching of the profile on the X axis. The three remaining profiles show the shape of the turbulence production profile in the wall jet, an initial production in the wall boundary region this dropping back at the peak V velocity region and then a large increase in the free shear region.

Figure 4.42a shows how the components of the production of turbulent kinetic energy vary against height above the ground board ($Y/Y_{½}$). As can be seen, it is the π_2 component which contributes to peak value of π. Therefore this indicates that it is work done by the rate of strain against the shear stress which accounts for the majority of the mean flow energy being converted to turbulent energy.

Figure 4.42b shows how the peak level of production varies with r/D_n. The peak level seems to occur at r/D_n between 1.5 and 2.5, the profiles seeming to converge to self similar values at around r/D_n=4.5. This compares well with the fluctuating velocity component profiles which also converged at this radial position. What is clear from the above graph is that as H_n/D_n decreases the production increases.

As the production of turbulent kinetic energy is an indication of the rate at which the mean velocity is dissipated to give turbulent energy, a higher value means that more of the energy contained in the mean flow is converted into turbulent energy. This suggests that as H_n/D_n decreases, the amount of energy contained in the mean flow of the wall jet is lower. It has been reported that at lower values of H_n/D_n, the momentum flux recovered in the wall jet is also lower (Schwantes 1973, Myszko 1993), this being

attributed to a less efficient turning process at lower H_n/D_n (Schwantes 1973, Miller and Wilson 1991). The recovered momentum flux was calculated using mean velocity measurements, but these data suggest that the energy stored in the mean flow, once self-symmetry of the profiles is obtained, is lower for lower H_n/D_n. As the change in value of the production occurs in the impingement region, it suggests that it is the conditions in the turning process which affect the recovery of wall jet momentum flux, this being consistent with the idea that at lower H_n/D_n the turning process is less efficient.

Figure 4.42c shows the variation of π_1 and π_2 profiles with H_n/D_n, again clearly showing that it is π_2 that changes with H_n/D_n, π_1 remaining fairly constant. This suggests that at lower nozzle heights, there is far greater shearing of the wall jet flow against the ambient air, so leading to a higher value of π_2. This is consistent with the observation that the wall jet thickness ($Y_{½}/D_n$) has a smaller initial value with lower H_n/D_n (Section 3.2.6), the change in the velocity gradient normal to the table (dV/dY) having to be greater because $Y/Y_{½}$ is smaller.

4.2.10 Phase One Summary

A dramatic improvement was noted in the settling chamber exit flow conditions following the insertion of the baffle and filter arrangement with a more uniform mean and turbulent velocity exit profile achieved with an exit turbulence intensity of 5.0%. Previous work using this chamber with a single nozzle (Bray 1992) should be treated with some degree of caution, especially at sub-critical NPR values (NPR < 1.89), and further investigations should be performed to see whether choking of the nozzle at NPR > 1.89 prevents the asymmetrical flow condition.

Mean wall jet velocity measurements indicate that self-similarity of the non-dimensional velocity profiles occurs soon after impingement, although nozzle height affects the exact radial location due to the thicker free jet entering the impingement region. For the largest nozzle height of 10 diameters, self-similarity is reached by r/D_n = 2.5 whereas for a height of 2 D_n, self-similarity occurs around r/D_n = 1.5. Nozzle height seemed to have a large effect of the peak wall jet velocity leaving the impingement

region, lower H_n/D_n cause a faster jet, although the peak velocity against radial location plots for the four different nozzle heights merged at $r/D_n > 4.0$.

The mean turbulent velocity components (both normal and shear stress) seem to reach self-similarity around $r/D_n = 4.5$, with a development region before this. Nozzle height appears to have a large effect on the level of turbulent fluctuations in this development region, the absolute levels being some 3 times higher for $H_n/D_n = 2.0$ compared with $H_n/D_n = 10.0$.

Wall jet half thickness was shown to grow almost linearly with radial distance, nozzle height seeming not the affect the rate of growth. The initial thickness of the jet leaving the impingement region was affect, increasing nozzle height causing an increased half thickness. This is believed to be due to the increased thickness of the free jet entering the impingement region at higher nozzle heights. There was a discrepancy in the experimental results concerning nozzle heights of 2 and 4 diameters and this data should be re-measured.

The production of turbulent kinetic energy was calculated for various radial locations and nozzle heights. Plots for differing r/D_n show that production of turbulent kinetic energy is self-similar in nature when non-dimensionalised with peak production at that radial location and wall jet half thickness although the results for $H_n/D_n = 4.0$ show considerably more scatter than other heights. Close to the wall, it is the normal stresses that account for most of the production where as above $Y/Y_{½} \approx 0.3$, it is the Reynolds shear stress that is the dominating factor. The increased shear stress at lower nozzle heights mentioned above causes a large increase in the production of turbulent kinetic energy at lower nozzle heights.

4.3 Phase Two

This section details measurements taken in Phase Two of the research project. The experimental apparatus and procedures used are detailed in Section 2.4

4.3.1 Ambient and Settling Chamber Conditions

For each profile, the ambient and settling chamber conditions were recorded whenever a sample was taken. Figure 4.43 shows typical ambient and settling chamber records for recorded wall jet profiles as well as the fluid flow temperature recorded which was used for the temperature compensation of the cross-wires. The data presented in Phase 2 represents over 550 hours of data collection, with a typical profile taking between 6 and 7.5 hours to acquire depending on the turbulence intensity of the flow in question.

For the 76 profiles taken and discussed in this section, the average atmospheric pressure was record as being 1.005 bar (753.59 mmHg), the highest and lowest recorded values were 1.017 bar (762.16 mmHg) and 0.983 bar (736.95 mmHg) respectively. The largest and smallest change during any one profile were 7.85 mbar (5.88 mmHg) and 0.33 mbar (0.25 mmHg) respectively. This recorded large change in atmospheric pressure of 7.85 mbar has justified the expense of fitting the atmospheric barometer to the pressure control system. The average atmospheric temperature recorded was 20.52 ^{0}C with the highest and lowest recorded values being 26.98 ^{0}C and 16.45 ^{0}C respectively. During any one profile, the largest and smallest change in atmospheric temperature were recorded as 3.05 ^{0}C and 0.30 ^{0}C.

The settling change temperature plot shows the dramatic temperature rise that can occur when using the centrifugal fan unit from cold. In this particular plot, the settling chamber temperature rose by 3.5 ^{0}C during the acquisition of the data, this being a typical value for most of the profiles. The largest single change was recorded at 10.38 °C, changes of this magnitude occurring on the first run of the rig after a weekend. Usually, the equipment would be left to run overnight collecting data and would finish around 5.00am. As the next profile would be started at around 8.00am the next morning, the fan would not have completely cooled down, so reducing the overall temperature rise. The equipment was rarely run over the weekend, and so the first run on the Monday morning would be with a fan unit at ambient temperature, hence giving the largest settling

chamber rise. A conscious effort was made to keep these large temperature increases to a minimum.

Fluid flow temperature across the impingement surface, and so the temperature used in the compensation for the cross-wires, followed the settling chamber trends closely. The average temperature recorded was 20.66 °C with the highest and lowest recorded values being 27.57 °C and 17.39 °C with the largest and smallest changes during any one profile being 4.38 °C and 0.56 °C respectively.

4.3.2 Non-Dimensional Wall Jet Profiles

Figure 4.44 shows non-dimensional V velocity component wall jet profiles similar to those in Phase 1 shown in Figure 4.32 and discussed in Section 4.2.5. The profiles show the same trend of self-similarity of the profile occurring shortly after impingement. For low nozzle heights ($H_n/D_n \leq 4.0$), it is only the profile at $r/D_n = 1.5$ which is distinguishable from the other profiles, although for plot (b), the profile at $r/D_n = 2.0$ is not included due to an experimental error. At $H_n/D_n = 8.0$ (plot c), profiles at low r/D_n are affected by the presence of the free jet which is wider due to the increased distance in which it can spread before impingement. It is unfortunate that at a height of $H_n/D_n = 10.0$ (plot d), all the inner radial location profiles have to be discarded due to errors made in their measurement. It is believed that the trend of self-similarity occurring later for higher nozzle to ground separation would continue in plot (d) as it had in the Phase 1 data (Figure 4.32).

Figure 4.45 shows how the non-dimensional profiles for Phase 1 and 2 differ, in this case the profiles are for $H_n/D_n = 8.0$ and $r/D_n = 8.0$ although the trend shown here is repeated in all the data. The Phase 2 profile has a peak velocity which occurs at a lower $Y/Y_{½}$ than previously shown, a shear layer which follows the Phase 1 data closely when the effect of the lower peak velocity height is taken into account and returns to a lower ambient velocity at higher $Y/Y_{½}$. There are a number of factors which could account for these differences in the profiles. There was a considerable amount of improvement performed on the experimental rig going from Phase 1 to 2 (Chapter 2), with improved

traverse performance, pressure control and data acquisition and sampling. Another major change was the replacement of the Howden compressors with the centrifugal fan unit as a source of compressed air for the settling chamber. It is believed by the author that the turbulence intensity of the jet at nozzle exit is lower for the fan than for the Howden compressors, although no precise measurements to confirm this point were taken using this settling chamber.

There are two factors which have lead the author to this conclusion. Firstly, the route the supply takes from the Howden compressors to the settling chamber is very tortuous, being in excess of 100 metres in length, with numerous changes in pipe diameter and many isolation valves and branch junctions before reaching the nozzle pressure control system. The centrifugal fan unit, on the other hand was connected to the pressure control system by a length of 4 metre rubber hosing which formed a smooth passage from the fan exit to the control valve. The second factor is that measurements performed in a similar study using this rig, but with a different settling chamber, showed lower exit turbulence intensities than would have been expected if the Howden compressors were used (Kirkham 1996). In Kirkham's work, an exit turbulence intensity of 0.4% was measured using Phase 2 equipment. It is not the author's intention to claim this as the exit turbulence intensity for the Phase 2 work, as the differences in the settling chamber design and construction are too great, but it does tend to infer a reduced turbulent component to the flow. This reduced turbulent component would reduce mixing with the ambient fluid and hence cause a jet with a different turbulence profile to enter the impingement region. Computational work presented later indicates that nozzle exit turbulence intensity has an effect on wall jet development.

Other factors which might be felt to account for the differences are associated with the rig improvements made for Phase 2. The traverse and position system was improved, but any position setting errors would show as an offset between the two profiles. Improved sampling techniques were used, although these are most likely to show in the turbulence profiles where sample frequency and period are far more important. Finally, hot-wire calibration was improved in Phase 2 with temperature compensation of the CTA

signal being used. This became necessary due to the heating effect that the centrifugal fan had on the nozzle exit flow.

The differences between the two Phases are important and need further investigation to be sure of the answer. The computational study reported in Chapter 5 has shown that exit turbulence intensity does have a predicted effect on jet flow factors and precise measurements of the flow conditions leaving the nozzle using the centrifugal fan need to be made.

Figure 4.46 shows Phase 2 non-dimensional v turbulent velocity profiles for the wall jet similar to those in Phase 1 (see Figure 4.34). It shows the development of the turbulence profile up to its self-similar value of 0.10 to 0.12 (giving a wall jet turbulence intensity $\sqrt{\overline{v^2}} / V_m$ of around 30%). It is clear when comparing the Phase 1 and 2 data that the later set of results have taken longer to reach self-similarity, in excess of r/D_n = 12.0 for Phase 2 compared with $r/D_n = 5.0$ for Phase 1. This is shown very clearly on Figure 4.47 (a) where a turbulence profile from Phase 1 and one from Phase 2 recorded under similar parametric conditions are compared. It shows that at the same radial location, there is a lower recorded turbulence level in Phase 2 compared to Phase 1. There are a number of possible reasons for this discrepancy. Firstly, an error could have been made in the calibration of the hot-wires for either phase of the project although this is unlikely due to the consistency of the difference over all the profiles. Secondly, the improved sampling period and length have enabled a more realistic turbulence level to be recorded. Finally, the turbulence level was lower to start with and hence takes time to develop to the levels seen in the self-similar profiles. It is the belief of the author that the explanation is most likely to be a mixture of these last two points.

Figure 4.47 (b) compares Phase 2 data with that of Guitton (1968) who performed accurate measurements in a 2-dimensional planar wall jet in still air using normal, slanted and cross-wires. As can be seen, the peak level of fluctuation is around 2.5 times smaller for the planar jet results, although it has to be stated that the profile of Guitton is at a far greater radial distance and the Reynolds number of his jet (based on slot height) is lower (3.1×10^4).

Figure 4.47 (c) compares Phase 2 data with that of Cooper et al. (1993) who collected cross-wire data for CFD validation in the impingement region of an impinging jet. The developing wall jet was generated by a 4" nozzle running at a nozzle exit Reynolds number of 7.1×10^4 at $H_n/D_n = 2.0$. The main difference between the data was the fully developed pipe flow profile at the nozzle exit in the Cooper et al. data. This would cause increased turbulence levels in the free jet before impingement compared to the Phase 2 data at a similar nozzle height. This is shown in the figure by the higher values of the fluctuating velocity in the Cooper et al. data. On the same plot is included the Phase 2 profile at $H_n/D_n = 10.0$ (and at a slightly larger radial distance from the impingement point) which shows slightly better agreement with Cooper et al. The higher nozzle height results in greater development of the free jet profile before impingement, in particular, the potential core has decayed before impingement, in contrast to $H_n/D_n=2.0$ where the potential core is impinging on the ground. This leads to the impingement region entry profile being closer for $H_n/D_n=10.0$ to that generated by the fully developed pipe flow exit condition.

Figure 4.48 shows the development of the turbulence profile in more detail, in this case for a nozzle height of 8.0 D_n, although the trend was repeated at the three remaining heights. Close to the stagnation point ($r/D_n < 4.5$), the peak value of turbulence occurs at a high value of $Y/Y_{½}$ in the profile, this being most likely due to the shear layer of the free jet penetrating the wall jet. At low values of $Y/Y_{½}$, the turbulence level seems to be constant with profile height, the value of turbulence growing with r/D_n. As r/D_n increases, a second peak seems to develop corresponding to the growth of the inner boundary layer of the wall jet profile. This second peak develops until it reaches the same magnitude as the peak due to the wall jet outer shear layer. At $r/D_n = 20.0$, the furthest profile measured away from the stagnation point, the dip in the turbulence profile corresponding to the peak wall jet velocity has not diminished to form a profile similar to those measured in Phase 1. It is believed that the longer sampling time used in Phase 2 has enabled a far more accurate profile to be measured when compared with those of Phase 1.

Figure 4.49 shows the surface-normal velocity fluctuations in non-dimensional form, similar to those of Phase 1 shown in Figure 4.35 with a direct comparison for one representative profile in Figure 4.50 (a). Similar to the stream-wise velocity fluctuation profiles discussed above, the peak recorded level is far lower for Phase 2 than Phase 1, with the level of change seeming to be even higher for this component. Figure 4.50 (b) shows a comparison with the data of Cooper et al. (1993) and, similar to the v turbulent velocity comparison in Figure 4.47 (c), the peak level of fluctuation is far lower for the Phase 2 data. This is believed to be due to the fully-developed pipe flow velocity profile at nozzle exit used by Cooper et al. Figures 4.51 and 4.52 show the development of the turbulent profile in more detail for two differing nozzle heights, one low and one high. For the low nozzle height of $H_n/D_n = 2.0$ (Figure 4.51), the development of the profiles at low r/D_n values is similar to those of the v turbulent component, with a peak occurring in the outer wall jet shear layer and a uniform value section close to the wall. As r/D_n increases, this uniform section reduces in height but increases in magnitude until around $r/D_n = 9.0$ where a profile is formed similar in shape to those of Phase 1. For the higher nozzle height of $H_n/D_n = 8.0$ (see Figure 4.52), this uniform section seems not to exist, the turbulence level increasing from the wall up to a peak in the outer shear layer and then falling away to ambient. This is most likely due to the fact that the potential core of the free jet, an area of constant velocity and low turbulence intensity has decayed away at these higher nozzle heights causing a fully turbulent free jet to impinge. These increased turbulence levels are then transmitted through the impingement process and into the developing wall jet.

Figure 4.53 shows the non-dimensional Reynolds shear stress profiles similar to those measured in Phase 1 and plotted in Figure 4.36. It is noted that far more of the negative shear stress (relative to the co-ordinate system used here) has been measured and resolved by the improvements in the experimental rig, this negative section being due to the shearing in the wall jet inner boundary layer. The positive peak, due to shearing in the wall jet outer layer is slightly lower in magnitude than Phase 1. This is confirmed in Figure 4.54 (a) where a comparison is made between Phase 1 and 2 profiles for the same geometric conditions. The positive peak is lower in magnitude and higher in position and forms a profile which is taller overall. Figure 4.54 (b) shows Phase 2 data compared with

the planar wall jet data of Guitton (1968) while plot (c) shows the radial wall jet data of Cooper et al. (1993). Once fully developed, the Phase 2 shear stress profiles have a peak value around 30% higher than those reported for planar jets, agreeing with previously published data (Launder 1983). Similar to the normal stress, the peak shear stress of Phase 2 when compared to Cooper et al.(1993) is far lower, this being attributed to the increased turbulent properties of the fully developed pipe flow nozzle exit condition used by Cooper et al.

4.3.3 Variation of Peak Wall Jet Values

Figure 4.55 shows how peak non-dimensional velocity values compare with the data collected in Phase 1. Plot (a) shows variation of peak wall jet velocity with radial location. Close to the impingement point, the recorded Phase 2 data is some 20% lower than the Phase 1 measurement, although it does show the same trend of falling rapidly with increasing r/D_n. Plots (b) and (c) show the turbulent normal stresses, $\overline{v^2}$ and $\overline{u^2}$, respectively. The Phase 2 measured peaks are dramatically lower than those of Phase 1, the peaks being removed by the late development of the turbulence profiles to their self-similar shape discussed in the earlier section. The peak in turbulence level also seems to occur later, i.e. Phase 2 peaks at around $r/D_n = 3.5 - 4.0$ compared to $r/D_n = 2.5$ for Phase 1.

Plot (d) compares the Reynolds shear stress between the two phases. As can be seen, the Phase 2 data has a slightly smaller peak value which occurs at a $r/D_n = 4.5$ compared with the peak at $r/D_n = 2.0$ for Phase 1.

4.3.4 Wall Jet Half Thickness

Figure 4.56 shows wall jet half thickness ($Y_{½}/D_n$) against radial location for the four differing nozzle heights. Similar to the Phase 1 data (see Figure 4.38 and Section 4.2.6), the plot shows the almost linear growth of wall jet thickness with radial distance. Like the Phase 1 data, nozzle heights of 2 and 4 diameters do not follow the trend of

increasing thickness with increasing H_n/D_n, the wall jet at a height of 4 D_n being thinner than that at a height of 2 D_n.

When compared to the half thickness calculated and plotted in Phase 1 (see Figure 4.57), it is clear that the Phase 2 wall jet is consistently thinner than that previously measured, although the rate of growth seems to remain the same. It appears to be the initial thickness of the wall jet leaving the impingement region that is causing the reduced value of $Y_{½}/D_n$. This is consistent with the peak in the non-dimensional wall jet profile occurring at a lower $Y/Y_{½}$ as discussed in the previous section. The reduction in initial wall jet thickness is consistent with the idea of a thinner free jet before impingement, possibly due to a reduced exit turbulence intensity.

Figure 4.58 compares the effect of nozzle height on wall jet half thickness for Phases 1 and 2. As mentioned above, the Phase 1 values are consistently higher than those for Phase 2, but both show a trend of increasing $Y_{½}/D_n$ with H_n/D_n (above H_n/D_n=4.0), the Phase 2 data in particular show this effect well at the larger radial locations. The discrepancy in this trend shown in Figures 4.56 and 4.38 for nozzle heights of 2 and 4 D_n is also clearly shown, with a turn-up in the line at $H_n/D_n = 2.0$ compared to $H_n/D_n = 4.0$. It appears to be that at a nozzle height of 2 diameters, a slightly thicker wall jet is produced although this is not as clear for the Phase 1 data (Figure 4.38).

4.3.5 Wall Jet Frequency Spectra

Following publication of the Phase 1 data, it was suggested that the apparently-anomalous wall jet thickness at $H_n/D_n = 4.0$ might be associated with impinging jet instability which can occur at certain critical nozzle heights. To investigate this, the spectral content of the Phase 2 hot-wire data was examined to see if there was any obvious variation with height.

Figure 4.59 shows a typical frequency spectrum calculated from the recorded sample data, one of these spectra generated for each sample position in a wall jet profile. The raw data were reduced using a Fast Fourier Transform (F.F.T) computer routine

which was written by Dr M. V. Finnis (the details of which are described in Appendix A). The plot shows the large range of frequencies that were present in the sample flow.

The frequency data were non-dimensionalised as a Strouhal number which has been used in the past to present frequency data for jets in cross-flow and impinging jet surface pressure fluctuations (Wilson 1995). Strouhal number is defined as:

$$St = \left[\frac{f l_m}{U}\right]$$

Equation 4.8

where l_m is a characteristic length scale and U is a characteristic velocity. In the case of this project, the wall jet half thickness, $Y_{½}$, and wall jet peak velocity, V_m, for each profile are used as the non-dimensionalising parameters.

Figure 4.60 shows a plot of Strouhal number against profile height for a number of radial locations at the same nozzle height, the remaining nozzle heights showing the same trends. The plots were generated by fitting a cubic-spline to the frequency spectra generated at each sample point (similar to Figure 4.59), finding the maximum frequency at that sample point and using that to generate a Strouhal number profile for that radial location. At low r/D_n, the Strouhal number profile indicates peak frequencies occur in the incoming shear layer with low frequency fluctuations near the wall, presumably due to the viscous damping effect close to the wall. As r/D_n increases, the peak magnitude of $St(f_m)$ also increases up to around a Strouhal number of 0.10 to 0.12. The magnitude of the Strouhal number close to the wall also increases rapidly between $r/D_n = 3.5$ and $r/D_n = 5.0$ to close to the peak value.

Figure 4.61 shows how the peak Strouhal number from a profile varies with radial location and for differing nozzle heights. St_m based on f_m rises rapidly from the impingement point up to a value of 0.16 at around a $r/D_n = 8.0$ -10.0 after which, it seems to remain reasonably constant at a round 0.16. It is clear that there are no unusual frequencies occurring at any of the heights tested.

4.3.6 Phase Two Summary

Cross-wire hot-wire anemometry measurements made in this phase confirm the rapid development of the self-similar wall jet velocity profiles, self similarity occurring before $r/D_n = 2.5$ to 3.0. There are differences between the Phase 1 and Phase 2 velocity profiles, the Phase 2 results indicating a wall jet with peak velocity that is closer to the wall and lower in magnitude. The development of the turbulent velocity profiles also differs from that of Phase 1, with self-similarity not occurring until $r/D_n = 9.0$. Peak values of normal and shear stresses non-dimensionalised with nozzle exit velocity show that levels of turbulent fluctuations in the Phase 2 wall jet are lower than those of Phase 1. The lower peak wall jet velocity results in a local wall jet turbulence intensity at a radial location, once self-similarity has been reached, of approximately the same magnitude as Phase 1.

The improvements made to the data collection system, and especially the increased sample times used in Phase 2, have improved the resolution of the turbulence profiles. These now show a damping effect on the turbulent fluctuations close to the wall when at small radial distances from the stagnation point, this effect seeming to be stronger at lower nozzle heights. Wall jet turbulence profiles at large radial distances indicate that the inner boundary layer has a level of turbulence similar to that in the outer shear layer, a dip occurring in the turbulence profile at the point of peak velocity.

The wall jet half thickness was lower than that measured in Phase 1 although the rate of growth of the wall jet was comparable, consistent with the non-dimensional wall jet profiles having a peak velocity closer to the surface. The Phase 2 data again suggests a discrepancy in the height effect for $H_n/D_n = 2.0$ and 4.0 similar to that shown in Phase 1. With the greater consistency of the Phase 2 data, it now appears that the anomalous wall jet height effect may be at $H_n/D_n = 2.0$, caused by a thicker wall jet leaving the impingement region, rather than an unusually thin wall jet at $H_n/D_n = 4.0$. More nozzle heights would need to be tested in this region to confirm this conclusion.

4.4 Phase Three

This section describes wall jet measurements taken above a moving surface for differing nozzle heights. The surface speed was fixed at 10ms^{-1} with an NPR = 1.05.

4.4.1 Ambient and Settling Chamber Conditions

During each run, ambient and settling chamber conditions were recorded at the time of each sample. Figure 4.62 shows typical plots that where acquired over the length of a profile, the typical time for which being around 60 minutes. This data presented in Phase 3 represents a total of 155 hours of data collection.

For the 162 profiles taken in this phase of the research, the average atmospheric pressure was 1.007 bar (754.78 mmHg), the highest and lowest recorded values being 1.010 bar (764.52 mmHg) and 0.987 bar (739.54 mmHg) respectively. During any one profile, the largest and smallest changes were 1.15 mbar (0.862 mmHg) and 0.07 mbar (0.052 mmHg) respectively. The average atmospheric temperature was 21.87^{0}C, the highest and lowest recorded values being 27.95^{0}C and 13.65^{0}C respectively, the largest and smallest changes being 8.97^{0}C and 0.14^{0}C respectively.

The settling chamber temperature recorded at the time of a sample shows the dramatic heating effect that the centrifugal fan has on the nozzle flow. The average settling chamber flow temperature for this phase was 25.66^{0}C, the highest and lowest recorded values being 32.89^{0}C and 16.01^{0}C respectively, the largest and smallest changes during any one profile being 6.31^{0}C and 0.48^{0}C respectively. A recommendation for future work using this system is to allow the fan to run for at least 1 hour at normal flow conditions to allow the settling chamber temperature to reach steady state.

4.4.2 Wall Jet Profiles

Figures 4.63, 4.64 and 4.65 show non-dimensional wall jet profiles at the three different nozzle heights for the three different ground speeds (V_g = -10.0, 0.0 & 10.0 ms^{-1}). At V_g = 0.0 (Figures 4.63(b), 4.64(b) & 4.65(b)), the wall jet profiles collapse onto

the standard non-dimensional shape with a defined inner boundary layer, followed by a peak velocity at around $Y_{½}/D_n = 0.2$ and then a free shear layer with velocity decay to ambient conditions. At low values of r/D_n, the profile is affected by the presence of the free jet, self-similarity being reached at $r/D_n = 4.0$ for the worst case of $H_n/D_n = 10.0$, this following the trends discussed in the previous sections.

For a $V_g = -10.0$ ms^{-1} (Figures 4.63(a), 4.64(a) & 4.65(a)), the profile shape is very different, with a very thin inner boundary layer formed, due to the reduced wall shear stress. It has to be noted that on most of the r/D_n profiles taken at $V_g = -10.0$ ms^{-1}, an inner boundary layer was not measured, the first point of the profile having the highest velocity. This would obviously happen at large r/D_n, where the wall jet peak velocity has decayed to that of the moving surface (in this case 10.0 ms^{-1}), but at low r/D_n the boundary layer was so thin that it could not be resolved with the experimental apparatus used. This has implications for the wall jet half thickness where the peak velocity is required, a low V_m causing too high a value of $Y_{½}$ to be calculated.

For a $V_g = 10.0$ ms^{-1} (Figures 4.63(c), 4.64(c) & 4.65(c)), profiles at low r/D_n are little affected by the surface speed with the formation of the inner boundary layer and outer shear layer. At $r/D_n \approx 7.0$, the inner boundary layer grows quickly and by $r/D_n \approx 8.0$, separation of the boundary layer from the surface occurs with a very turbulent velocity profile formed. The profiles for $V_g = 10.0$ tend not to become self-similar unlike $V_g = 0.0$, as r/D_n increases, the non-dimensional velocity profile becomes thinner, the non-dimensional velocity gradient in the outer shear layer increasing. The separation of the wall jet is shown more clearly on Figure 4.66 where the velocity profiles around the separation point are shown in dimensional terms. These plots show how the development of the velocity profile changes rapidly between $r/D_n = 8.0$ and 9.0. All three plots on Figure 4.66 show the dramatic decrease in peak velocity and increase in profile height going from 8.0 to 9.0 diameters from the stagnation point.

4.4.3 Effect of V_g on Wall Jet Half Thickness and Peak Velocity Decay

Figures 4.67, 4.68 and 4.69 show wall jet half thickness (a) and wall jet peak velocity (b) at the three different surface conditions for the different nozzle heights. The plots of $Y_{½}/D_n$ against r/D_n shows how for a V_g = -10.0, a far thinner wall jet is formed due to the reduced surface shear stress causing a reduced inner boundary layer. It is worth remembering at $Y_{½}/D_n$ for V_g = -10.0 may be too high due to difficulties in measuring the peak profile velocity (see section 4.4.2).

The decay of peak velocity plots for the three different nozzle heights all show the same trend. For V_g = -10.0, the decay is similar to the zero ground speed condition for low r/D_n, the decay reducing at around r/D_n = 4.0 causing a faster jet than for V_g = 0.0. All three heights show that V_g = -10.0 had the lowest peak velocity leaving the impingement region, approximately 7-8 ms^{-1} (10%) slower than for V_g = 0.0 although this could be due to the uncertainties over the value of the peak velocity for this surface speed.

The decay of velocity when V_g = 10.0 also follows closely the decay when V_g = 0.0, the line departing the base condition around r/D_n = 7.0, this being consistent with the separation of the boundary layer described in the above sections. Hereafter, the peak velocity decays at a much faster rate due to the rapidly increasing mixing with the ambient fluid. It has to be noted that although no cross-flow as described in Chapter One was used in these tests, the moving surface would have a tendency to drag fluid along with it due to viscous forces. This would cause an ambient fluid flow, and hence fluid momentum, to stagnate against the wall jet. Due to the method of generation of this "cross-flow" profile, it would be predominately low in height and so have the greatest effect on the inner boundary layer region on the wall jet profile. Therefore it is not possible to state whether the separation is due to the increased shear or "cross-flow" momentum. Further detailed measurements would be required in the wall jet around separation and measurement of the ambient fluid profile close to the surface to answer this question.

Following separation, this ambient flow would increase mixing by causing two free flow shear layers on the wall jet flow, an outer wall jet layer developing from the stagnation point and an inner layer due to ambient flow getting underneath the profile because of the separated region of flow. This is shown to some degree on Figure 4.66 where profiles for $r/D_n = 9.0$ show a marked dip at low profile heights and a point of inflection in the velocity gradient dV/dY. This increased turbulence generation would cause greater mixing with the ambient fluid and hence a rapid increase in peak wall jet velocity decay.

4.4.4 Effect of H_n/D_n on Wall Jet Half Thickness and Peak Velocity Decay

The effect of nozzle height on the wall jet half thickness against radial distance (see Figure 4.70) is consistent with previous results discussed in earlier sections. Increasing H_n/D_n caused the wall jet initial thickness to increase for all three surface speeds (v_g = -10.0, 0.0 & 10.0 ms^{-1}). Figure 4.70 (c) clearly shows the separation of the wall jet from ground plane, around $r/D_n = 7.5$, with the sudden increase in the rate of growth of the half thickness. It shows that the wall jet at $H_n/D_n = 4.0$ separates first followed by 8.0 and then 10.0, although the difference is small.

Figure 4.71 shows how wall jet peak velocity decays with radial distance for different nozzle heights and how that changes for differing surface speeds. Trends shown here for the nozzle height effect are consistent with those discussed in previous sections.

4.4.5 Wall Jet Momentum Flux

Wall jet momentum flux was calculated for these profiles in a similar way to Phase One (see section 4.2.8) by the integration of the velocity profiles at a fixed r/D_n. Figure 4.72 (a) shows the effect different surface speeds have on the momentum flux at H_n/D_n=10.0, the two remaining nozzle heights showing the same trends. For a V_g=-10.0 ms^{-1}, the decay of momentum flux with radial distance is reduced due to the decreased shearing of the wall jet inner boundary layer compared with V_g=0.0. For the case of

V_g=10.0, the rapid decay of the wall jet at around r/D_n=7.0 is clearly shown with a dramatic decrease in the measured momentum flux.

The variation of momentum flux for different nozzle heights is shown in Figure 4.72(b) for V_g = 10.0 ms^{-1}. The nozzle height effect of lower momentum flux in the wall jet for low H_n/D_n is shown clearly with the rapid decrease in momentum flux after r/D_n = 7.0. This supports the evidence discussed in previous sections for the wall jet separation occurring earlier at low nozzle heights.

4.4.5 Phase Three Summary

This preliminary investigation of the development of a radial wall jet on a moving surface has shown a number of interesting features. The wall jet profile formed when V_g = -10.0 ms^{-1} (i.e. surface moving away from the impingement point with the wall jet) has a very thin inner boundary layer region, causing difficulties in measuring accurately the peak profile velocity. When V_g=10.0 ms^{-1} (i.e. surface moving towards the impingement point against the wall jet), the initial development seems very similar to the case with the surface is stationary (V_g = 0.0). At round r/D_n = 4.0, an increase in the wall jet half thickness is noticeable over the stationary case and at r/D_n = 7.0 there is a sudden rapid increase. This is believed to be due to the separation of the wall jet inner boundary layer due to the increased surface shear stress causing dramatically increased turbulence generation and mixing with the ambient surrounding. The wall jet momentum flux has also been investigated and is consistent with the above.

A more detailed investigation now needs to be performed, using cross-wires or Laser Doppler Anemometry (L.D.A.) to measure the turbulent quantities involved in this process.

BLANK IN ORIGINAL

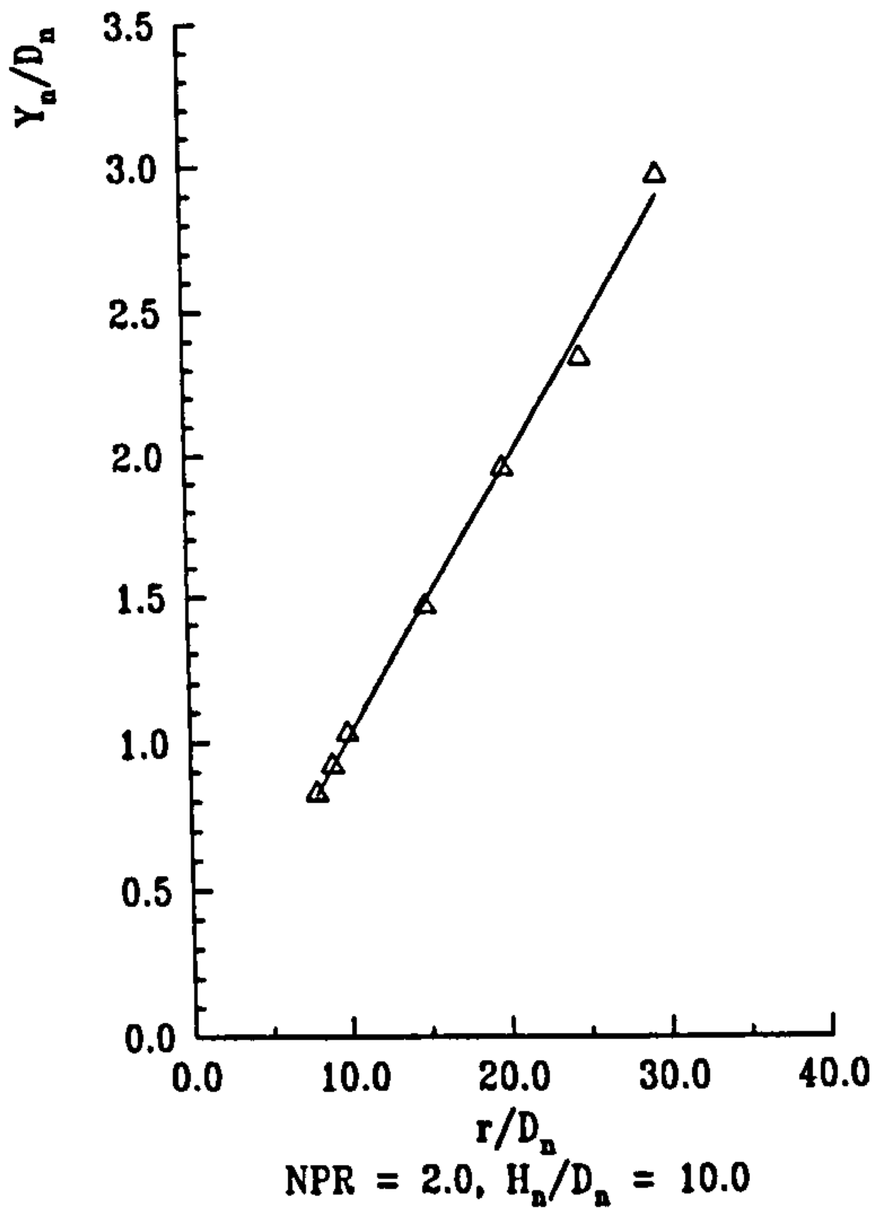

Figure 4.1 : Variation of Wall Jet Thickness with Radial Distance

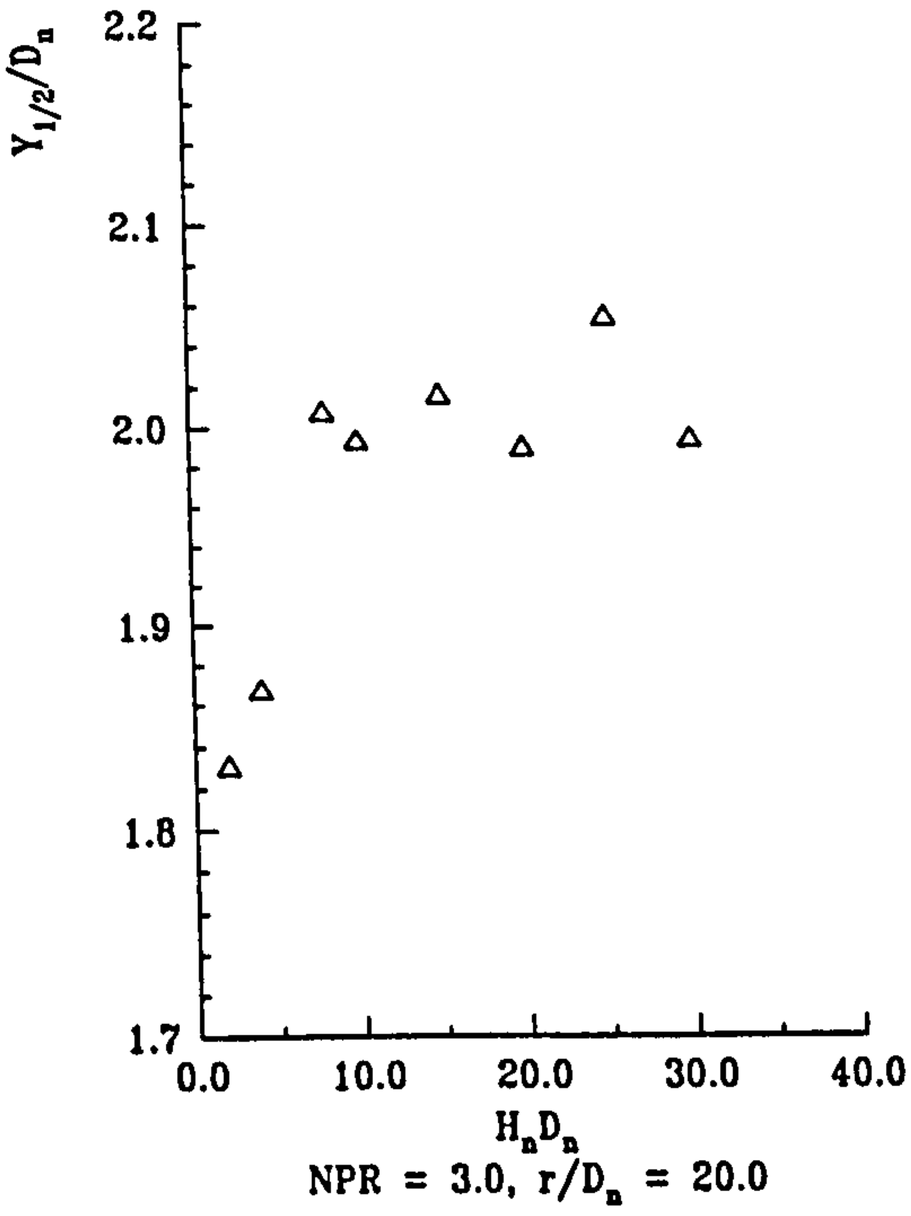

Figure 4.2 : Variation of Wall Jet Thickness with Nozzle Height

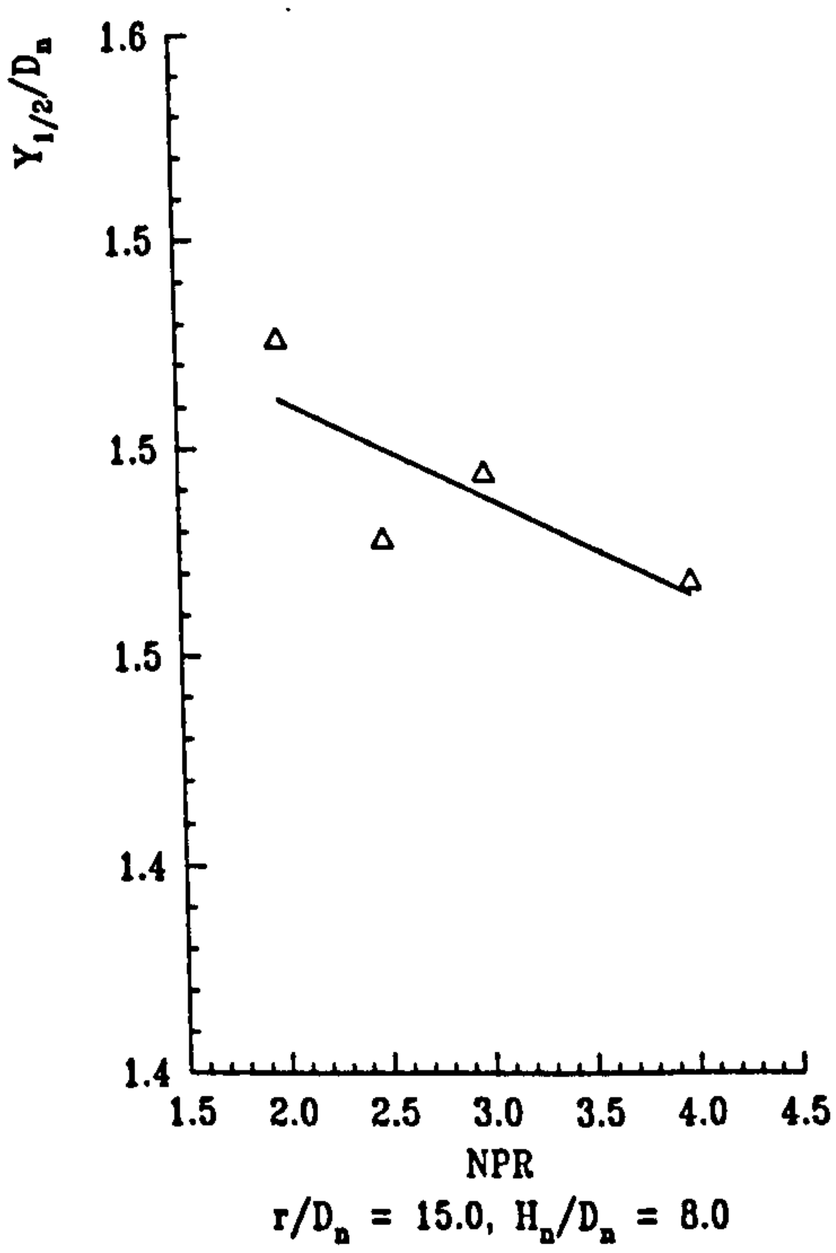

Figure 4.3 : Variation of Wall Jet Thickness with Nozzle Pressure Ratio

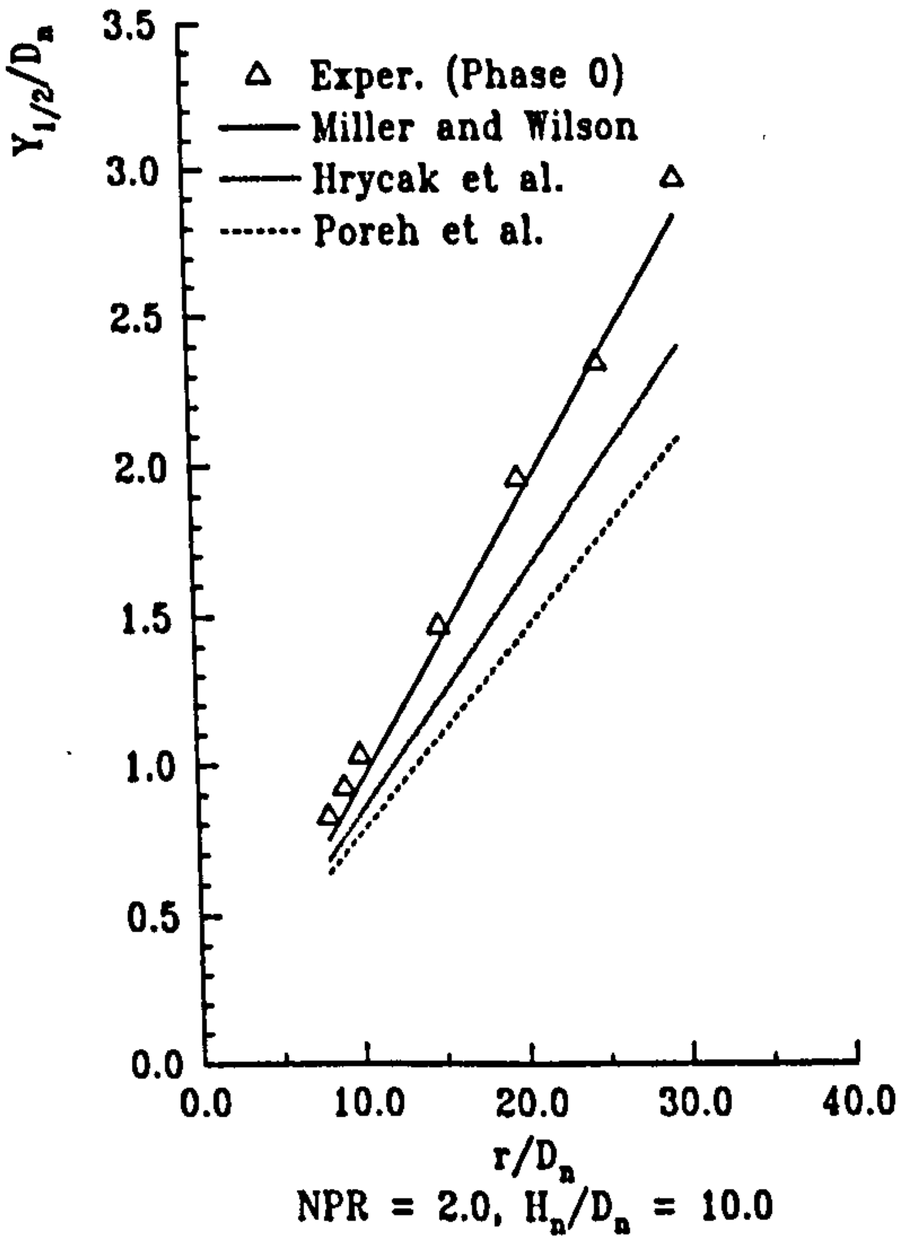

Figure 4.4 : Comparison of Phase 0 Data with Previous Correlations

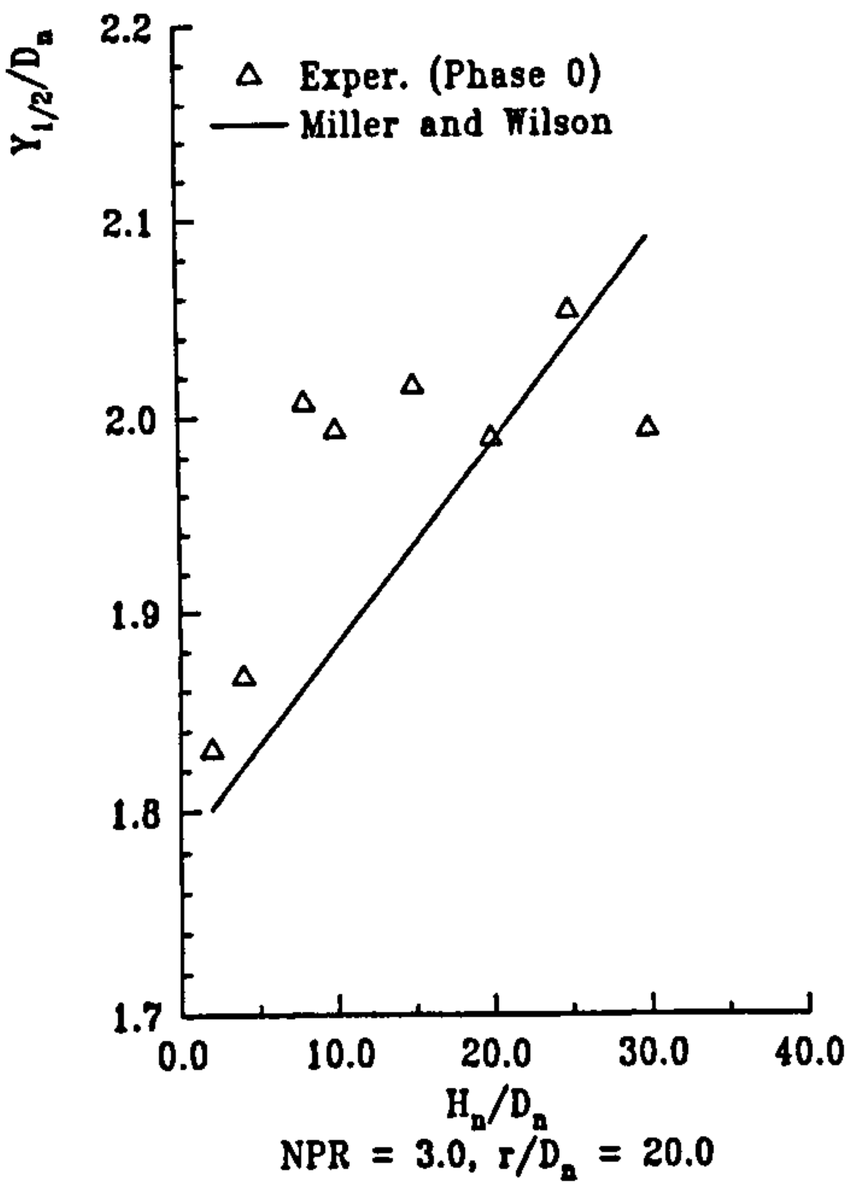

Figure 4.5 : Comparison of Height Effect with Correlation of Miller and Wilson

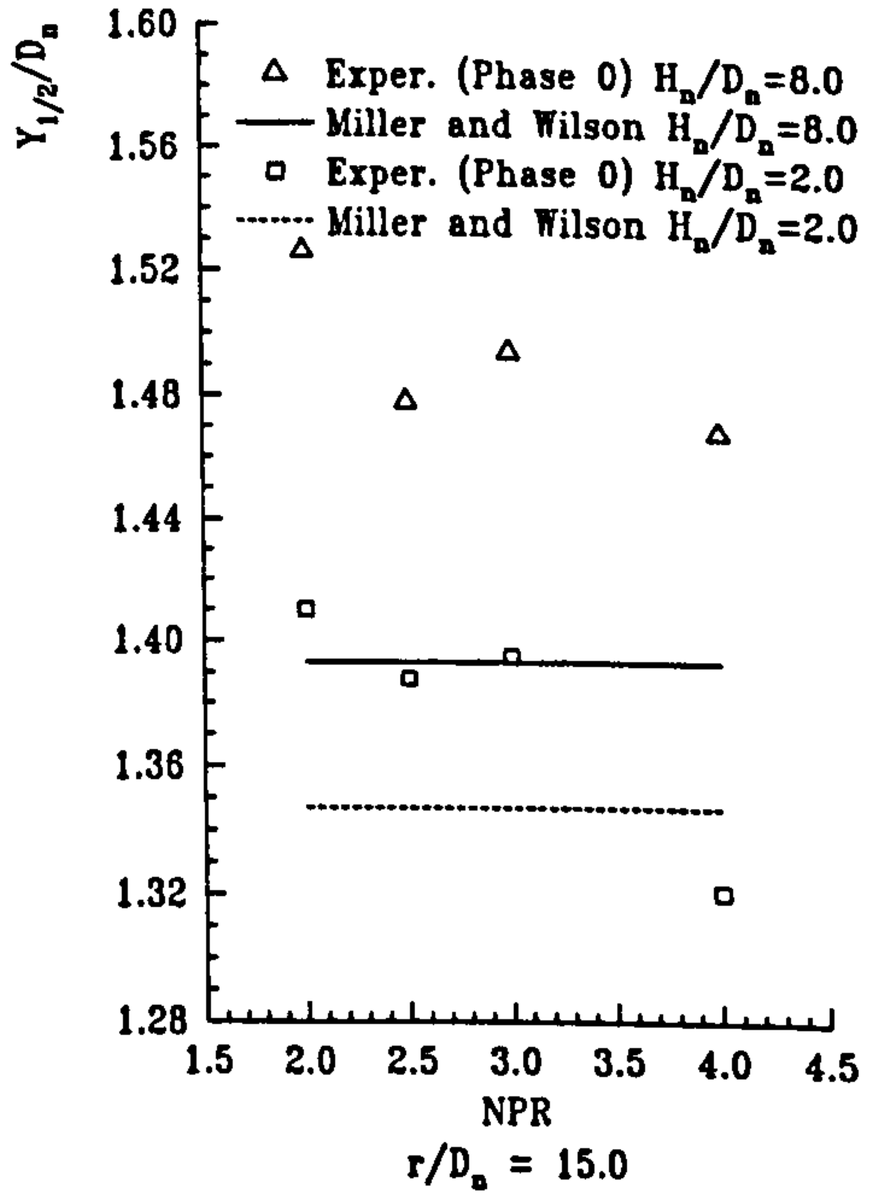

Figure 4.6 : Comparison of NPR Effect with Correlation of Miller and Wilson

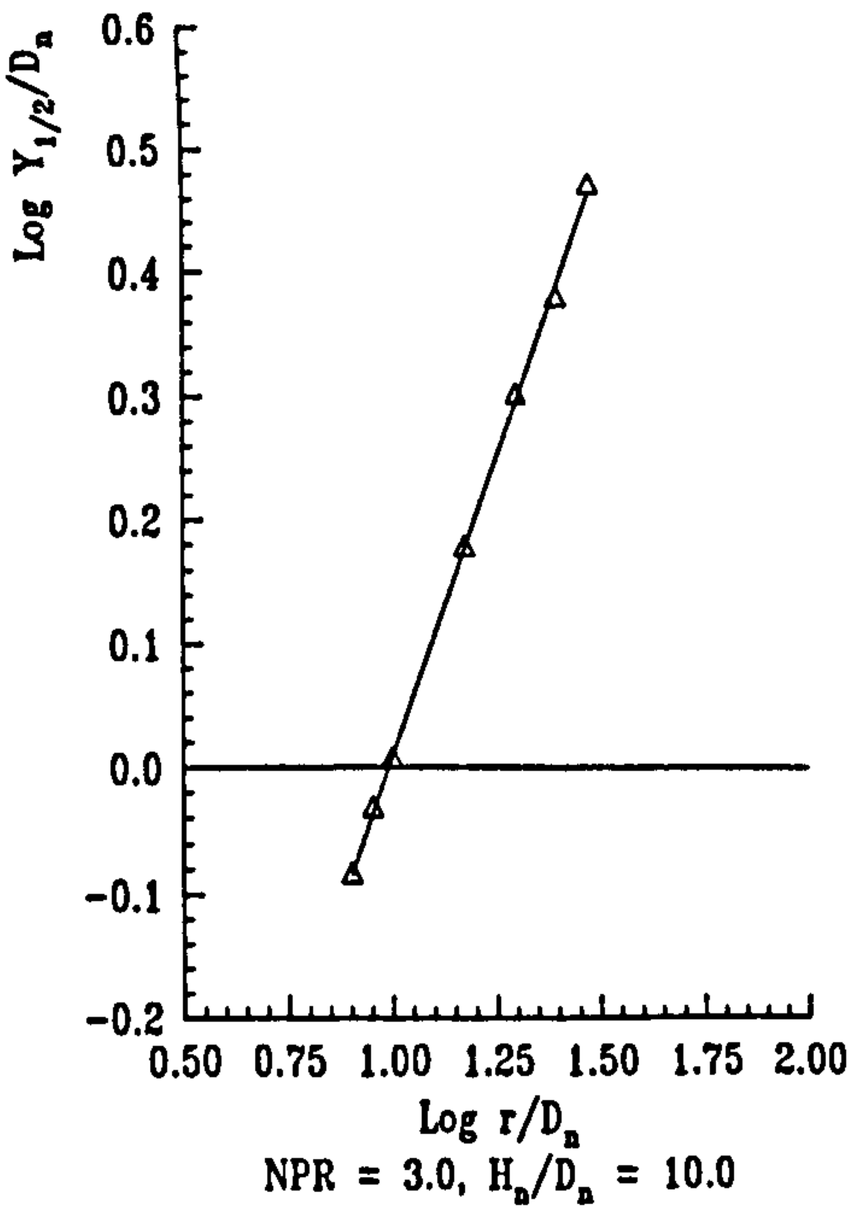

Figure 4.7 : Logarithmic Plot of Half Thickness against Radial Position

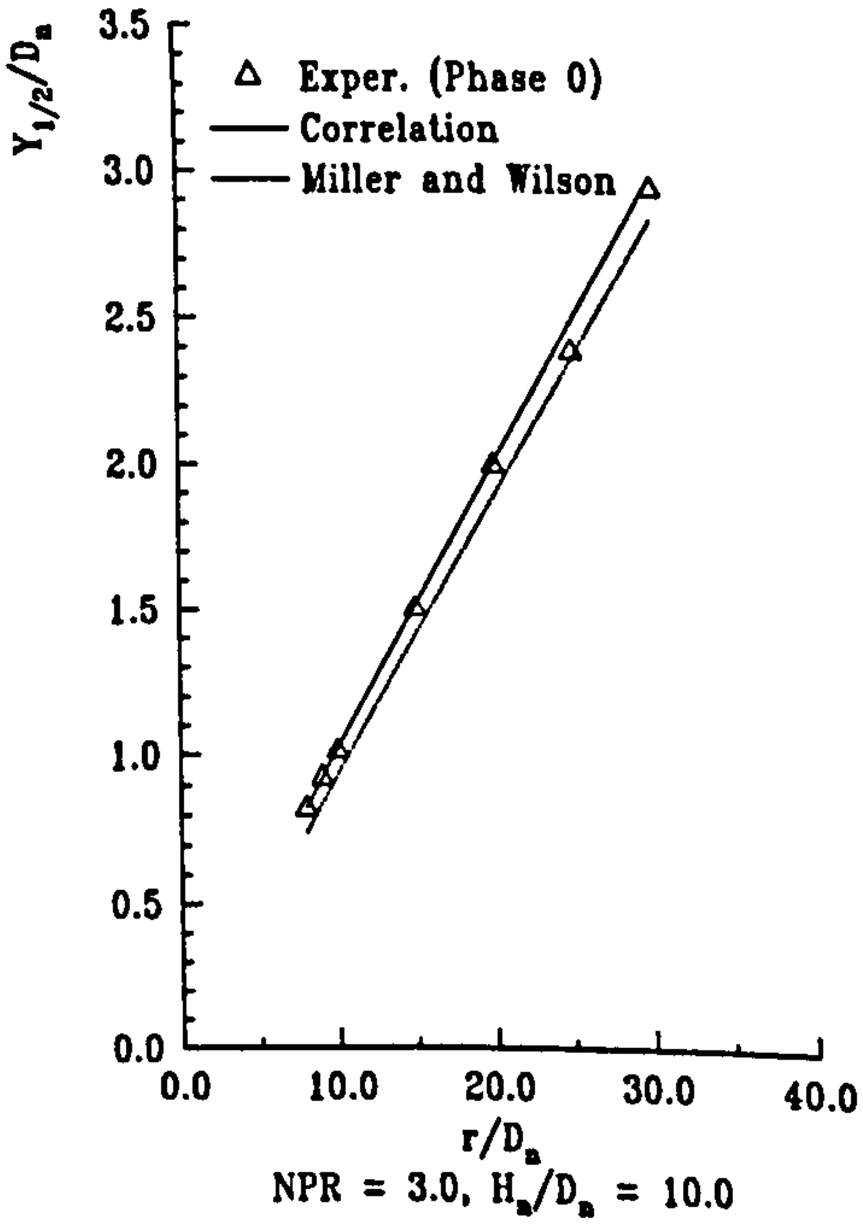

Figure 4.8 : Comparison of Correlations with Phase 0 Data

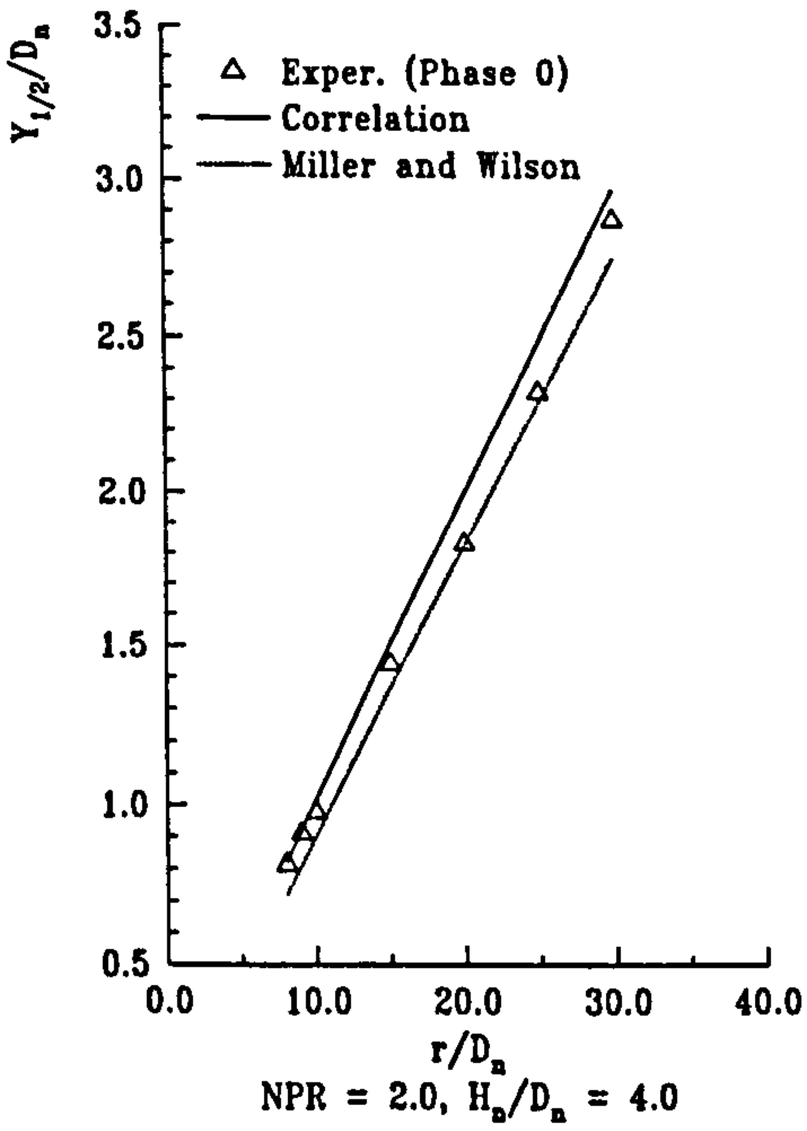

Figure 4.9 : Comparison of Correlations with Phase 0 Data

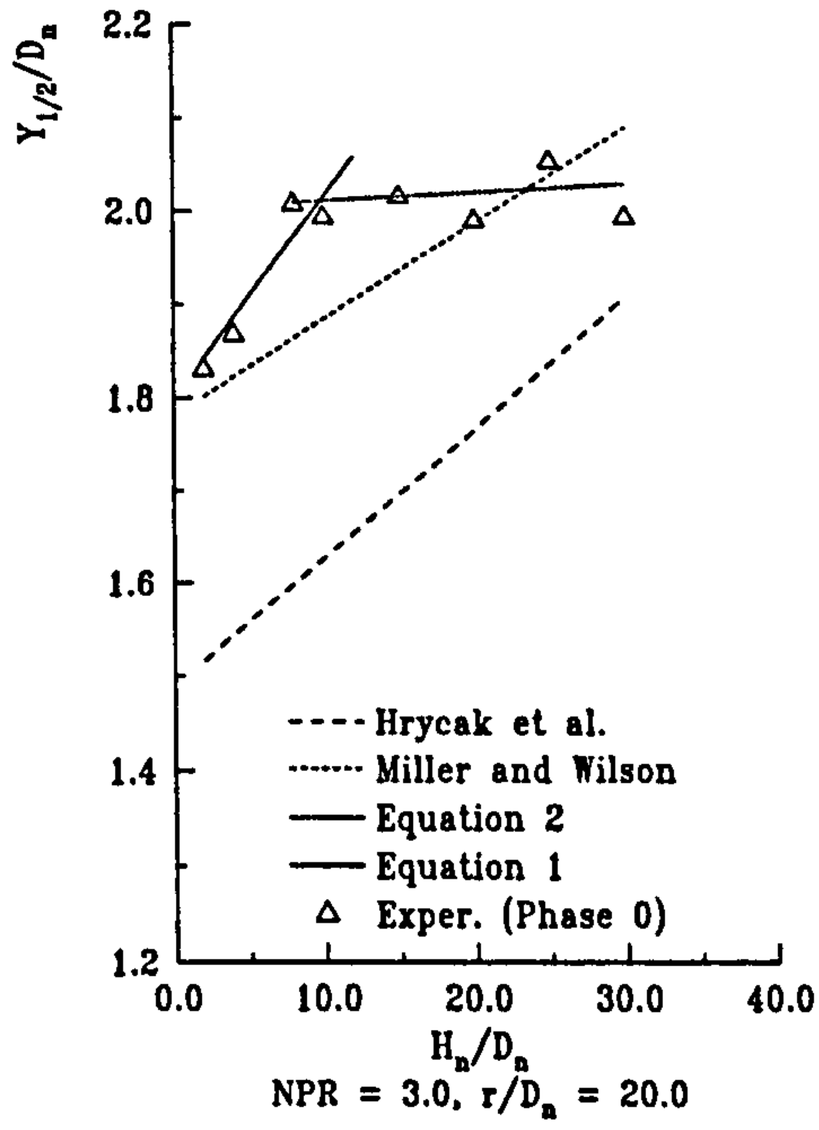

Figure 4.10 : Comparison of Correlations with Height Effect

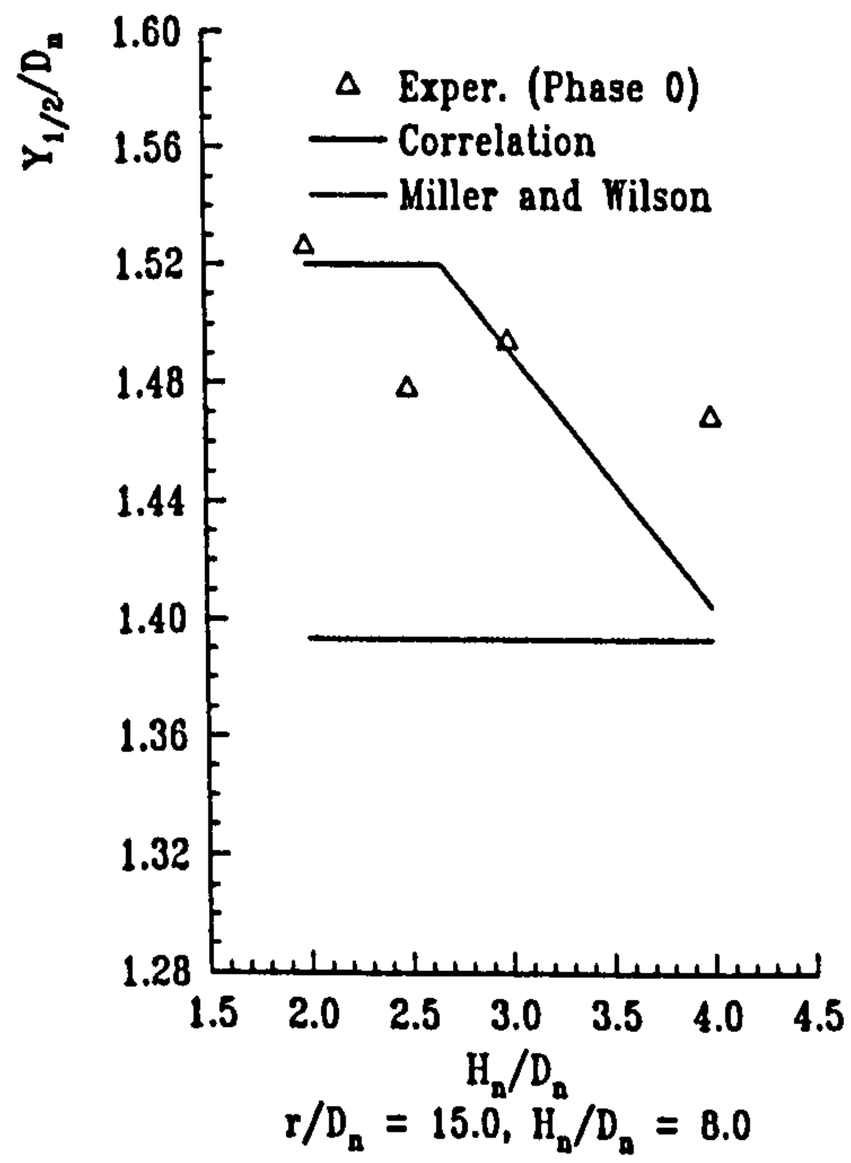

Figure 4.11 : Comparison of Correlations with NPR Effect

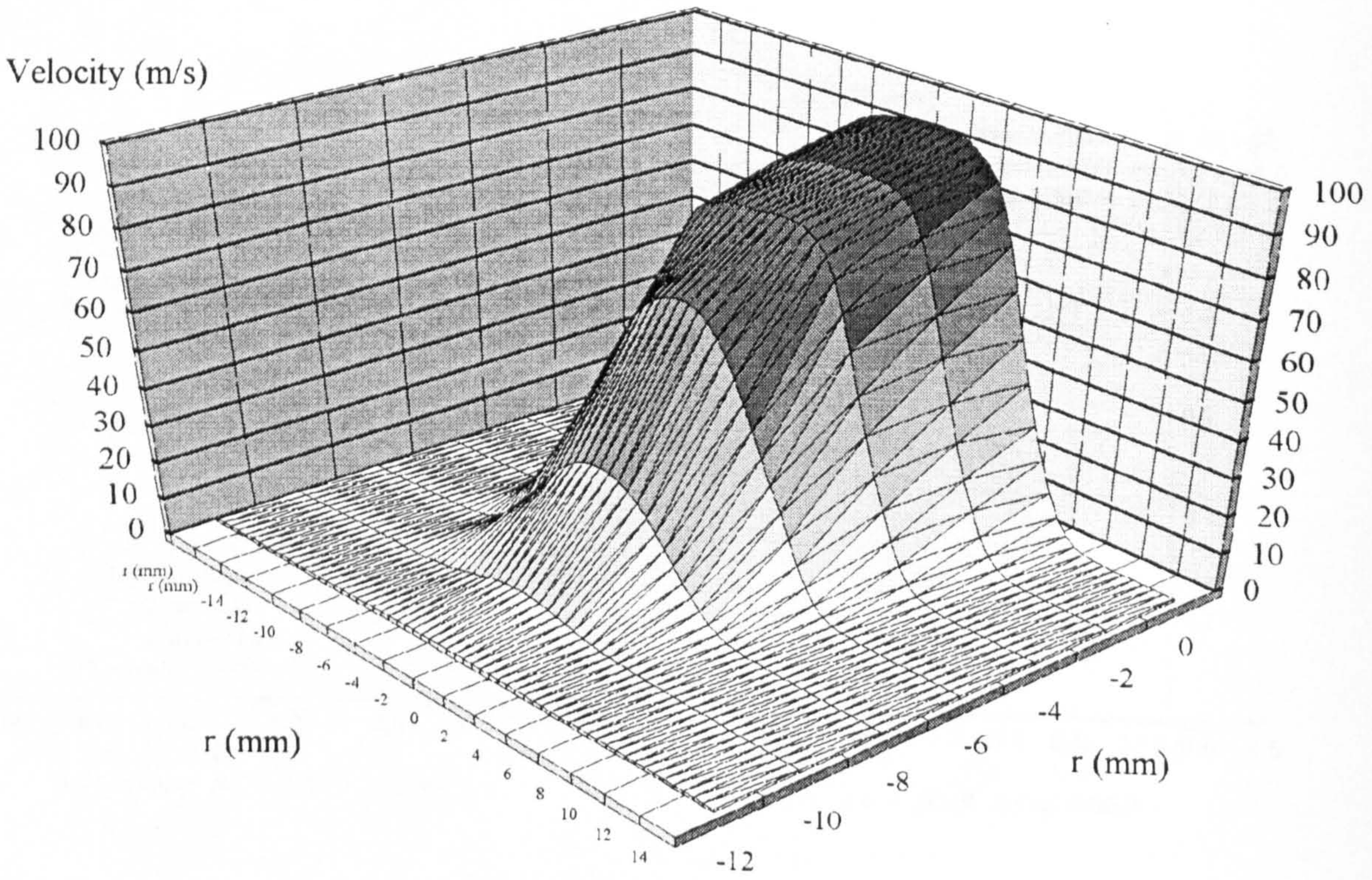

Figure 4.12 : 3-Dimensional Velocity Profile in the Free Jet, NPR=1.05, H_n/D_n=10.0 and H_p/D_n=8.0

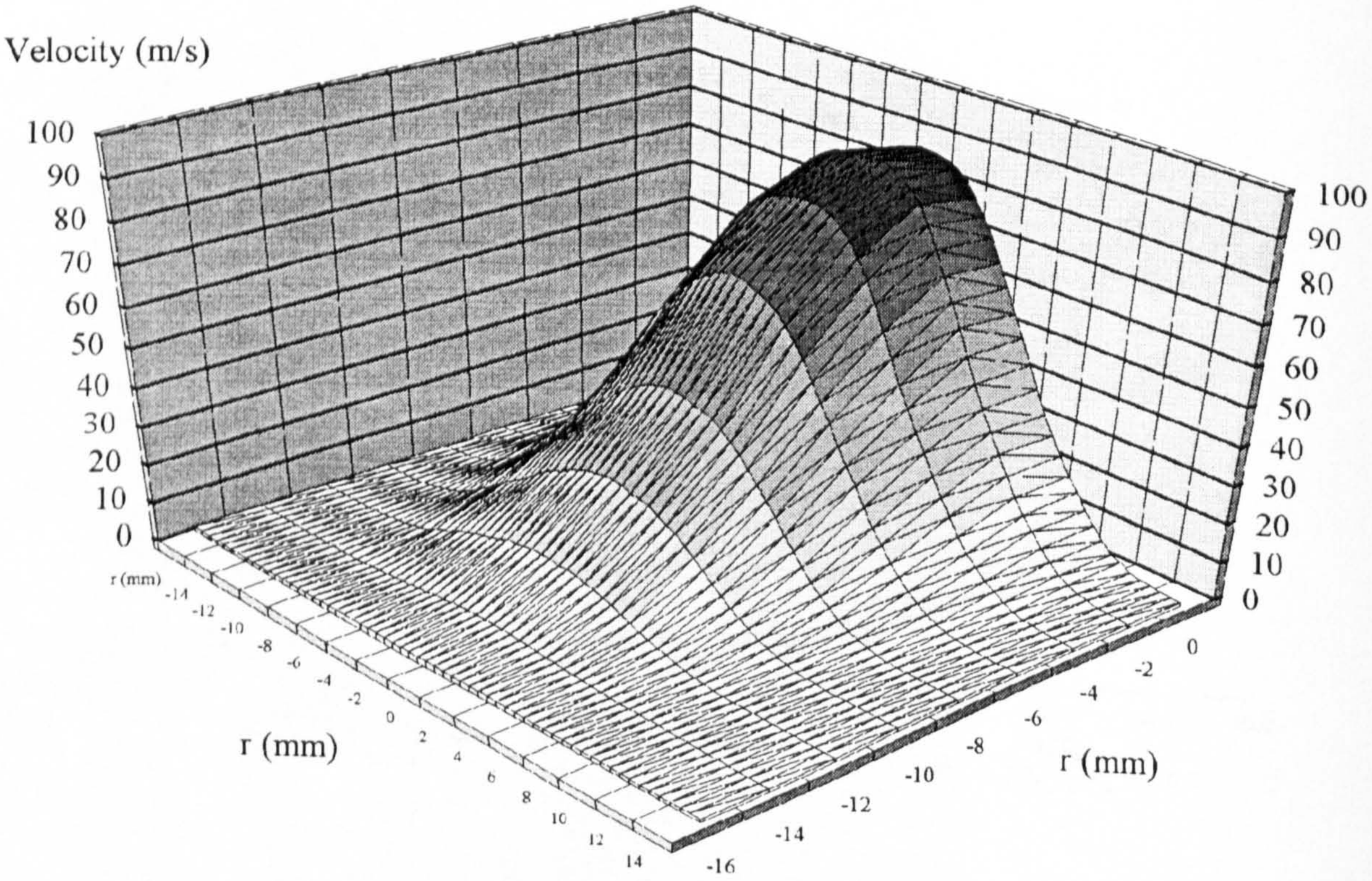

Figure 4.13 : 3-Dimensional Velocity Profile in the Free Jet, NPR=1.05, H_n/D_n=10.0 and H_p/D_n=6.0

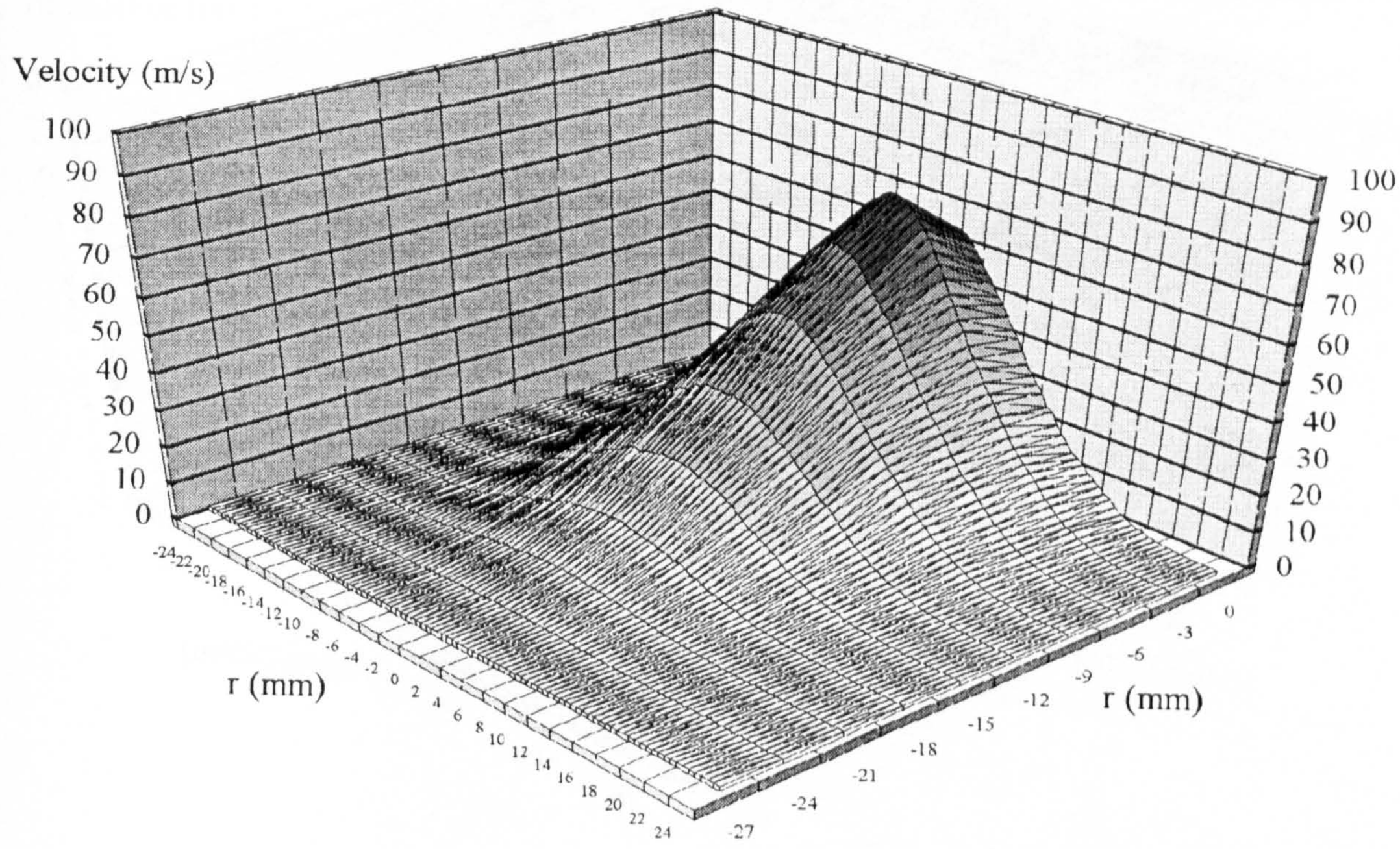

Figure 4.14 : 3-Dimensional Velocity profile in the Free Jet, NPR=1.05, H_n/D_n=10.0 and H_p/D_n=4.0

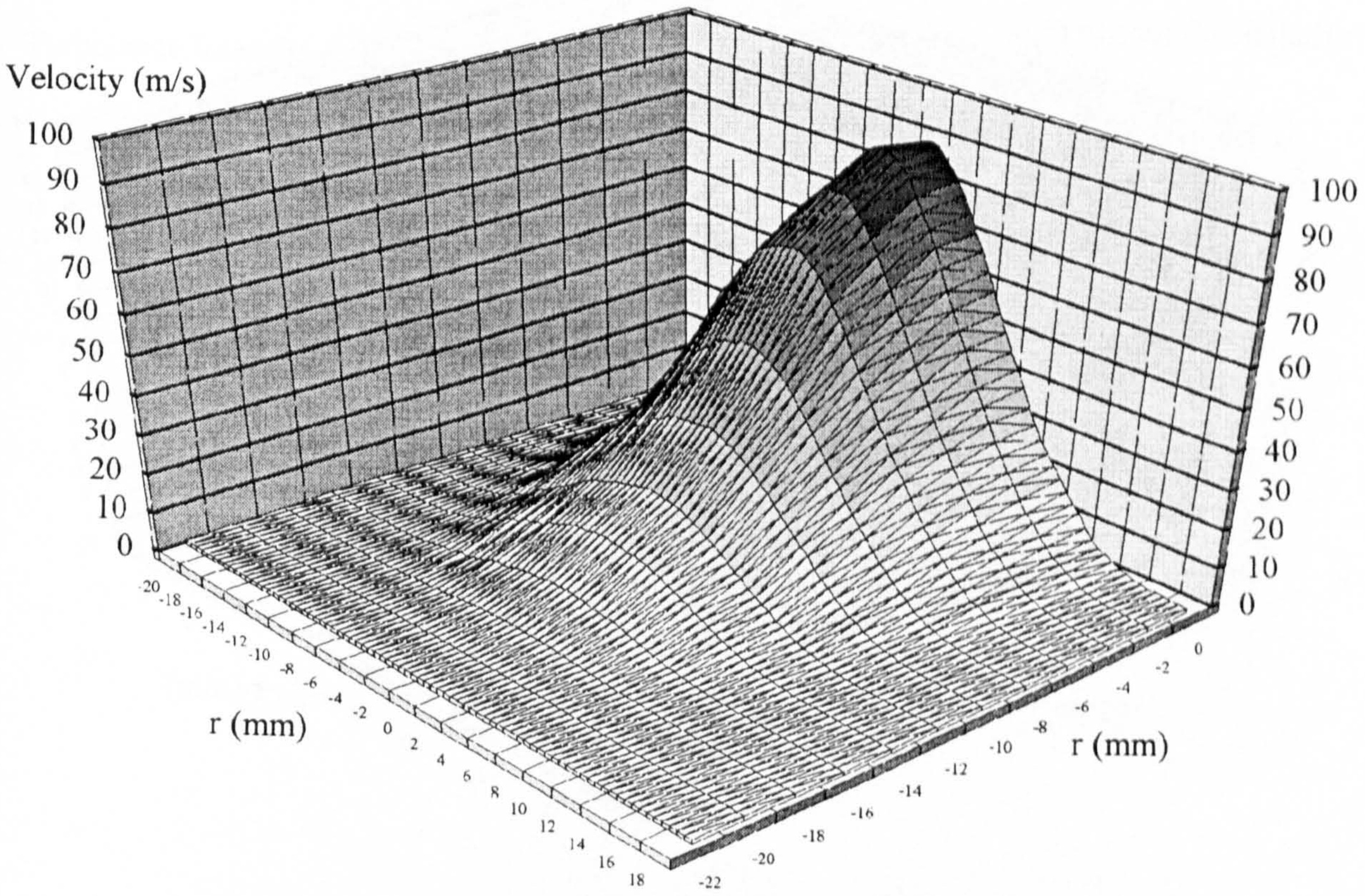

Figure 4.15 : 3-Dimensioanl Velocity Profile in the Free Jet, NPR=1.05, H_n/D_n=10.0 and H_p/D_n=2.0

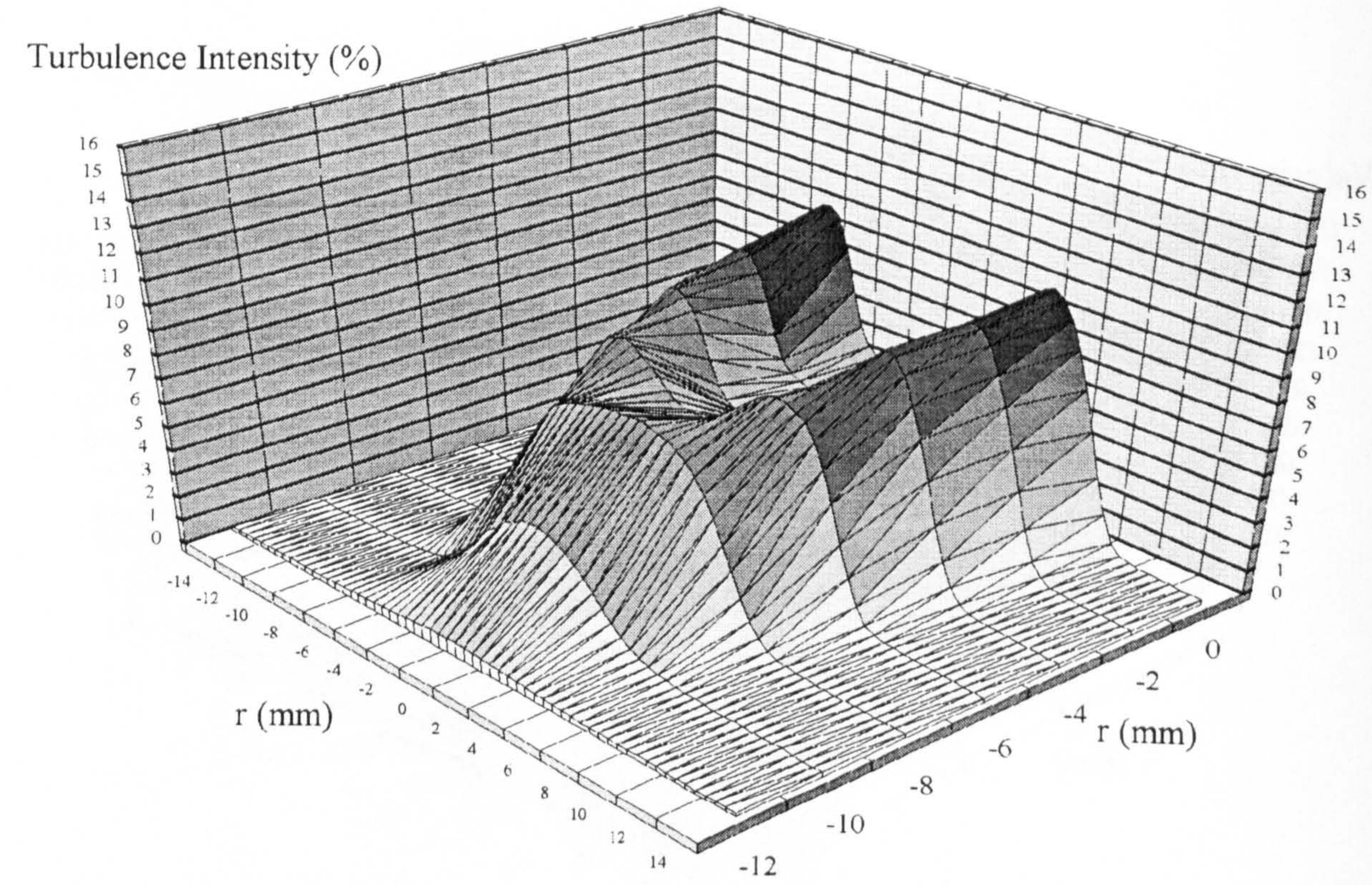

Figure 4.16 : 3-Dimensional Turbulence Intensity Profile in the Free Jet, NPR=1.05, H_n/D_n=10.0 and H_p/D_n=8.0

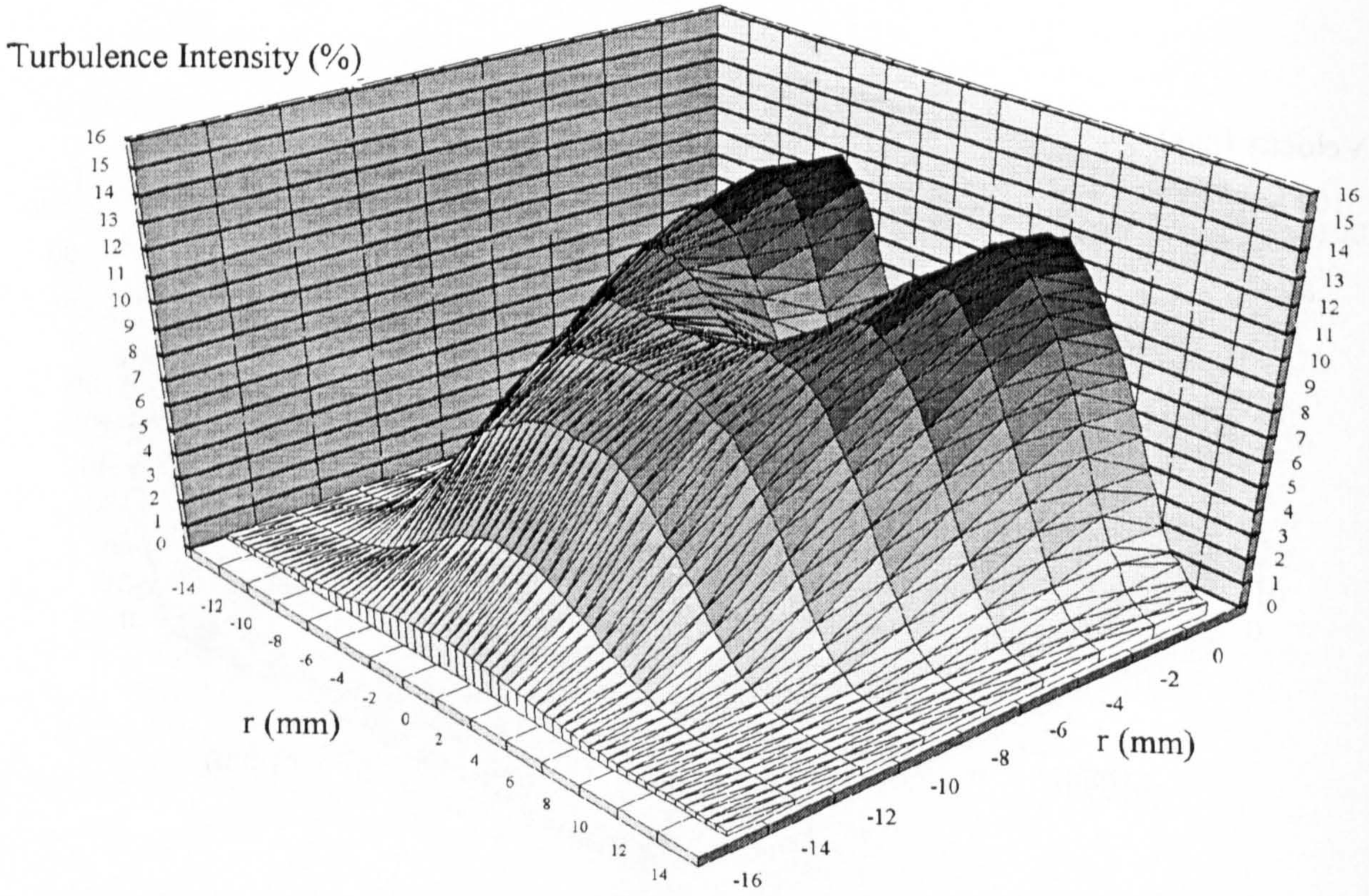

Figure 4.17 : 3-Dimensional Turbulence Intensity Profile in the Free Jet, NPR=1.05, H_n/D_n=10.0 and H_p/D_n=6.0

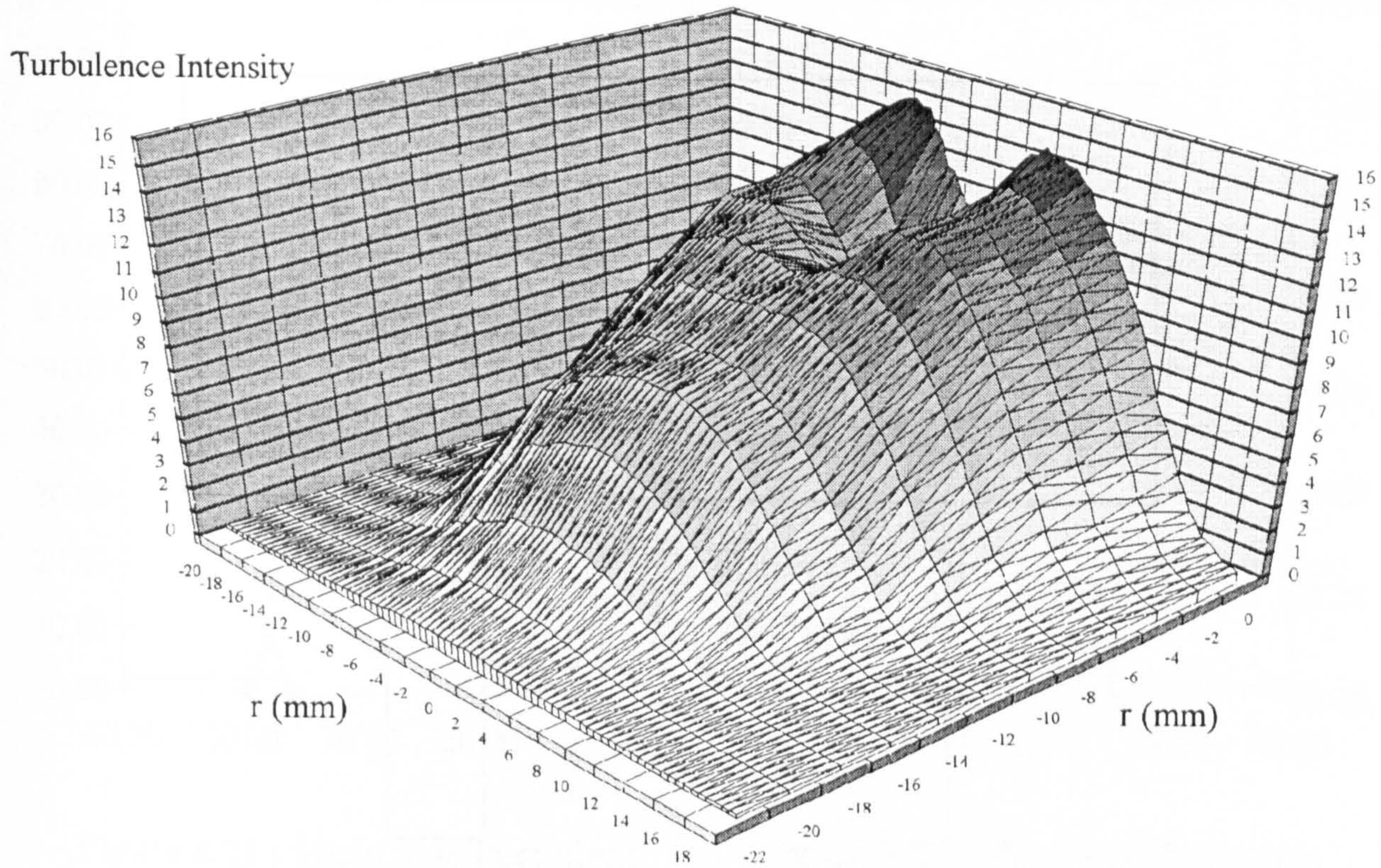

Figure 4.18 : 3-Dimensional Turbulence Intensity Profile in the Free Jet, NPR=1.05, H_n/D_n=10.0 and H_p/D_n=4.0

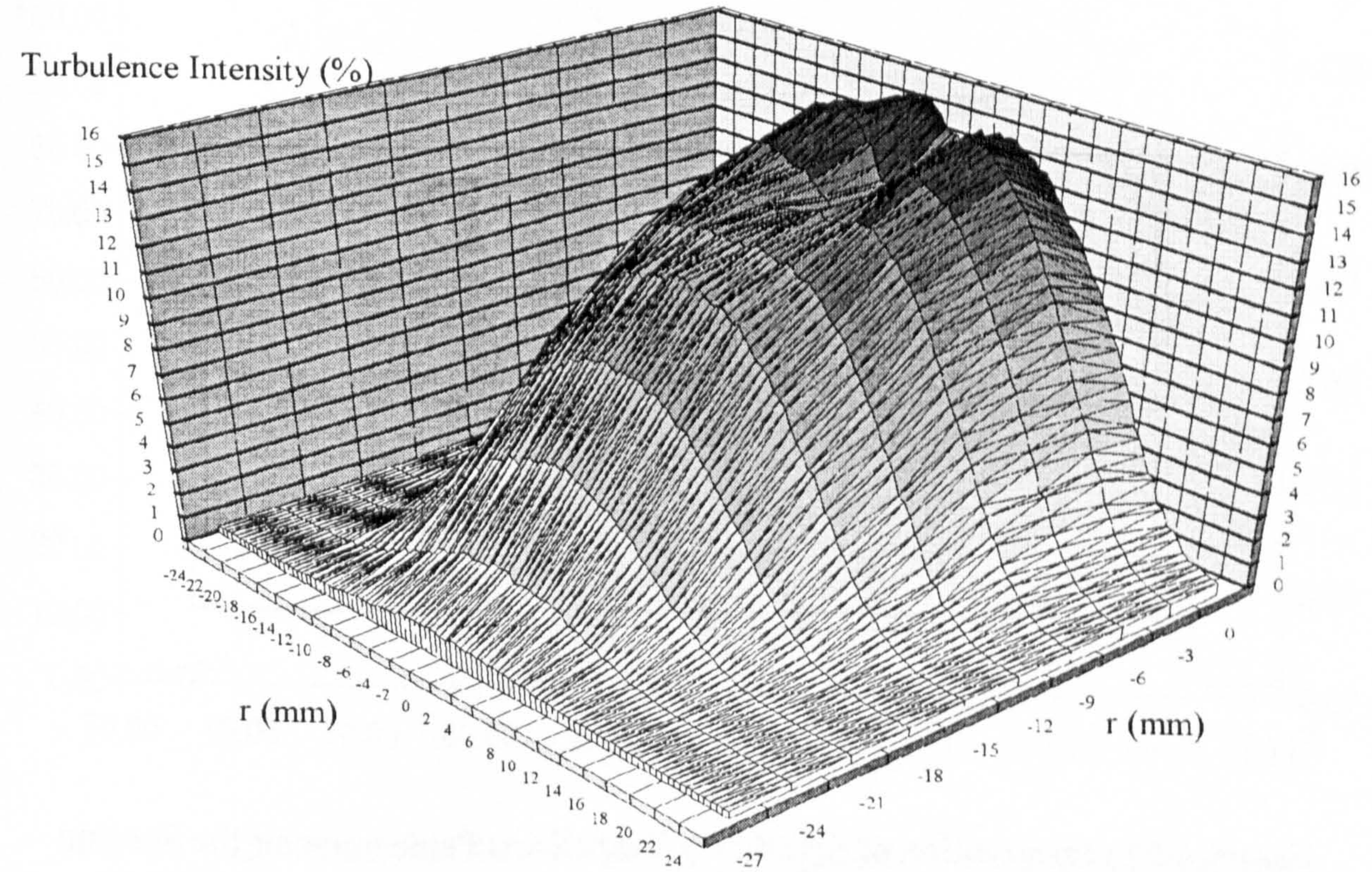

Figure 4.19 : 3-Dimensional Turbulence Intensity Profile in the Free Jet, NPR=1.05, H_n/D_n=10.0 and H_p/D_n=2.0

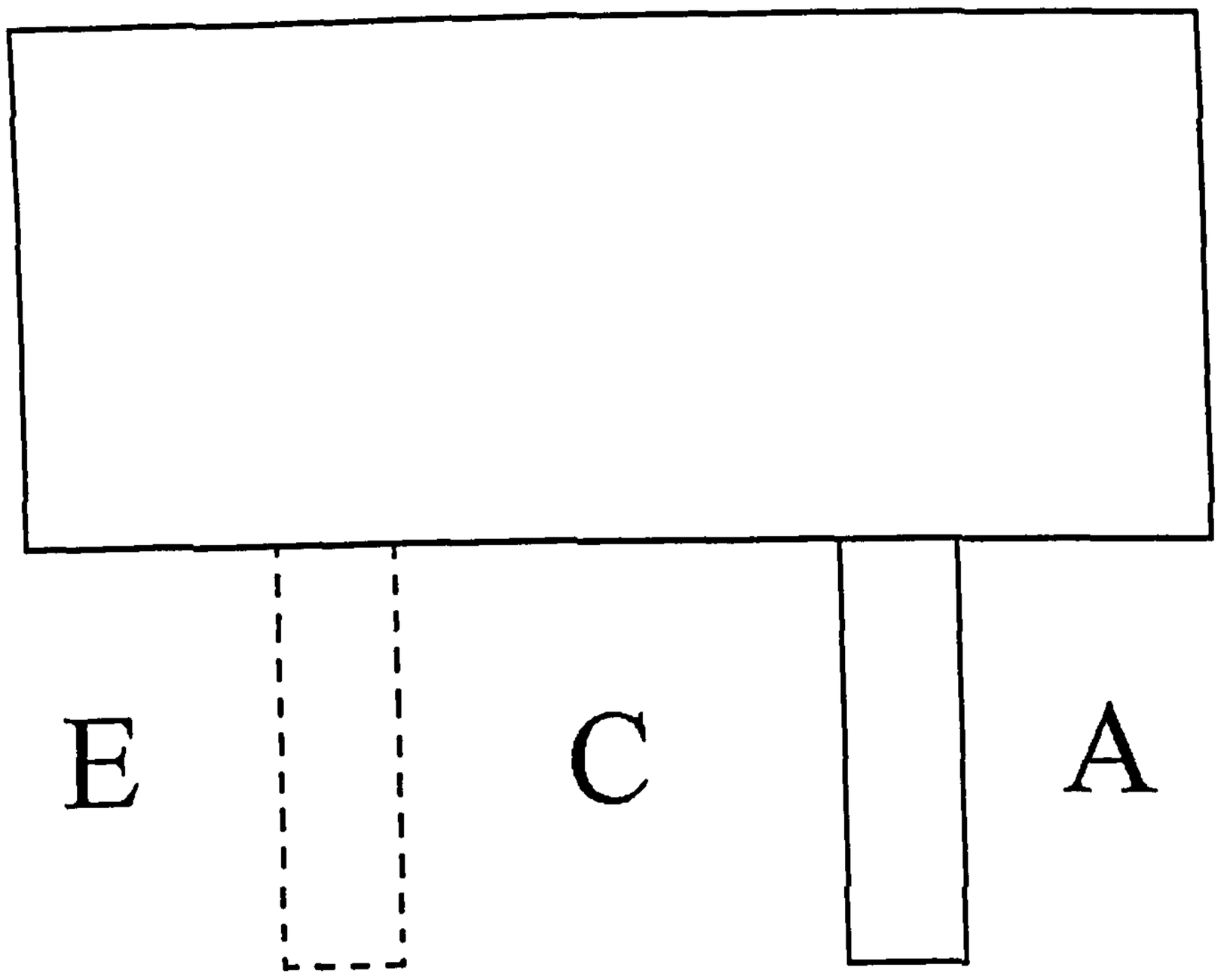

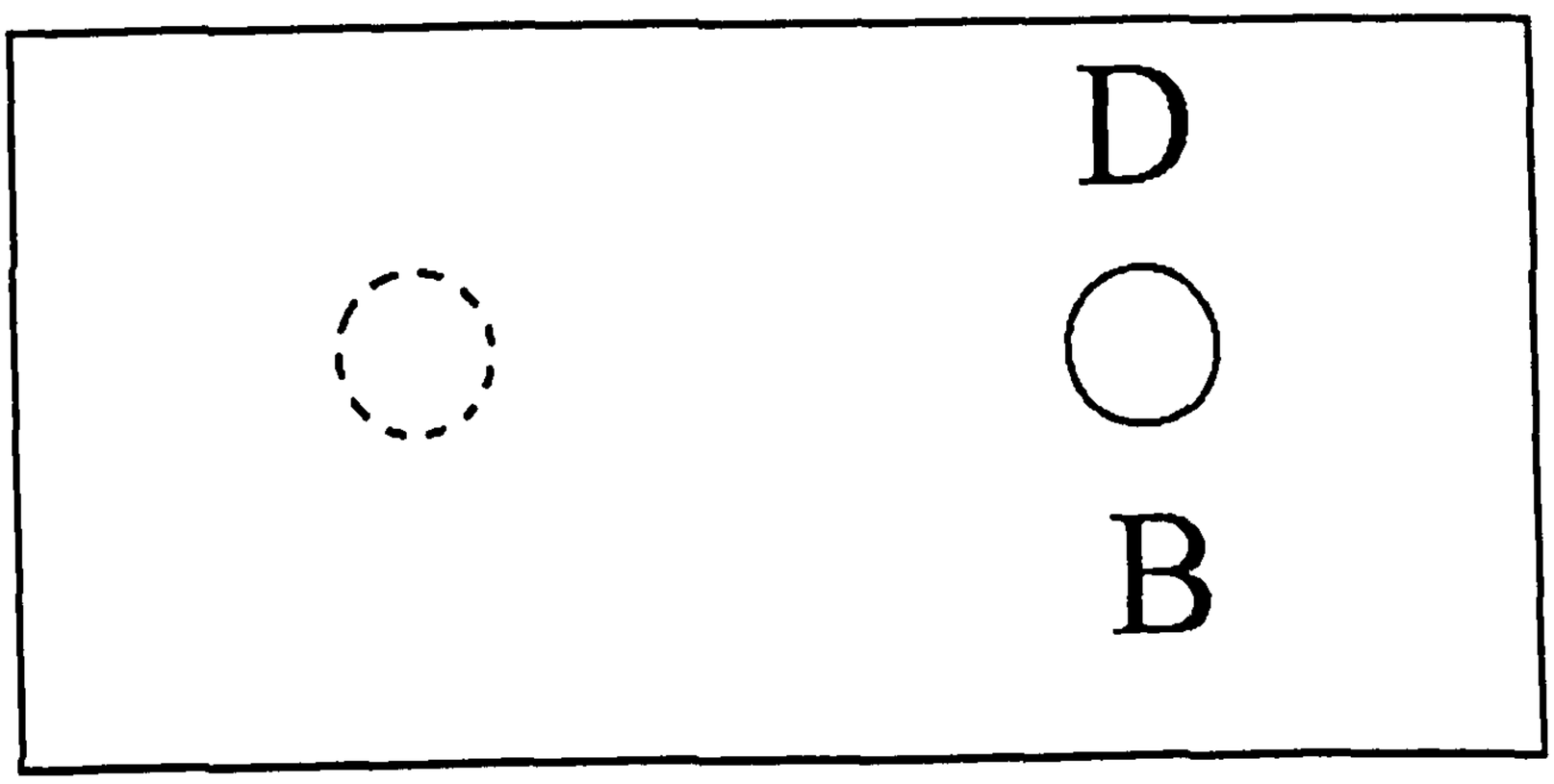

Figure 4.20 : Orientation of Symmetry Tests Runs Performed on the Settling Chamber

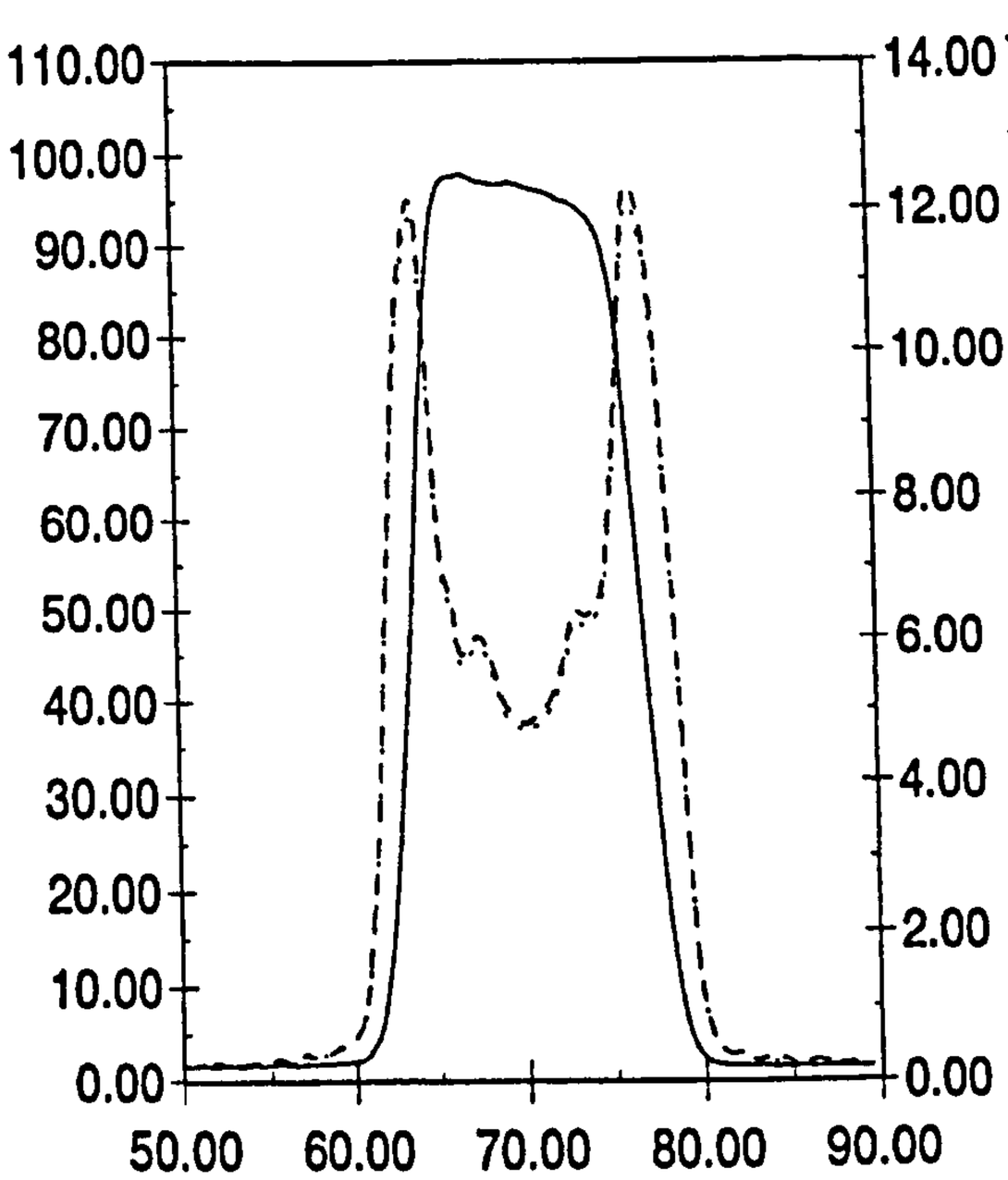

Figure 4.21 : Mean and Turbulent Velocity Profiles (D-B)

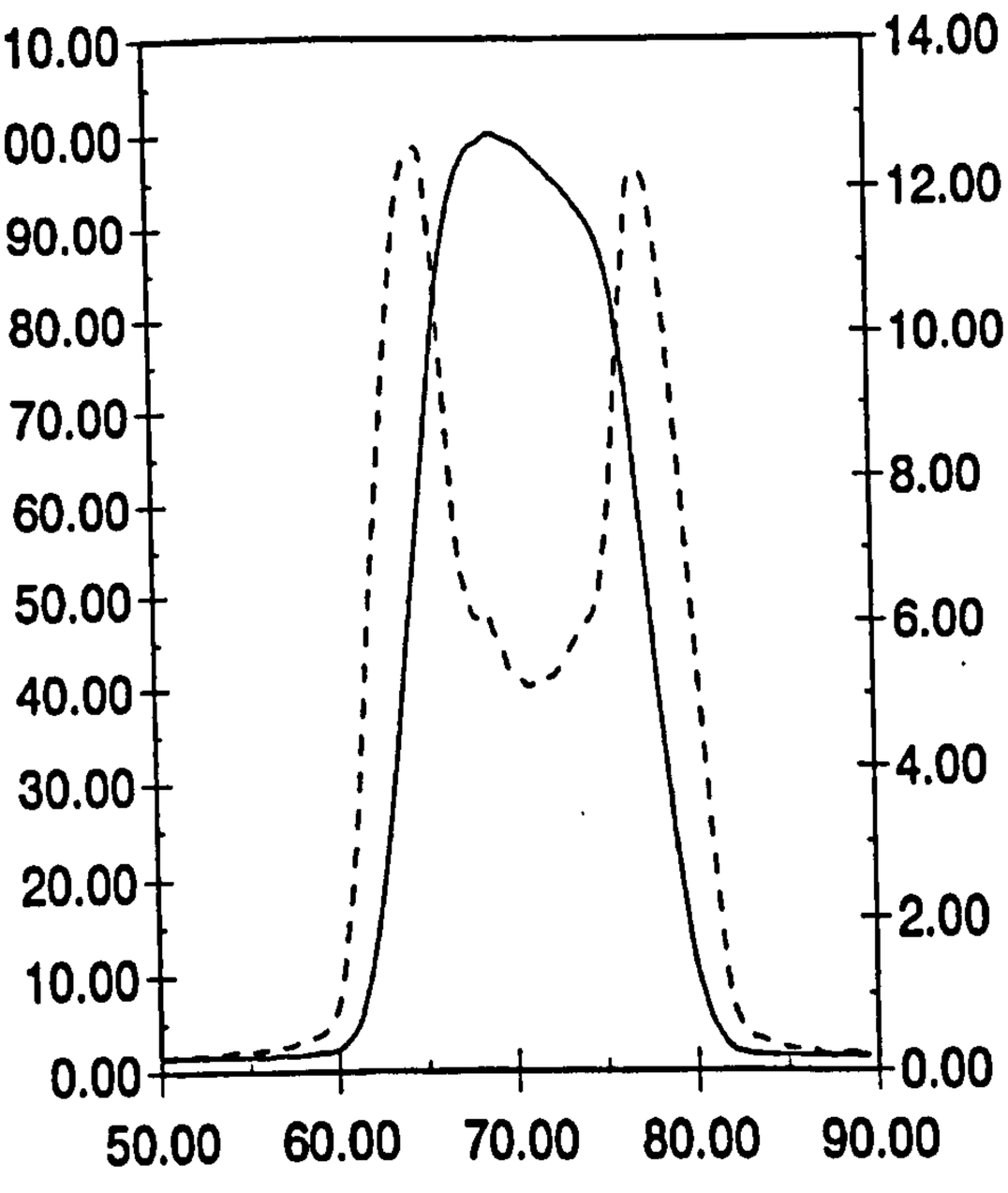

Figure 4.22 : Mean and Turbulent Velocity Profiles (C-A)

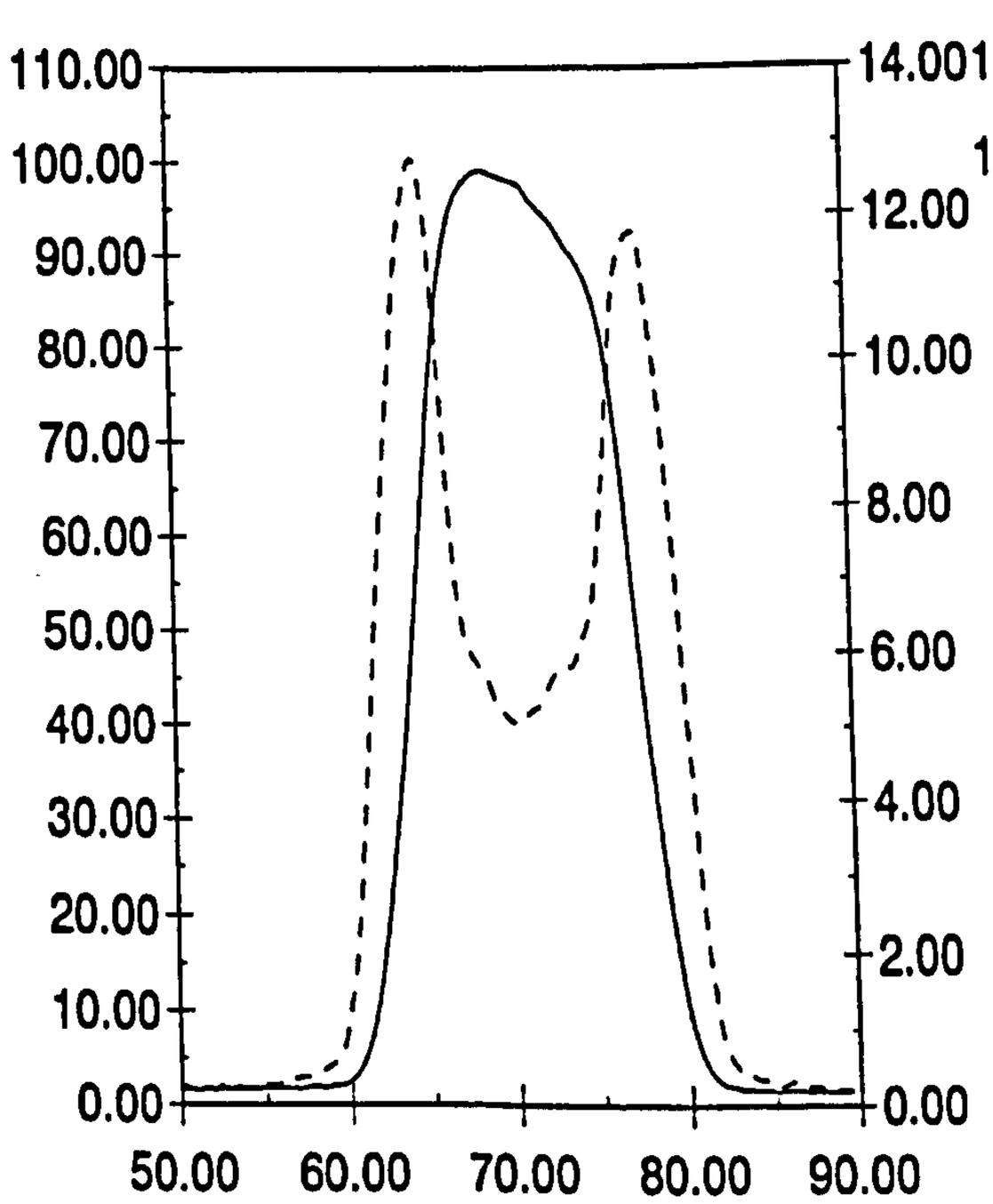

Figure 4.23 : Mean and Turbulent Velocity Profiles (C-A)

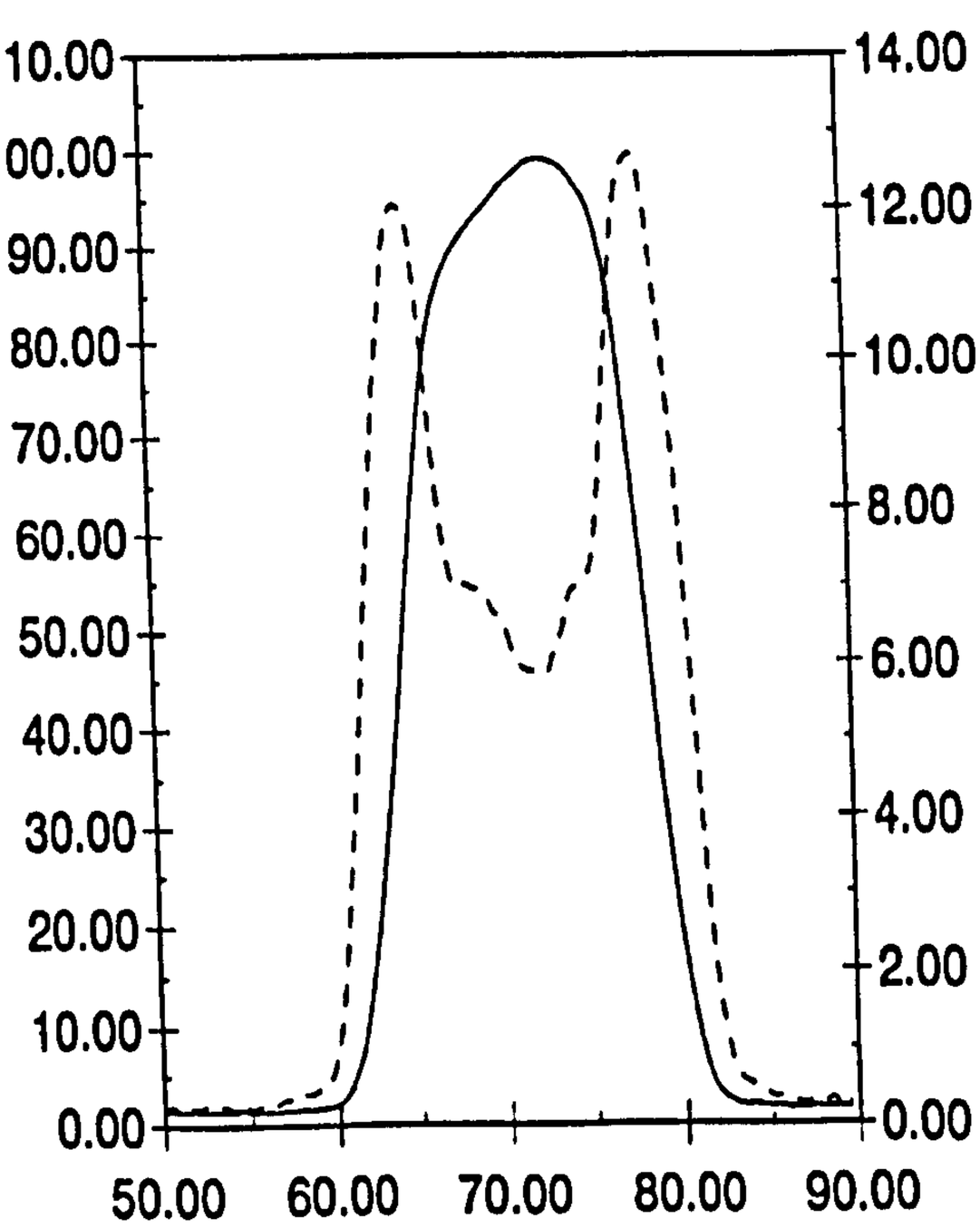

Figure 4.24 : Mean and Turbulent Velocity Profiles (E-C)

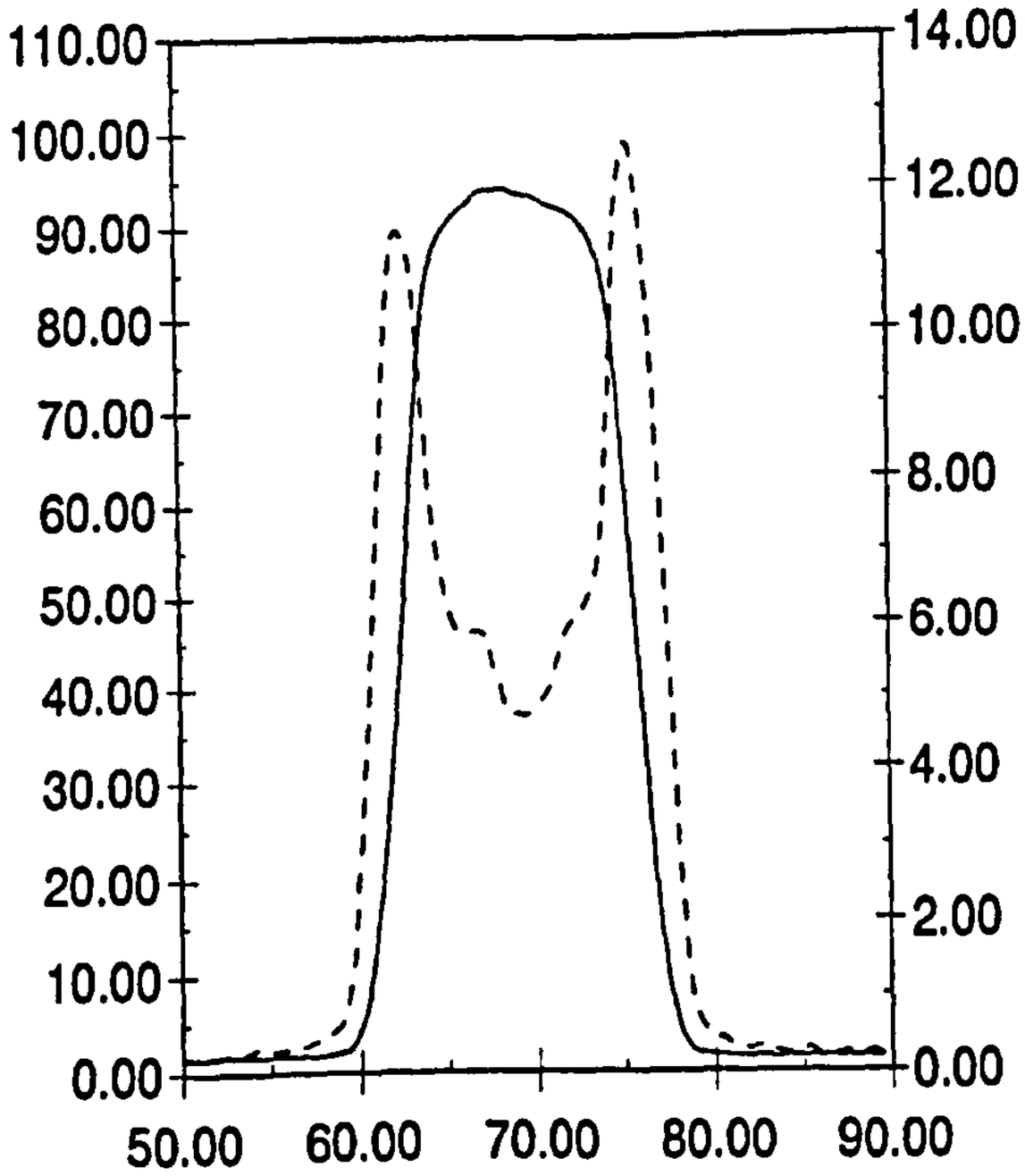

Figure 4.25 : Mean and Turbulent Velocity Profiles (C-A)

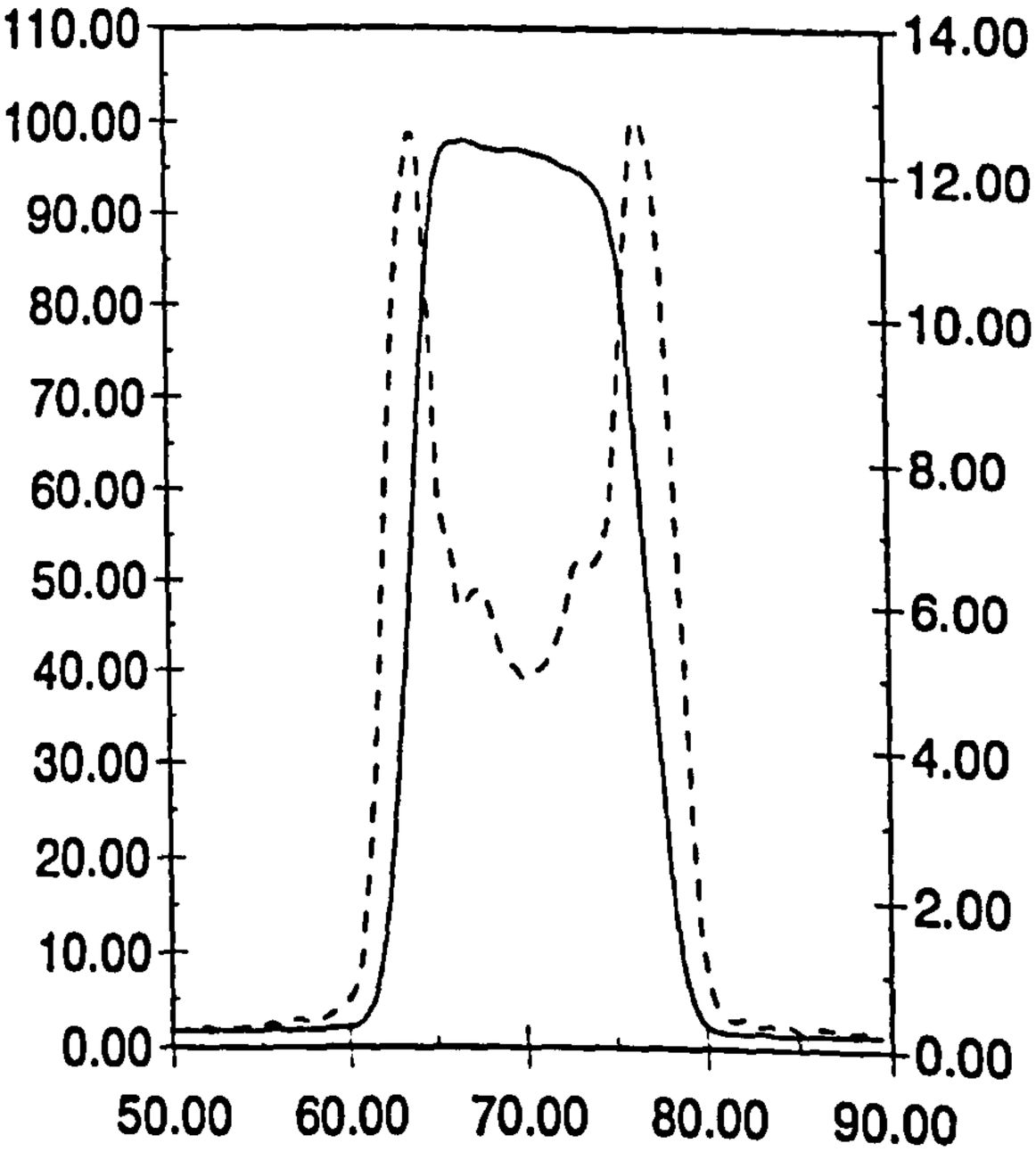

Figure 4.26 : Mean and Turbulent Velocity Profiles (C-A)

Figure 4.27 : Mean and Turbulent Velocity Profiles (C-A)

Figure 4.28 : Mean and Turbulent Velocity Profiles (D-B)

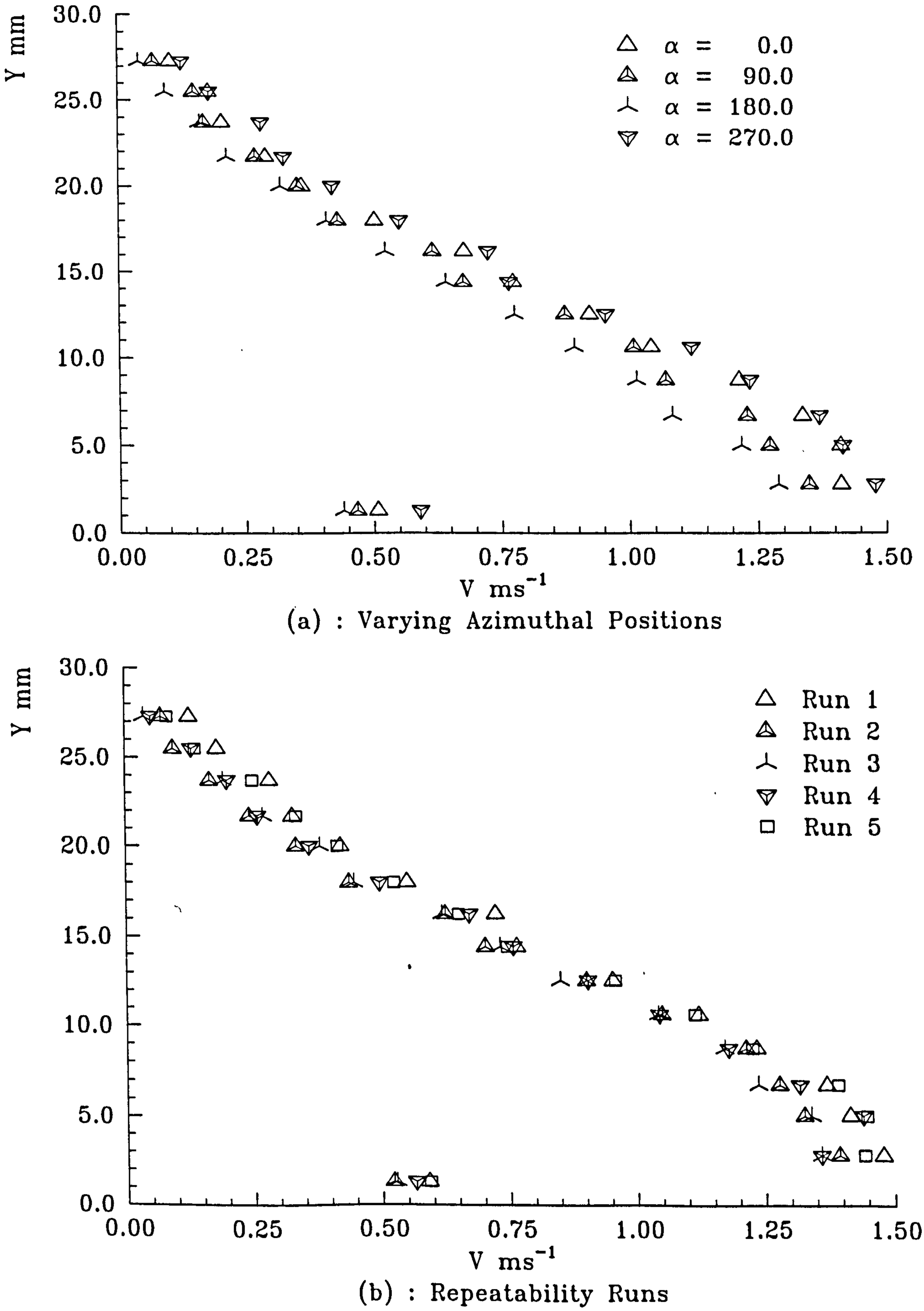

(a) : Varying Azimuthal Positions

(b) : Repeatability Runs

Figure 4.29 : Symmetry Checks of Wall Jet Profiles

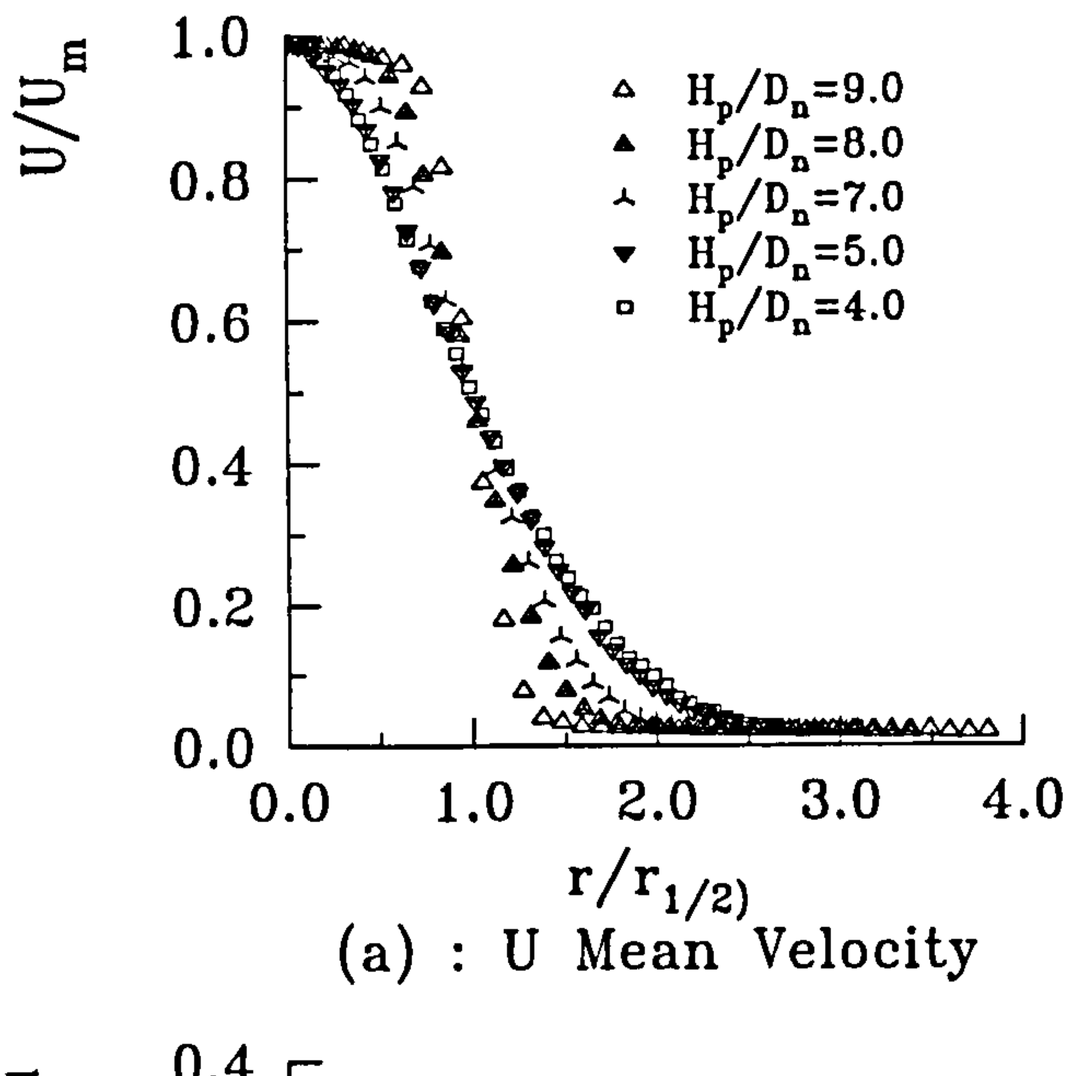

(a) : U Mean Velocity

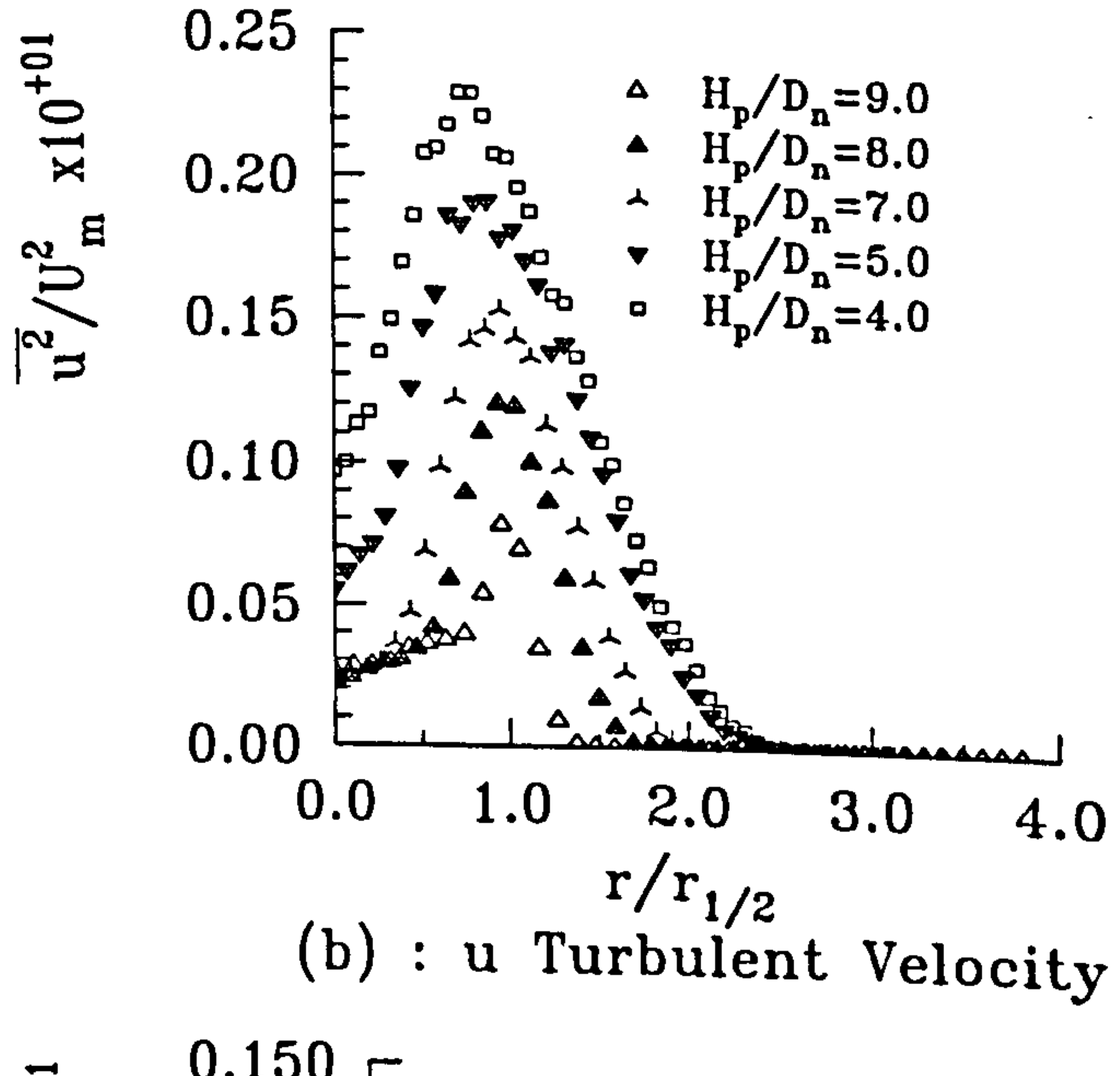

(b) : u Turbulent Velocity

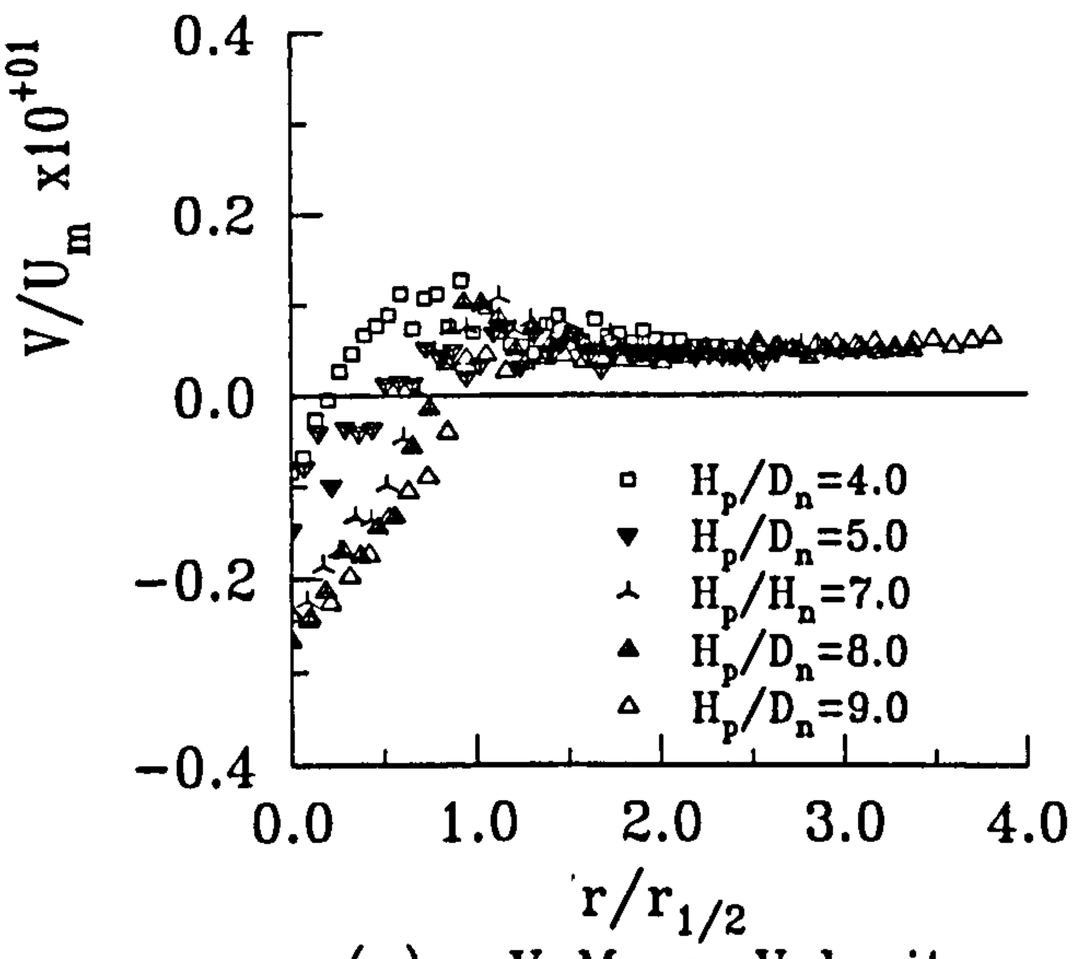

(c) : V Mean Velocity

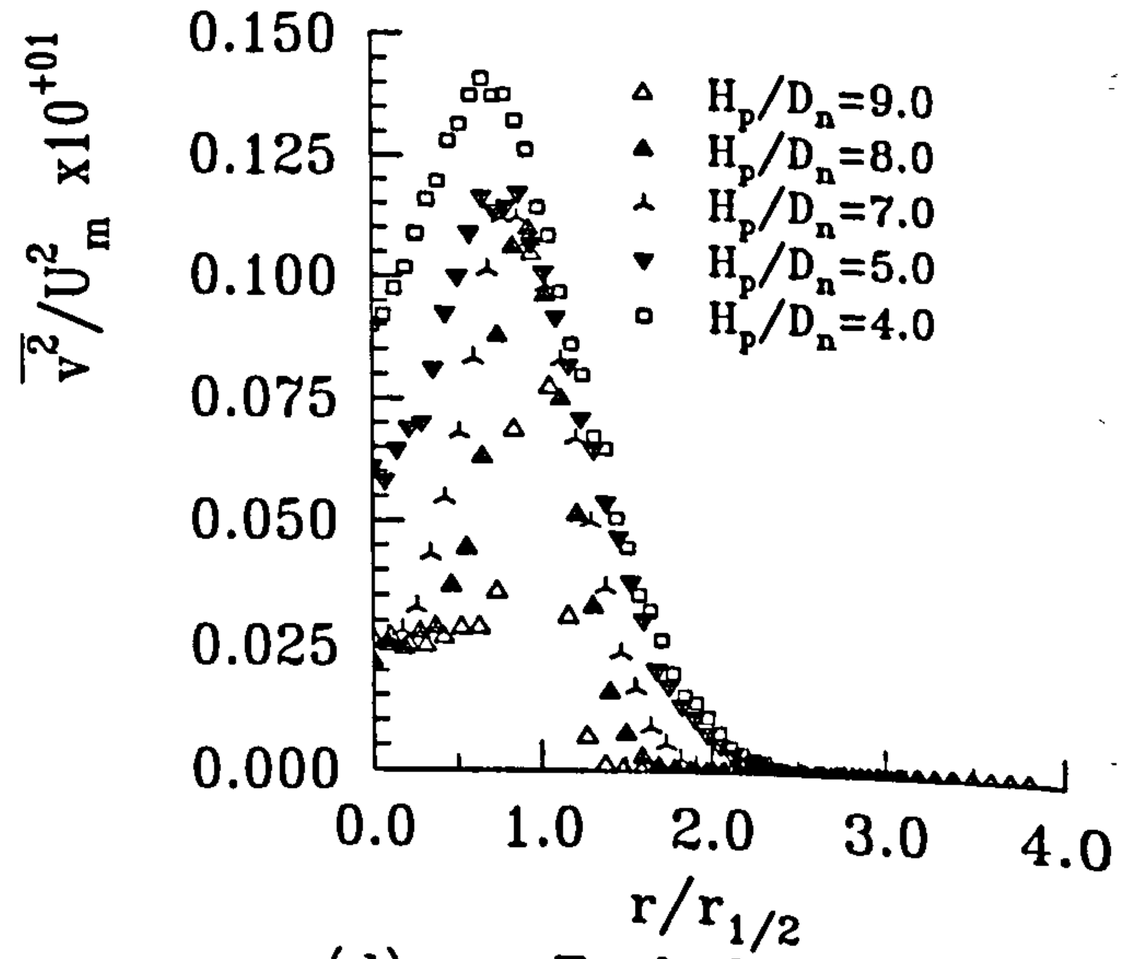

(d) : v Turbulent Velocity

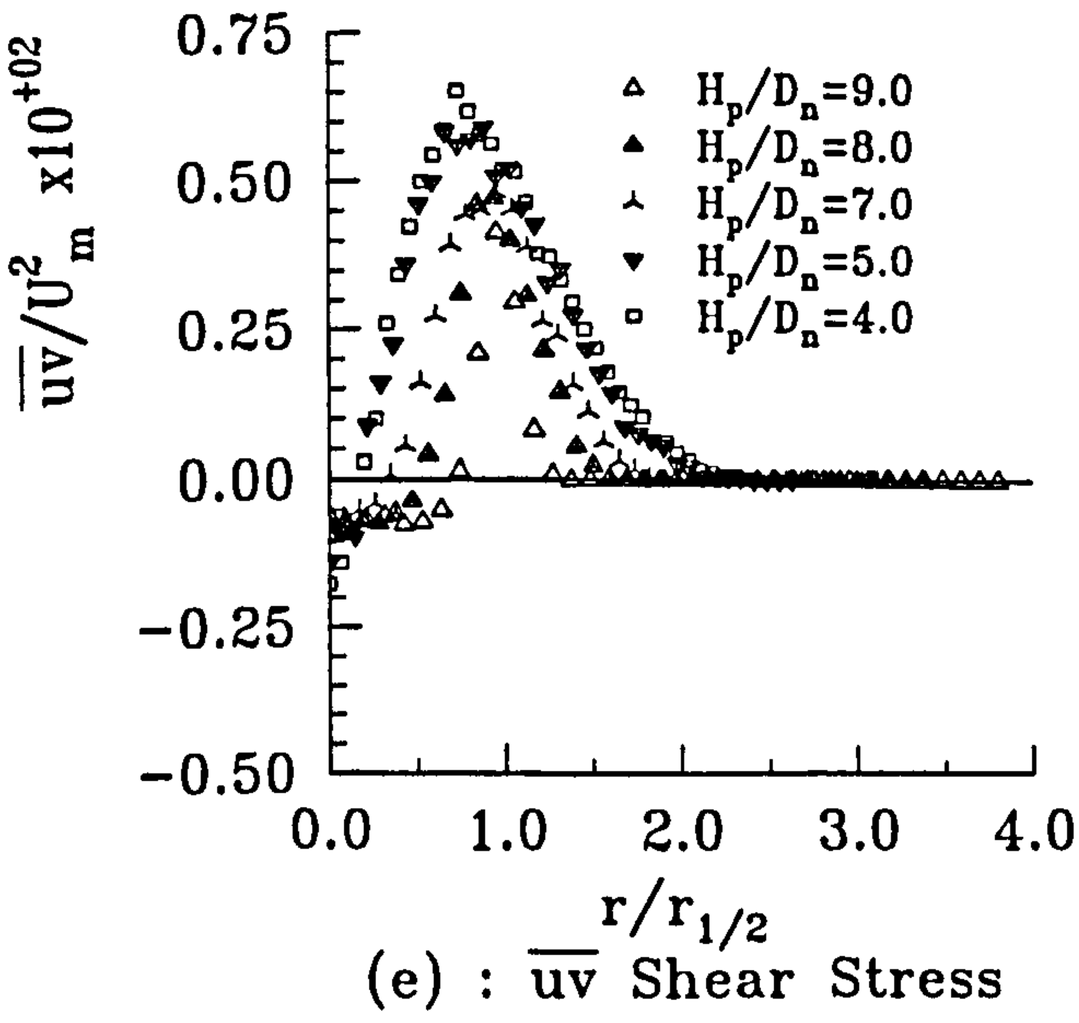

(e) : $\overline{uv}$ Shear Stress

Figure 4.30 : Non-dimensional Free Jet Profiles for Varying H_p/D_n, H_n/D_n = 10.0 and NPR = 1.05

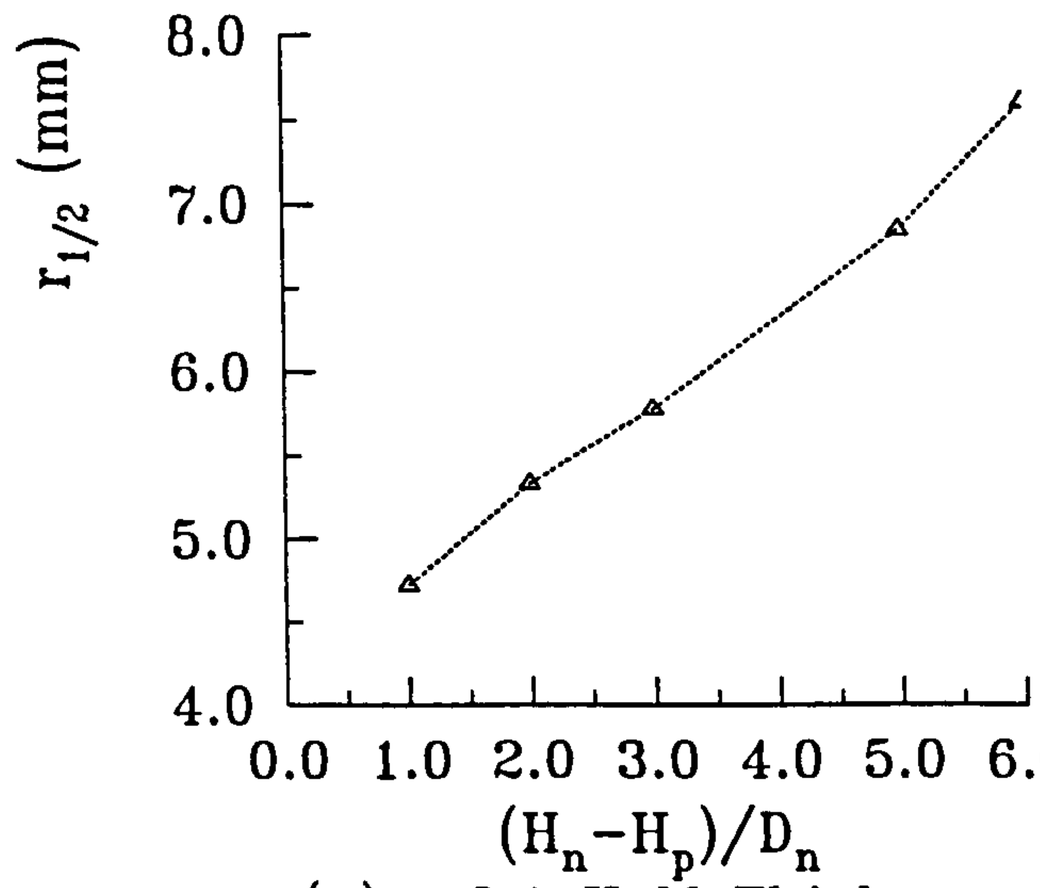

(a) : Jet Half Thickness

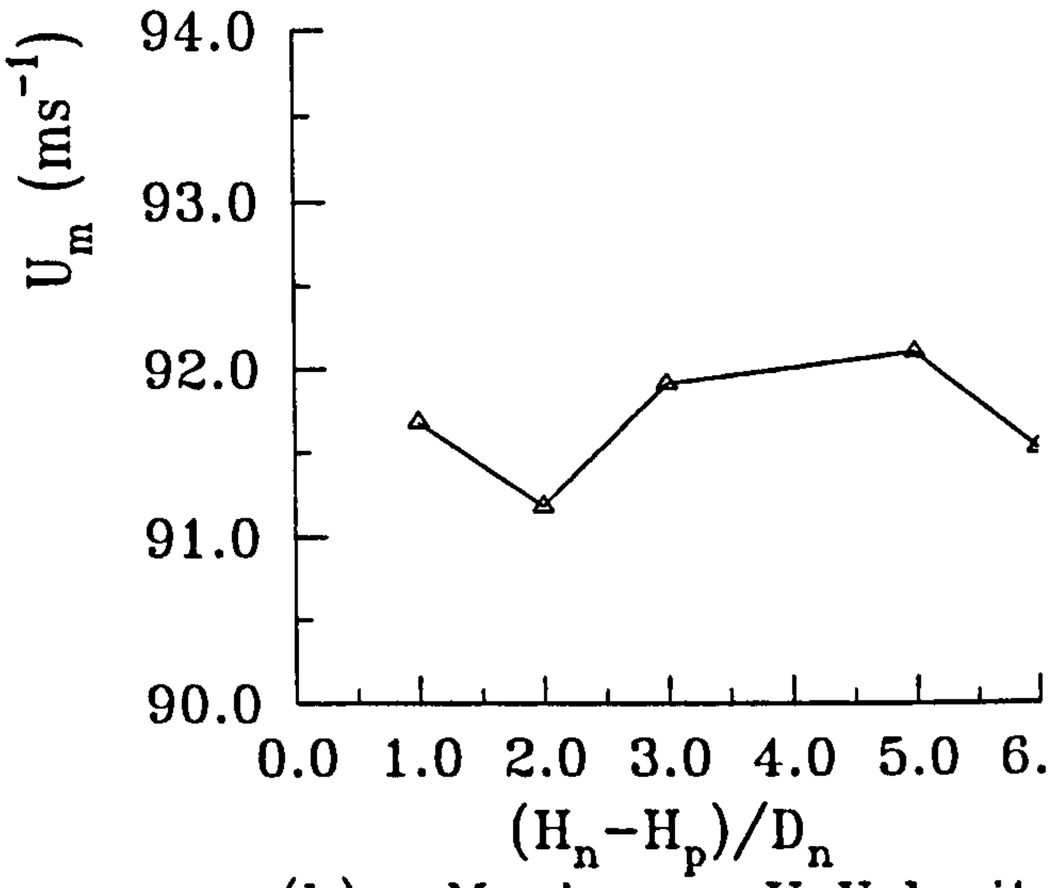

(b) : Maximum U Velocity

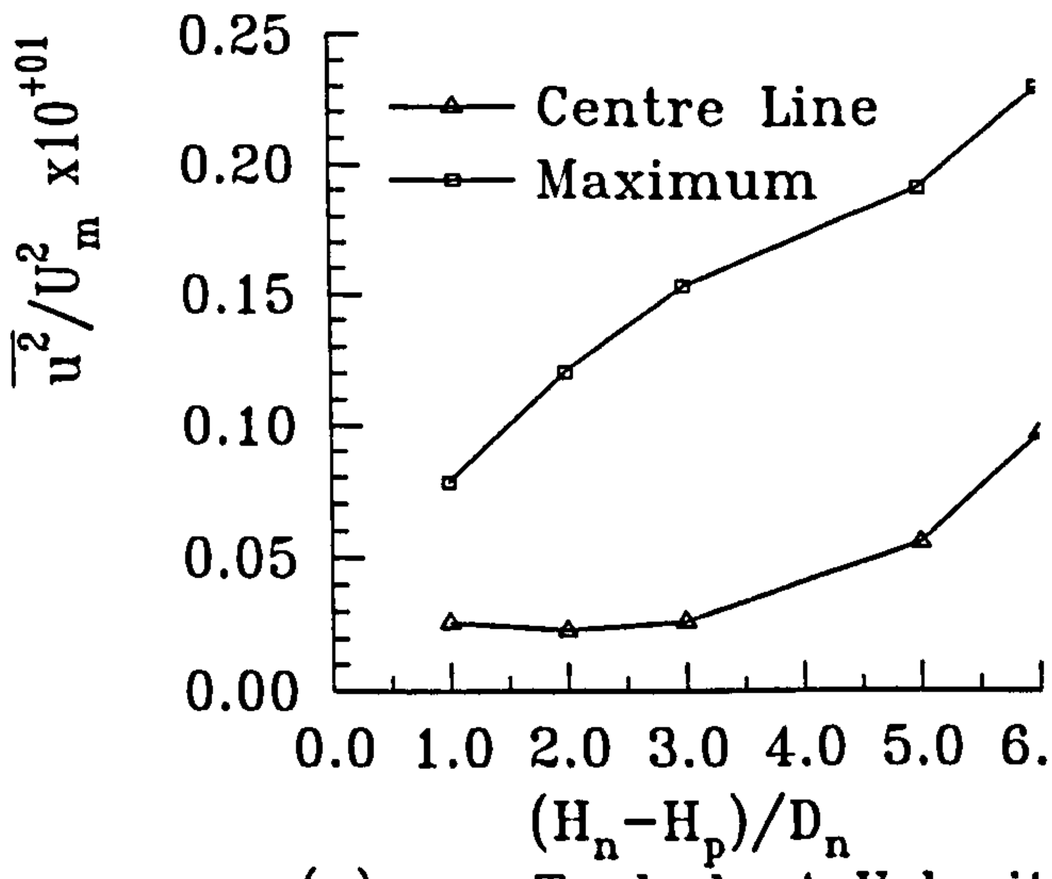

(c) : u Turbulent Velocity

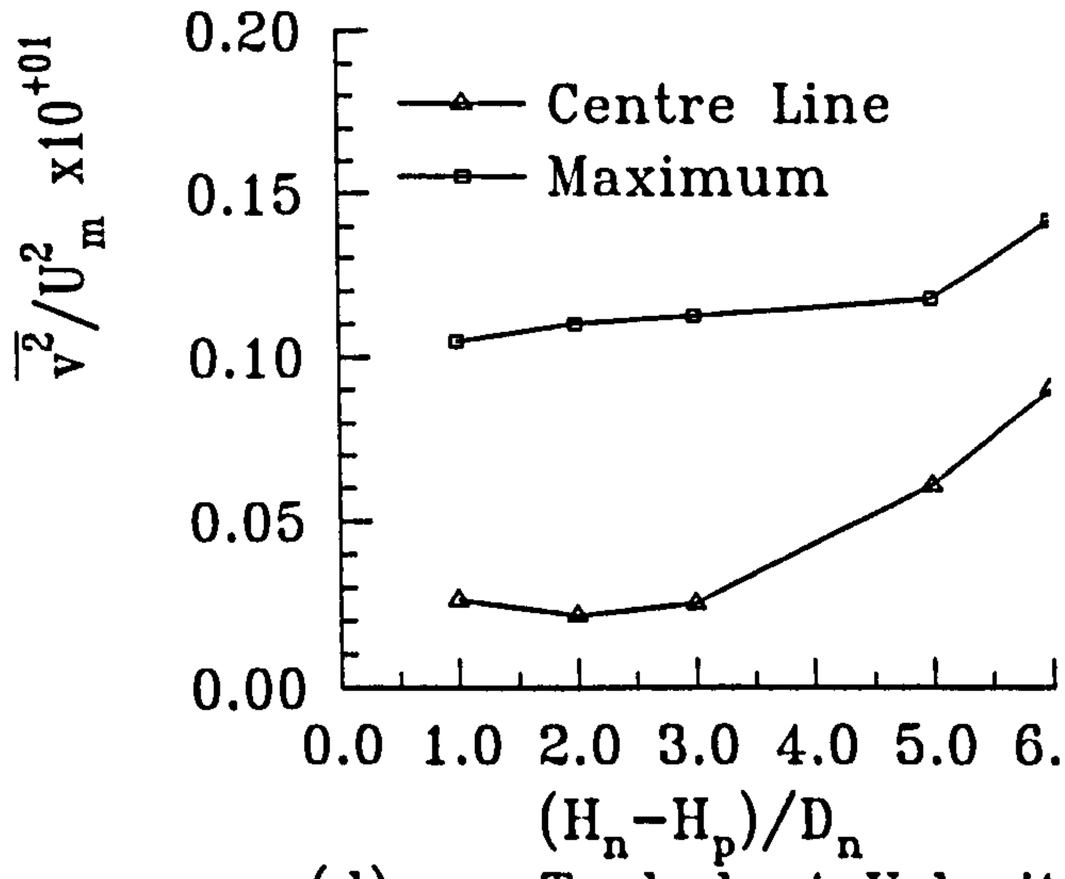

(d) : v Turbulent Velocity

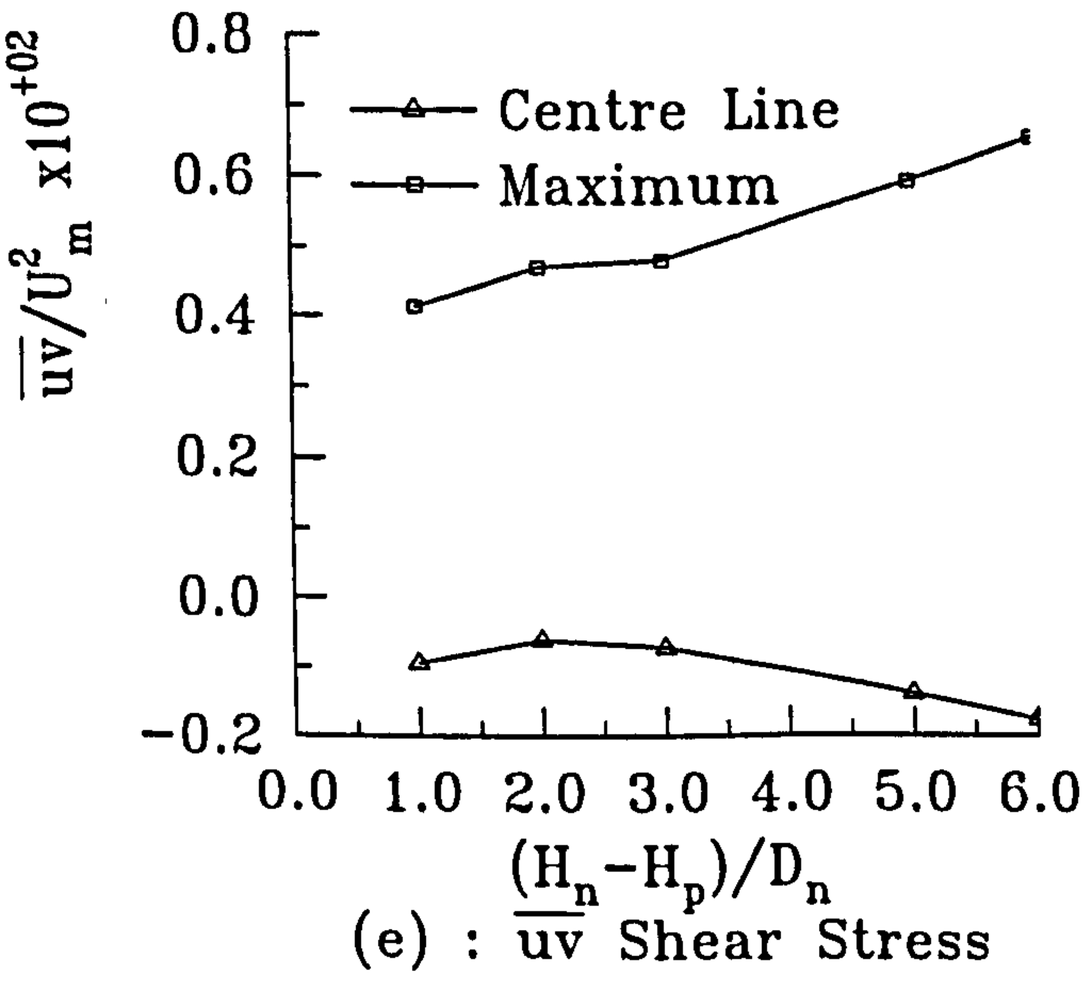

(e) : $\overline{uv}$ Shear Stress

Figure 4.31 : Free Jet Details for Varying H_p/D_n, H_n/D_n = 10.0 and NPR = 1.05

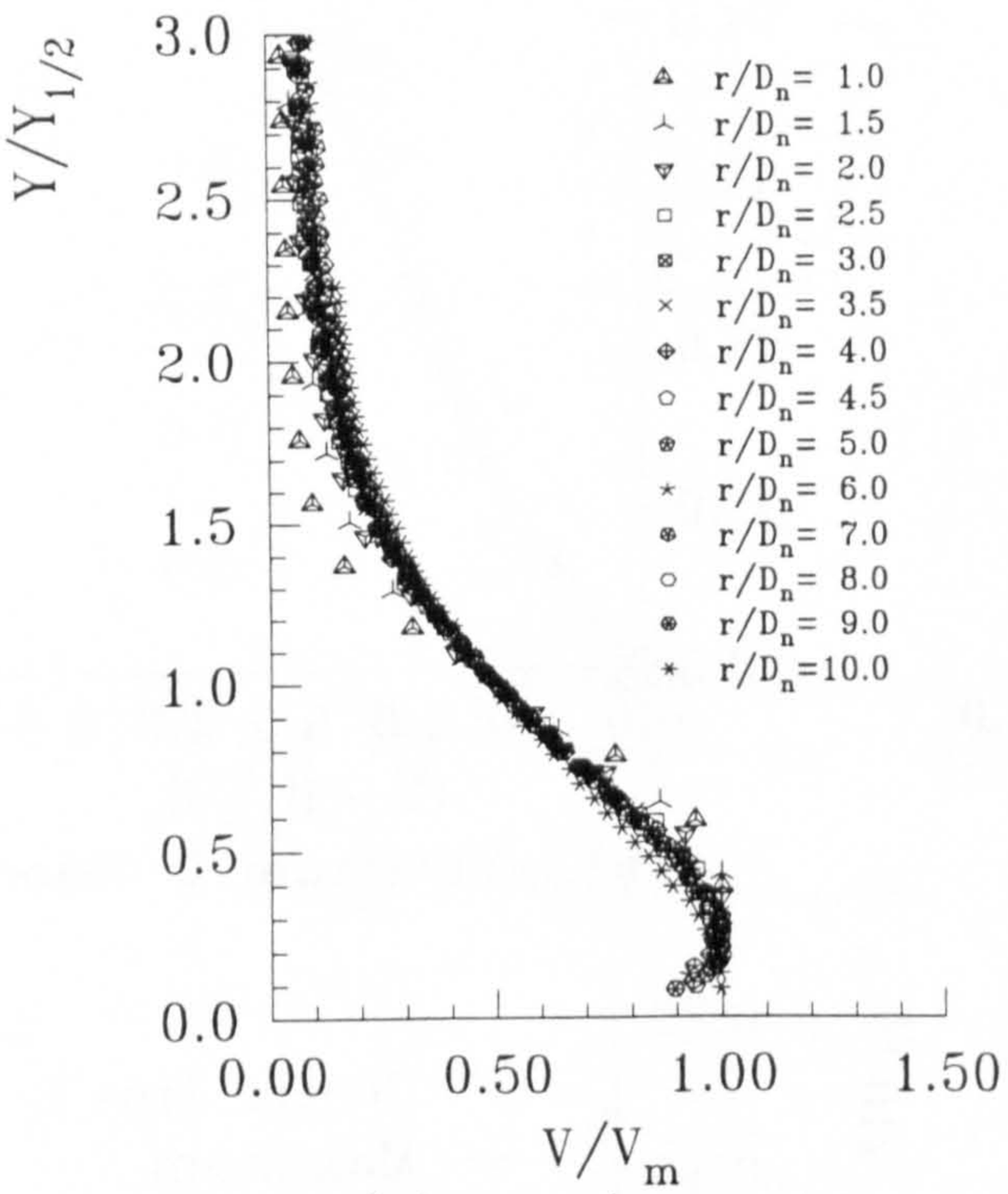

(a) : H_n/D_n = 2.0

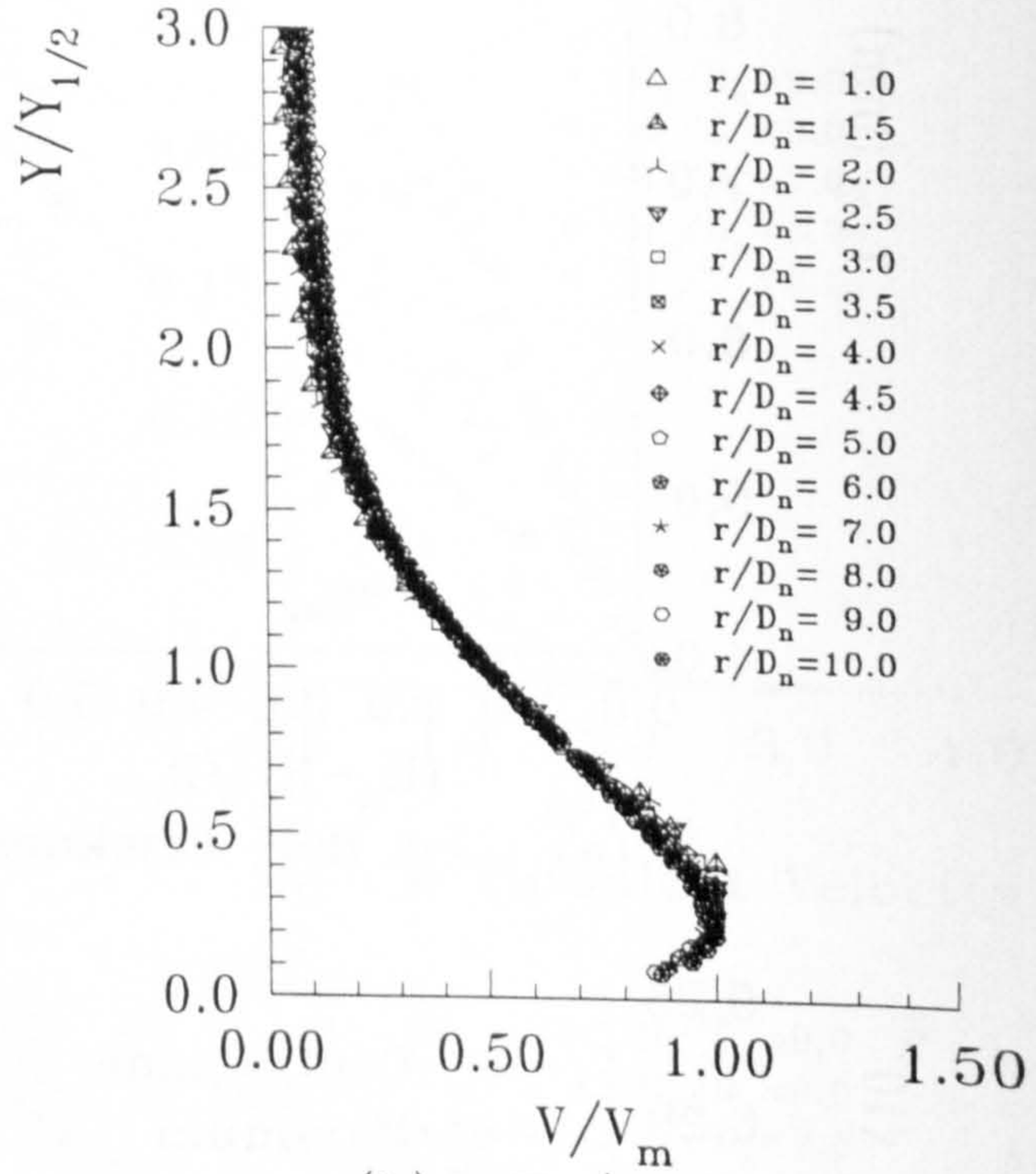

(b) : H_n/D_n = 4.0

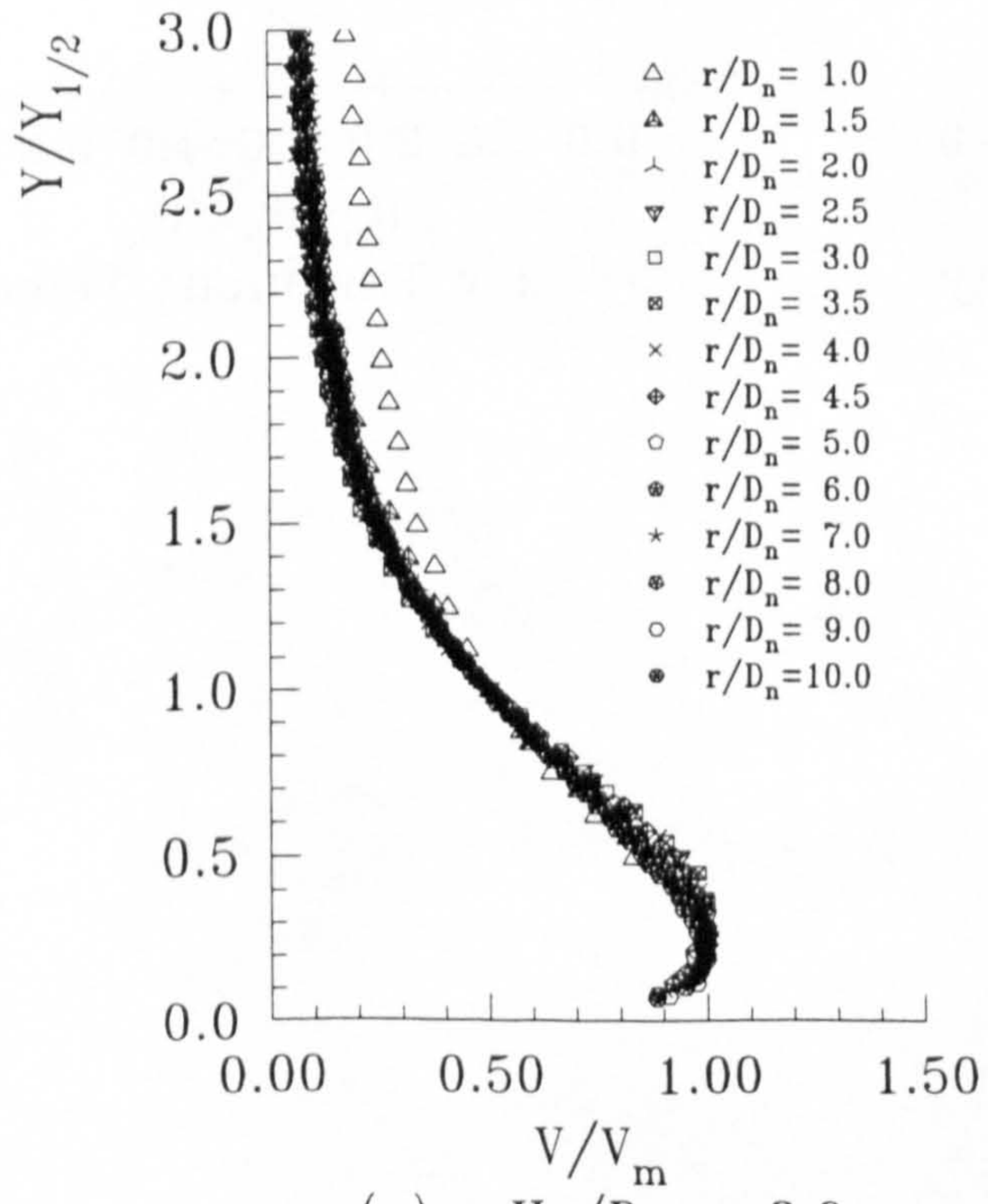

(c) : H_n/D_n = 8.0

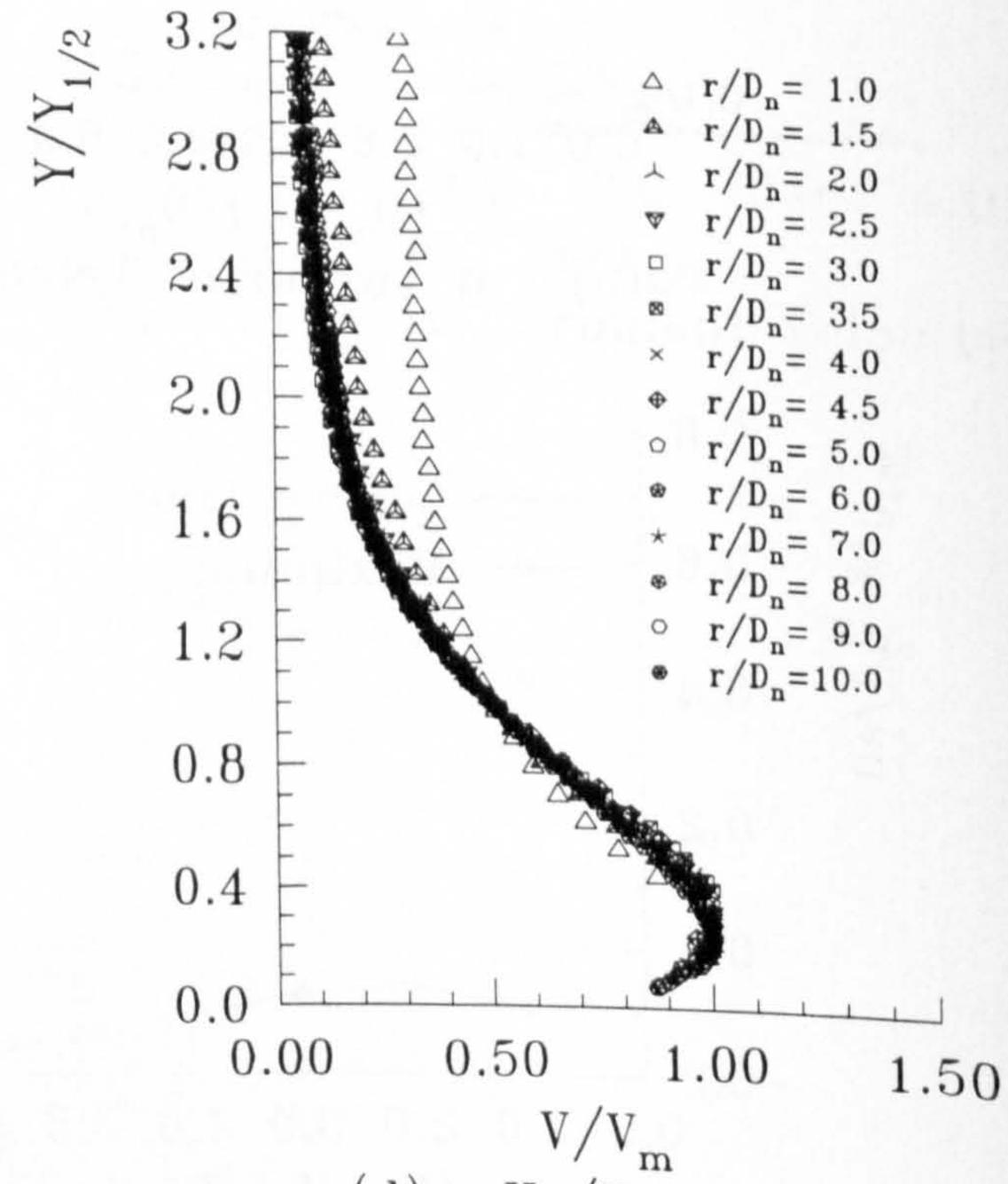

(d) : H_n/D_n = 10.0

Figure 4.32 : Non-dimensional V Mean Velocity Component Profiles at Different r/D_n for Varying H_n/D_n, NPR=1.05

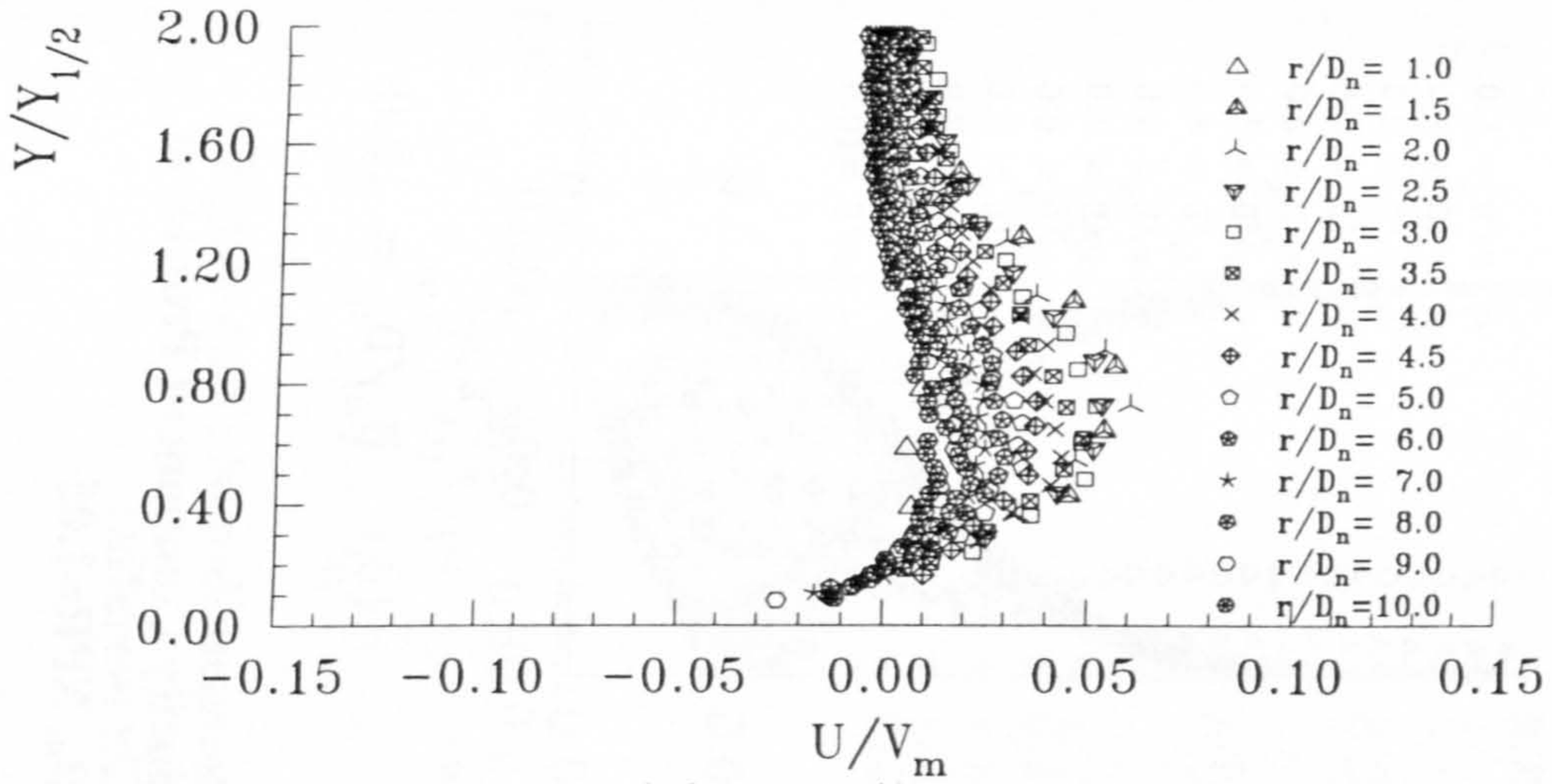

(a) : H_n/D_n = 2.0

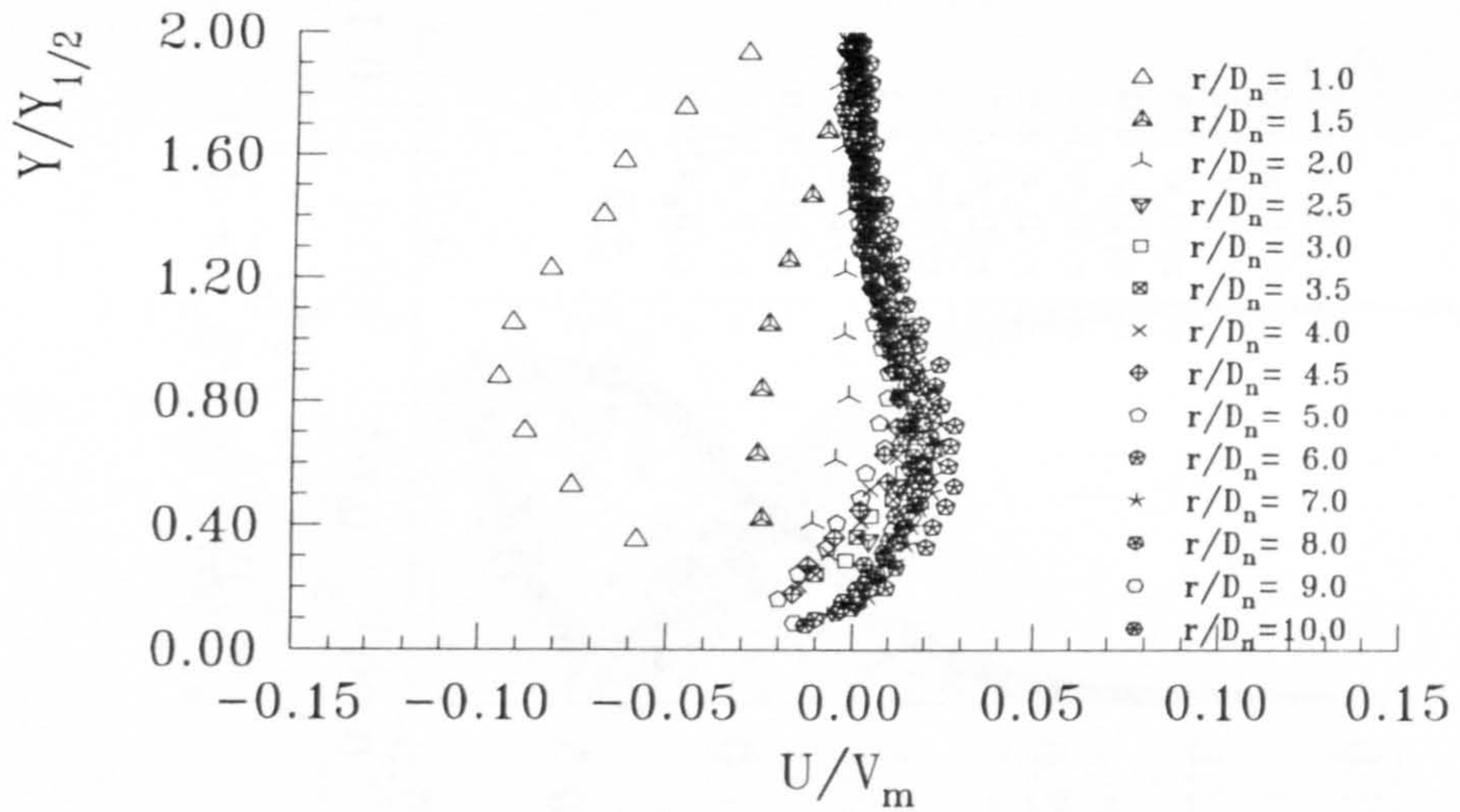

(b) : H_n/D_n = 4.0

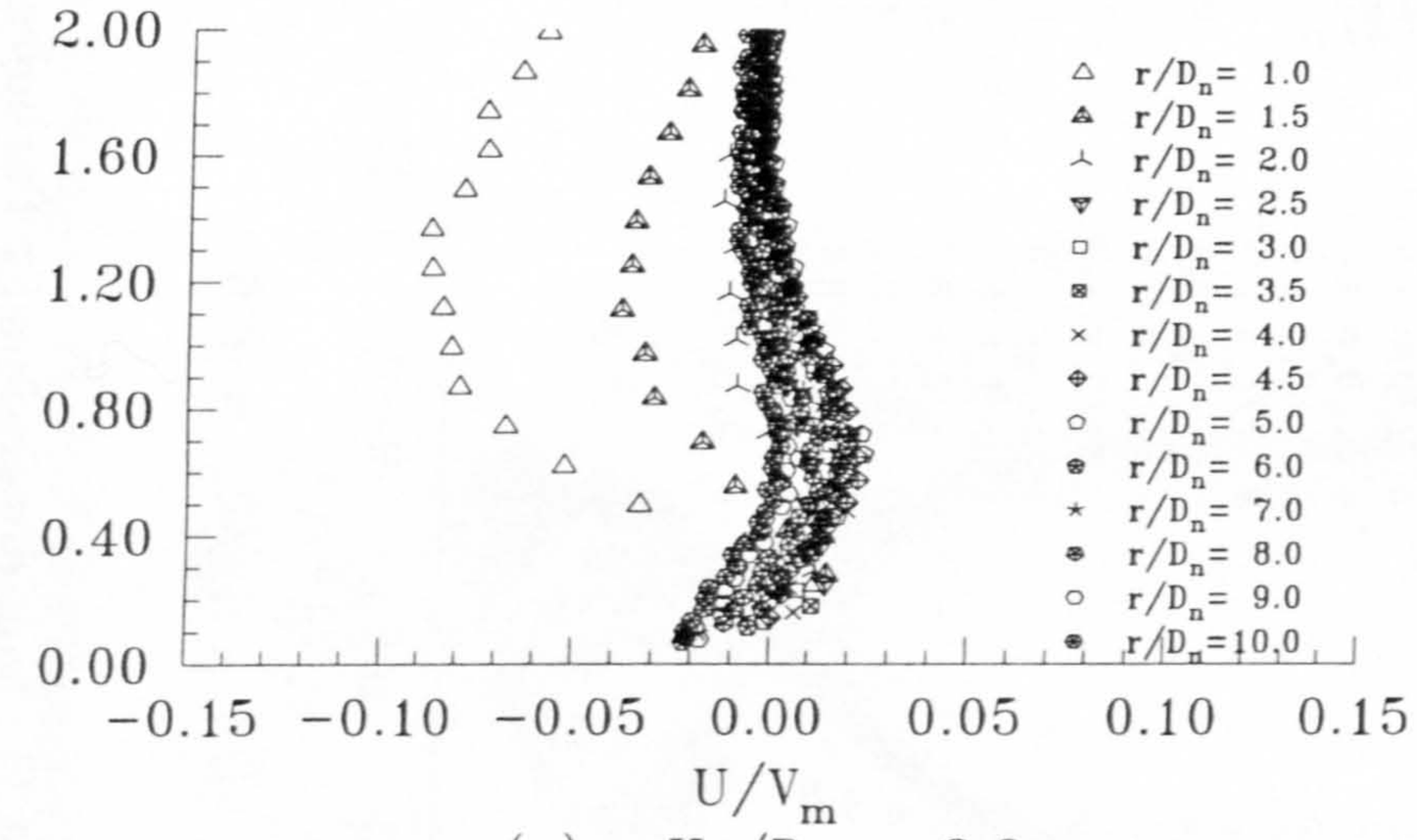

(c) : H_n/D_n = 3.0

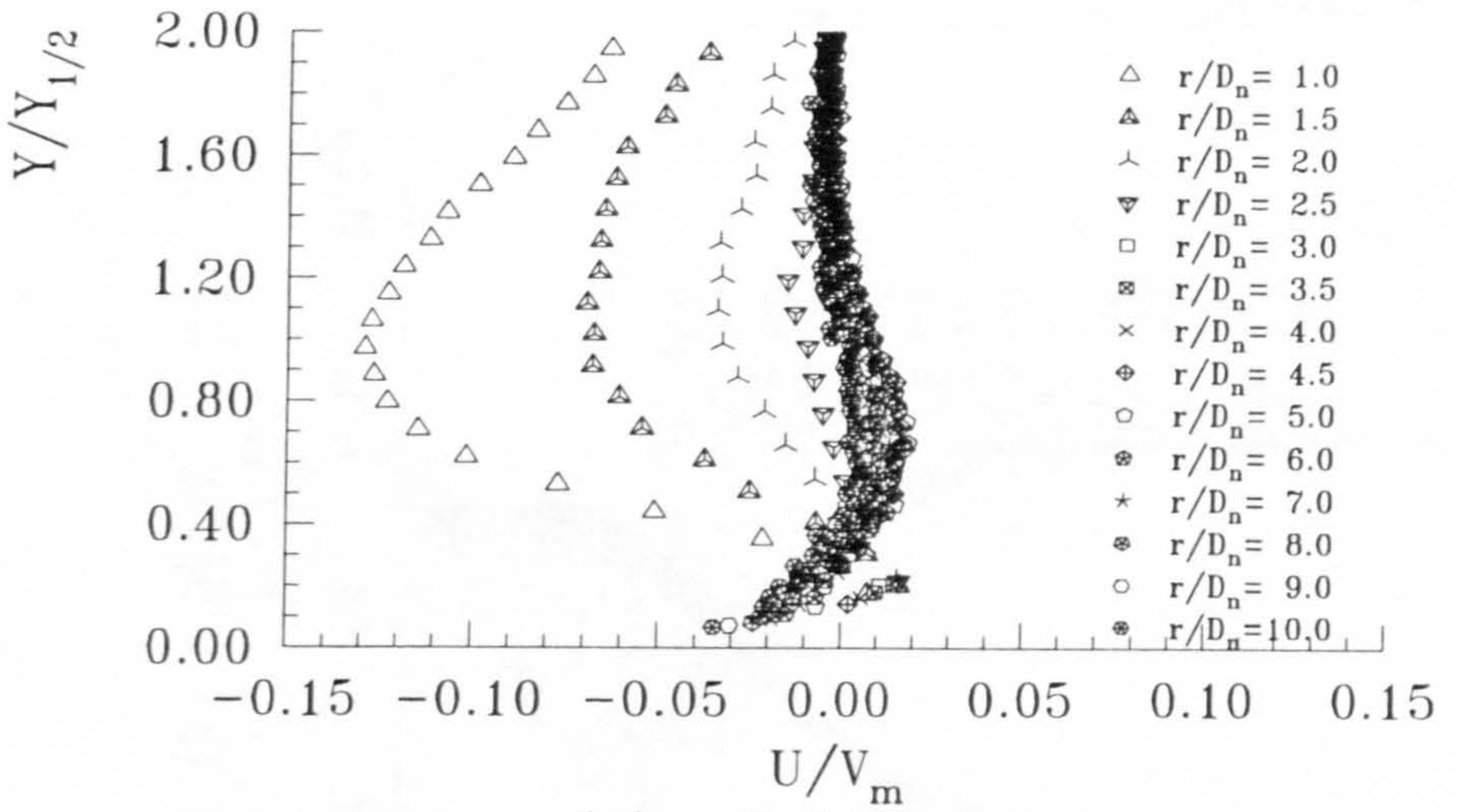

(d) : H_n/D_n = 10.0

Figure 4.33 : Non-dimensioanl U Mean Veloocity Component Profiles at Different Radial Locations for Varying Nozzle Height, NPR=1.05

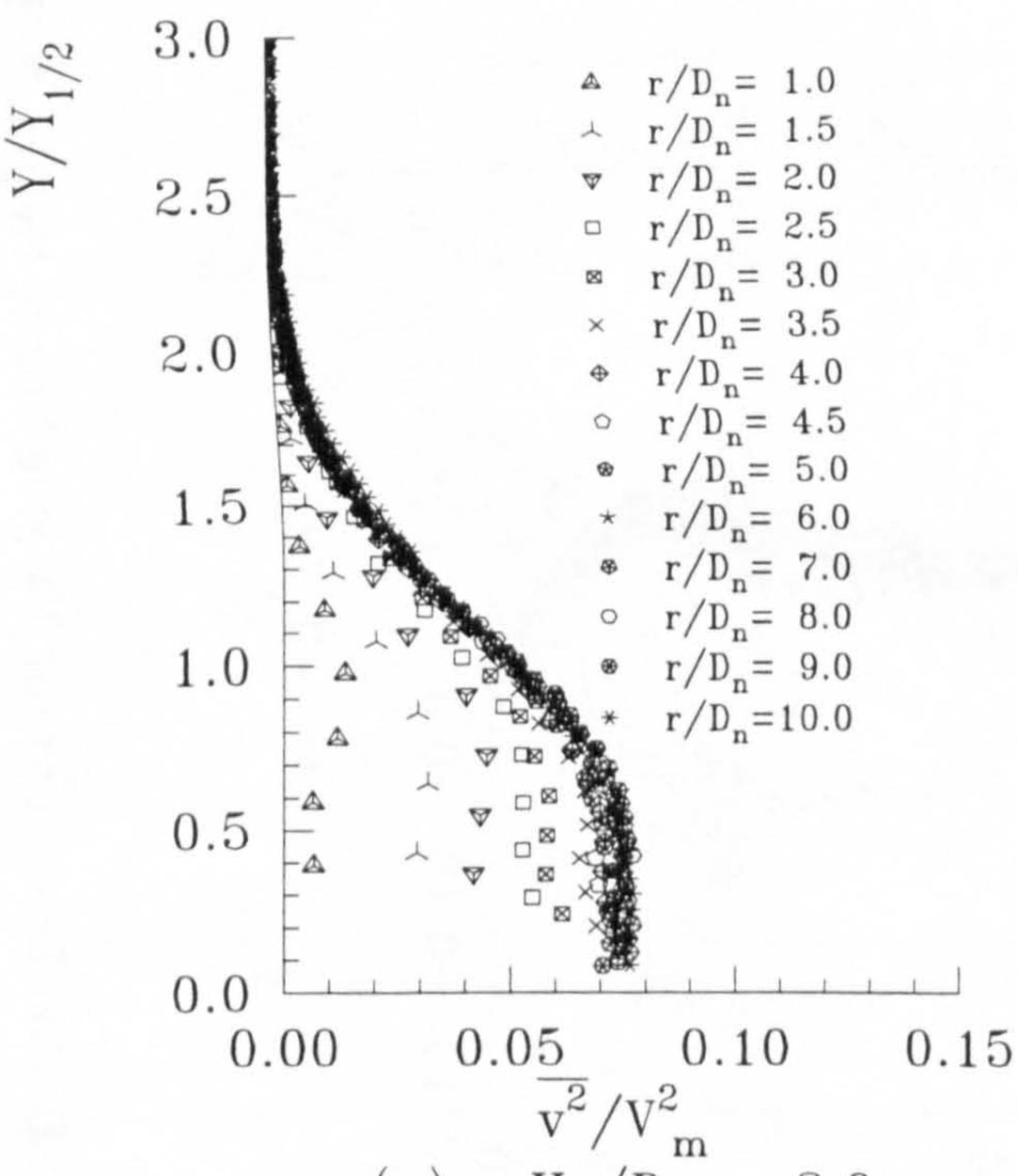

(a) : H_n/D_n = 2.0

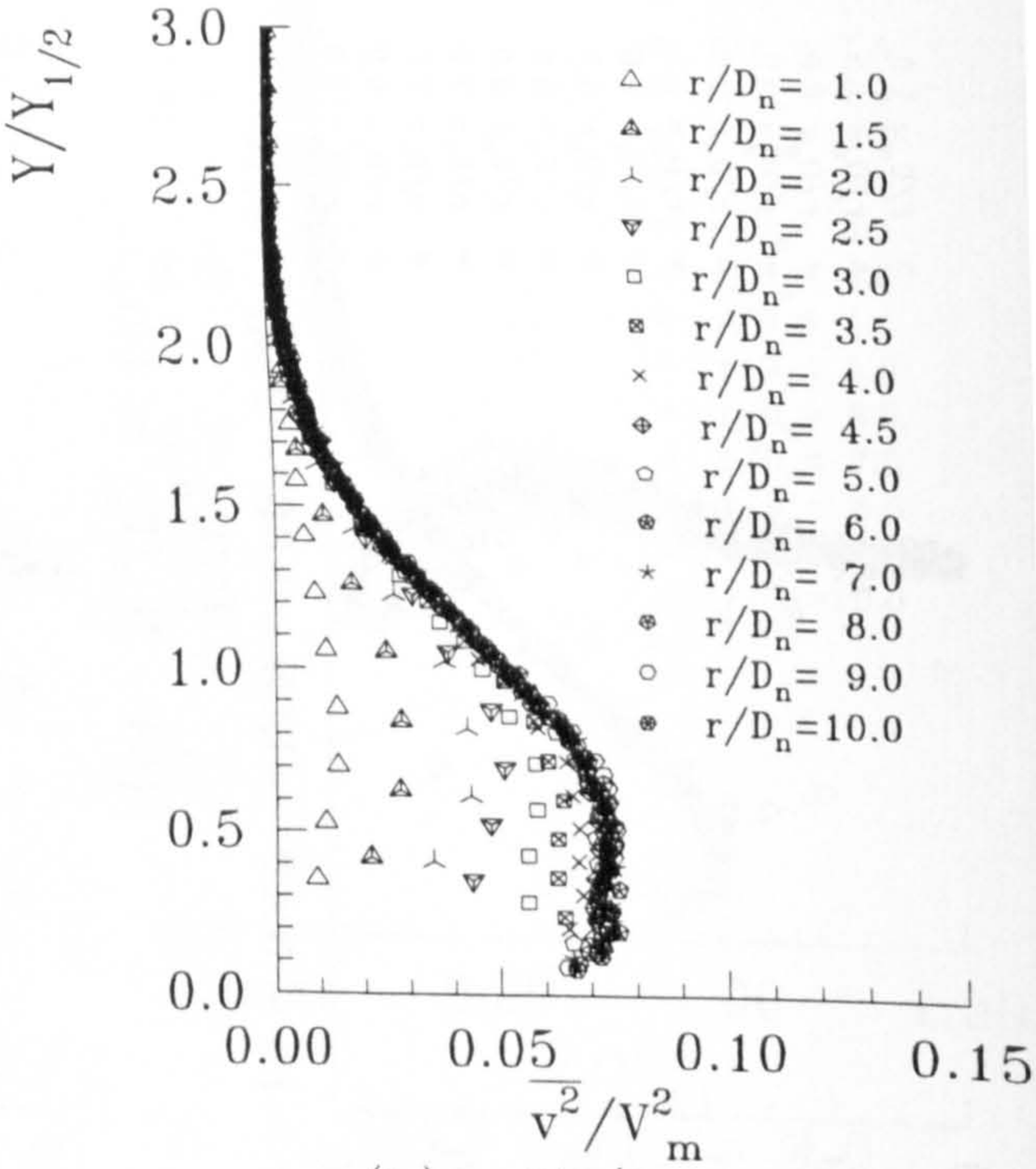

(b) : H_n/D_n = 4.0

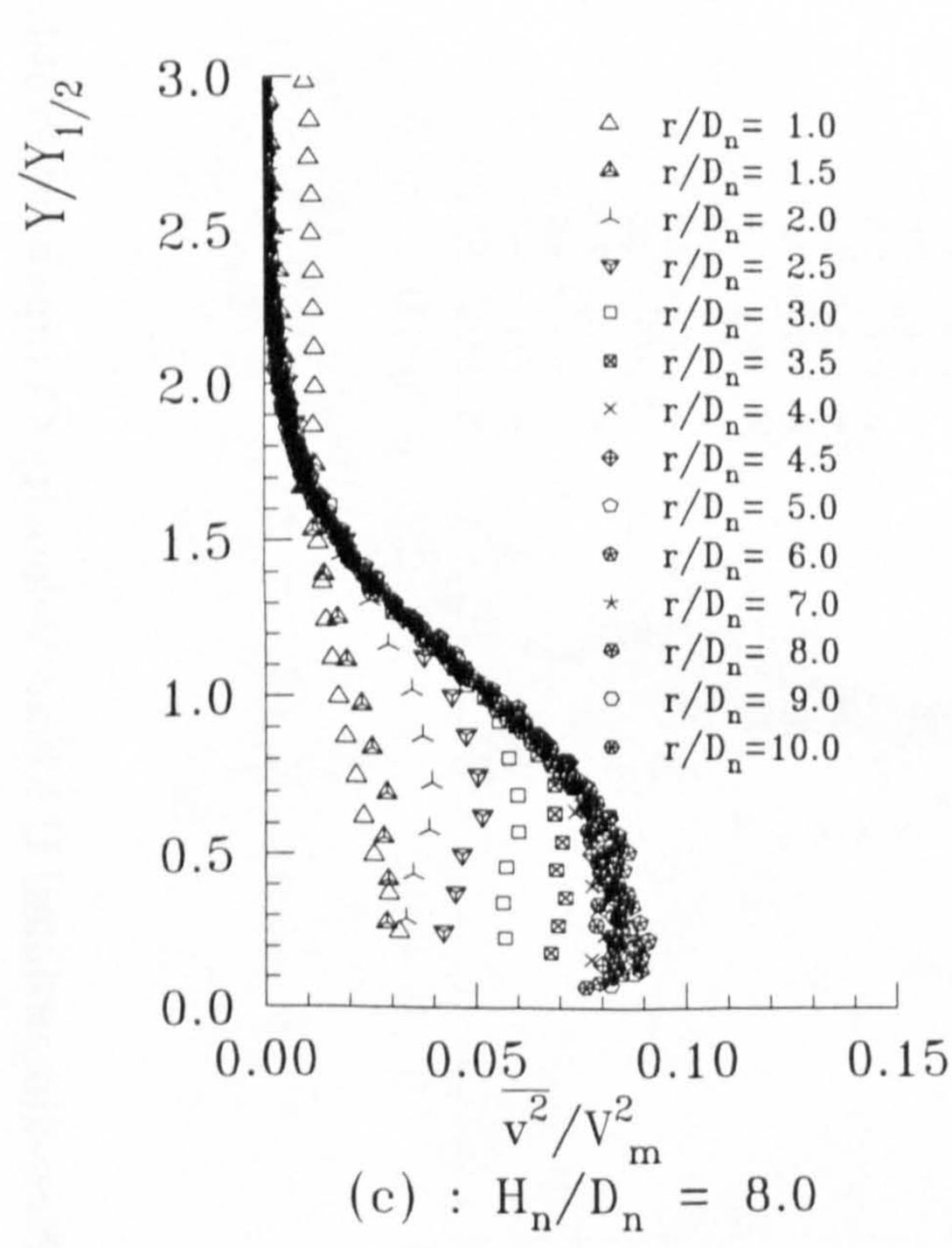

(c) : H_n/D_n = 8.0

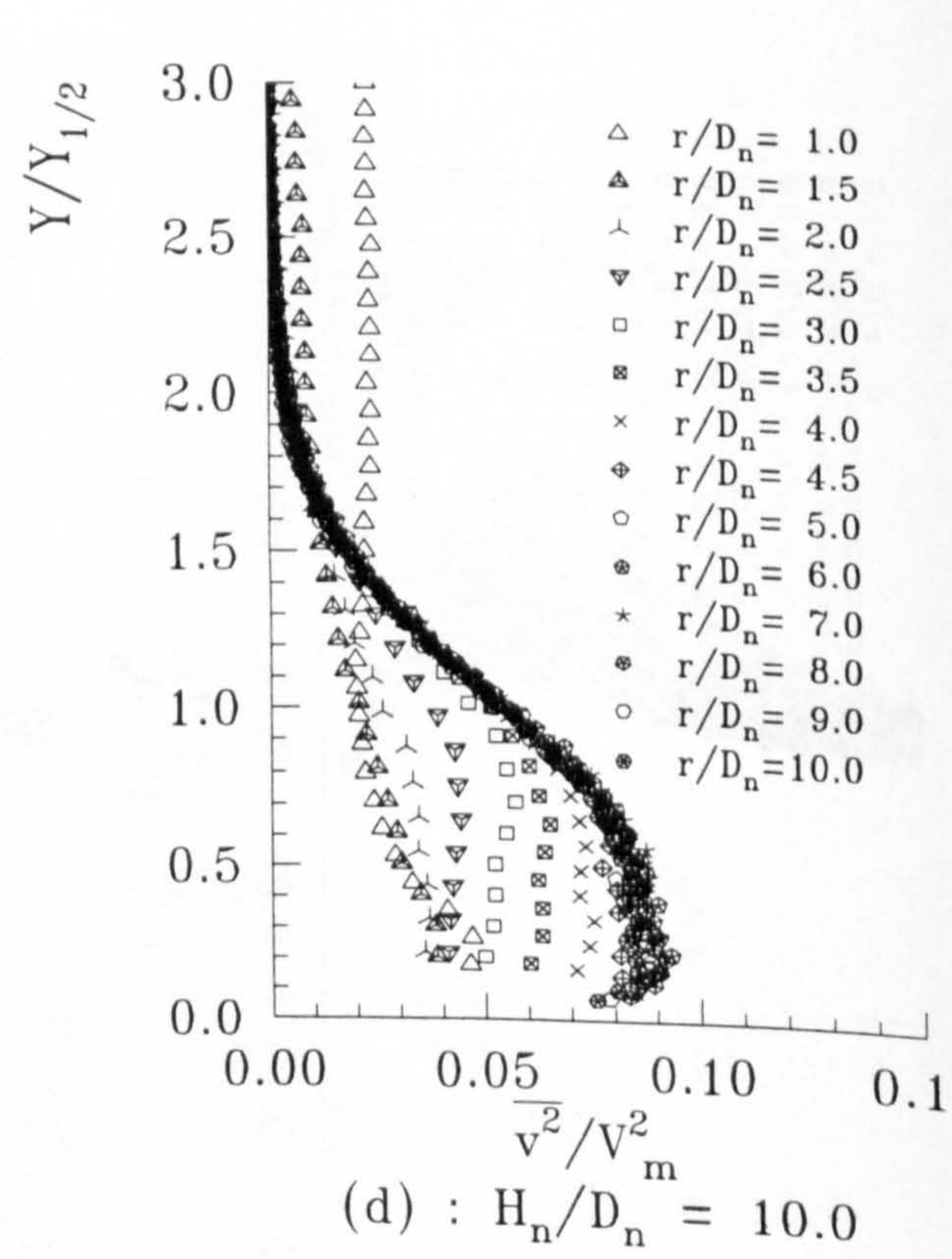

(d) : H_n/D_n = 10.0

Figure 4.34 : Non-dimensional v Turbulent Velocity Component Profiles at Different r/D_n for Varying H_n/D_n, NPR=1.05

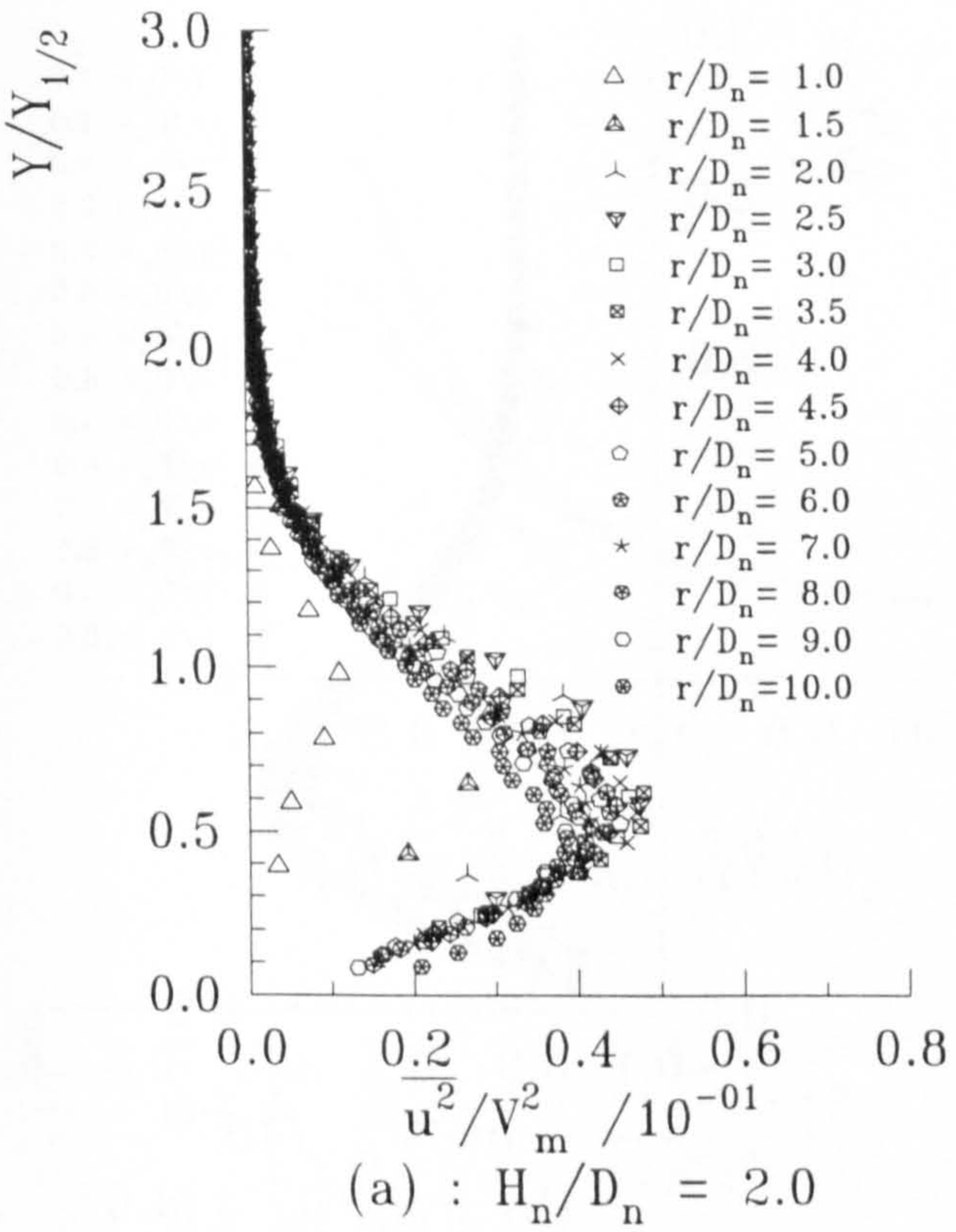

(a) : H_n/D_n = 2.0

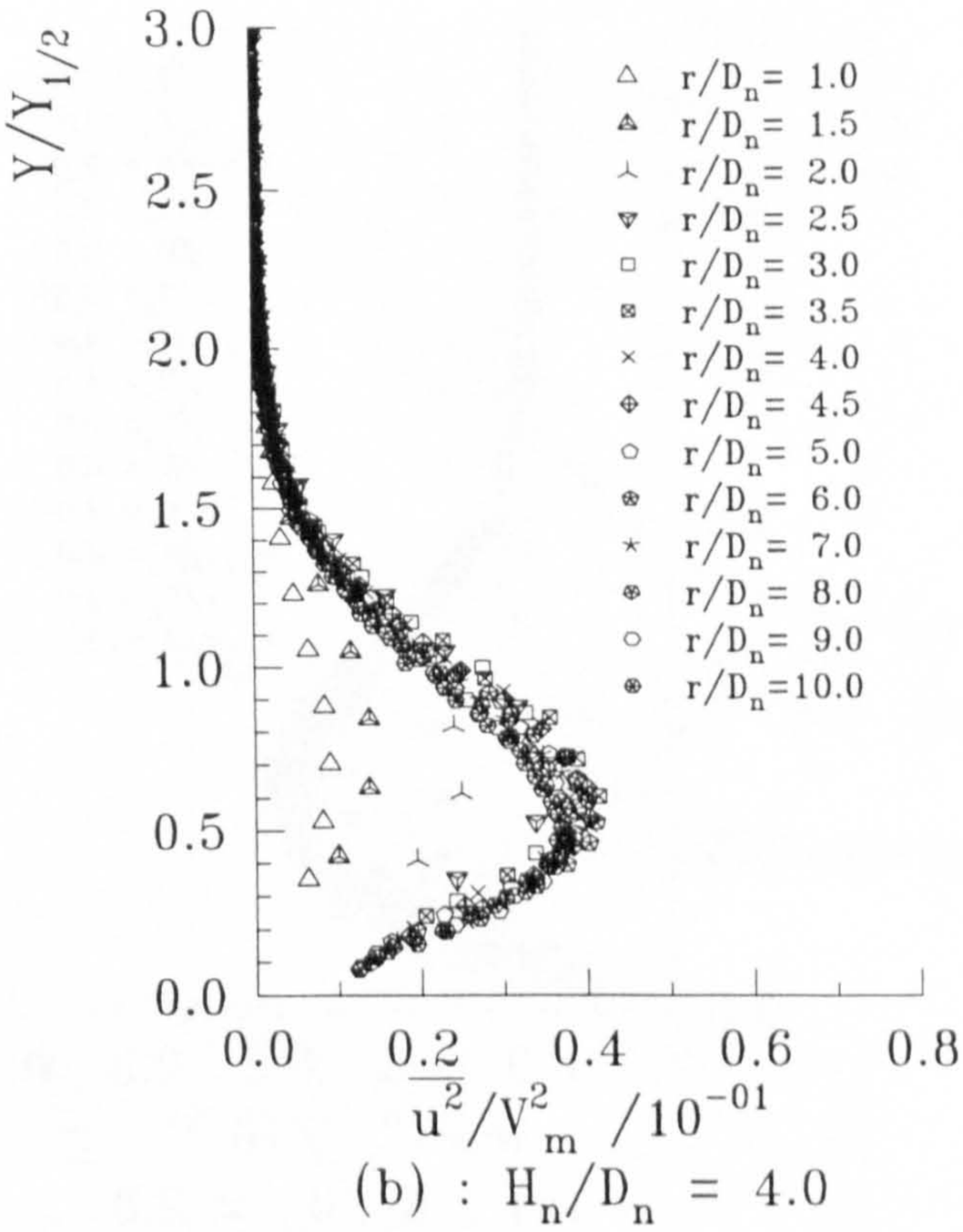

(b) : H_n/D_n = 4.0

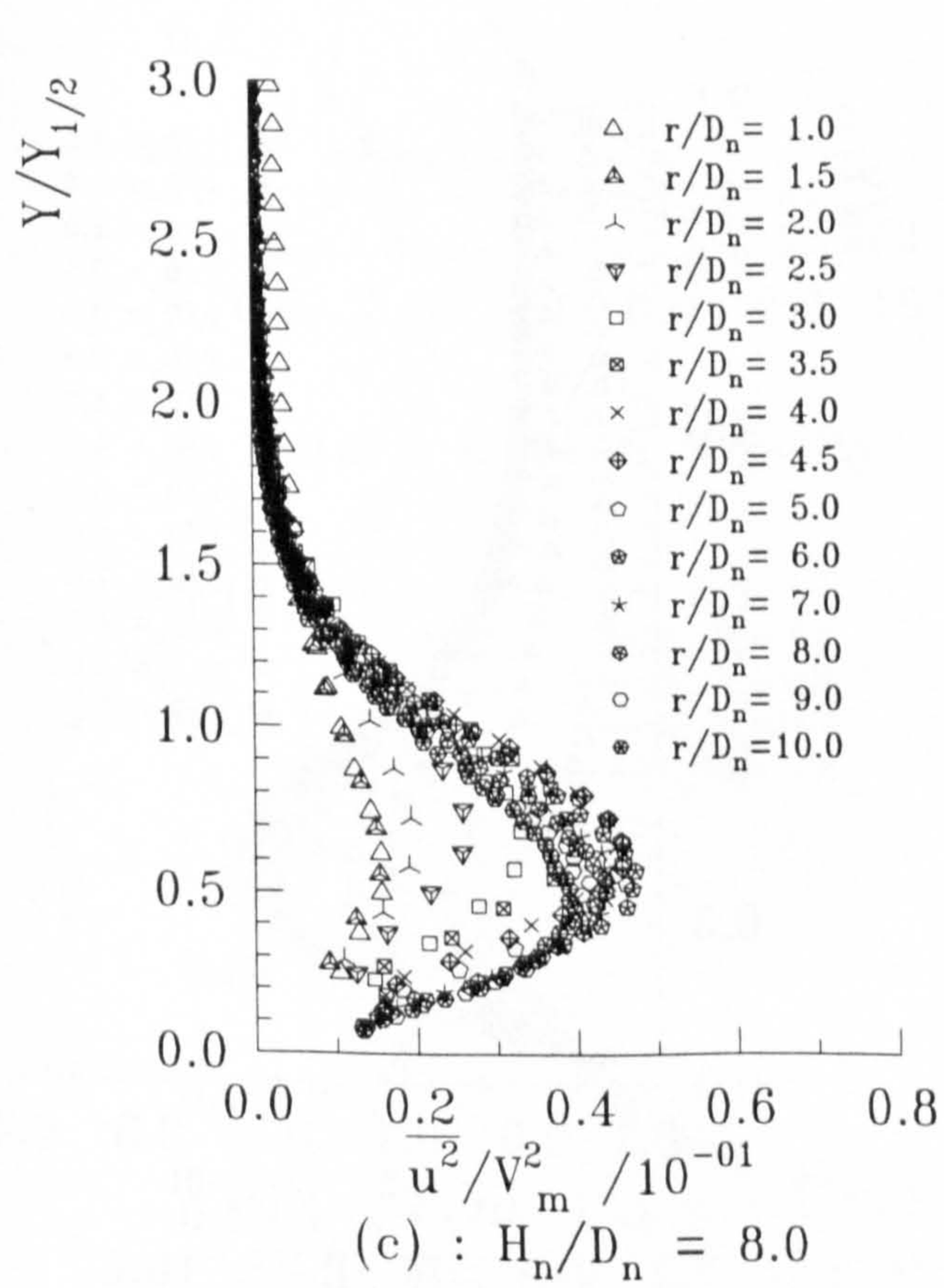

(c) : H_n/D_n = 8.0

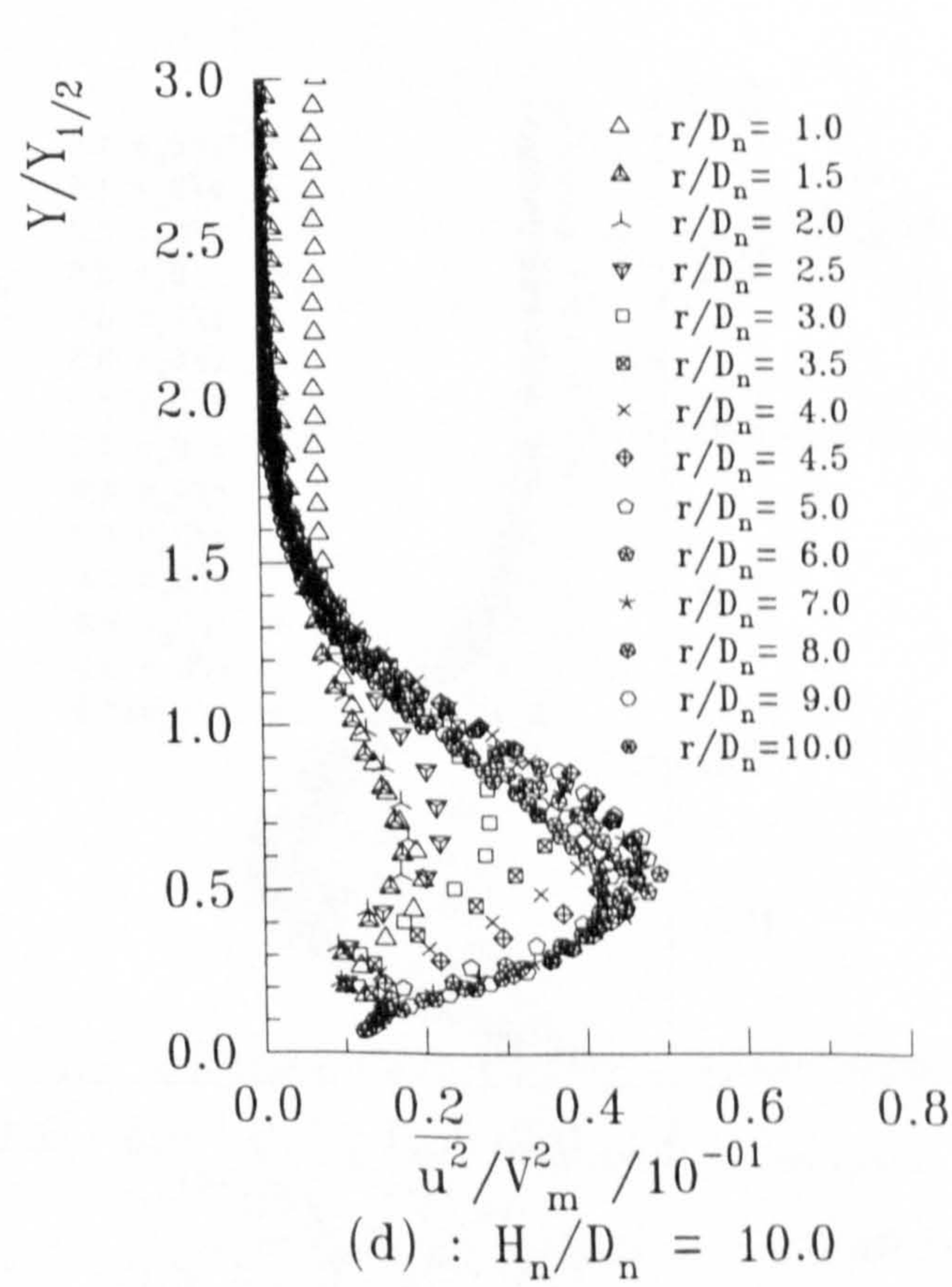

(d) : H_n/D_n = 10.0

Figure 4.35 : Non-dimensional u Turbulent Velocity Component Profiles at Different r/D_n for Varying H_n/D_n, NPR=1.05

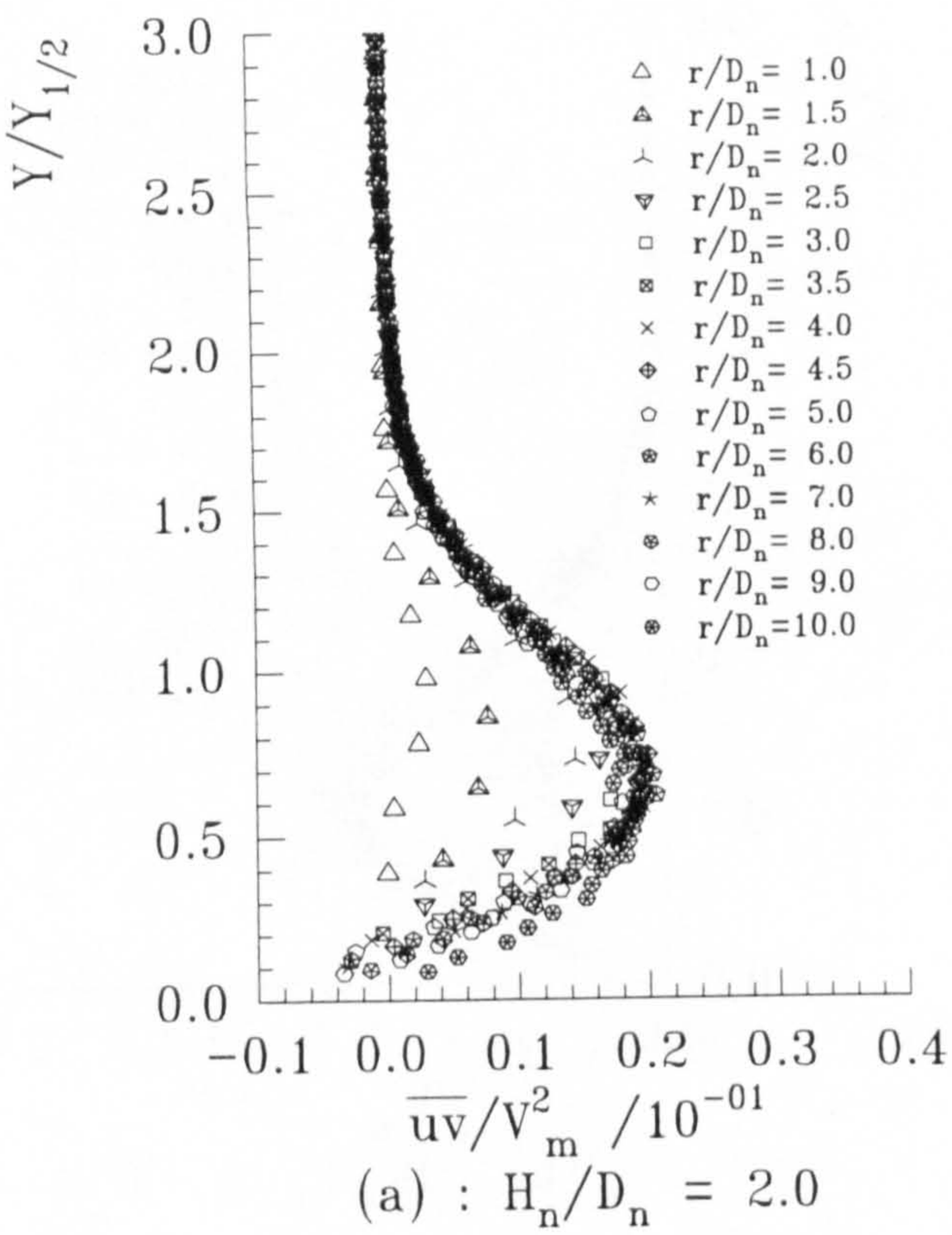

(a) : H_n/D_n = 2.0

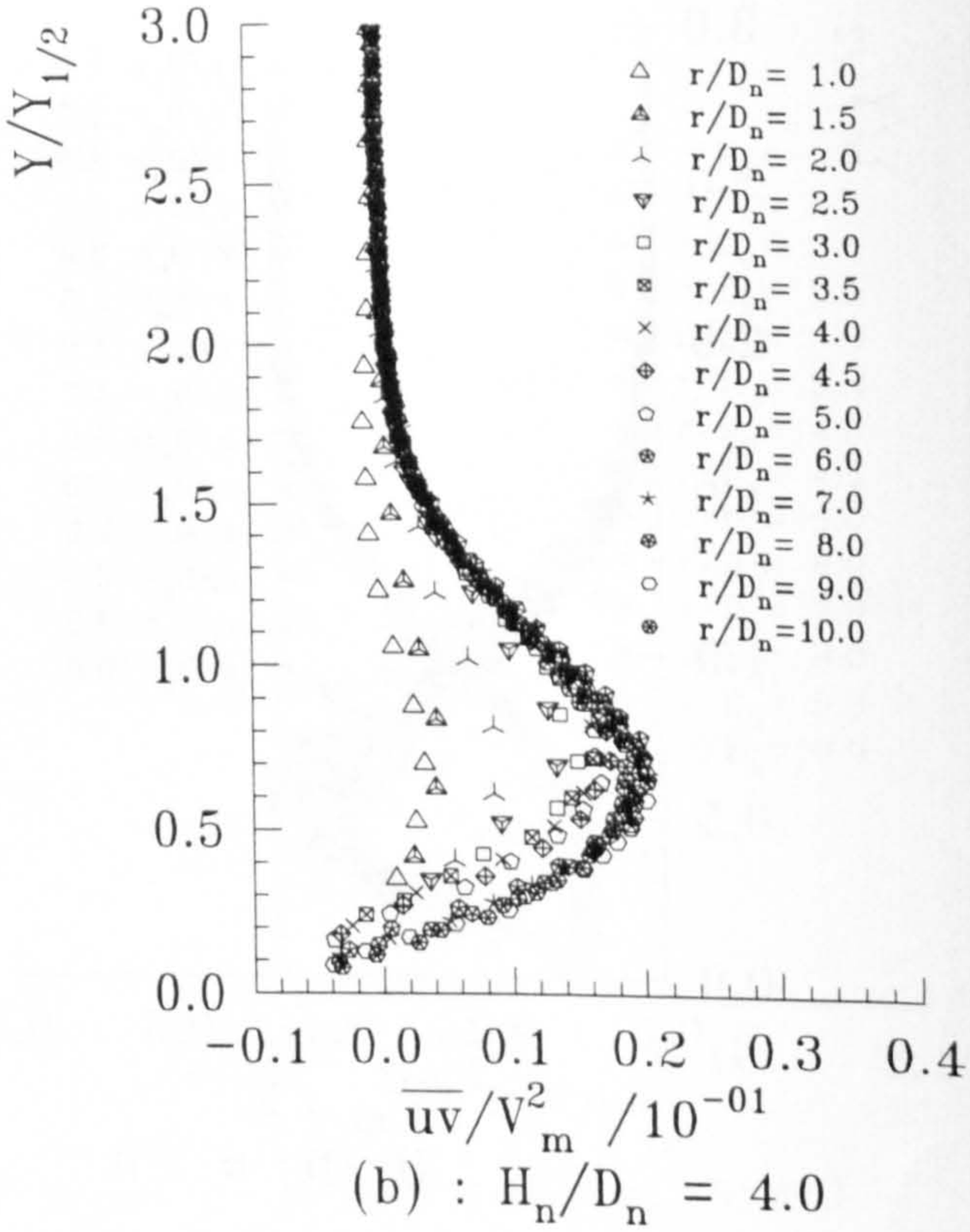

(b) : H_n/D_n = 4.0

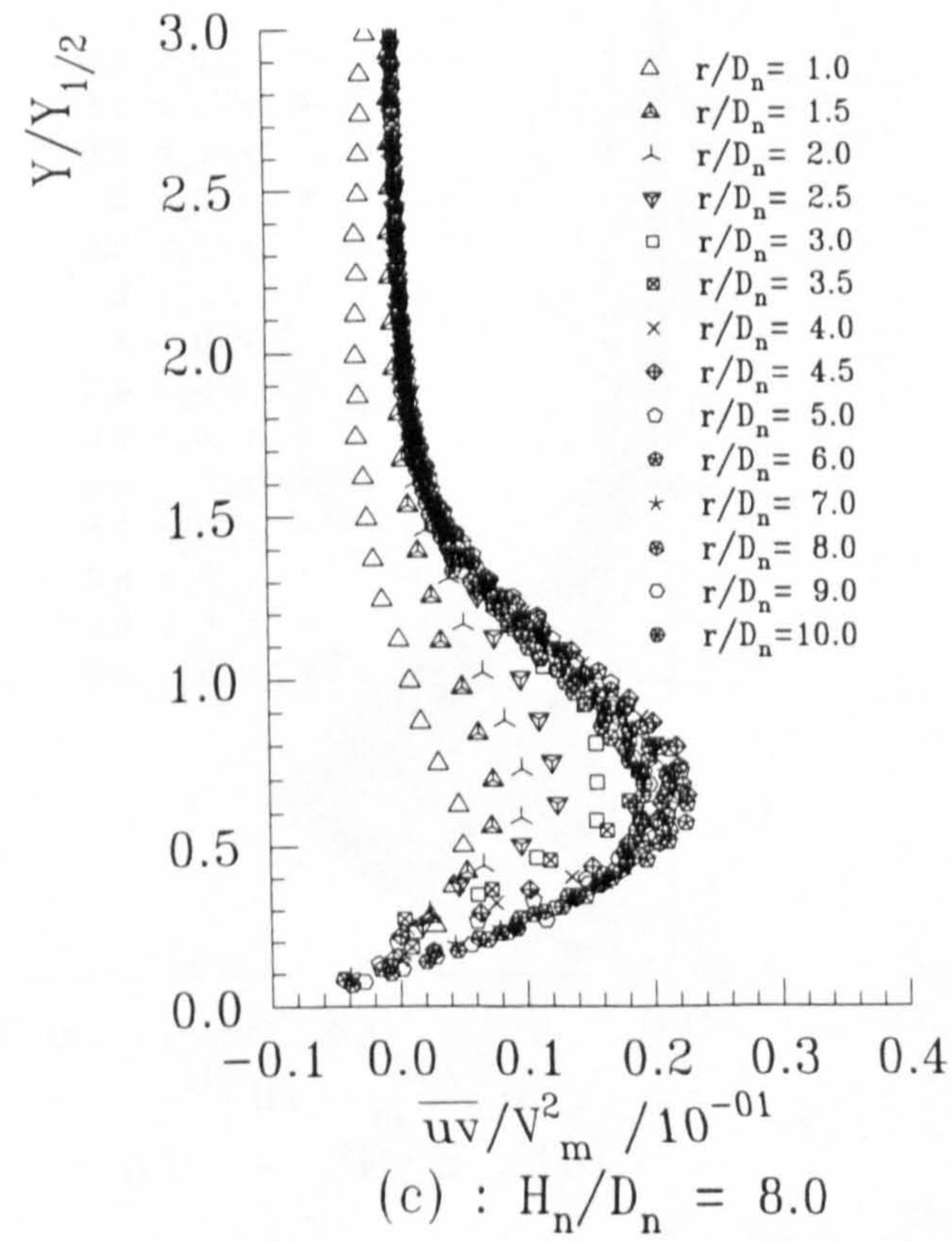

(c) : H_n/D_n = 8.0

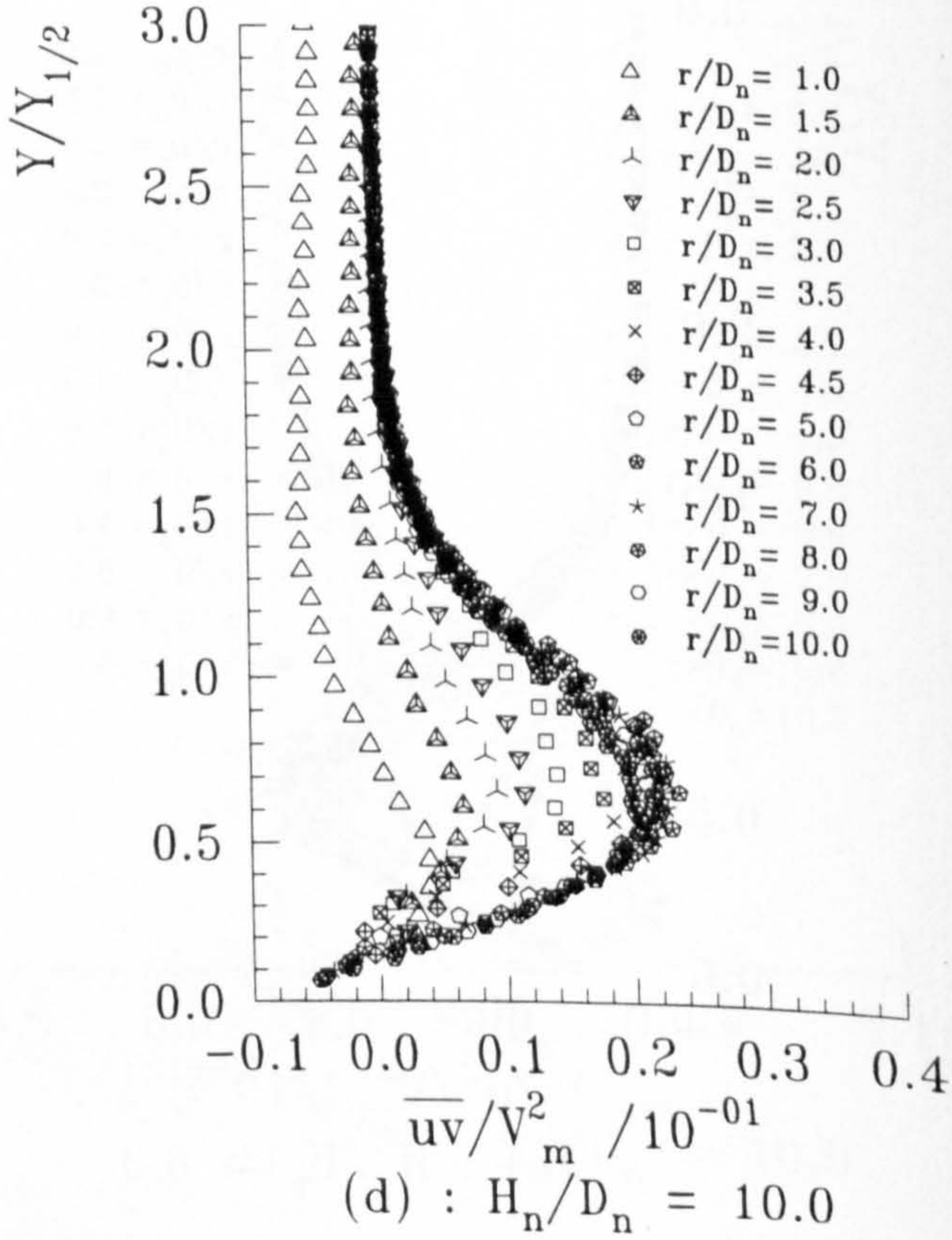

(d) : H_n/D_n = 10.0

Figure 4.36 : Non-dimensional Reynolds Shear Stress Component Profiles at Different r/D_n for Varying H_n/D_n, NPR=1.05

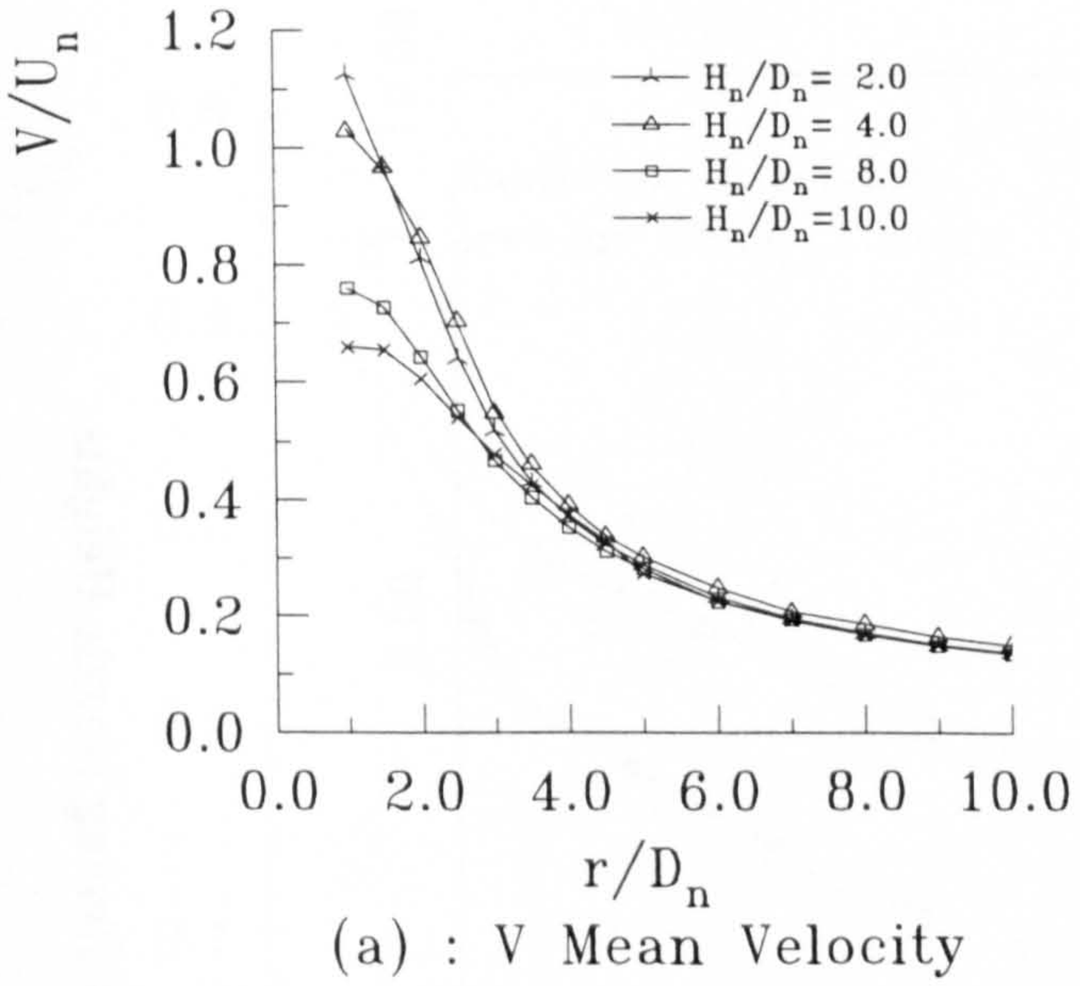

(a) : V Mean Velocity

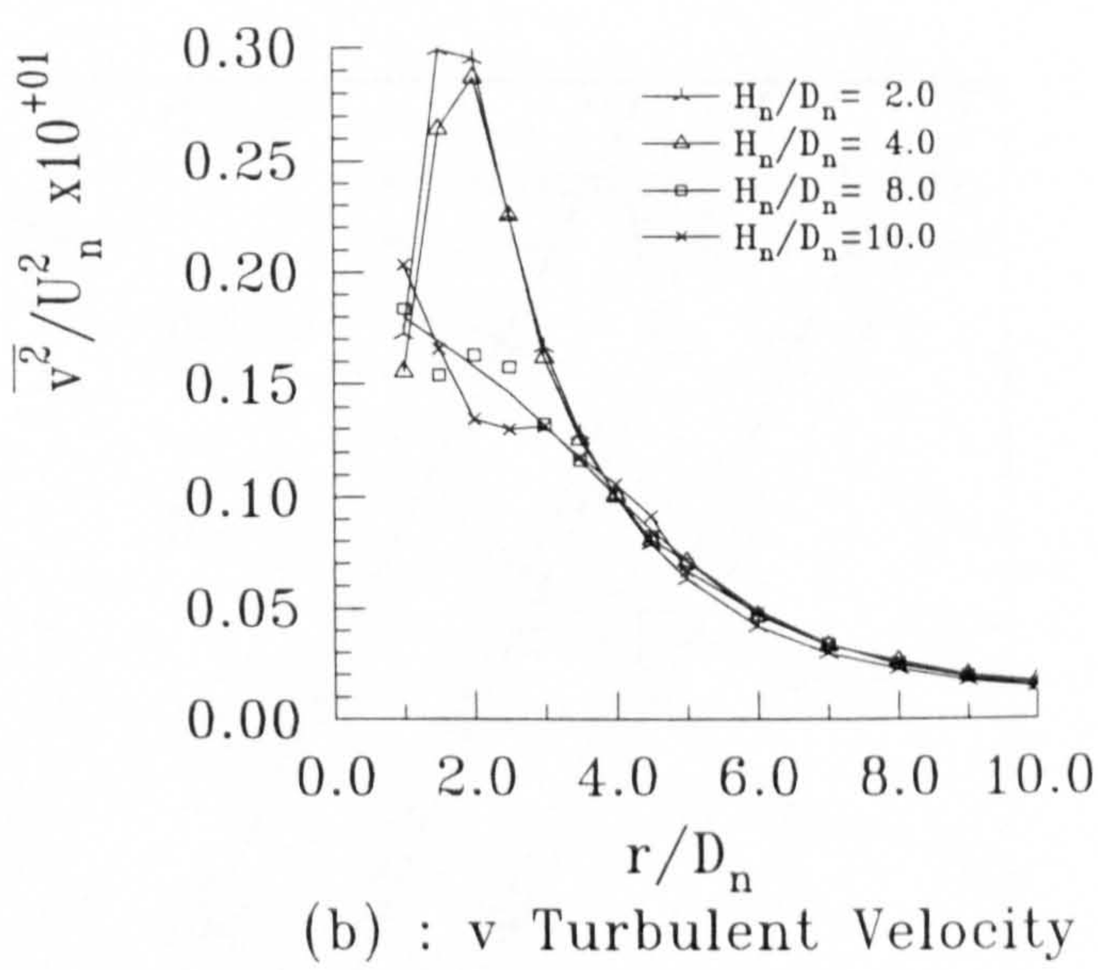

(b) : v Turbulent Velocity

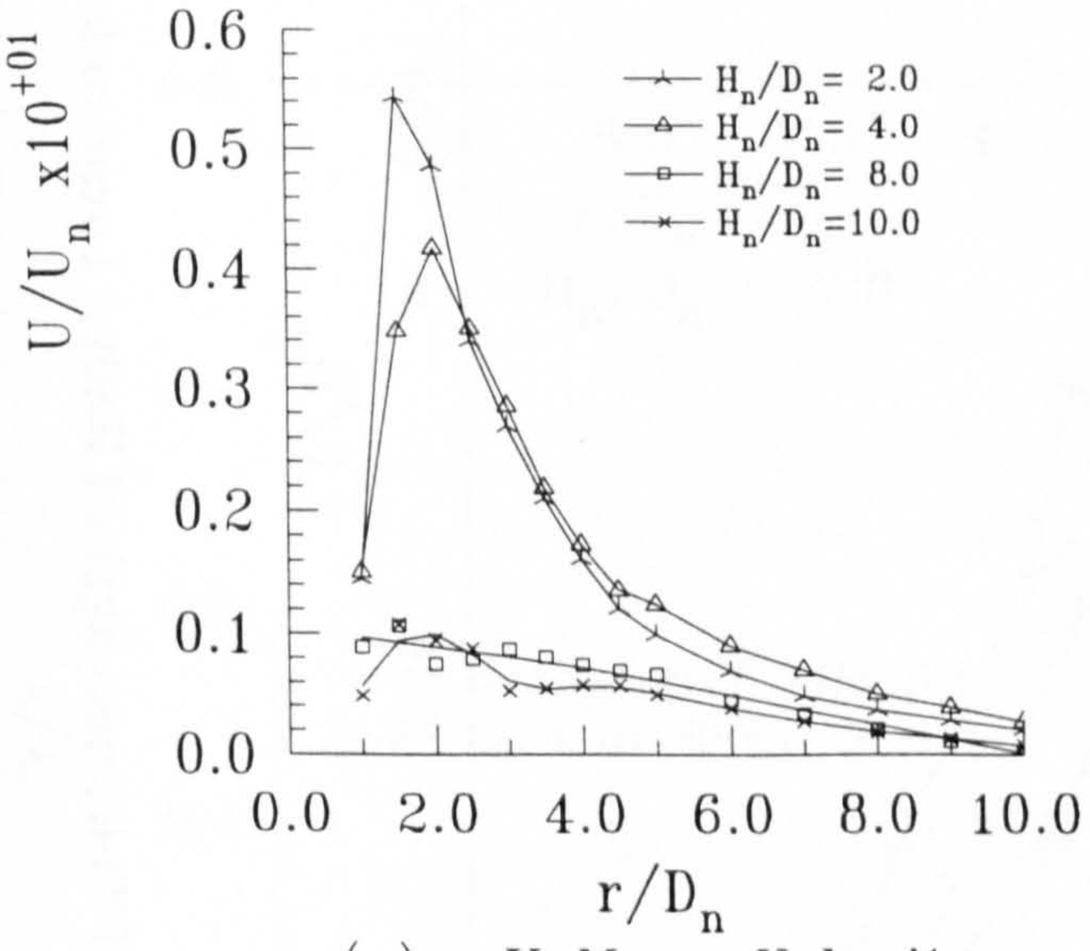

(c) : U Mean Velocity

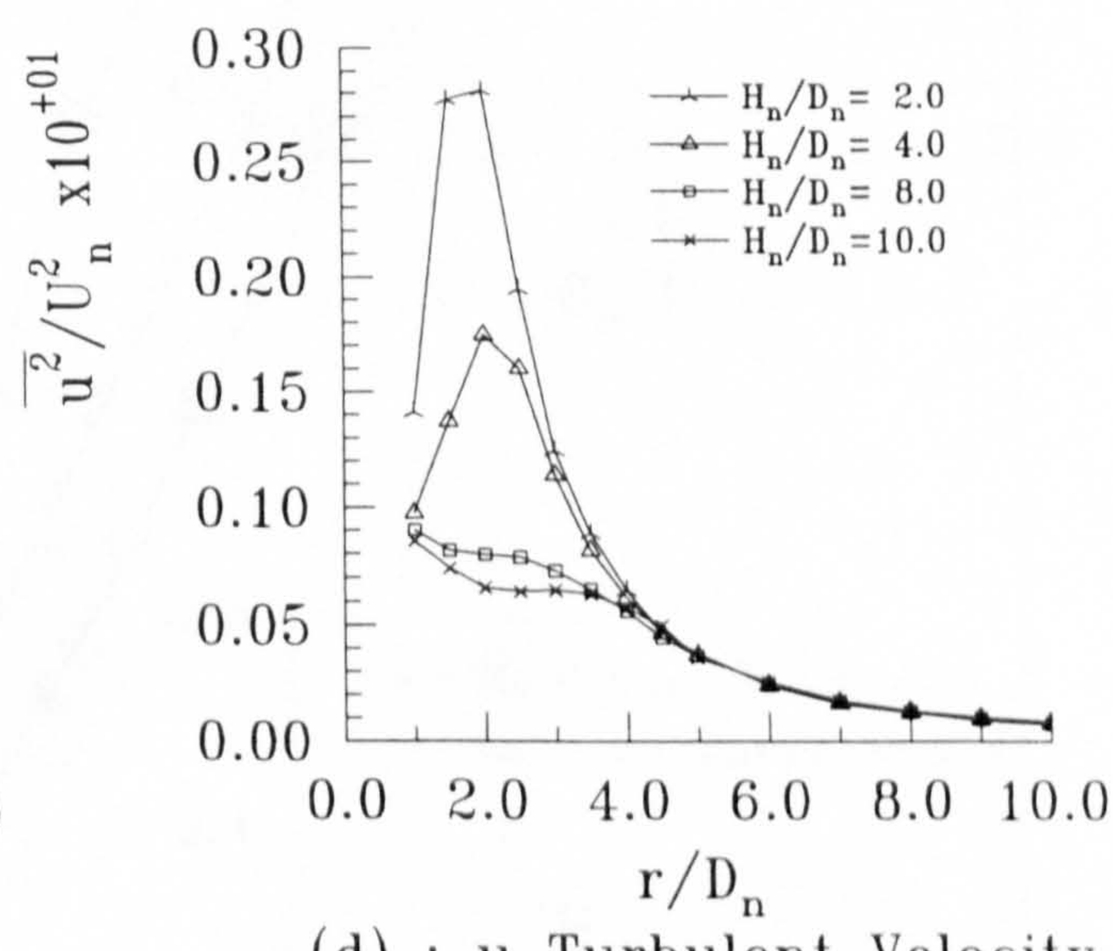

(d) : u Turbulent Velocity

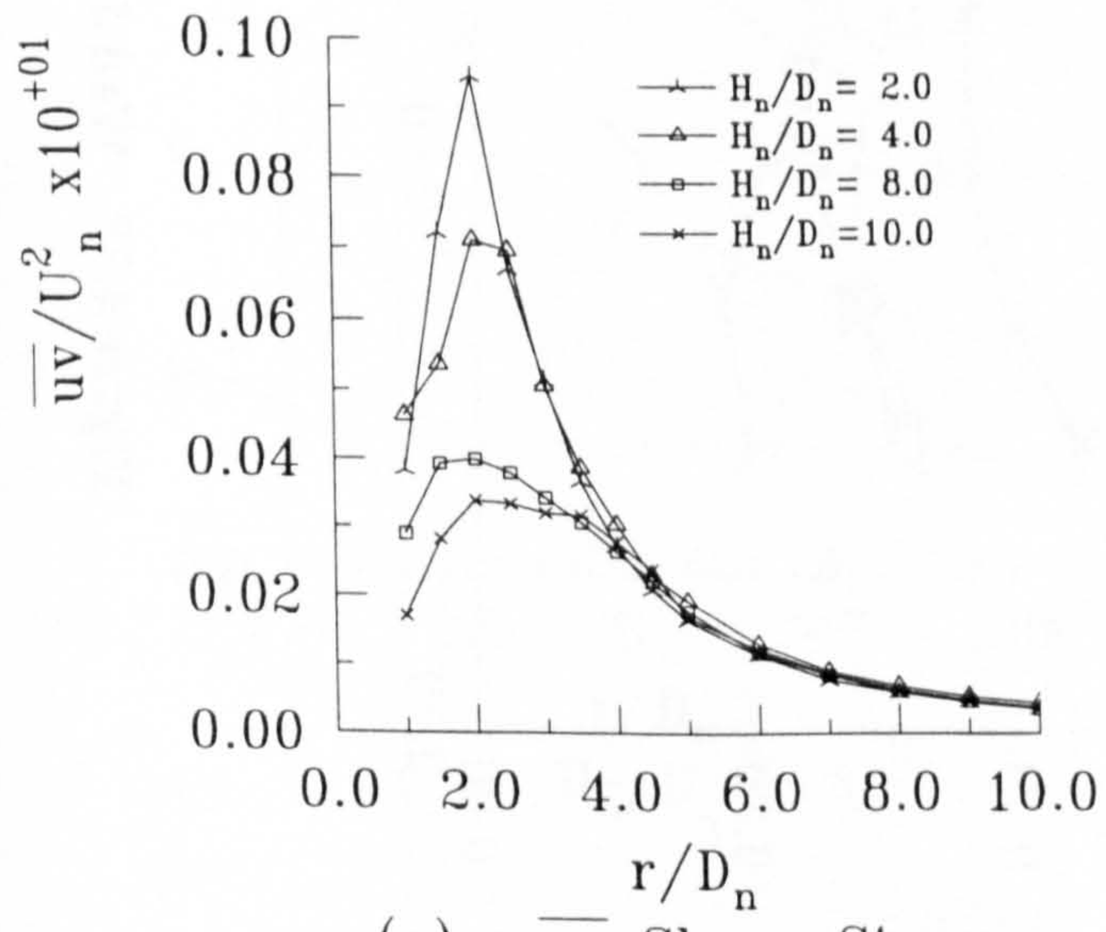

(e) : $\overline{uv}$ Shear Stress

Figure 4.37 : Peak Non-dimensional Values of Measured Mean and Turbulent Quantities in the Wall Jet against r/D_n for Varying H_n/D_n, NPR=1.05

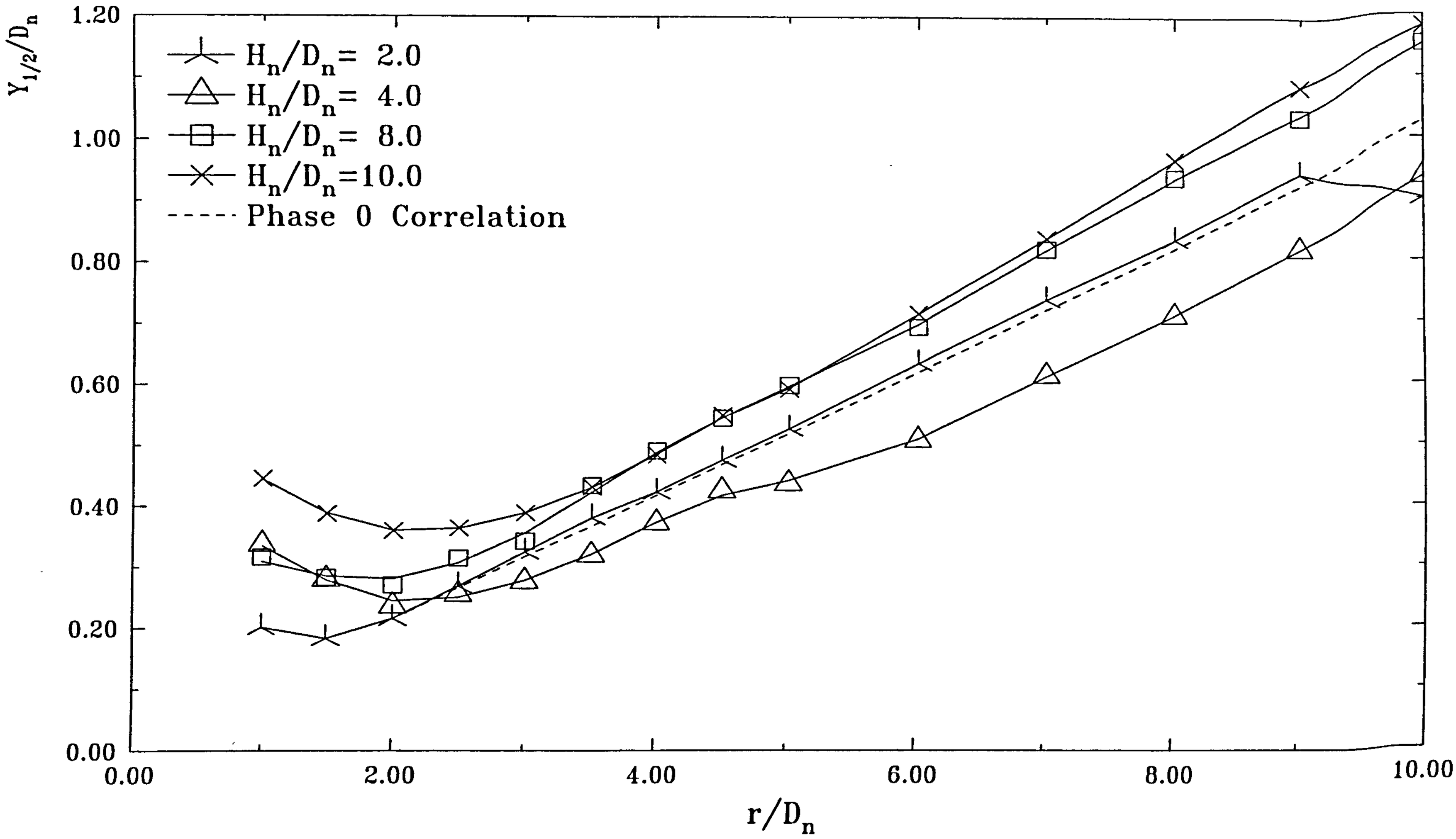

Figure 4.38 : Wall Jet Half Thickness against Radial Location for Differing Nozzle Heights

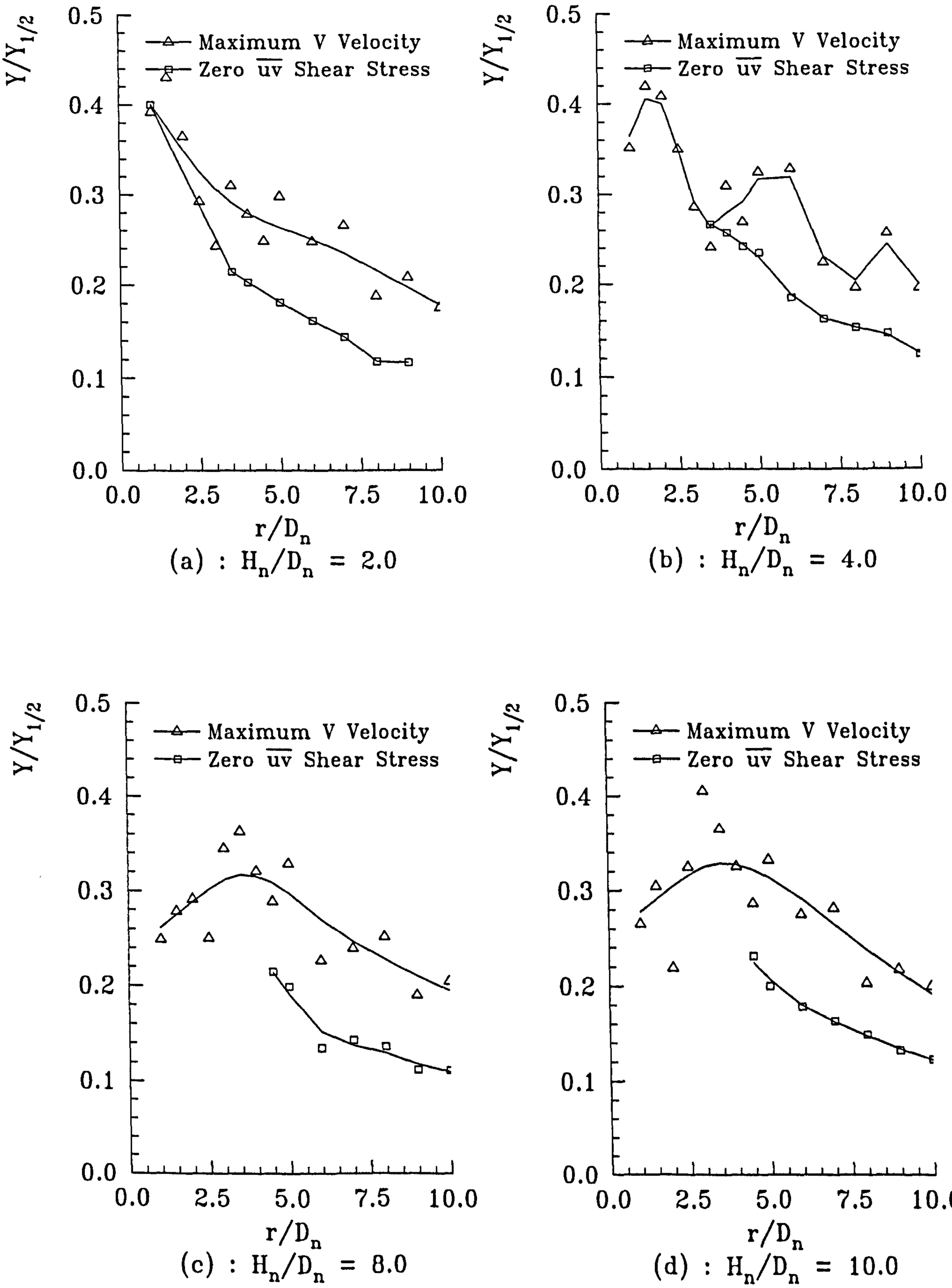

Figure 4.39 : Variation of the height of V_m and Zero Reynolds Stress above the Impingement Plate against r/D_n

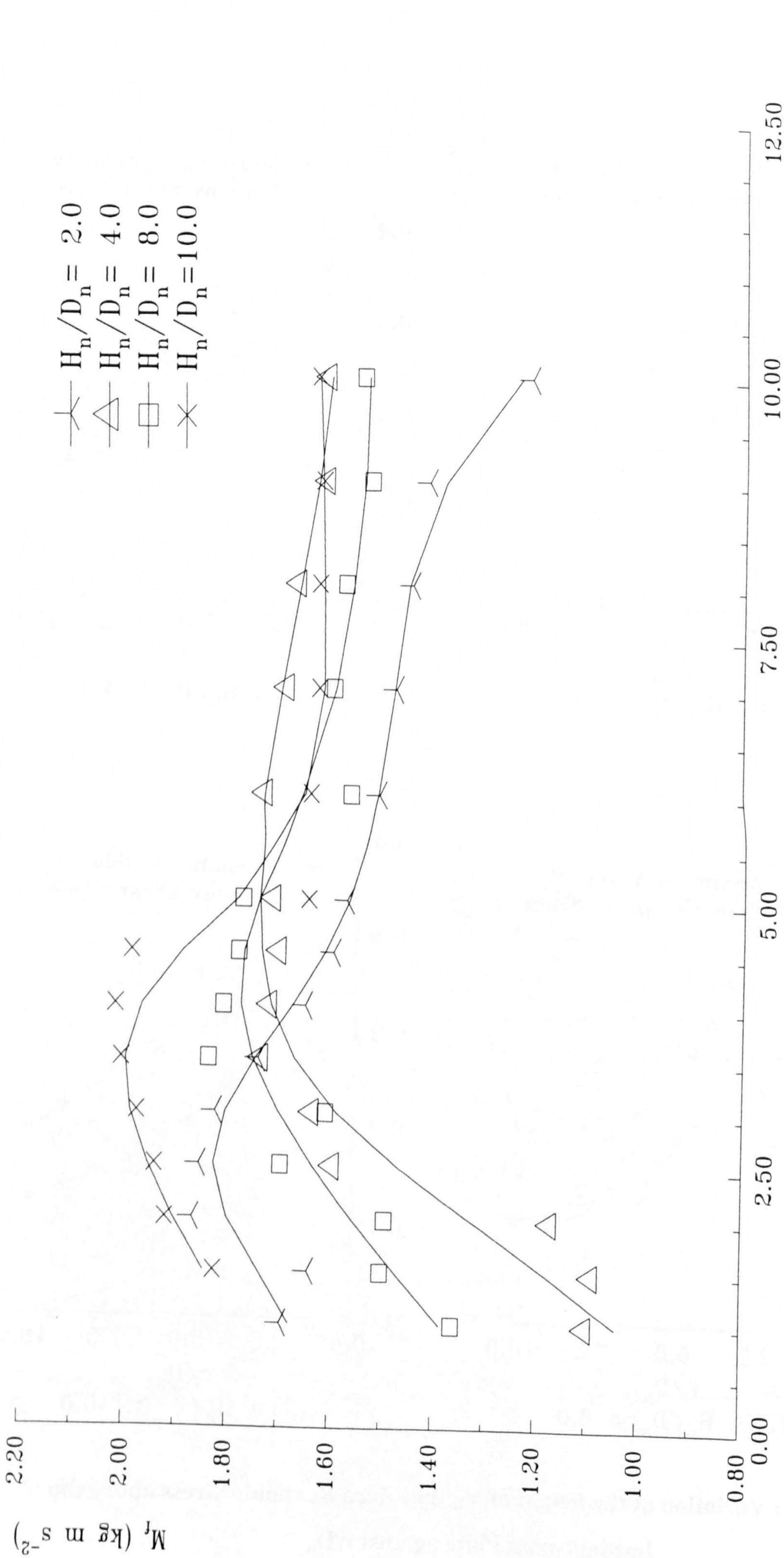

Figure 4.40 : Variation of Wall Jet Momentum Flux with Radial Distance for Different Nozzle Heights

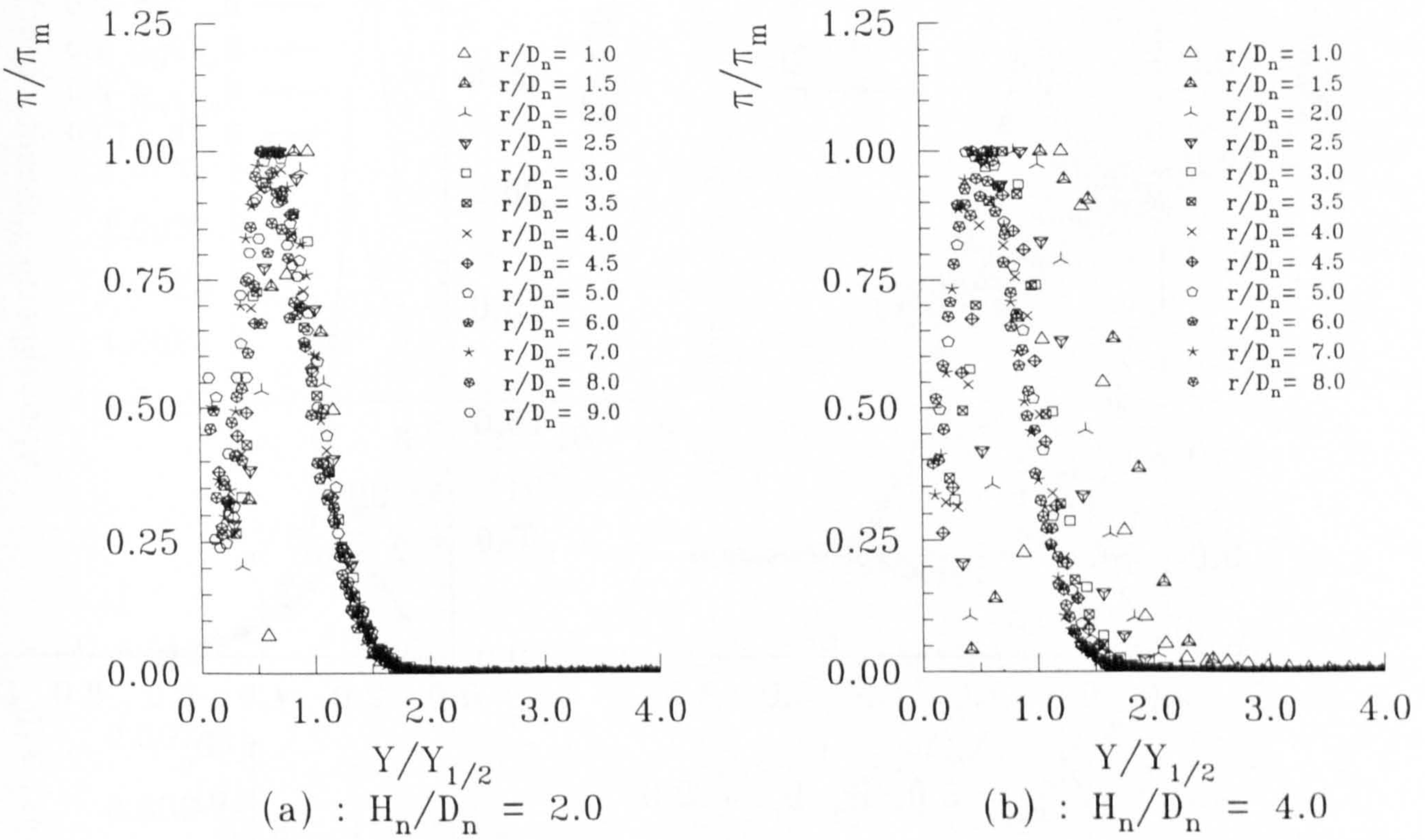

(a) : H_n/D_n = 2.0

(b) : H_n/D_n = 4.0

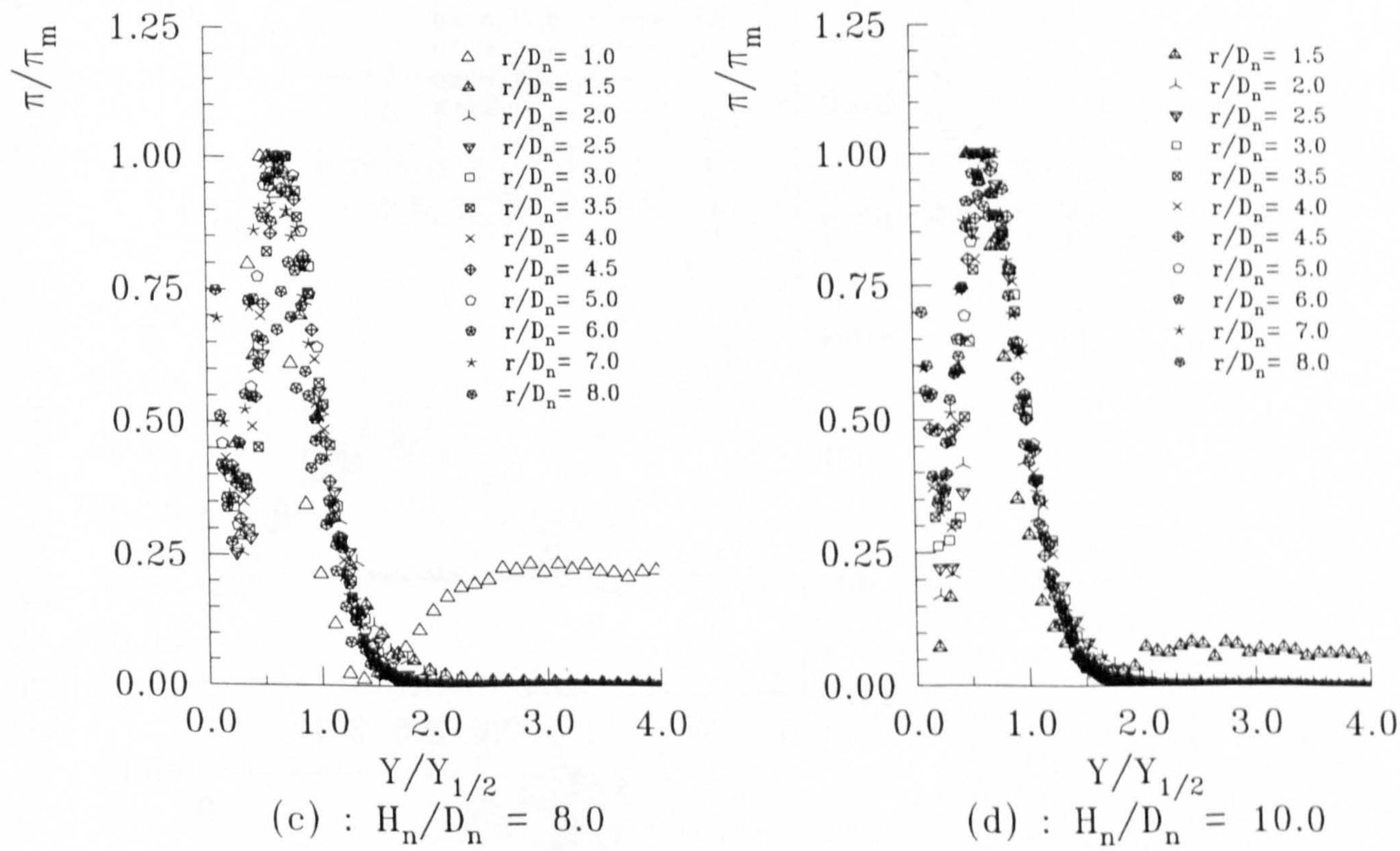

(c) : H_n/D_n = 8.0

(d) : H_n/D_n = 10.0

Figure 4.41 : Non-dimensional Production of Turbulent Kinetic Energy for the Wall Jet for Varying r/D_n, NPR=1.05

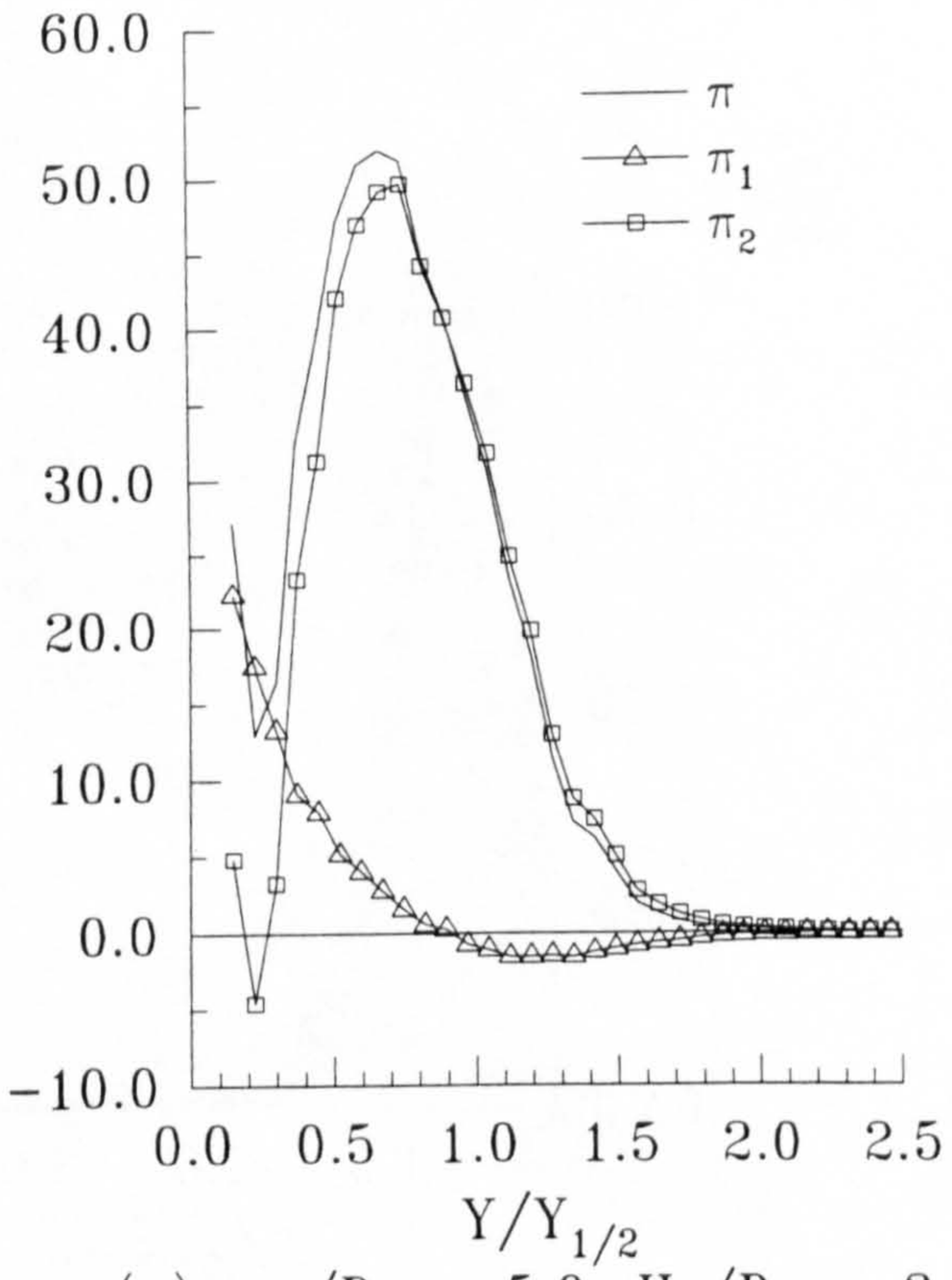

(a) : r/D_n = 5.0, H_n/D_n = 2.0

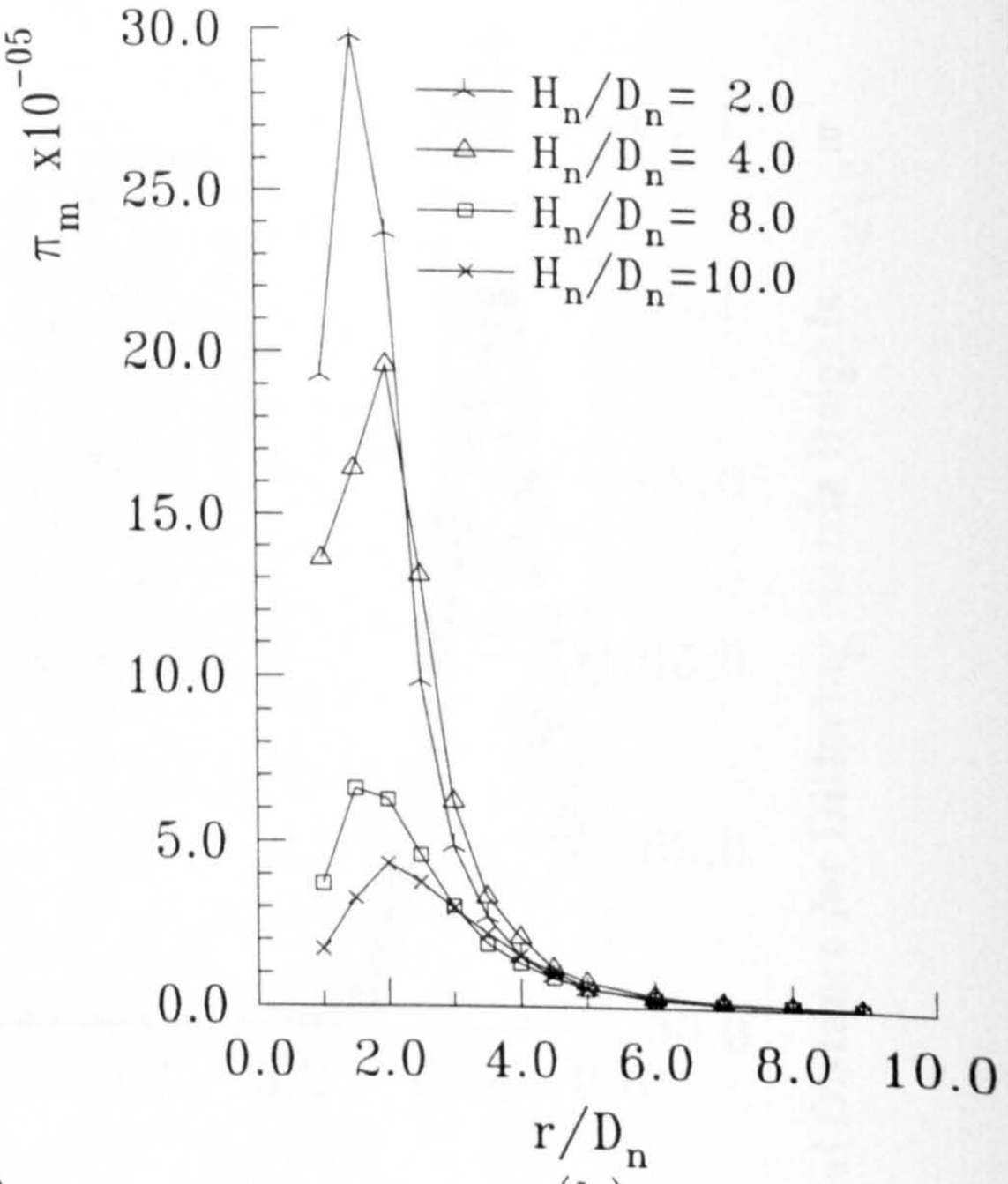

(b)

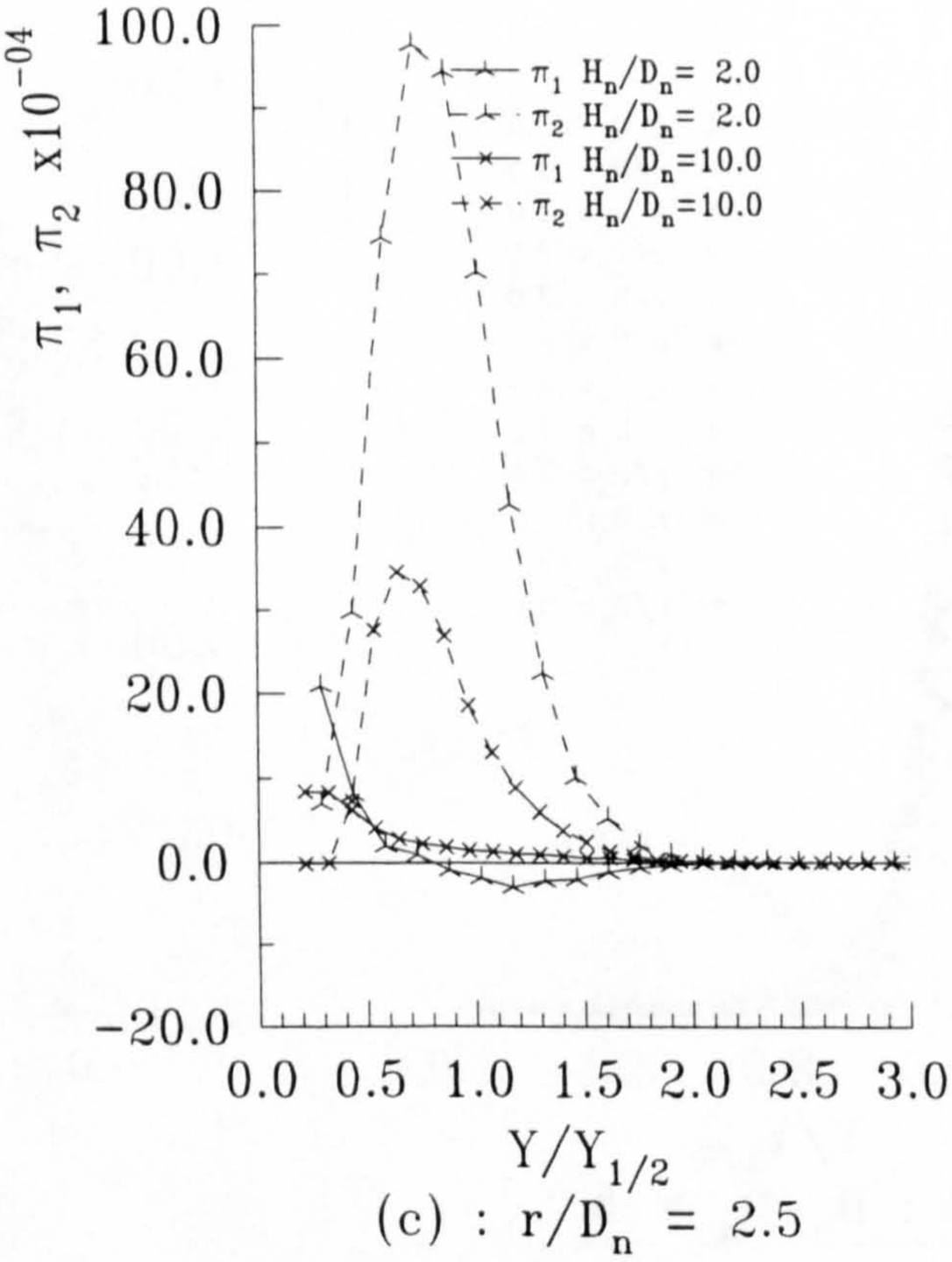

(c) : r/D_n = 2.5

Figure 4.42 : Details of Production of Turbulent Kinetic Energy for the Wall Jet

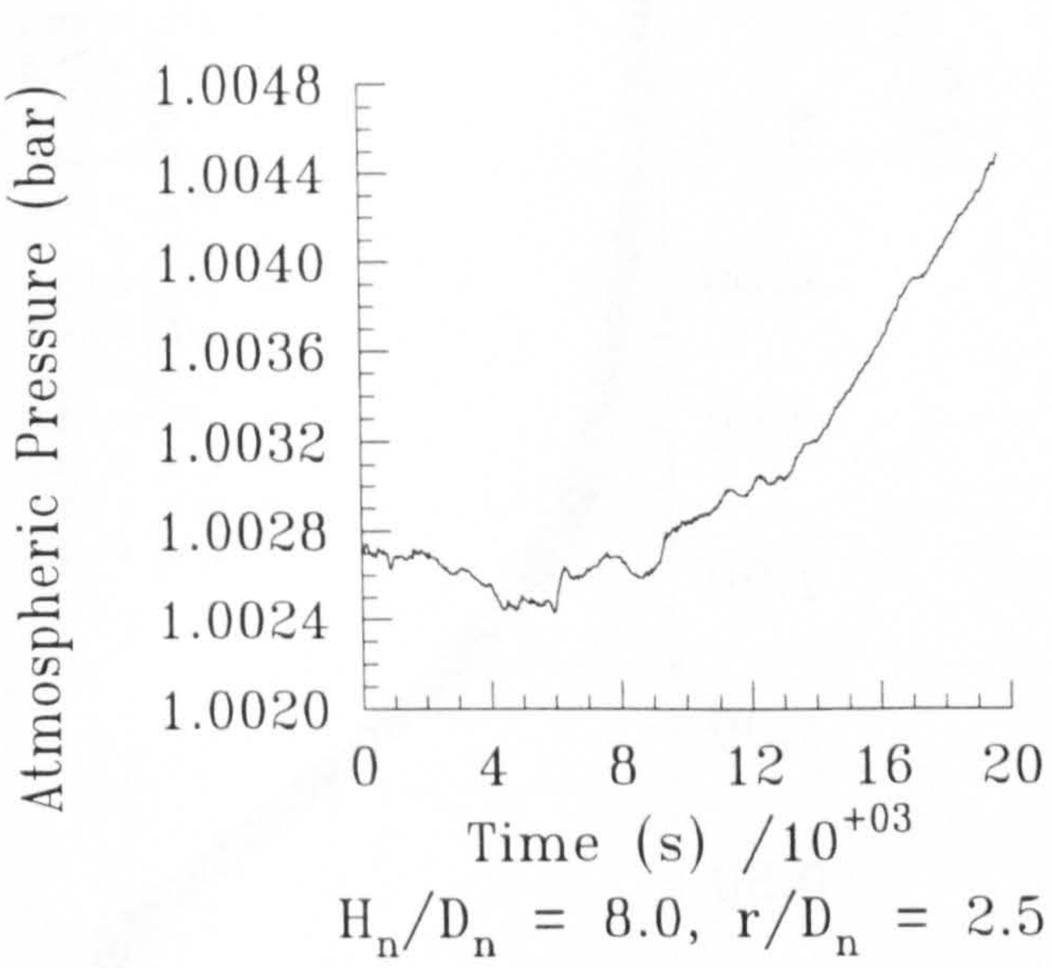

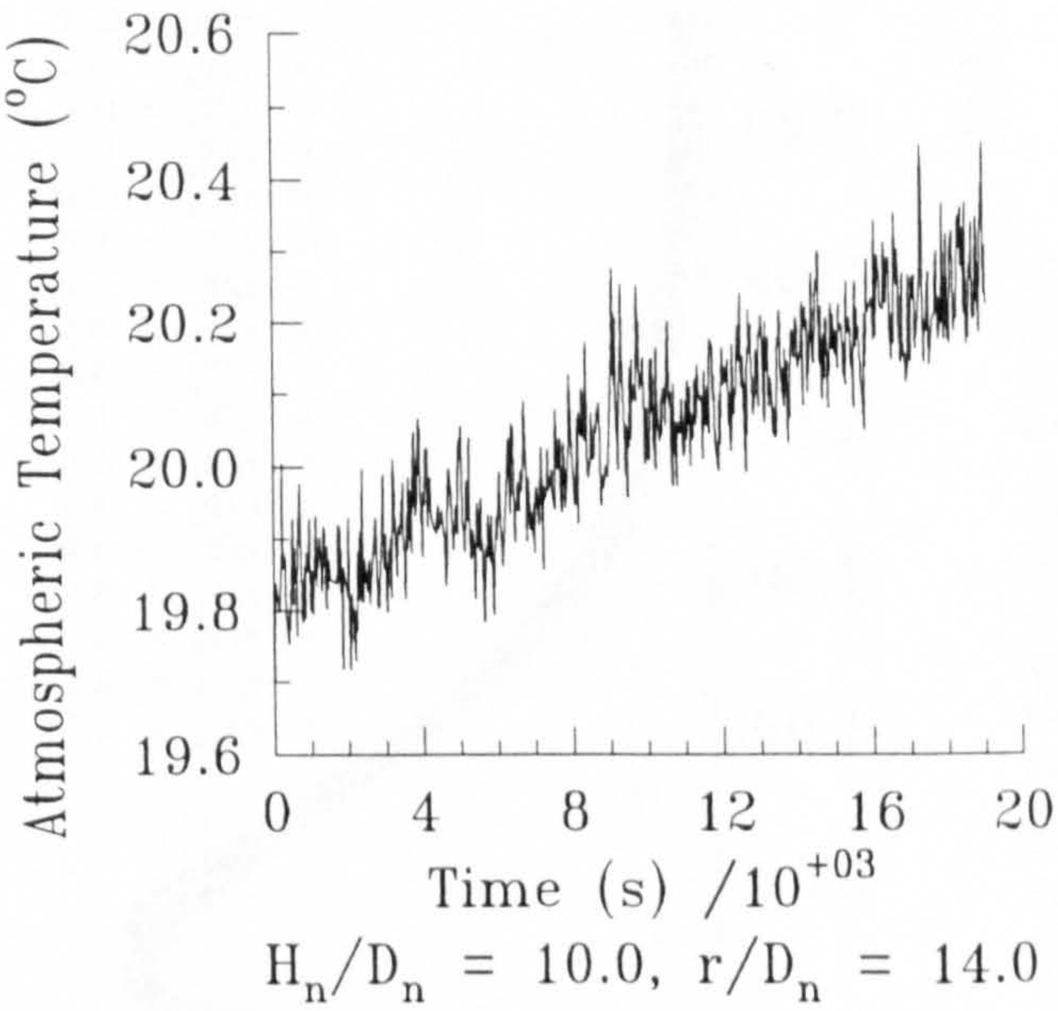

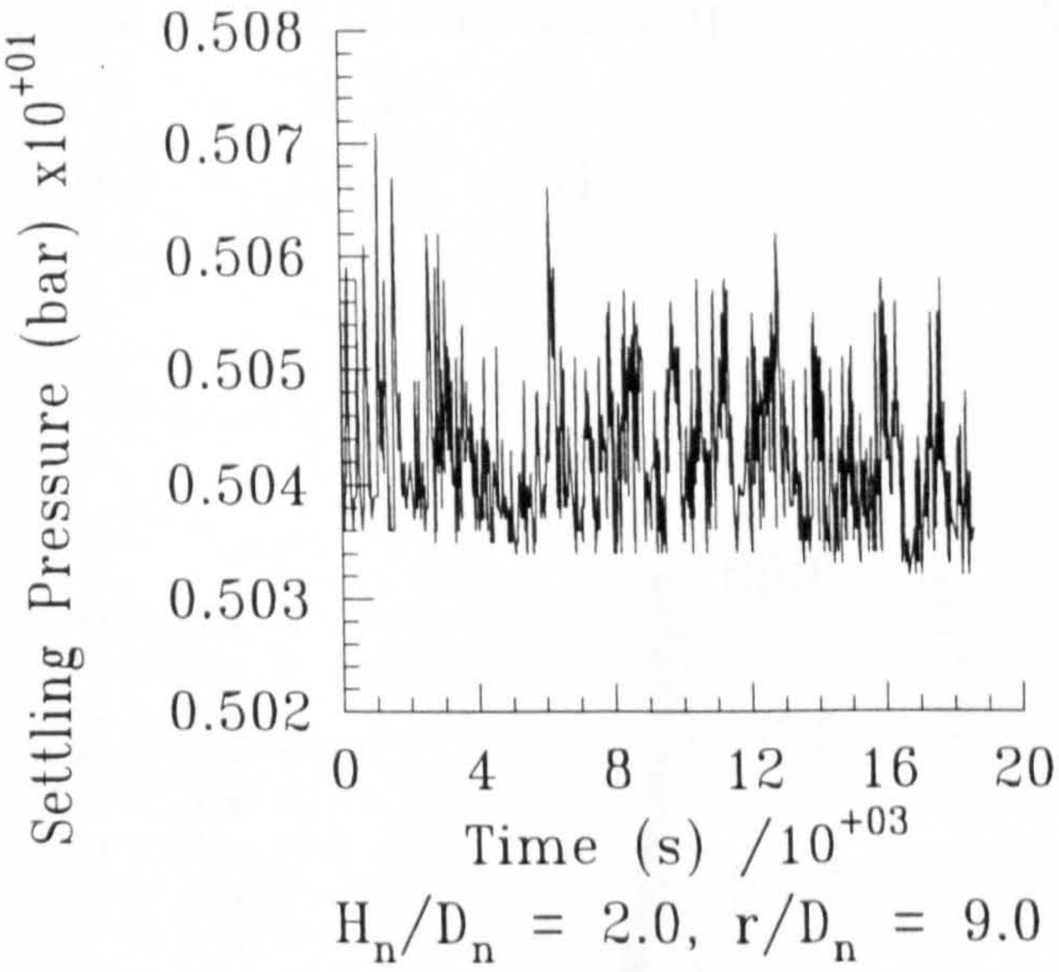

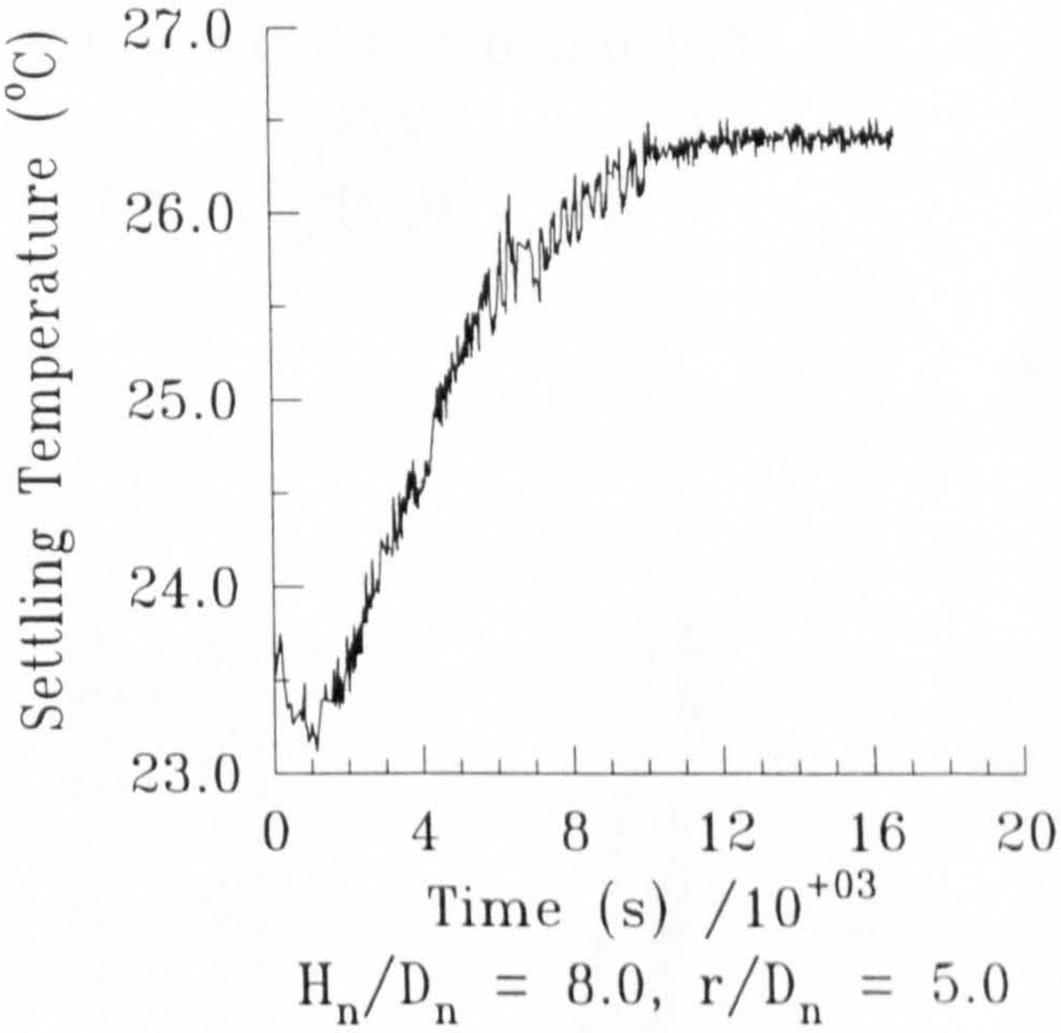

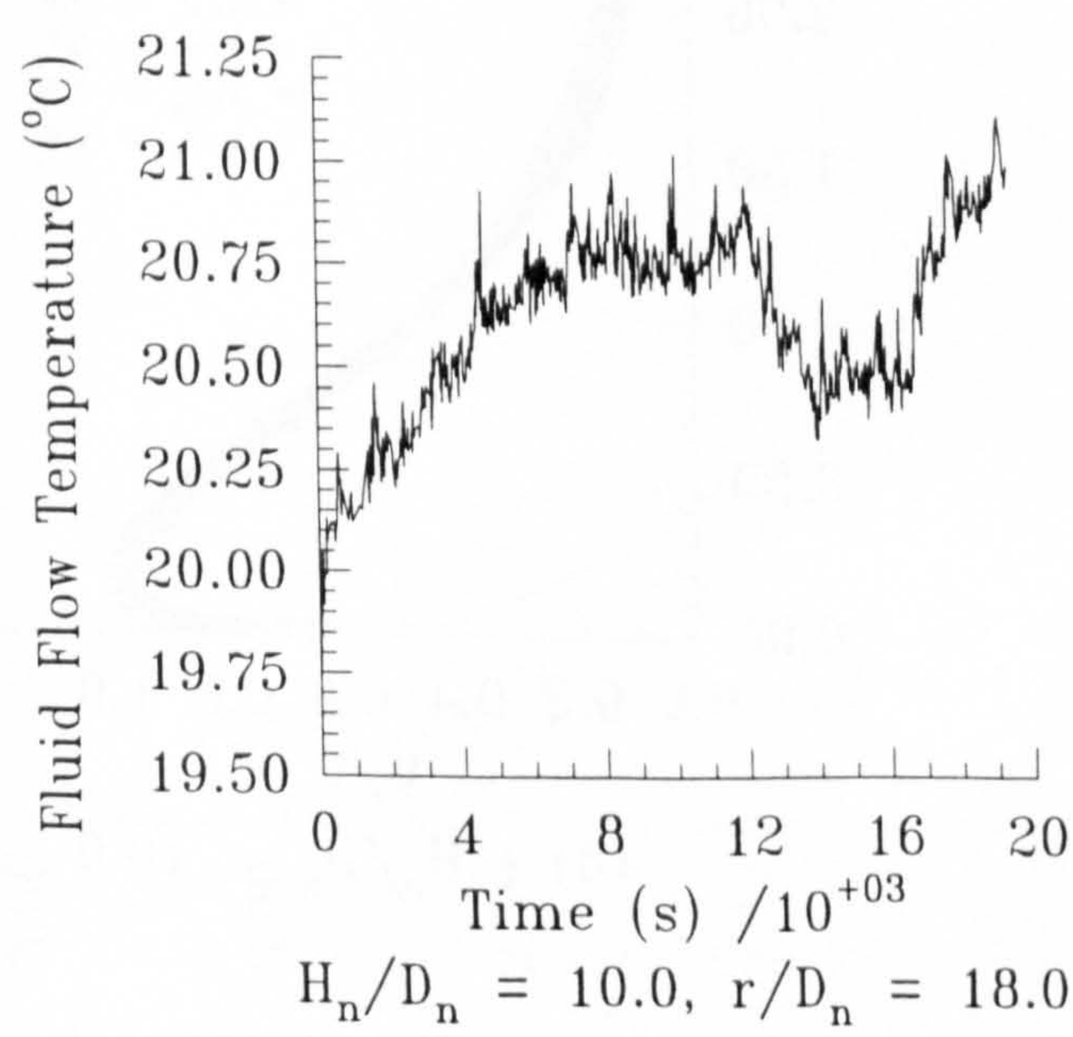

Figure 4.43 : Typical Ambient and Settling Chamber Conditions during a Run

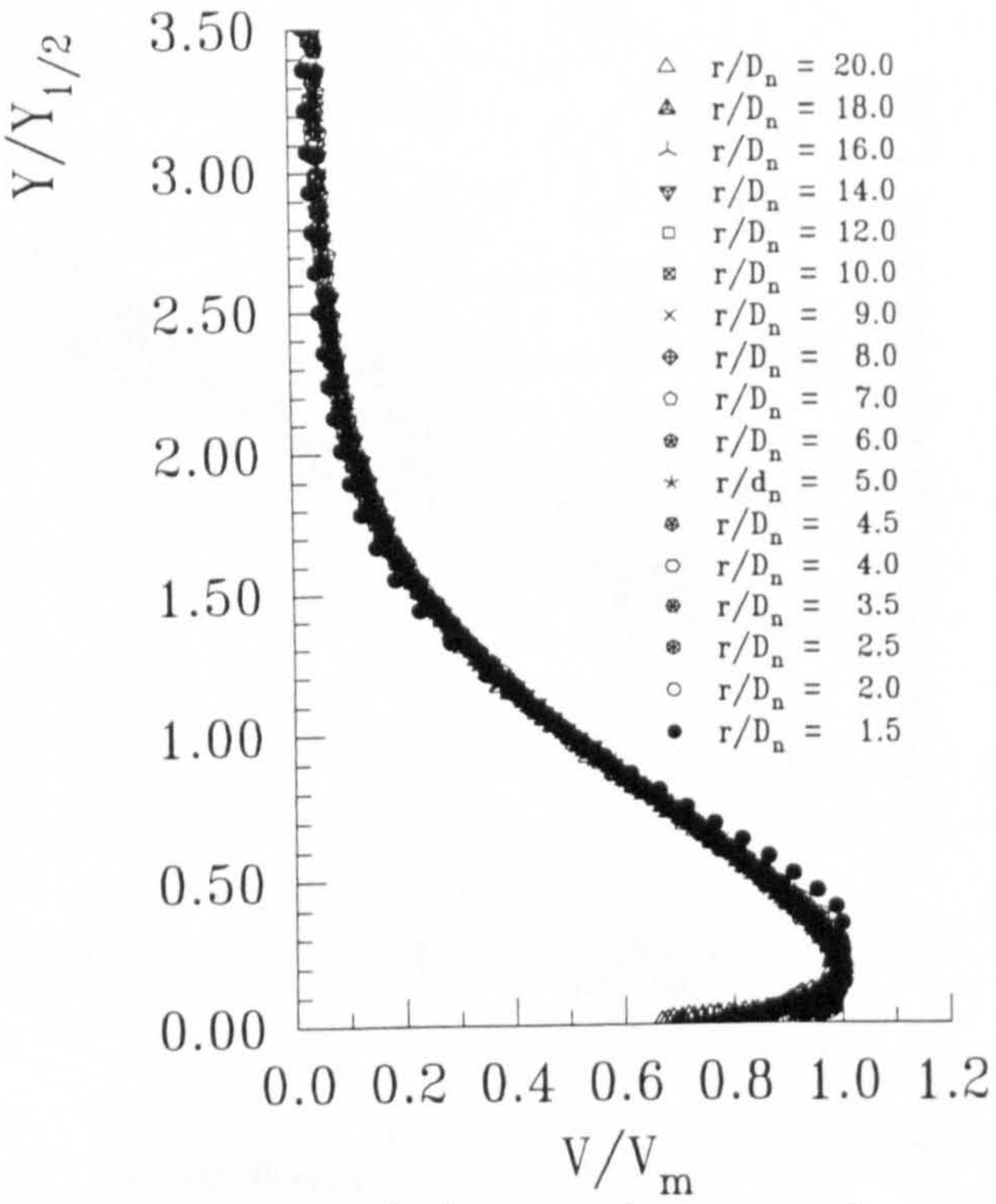

(a) : H_n/D_n = 2.0

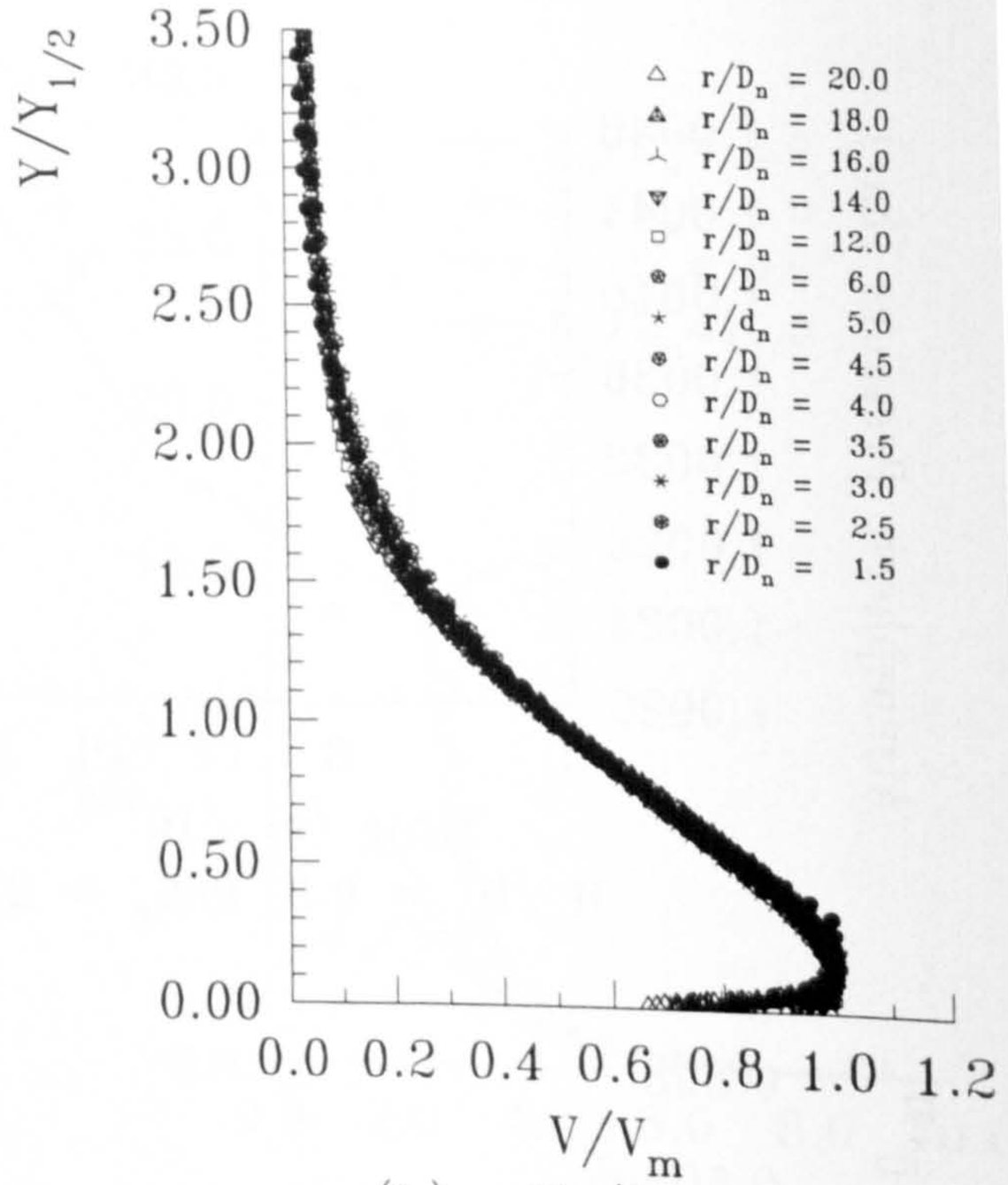

(b) : H_n/D_n = 4.0

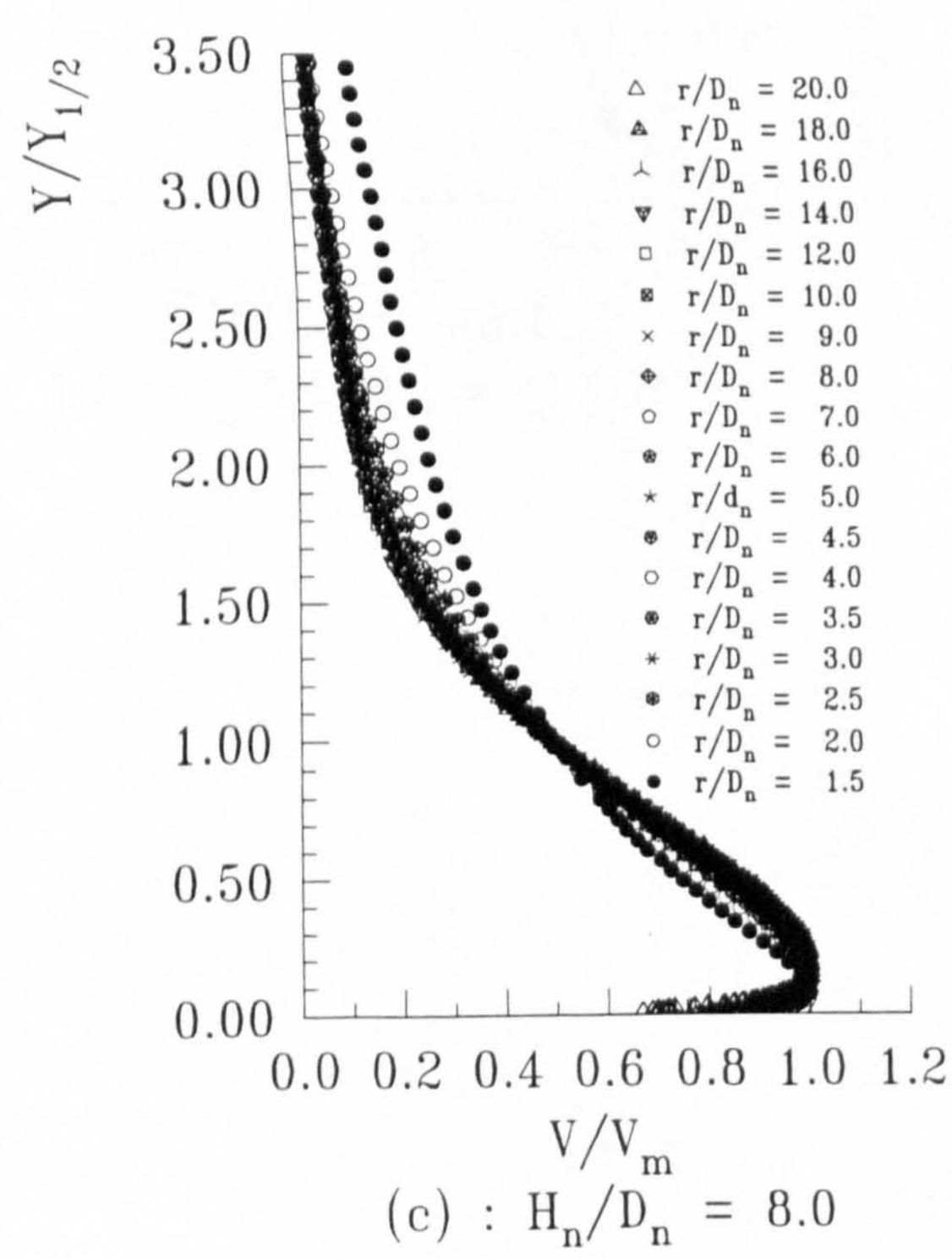

(c) : H_n/D_n = 8.0

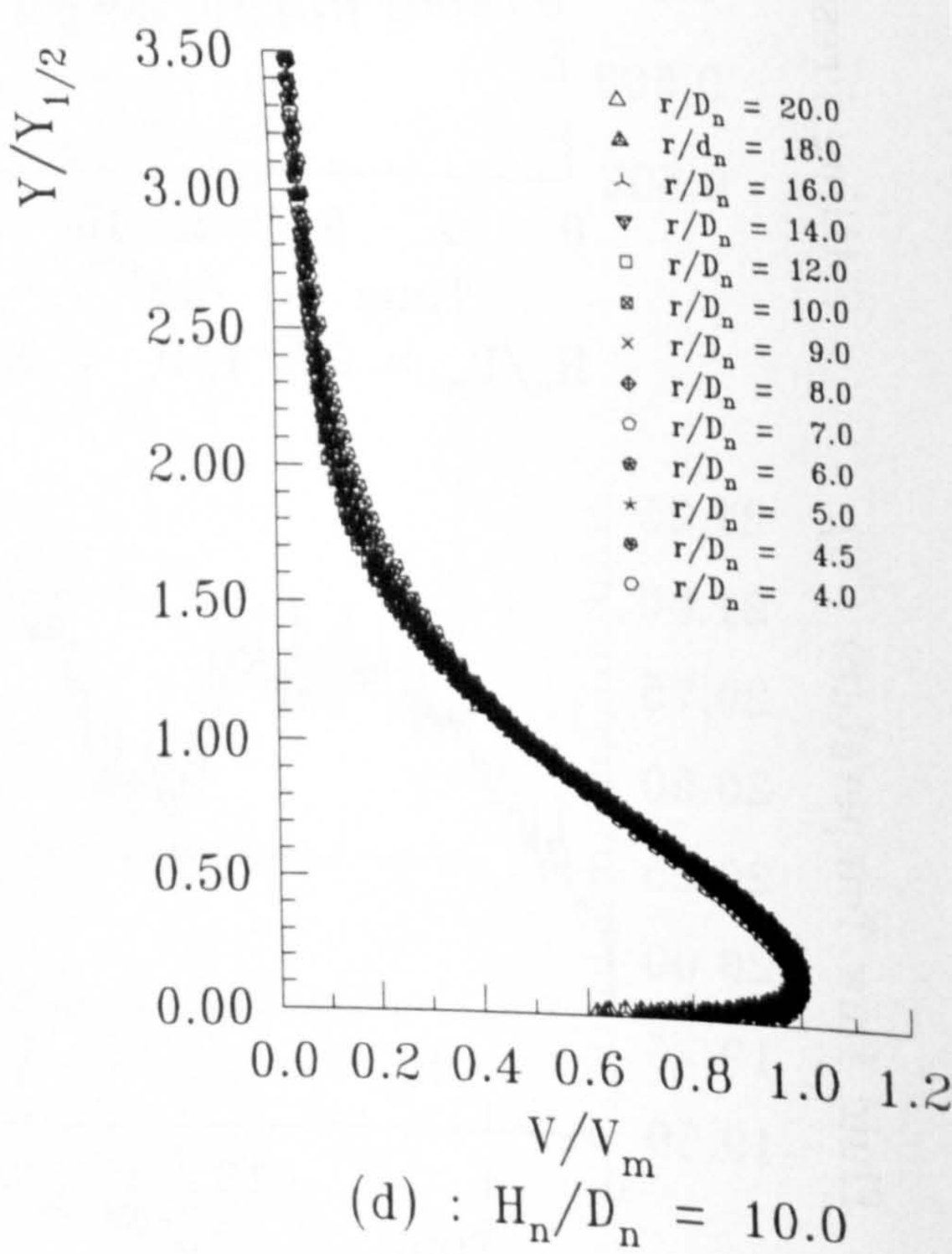

(d) : H_n/D_n = 10.0

Figure 4.44 : Non-dimensional V Mean Velocity Component Profiles at Different r/D_n for Varying H_n/D_n, NPR = 1.05

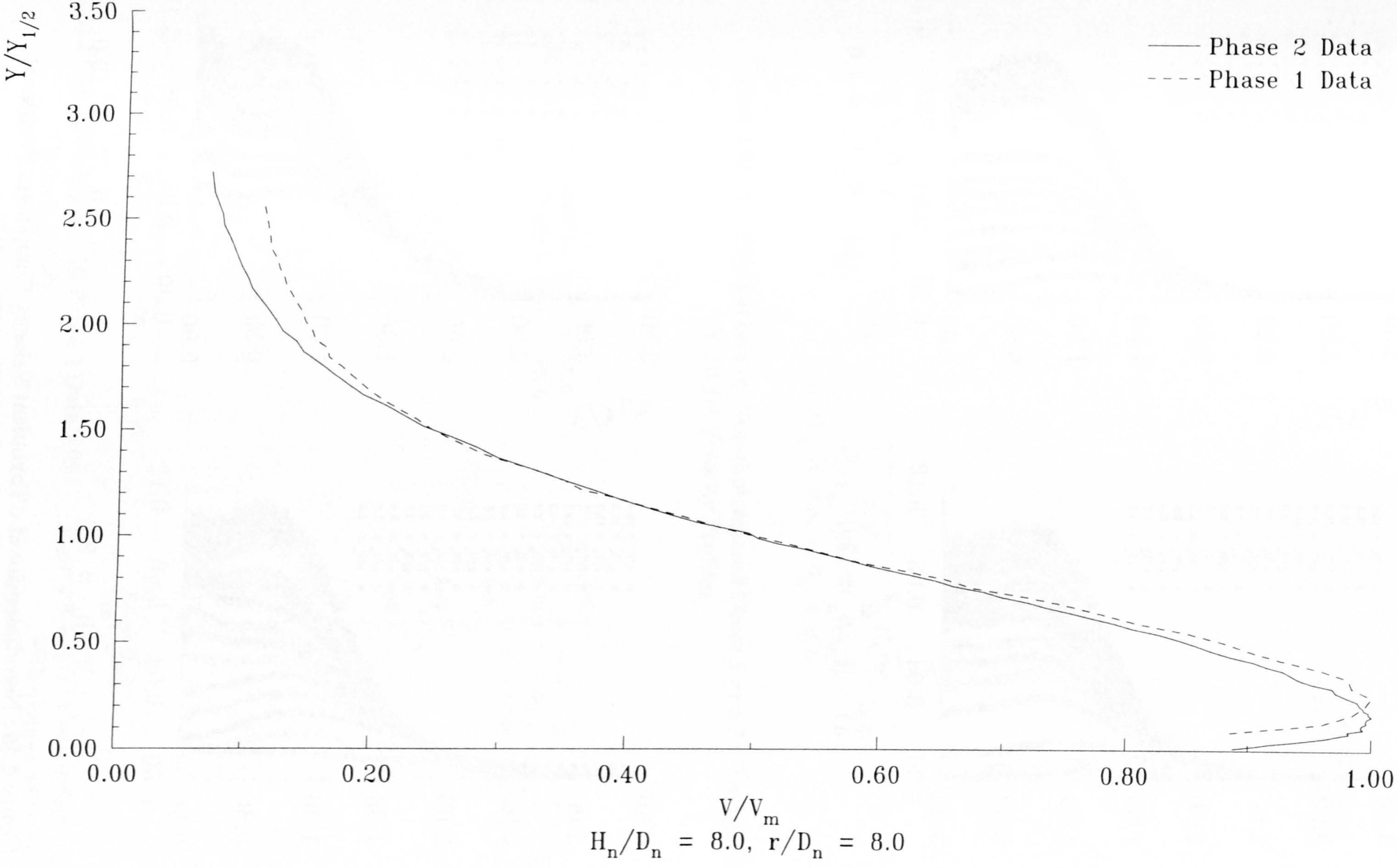

Figure 4.45 : Comparison of Non-dimensional Phase 1 and Phase 2 V Component Wall Jet Velocity Profiles

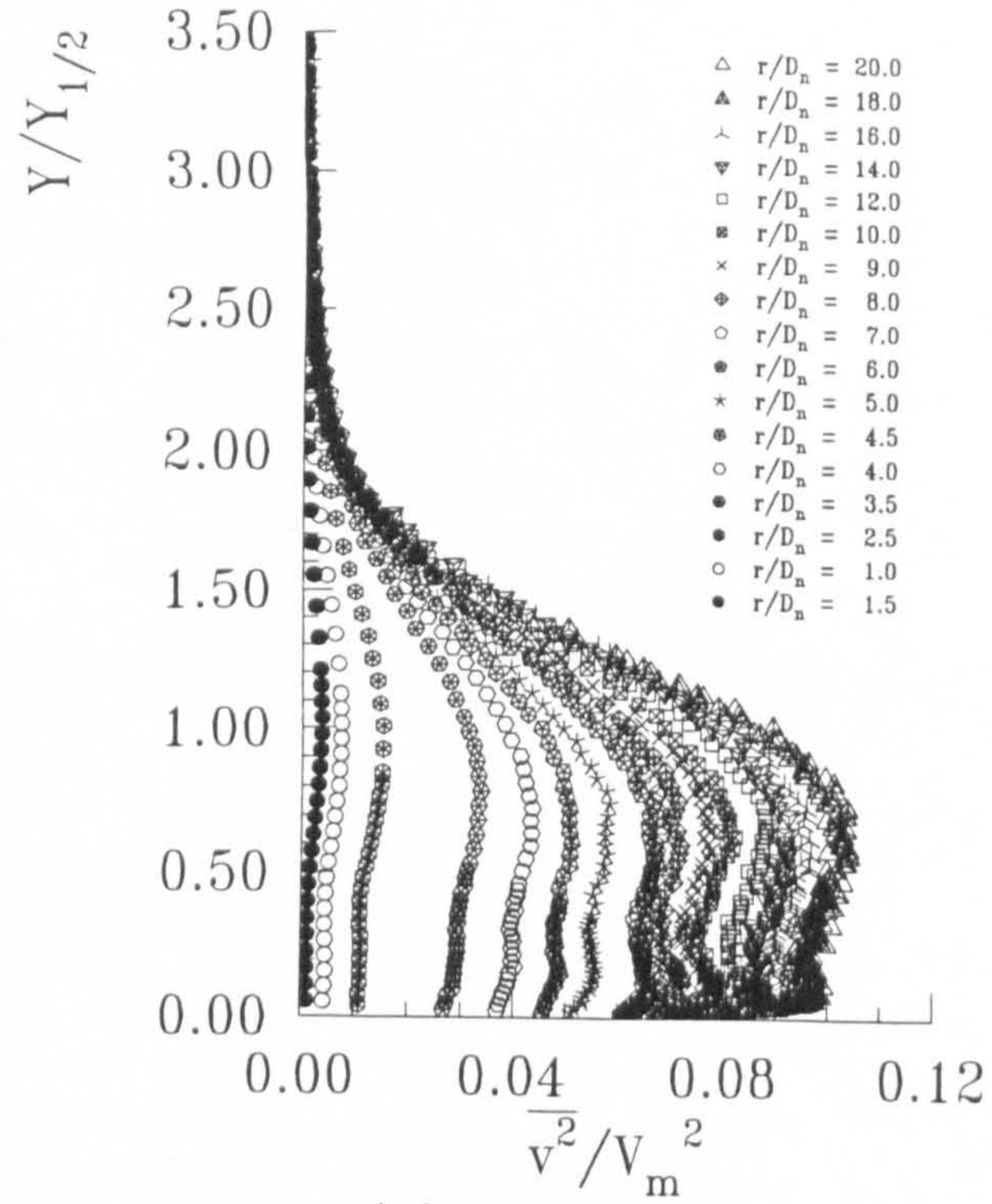

(a) : H_n/D_n = 2.0

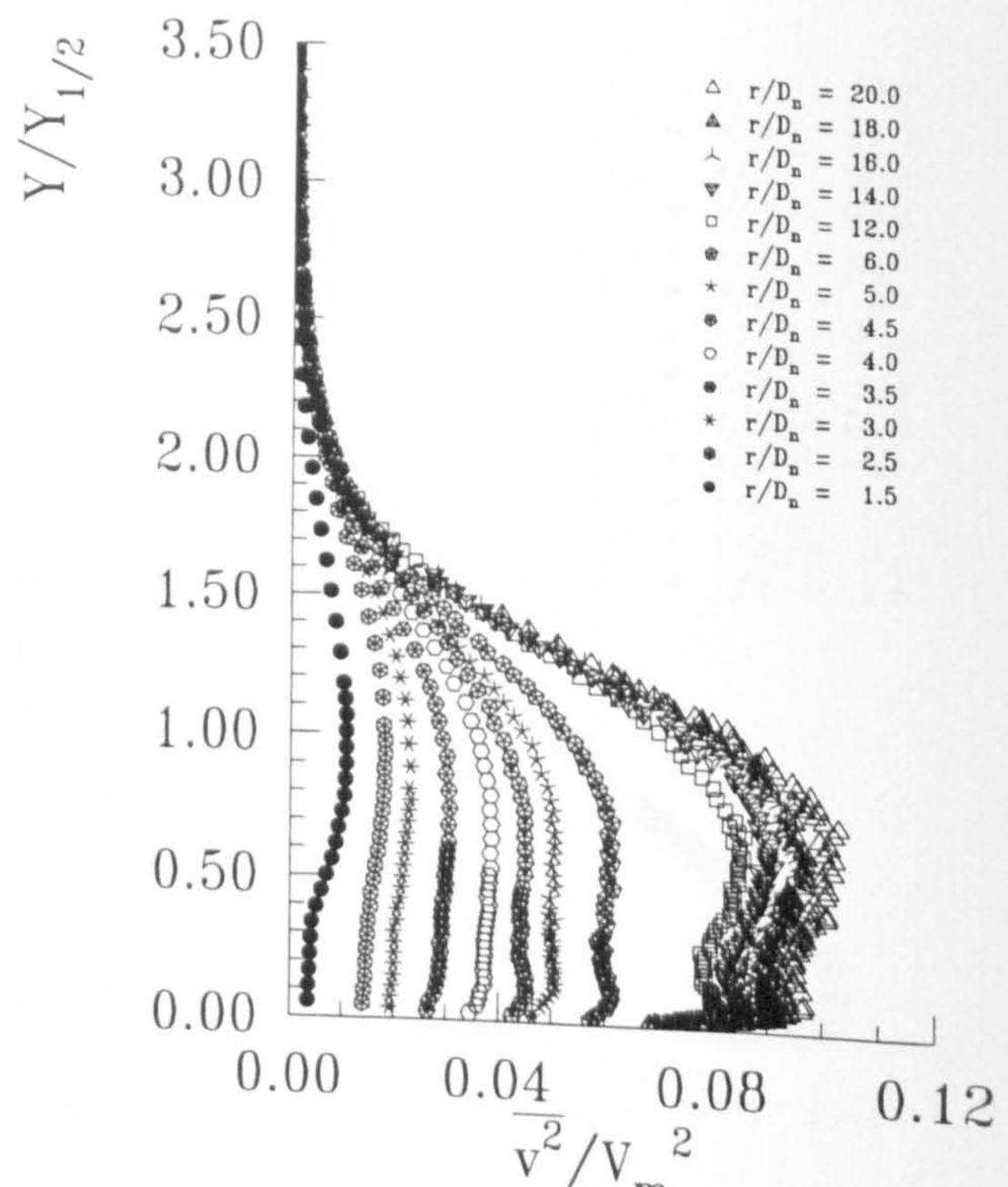

(b) : H_n/D_n = 4.0

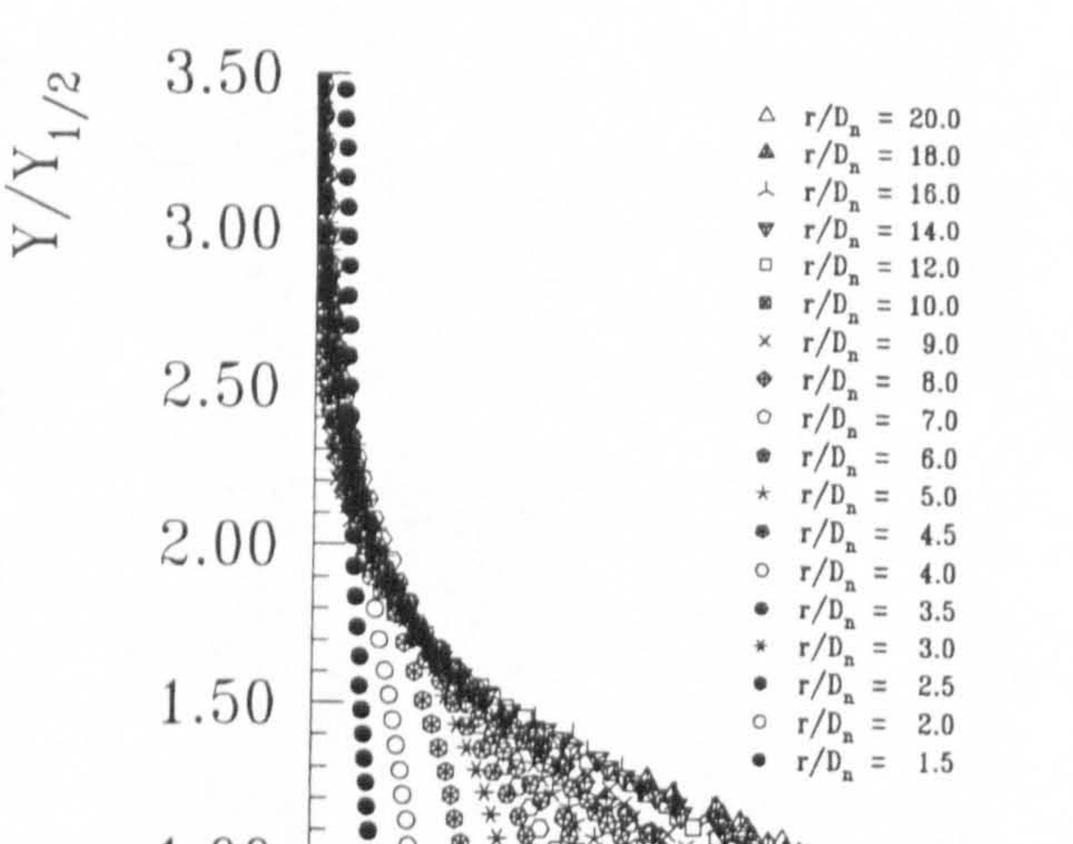

(c) : H_n/D_n = 8.0

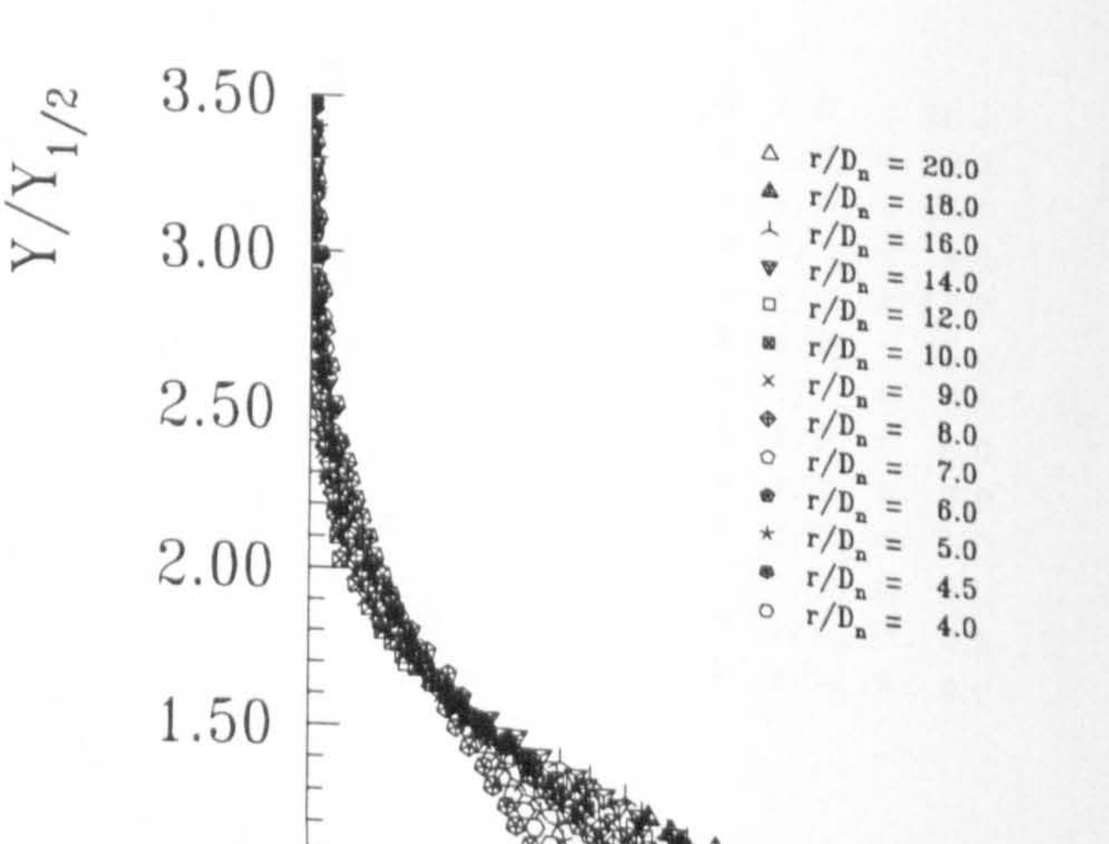

(d) : H_n/D_n = 10.0

Figure 4.46 : Non-dimensional v Turbulent Velocity Component Profiles at Different r/D_n for Varying H_n/D_n, NPR = 1.05

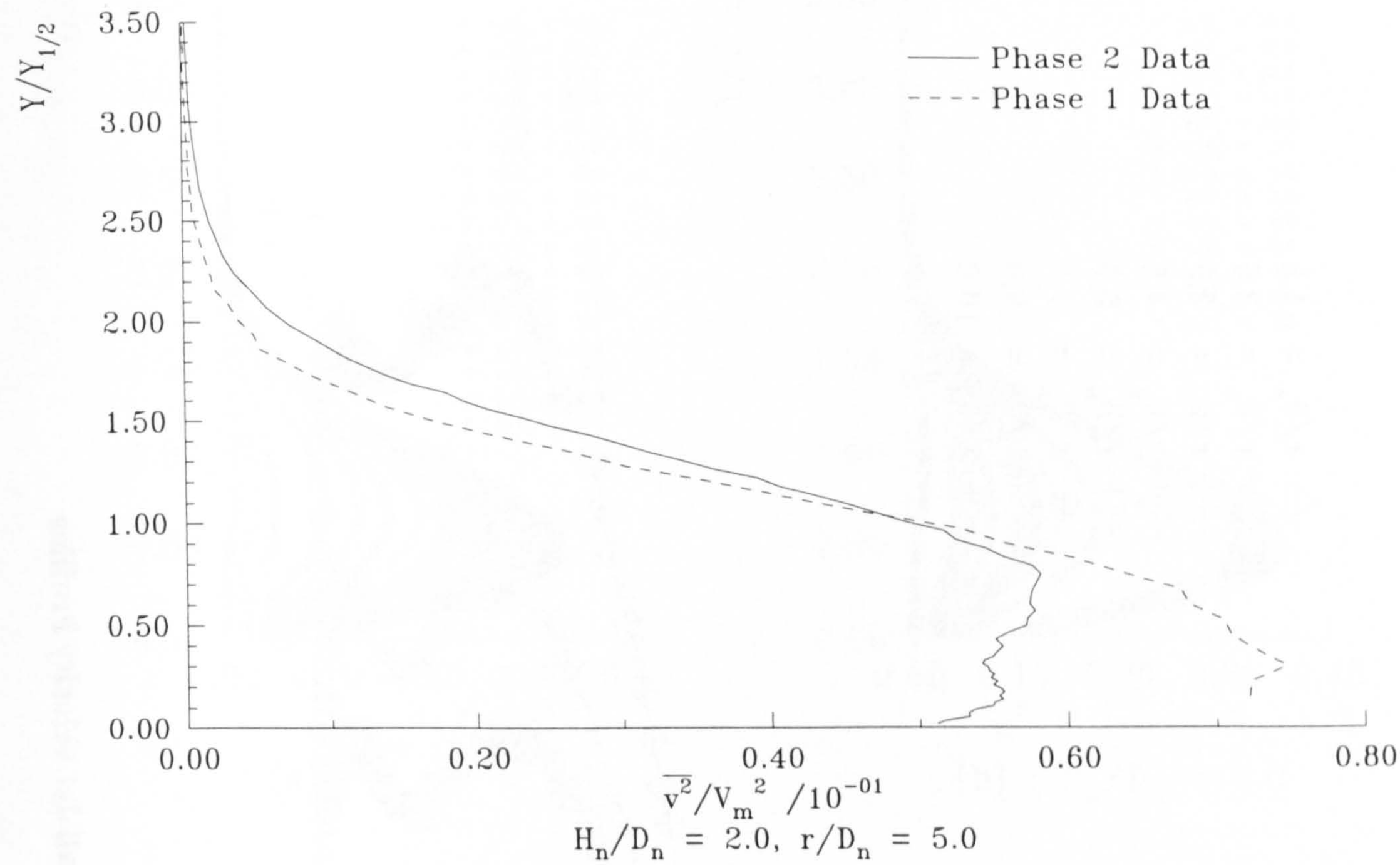

Figure 4.47 (a) : Comparison of Non-dimensional Phase 1 and 2 v Turbulent Wall Jet Velocity Profiles

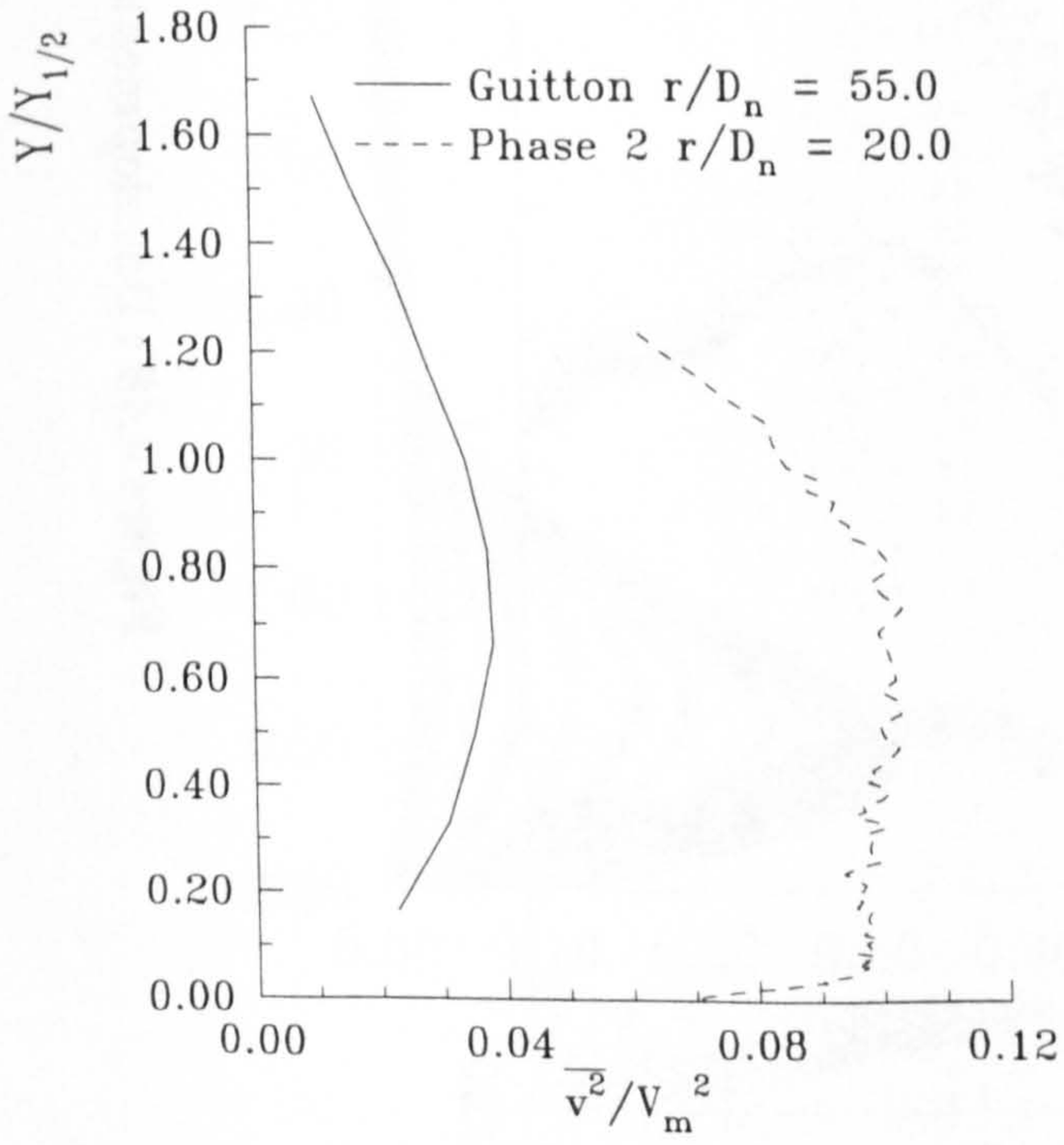

Figure 4.47 (b) : Comparison of Phase 2 Data with Guitton (1968)

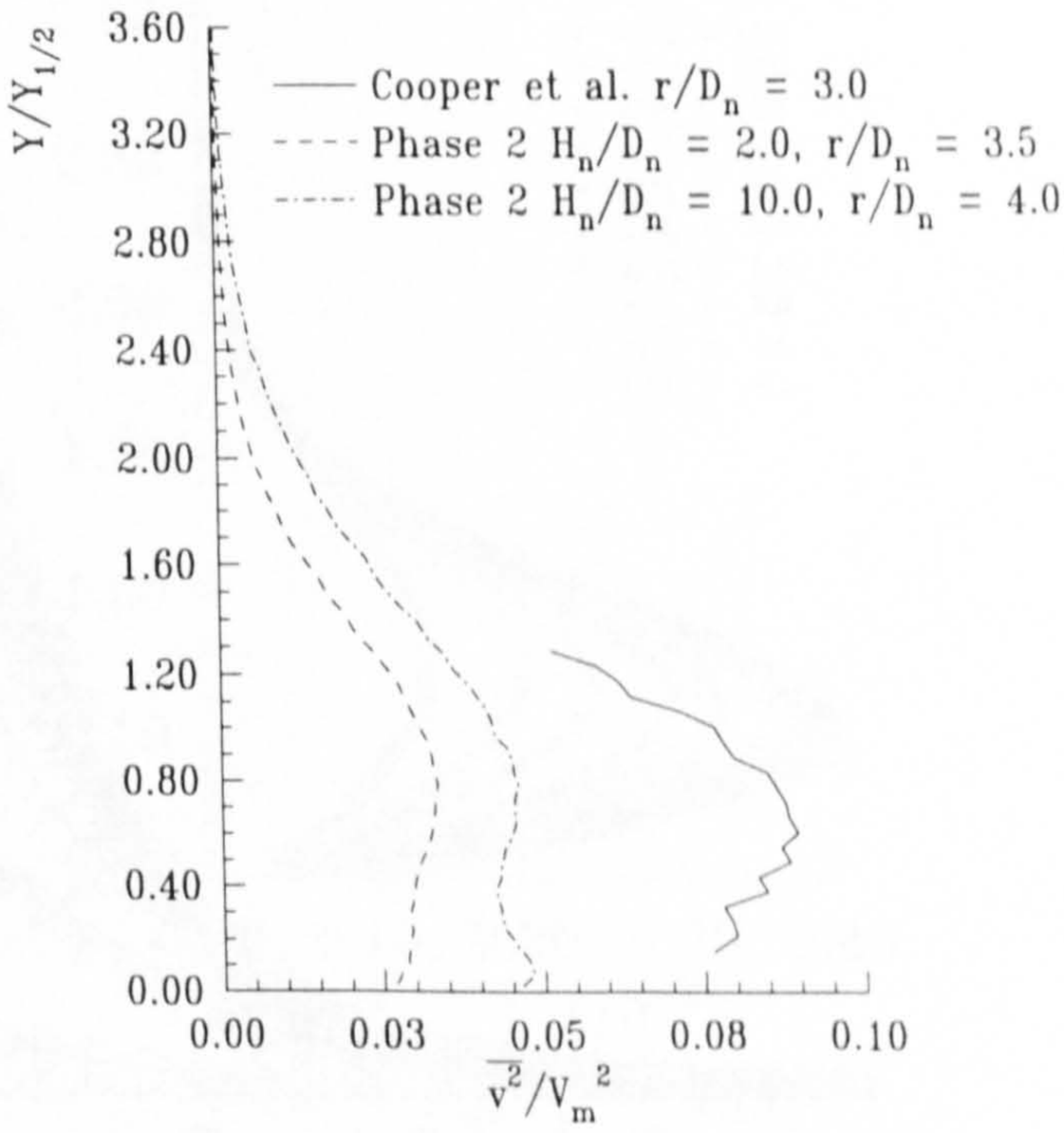

Figure 4.47 (c) : Comparison of Phase 2 Data with Cooper et al. (1993)

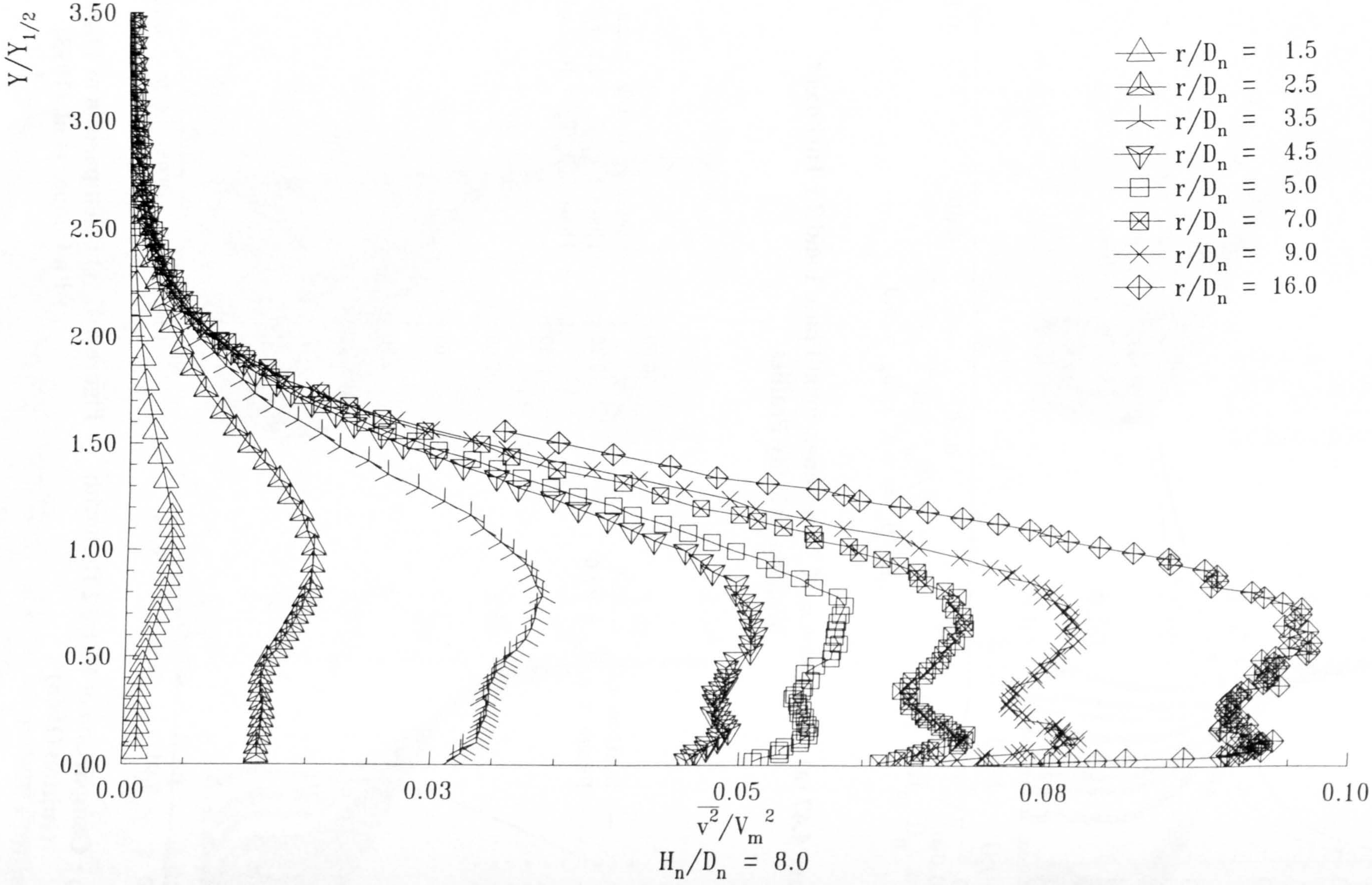

Figure 4.48 : Development of v Turbulent Wall Jet Velocity Profiles

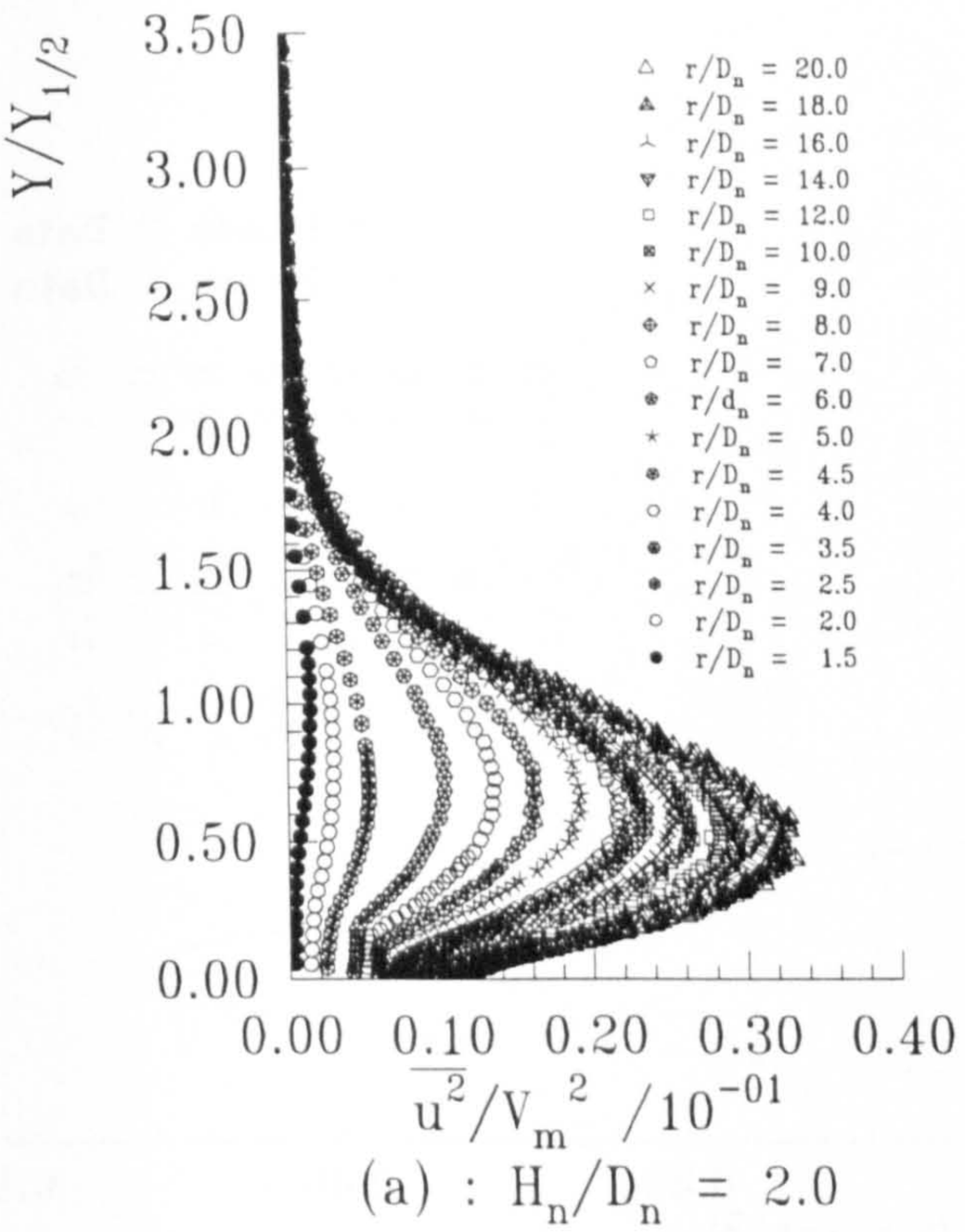

(a) : H_n/D_n = 2.0

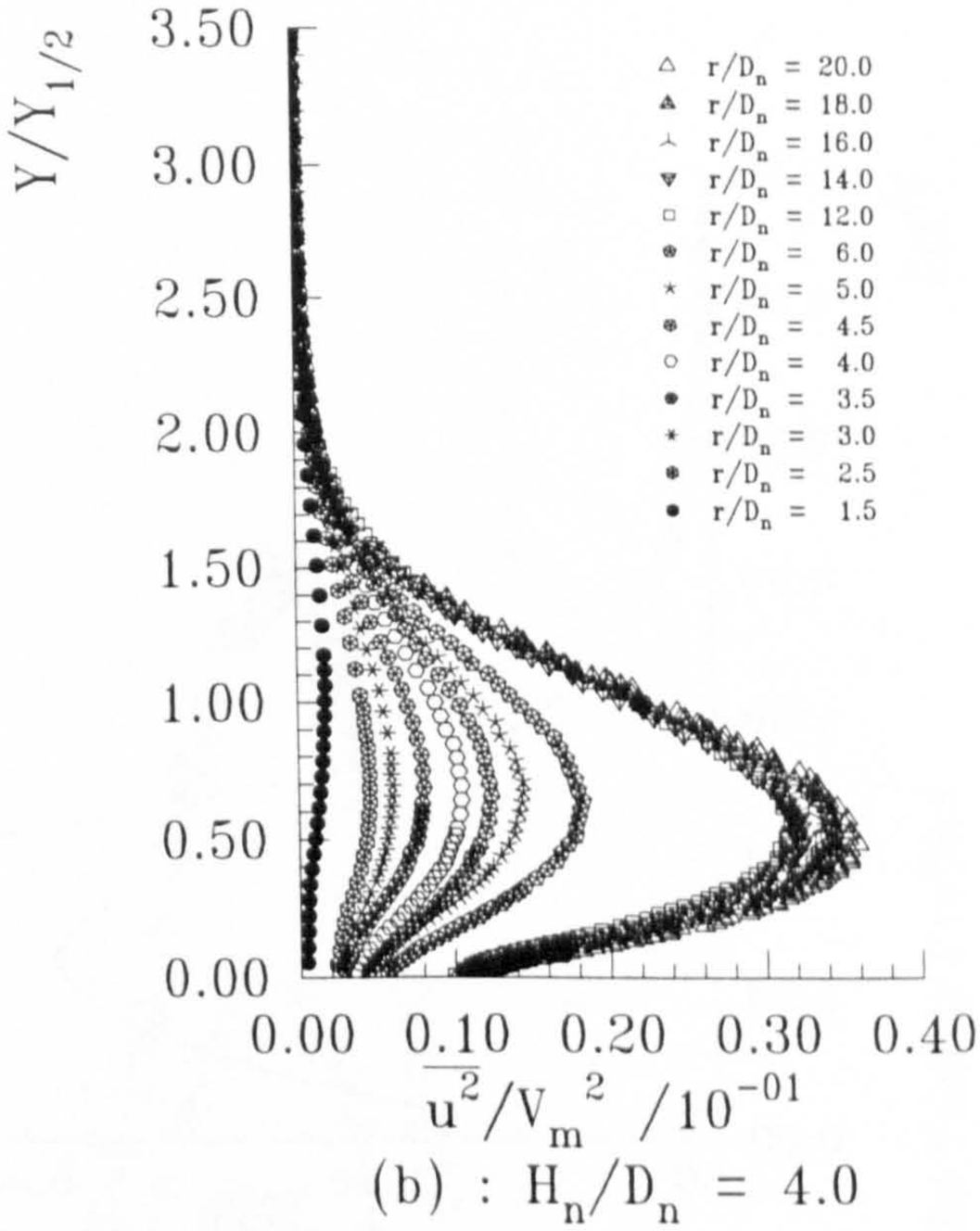

(b) : H_n/D_n = 4.0

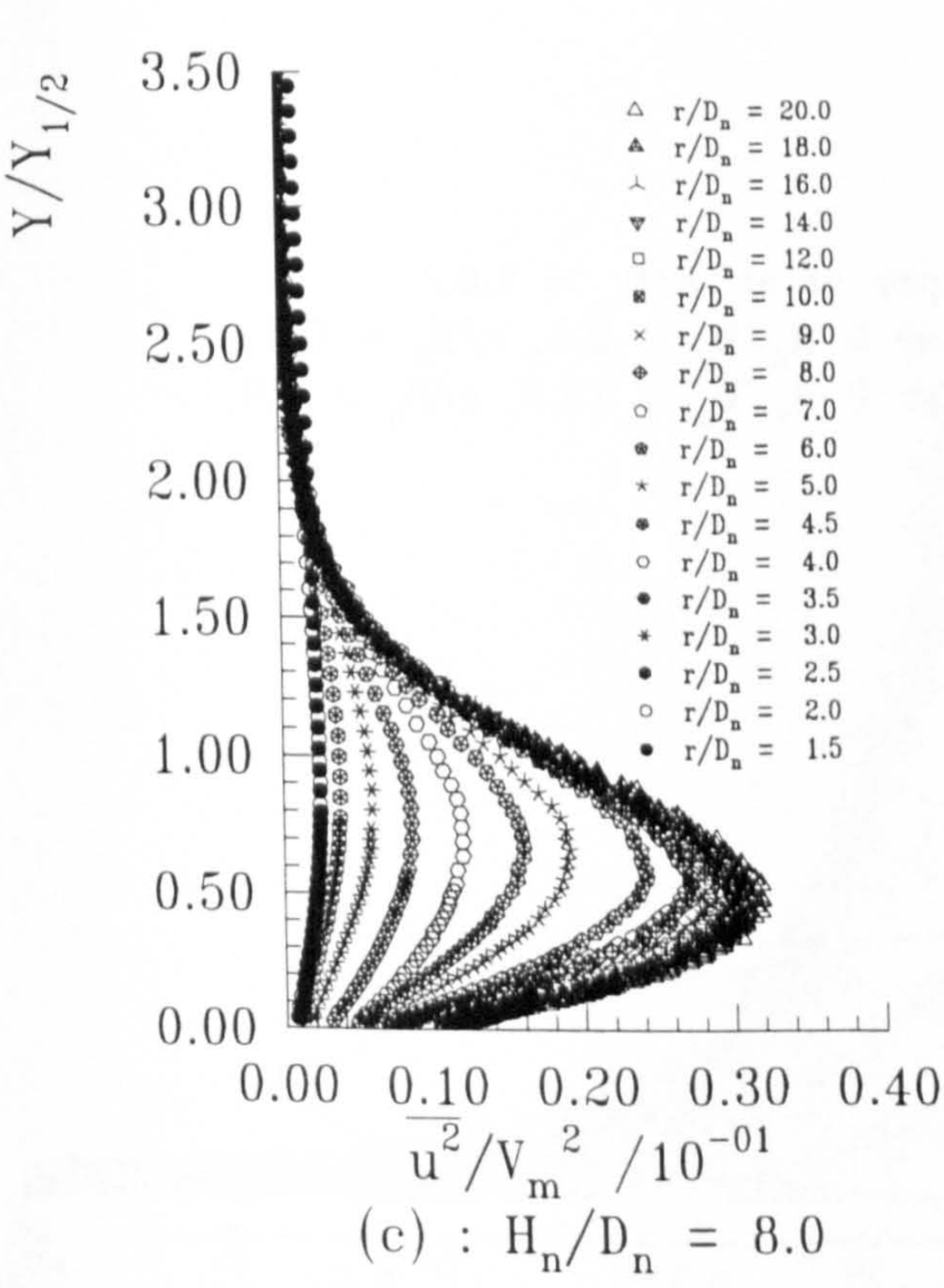

(c) : H_n/D_n = 8.0

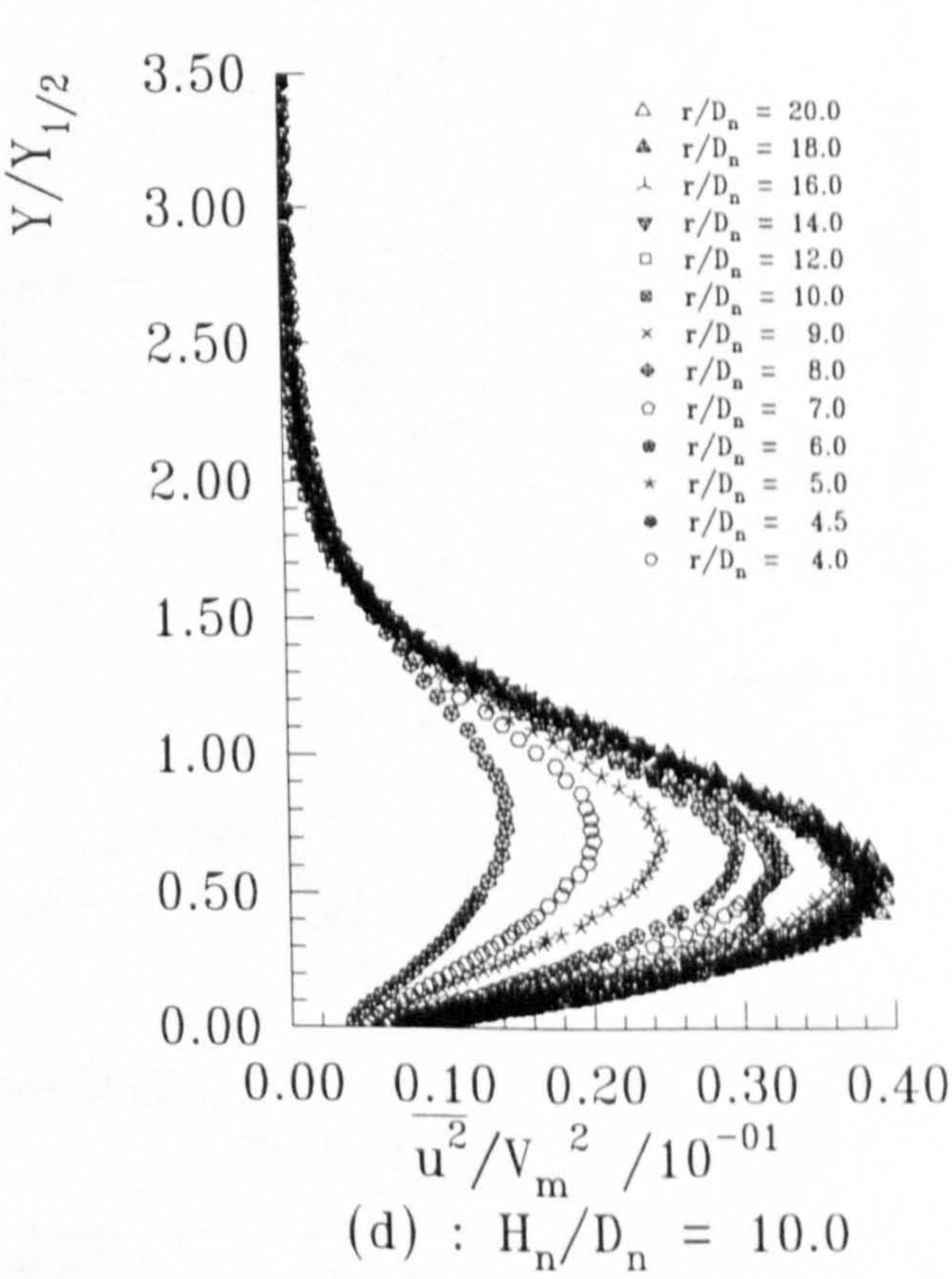

(d) : H_n/D_n = 10.0

Figure 4.49 : Non-dimensional u Turbulent Velocity Component Profiles at Different r/D_n for Varying H_n/D_n, NPR = 1.05

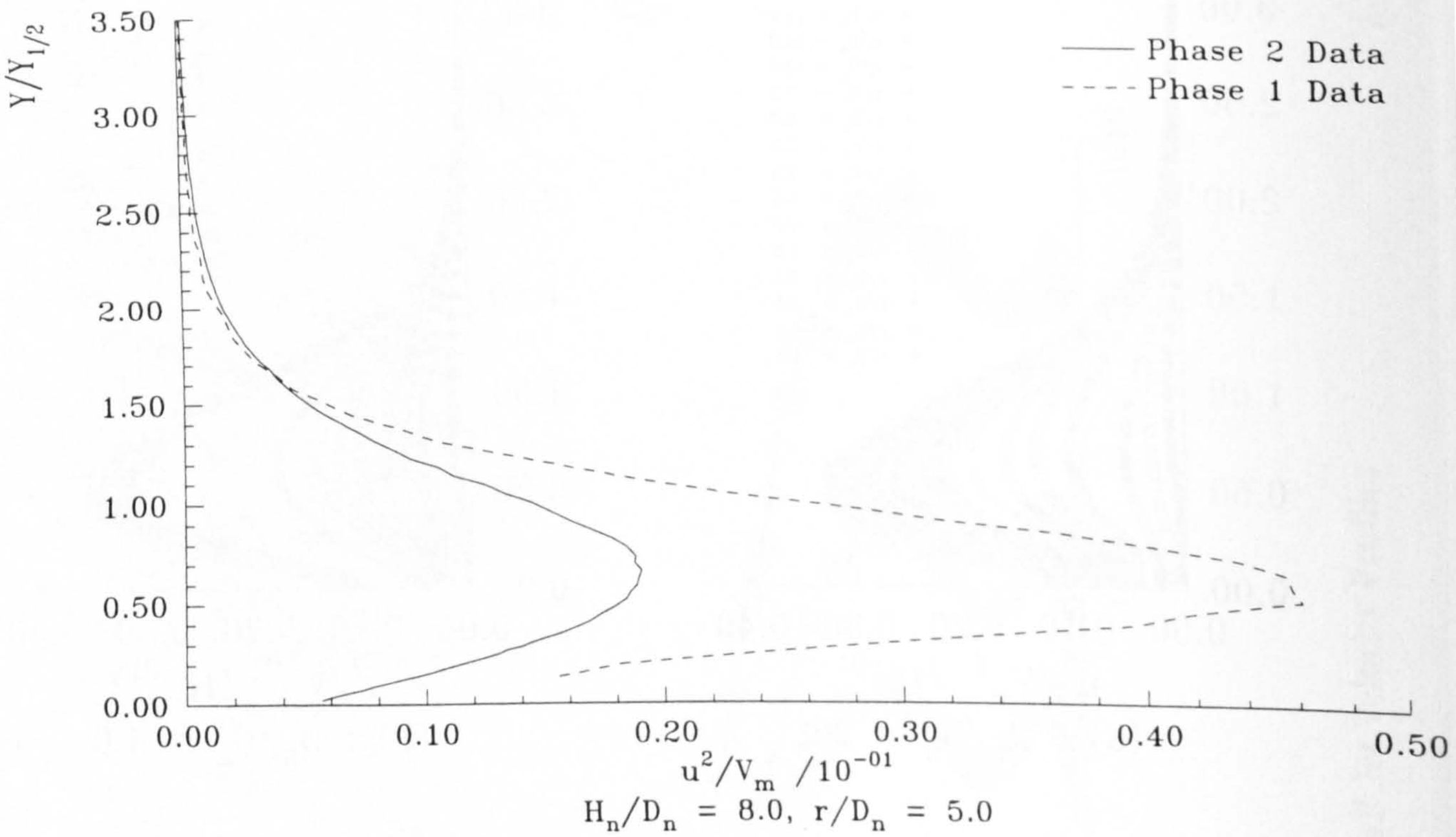

Figure 4.50 (a) : Comparison of Phase 1 and 2 u Turbulent Wall Jet Velocity Profiles

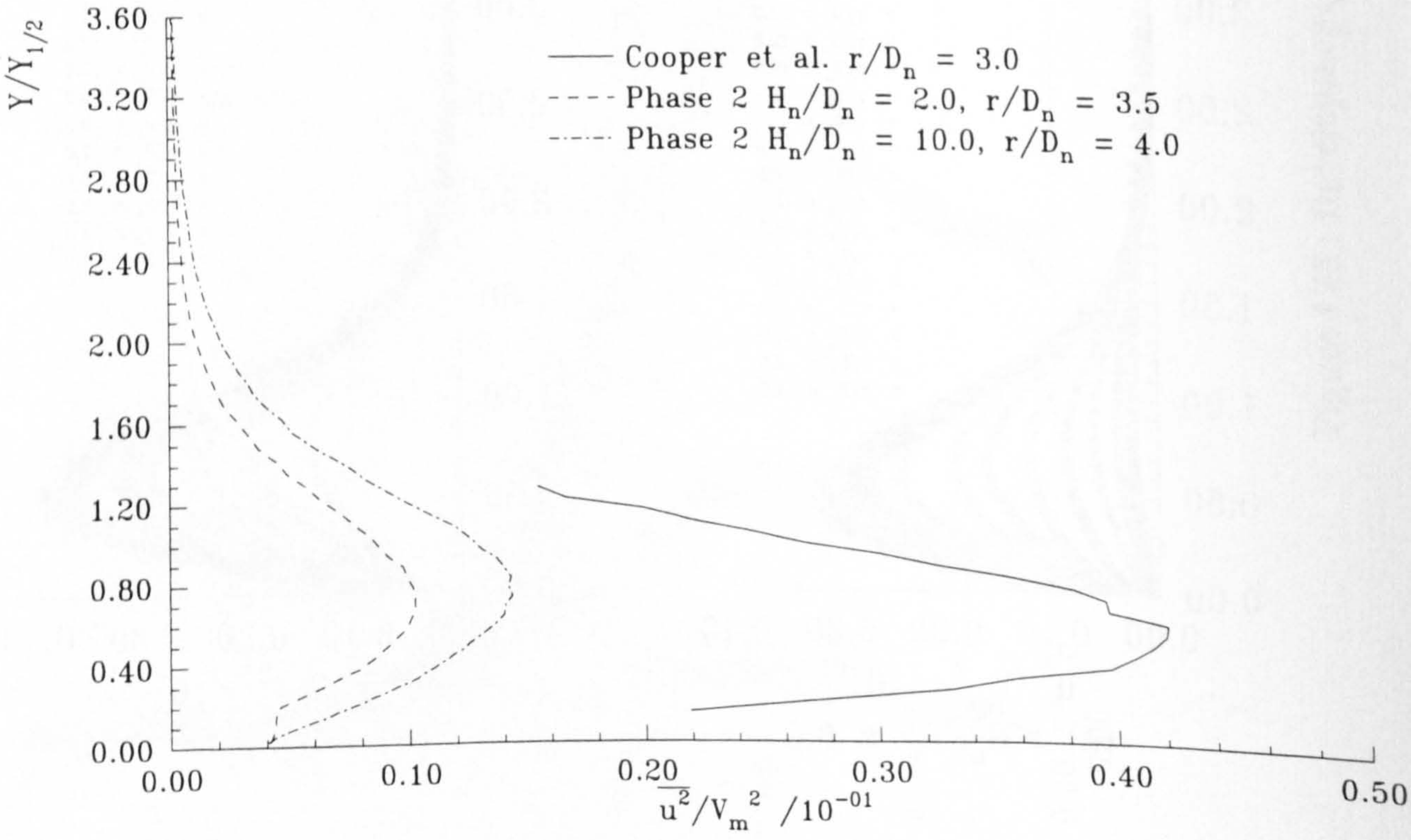

Figure 4.50 (b) : Comparison of Phase 2 Data with Cooper et al. (1993)

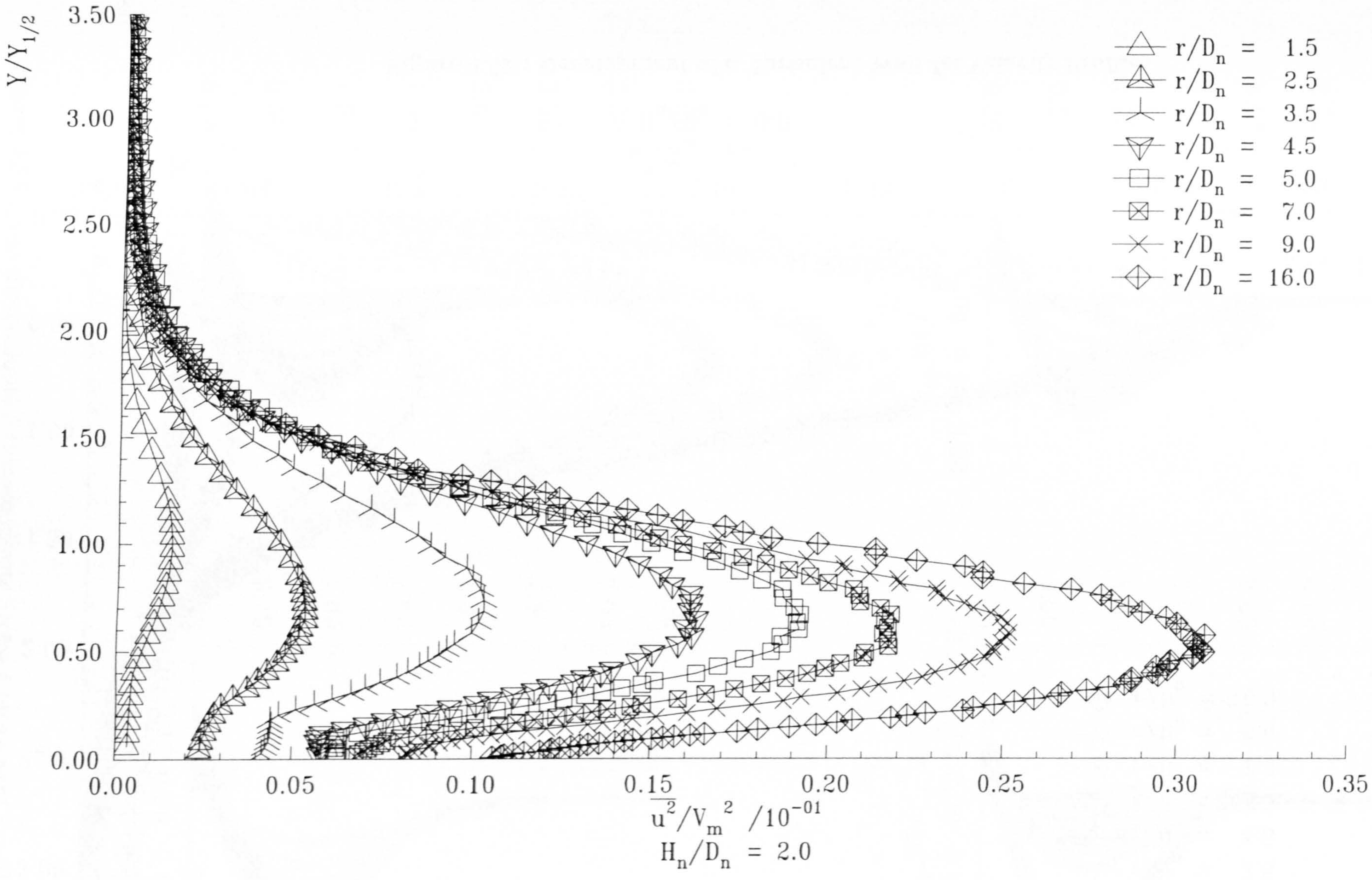

Figure 4.51 : Development of u Turbulent Wall Jet Velocity Profiles

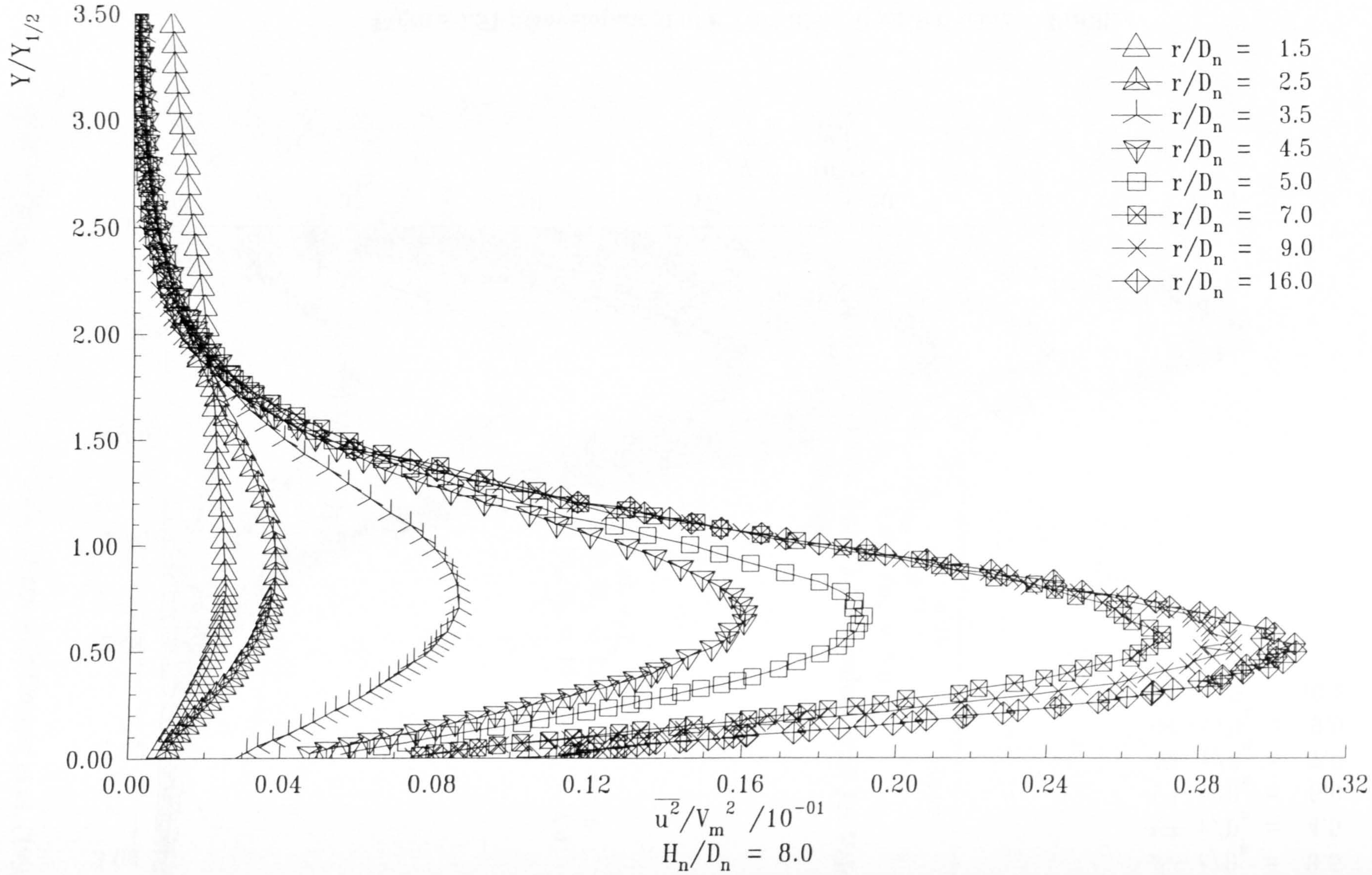

Figure 4.52 : Development of u Turbulent Wall Jet Velocity Profiles

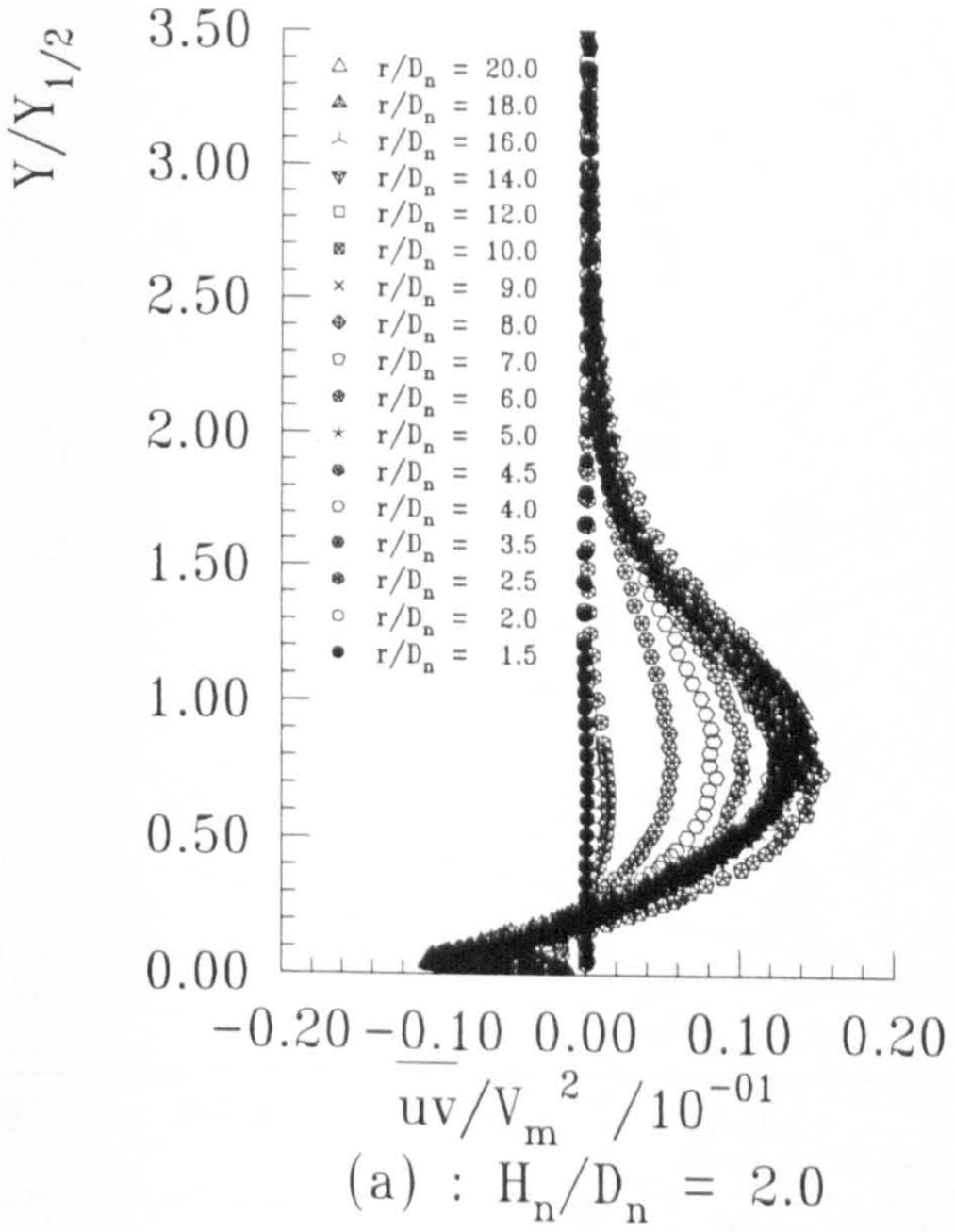

(a) : H_n/D_n = 2.0

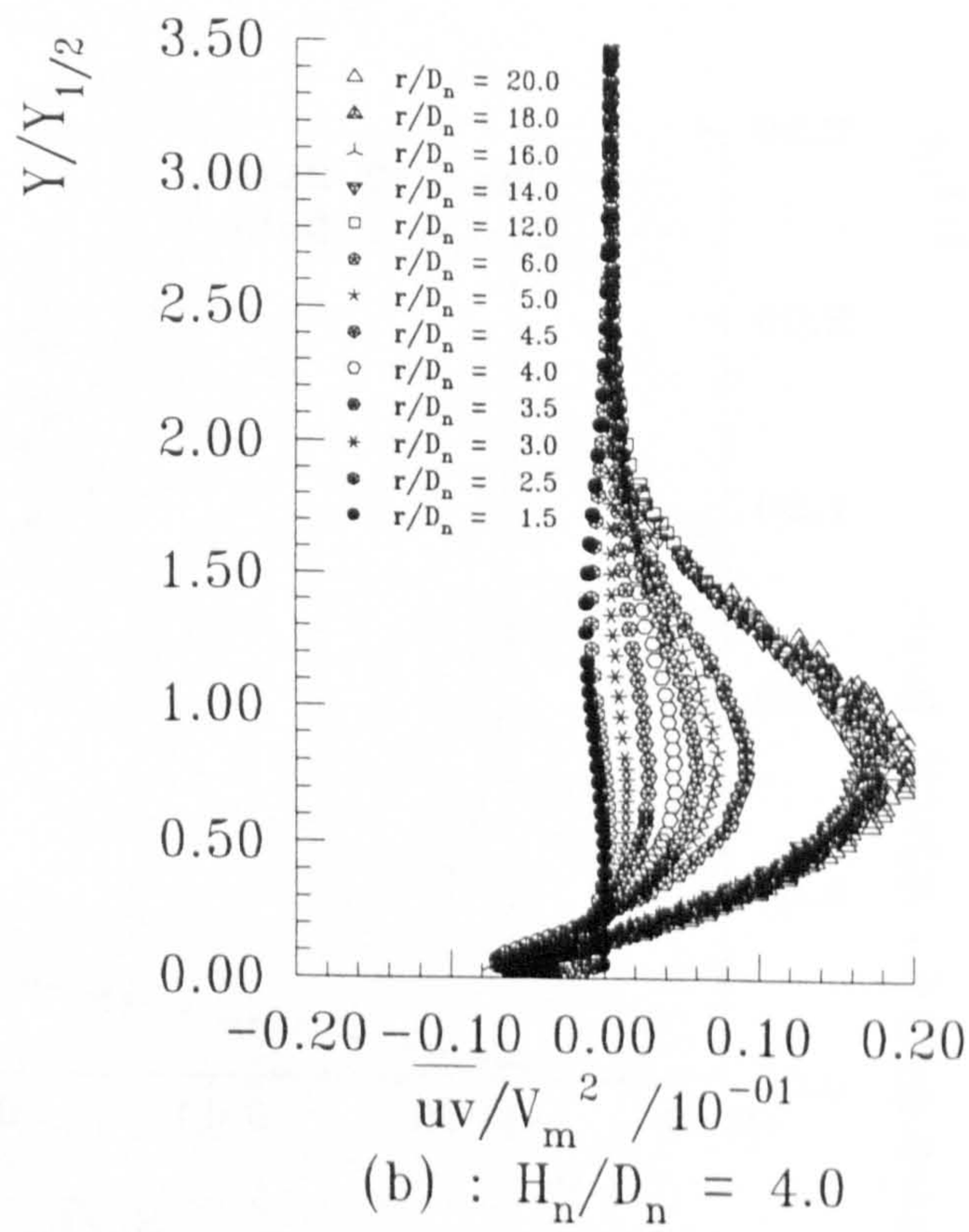

(b) : H_n/D_n = 4.0

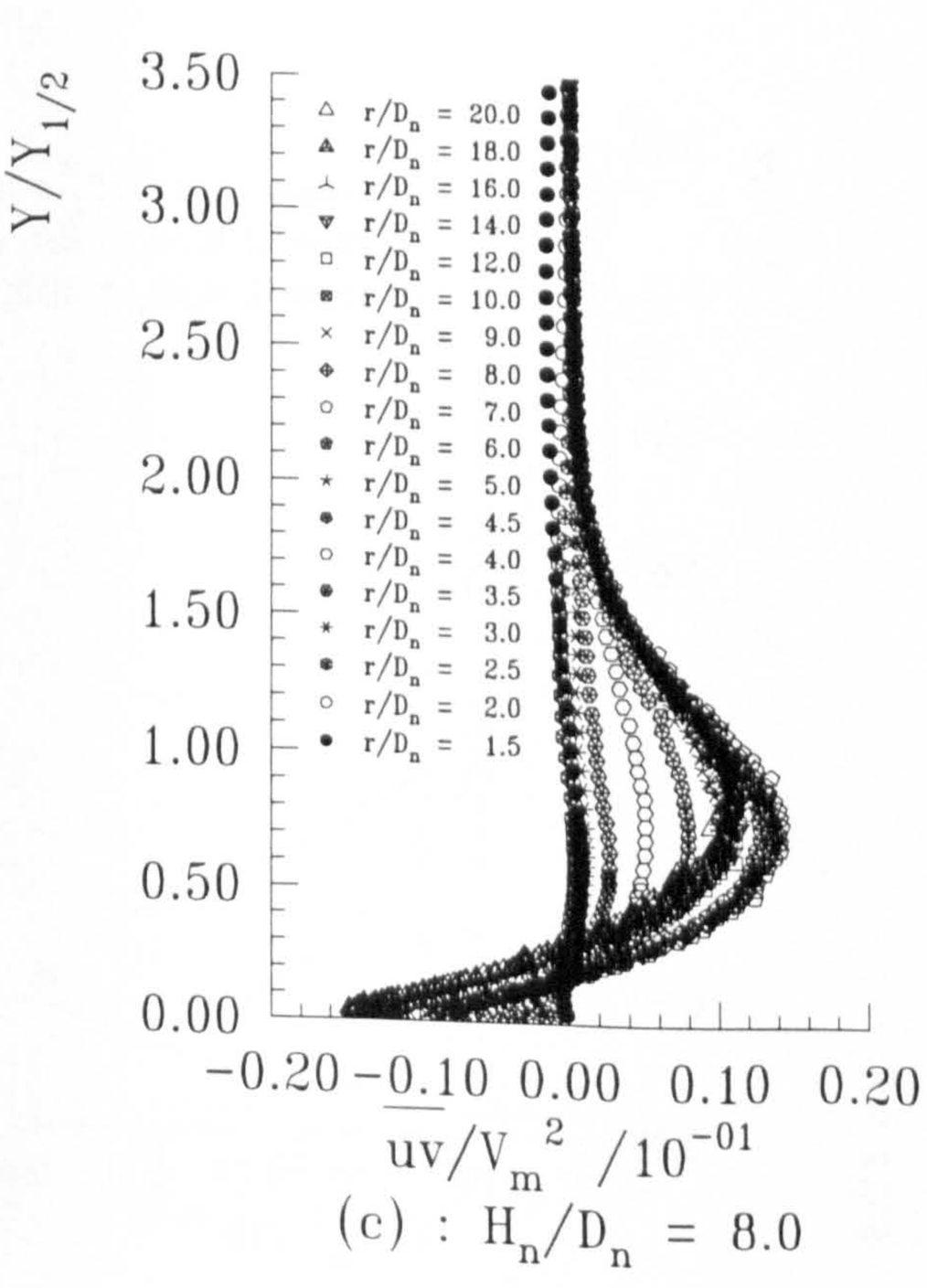

(c) : H_n/D_n = 8.0

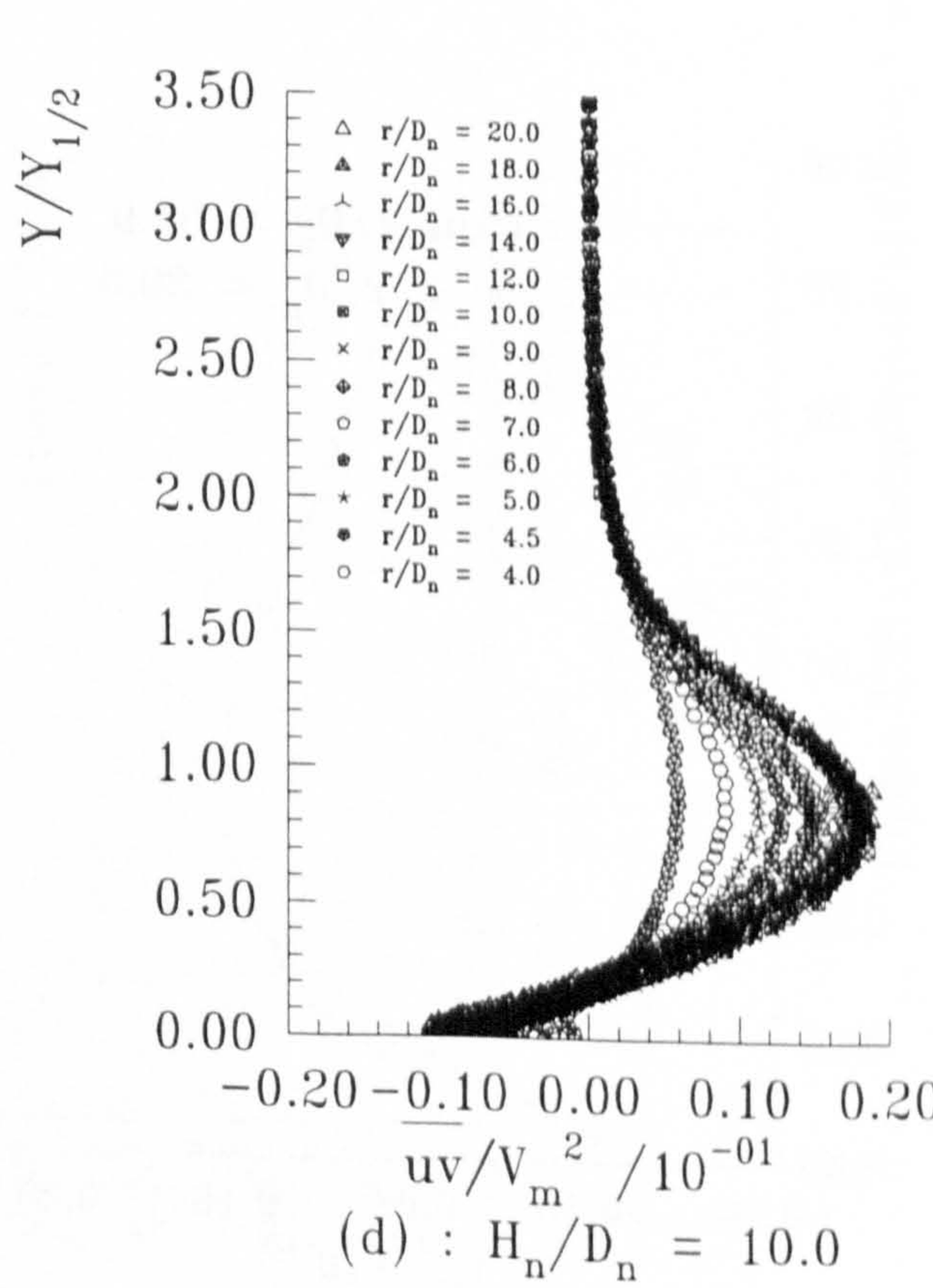

(d) : H_n/D_n = 10.0

Figure 4.53 : Non-dimensional Reynolds Shear Stress Component Profiles at Different r/D_n for Varying H_n/D_n, NPR = 1.05

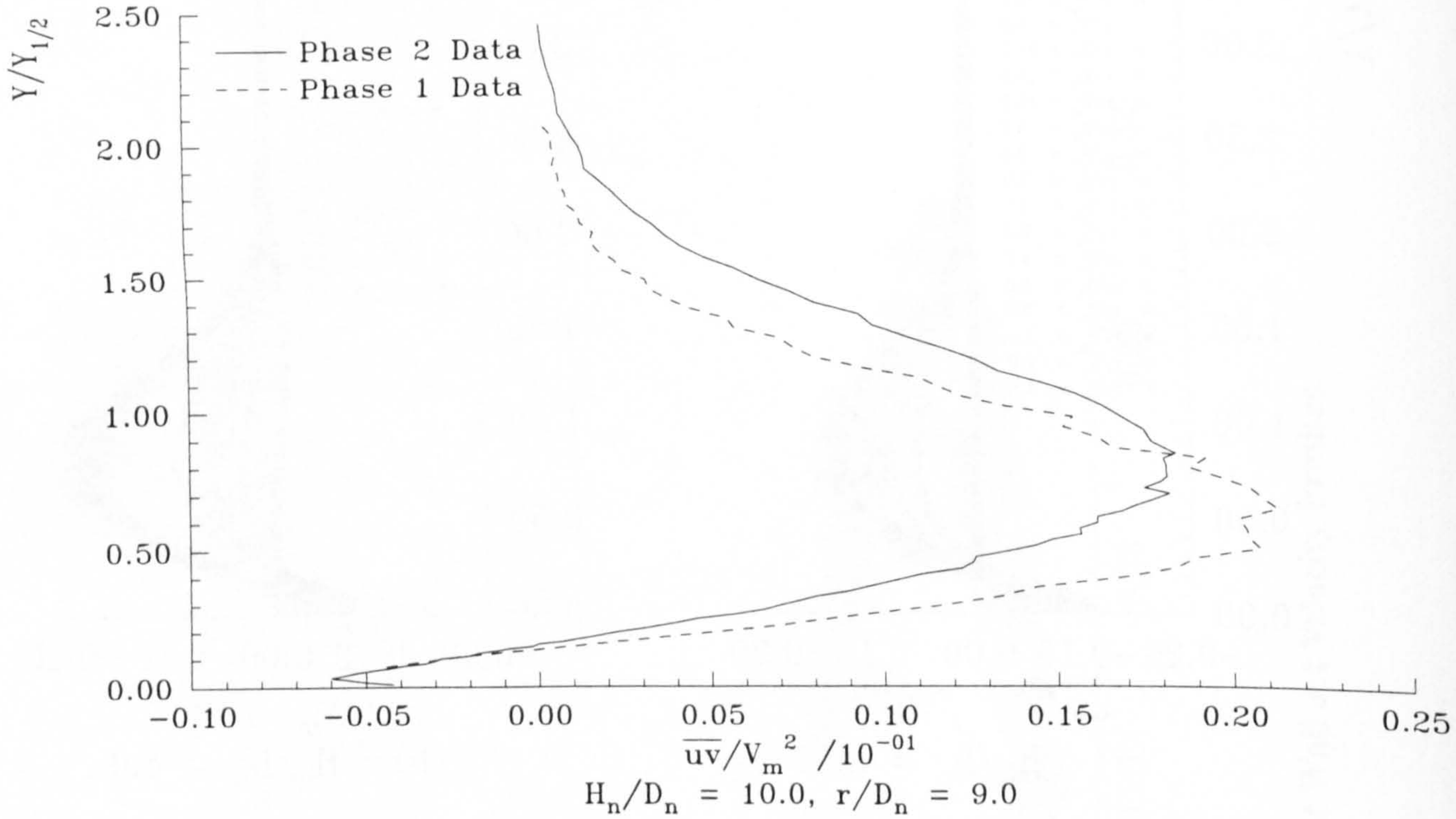

Figure 4.54 (a) : Comparison of Phase 1 and 2 Reynolds Shear Stress Profiles

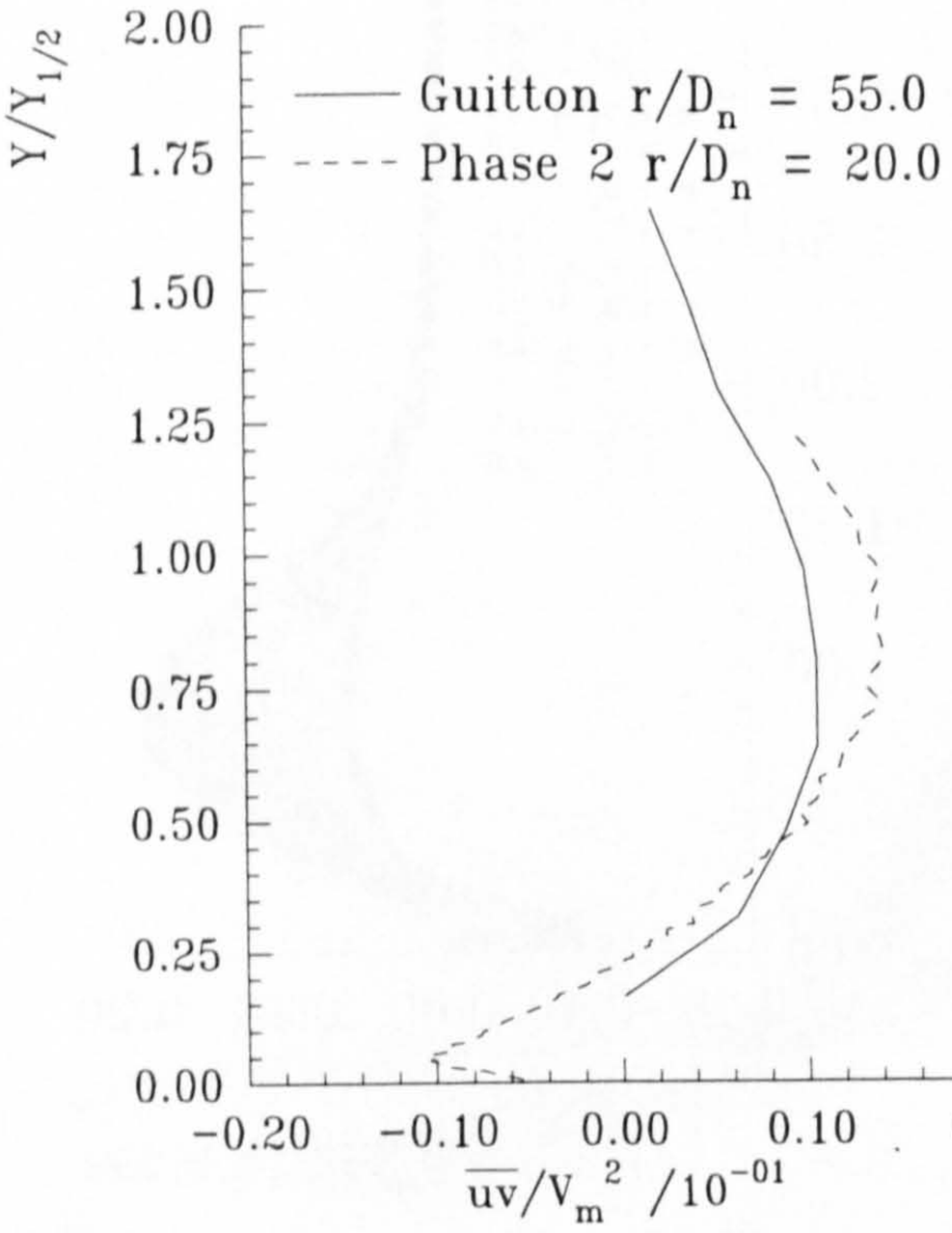

Figure 4.54 (b) : Comparison of Phase 2 Data with Guitton (1968)

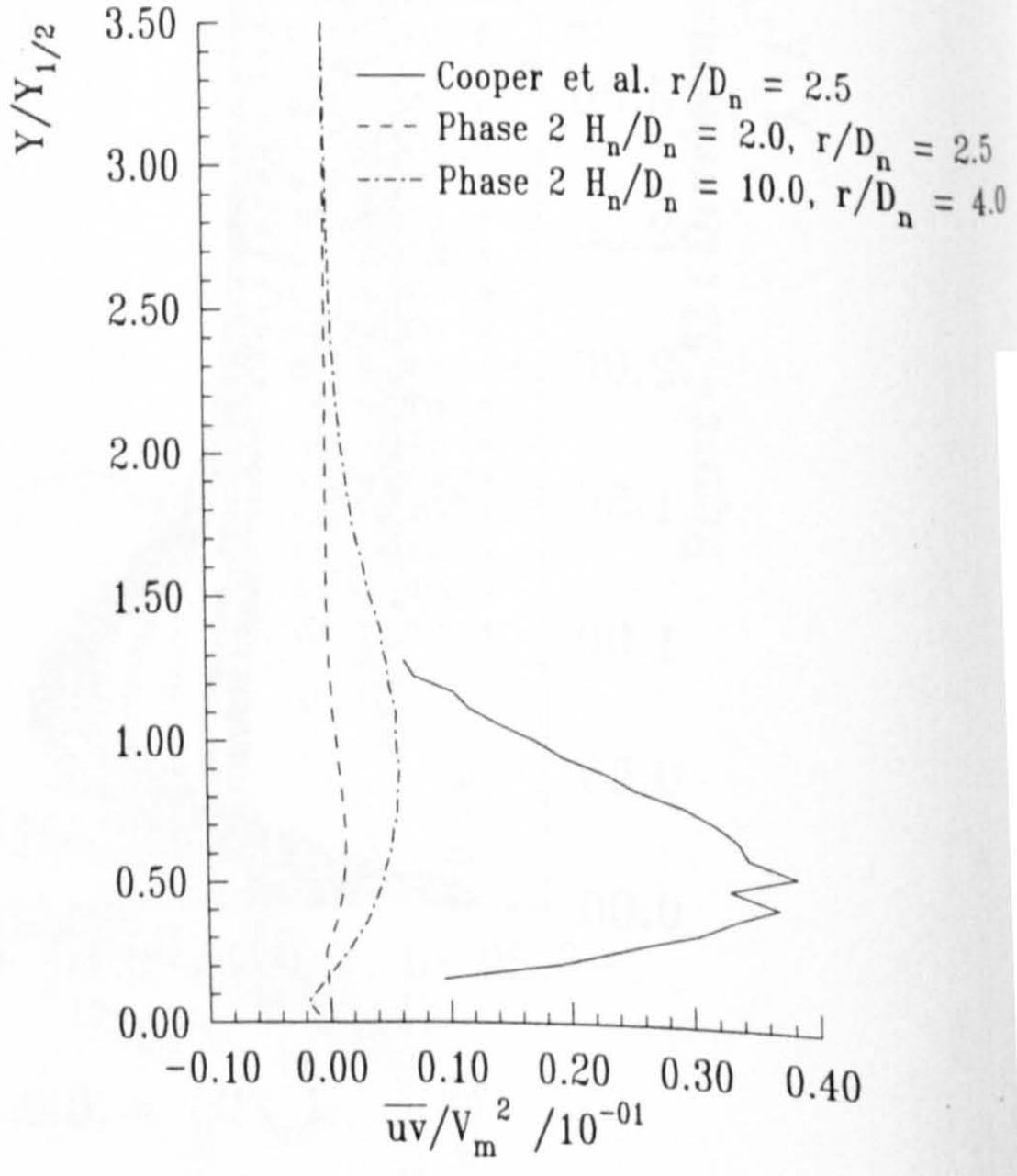

Figure 4.54 (c) : Comparison of Phase 2 Data with Cooper et al. (1993)

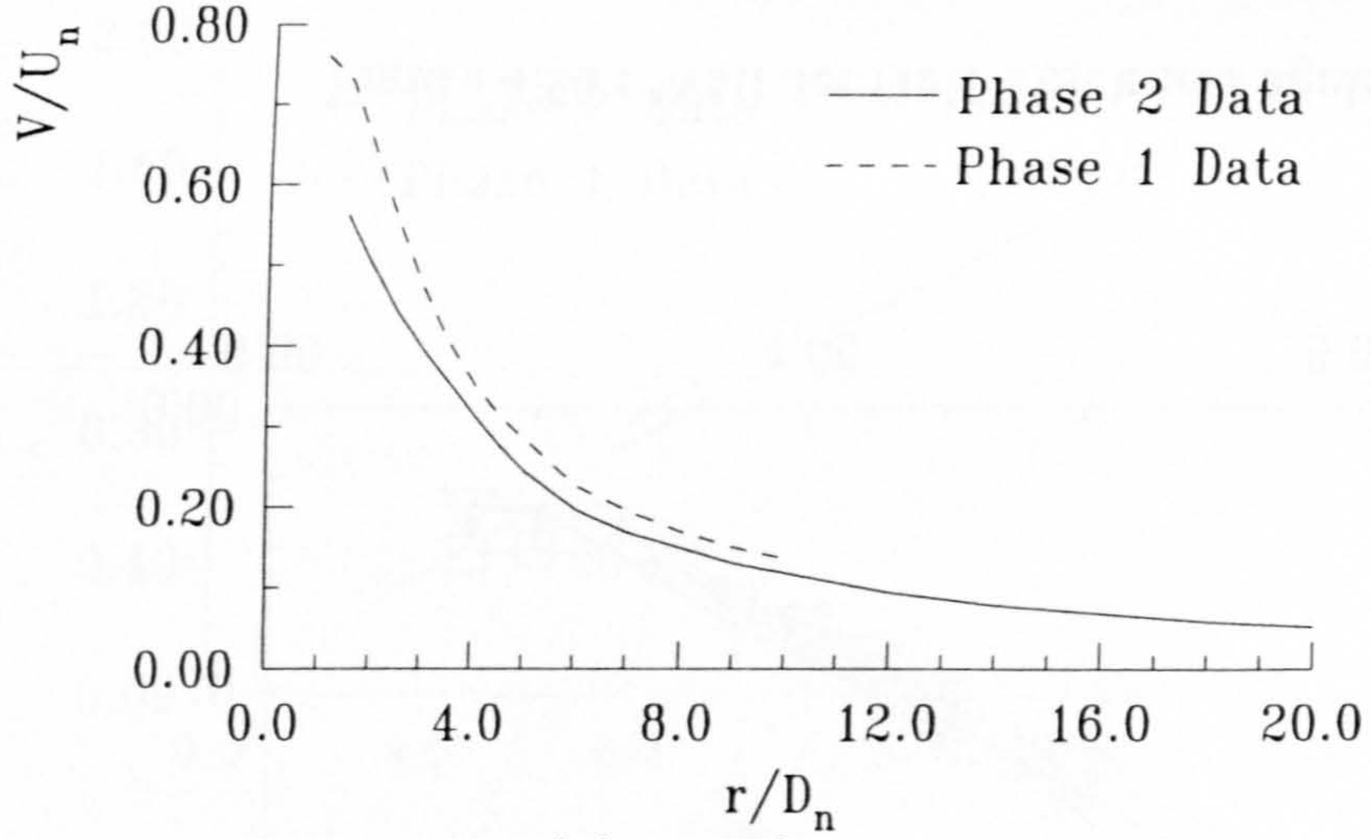

(a) : H_n/D_n = 8.0

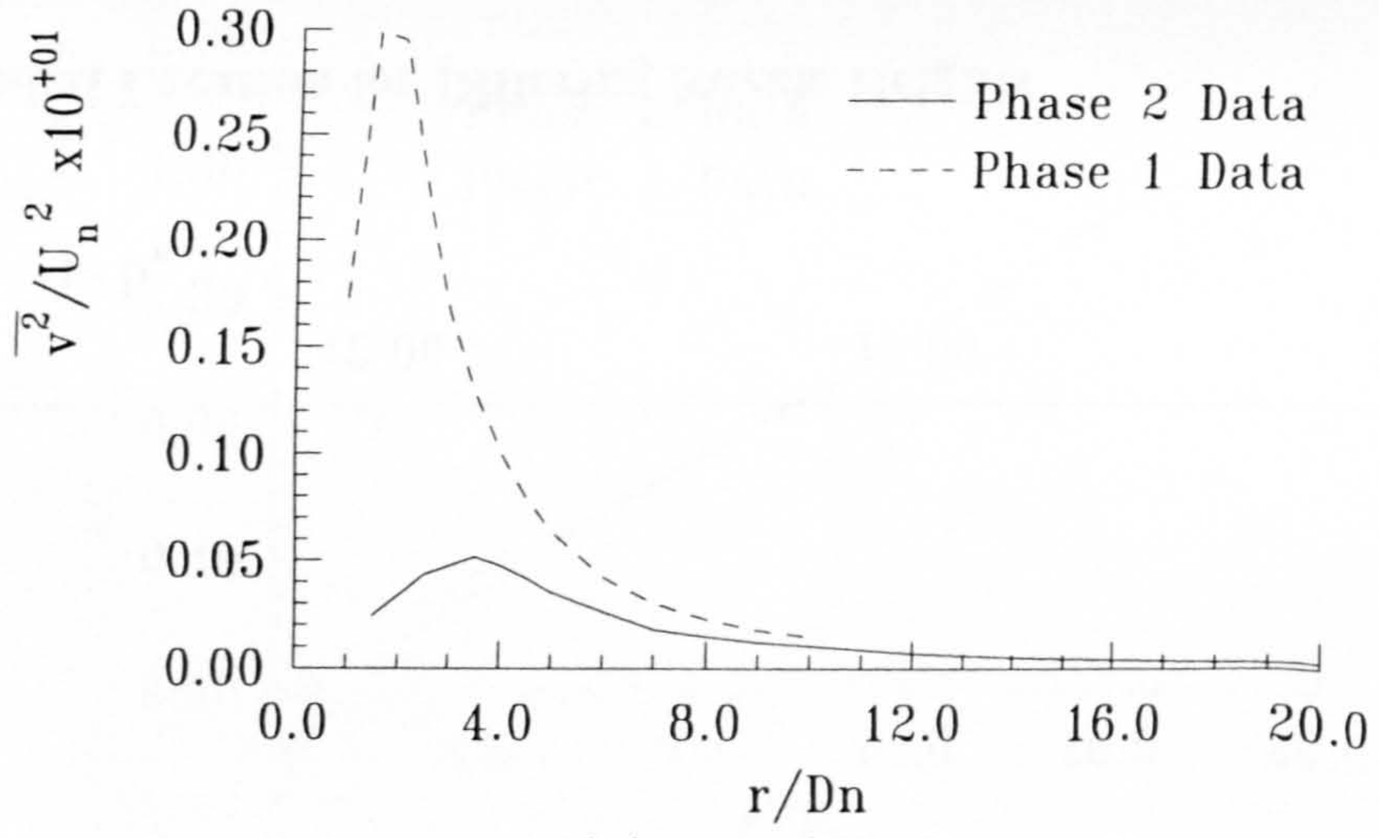

(b) : H_n/D_n = 8.0

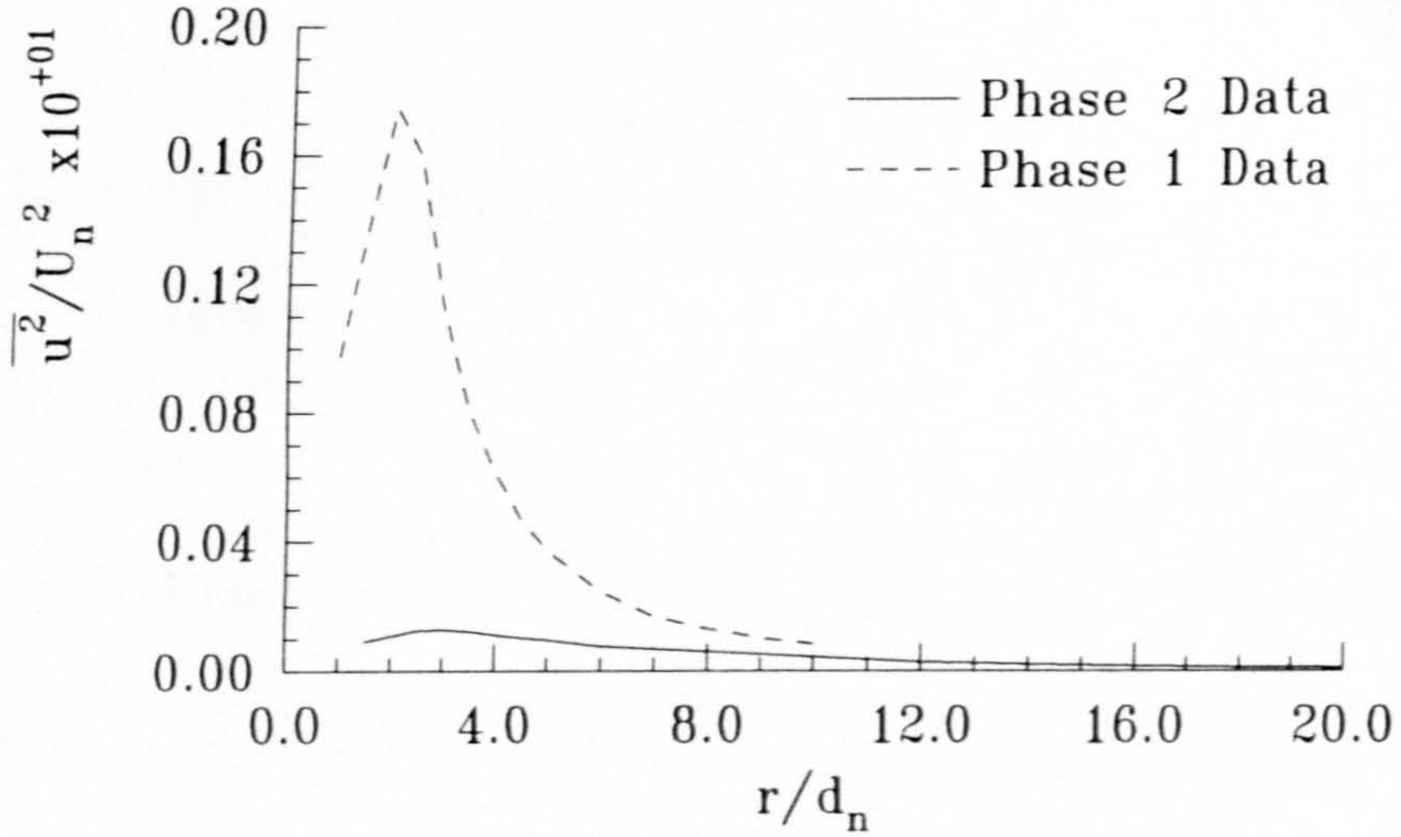

(c) : H_n/D_n = 4.0

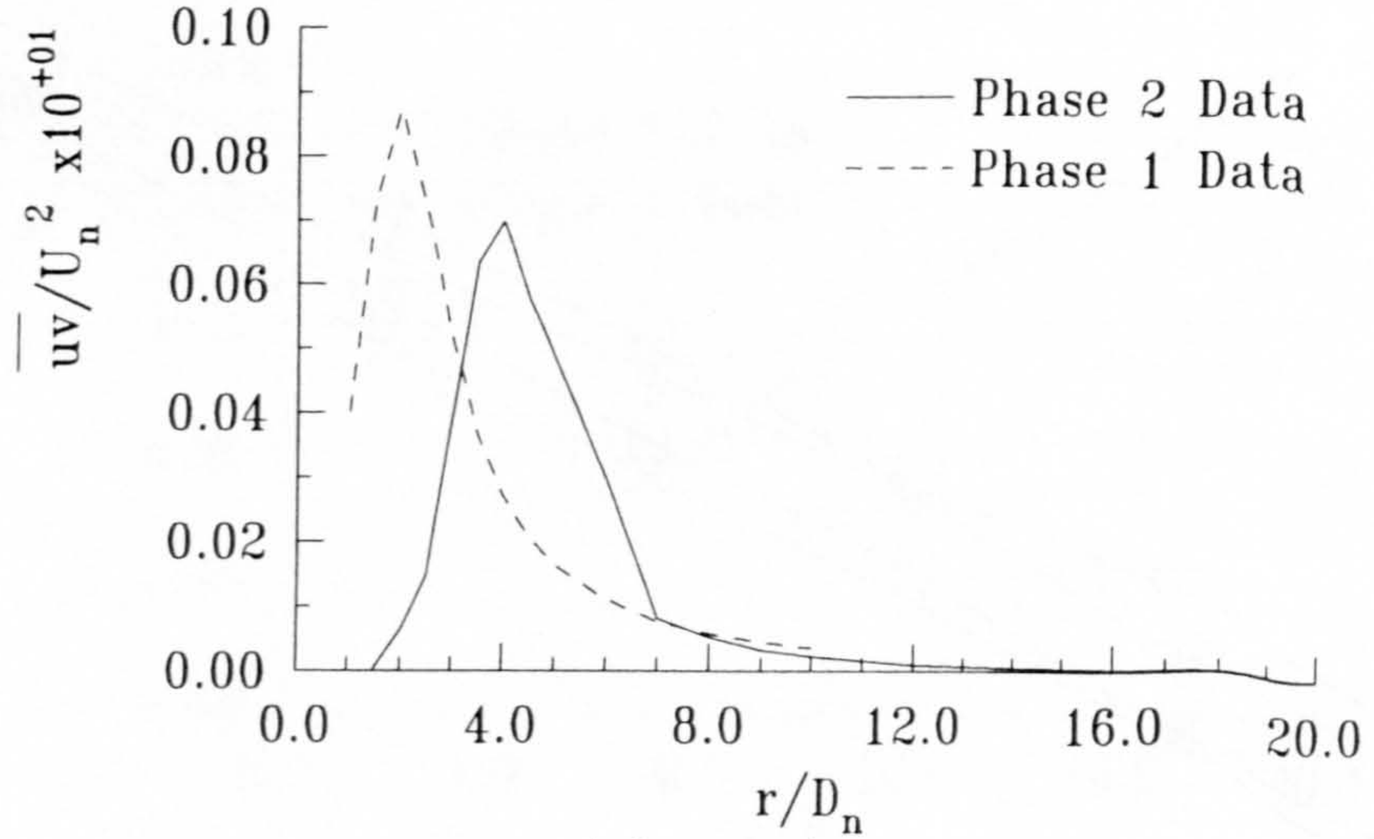

(d) : H_n/D_n = 2.0

Figure 4.55 : Comparison of Phase 1 and Phase 2 Peak Wall Jet Velocity Data

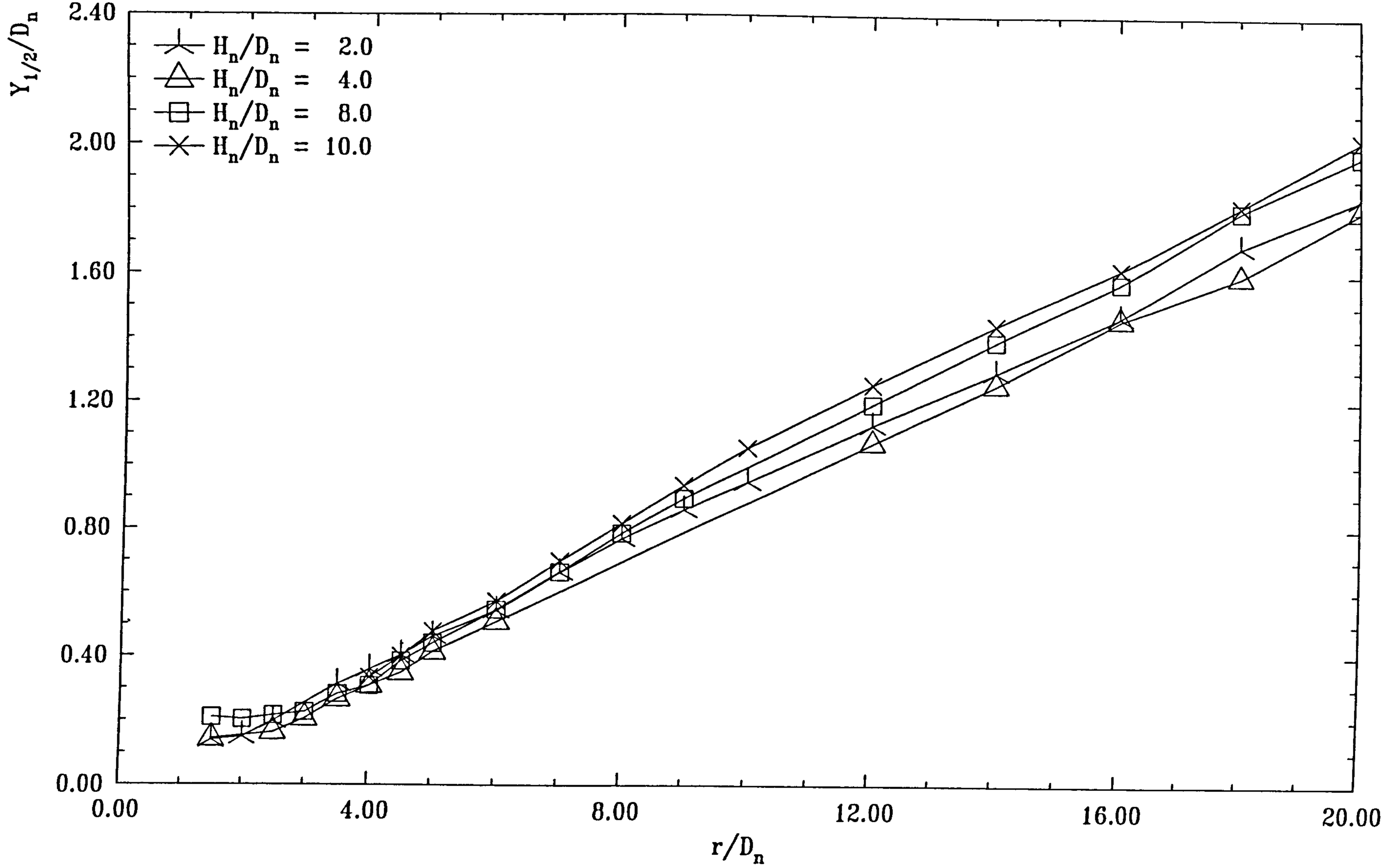

Figure 4.56 : Wall Jet Half Thickness against Radial Location for Differing Nozzle Heights

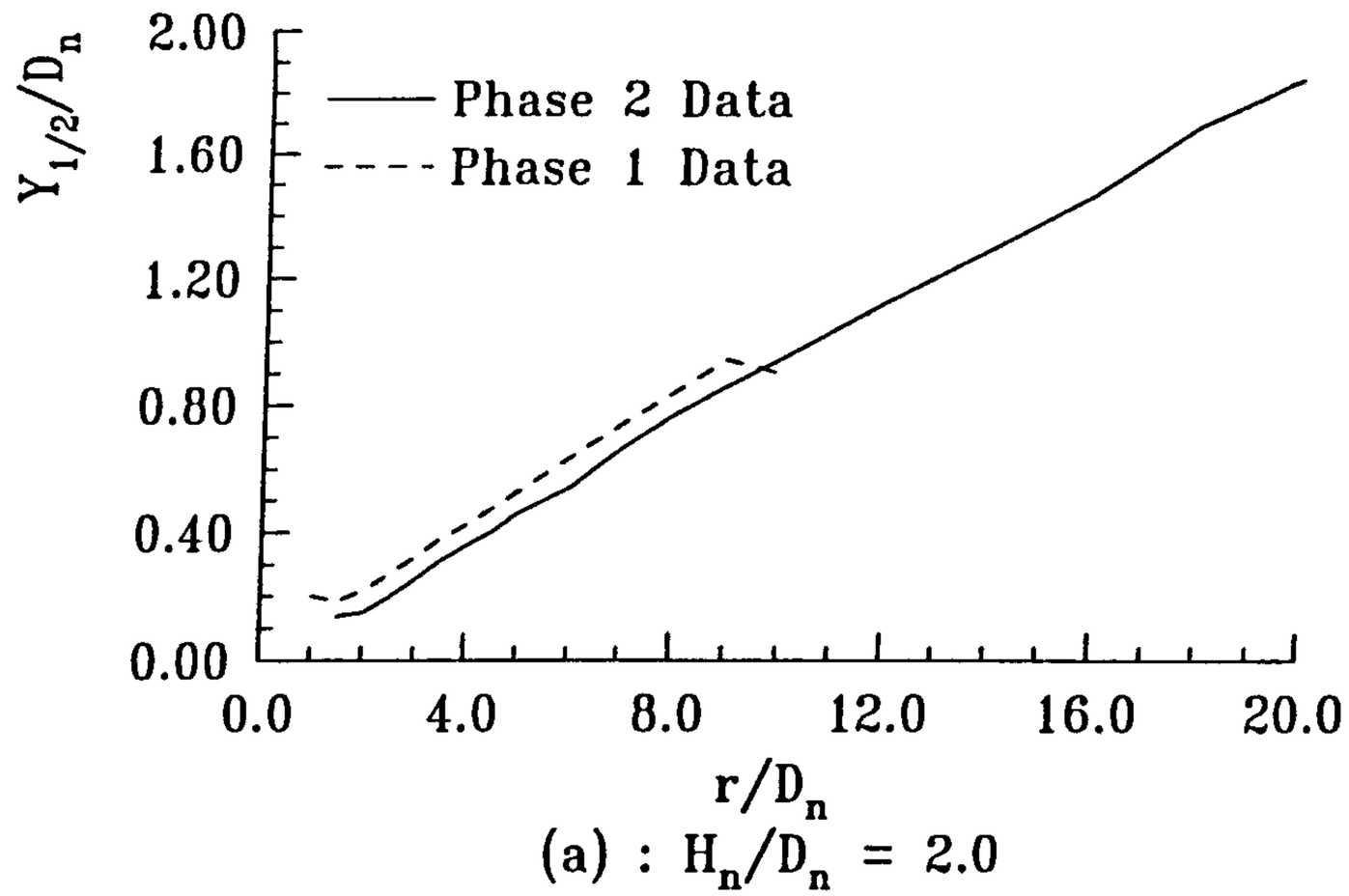

(a) : H_n/D_n = 2.0

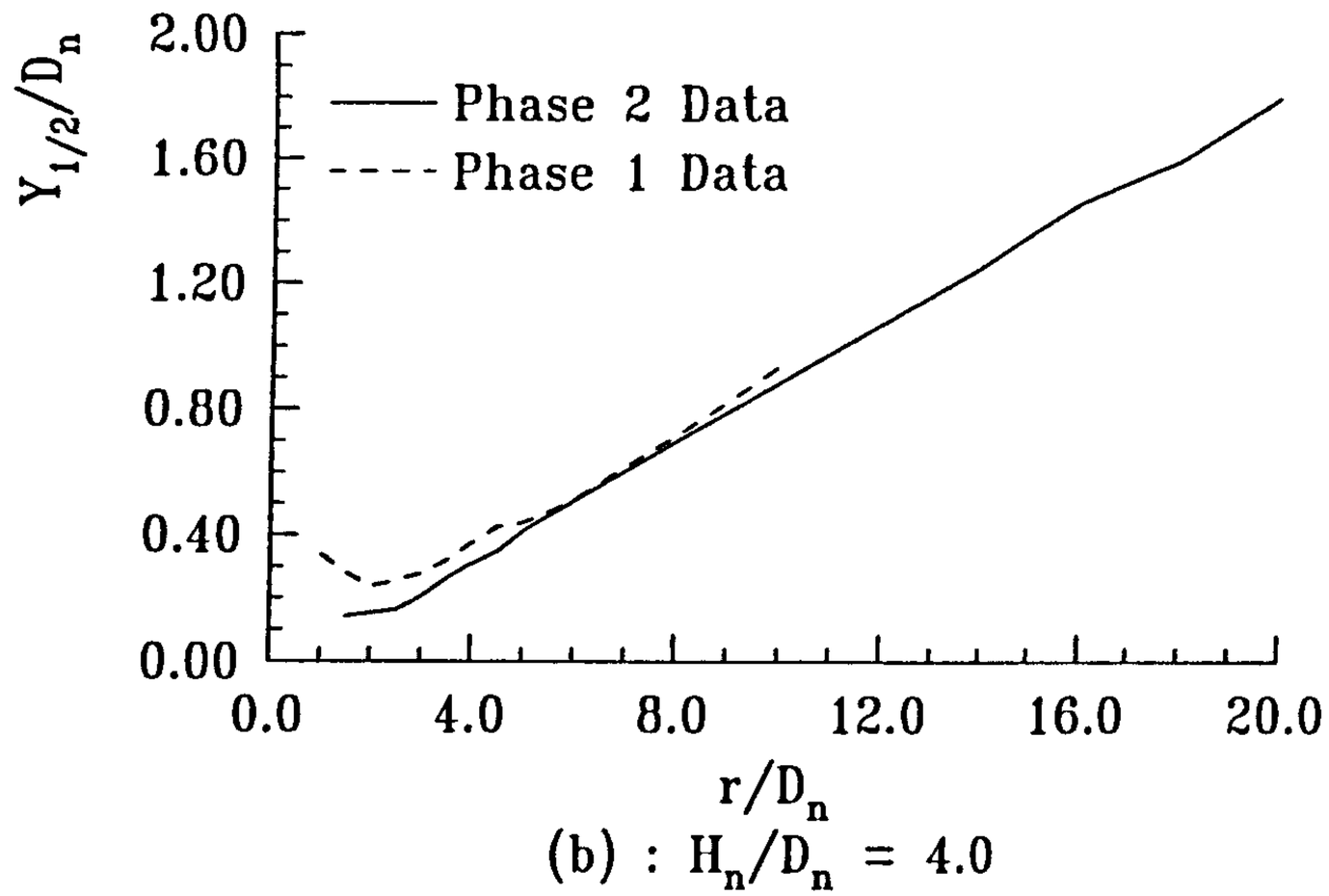

(b) : H_n/D_n = 4.0

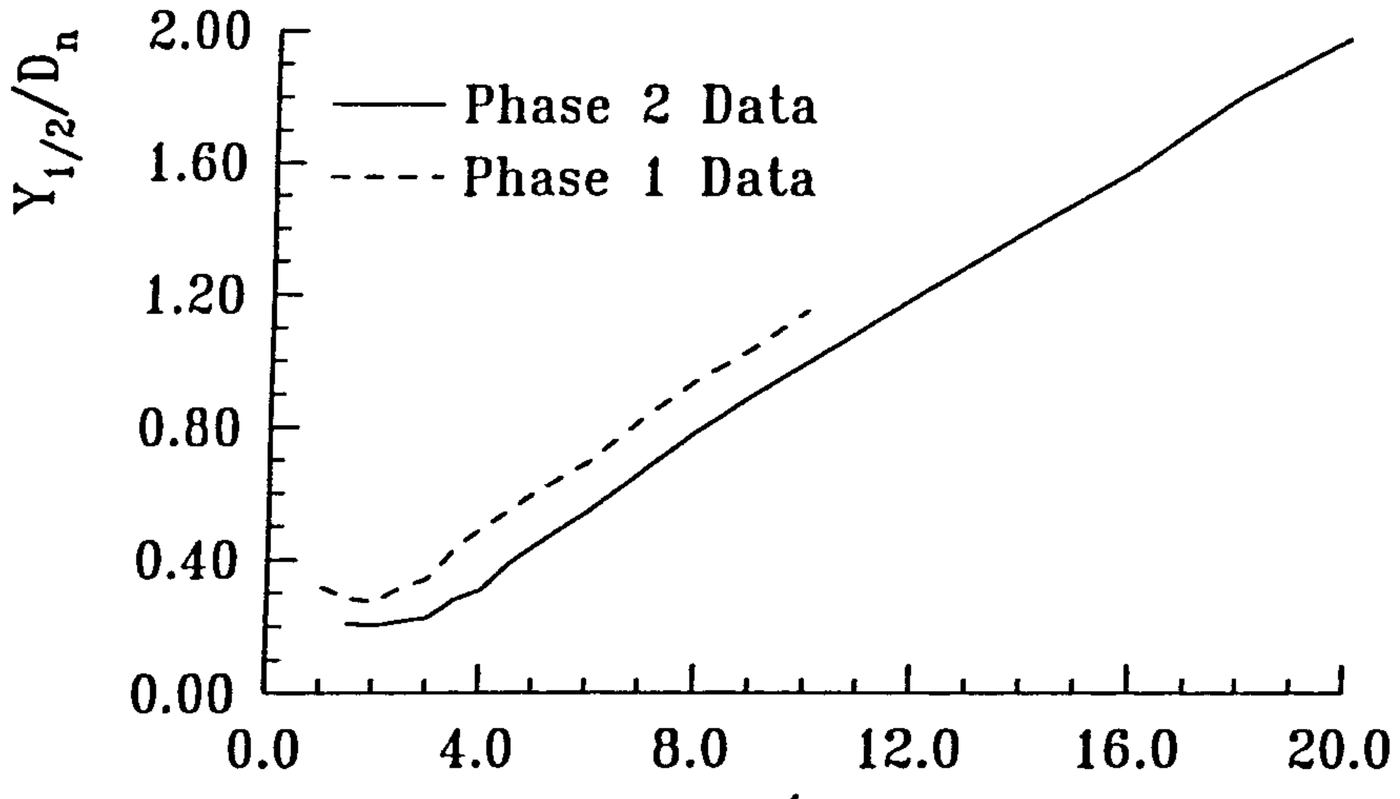

(c) : H_n/D_n = 8.0

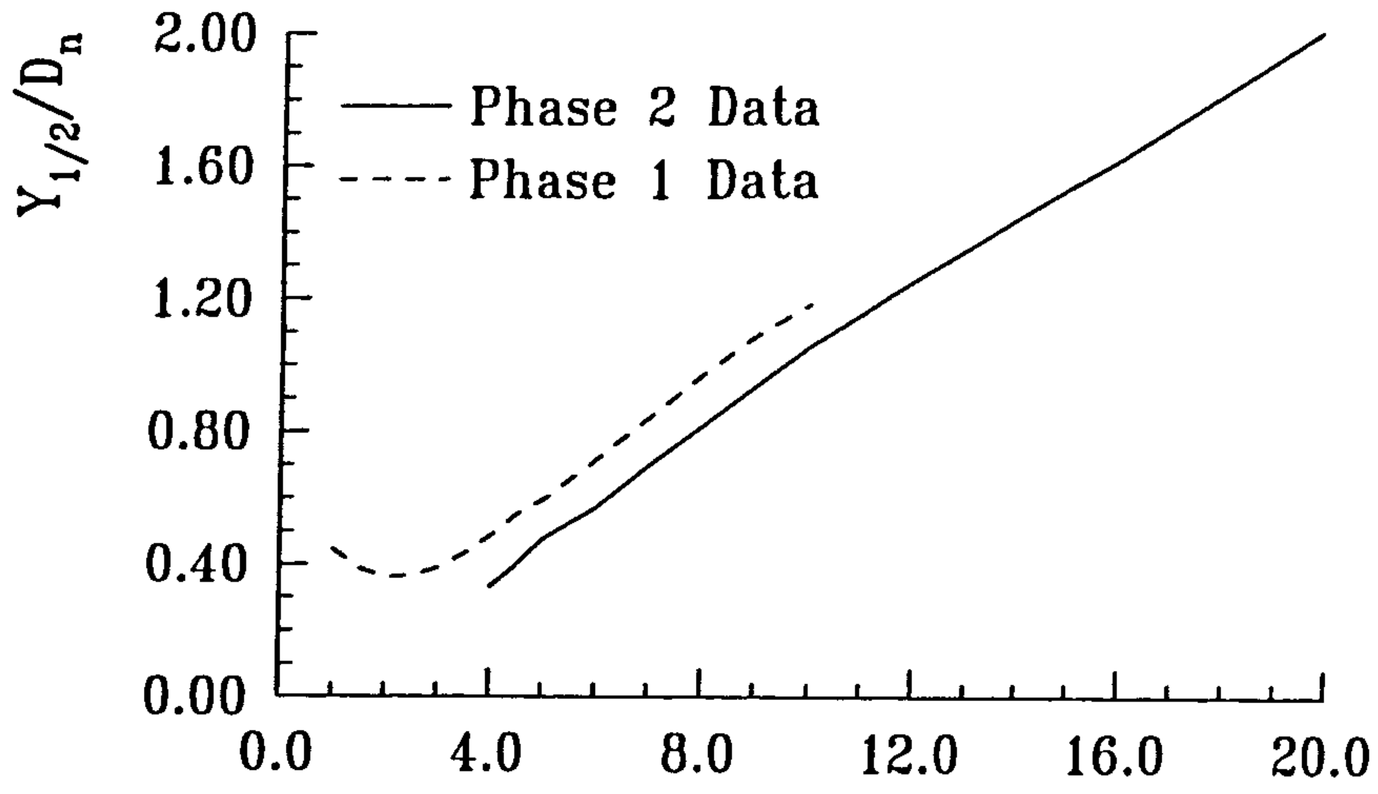

(d) : H_n/D_n = 10.0

Figure 4.57 : Comparison of Phase 1 and Phase 2 Wall Jet Half Thickness against Radial Location

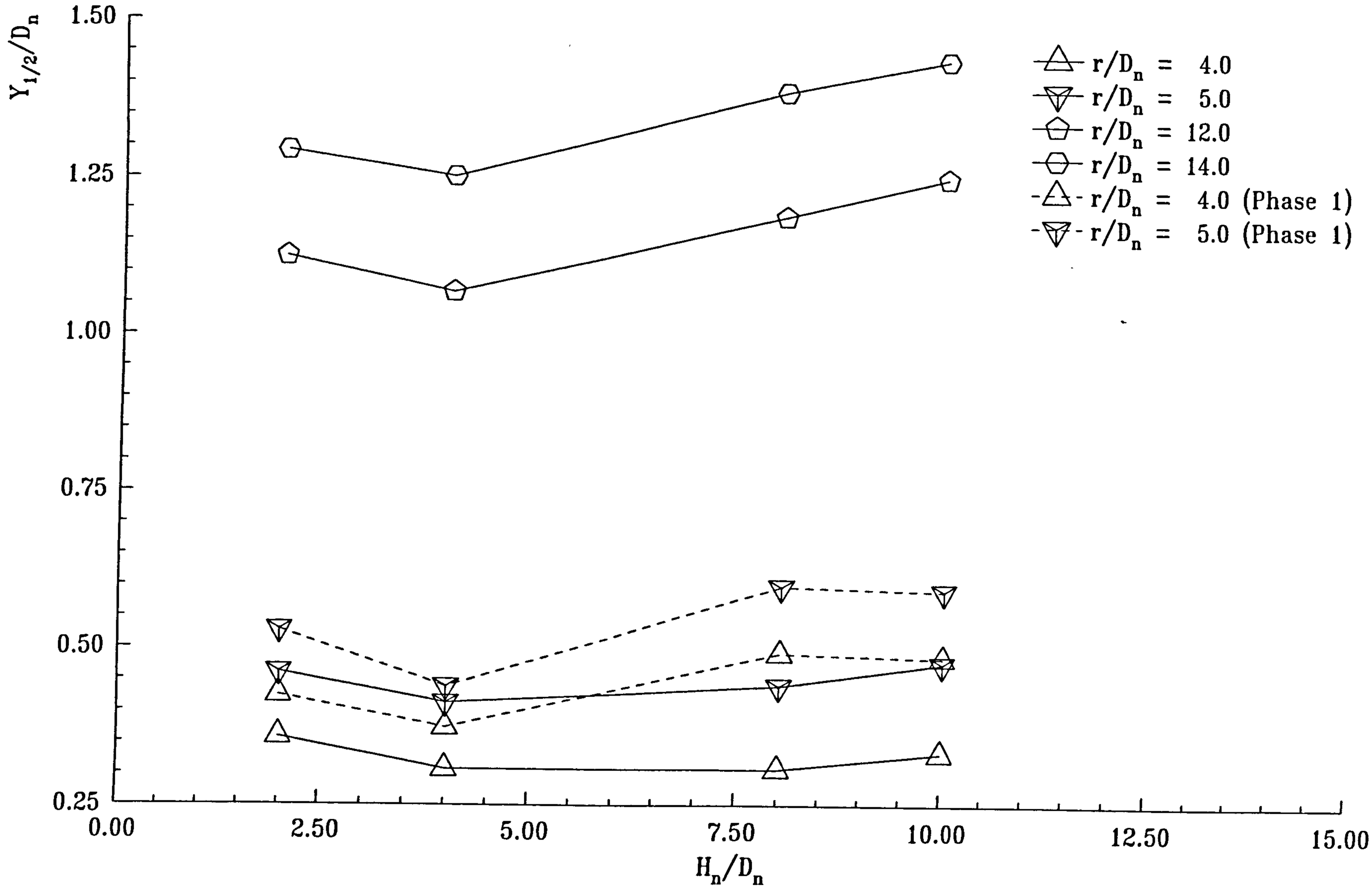

Figure 4.58 : Comparison of Phase 1 and Phase 2 Nozzle Height Effect

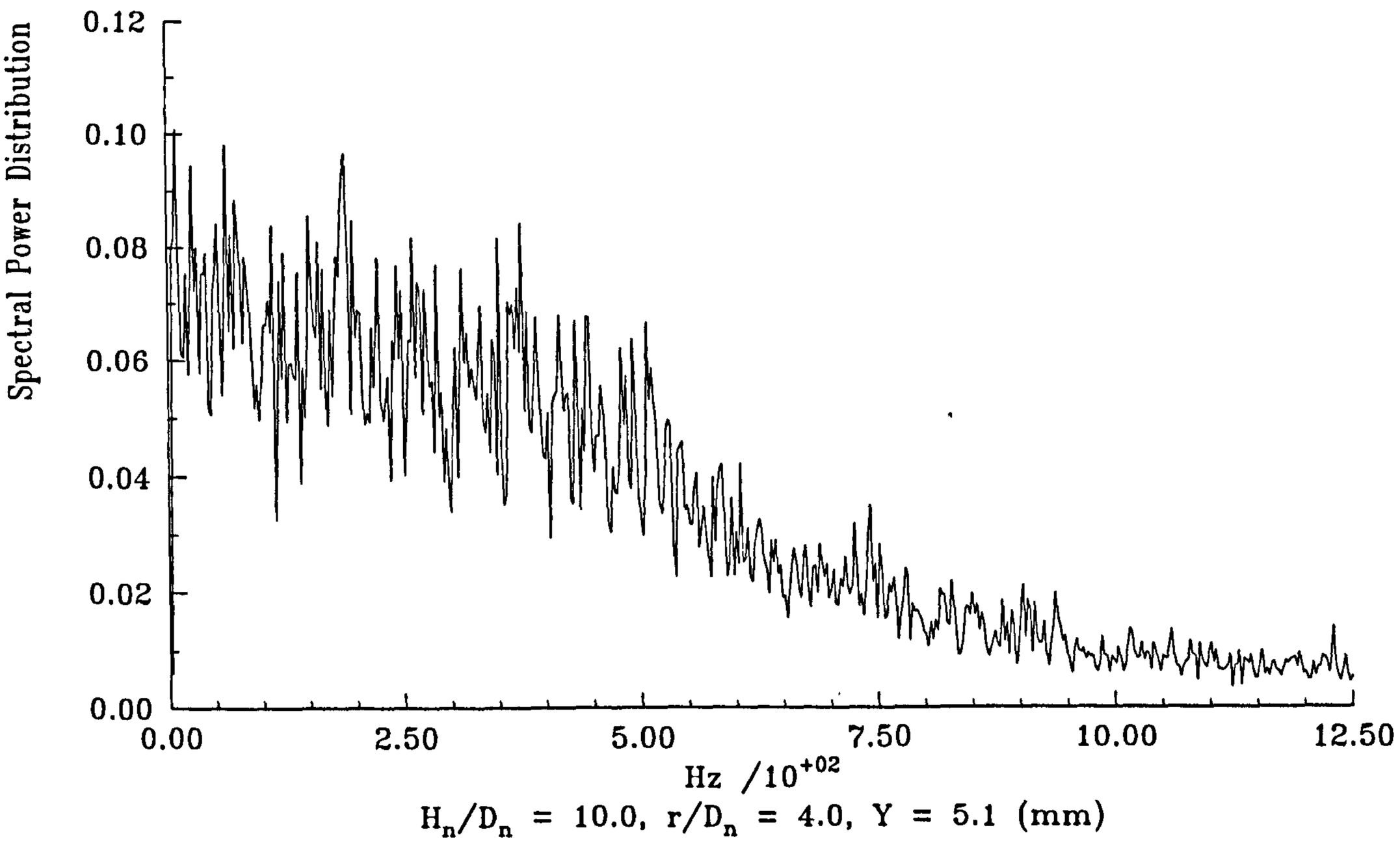

Figure 4.59 : Typical Profile Sample Frequency Spectrum

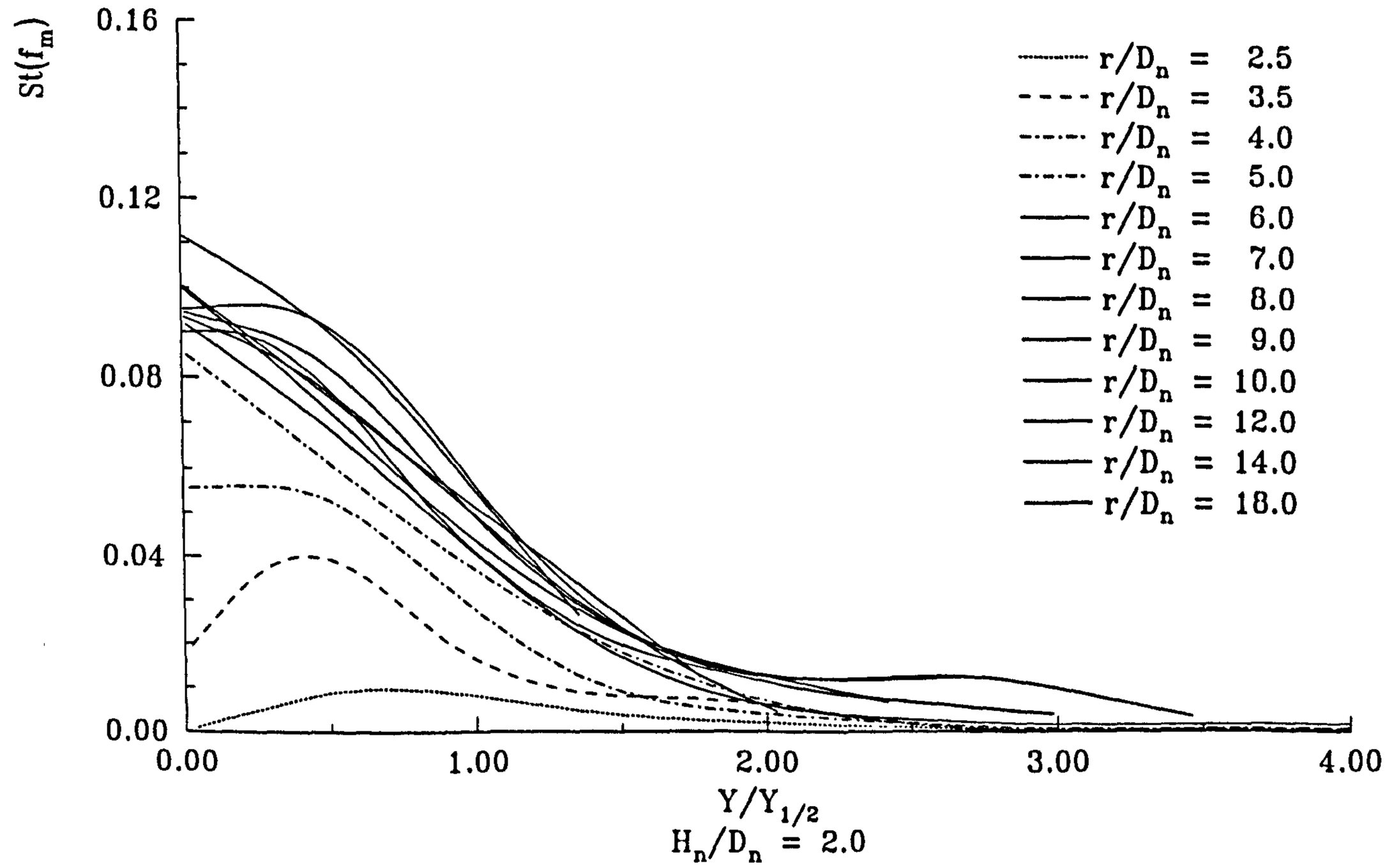

Figure 4.60 : Non-dimensional Strouhal Number

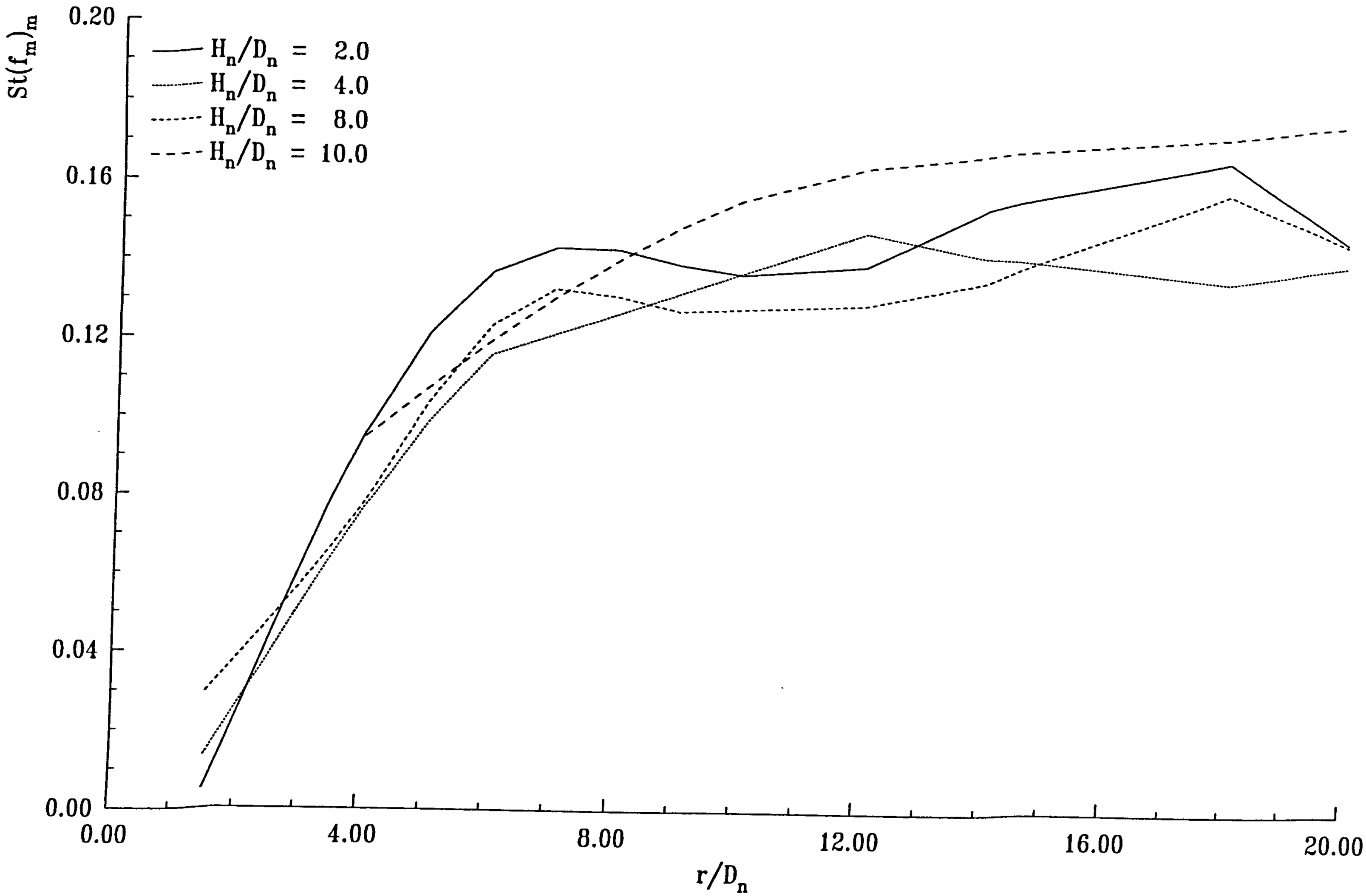

Figure 4.61 : Peak Strouhal Number against Radial Location for Varying Nozzle Height

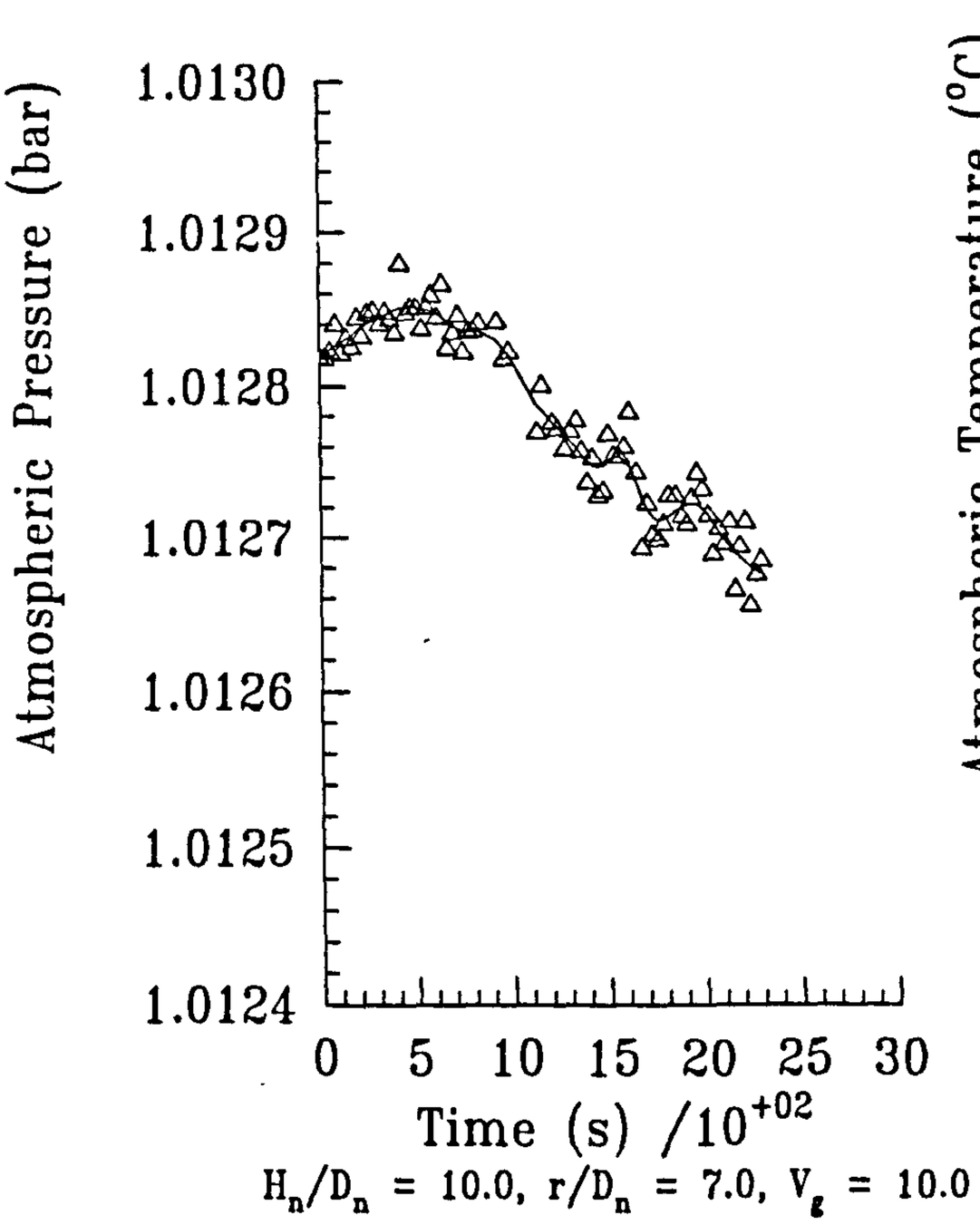

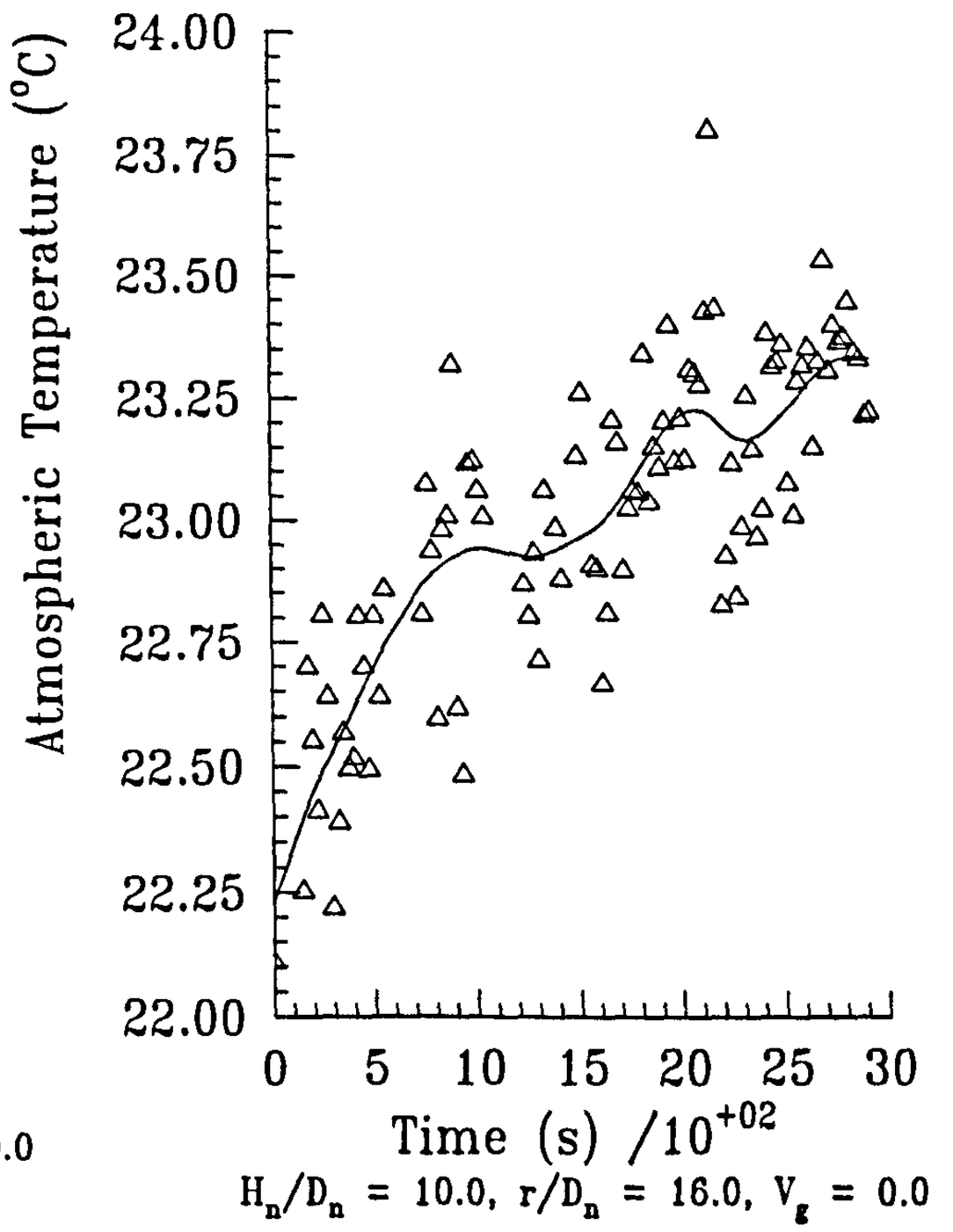

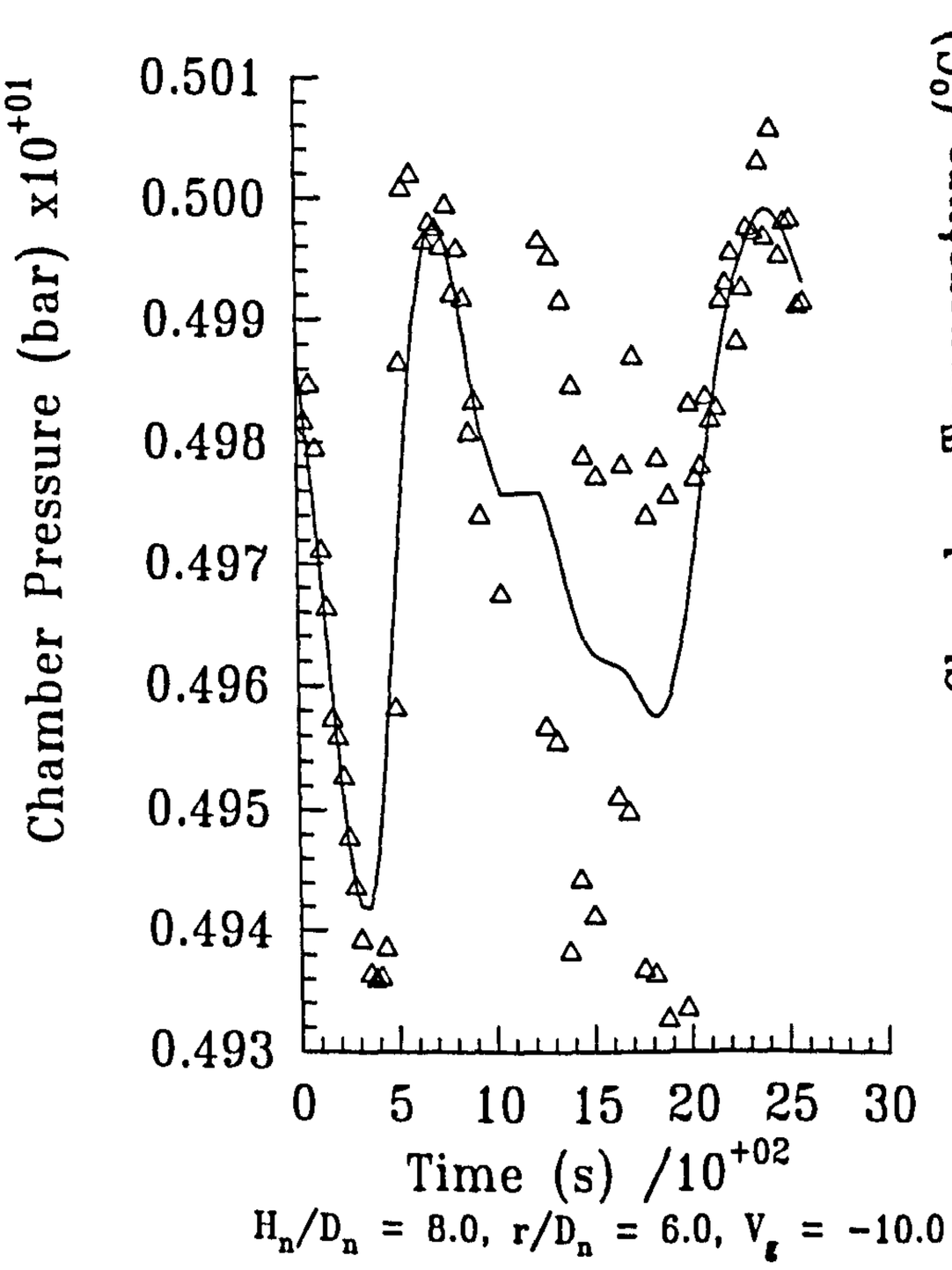

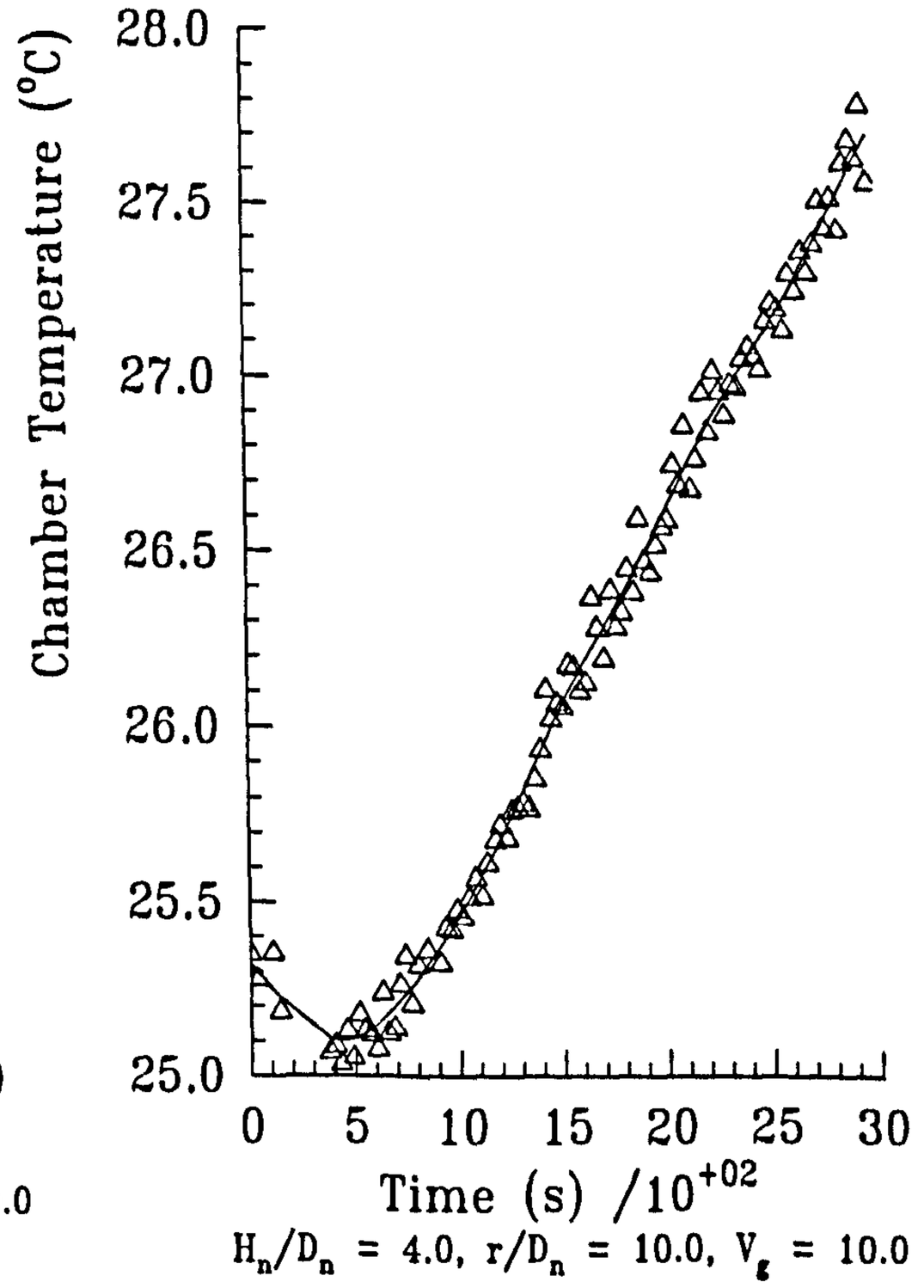

Figure 4.62 : Typical Ambient and Settling Chamber Conditions during a Run

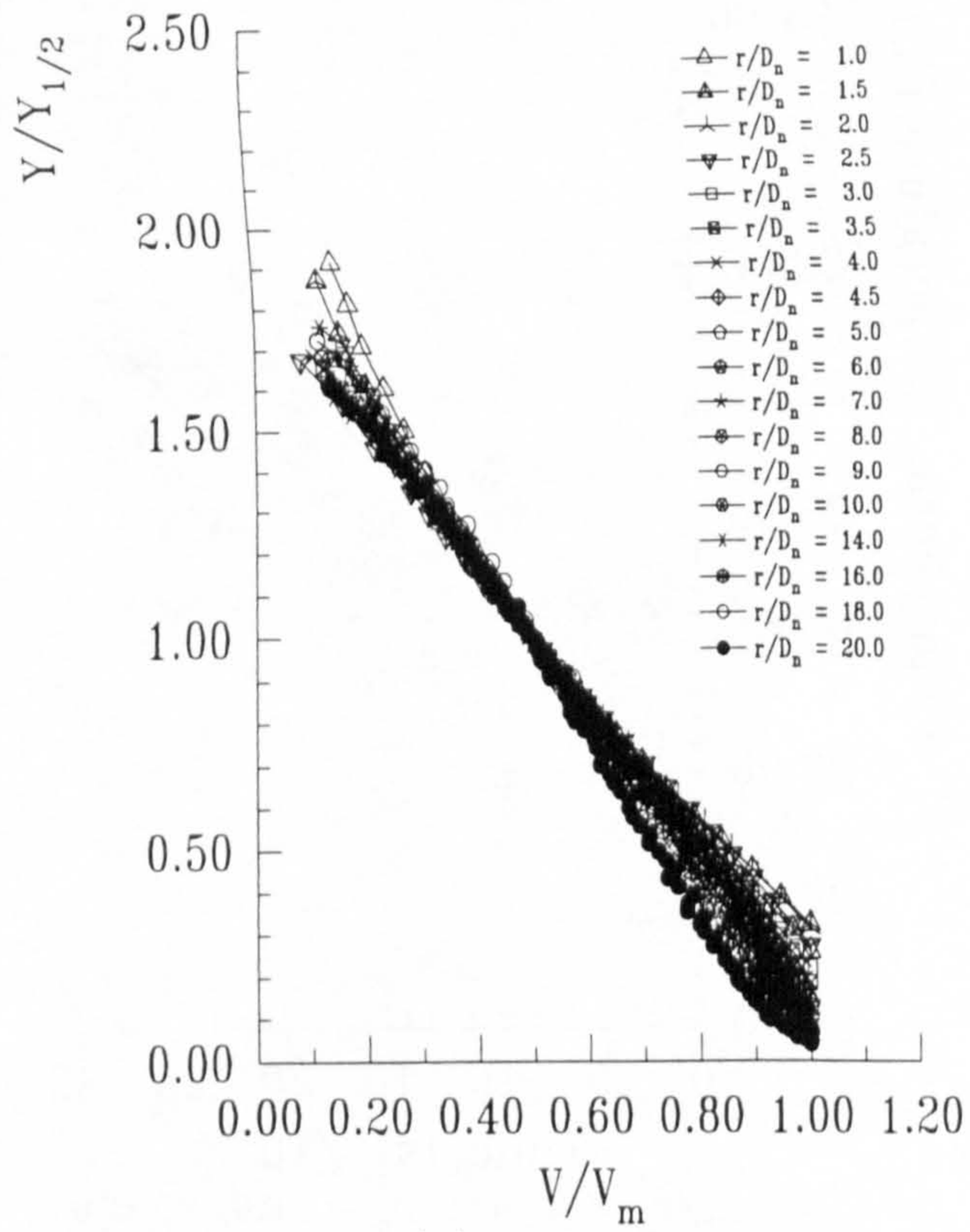

(a) : V_g = -10.0

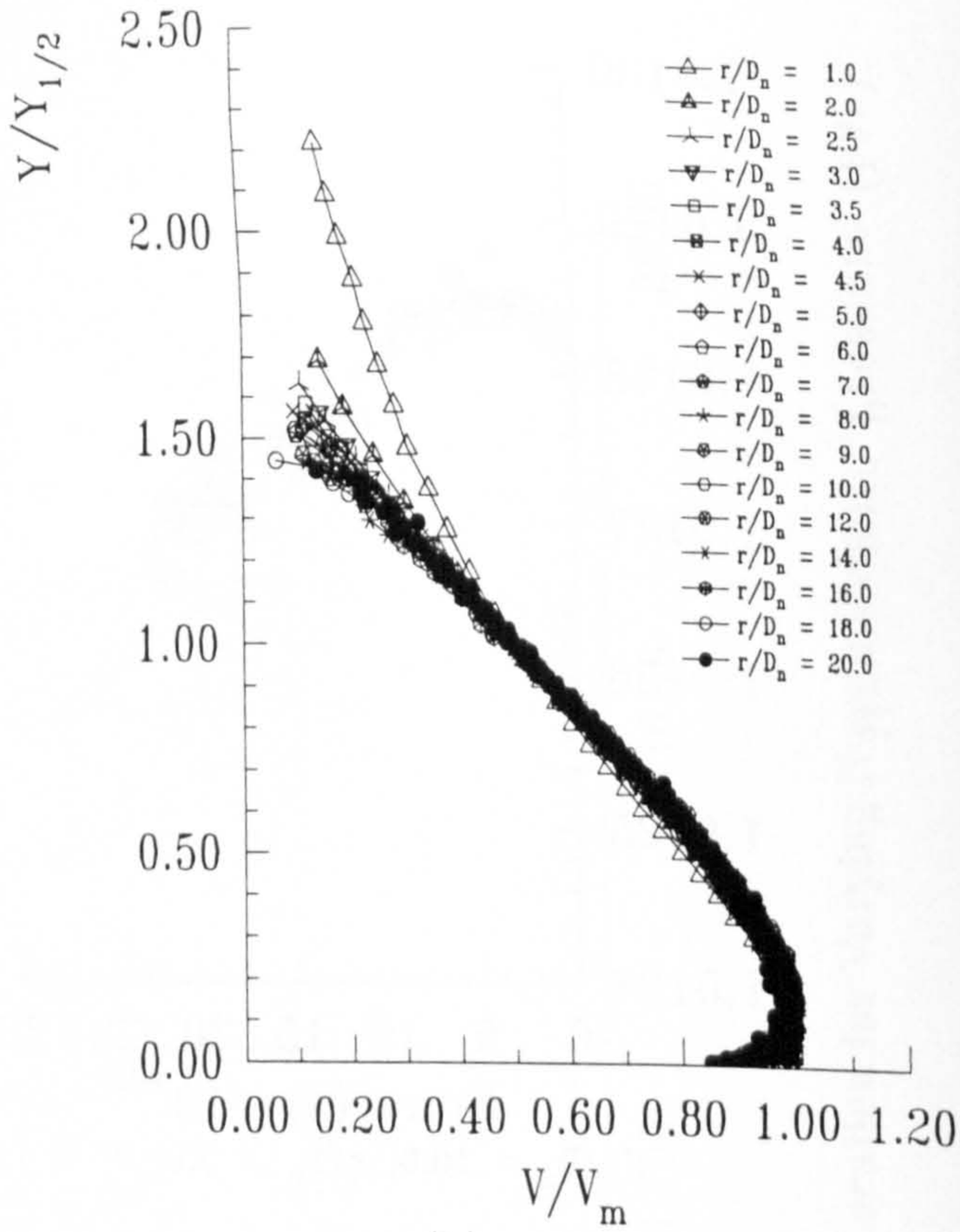

(b) : V_g = 0.0

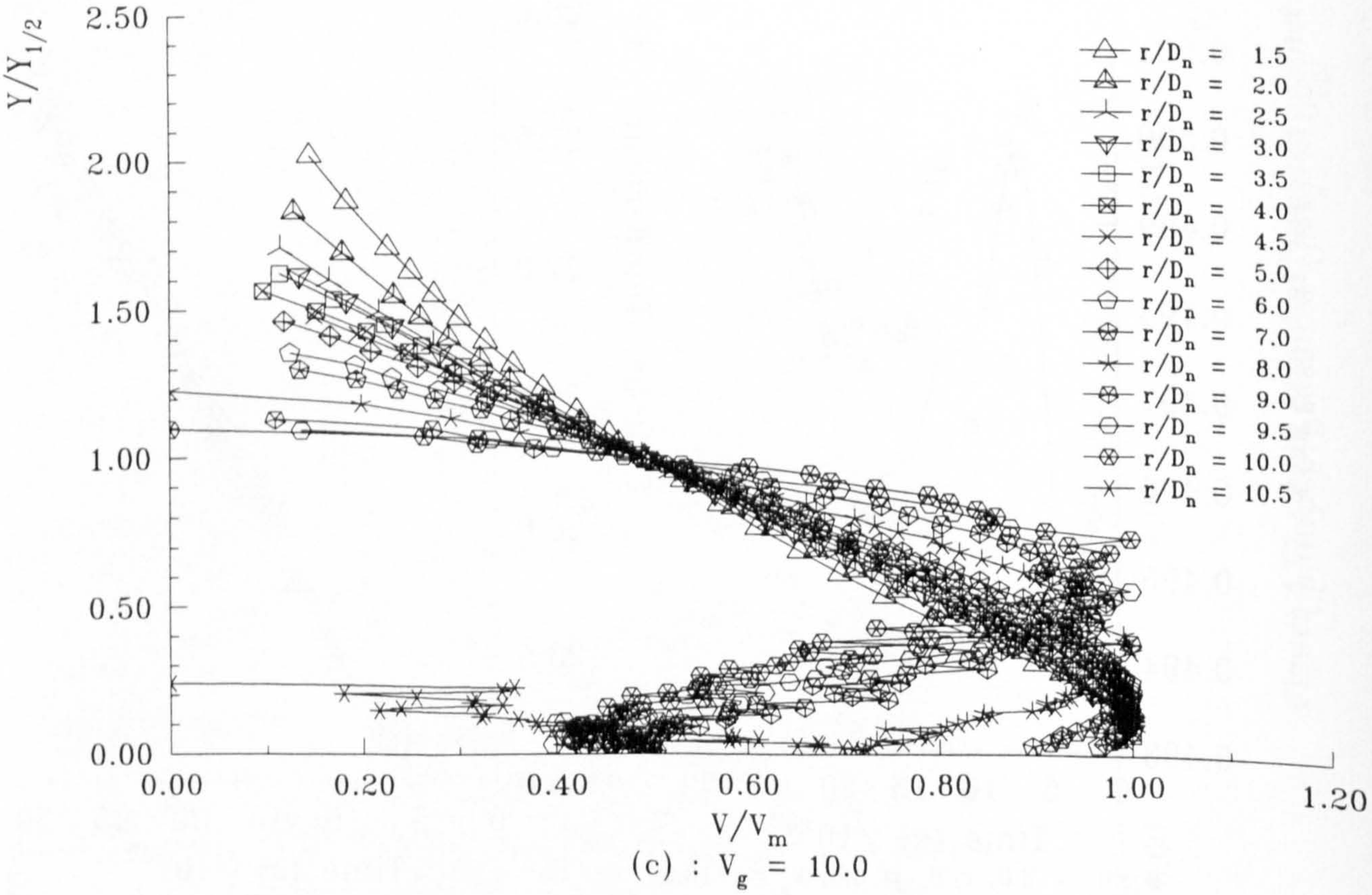

(c) : V_g = 10.0

Figure 4.63 : Non-dimensional Wall Jet profiles for differeing V_g, H_n/D_n = 4.0 & NPR = 1.05

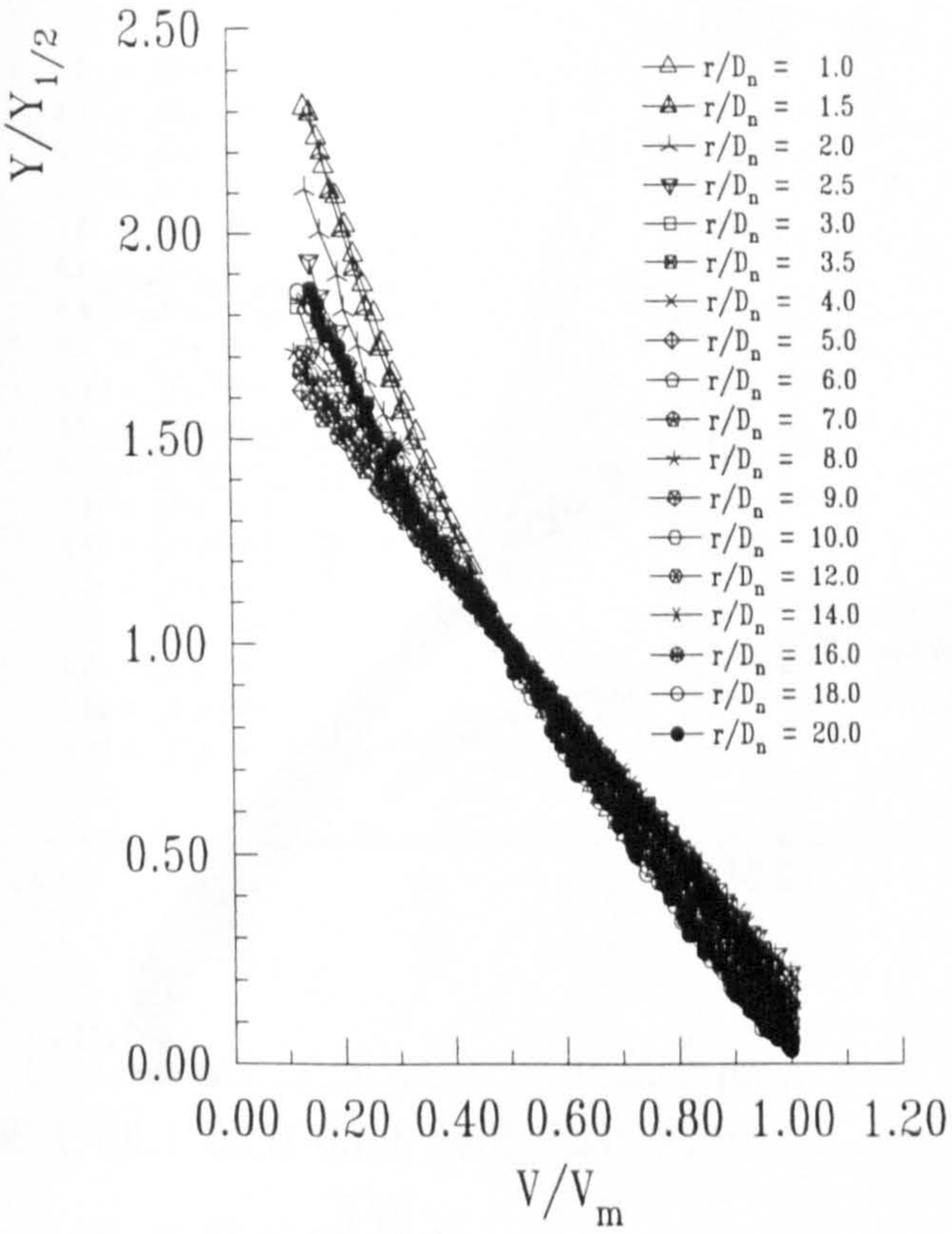

(a) : V_g = -10.0

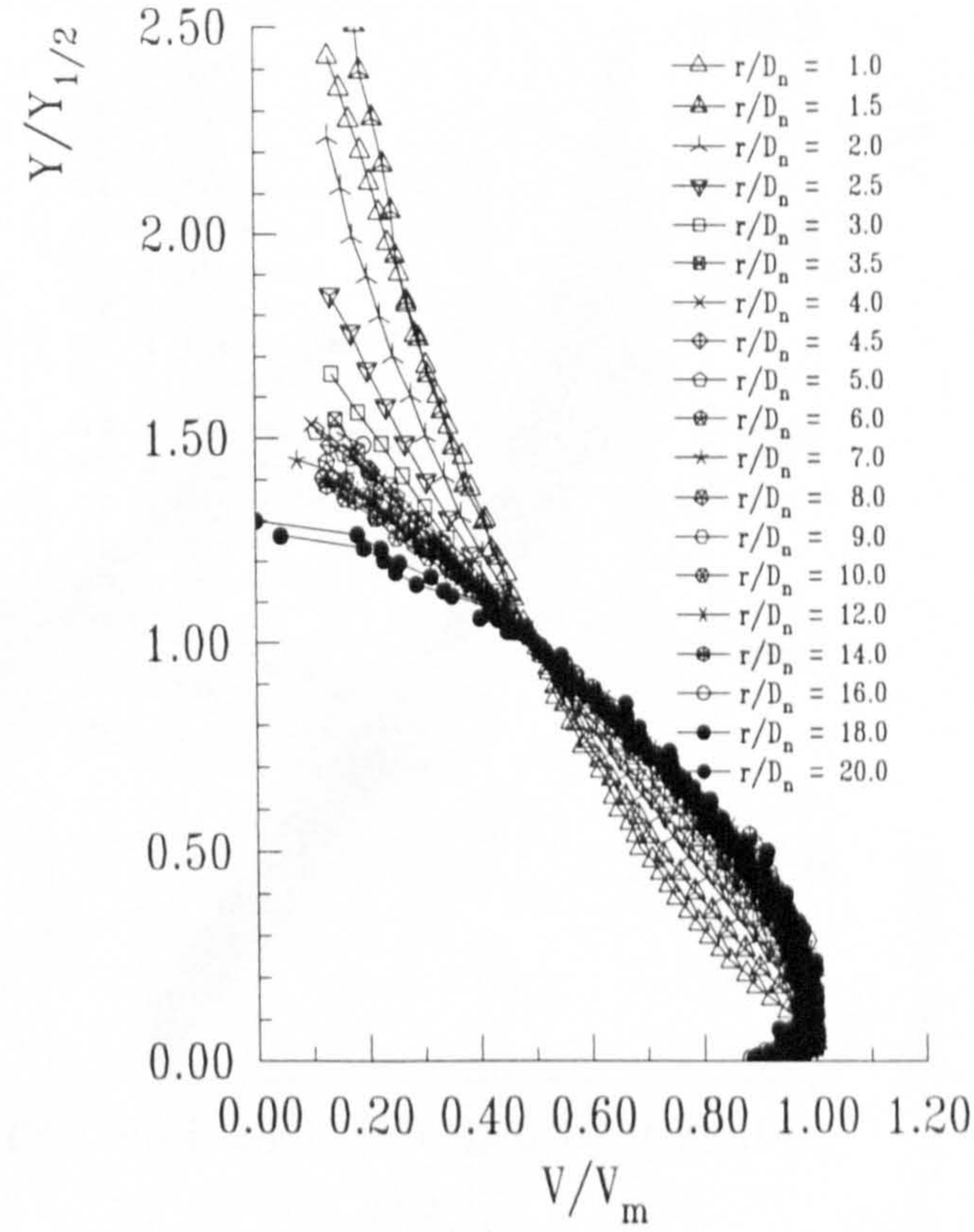

(b) : V_g = 0.0

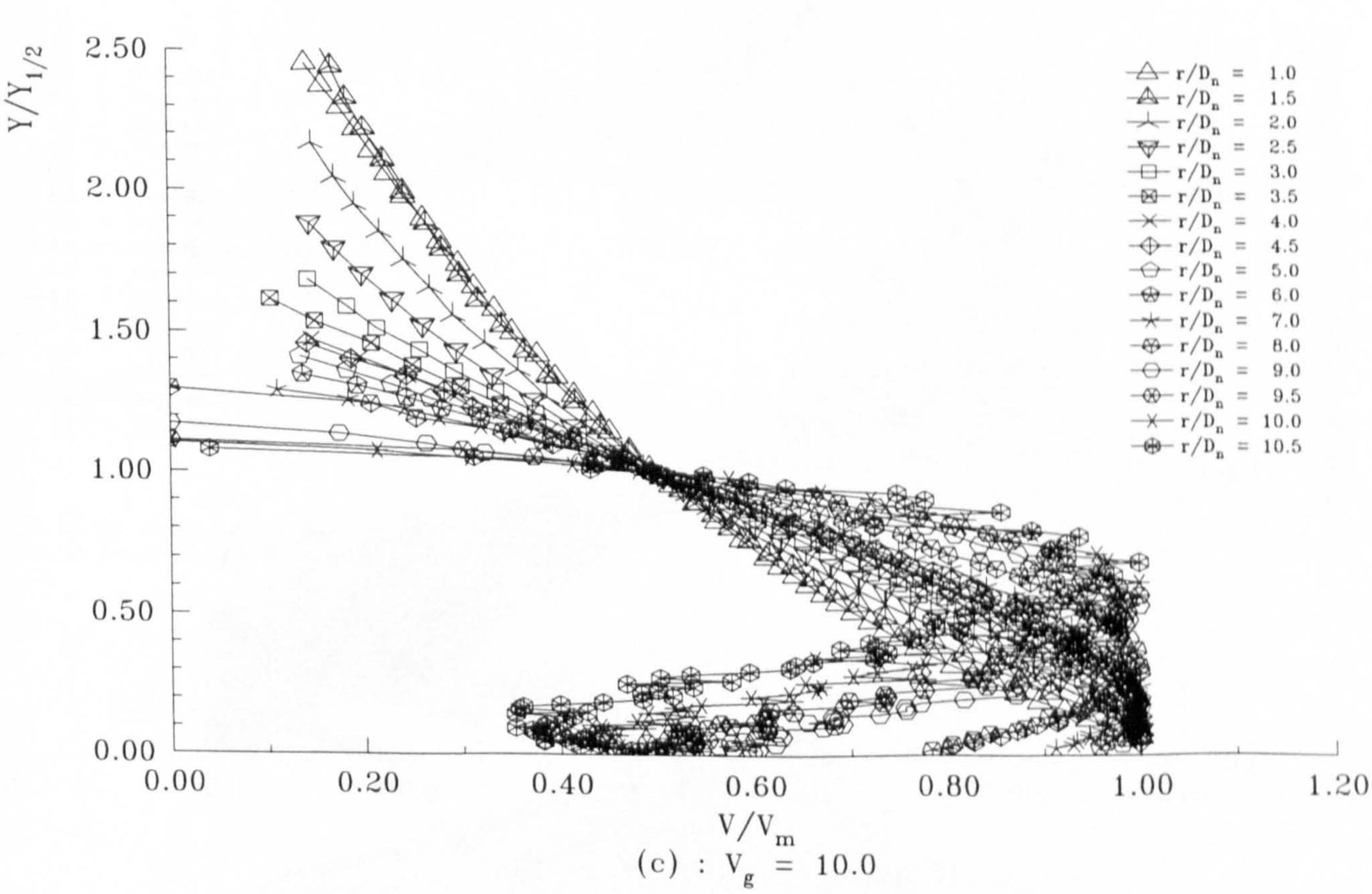

(c) : V_g = 10.0

Figure 4.64 : Non-dimensional Wall Jet Profiles for differing V_g, H_n/D_n = 8.0 & NPR = 1.05

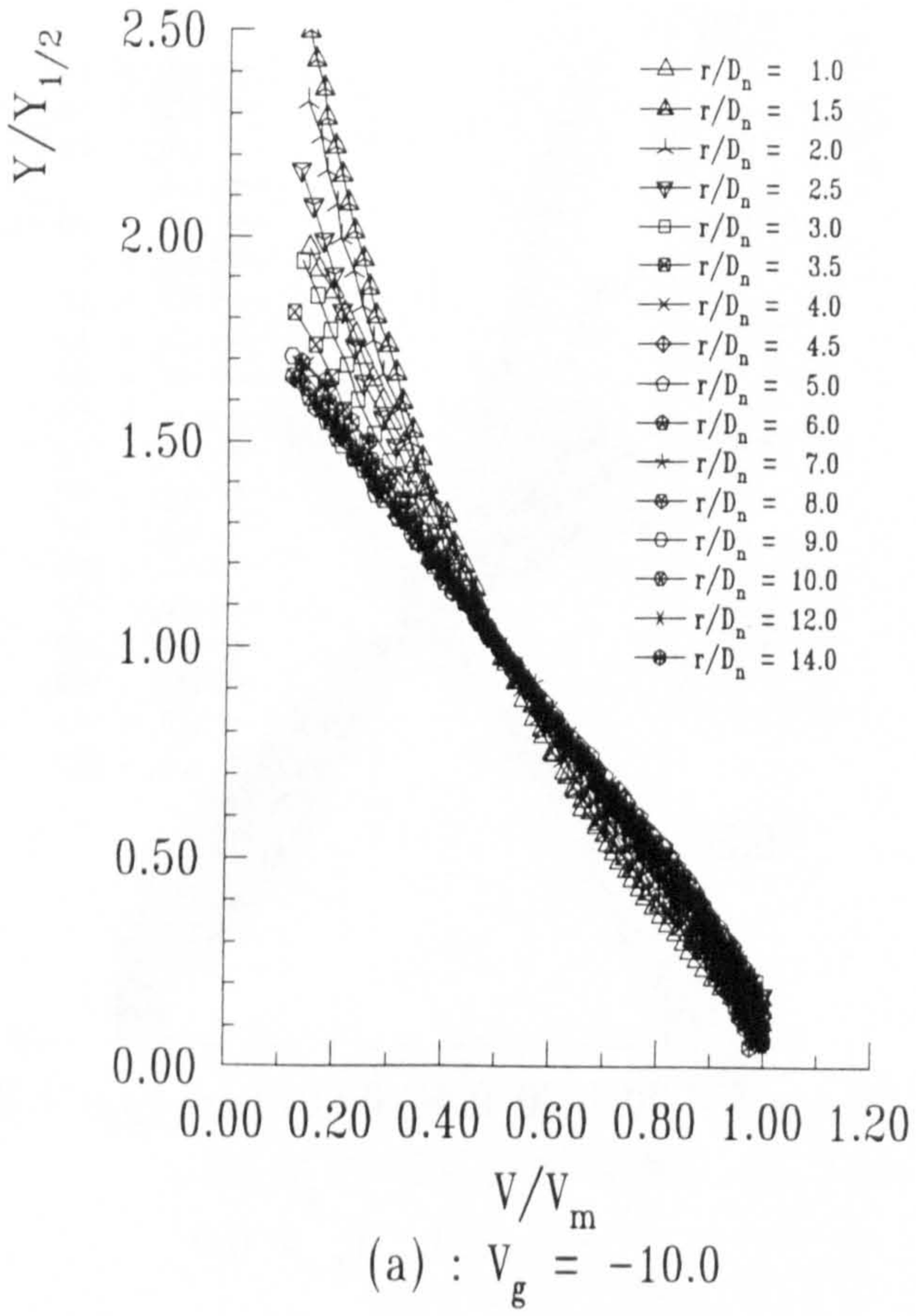

(a) : V_g = -10.0

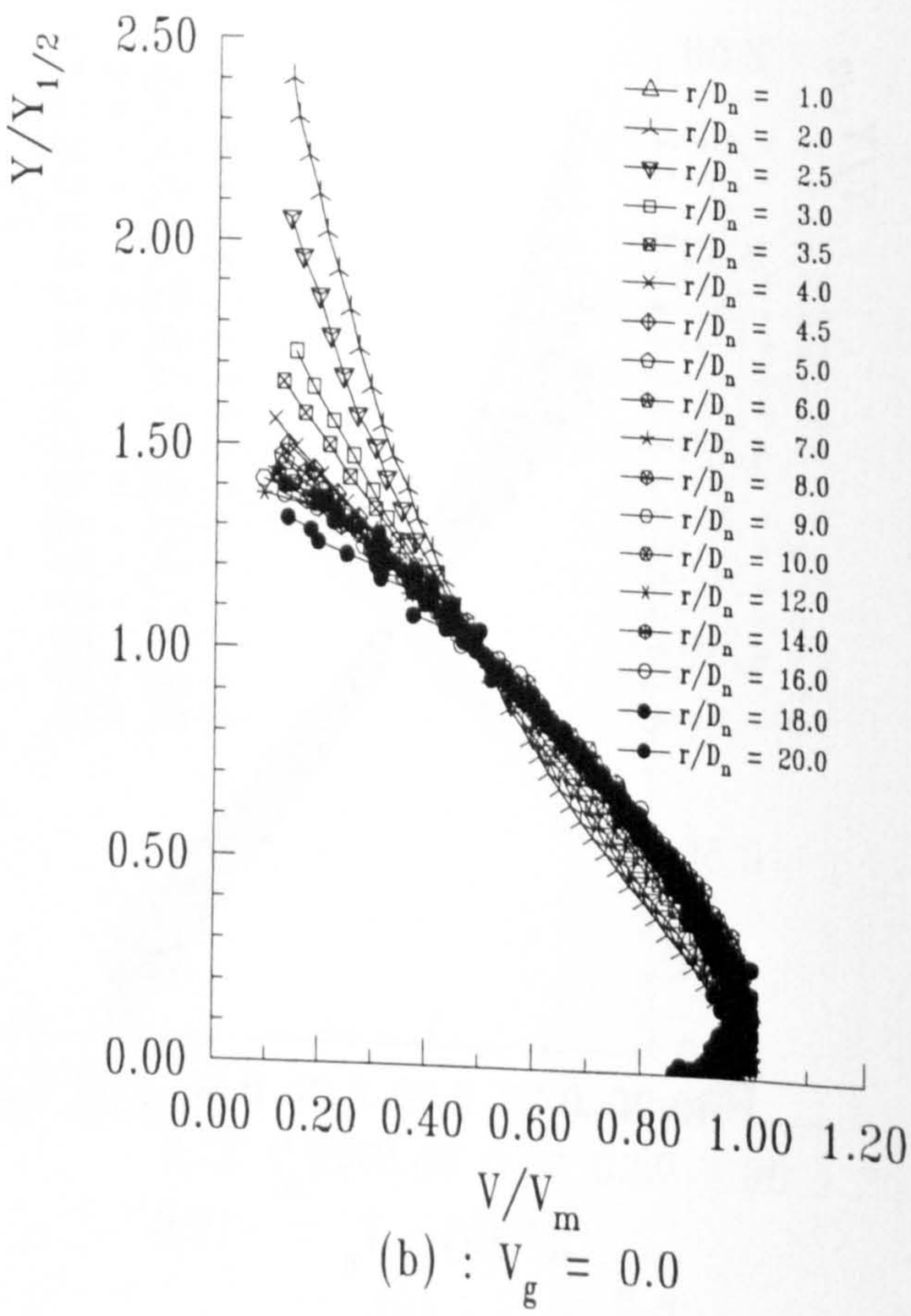

(b) : V_g = 0.0

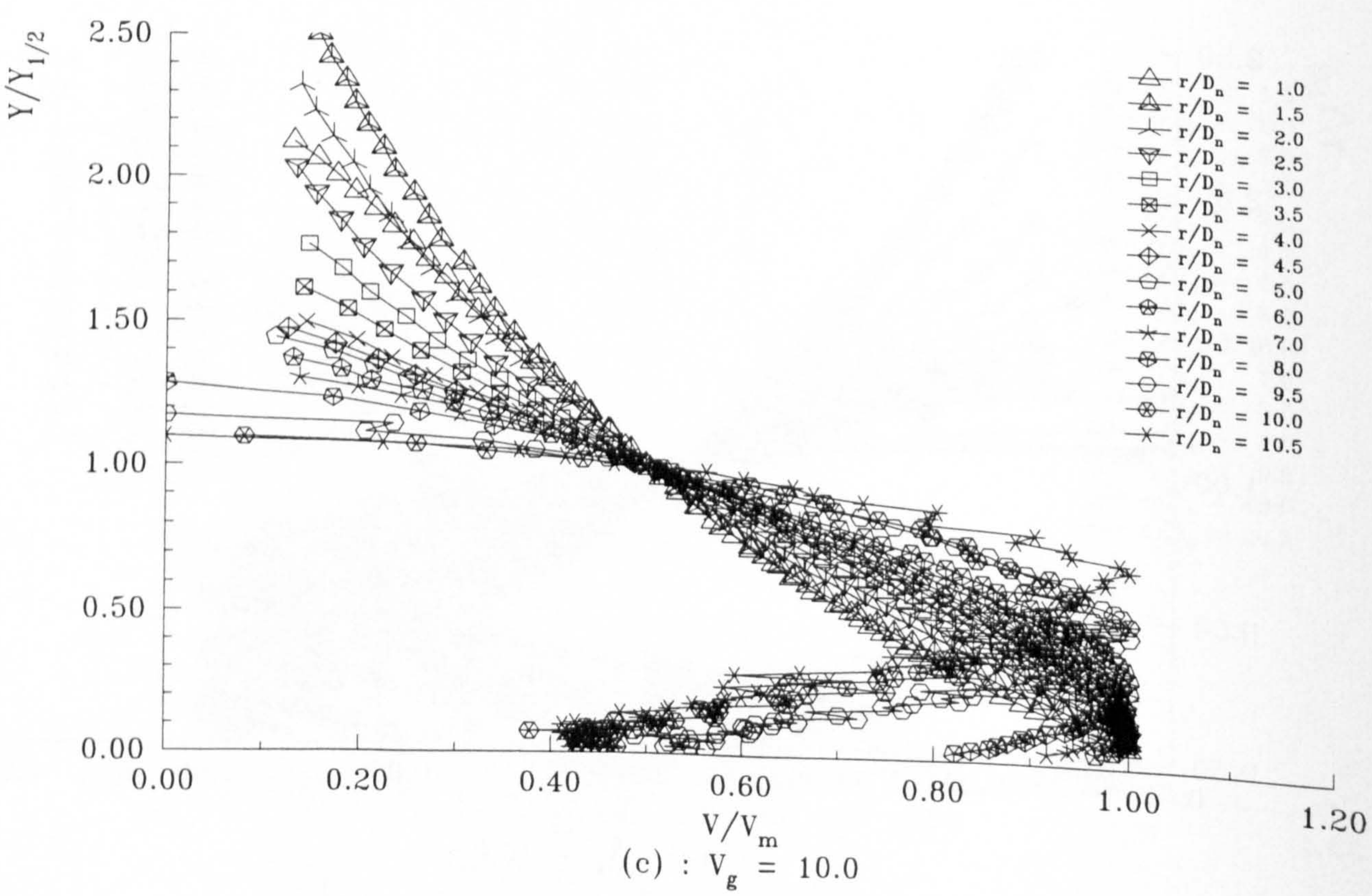

(c) : V_g = 10.0

Figure 4.65 : Non-dimensional Wall Jet Profiles for differing V_g, H_n/D_n = 10.0 & NPR = 1.05

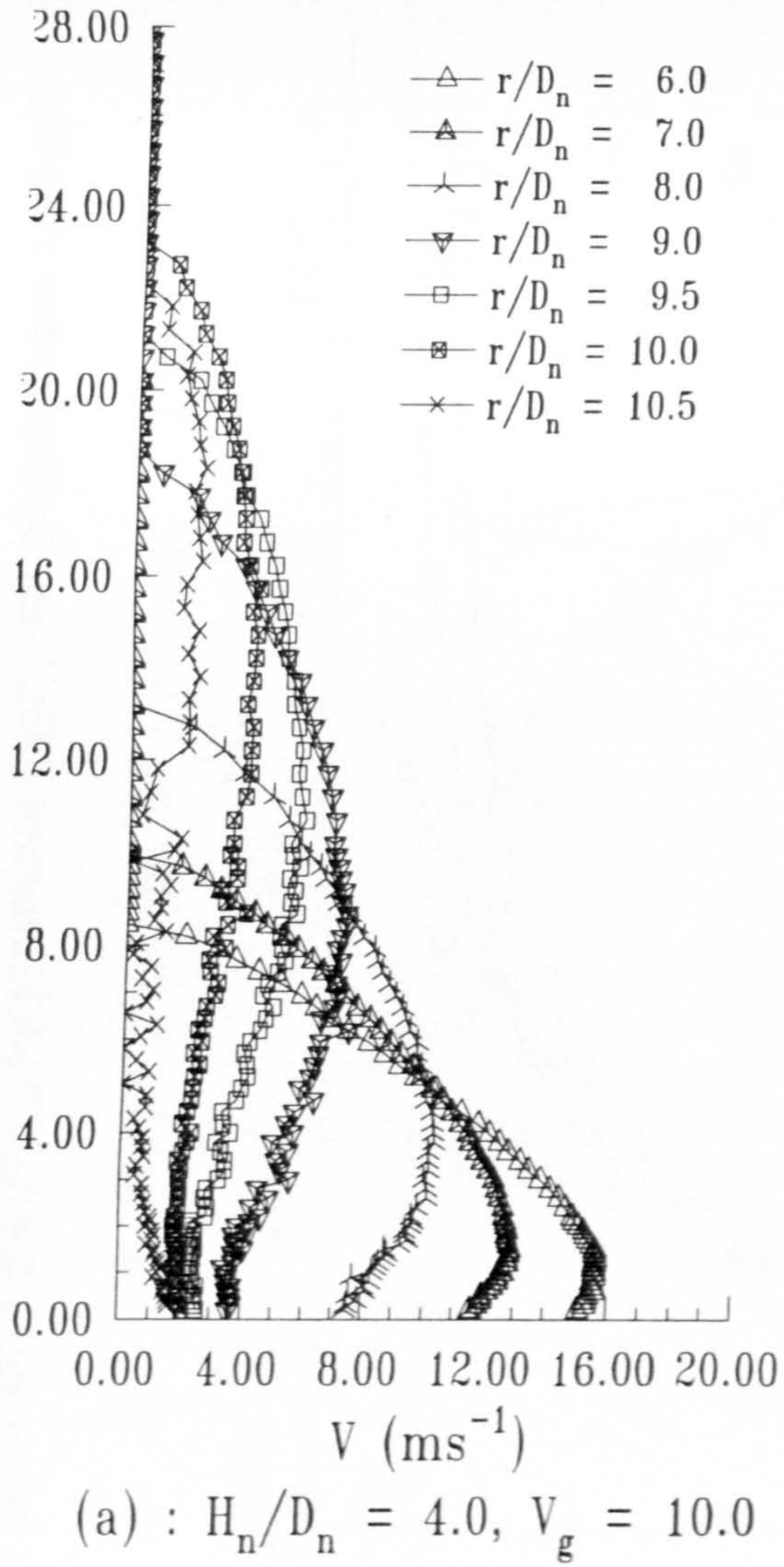

(a) : H_n/D_n = 4.0, V_g = 10.0

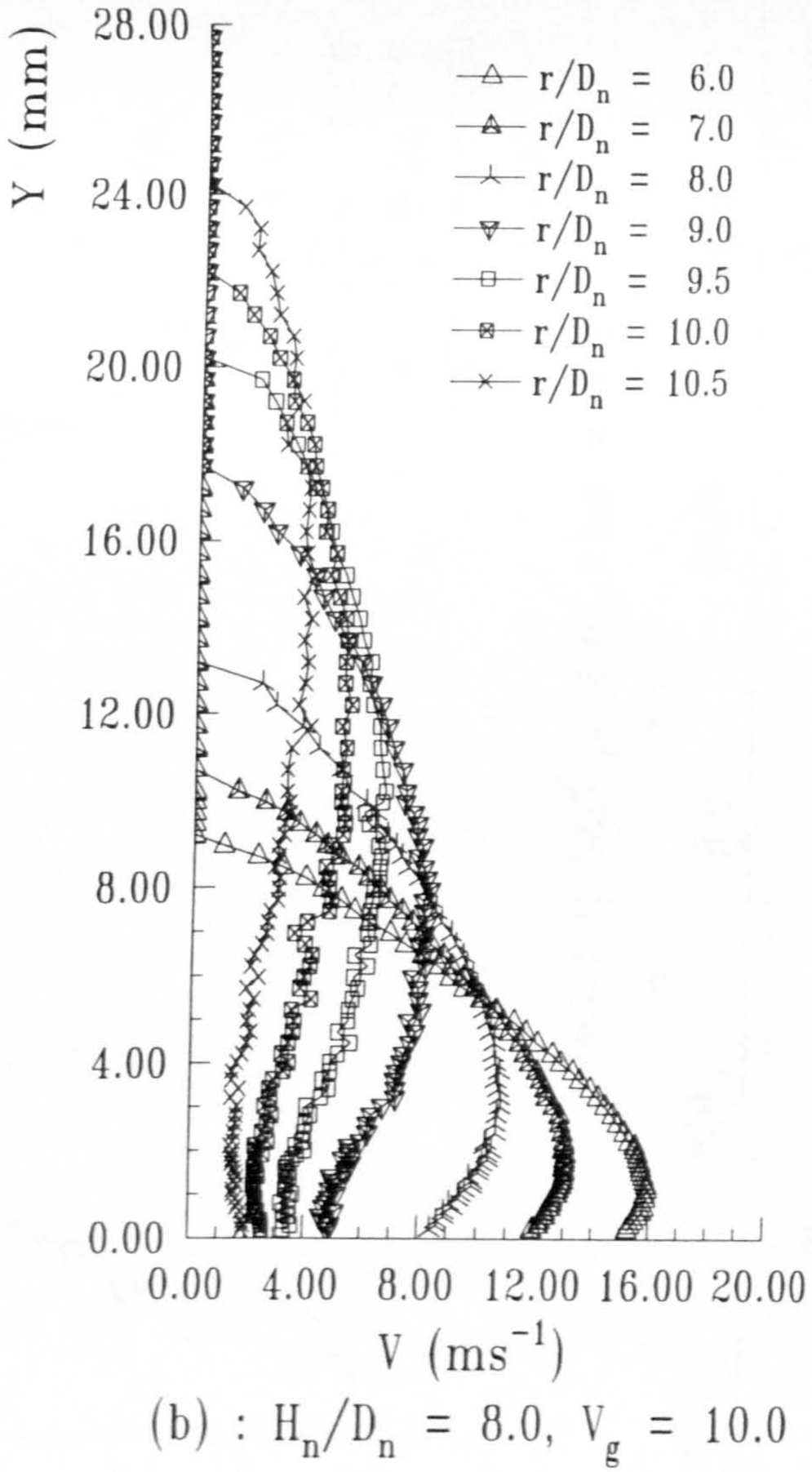

(b) : H_n/D_n = 8.0, V_g = 10.0

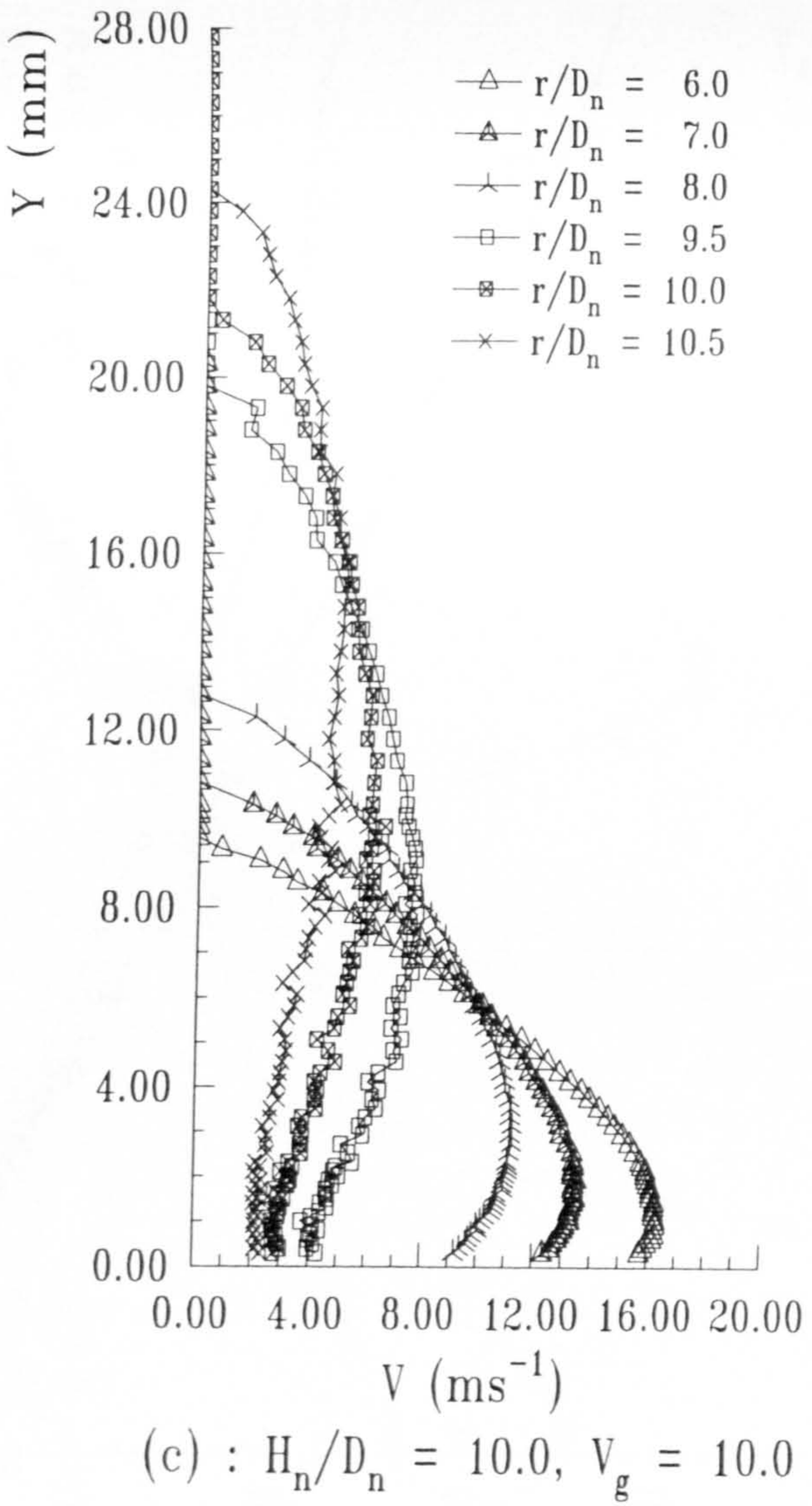

(c) : H_n/D_n = 10.0, V_g = 10.0

Figure 4.66 : Wall Jet Velocity Profiles showing Separation

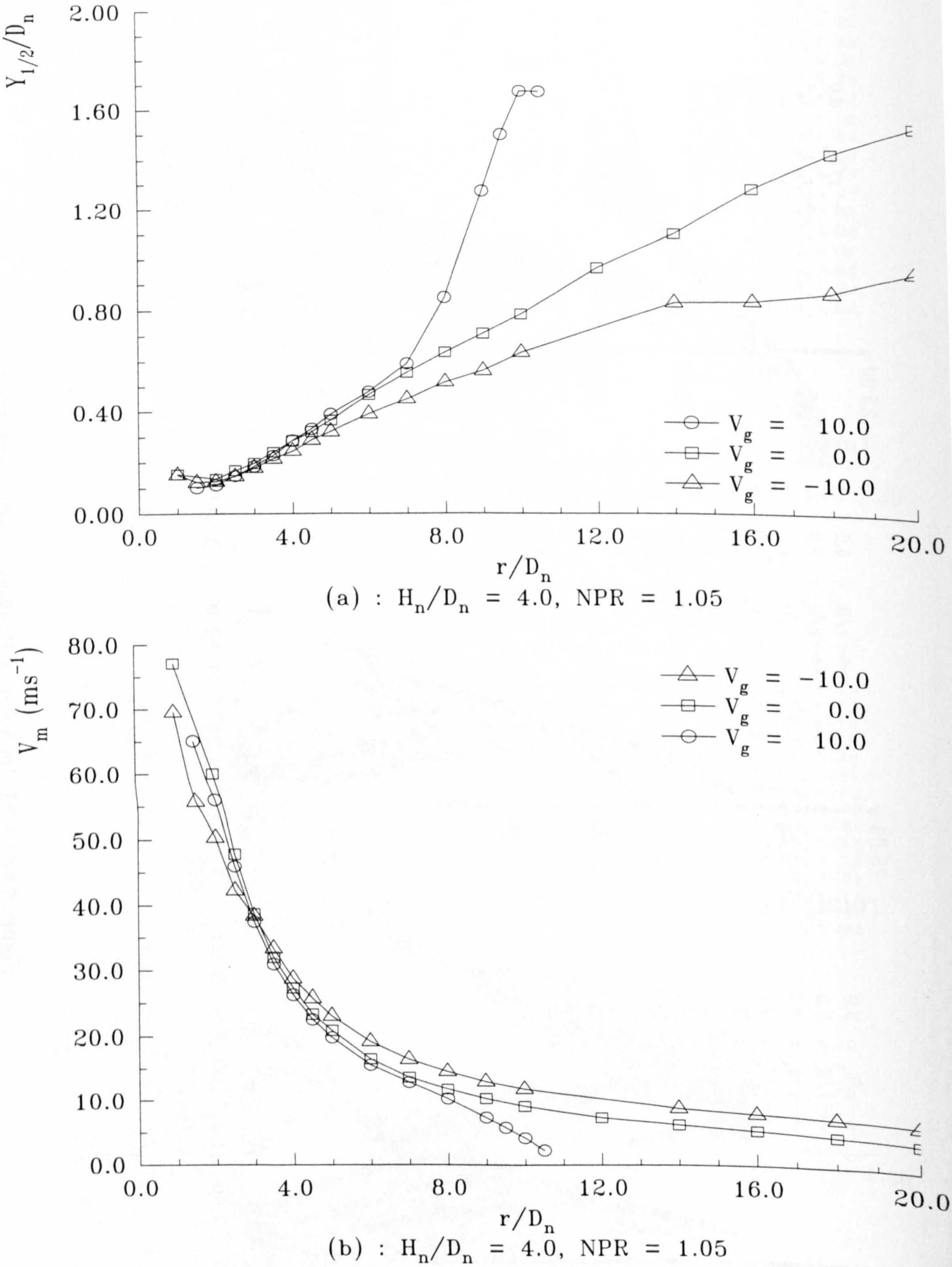

Figure 4.67 : Wall Jet Half Thickness and Peak Velocity Decay for Varying Surface Speeds

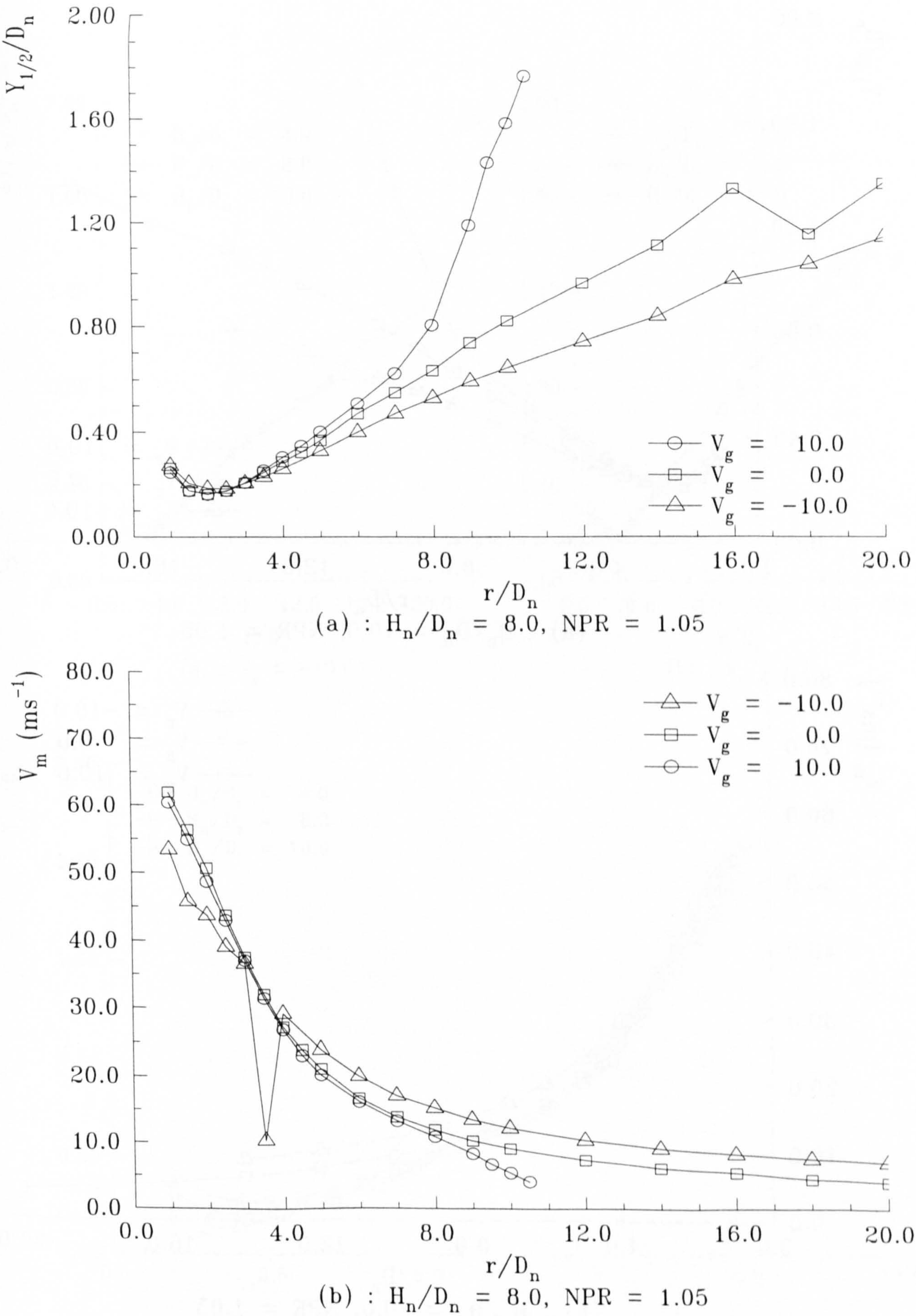

Figure 4.68 : Wall Jet Half Thickness and Peak Velocity Decay for Varying Surface Speeds

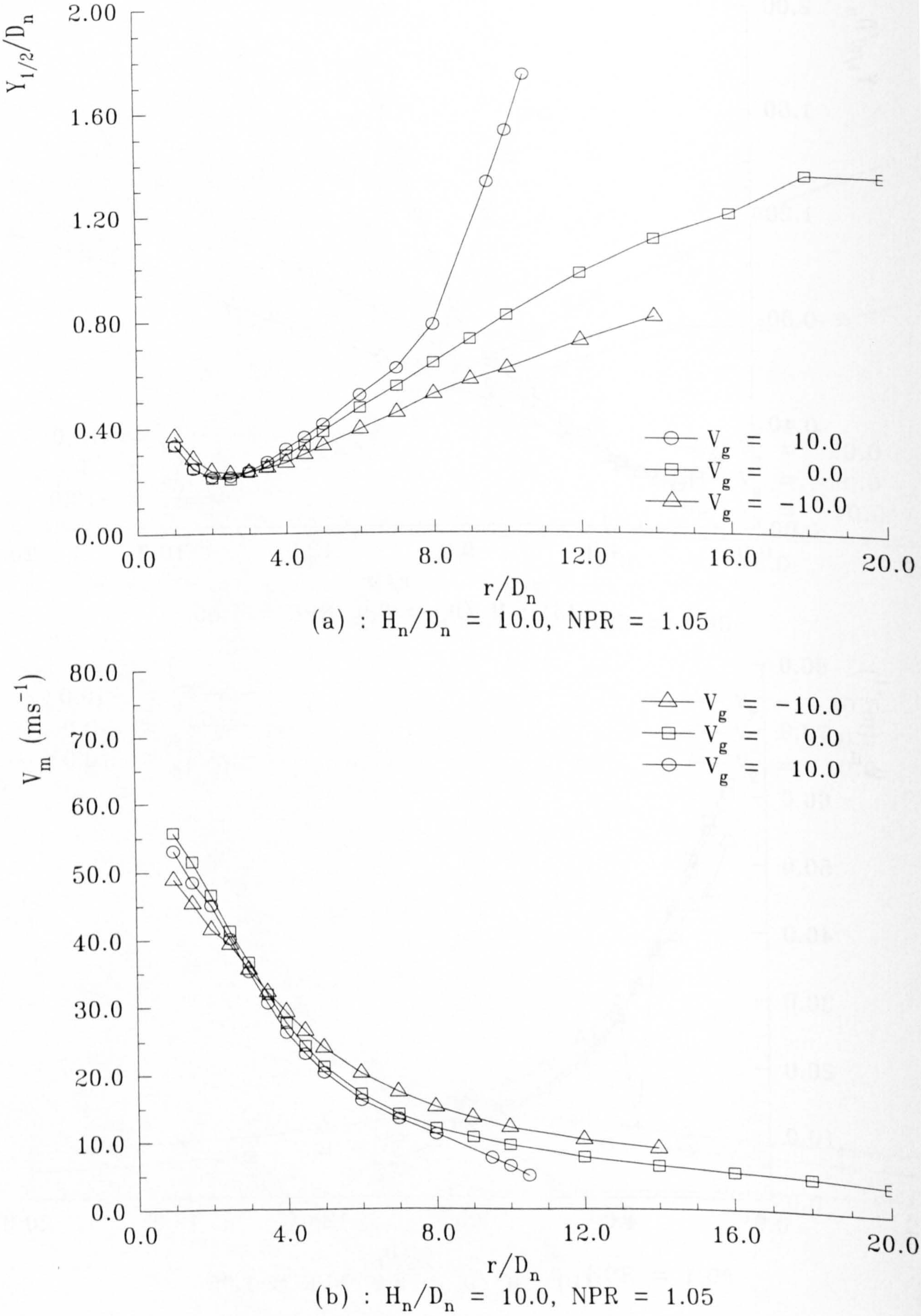

Figure 4.69 : Wall Jet Half Thickness and Peak Velocity Decay for Varying Surface Speeds

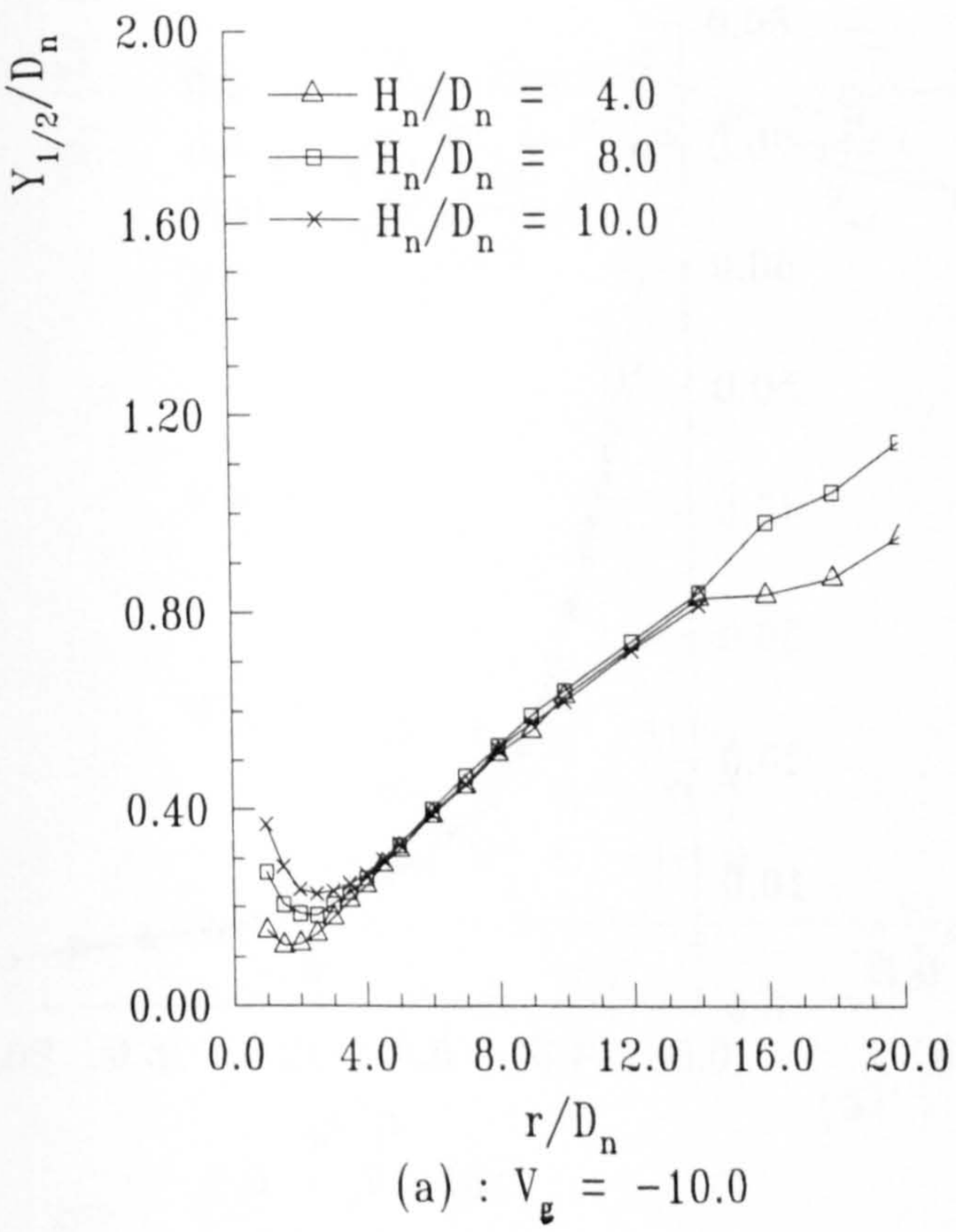

(a) : V_g = -10.0

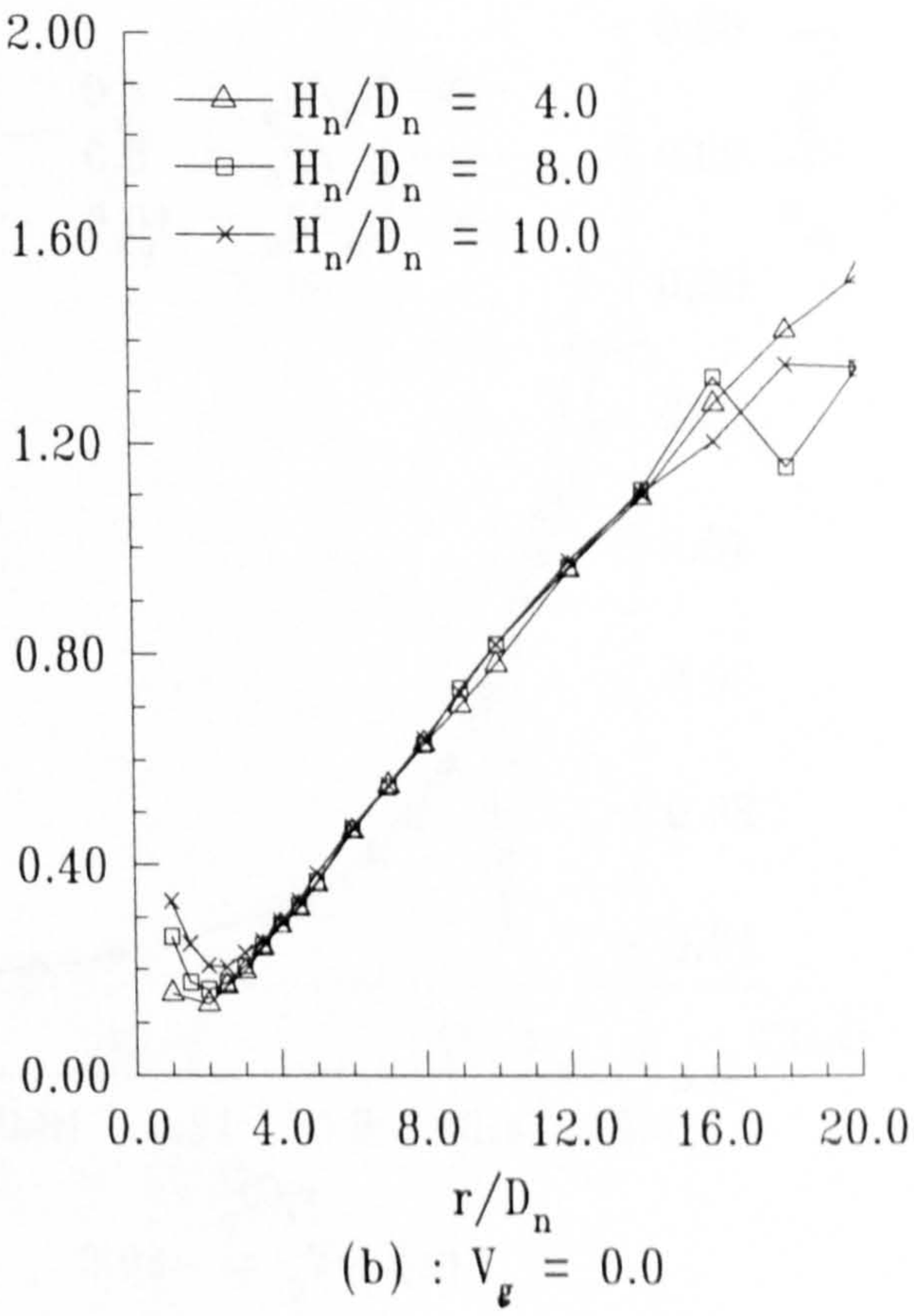

(b) : V_g = 0.0

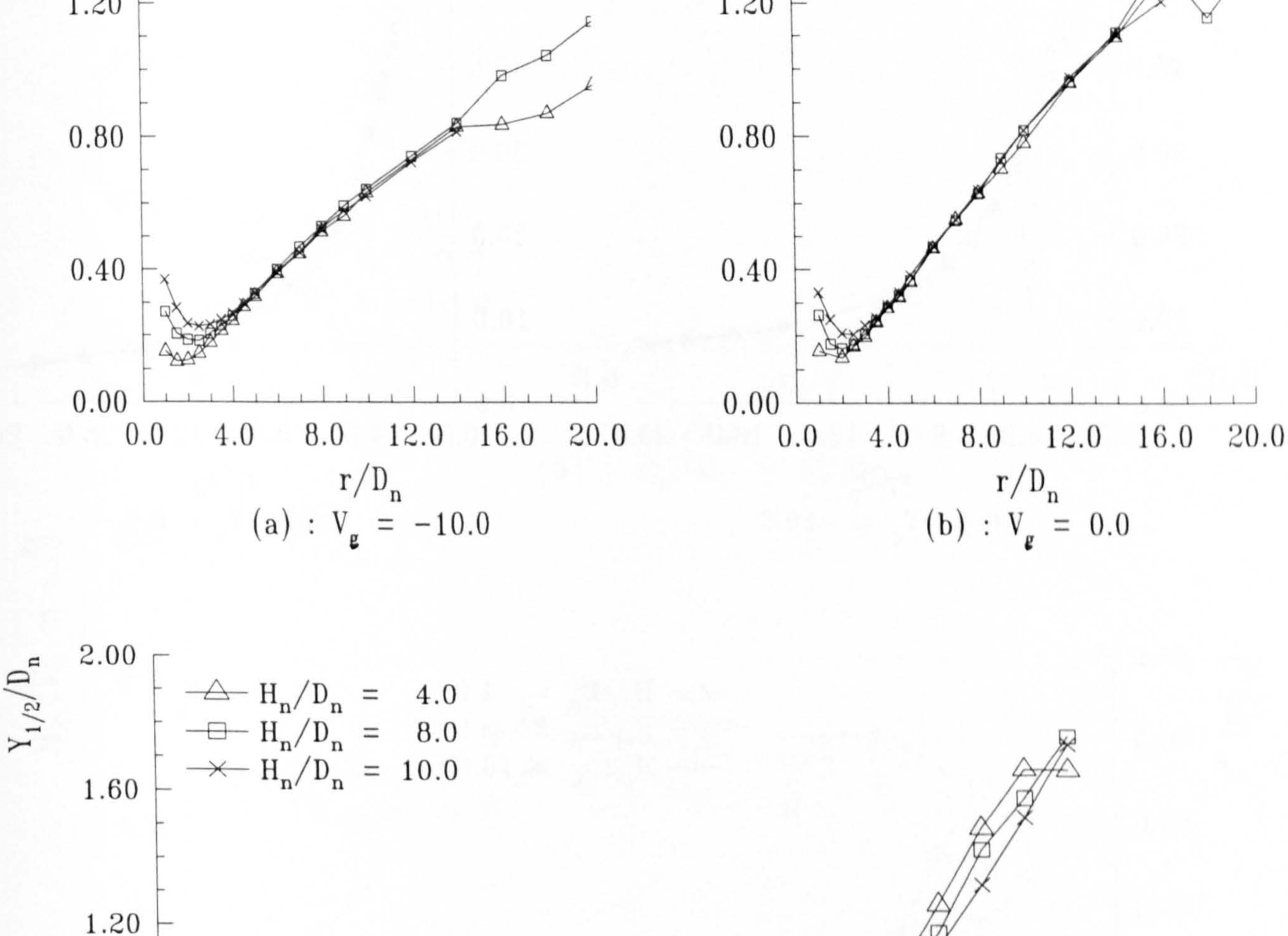

(c) : V_g = 10.0

Figure 4.70 : Wall Jet Half Thickness for Varying Nozzle Heights

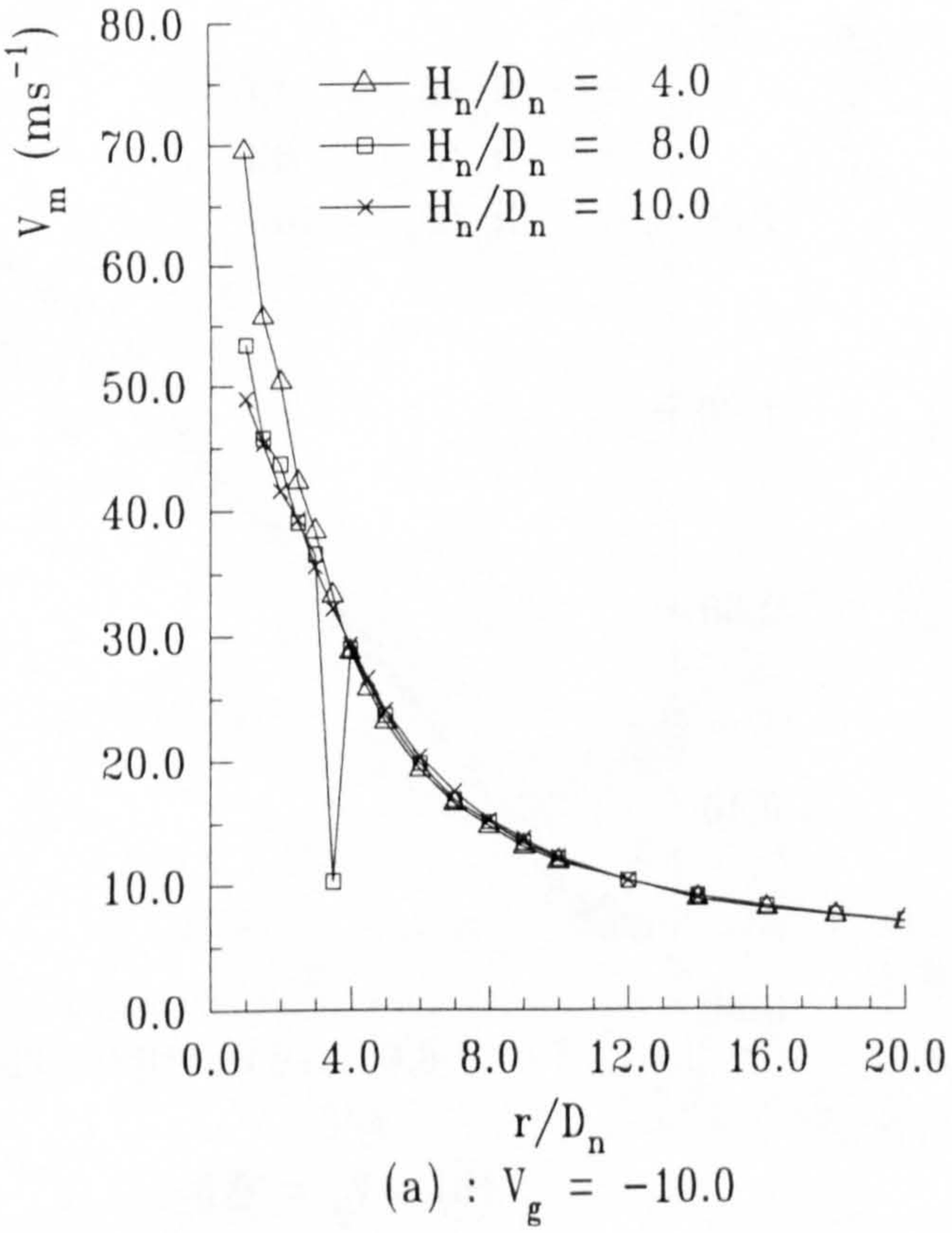

(a) : V_g = -10.0

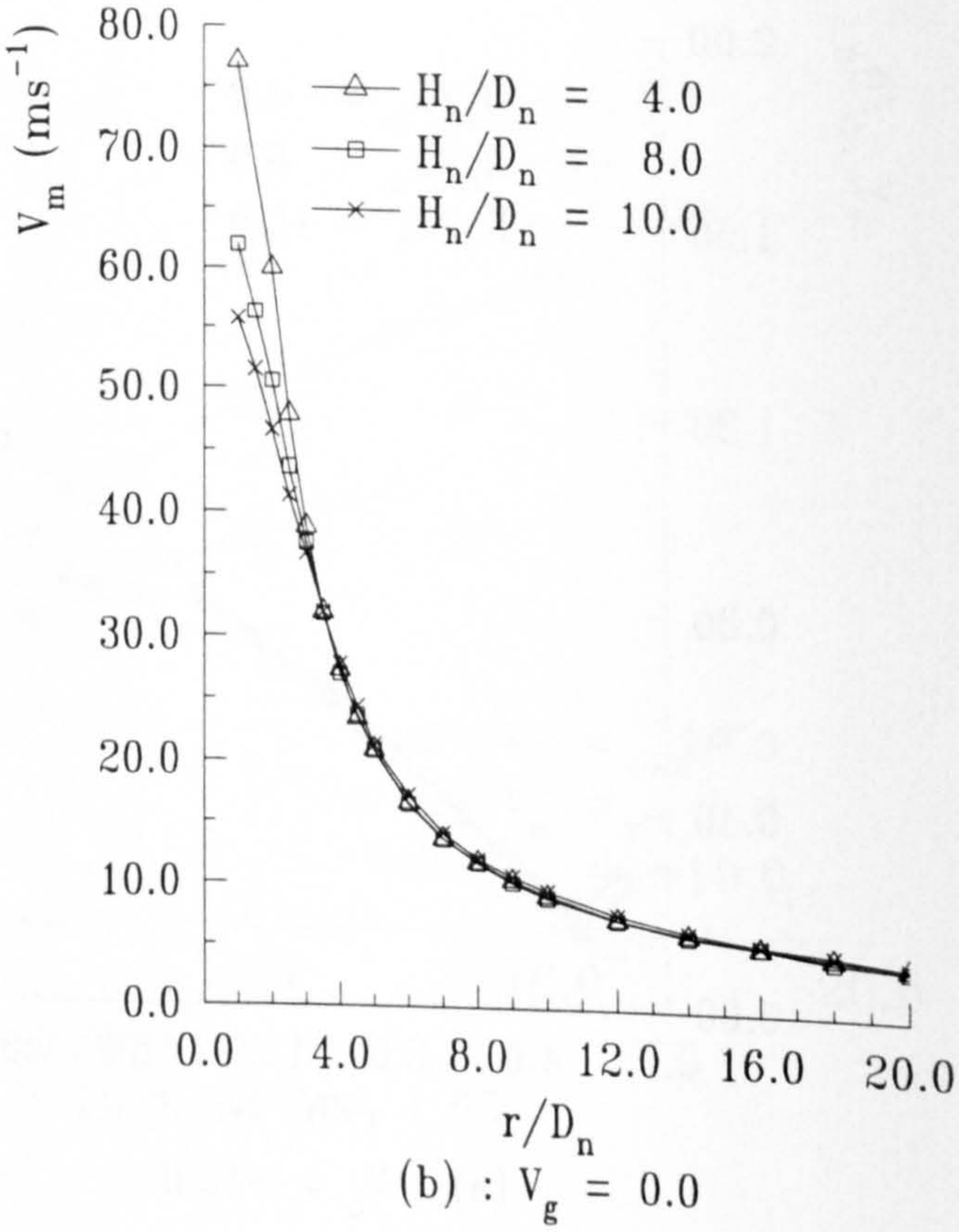

(b) : V_g = 0.0

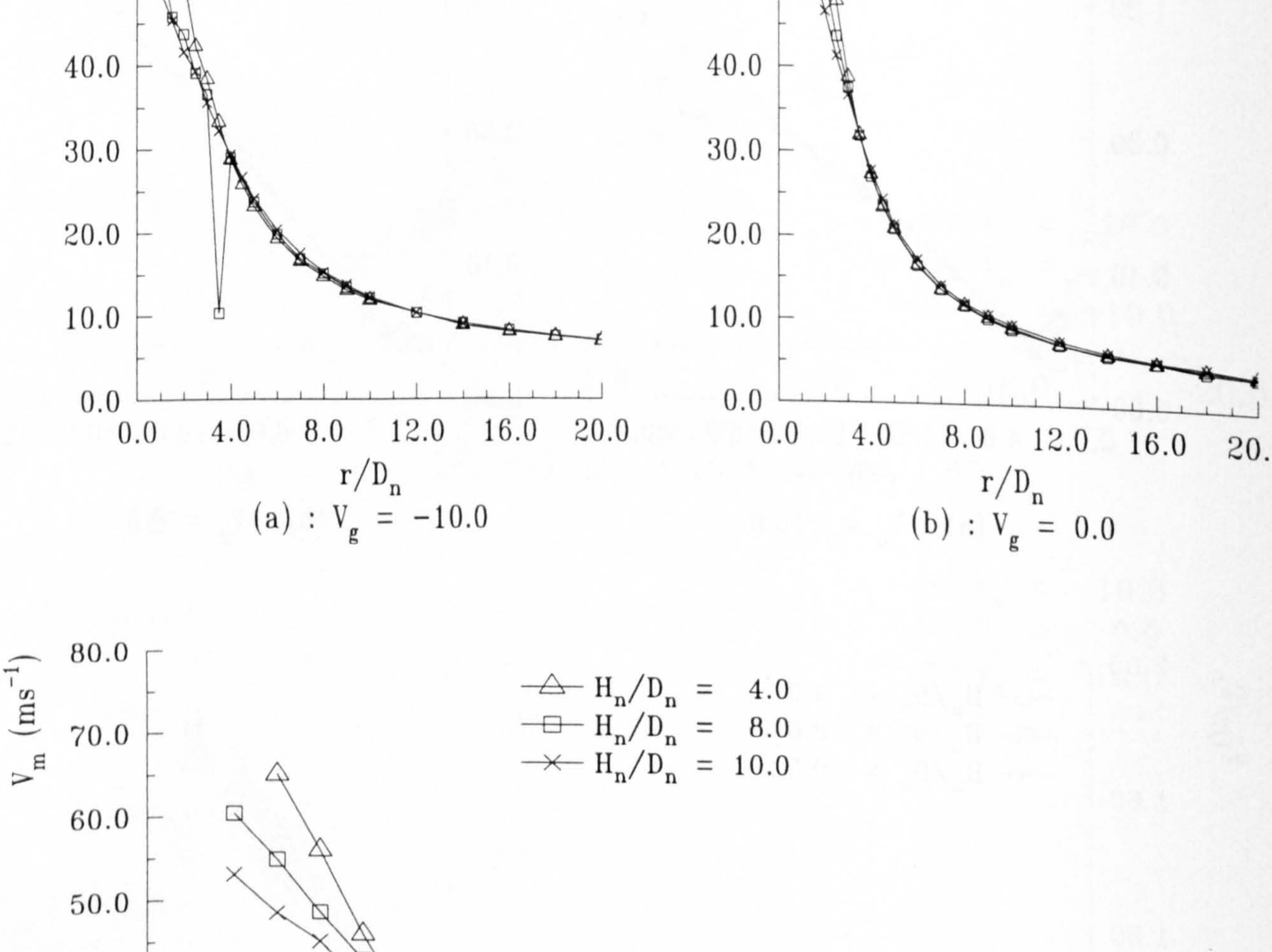

(c) : V_g = 10.0

Figure 4.71 : Wall Jet Peak Velocity Decay for Varying Nozzle Heights

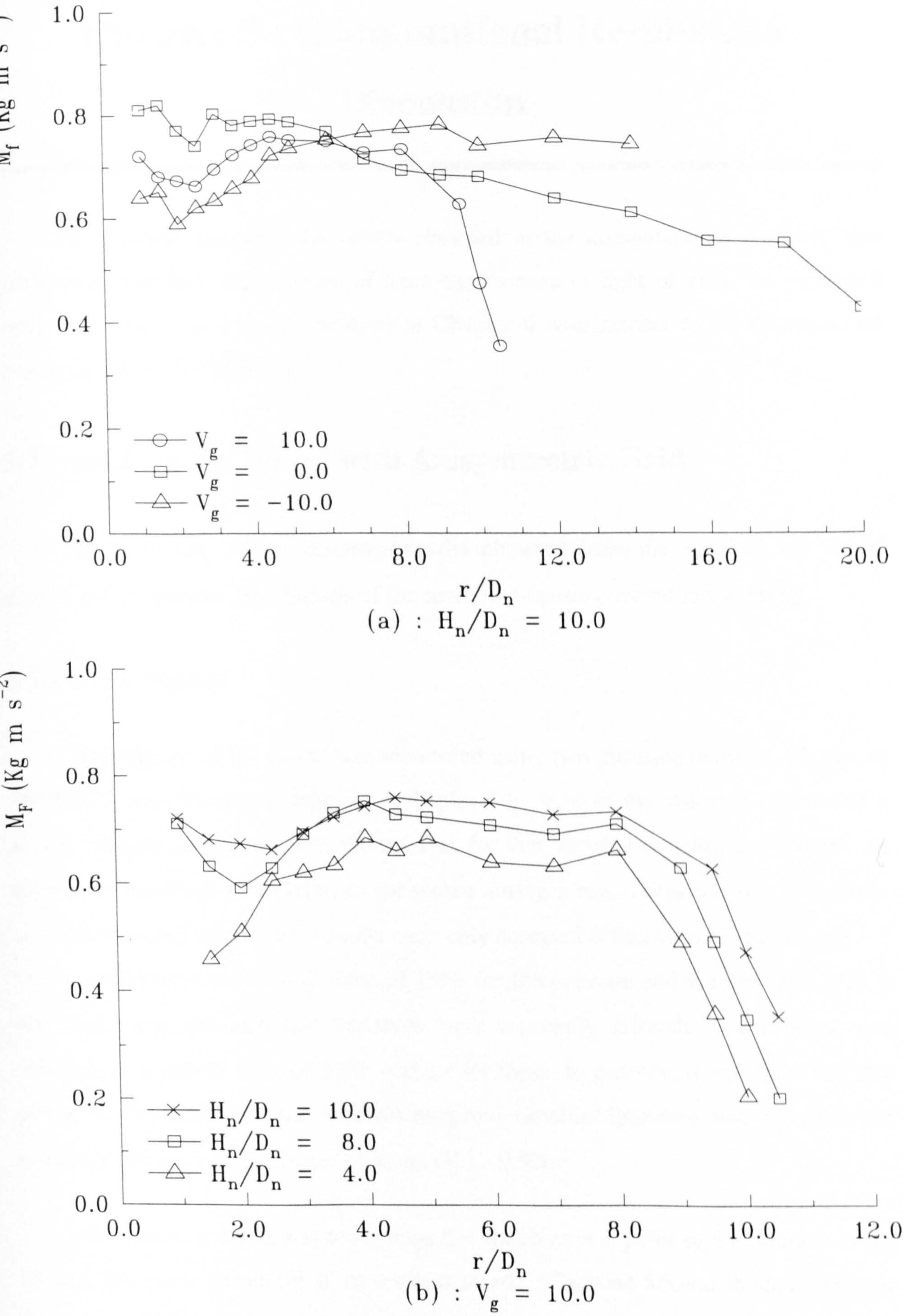

Figure 4.72 : Wall Jet Momentum Flux against Radial Location

BLANK IN ORIGINAL

Chapter 5 : Computational Results and Discussion

This chapter describes the results obtained in the computational phase of this project together with a discussion of their significance in light of previous published work. A further discussion is included in Chapter 6 with respect to the experimental results contained in Chapter 4.

5.1 Standard k-ε Model with Axisymmetric Grid

The following section describes results obtained from the standard k-ε model using a polar-cartesian grid. Details of the model set-up are covered in Chapter 3.

5.1.1 Convergence

Convergence of the model was monitored using two differing methods. Firstly, as PHOENICS runs through a solution, it displays the sum of the absolute residual of a solved variable normalised with the net flux for that variable entering the domain. As these were continually displayed to the screen during a run, it was possible to monitor how well a model converged. Results were only accepted if this normalised residual fell below a predetermined cut-off value of 1.0% for the pressure and velocity variables. It was found that the turbulent variables were especially difficult to get below this criterion, so a cut-off level of 2.0% was set for these. In practice, it was the k variable which was the limiting factor, the remaining four variables (pressure, two velocities and ε) usually finishing with an error of around 0.1 - 0.5%.

The second method was to monitor the variables at a point in the domain during the run. The point chosen for all runs was at an r/D_n of around 5.5 and about 16.5mm up from the wall. Figure 5.1 shows how the variables quickly reach their final values, this normally happening at around 1000 sweeps. The runs were normally continued for a

further 2000 sweeps (total of 3000 sweeps) to enable the first convergence criterion to be met.

5.1.2 Grid Development

As basic grid independence tests had been performed by Bray (1992), no further independence tests were conducted. The Y^+ value along the impingement wall was investigated to confirm that it fell within the required range of $30.0 < Y^+ < 160.0$ for operation of the logarithmic-law-of-the-wall function (see Appendix B for further details). Y^+ values were printed in the PHOENICS result file at the completion of a run by the addition of YPLS=TRUE in the Q1 input file.

Figure 5.2 shows how Y^+ varies with radial position starting at the impingement point for various grids. The grid of Bray (1992) is at a $H_n/D_n = 10.0$ and NPR = 1.05 and here the Y^+ value is zero due to the stagnation point underneath the jet, but quickly rises as the flow accelerates away because of the stagnation point pressure gradient. The value peaks at around 1.5 - 2.5 D_n due to the contribution made to Y^+ by the high shear stress values in this region. Y^+ then falls as the wall jet develops, dropping below the $Y^+ = 30.0$ minimum at $r/D_n \approx 5.0$. As this meant a large portion of the flow domain was calculated incorrectly, a number of grids were tried (Grid 1 and Grid 2, Table 5.1) to try and optimise the thickness of the lowest cell to achieve Y^+ in the required region for the largest portion of the grid possible. Increasing the thickness of the first cell next to the wall increased the value of Y^+ in the impingement region, but seemed to have little effect in the developed flow domain. At the lower height of $H_n/D_n = 2.0$ (Grid 2, Case 2), the trend is the same, the peak in Y^+ being higher due to the greater shear stress, but the lower limit being reached at around $r/D_n = 5.0$.

Grid 2 was chosen because although the lower limit was only reached at $r/D_n = 12.5$, any further increase in the first cell thickness would lead to an excessively high maximum Y^+ value in the impingement region at lower nozzle heights as shown in Figure 5.2. This shows the difficulties of using a grid with a fixed height first cell (as with Polar-Cartesian and Cartesian) grid with this form of flow. It is extremely hard to

design the grid so that the Y^+ is beneath the upper limit in the high shear stress region but remains above the lower limit in the rest of the developing flow. Ideally, the height of the first cell needs to change as r/D_n increases, so altering Y^+. This could be performed in one of two ways using the presently available versions of PHOENICS. Firstly, a Body Fitted Co-ordinate (BFC) grid could be developed in which the first cell thickness increases with r/D_n. This, unfortunately, would lead to alternative problems of grid dependence due to the distortion of the cells. PHOENICS version 2.1 and higher allows for multi-block griding where a block of finer cells can be inserted into a domain. It did not prove possible, during this project, to implement this function successfully into a model, but the possibilities it presents means it deserves further study.

5.1.3 Flow Domain

Figure 5.3 shows a typical vector plot obtained from PHOENICS. It clearly shows the decay and spread of the free jet, the turning of the flow in the impingement region, and the consequent development of the wall jet.

5.1.3.1 Free Jet

The development of the free jet is shown in greater detail in Figure 5.4, a plot of U mean velocity normalised with local maximum against radial distance, r, normalised with the jet's half width. This shows the decay of the jet's top hat profile close to the nozzle exit, the profile becoming nearly self-similar at around 5.0 - 6.0 D_n below the nozzle exit. This is similar to the experimental results obtained in Phase One (see section 4.2.4).

Figure 5.5 shows selected non-dimensional free jet profiles plotted against their corresponding experimental profile taken during Phase One. As can be seen, the predicted free jet shapes match the experimental data well, the jet being slightly too wide in the lower half of the plot, most likely due to an over-prediction of entrainment of ambient fluid into the jet. When the normalising parameters are compared with the experimental values ($r_{½}$ in Figure 5.6 (a) and U_m in 5.6(b)), it is clear that the thickness of the jet is dramatically over-predicted at the nozzle exit (in this case by some 40%)

and that the rate of growth of the jet is too low, the experimental thickness almost matching the predicted result after 6 D_n. The peak velocity in the jet also is shown to decay too fast when compared to the experiments, although there is too little experimental data shown to make a conclusive comparison. It is well known that the k-ε model over-predicts the free jet spreading by some 25% (Rodi 1980) due to too high a level of mixing. Figures 5.5 and 5.6 show that in this case the level of entrainment into the jet is too high, leading to an over predicted jet half thickness and an under-predicted jet core length.

5.1.3.2 Wall Jet

Figure 5.7 shows predicted normalised wall jet profiles for various r/D_n values. As with the experimentally obtained results, the V velocity profiles become self-similar at around r/D_n=2.5, the free jet affecting profiles before this. Also included are normalised experimental wall jet profiles taken in Phase One and Two at the same nozzle height and NPR. As can be seen, the shape of the predicted velocity profile is wrong at the high V/V_m values, especially for the Phase One profile where the boundary layer formed on the table is far too thin. This is most likely due to the errors in the Y^+ values for the grid used as discussed in section 5.1.2 or with problems with the wall function used with the k-ε model. The predicted profile also goes negative (i.e., $V/V_m < 0.0$) after $Y/Y_{½} > 2.0$ which is not shown in the experimental results.

When the wall jet normalising parameters are compared with experimental data from Phase One and Two ($Y_{½}/D_n$ in Figure 5.8(a) and V_m/U_n in 5.8(b)), they show how the developed wall jet half-thickness is under-predicted by the numerical model, the growth rate being approximately 50% lower than that measured in Phase One. The model also fails to predict the dip in $Y_{½}/D_n$ at low r/D_n due to the free jet, presumably because of the over-predicted free jet diffusing the edge of the turning region.

5.1.4 Effect of H_n/D_n

Figure 5.9(a) shows the variation of wall jet thickness, $Y_{½}$, with radial location for the four different nozzle heights showing that PHOENICS does predict an increase in wall jet thickness with H_n/D_n. Although there seems to be little change in the rate of wall jet growth, this remaining practically constant for varying nozzle height, the initial wall jet thickness following impingement is increased. This is most likely due to a thicker free jet entering the impingement region (due to the greater nozzle to ground plane separation) causing a larger impingement region. At higher values of H_n/D_n, the typical turn up of the growth line at low values of r/D_n, as shown in the experimental data (see section 4.2.6 and 4.3.4), is no longer predicted, the extra spreading of the free jet diffusing this turning region effect. Figure 5.9(b) shows the effect of H_n/D_n on the wall jet half thickness at two representative radial locations non-dimensionalised with the wall jet half thickness at a nozzle height of 10 D_n for that radial location. Also shown are the comparable results from the experimental Phase 2 work. The nozzle height effect predicted by the k-ε model is too large when compared to the experimental results of phase 2, the decrease in $Y_{½}$ with H_n/D_n being over predicted by some 10% for a nozzle height of 4 D_n. The small increase in $Y_{½}$ at $H_n/D_n = 2.0$ shown in the experimental results is completely missed in the computational prediction.

Figure 5.10 shows peak wall jet velocity against radial location for the four different nozzle heights. This shows the very rapid decay of the predicted peak velocity at the higher heights, the non-dimensional value obtaining self-symmetry at around an r/D_n of 15.0. This is far higher than that observed in the experimental phases where self-symmetry of the peak wall jet velocity is reached at around $r/D_n = 4.0$ (see section 4.2.5 and section 4.3.3). It has already been commented on how the peak wall jet velocity is far closer to the wall than that measured experimentally at the lower r/D_n values (see section 5.1.3.2). This error seems to reduce at lower H_n/D_n; at a height of 2 diameters, the peak velocity is under-predicted by 35% compared to around 50% at $H_n/D_n = 10.0$ when compared to Phase One data. This can be accounted for by the over-prediction of the free jet thickness entering impingement, at lower H_n/D_n, the

over-prediction has had less influence on the free jet and consequently, the conditions entering the impingement region match experimental data far closer.

5.1.5 Effect of Initial Turbulence Intensity

The initial turbulence intensity was varied (10%, 5%, 3% and 1% of nozzle exit velocity) to investigate its effect on wall jet spreading. A major observation noted in running different initial turbulence intensity models was that as Tu was increased, a converged solution became progressively easier to obtain. This was noted by Bray (1992) and is possibly due to the extra turbulence improving the speed at which variables are transported through the computational domain.

Figures 5.11 and 5.12 show the rate of growth and centre-line velocity decay of the free jet with varying initial turbulence intensities. As can be seen, increasing initial Tu has a very marked effect on the rate of spread and velocity decay of the jet, causing increased free jet growth and the corresponding increase in velocity decay. The length of the predicted potential core, shown by the unchanging U_m/U_n with increasing $(H_n-H_p)/D_n$ on Figure 5.12, is greatly reduced with increasing Tu, the centre-line velocity being around 30% lower on entering the impingement region for T_u=10.0% compared with Tu=1.0%. This is an expected result, as increased mixing due to higher values of initial turbulence would cause a quicker transfer of momentum from the fast-moving core to the jet edge and so increased free jet growth and peak velocity decay.

Figures 5.13 and 5.14 show the effect of varying initial turbulence intensity on the predicted wall jet growth and peak velocity decay. These show that Tu has very little effect on the thickness of the wall jet, other than a slightly increased initial thickness leaving the impingement region for higher leaves of Tu. The increased turbulence at nozzle exit does not seem to increase the rate of growth of the wall jet. The decay of the peak velocity seems to be similarly little affected by the initial Tu, there being approximately 10% change in the peak value of V_m/U_n for a Tu of 1% and 10% with the profiles merging at round r/D_n = 12.0. These results are similar to those for varying nozzle height at constant Tu, where changes in nozzle conditions affected the free jet

and the impingement entry and exit flow but seemed to have comparatively little affect on the wall jet flow.

The trend of reducing the value of turbulence causing reduced wall jet thickness agrees with the results of Bray (1992) and Knowles et al. (1993). This trend is expected as, for the free jet, reduced turbulence would mean reduced transfer of momentum (reduced mixing) from the fast-moving potential core to the ambient air, so decreasing the jet's rate of growth. It is a little surprising, however that the initial turbulence level does not affect the rate of wall jet growth, any change being due to an increased initial thickness.

5.1.6 Effect of NPR

A range of different NPR were tested (NPR=1.05, 1.25, 1.50 & 1.75) for H_n/D_n=10.0 and for an initial turbulence level of 3%. A subsonic jet was retained at all times as modelling the experimental set-up running supersonic jets would require modifications to the model to obtain a choked exit and increased grid resolution for shock definition and was outside the realm of this phase of the project.

Figure 5.15 shows how the half thickness for the free jet decreases with increasing NPR, following the trend described in the literature. To date this is believed to be due to increased compressibility reducing the level of turbulent mixing in the outer shear layer surrounding the jet (Strykowski 1996). It is worth noting the relatively thicker free jet close to the nozzle exit ($(H_n-H_p)/D_n$ = 1.0) for the higher NPR jets of Figure 5.15. The reason for this expansion of the jet following the nozzle exit is unknown. Figure 5.16 shows the normalised centre-line peak velocity for the free jet, showing the effect NPR has on the length of the potential core. Increasing NPR increases this potential core length, increasing the flow velocity on entrance to the impingement region. It is also worth noting the dip in the velocity line for NPR = 1.75, and the following relatively lower non-dimensional value of the potential core. As with the free jet half-thickness, the reason for this unexpected behaviour is unknown.

Figure 5.17 shows the effect that increasing NPR has on the wall jet spreading rate. As can be seen, the rate of spread of the wall jet does not seem to be affected by the value of NPR, but increasing NPR does decrease the thickness at a given radial position. This is due to the wall jet leaving the impingement region being thicker for lower values of NPR. This result is similar to the effect that H_n/D_n has on the wall jet stated in Section 5.1.4, the NPR effect also following the trends of experimental data (Miller and Wilson 1993, Myszko 1993).

The change in initial thickness of the wall jet for varying NPR and H_n/D_n can not be explained by differing shock structure losses as the jet remains subsonic at all times, the difference being the speed of the free jet entering the impingement region. As NPR is increased, the free jet speed will increase and so will the turning region entry speed, while increased H_n/D_n will decrease this effect due to greater free jet decay. These computational results seem to suggest that the H_n/D_n and NPR effects do not change the rate of growth of the wall jet, but do change initial thickness of the jet. This observation is in agreement with experimental data presented in this report (see Section 4.2.6 and 4.3.4) where changes in H_n/D_n changed the initial value of $Y_{½}/D_n$ and not the rate of spread of the wall jet.

5.2 Modifications to Standard k-ε Models

The following sections describes the results of three modifications made to the standard k-ε turbulence model.

5.2.1 Rodi Correction

The Rodi correction (Rodi 1980) described in section 3.2.1 was applied to the free jet portion of an impinging jet model. The model used a 1" (25.4mm) nozzle and ran at an NPR of 1.079 so that the results could be compared with previous work of Bray (1992) and with the experimental work of Poreh et al. (1967)

The first checks made were for convergence. The new varying coefficients used did not seem to affect this, it continuing to take around 3000 sweeps for a 51 by 49 cell domain.

With the Rodi correction applied (see Figure 5.19, which also includes results of other corrections discussed later), the rate of spread of the free jet compared with the standard k-ε version is reduced, especially as the flow nears the impingement region. When a lower initial turbulence intensity was used (see Figure 5.20), the rate of growth of the free jet was reduced in line with results discussed earlier. The effect of the Rodi correction on peak centre line velocity decay for the free jet is shown in Figures 5.21 and 5.22. The reduced momentum transfer from the fast-moving core to the jet edge associated with this correction caused a reduction in velocity decay, this being slightly further reduced by reduced initial turbulence intensity. This ties in with the reduced free jet growth shown in Figure 5.19, the correction causing a thinner, faster jet to enter the impingement region.

As the standard k-ε model was used for the wall jet portion, it was found that the rate of wall jet growth remained the same (see Figure 5.23) although the initial thickness had been reduced on leaving the impingement region. This was most likely due to the free jet being thinner before the turning process starts so causing a thinner wall jet to emerge. This means that although the free jet thickness is now better predicted, the wall jet is even more under-predicted than by the standard model. The effect of the Rodi correction on the wall jet for differing initial turbulence levels (see Figure 5.24) is similar to that described in section 5.1.5, a lower value of Tu causing a thinner wall jet.

The Rodi correction is shown to increase dramatically the wall jet peak velocity, especially in the impingement region (see Figure 5.25), the value falling quickly to reach the standard k-ε value at around $r/D_n = 18.0$. This is expected as the correction produced a faster thinner jet entering the impingement region causing a faster, thinner wall jet to leave. The effect of initial turbulence level (see Figure 5.26) is as described in section 5.1.5

5.2.2 Malin Correction

The Malin correction as described by Glynn and Jal (1987) was applied to the wall jet portion of an impinging jet model. The model used a 1" (25.4mm) nozzle and ran at an NPR = 1.079. Convergence of the model was found to be similar to the Rodi correction (see section 5.2.1).

When the Malin correction was applied to the wall jet (see Figure 5.23), the rate of spread was slightly increased, indicating that the correction was working as intended, but the improvement was not enough to bring the results up to those measured by Poreh (1967). Not only was the spreading rate too low, but the initial thickness was also too small. The spreading rate could be increased by further adjustment to the constants in the applied correction, this also being the conclusion of Glynn and Jal (1987). This will not, however, improve the prediction of the turning process where a correctly-predicted free jet causes the wall jet to have approximately half the required initial thickness. The effect of initial turbulence intensity (see Figure 5.24 and 5.26) was consistent with previous results.

A CFD run was also performed with the Rodi correction applied to the free jet and Malin to the wall jet at the same time (see Figure 5.23 and Figure 5.25), this theoretically giving the best result. The free jet is now more accurately predicted with the Rodi correction reducing the over-prediction of the standard k-ε model. The wall jet, although slightly better than the Rodi correction on its own, is still worse than the standard k-ε because of the thinner free jet cause a much reduced wall jet thickness leaving the impingement region.

The applied corrections are, as their name implies, trying to correct and compensate for inadequacies within the standard turbulence model. With further work, these compensations could be adjusted to give adequate predictions of free and wall jet spreading rates, but it is most likely that different values would be required for different initial conditions and that the corrections would not be valid for all cases.

5.2.3 Chen Correction

The Chen correction was applied as part of the standard implementation of PHOENICS, the activation of which is described in section 3.2.3. The grid was that used in the standard k-ε study, with a ½" (12.7mm) nozzle running at an NPR = 1.05 at a H_n/D_n =10.0 and Tu=3.0%.

Figures 5.27 and 5.28 show predicted free jet growth and peak velocity decay respectively compared to the standard k-ε and Phase 1 experimental results. The Chen correction has predicted a thinner free jet, especially close to the impingement region, similar to that of the Rodi correction (see section 5.2.1). It has also predicted a far slower peak velocity decay, the agreement with Phase 1 experimental results being much better than the standard k-ε model where the over-predicted free jet spread caused too fast a peak velocity decay.

Figures 5.29 and 5.30 show predicted wall jet growth and peak velocity decay respectively. The thinner wall jet predicted by the use of the Chen correction has produced a thinner wall jet than the standard k-ε model leaving the impingement region and has caused it to spread even slower. As the standard k-e model under-predicts the wall jet growth the use of the Chen correction on the wall jet has increased the inaccuracy of the predicted growth. This thinner wall jet has caused a higher peak wall jet velocity leaving the impingement region, this increased exit velocity agreeing far better with experimental data than the standard k-ε model.

5.3 Low Reynolds Number k-ε Model with Axisymmetric Grid

The following section describes results obtained with the use of a low Reynolds number k-ε turbulence model on a polar-cartesian grid. Details of the model set-up are covered in section 3.3.

5.3.1 Convergence

Convergence of model runs was monitored in a similar way to that used with the standard k-ε turbulence model. The normalised absolute residuals, displayed as the solution progressed were monitored, convergence accepted when the percentage errors where less than 1.0% for velocity and pressure variables and 2.0% for the turbulence variables. As with the standard k-ε model, it was the k variable that was the limiting factor, the velocity and pressure percentage errors being as low as 0.1% at convergence.

The variations of variables at a spot value in the solution domain ($r/D_n = 5.5$ and 16.5mm up from the wall) were also monitored and are shown in Figure 5.31. This shows that the variables reach an unchanging value at around 3000 sweeps, runs continuing until 5000 sweeps to meet the first convergence criteria.

5.3.2 Grid Development

The implementation of the low Reynolds number k-ε model requires the Y^+ value of the first cell to below 5.0 and preferably below 1.0. For this, a number of grids with differing first cell thicknesses were tried (see table 5.2), the variation of Y^+ with radial location being shown in Figure 5.32. Twelve grids were tried in total, in general, the first cell thickness being reduced by 35% in moving from one grid to the next. Figure 5.32 shows that by around grid 10, the peak Y^+ value had been reduced from 100.0 to around 5.0. Grids 10, 11 and 12 are shown in more detail in Figure 5.33, showing that although grid 11 has a peak value below the limit, grid 12 reaches a $Y^+ < 1.0$ earlier, this grid being chosen to continue this study with.

5.3.3 Flow Domain

The following section describes details of the flow domain predicted by the low Reynolds number k-ε turbulence model.

5.3.3.1 Free Jet

Figure 5.34 shows a comparison of the low Reynolds number and standard k-ε predicted free jet growth. The low Reynolds number model has predicted a slightly faster growth which is surprising as the models should be the same away from the wall. The low Reynolds number corrections could be causing a larger predicted stagnation region and hence larger impingement region, this influencing the growth rate of the free jet. The rate of peak velocity decay, shown in Figure 5.35, has also increased, this being consistent with the slightly quicker free jet growth.

5.3.3.2 Wall Jet

Figure 5.36 shows non-dimensional wall jet profiles for various radial locations predicted by the low Reynolds number model. Similar to the standard k-ε prediction (see Figure 5.7) the profiles collapse well to a self-similar shape. Figure 5.37 shows the profile at $r/D_n = 5.0$ in more detail with corresponding standard k-ε and experimental profiles from both phases for comparison. Although the boundary layer predicted by the low Reynolds number model is still too thin compared with the experimental results from Phase One, it is a reasonable good fit to the profile of Phase Two. It is also noted that the low Reynolds number profile is fuller at the higher values of V/V_m when compared to the standard model, comparing better with both experimental profiles.

Figures 5.38 and 5.39 show wall jet thickness and peak velocity decay respectively for the low Reynolds number, k-ε and experimental data. It shows that the wall jet thickness is increased using the low Reynolds number wall model, seemingly a uniform increase in thickness across the r/D_n range for $r/D_n > 4.0$. This could be due to the thicker boundary layer now predicted as shown in Figure 5.37. As both turbulence models use the standard k-ε model away from the wall, it is unsurprising that the rate of growth of the wall jet has not changed as this would be dominated by the free shear flow with the ambient air. The rate of growth of the wall jet is still vastly under-predicted by both turbulence models.

The decay of peak wall jet velocity is in line with the trends seen in the standard k-ε study. The thicker initial wall jet predicted by the lower Reynolds number model due to a greater over-prediction of the free jet thickness, leads to a low impingement region exit velocity. The velocity then decays at almost the same rate as the standard k-ε model, the experimental data agreeing better with this standard model.

5.4 Summary

The following conclusions were drawn from this phase of the project.

i. Due to high levels of surface shear stress in the impingement region compared to the developed wall jet, there is great difficulty in using a uniform first cell thickness grid (as with the Polar-cartesian grid in PHOENICS) and the logarithmic law of the wall. The variation of Y^+ value is too great to satisfy the limits placed upon it.

ii. The k-ε model over-predicts the spreading rate, and hence the peak velocity decay, of the free jet, and under-predicts the spreading rate of the wall jet. Nozzle height, exit NPR and initial turbulence intensity have an affect on the free jet, but only seem to affect the initial thickness of the wall jet as it leaves the impingement region.

iii. Wall jet velocity profiles are poorly predicted, the logarithmic law of the wall failing to resolve the boundary layer.

iv. The corrections to the standard k-ε model investigated here were disappointing, none used was able to come close to the experimental data in all the flow regions of an impinging jet.

v. The use of the low Reynolds number k-ε model has improved the wall jet velocity profile boundary layer thickness. This has caused a thicker wall jet, although it has not corrected the under-predicted rate of growth. The results are

disappointing considering the extra computational time required due to the finer grid resolution.

5.5 Important Note

Since this phase of the project was completed, and the results processed and discussed in the above section, it has been discovered (my thanks to A. J. Saddington) that an error had been made in the input file for the above predictions. In specifying the mass flow entering the domain through the nozzle, the stagnation density was used instead of the static density, thus giving a higher value of mass flow for the appropriate value of NPR.

At the main test value of NPR = 1.05, this error caused the mass flow to be around 3.5% higher than would be expected, this rising to 49% at NPR = 1.75. This mass flow imbalance is a potential reason for the increased convergence times required with these models compared with an estimate given by CHAM. The larger error at higher NPRs means these results can not be relied upon, although trends shown should still be representative. For a NPR=1.75, there were some unusual results (Figures 5.15 and 5.16, see section 5.1.6) which could be explained by a supersonic jet emerging from the nozzle caused by the increased mass flow. This would cause some degree of expansion of the jet following the exit as shown on Figure 5.15 and a weak shock wave dropping the velocity to subsonic values, possibly shown by the dip in the normalised centre line velocity shown on Figure 5.16.

Grid	First Cell Thickness (mm)	Peak Y^+
1	0.63480	77.74
2	1.26960	99.05

Table 5.1 : Table of First Cell Thickness and Corresponding Peak Y^+ Value for Grids used during Standard k-ε Study

Grid	First Cell Thickness (mm)	Peak Y^+
1	0.12690	99.05
2	0.09520	69.83
3	0.06350	49.02
4	0.04760	38.23
5	0.03174	27.00
6	0.02380	21.15
7	0.01587	15.03
8	0.01190	11.83
9	0.00794	8.41
10	0.00595	6.60
11	0.00397	4.70
12	0.00298	3.66

Table 5.2 : Table of First Cell Thickness and Corresponding Peak Y^+ Value for Grids used during Low Reynolds Number k-ε Study

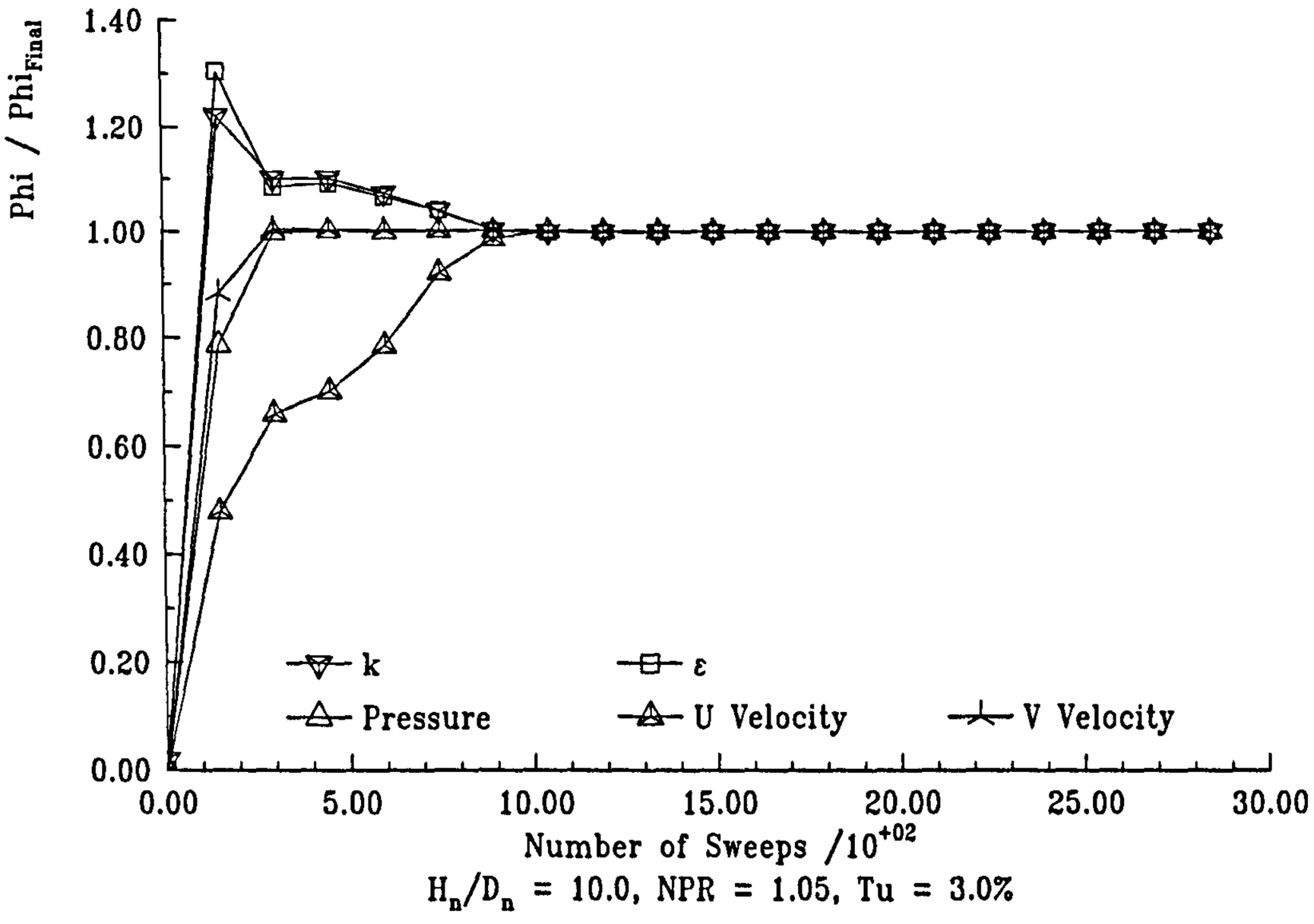

Figure 5.1 : Convergence of k-ε Solved Variables against Number of Sweeps

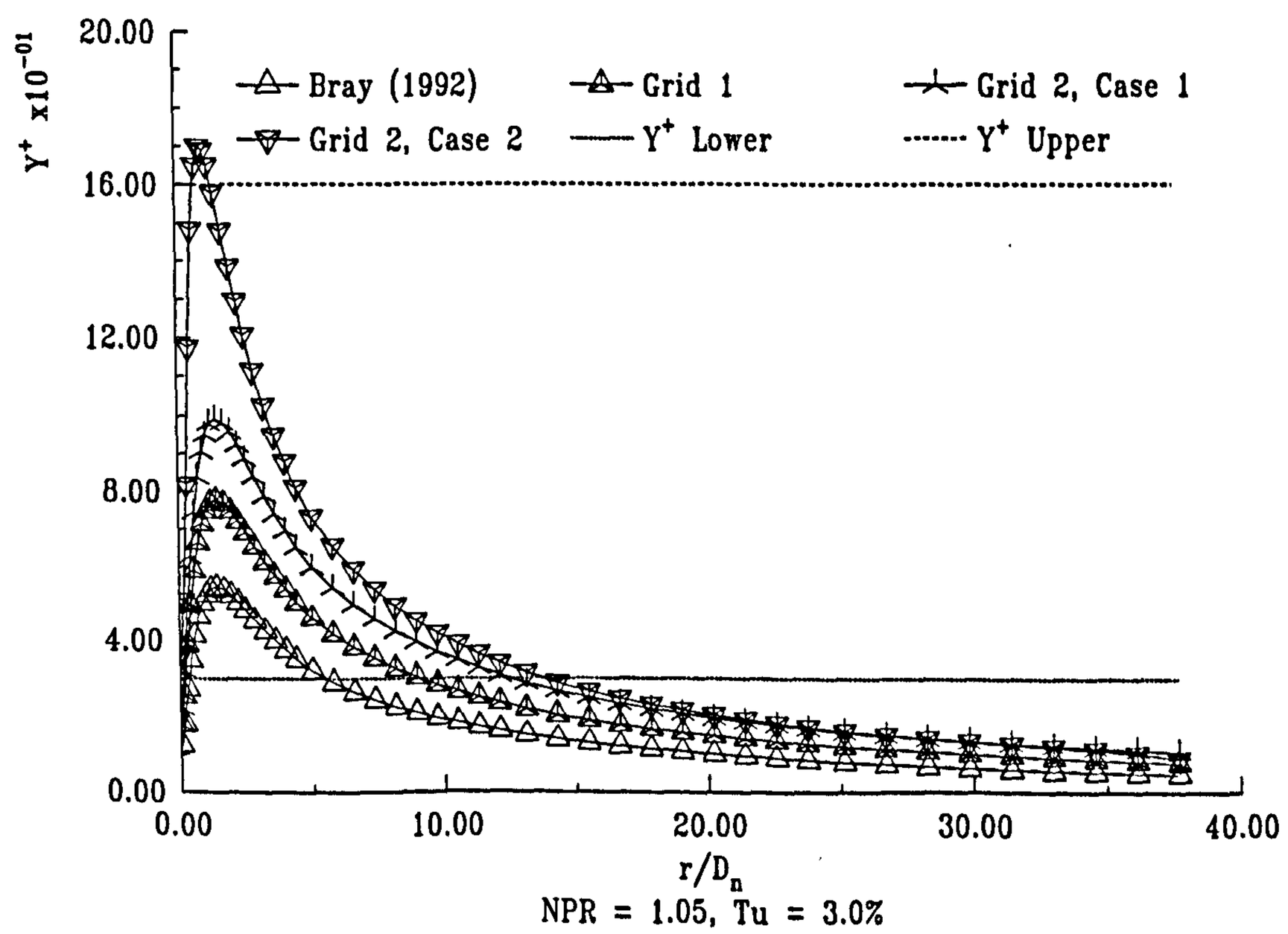

Figure 5.2 : Y$^+$ against Radial Location for Grids used in k-ε Study

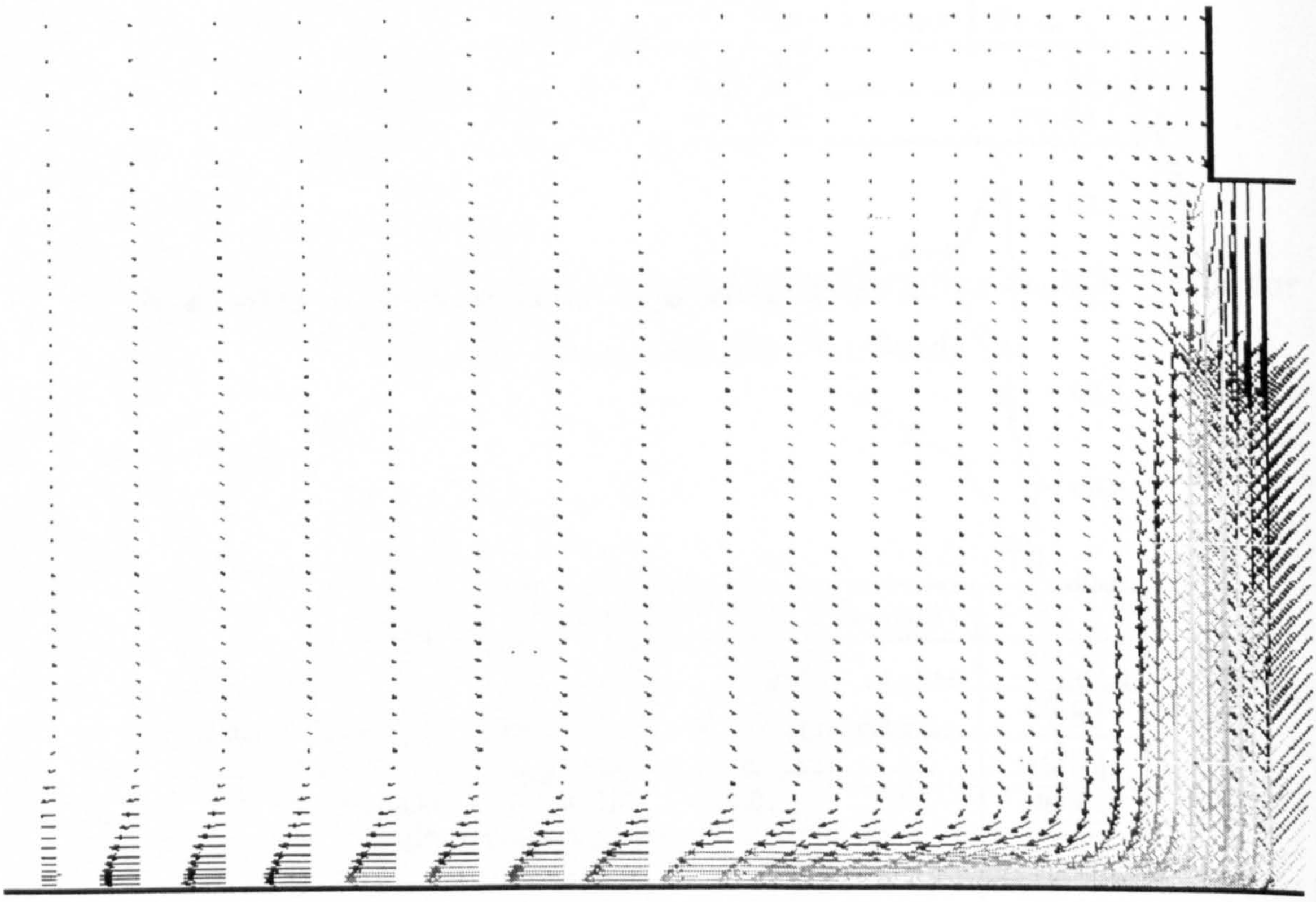

Figure 5.3 : Velocity Vector Plot for an Impinging Jet Using the k-ε Turbulence Model

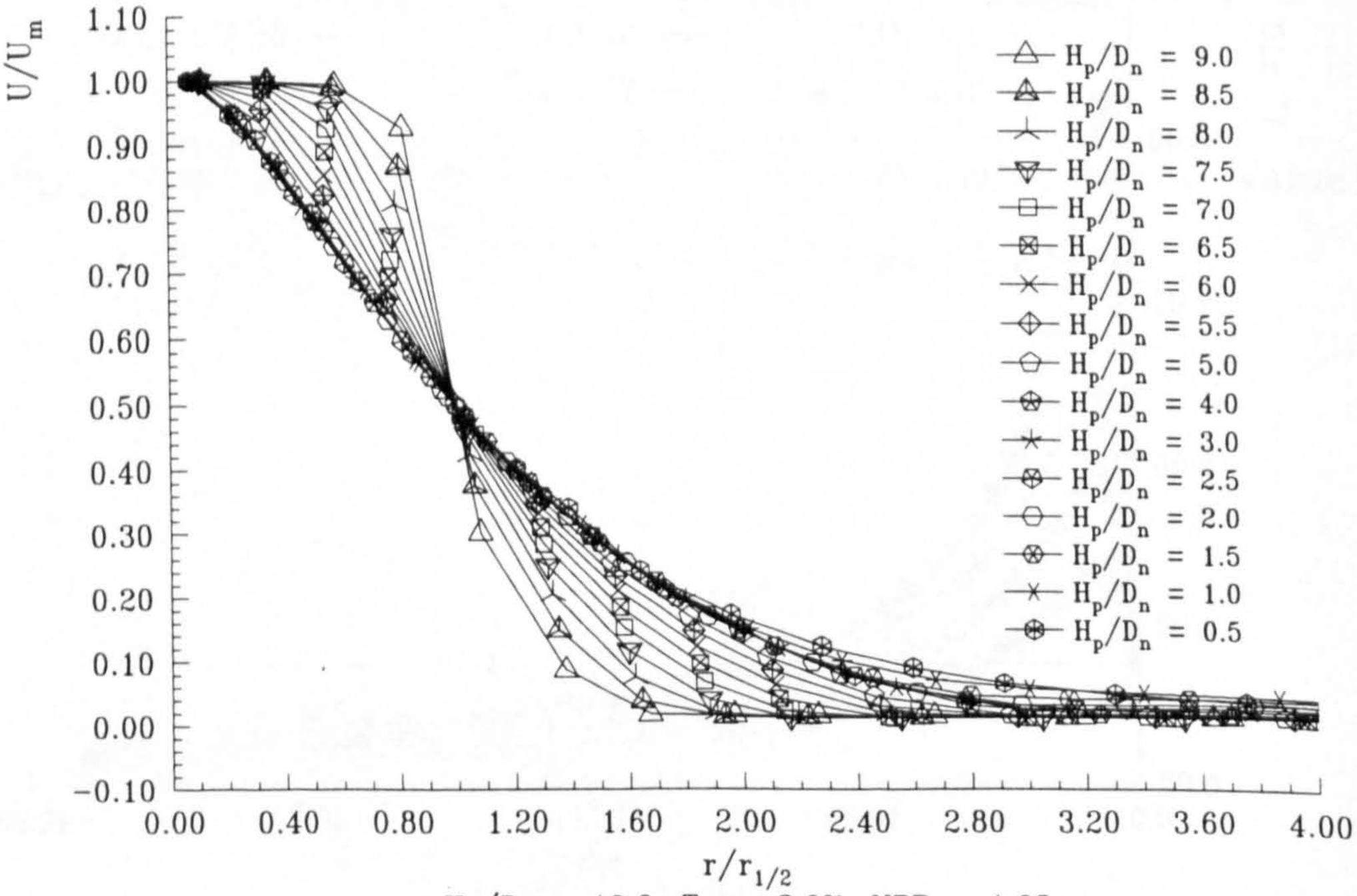

Figure 5.4 : Non-dimensional Free Jet Velocity Profiles

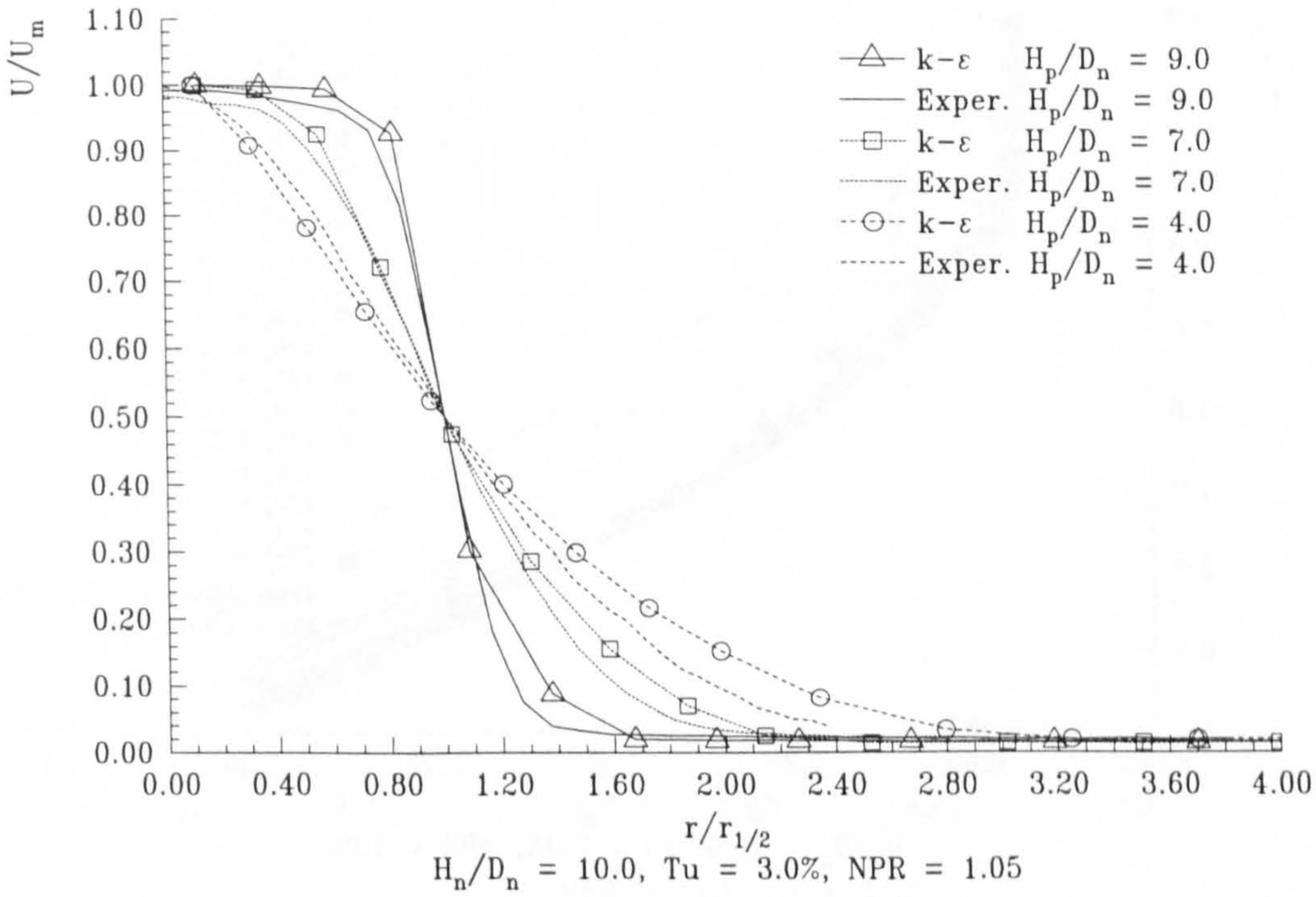

Figure 5.5 : Comparison of k-ε Free Jet Development with Phase One Experimental Results

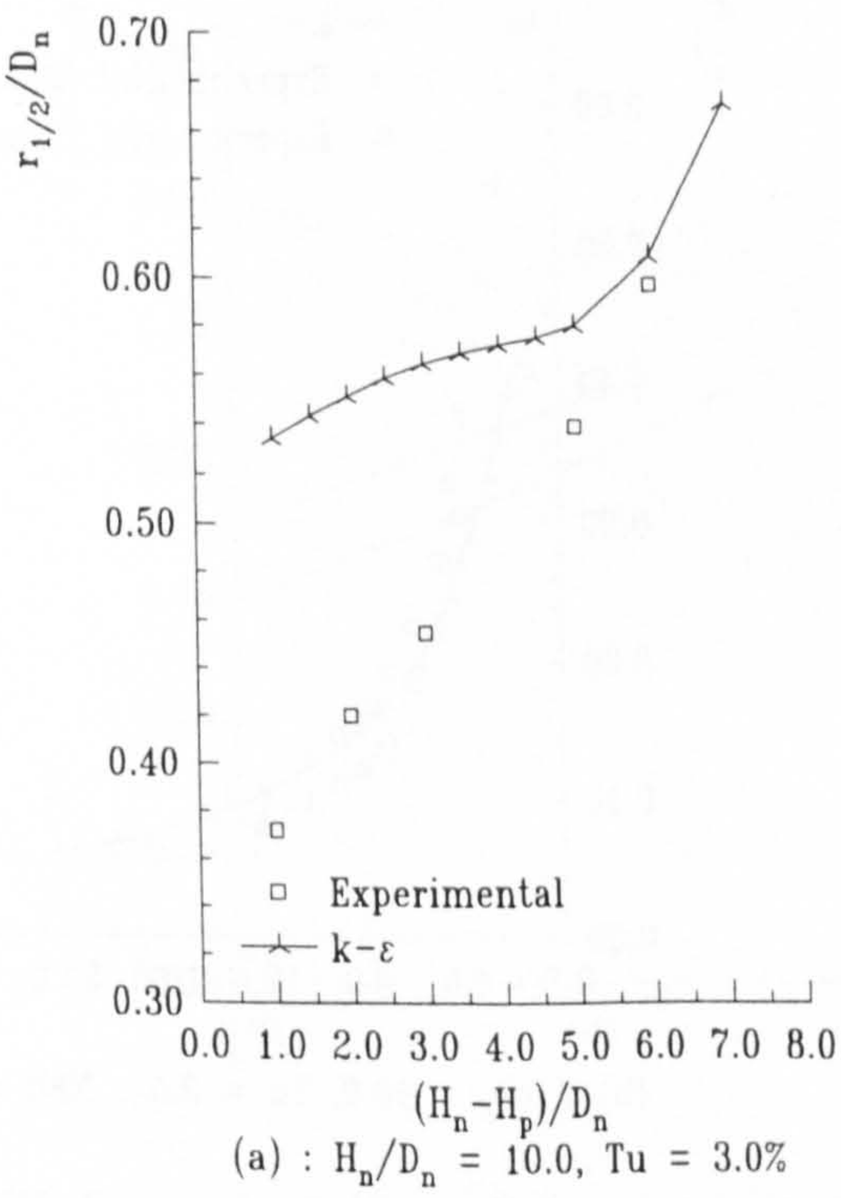

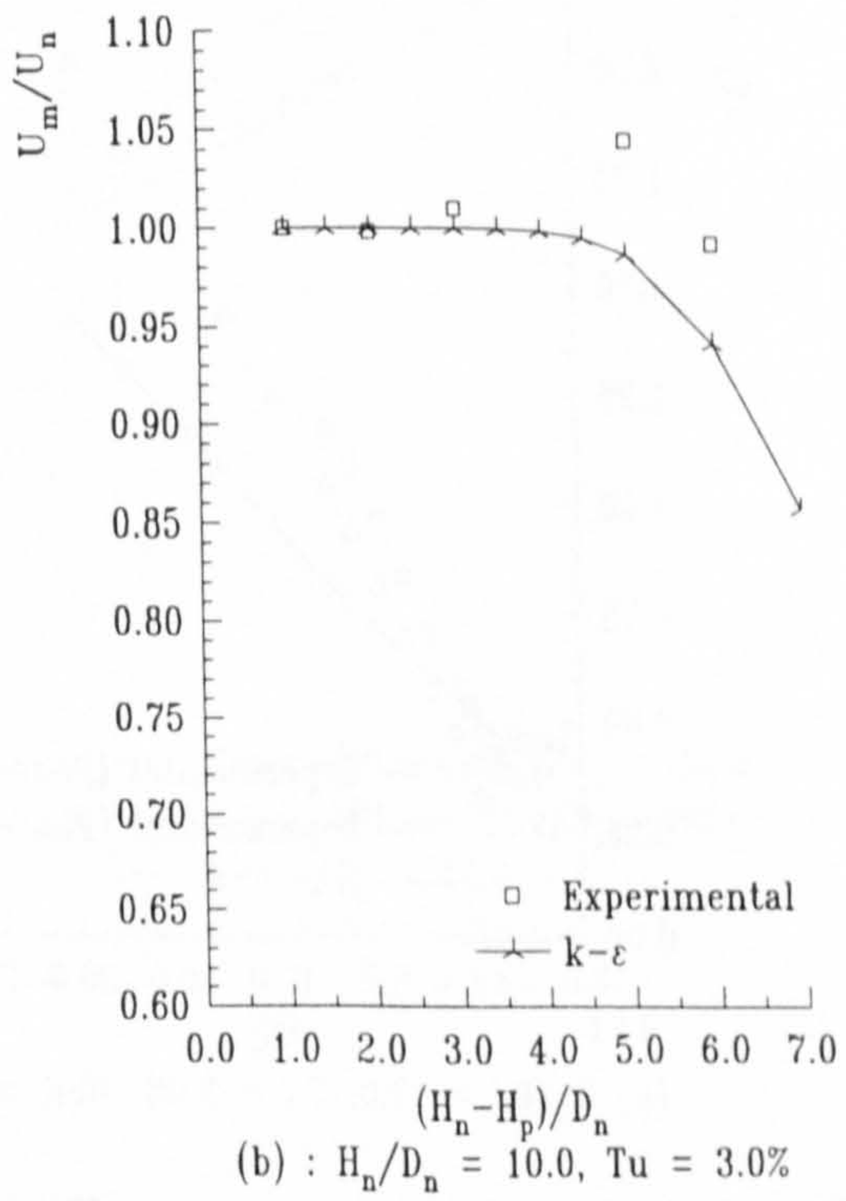

Figure 5.6 : Comparison of k-ε Free Jet Thickness and Peak Velocity with Phase One Experimental Results

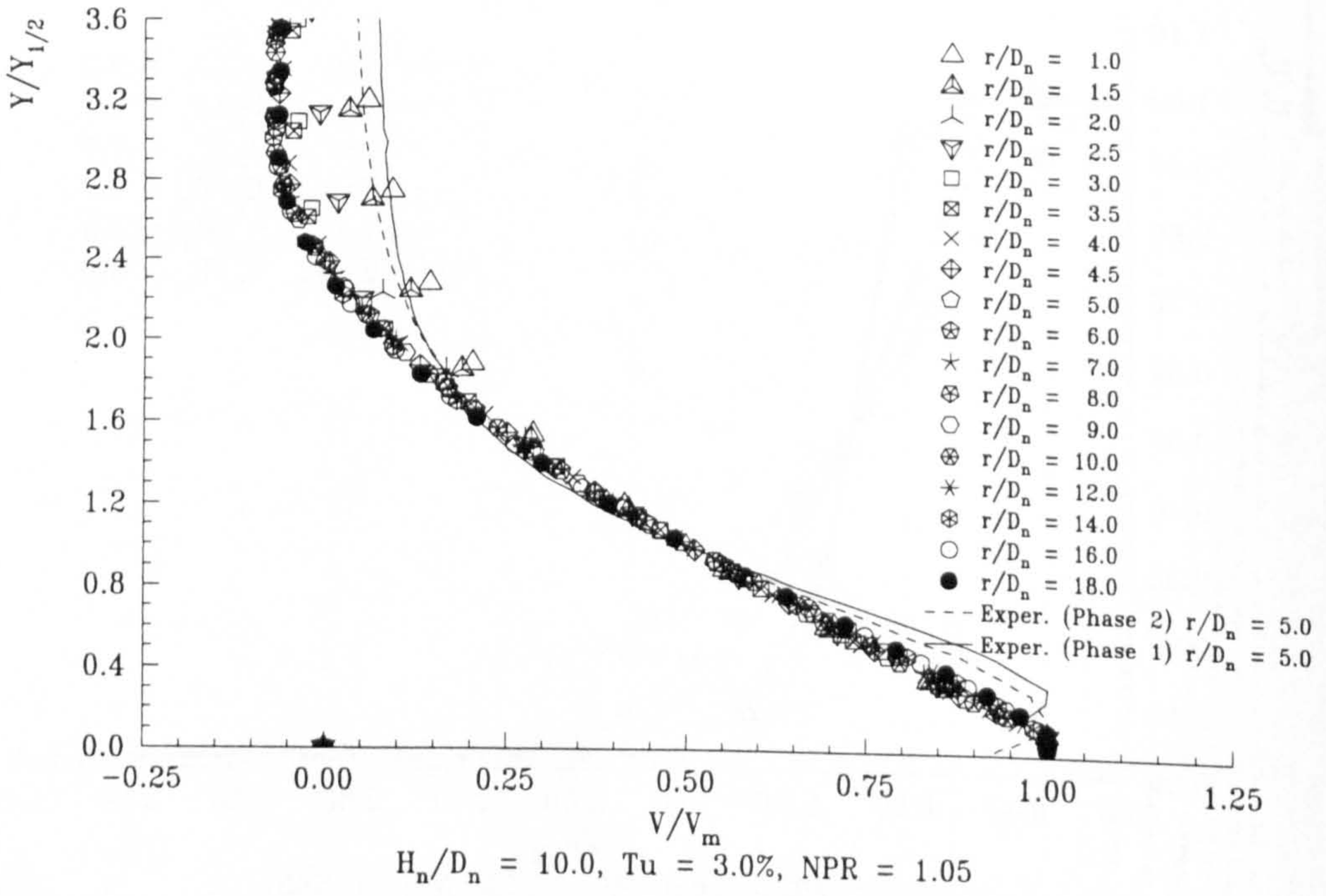

H_n/D_n = 10.0, Tu = 3.0%, NPR = 1.05

Figure 5.7 : Comparison of k-ε Wall Jet Development with Phase One and Two Experimental Results

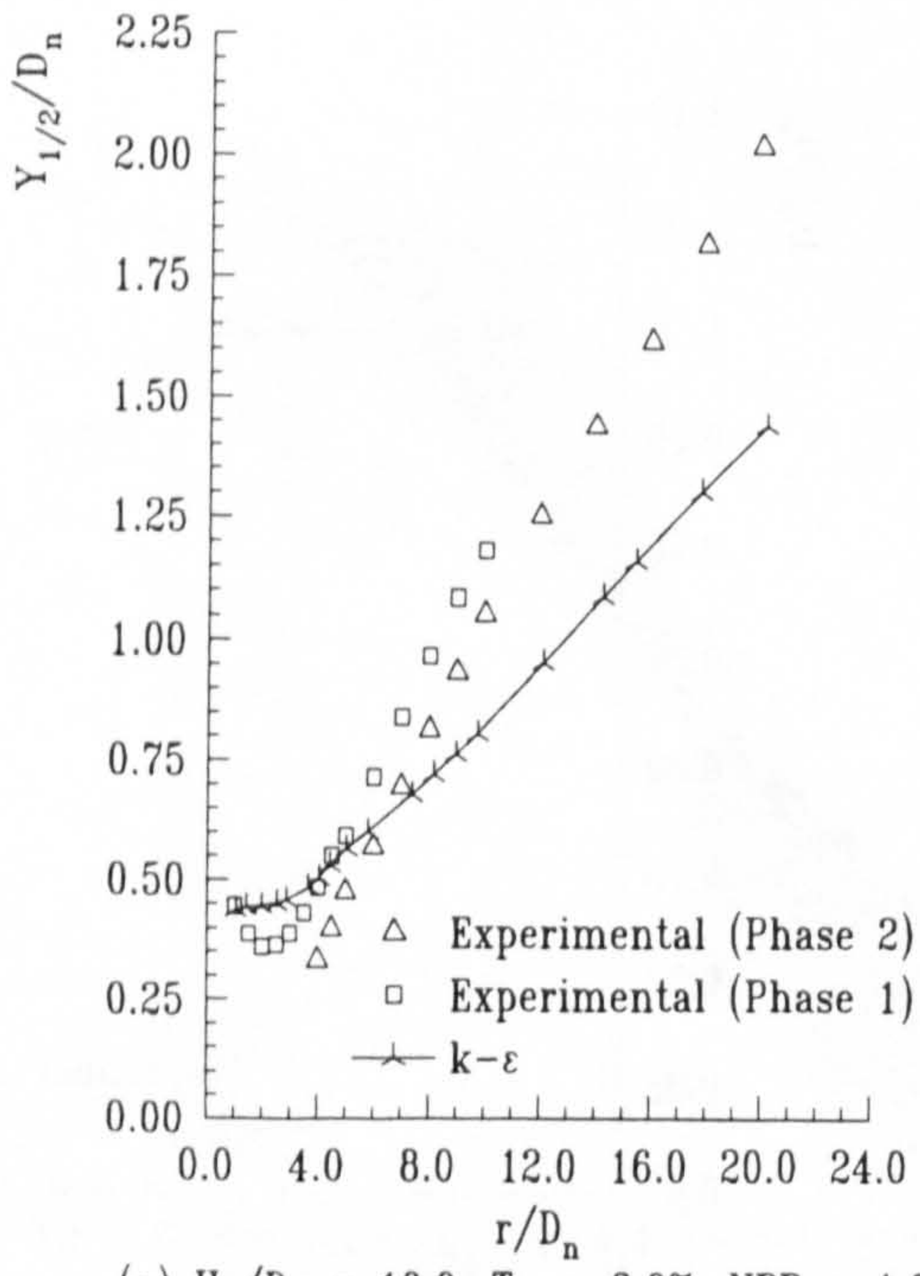

(a) H_n/D_n = 10.0, Tu = 3.0%, NPR = 1.05

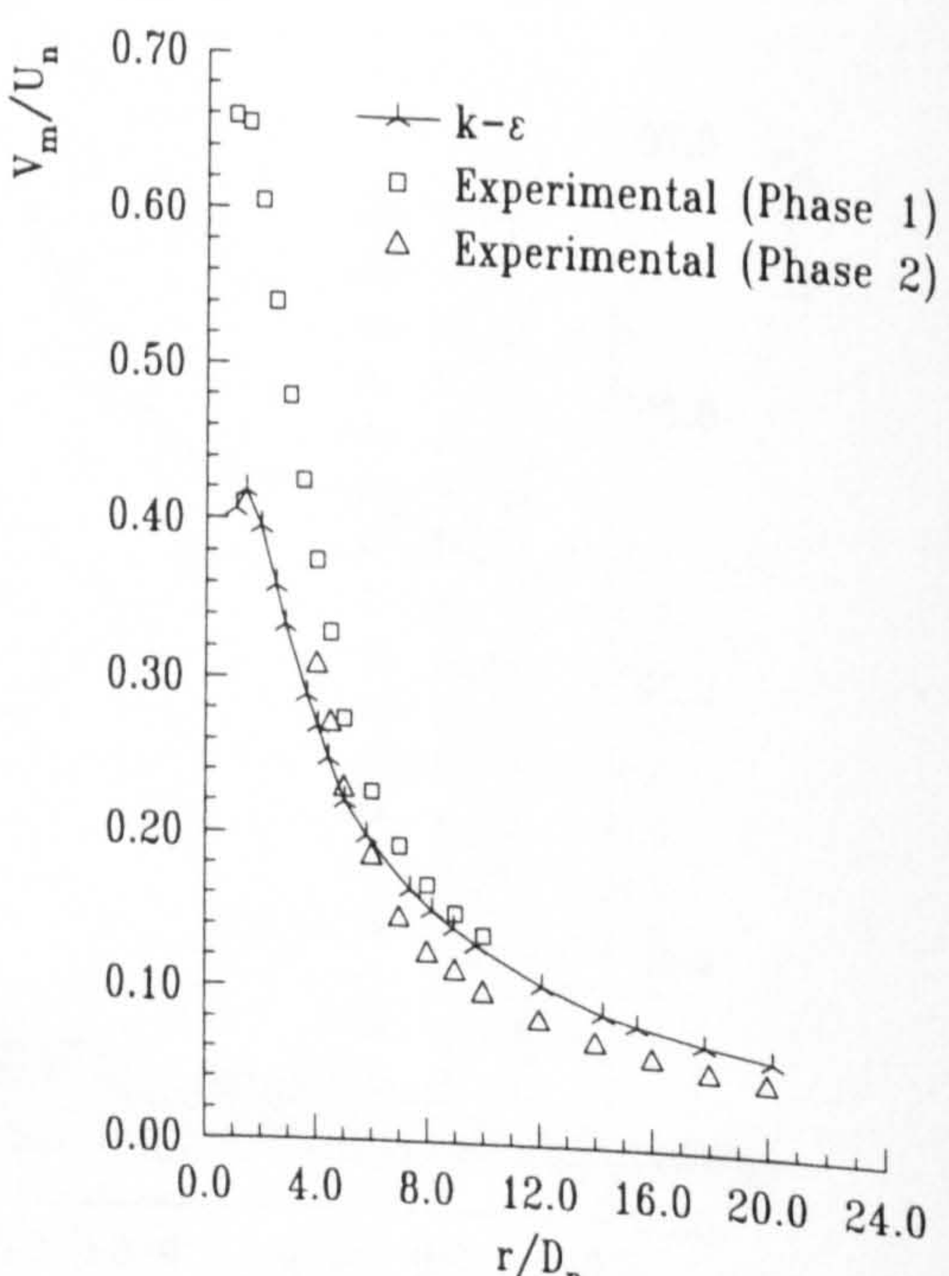

(b) H_n/D_n = 10.0, Tu = 3.0%, NPR = 1.05

Figure 5.8 : Comparison of k-ε Wall Jet Thickness and Peak Velocity with Phase One and Two Experimental Results

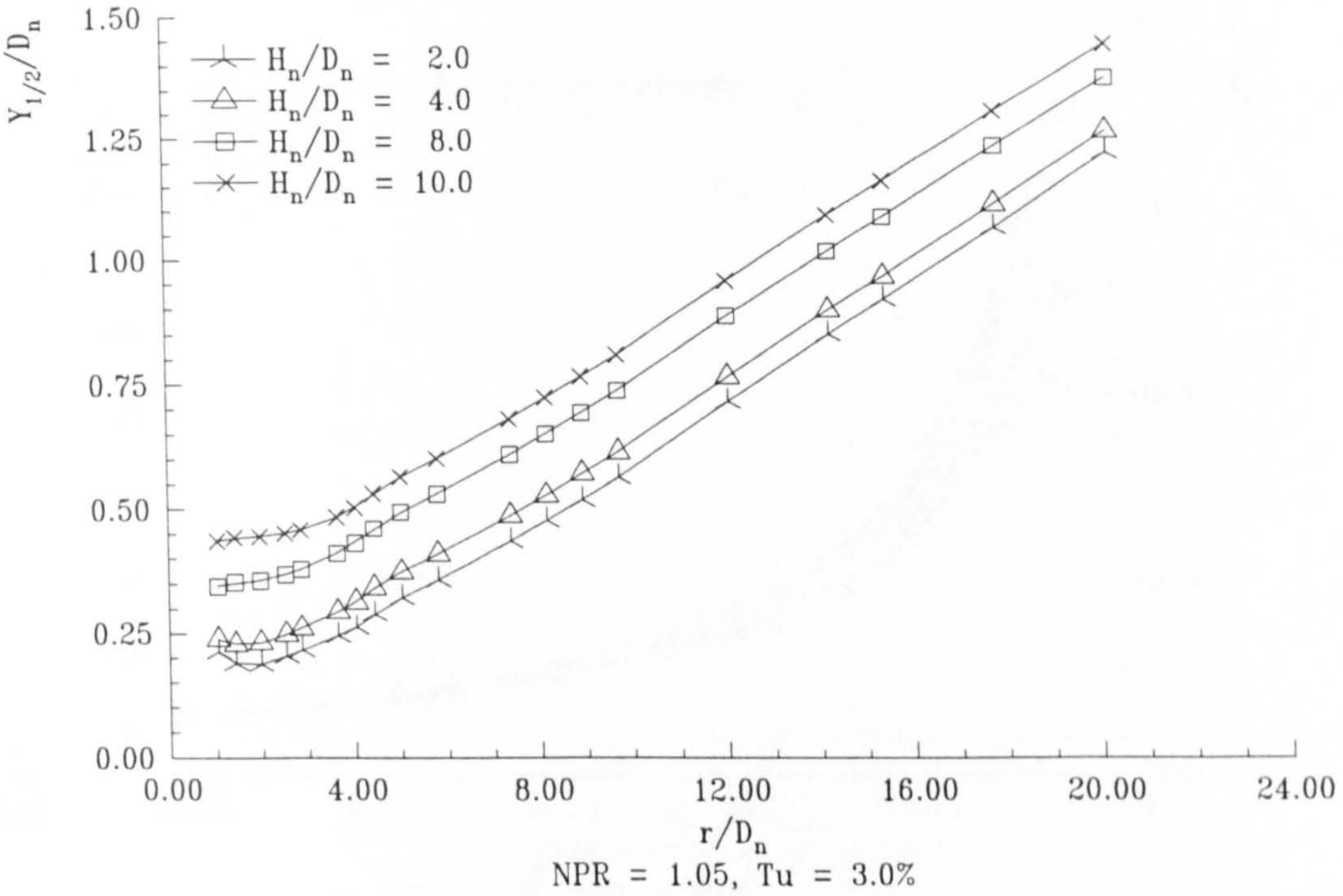

(a) : Radial Location

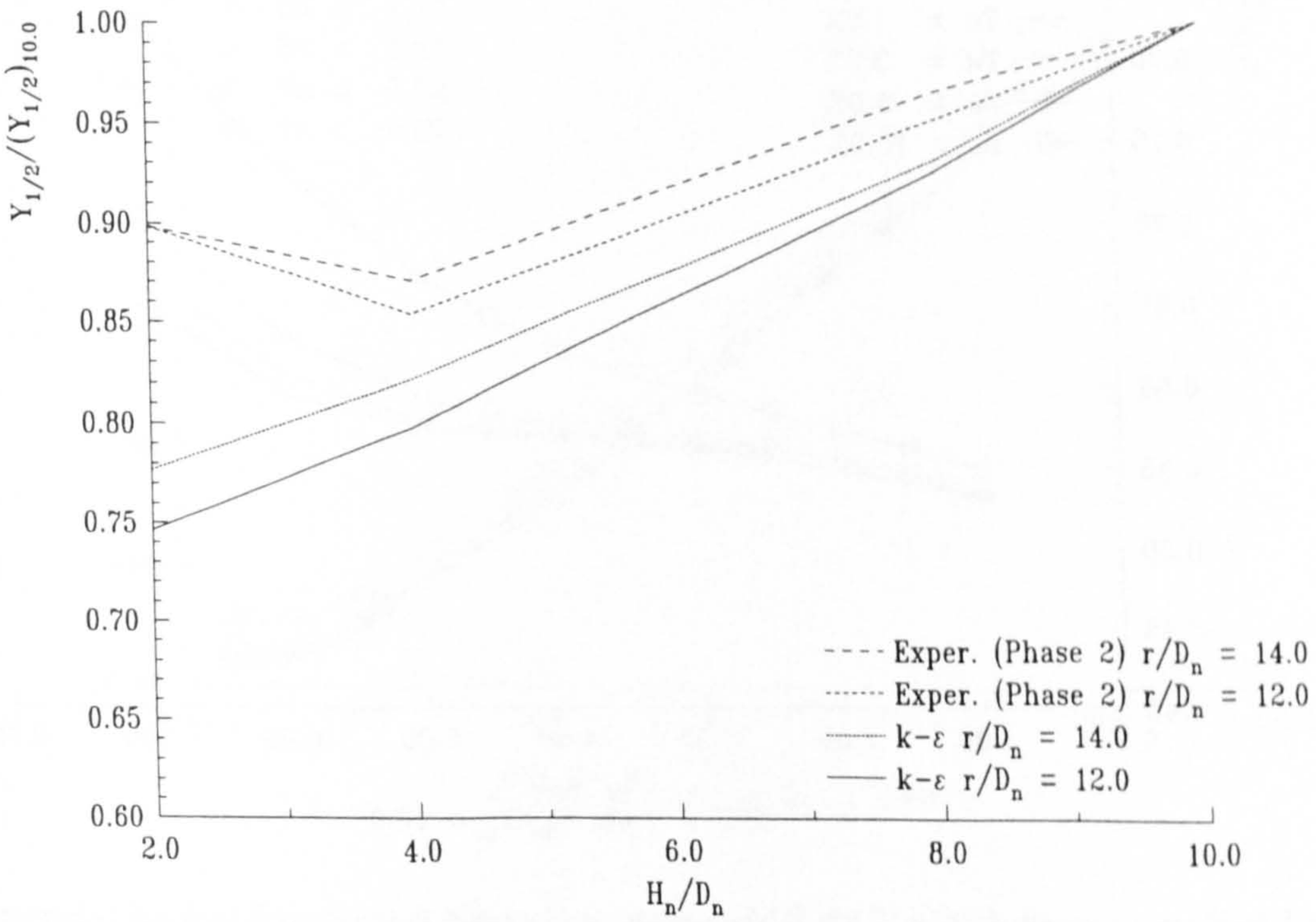

(b) : Nozzle Height Effect

Figure 5.9 : k-ε Predicted Non-dimensional Wall Jet Thickness

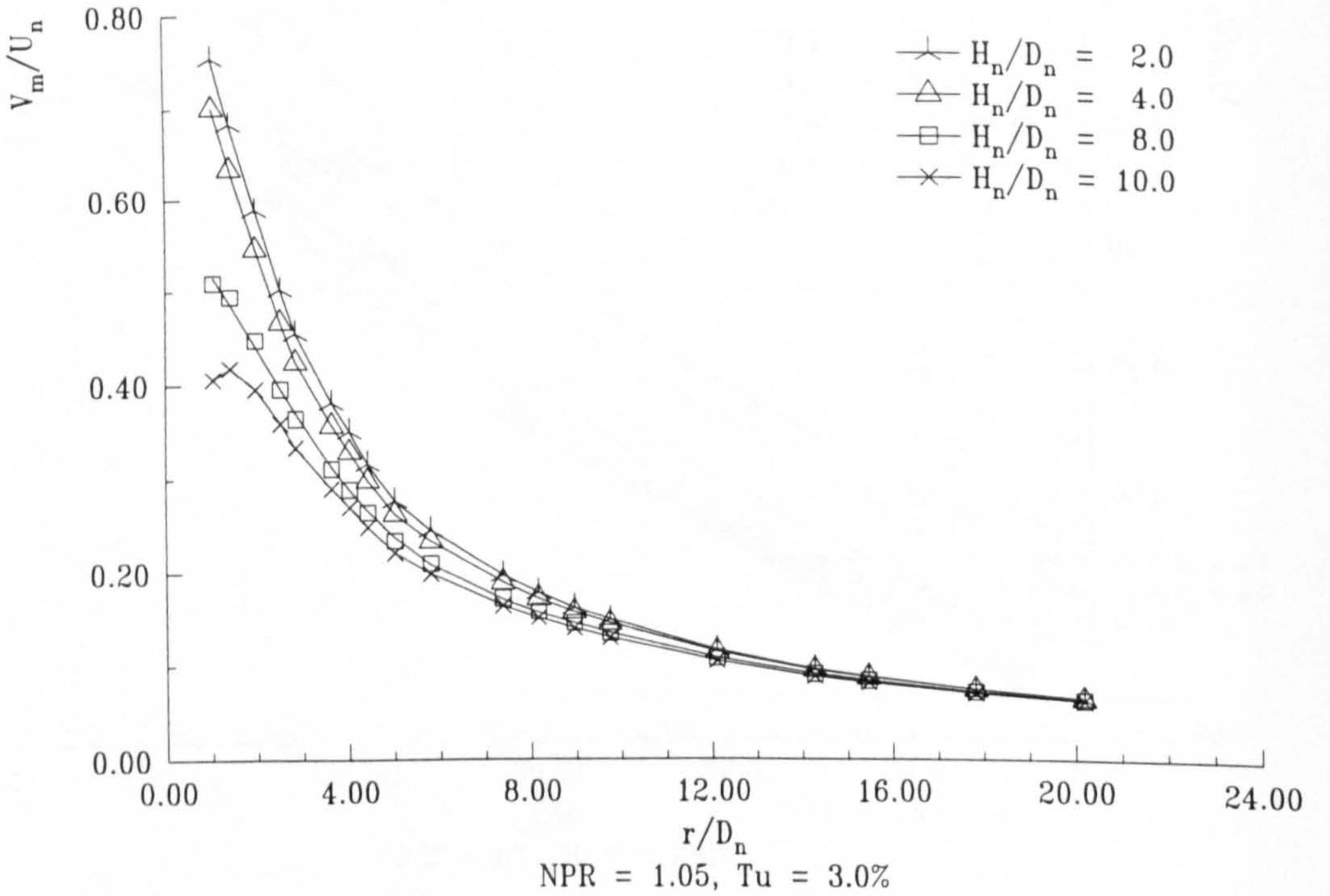

Figure 5.10 : k-ε Predicted Non-dimensional Wall Jet Velocity Decay against Radial Location for Differing Nozzle Heights

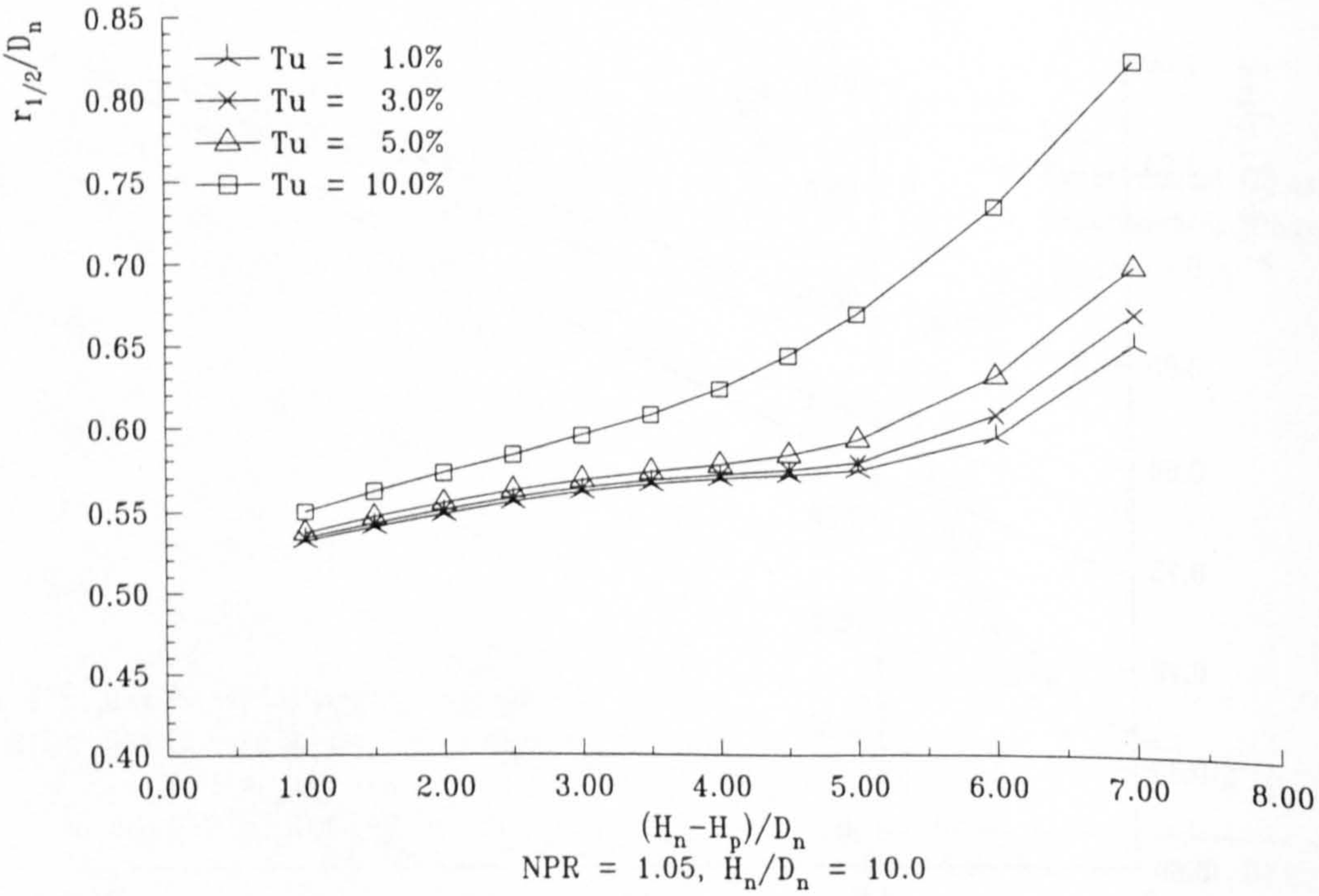

Figure 5.11 : k-ε Predicted Non-dimensional Free Jet Thickness for Differing Initial Turbulence Intensity

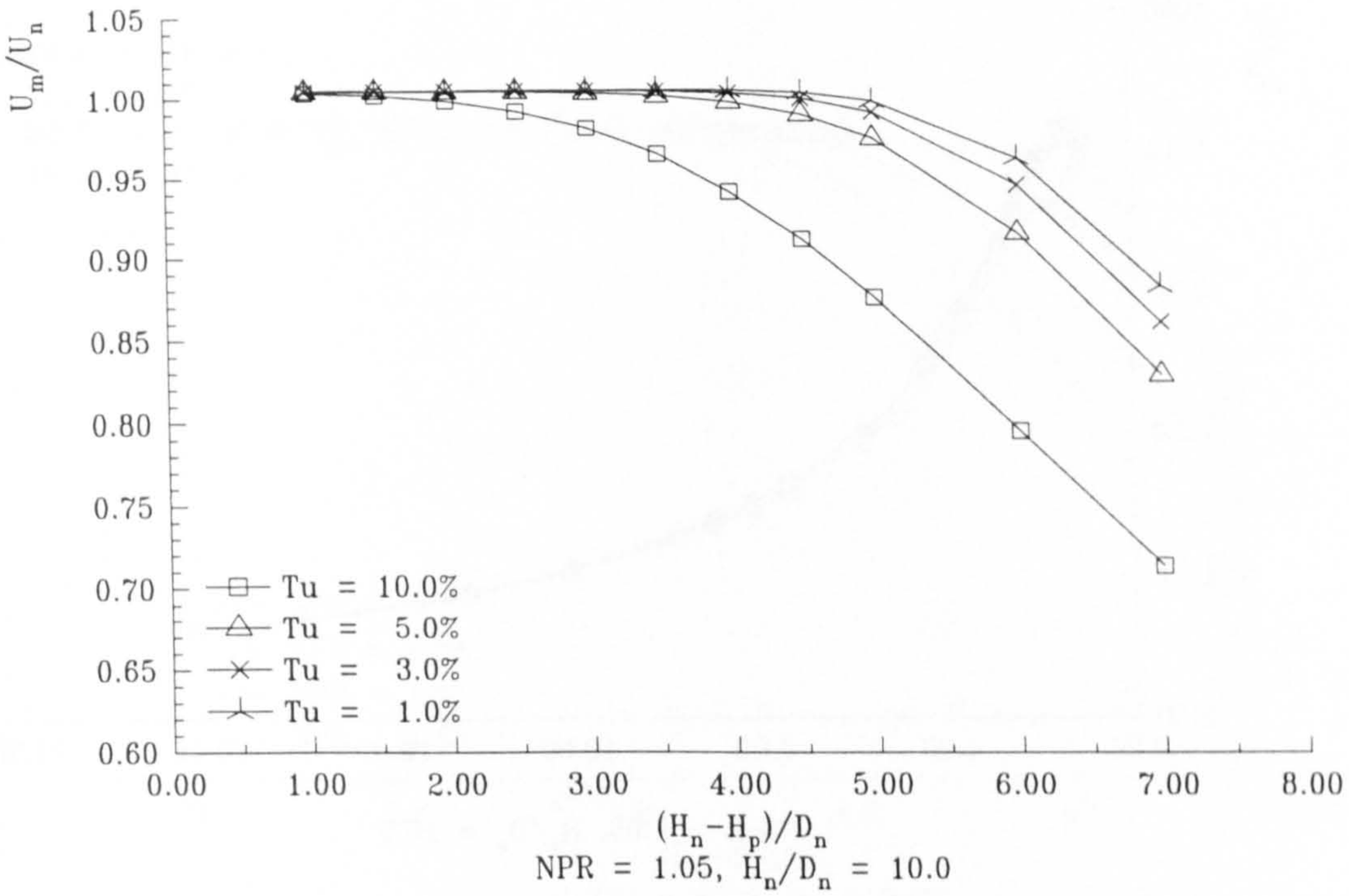

Figure 5.12 : k-ε Predicted Non-dimensional Free Jet Velocity Decay for Differing Initial Turbulence Intensity

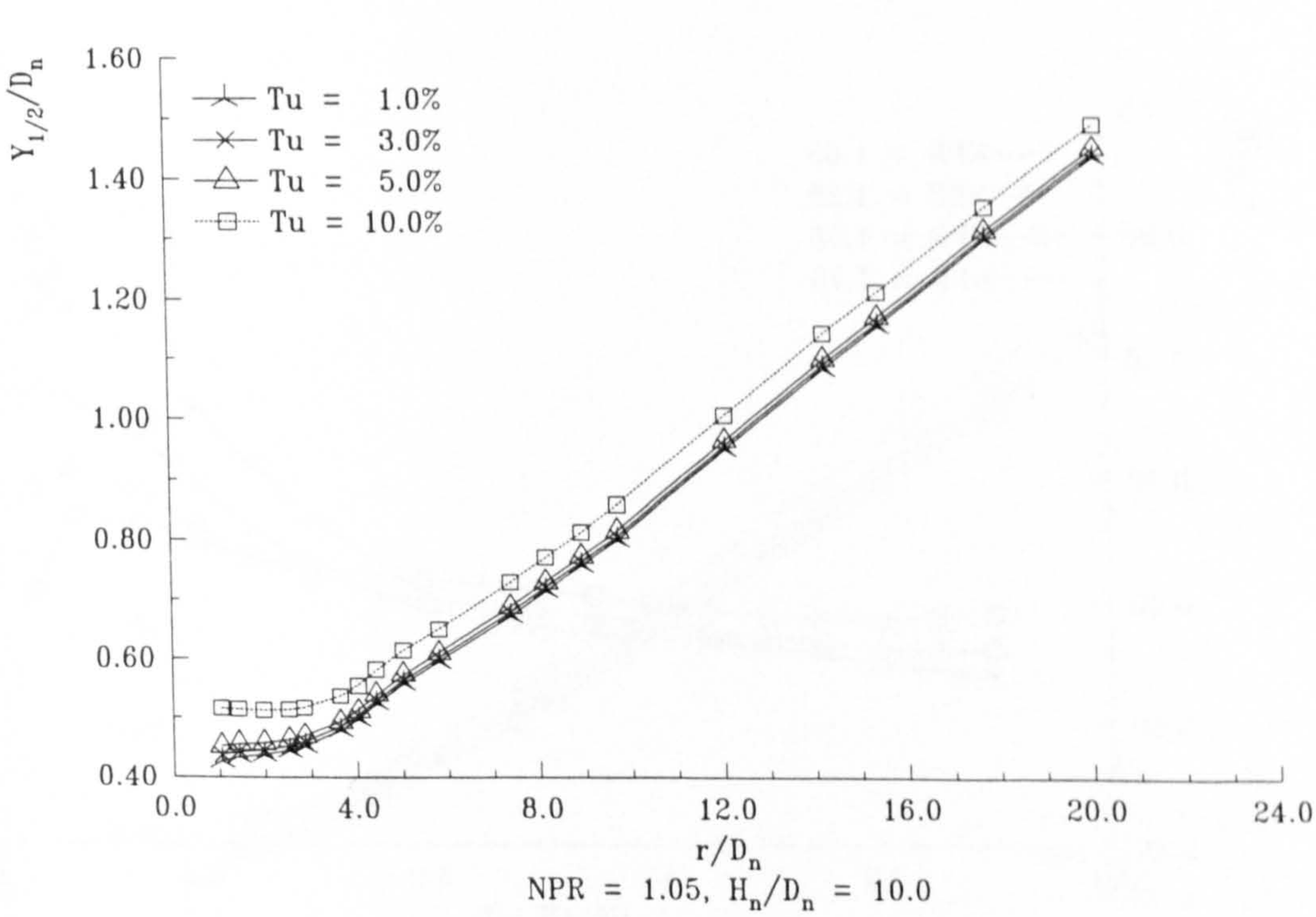

Figure 5.13 : k-ε Predicted Non-dimensional Wall Jet Thickness against Radial Location for Differing Initial Turbulence Intensity

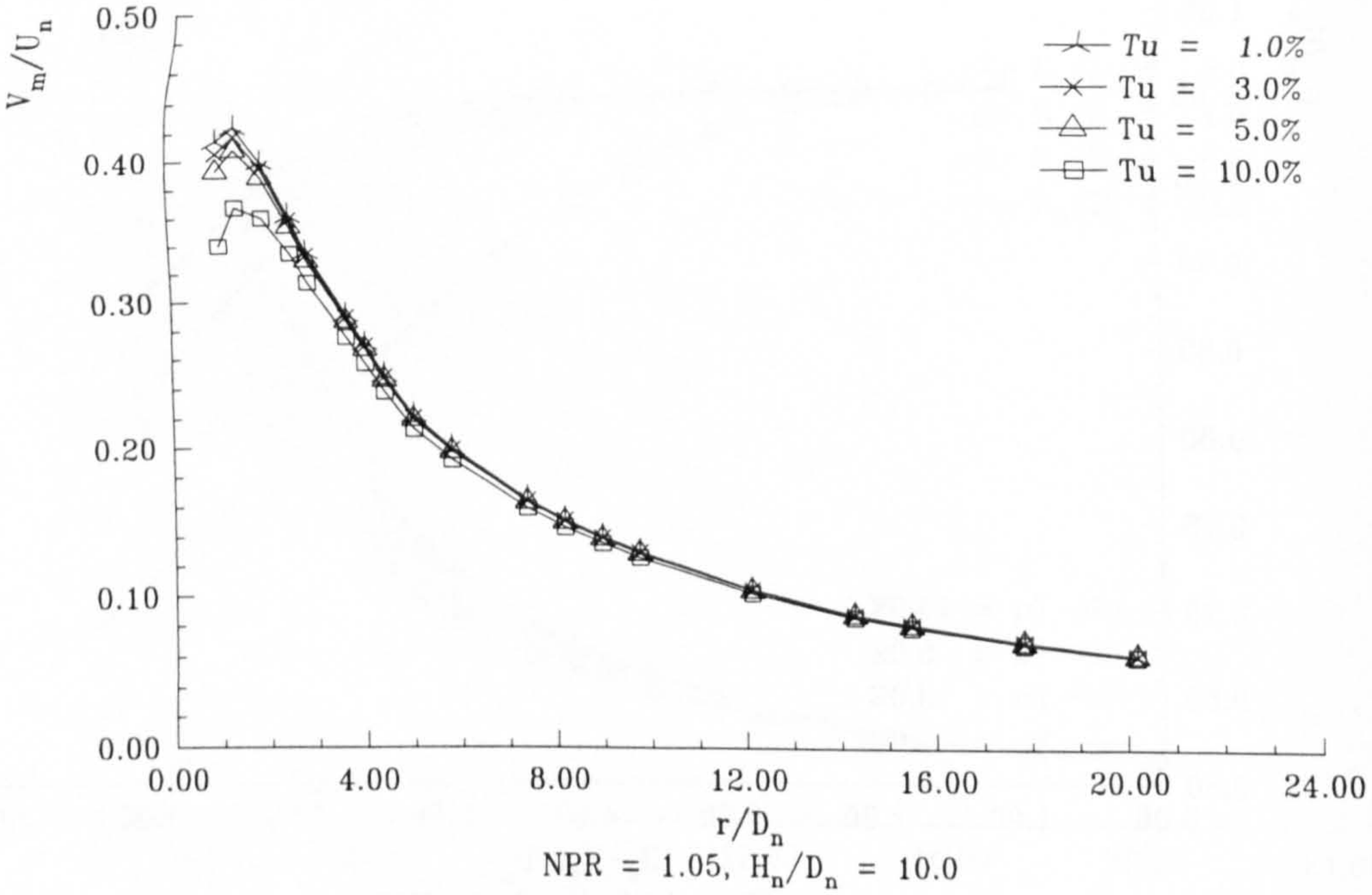

Figure 5.14 : k-ε Predicted Non-dimensional Wall Jet Velocity Decay against Radial Location for Differing Initial Turbulence Intensity

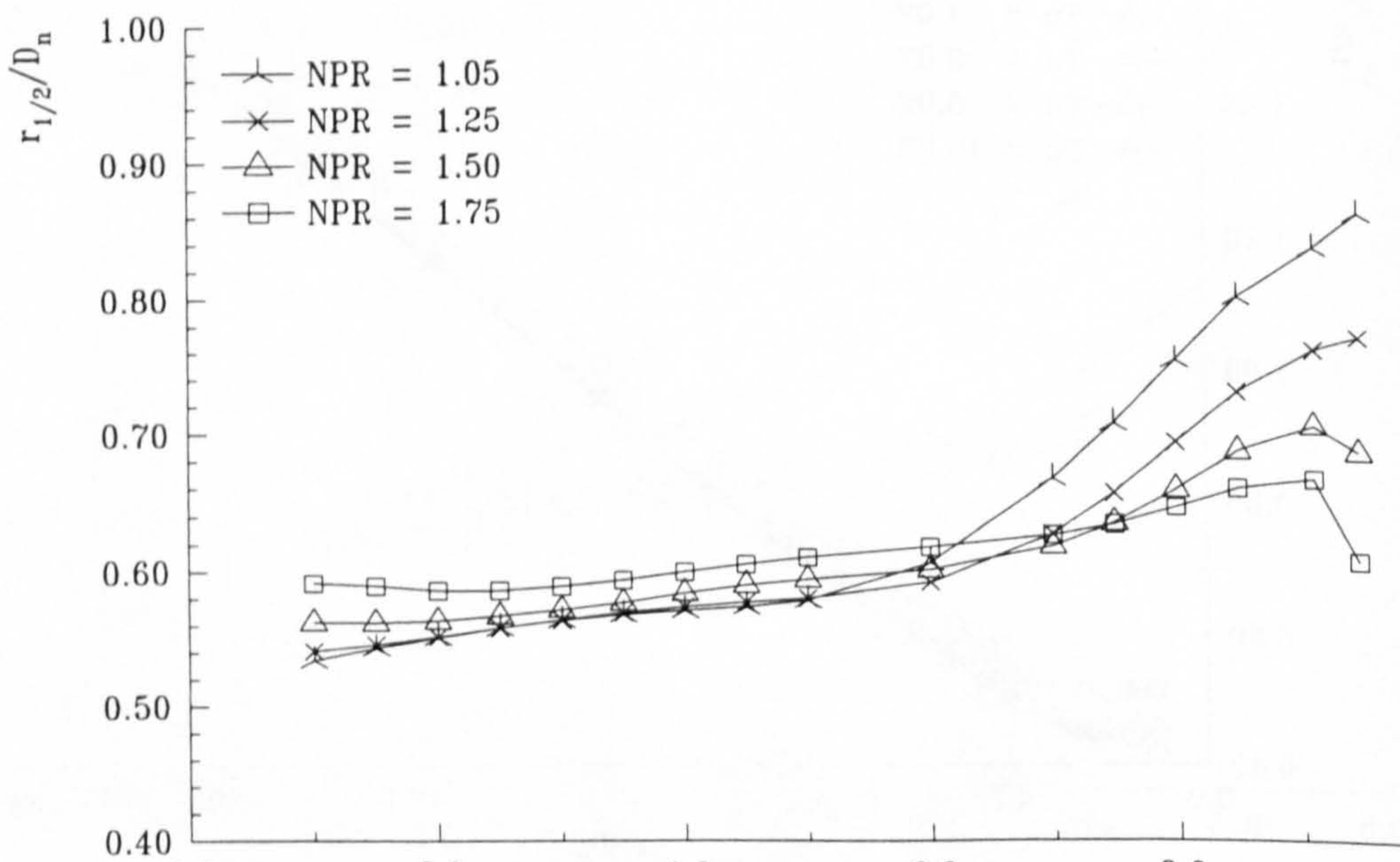

Figure 5.15 : k-ε Predicted Free Jet Thickness for Differing NPR

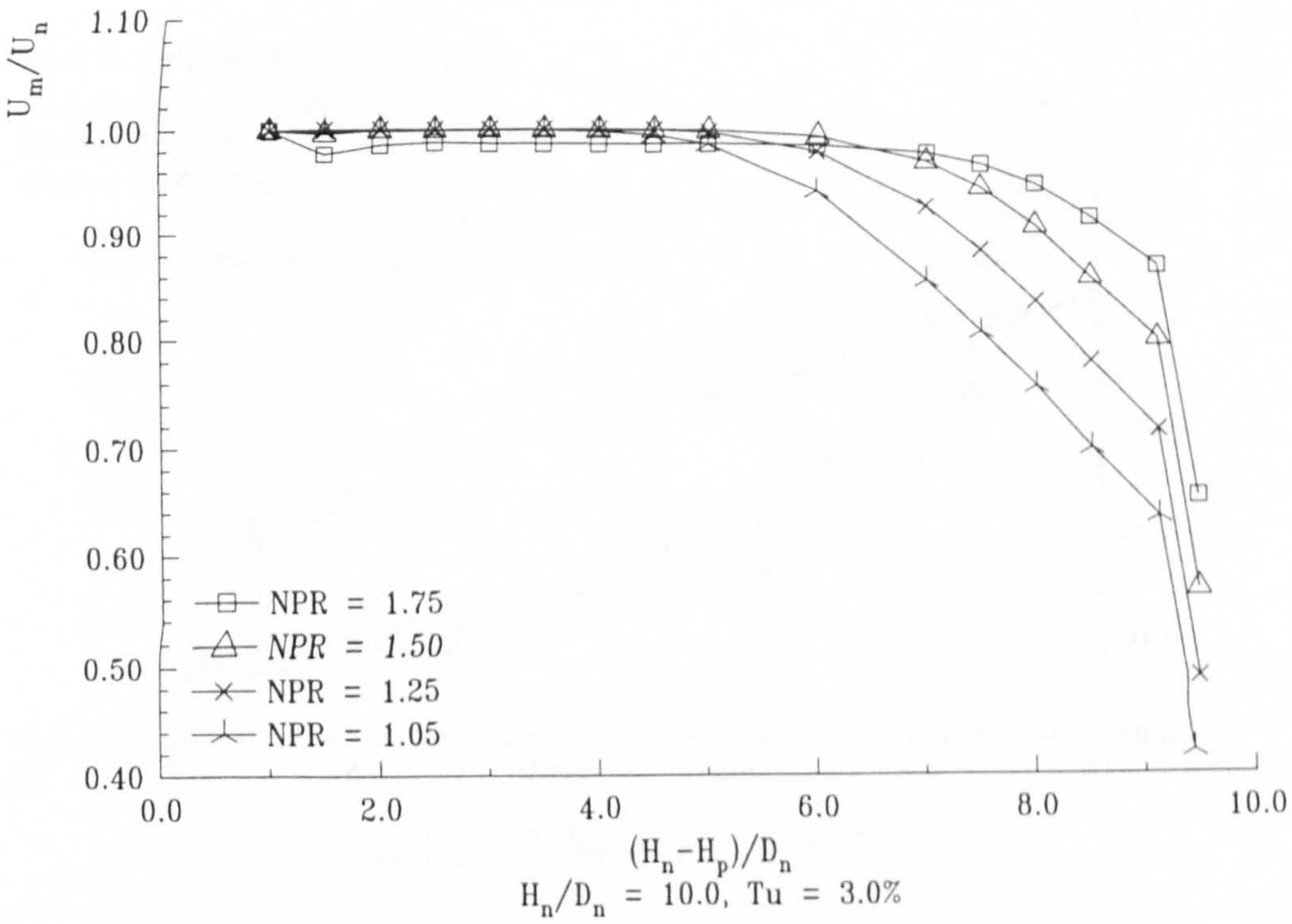

Figure 5.16 : k-ε Predicted Non-dimensional Free Jet Peak Velocity Decay for Differing NPR

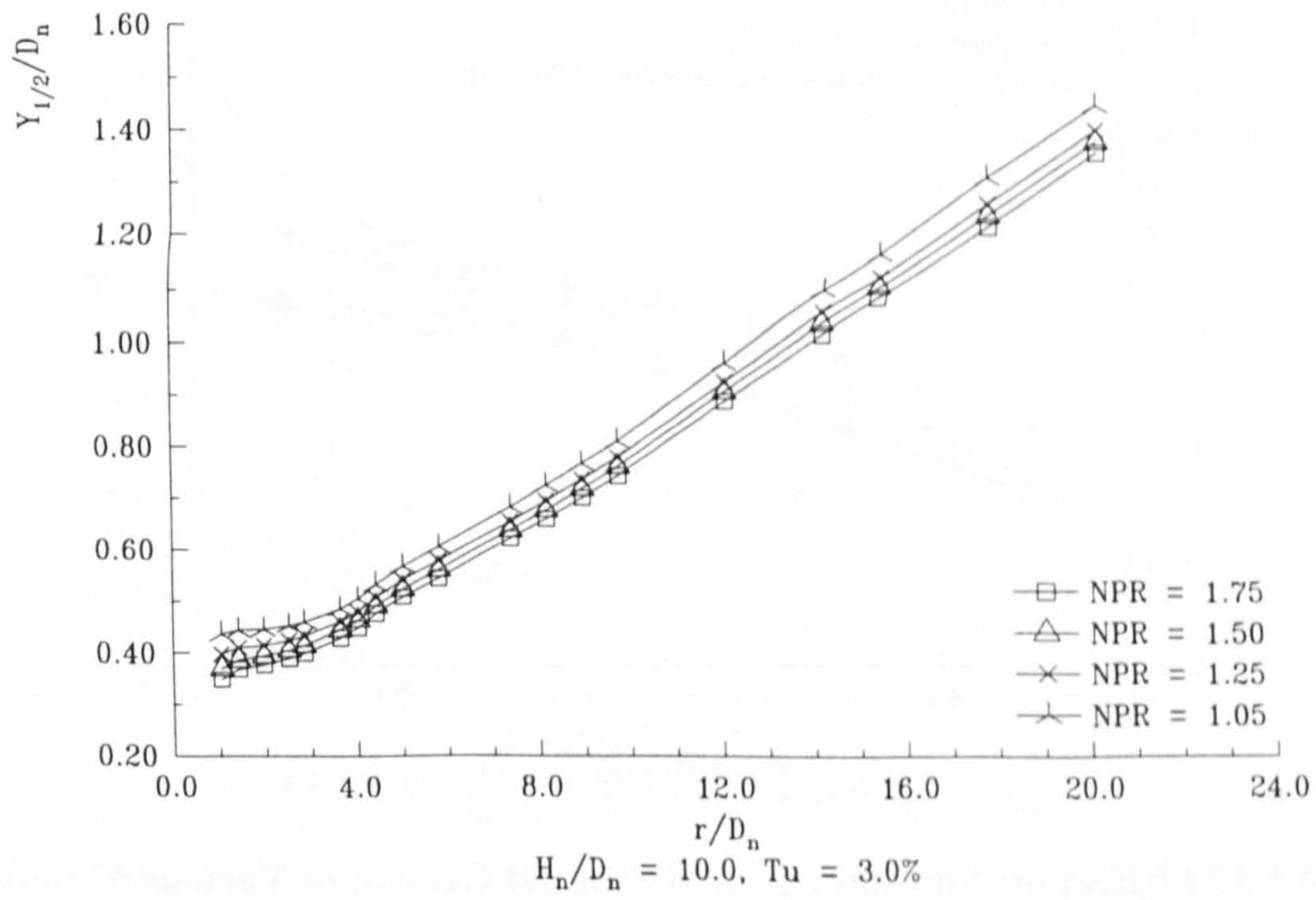

Figure 5.17 : k-ε Predicted Non-dimensional Wall Jet Thickness against Radial Location for Differing NPR

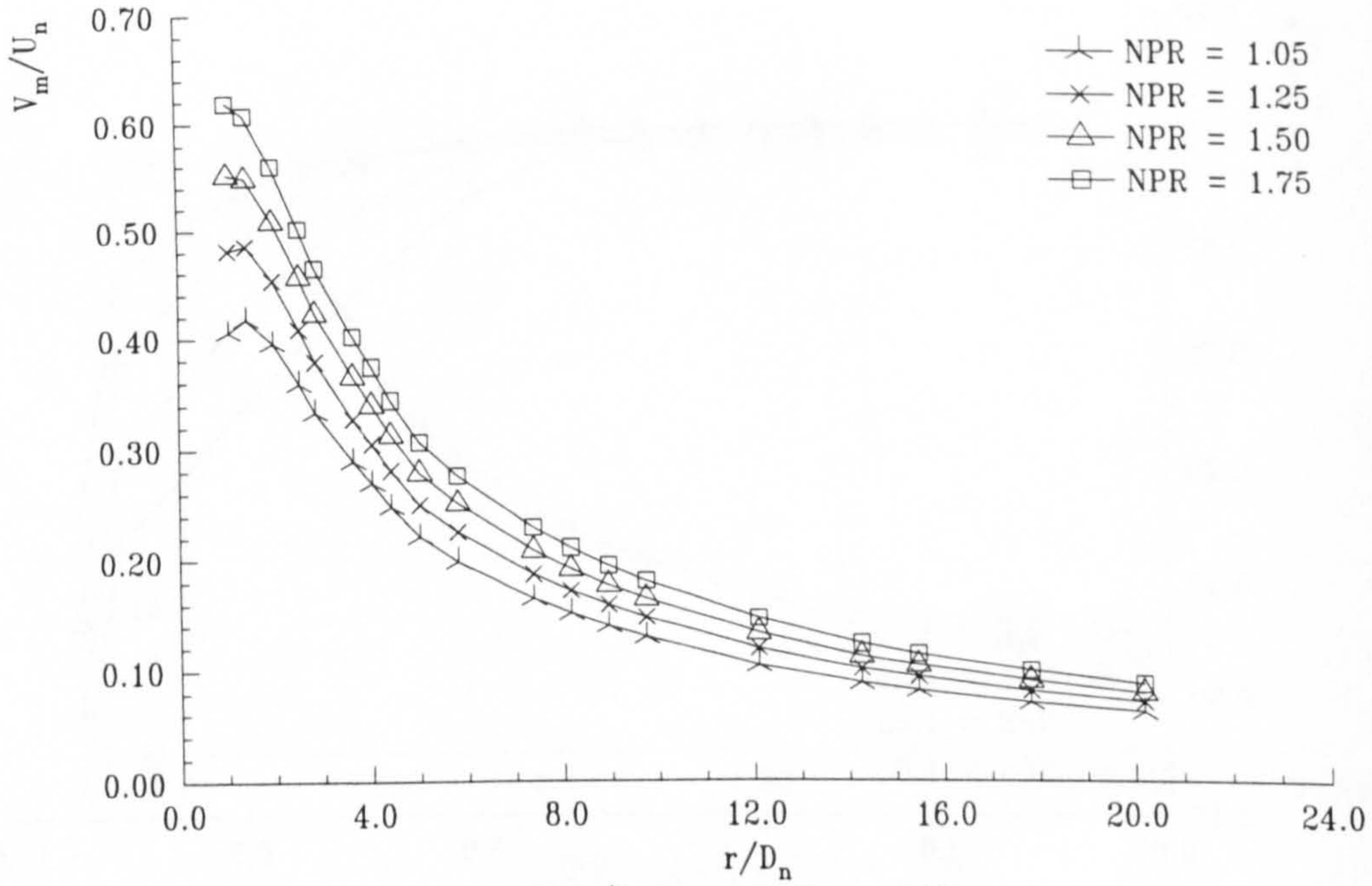

Figure 5.18 : k-ε Predicted Non-dimensional Wall Jet Peak Velocity Decay against Radial Location for Differing NPR

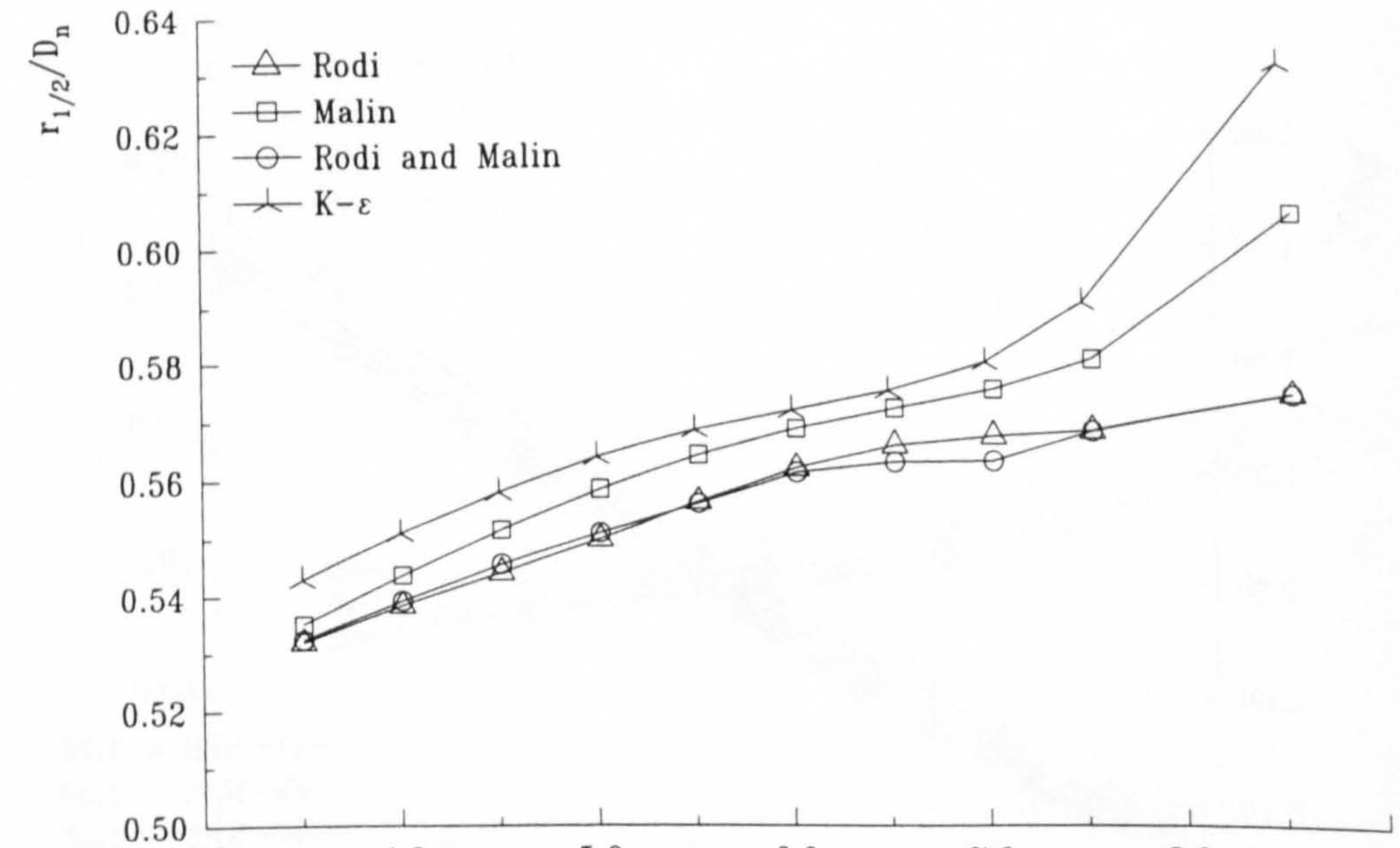

Figure 5.19 : Effect on Non-dimensional Free Jet Growth of Various Modifications to the Standard k-ε Turbulence Model

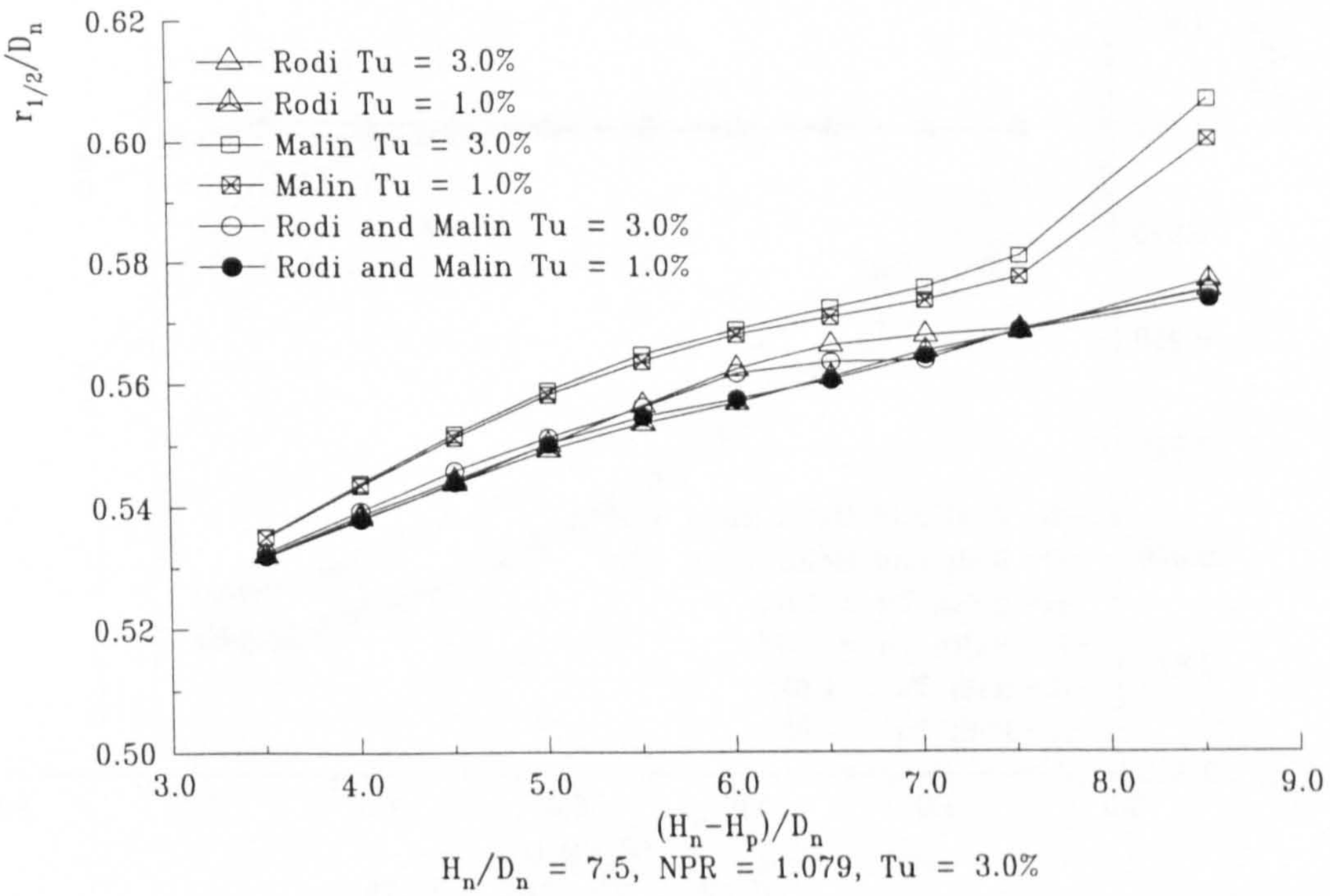

Figure 5.20 : Effect of Differing Initial Turbulence Intensities on the Prediction of Non-dimensional Free Jet Growth using Various Modifications to the Standard k-ε Turbulence Model

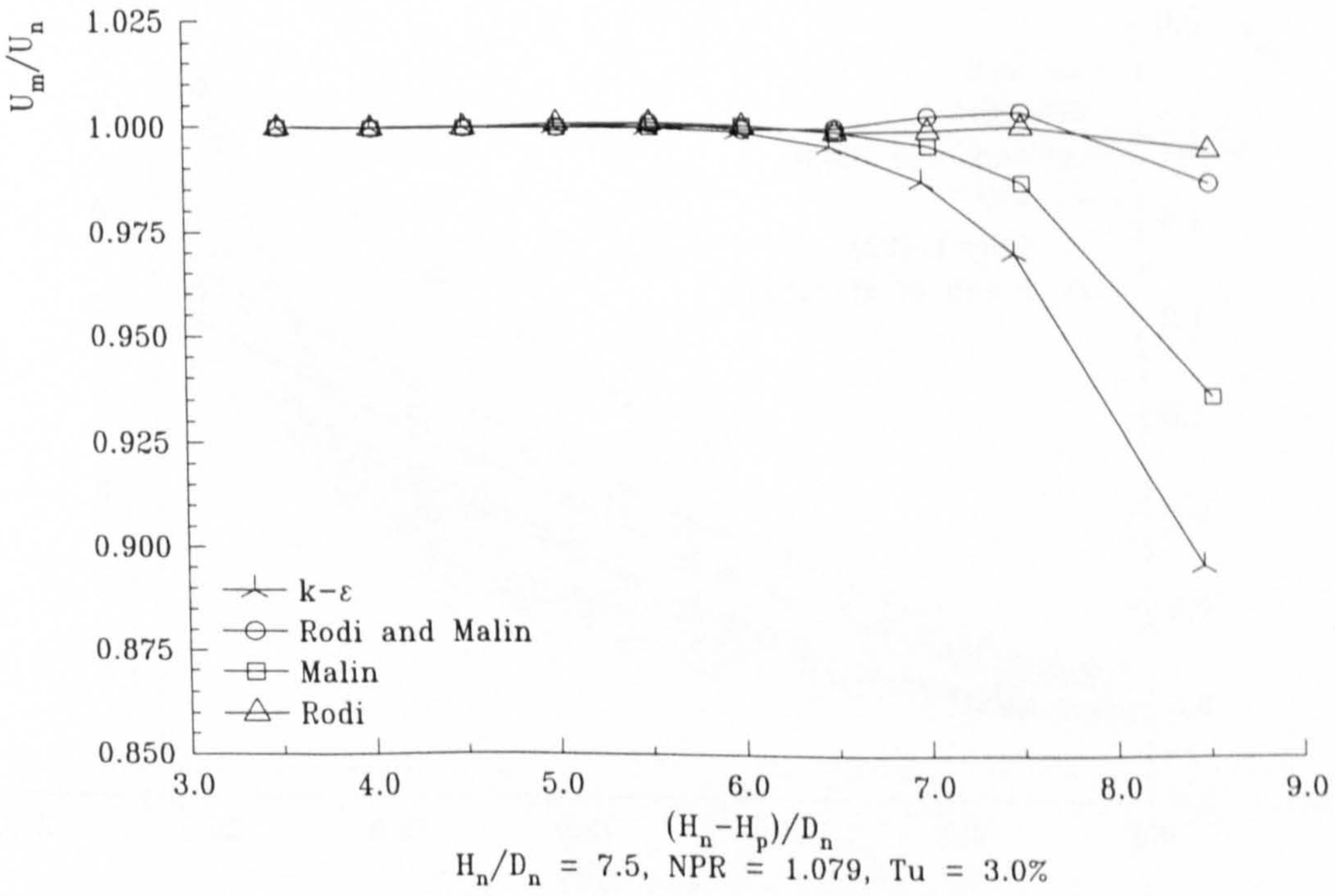

Figure 5.21 : Effect on Non-dimensional Free Jet Peak Velocity Decay of Various Modifications to the Standard k-ε Turbulence Model

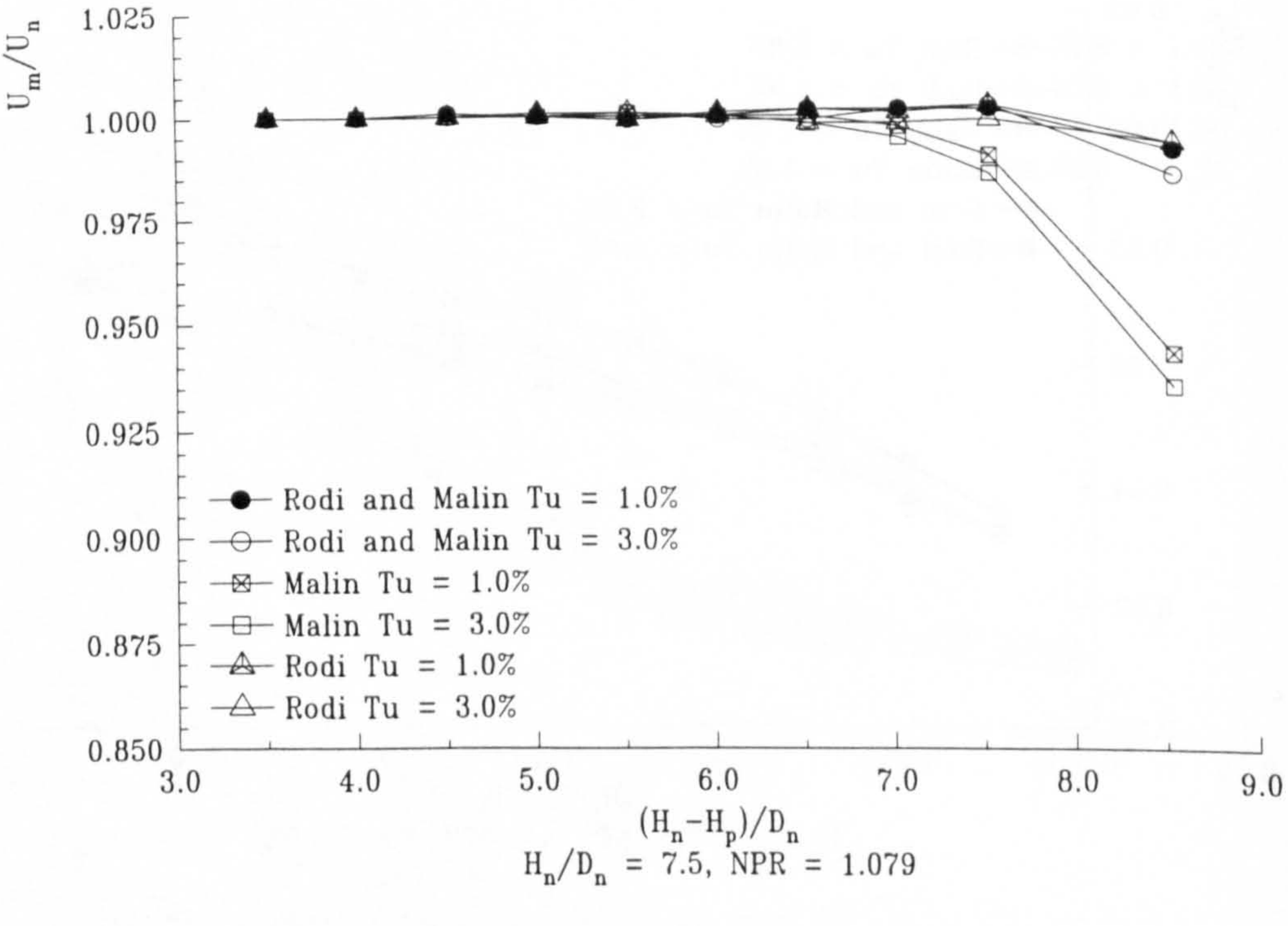

Figure 5.22 : Effect of Differing Initial Turbulence Intensities on the Prediction of Non-dimensional Free Jet Peak Velocity Decay using Various Modifications to the Standard k-ε Turbulence Model

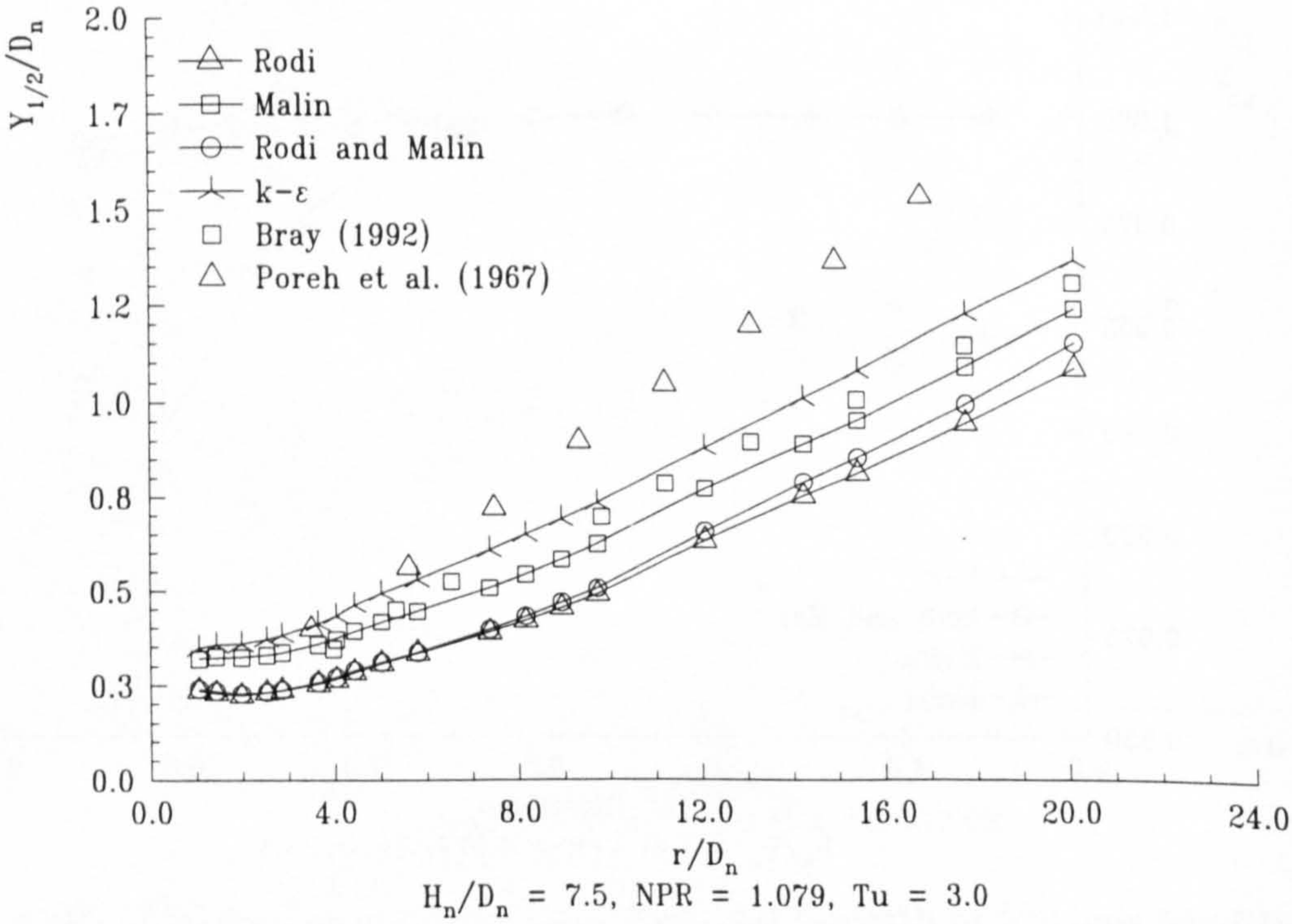

Figure 5.23 : Effect on Non-dimensional Wall Jet Growth of Various Modifications to the Standard k-ε Turbulence Model

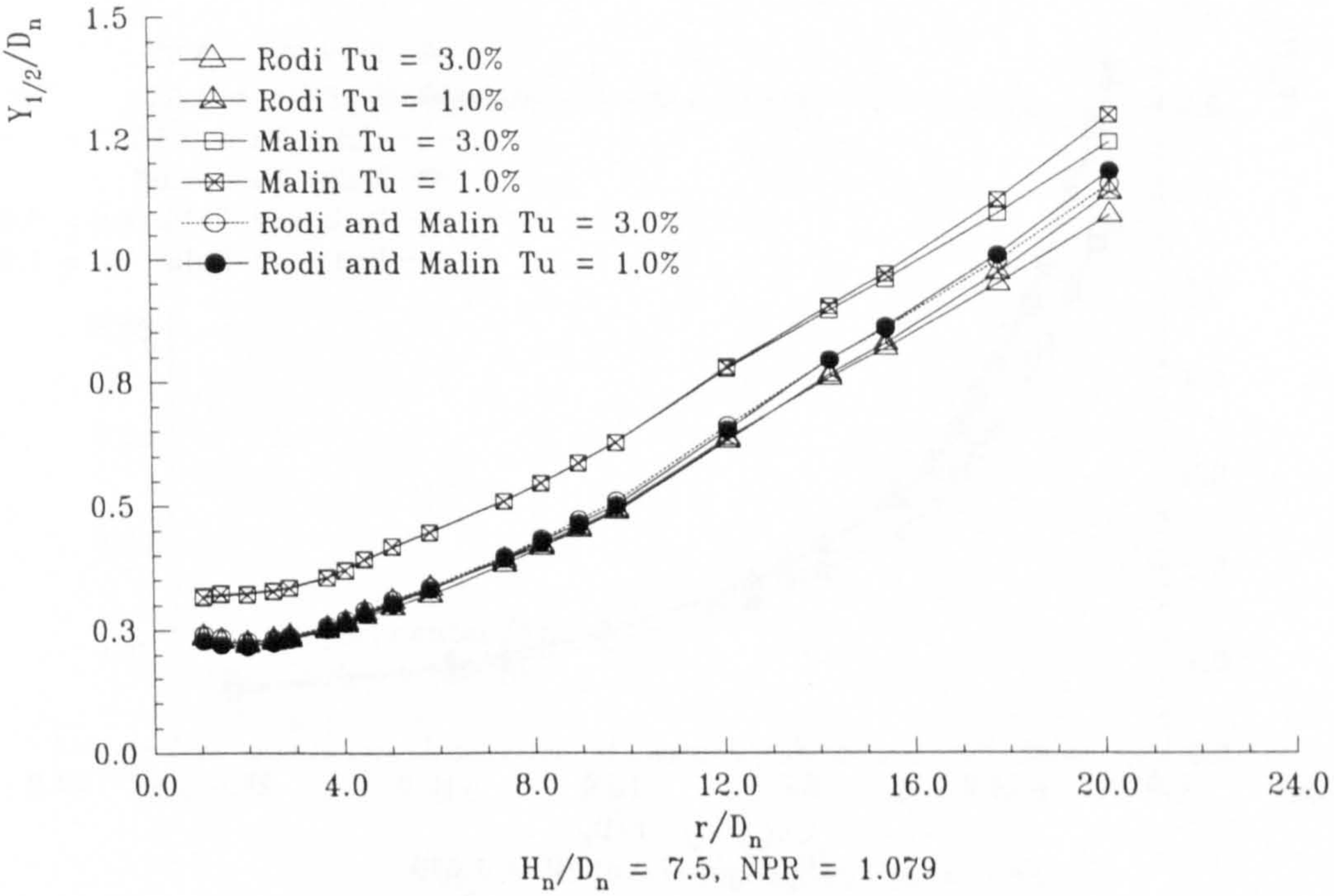

Figure 5.24 : Effect of Differing Initial Turbulence Intensities on the Prediction of Non-dimensional Wall Jet Growth using Various Modifications to the Standard k-ε Turbulence Model

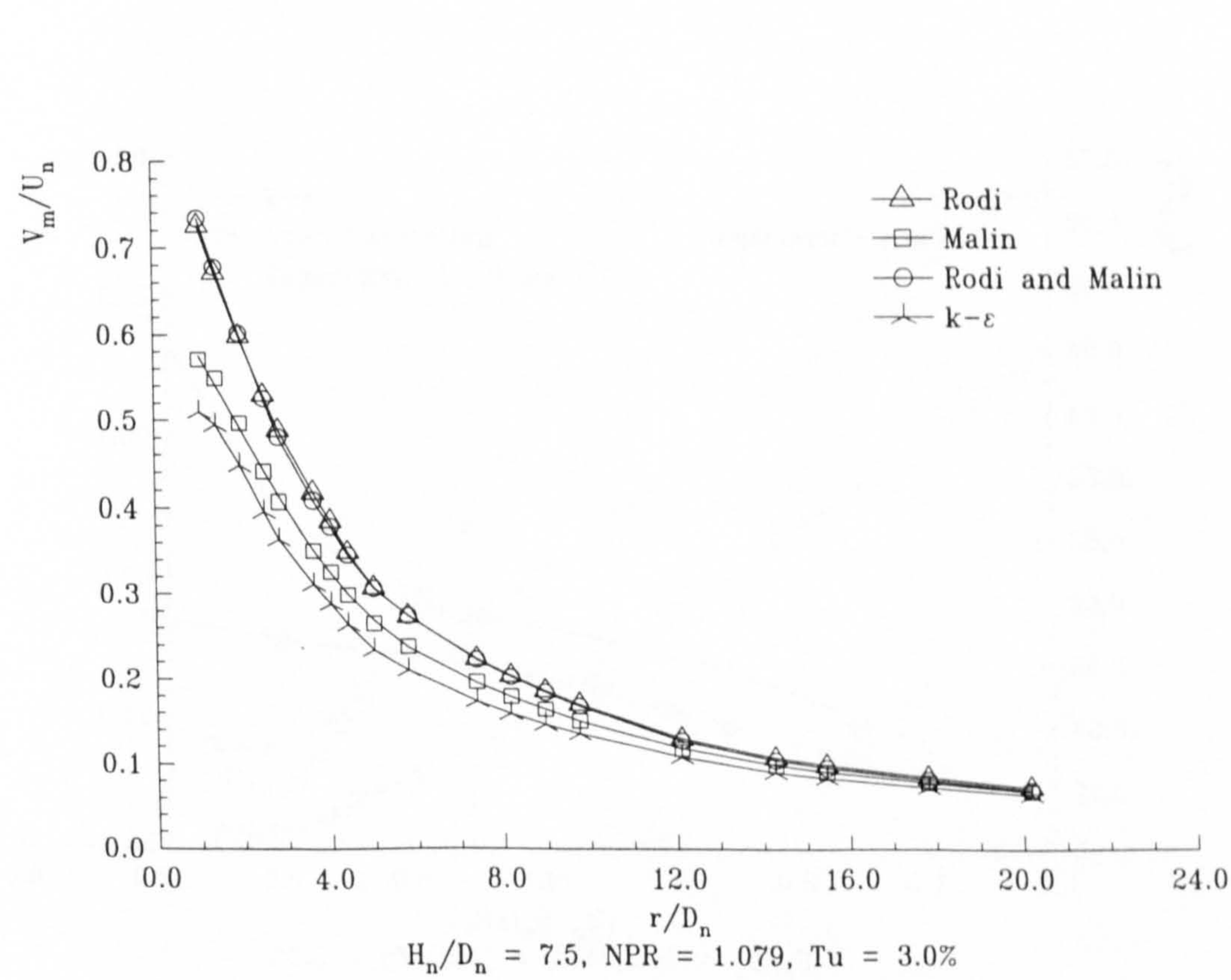

Figure 5.25 : Effect on Non-dimensional Wall Jet Peak Velocity Decay of Various Modifications to the Standard k-ε Turbulence Model

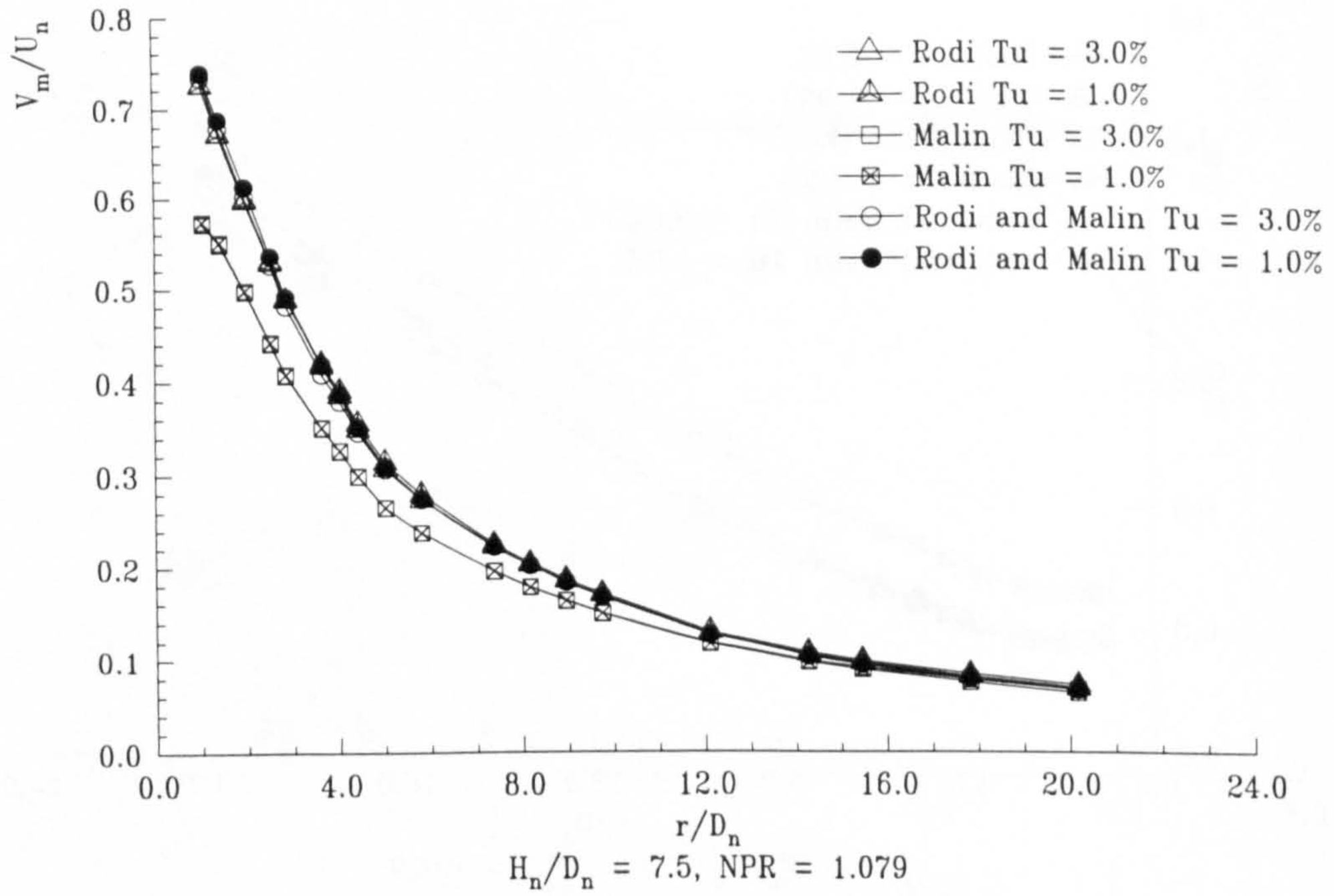

Figure 5.26 : Effect of Differing Initial Turbulence Intensities on the Prediction of Non-dimensional Wall Jet Peak Velocity Decay using Various Modifications to the Standard k-ε Turbulence Model

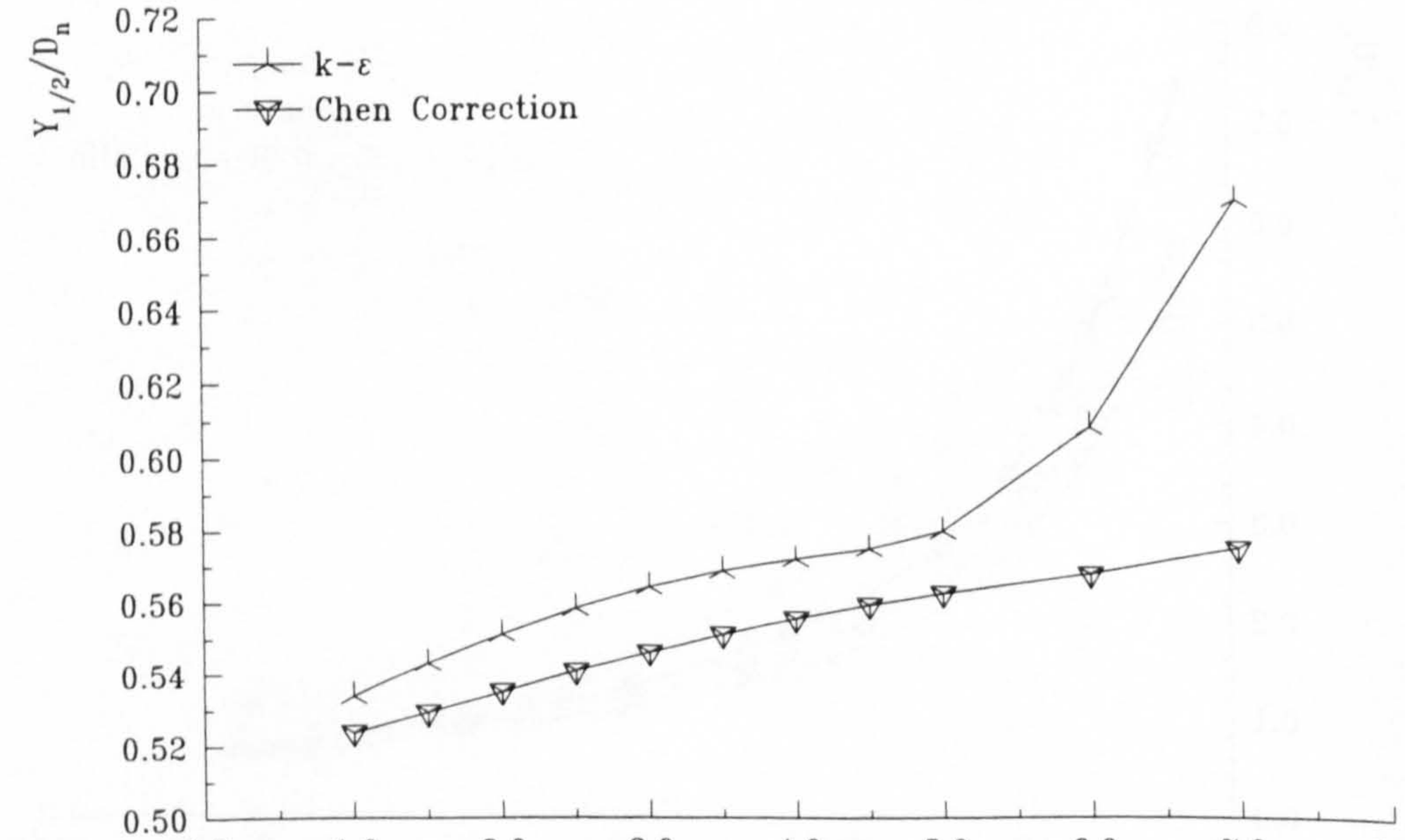

Figure 5.27 : Effect of Chen Correction on the Prediction of Non-dimensional Free Jet Growth

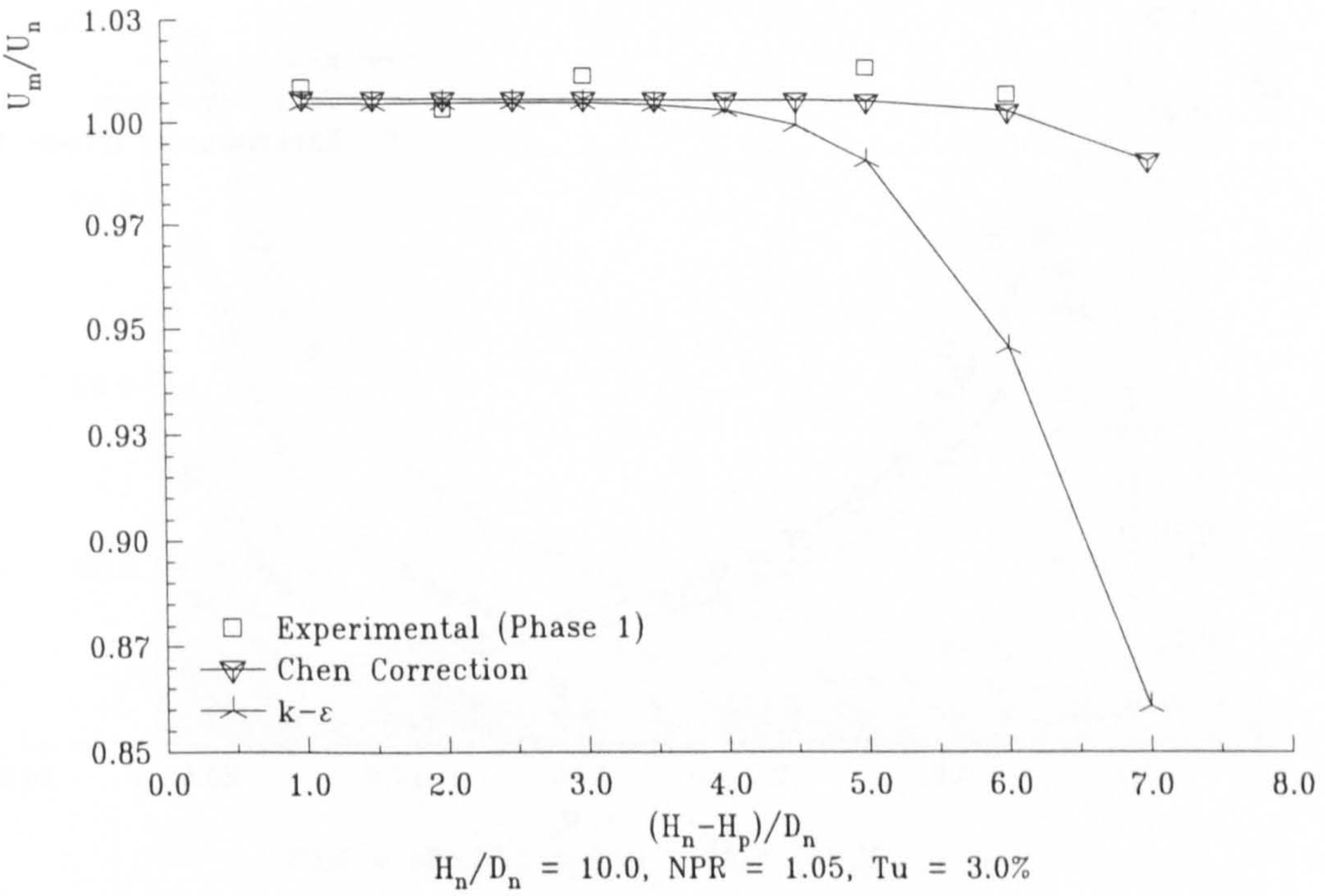

Figure 5.28 : Effect of Chen Correction on the Prediction of Non-dimensional Free Jet Peak Velocity Decay

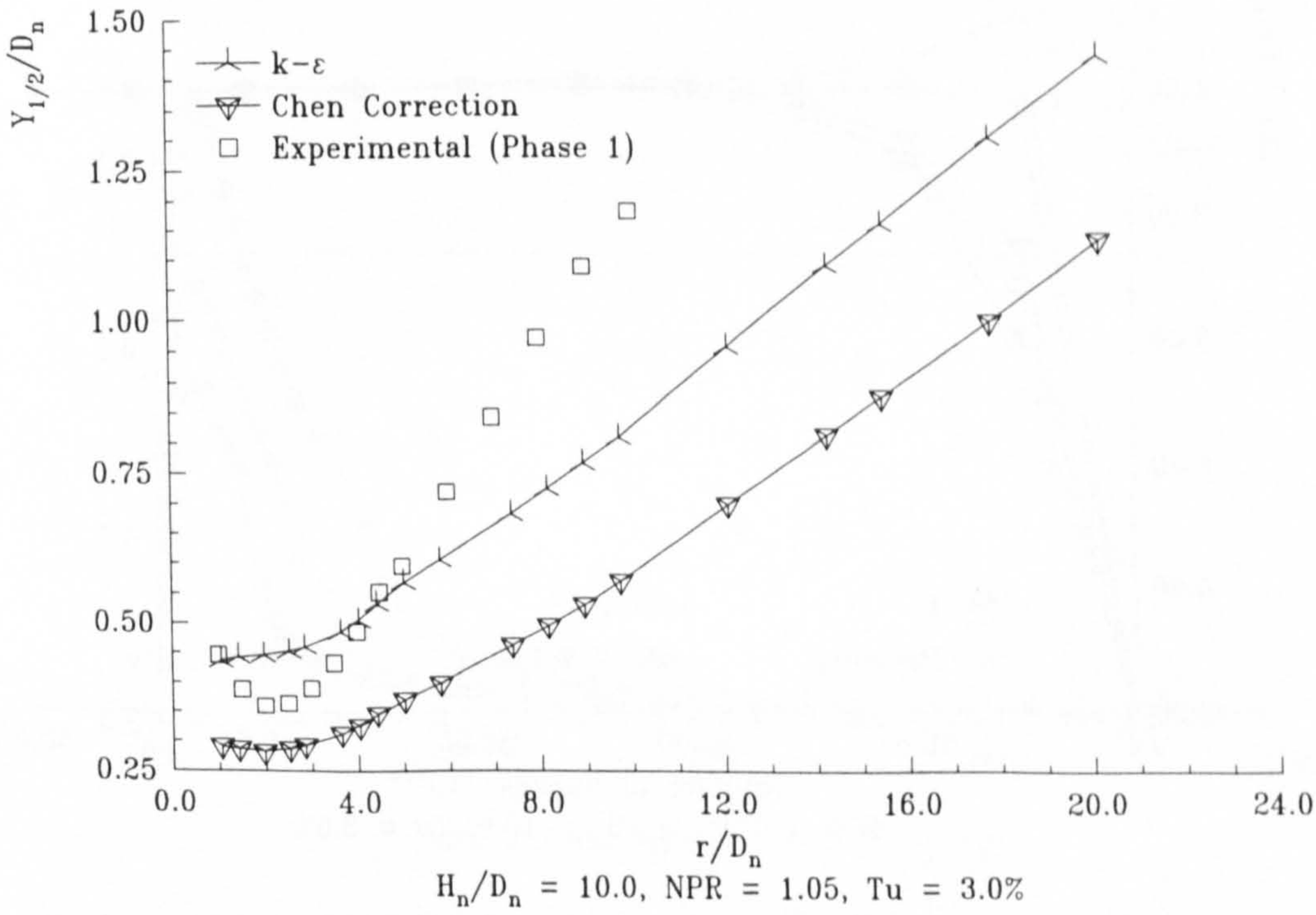

Figure 5.29 : Effect of Chen Correction on the Prediction of Non-dimensional Wall Jet Growth

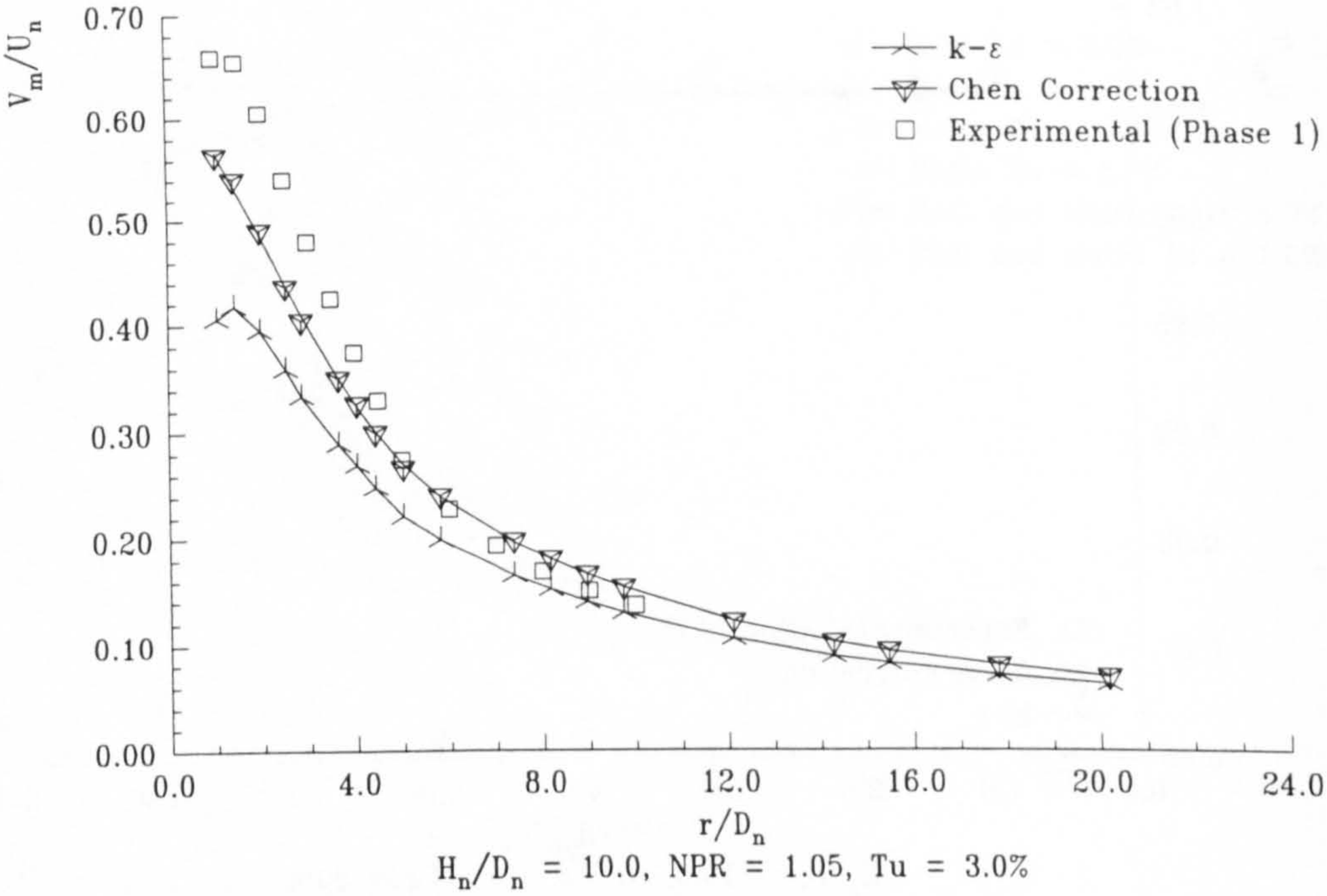

Figure 5.30 : Effect of Chen Correction on the Prediction of Non-dimensional Wall Jet Peak Velocity Decay

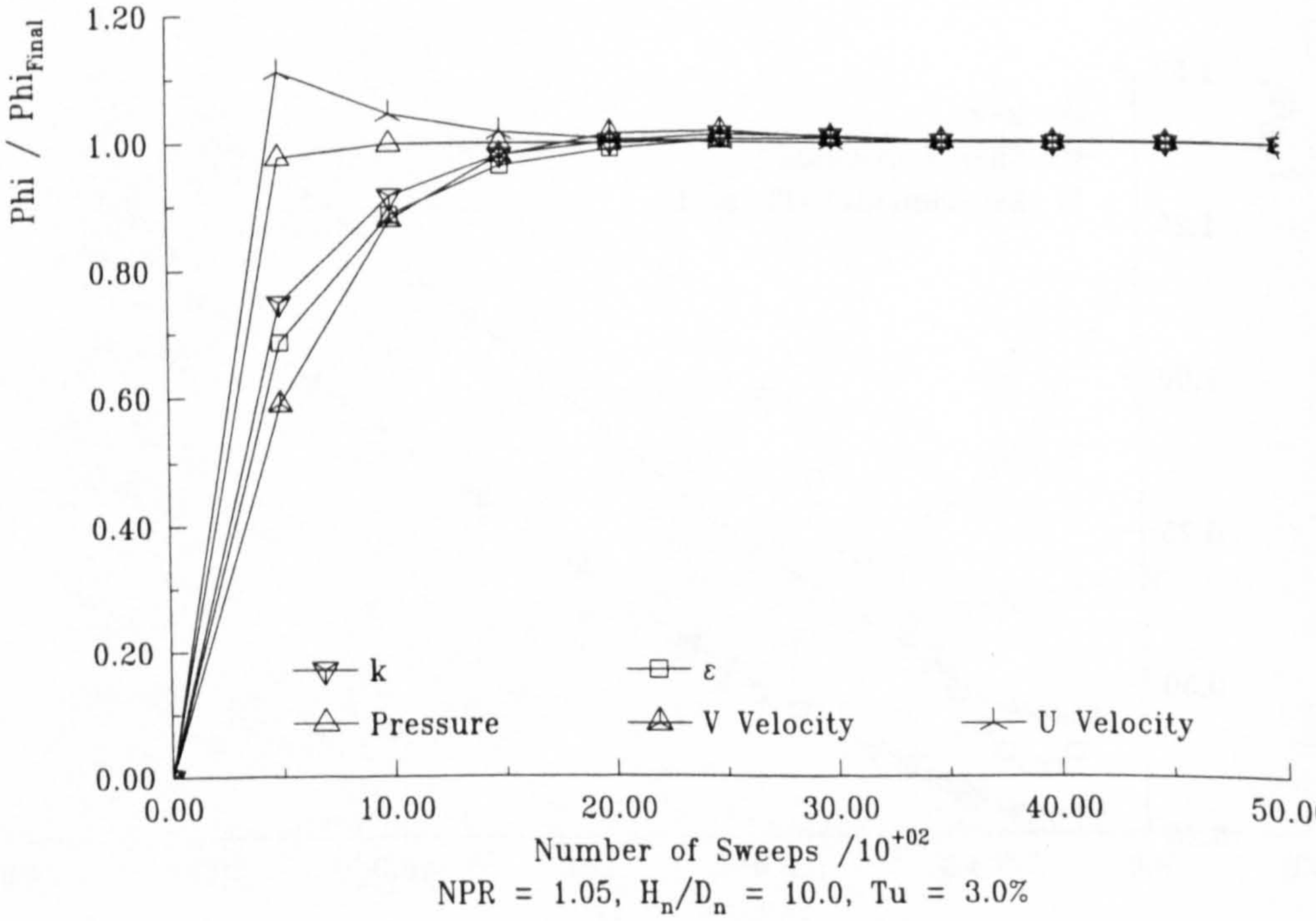

Figure 5.31 : Convergence of Low Reynolds Number k-ε Variable against Number of Sweeps

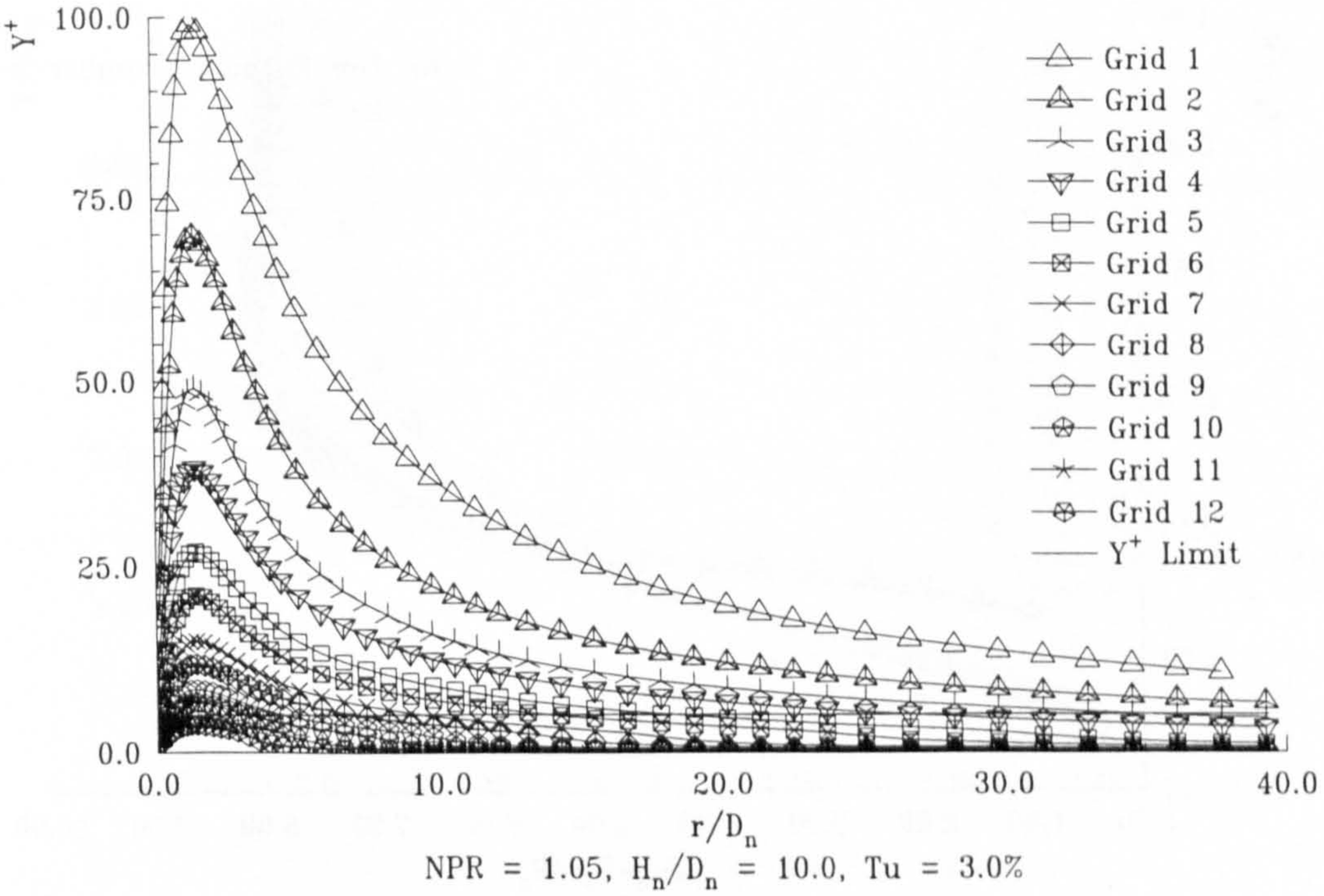

Figure 5.32 : Y^+ Against Radial Location for Grids used in Low Reynolds Number k-ε Study

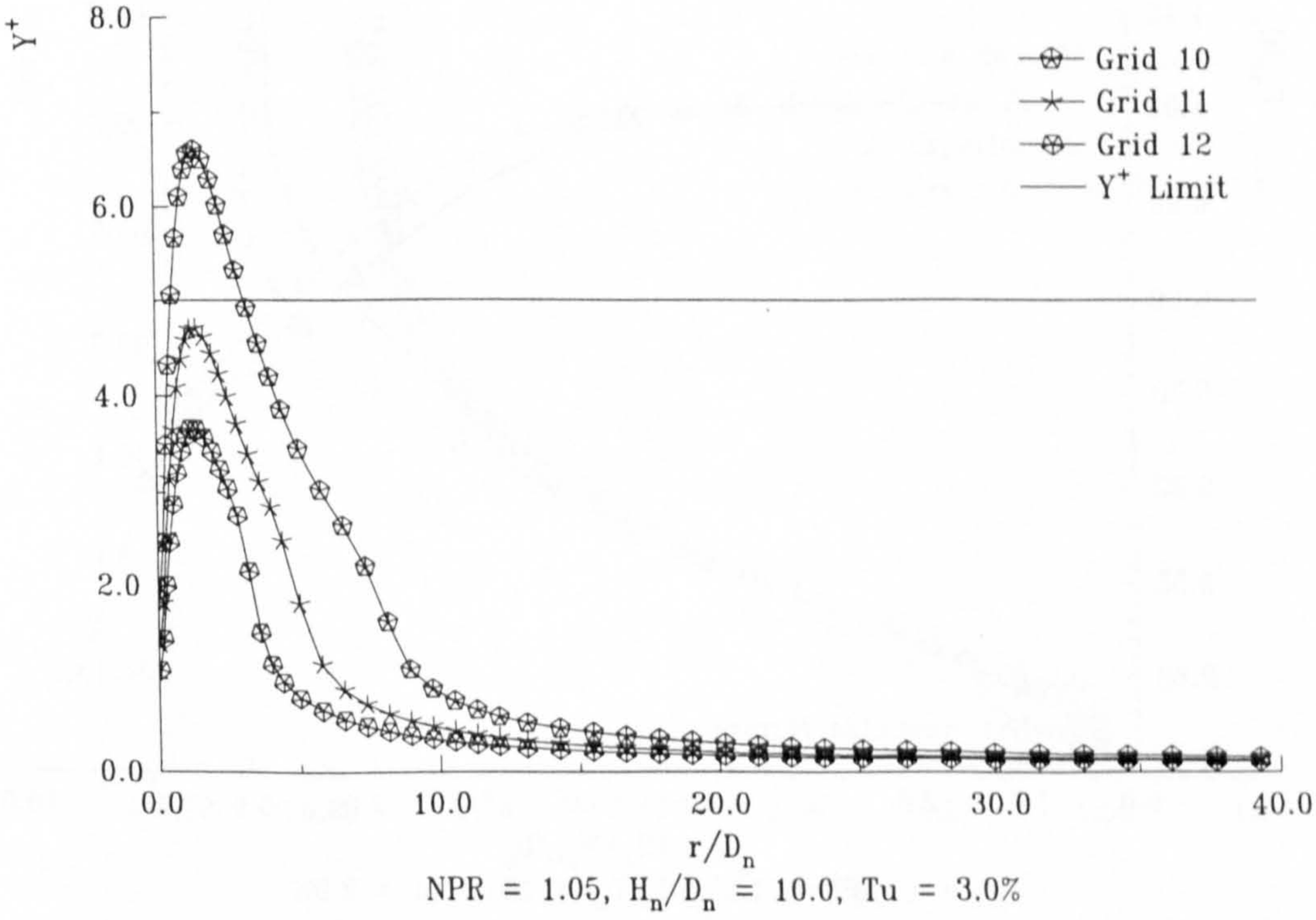

Figure 5.33 : Y^+ against Radial Location for Grid used in Low Reynolds Number k-ε Study

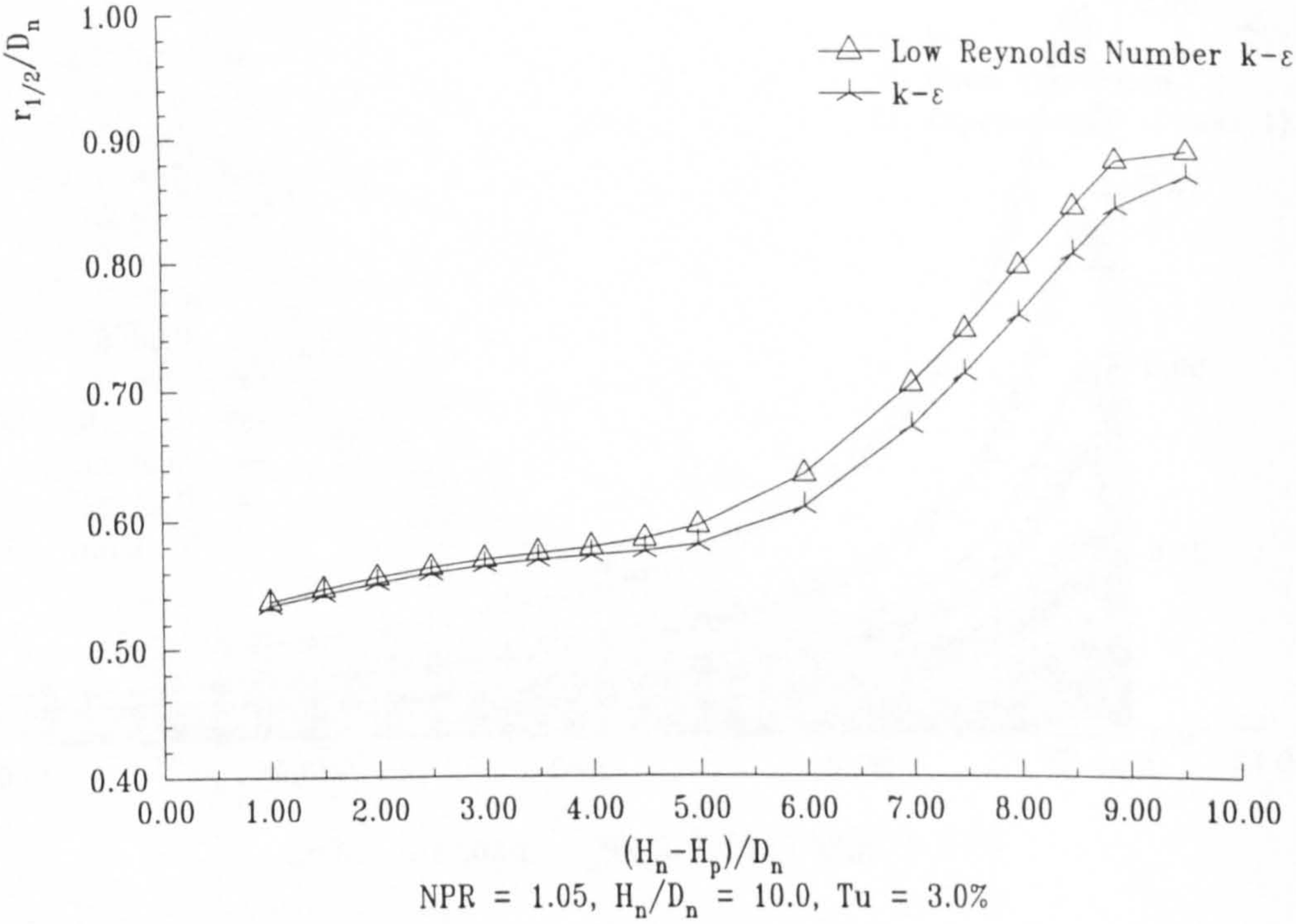

Figure 5.34 : Comparison of Low Reynolds Number and Standard k-ε Predicted Free Jet Thickness

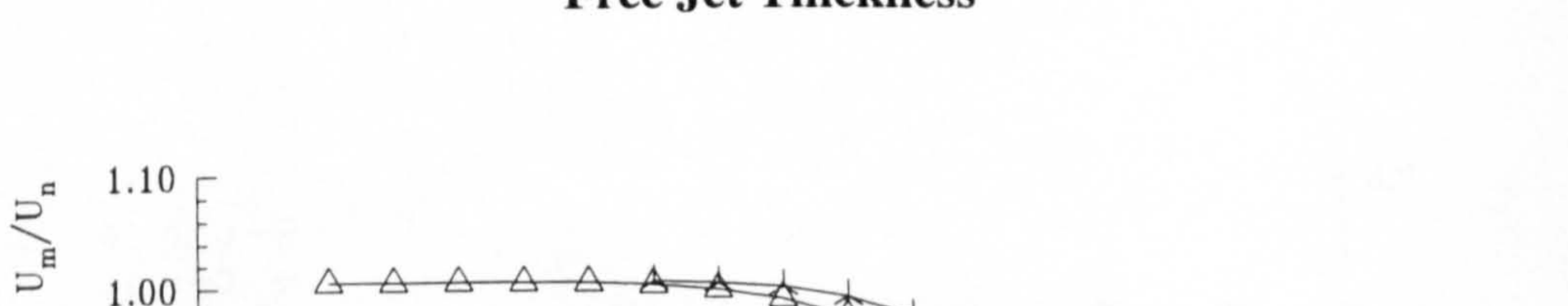

Figure 5.35 : Comparison of Low Reynolds Number and Standard k-ε Predicted Free Jet Peak Velocity

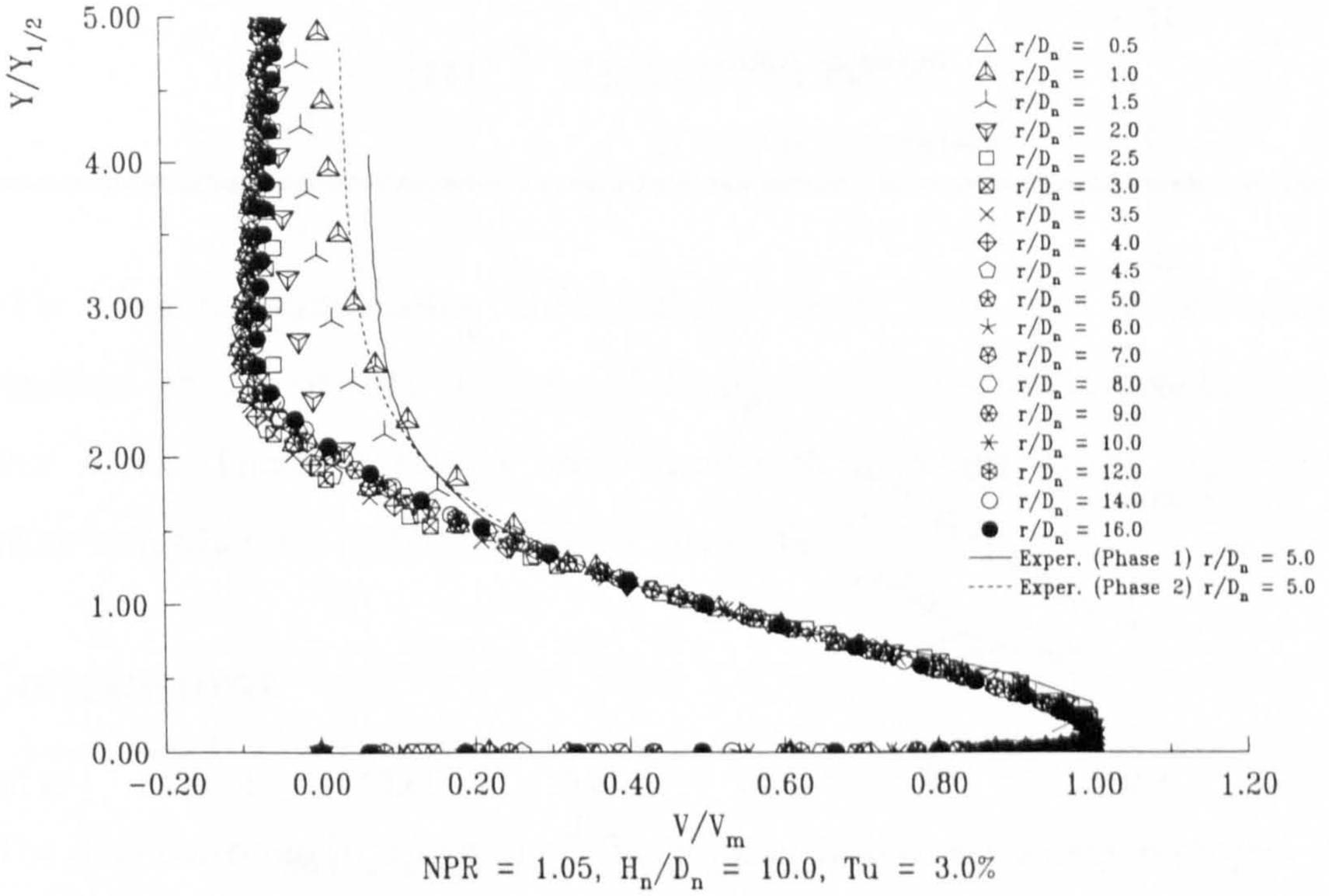

Figure 5.36 : Low Reynolds Number k-ε Non-dimensional Wall Jet Profiles

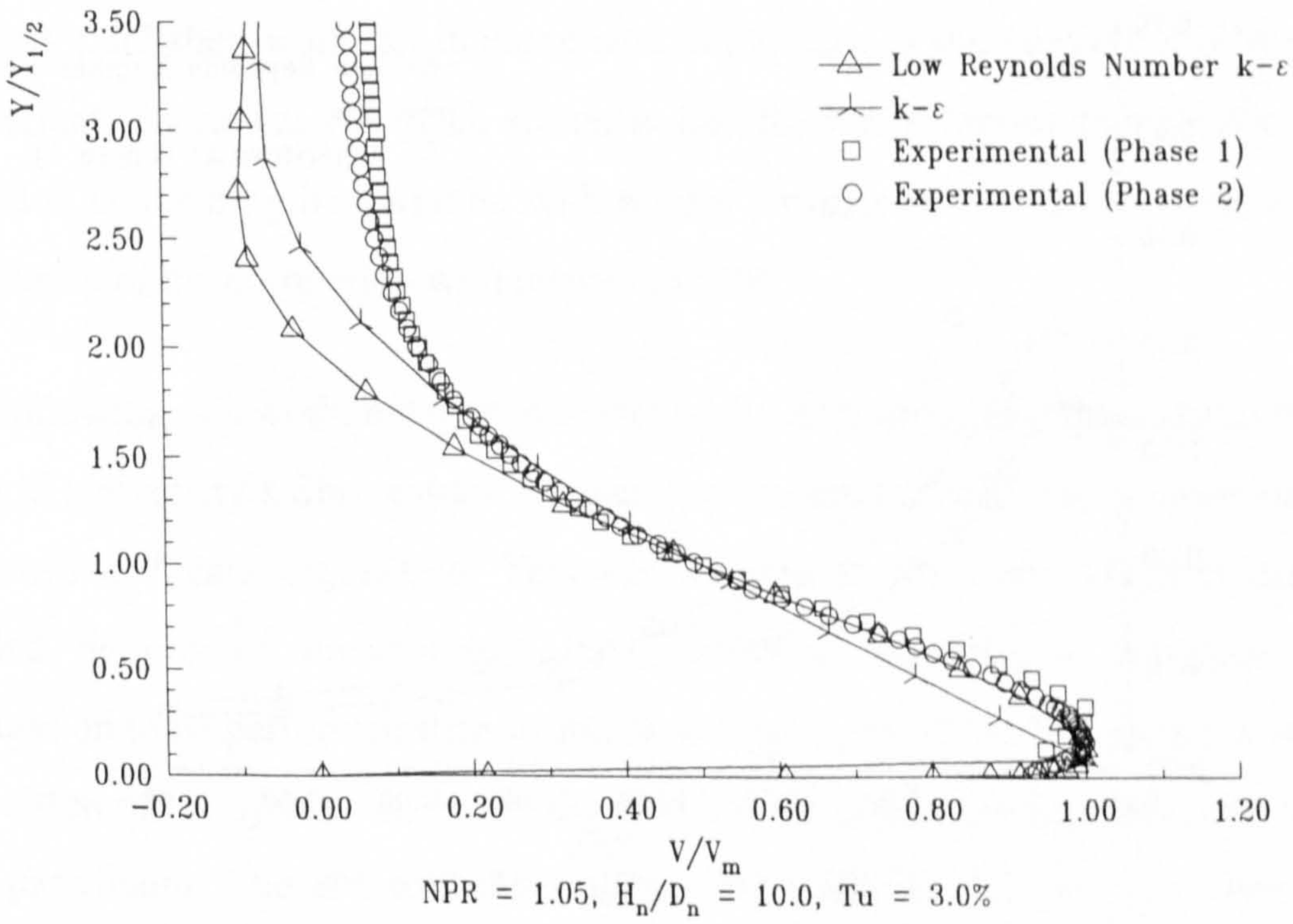

Figure 5.37 : Comparison of low Reynolds Number and Standard k-ε with Experimental Data

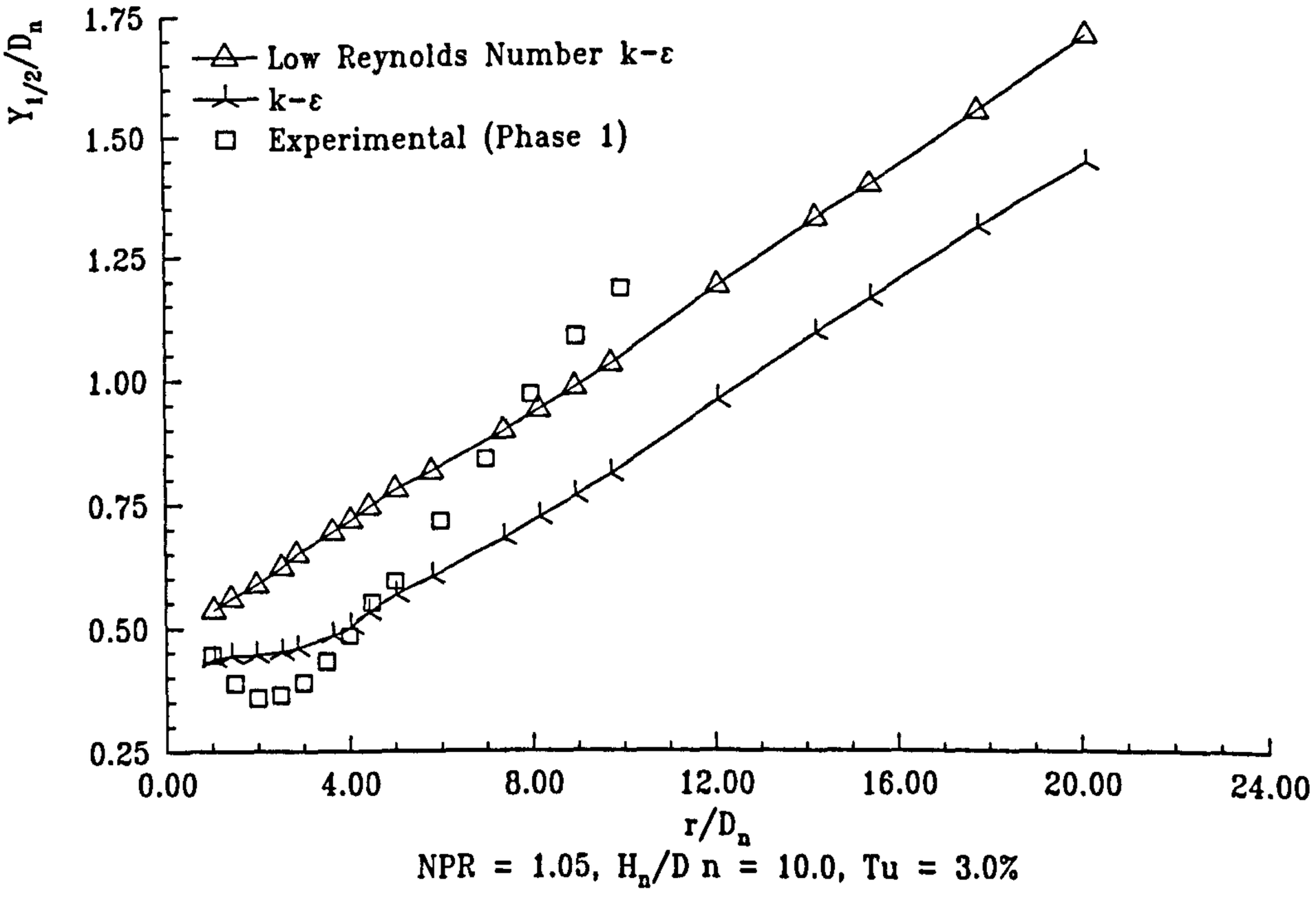

Figure 5.38 : Comparison of Low Reynolds Number and Standard k-ε with Experimental Data

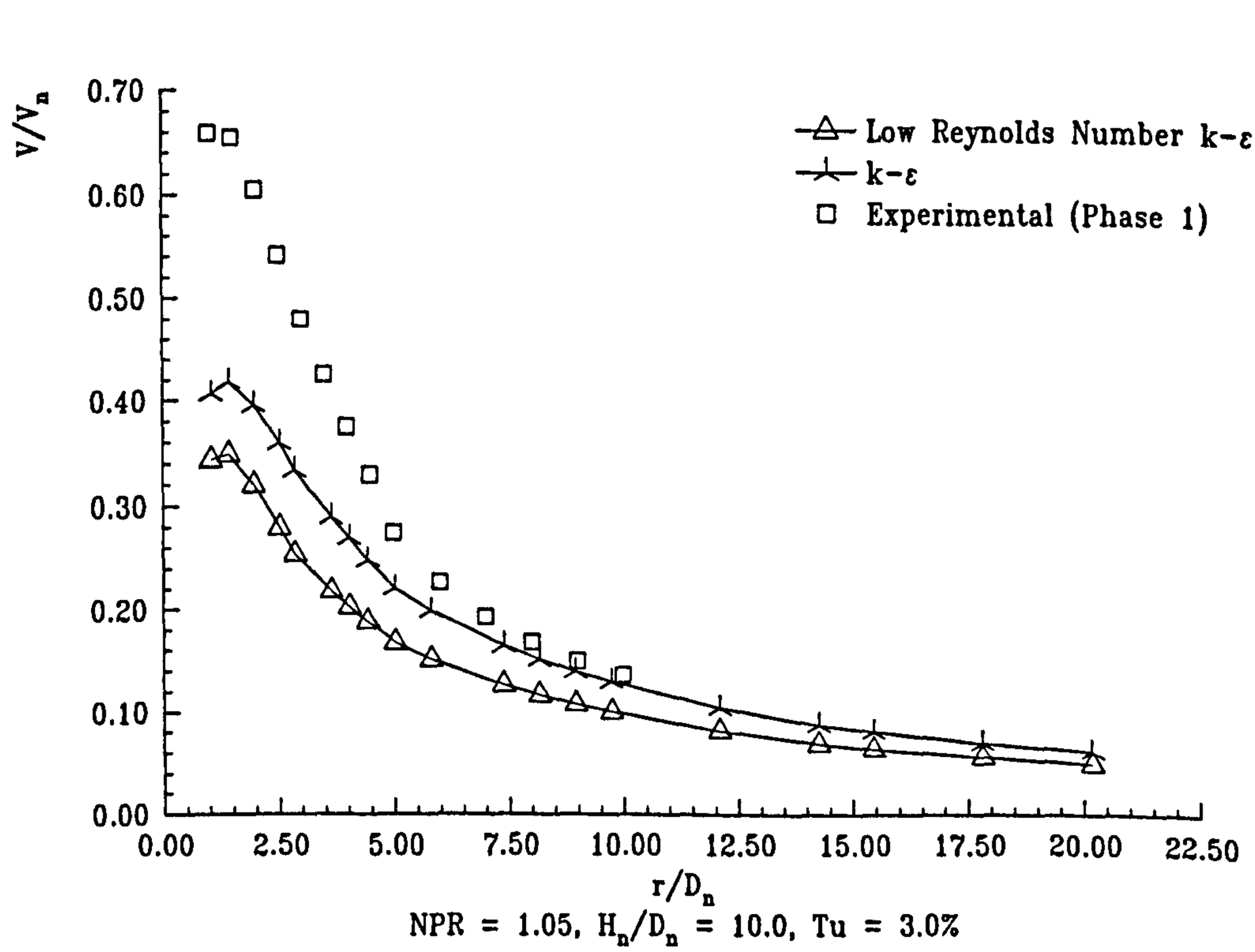

Figure 5.39 : Comparison of Low Reynolds number and Standard k-ε with Experimental Data

Chapter 6 : Conclusions and Recommendations for Future Work

This chapter summarises the findings from both the experimental and computational phases of this project and re-emphasises the main conclusions drawn from that work. There is also a brief discussion of future work suggested to be undertaken to further our understanding of this subject.

6.1 Conclusions

The data collected in the author's Bachelor of Engineering degree project (Myszko 1993) have been further reduced to form an engineering correlation for the growth in wall jet half thickness with radial distance. This includes terms for the previously experimentally measured nozzle height and nozzle pressure ratio effects, the latter apparently not included in earlier correlations. Its performance compared well with previously published work, an improvement being seen in the prediction of the nozzle height effect. There was too much scatter in half thickness data to gain a fully accurate description concerning its variation with nozzle pressure ratio and this is shown in the performance of the correlation with respect to NPR.

Following this work, a major overhaul of the impinging jet experimental facility at Cranfield University's Shrivenham campus was undertaken with the computerisation of rig control and data acquisition. This has resulted in a system which is capable of extended periods of unsupervised data collection enabling a far more detailed investigation to be performed than would otherwise be possible. The accuracy and speed of operation of the system has been improved over this period with safety and reliability being paramount. The are still areas of the experimental facility which need further improvements (e.g. the calibration of cross-wires) but the fundamentals of the system have worked well and should enable the continuation of this line of research.

An initial investigation into the flow leaving the settling chamber indicated problems with the flow symmetry due to the chamber design. These problems were corrected and later measurements have provided detailed information of the mean and turbulent velocity distributions at nozzle exit. Basic radial wall jet flow symmetry tests have been performed and have indicated that the variations in wall jet profiles were within the measurement tolerances of the equipment used.

A detailed set of wall jet profiles covering r/D_n = 1.5 - 20.0 has been collected for four nozzle heights and various impingement surface speeds at an NPR = 1.05 using cross-wire anemometry and pitot pressure measurements, representing nearly 900 hours of data collection in total. A CFD investigation into the effect of parametric changes to wall jet development has been conducted in parallel using the k-ε turbulence model and various modifications to it.

The experimental results and CFD predictions both indicated that self-similarity of the mean wall jet velocity profiles occurs soon after impingement, although the exact radial location varies with nozzle height. For the largest investigated nozzle-to-ground plane separation of 10 D_n, self-similarity occurs by $r/D_n < 3.0$ where as for a height of 2 D_n, this has reduced to $r/D_n < 2.0$. The data were not as repeatable for the turbulent velocity components, Phase 1 indicating self-similarity occurring at $r/D_n = 4.5$ where as the data of Phase 2 did not reaching self-similarity until $r/D > 9.0$. Improvements made in the measurement techniques and a change in the source of the compressed air supplying the nozzle have provided possible reasons for this discrepancy and further work is required to resolve this matter.

Non-dimensional wall jet profiles predicted by the k-ε model have shown a problem with the use of the logarithmic law-of-the-wall function, the height of peak wall jet velocity above the surface being too low when compared to both experimental phases. It is believed that the major source of error is in the height of the grid cell closest to the wall, the grid geometry used being unable to satisfy the criteria for the use of this wall function. The use of the low Reynolds number k-ε model which removes the need

for the use of this wall function has shown an improved prediction for the non-dimensional wall jet profile, especially when compared to Phase 2 data.

Nozzle height seems to have a large effect on the peak velocity and fluctuation levels in the wall jet development region, this being shown both experimentally and computationally. Decreasing nozzle height increased the peak wall jet velocity leaving the impingement region and increased the relative magnitude of the turbulence level. The absolute level of peak Reynolds shear stress measured in the wall jet was nearly three times higher for $H_n/D_n = 2$ compared with $H_n/D_n = 10.0$, although the non-dimensional values were very similar.

Wall jet growth, measured by the height to half the peak wall jet profile velocity, has been shown to increase almost linearly with increasing radial location, except for low r/D_n values where the flow is affected by the presence of the free jet. Comparisons with the CFD results show that the k-ε model is poor at predicting the correct growth of the wall jet, tending to over-predict at low radial locations and vastly under-predict at high r/D_n. The low Reynolds number k-ε model predicted a slightly thicker wall jet, presumably due to the more accurately predicted inner boundary layer, although the rate of growth with radial location was still the same as the standard k-ε model causing the over prediction at low r/D_n to be worse. Nozzle height seemed not to affect the measured rate of growth of the wall jet, but did affect the initial thickness leaving the impingement region. Increasing H_n/D_n tended to increase this initial thickness although there was some discrepancy concerning the nozzle heights of 2 and 4 diameters. This trend of increased thickness with increased H_n/D_n was captured by the k-ε model, although it did over-predict the effect.

The production of turbulent kinetic energy was calculated for various radial wall jet locations and nozzle heights. Plots of production were shown to be self-similar in nature when non-dimensionalised with peak production and wall jet half thickness, although there was a marked increase in the amount of scatter at a nozzle height of 4 diameters. Close to the wall, it was shown that it is the normal stresses ($\overline{u^2}$ and $\overline{v^2}$) that account for most of the production whereas above $Y/Y_{½} \approx 0.3$ (just above the height of

peak wall jet velocity), it is the shear stress that is the dominating factor. The dramatically increased magnitude of the shear stress for lower nozzle heights causes the peak production of turbulent kinetic energy to be far higher for lower H_n/D_n, the variation with radial location found to peak at around $r/D_n = 2.5$ (similar to the Reynolds shear stress profiles).

The impingement of a jet onto a moving surface was briefly investigated experimentally, the data collected indicated the areas of interest where a more detailed investigation could be performed. The half thickness of the wall jet formed by impingement on a moving surface was found to be almost unaffected by the direction of the moving surface up to a radial location of 4 diameters away from the stagnation point. Beyond this point, the inner boundary layer of the wall jet was found to separate when flowing against the moving surface. It is suggested that this allows ambient fluid to penetrate underneath the wall jet, together with the dramatically increased turbulence generation due to separation, causing an extremely rapid decay of peak radial wall jet velocity and increased wall jet half thickness. For a jet at NPR = 1.05 impinging on a surface moving at 10.0 ms^{-1} towards the stagnation point, separation was found to occur at a around $r/D_n = 7.0 - 8.0$ with the wall jet being almost completely diffused by $r/D_n = 10.0$. It is unclear to what extent this separation is contributed to by stagnation against oncoming fluid dragged along by the moving surface. The primary factor is almost certainly the increased surface shear stress due to the moving surface but this still needs further investigation. When the surface is moving with the wall jet away from the stagnation point, the rate of wall jet growth and peak velocity decay are reduced causing a thinner, faster wall jet to exist.

Further parametric trends shown in the computational phase were the effect of nozzle pressure ratio and exit turbulence intensity. NPR was shown to reduce the predicted free jet and wall jet thickness and increase the free jet potential core length. These NPR results have to be treated with a degree of scepticism due to an error found in the initial model set-up which caused a large massflow discrepancy, although the trends predicted do agree with previously published experimental work. An increase in the exit turbulence intensity was found to increase free jet growth and peak velocity decay. The

initial thickness of the wall jet leaving the impingement region was also found to increase although the rate of growth with radial distance remained the same.

The three modifications made to the k-ε model have been disappointing in performance, none being able to produce a significant improvement over the standard model. The correction suggested by Rodi (1981) improved the free jet prediction, decreasing the predicted spreading rate compared to k-ε. This, unfortunately, generated a far thinner wall jet than measured experimentally (and thinner than predicted by the standard model) and the wall jet correction of Malin (1988) was unable to compensate for this. The coefficients in these corrections could be tuned to improve their performance, although it appears to be the prediction of the stagnation point flow by the standard k-ε model which is the main cause of the inaccuracy. The Chen (1987) correction had the same effect as the use of the Rodi correction, a better predicted free jet causing an increased under-prediction of the wall jet thickness.

This experimental and computational study has indicated that a number of factors will affect the development of a wall jet. Experimentally, increasing nozzle height was shown to increase the initial thickness of the wall jet leaving the impingement region, although there seems to be a discrepancy in the results for H_n/D_n = 2.0 & 4.0 which has not been explained. Nozzle height was also shown to affect the turbulence profiles close to the impingement region, lower H_n/D_n causing increased turbulent fluctuations, increased shear stress and increased turbulence generation.

The computational study has shown that the nozzle height, NPR and Tu effects can be predicted using the k-ε model although the absolute accuracy of the predictions is poor. The use of the low Reynolds number k-ε model showed that an improved wall jet velocity profile was possible, although the dependency of this model on the standard k-ε model at high Reynolds numbers meant that overall predictions were not much better. None of the modifications tried in this project gave noticable improvements over the standard model, although it is believed further tuning of the results would improve the prediction for those cases considered.

6.2 Recommendations for Future Research

Included below are a few recommendations for further research on the subject contained within this thesis.

1. A systematic experimental investigation into the effects nozzle exit turbulence has on the development of a radial wall jet should be undertaken.

2. The techniques used to calibrate the cross-wires should be re-examined and the calibration equipment further improved if possible. The performance of the cross-wire probe in highly turbulent flows should be further investigated.

3. Even more nozzle heights should be examined, especially at the lower values where discrepancies in the experimental data were noted.

4. Detailed turbulence measurements should be taken in an impinging jet on a moving surface and compared with the results presented here. This may require the use of an LDA system to perform measurements close to the moving surface.

5. All the computational models should be rerun with the correct value of density used to define the inlet massflow.

6. A number of newer turbulence models have shown improvements over the standard k-ε model in other fields, most noticeably, the two-layer model suggested by Rodi (1991). These should be looked at with respect to impinging jets and a possible comparison made with the standard k-ε turbulence model.

References

BAKKE B. (1957)
"An Experimental Investigation of the Wall Jet." *J. Fluid Mechanics*, Vol.2, pt. 5, pp 467-472.

BARATA J. M. M., DURÃO D. F. G., HEITOR M. V. (1986)
"Experimental and Numerical Study on the Aerodynamics of Jets in Ground Effect." *10th Symposium on Turbulence*, Univ. of Rolla-Missouri, Missouri, 22-24 September.

BARATA J. M. M., DURÃO D. F. G., HEITOR M. V. & MCGUIRK J. J. (1987)
"The Turbulence Characteristics of a Single Impinging Jet Through a Cross Flow." *6th Symposium on Turbulence Shear Flows*, Toulouse, France.

BARATA J. M. M., DURÃO D. F. G. & MCGUIRK J. J. (1989)
"Numerical Study of Single Impinging Jets Through a Crossflow." *J. Aircraft*, Vol. 26, No. 11, pp 1002-1008.

BAUGHN J. W. B. & SHIMIZU S. (1989)
"Heat Transfer Measurements from a Surface with Uniform Heat Flux and an Impinging Jet." *A.S.M.E. J. Heat Transfer*, Vol. 111, pp 1096.

BEDÍÍ-ÖZDEMÍR İ. & WHITELAW J. H. (1992)
"Impinggement of an Axisymmetric Jet on Unheated and Heated Flat Plates." *J. Fluid Mech.*, Vol. 240, pp 503-532.

BLASIUS H. (1913)
"Das Ahnlichkeittsyessetz bei Reibungsvorgängen in Flüssigkeiten" *Forschy. Arb. Ing.-Wes.*, No 134.

BOUSSINESQ J. (1877)
"Théorie de l`écoulement tourbilliant." Mén. Présentés par divers Savants Acad, Sci. Inst. Fr., Vol 23, pp 46-50.

BRADBURY L. J. S. (1972)
"The Impact of an Axisymmetric Jet onto a Normal Ground." *Aeronautical Qrt.*, Vol. May, pp 141-147.

BRADSHAW P & LOVE E. M (1959)
"The Impingement of a Circular Air Jet on a Flat Surface." *Aeronautical Research Council*, Report No. R&M-3205.

BRAY D. (1992)
"Jets in Cross-FLow and Ground Effect." *PhD Thesis*, Aeromechanical Systems Group, Cranfield Institute of Technology, Shrivenham, Wiltshire, UK.

BRISON J. F. & BRUN G. (1991)
"Round Normally Impinging Turbulent Jets" *Proc. 15th Meeting IAHR Working Group on Refined Flow Modelling*, Lab. Méc. Fluides, ECL, Lyon, France.

BRUNN H. H. (1971)
"Interpretation of a Hot-wire Signal Using a Universal Calibration Law." *J. Phys. E. : Sci. Instr.*, Vol. 4, pp 225-231.

BRUNN H. H. (1995)
"Hot-wire Anemometry : Principles and Signal Analysis." Oxford University Press, Oxford.

BRUNN H. H., KHAN M. A., AL-KAYIEM H. H. AND FARDAD A. A. (1988)
"Velocity Calibration Relationships for Hot-wireAnemometry." *J. Phys. E. : Sci. Instr.*, Vol. 21, pp 225-232.

CHEN Y. S. & KIM S. W. (1987)
"Computation of Turbulent Flows using an Extended k-ε Turbulence Closure Model." NASA CR-179204

CHIEN K. T. (1982)
"Predictions of Channel and Boundary Layer Flows with a Low Reynolds Number Turbulence Model." *AIAA Journal*, Vol. 20, No. 1, pp 33-38.

CHILDS E. P. & PATEL B. R. (1990)
"Turbulence Model Preformance in V/STOL Flow Field Simulation." AIAA 90-2248, *26th Joint Propulsion Conference*, Orlando, FL, USA, 16-18 July.

CHILDS R. E. & NIXON D. (1987)
"Turbulence and Fluid/Acoustic Interaction in Impinging Jets." *Proceedings of the International Powered Lift Conference*, Santa Clara, CA, USA, 7-10 December.

CIMBALA J.M., BILLET M. L., GAUBLOMME D.P & OEFELEIN J. C. (1991)
"Experiments on the Unsteadiness Associated with a Ground Vortex.", *J. Aircraft*, Vol 28, No. 4, pp 261 - 267.

CIMBALA J. M., STINEBRING D. R. , TREASTER A. L. & BILLET M. L. (1987)
"Experimental Investigation of a Jet Impinging on a Ground Plane in the Presence of a Cross-flow." *Proceedings of the International Powered Lift Conference*, Santa Clara, CA, USA, 7-10 December.

COLIN P. E & OLIVARI D. (1969)
"The Impingement of a Circular Jet Normal to a Flat Surface with and without Cross-flow." *European Research Office*, U.S. Army, Contract No DAJA 3768-C-0352.

COOPER D., JACKSON D. C., LAUNDER B. E. & LIAO G. X. (1993)
"Impinging Jet Studies for Turbulence Model Assessment - I. Flow Field Experiments." *International Journal of Heat and Mass Transfer*, Vol. 36, No. 10, pp 2675-2684.

COUSTEIX J & HOUDEVILLE R. (1983)
"Effects of Unsteadiness on Turbulent Boundary Layers." Lecture Series 1983-03, von Karman Inst. for Fluid Dynamics, Rhode-Saint Genese, Belgium.

COX M. & ABBOT W. A. (1964)
"Experiments with a Single Vertical Jet Simulating an Engine for Vertical Take-off." NGTE Memo M.390.

CRAFT T. J., GRAHAM L. J. W. & LAUNDER B. E. (1993)
"Impinging Jet Studies for Turbulence Model Assesement - II. An examination of the Performance of Four Turbulence Models." *International Journal of Heat and Mass Transfer*, Vol. 36, No. 10, pp 2685-2697.

CURTIS P. (1987)
"Investigation into the Behaviour of a Single Jet in Free Air and Impinging Perpendicularly on the Ground." *BAe Report*, KAD-R-RES-3349.

DAVIES T. W. & PATRICK M. A. (1972)
"A Simplified Method of Improving the Accuracy of Hot-wire Anemometry." *Proc. Conf. on Fluid Dynamic Measurements in the Industrial and Medical Enviroment*, Leicester University, pp 152-155.

DECLERCQ J. & DUTRÉ W. (1994)
"Simulation of Impinging Jets with a Reynolds-Stress Turbulence Model and Turbulent Heat Fluxes." *ICHMT Internation Symposium on Turbulence, Heat and Mass Transfer*, Lisbon, Portugal, 9-12 August.

DONALDSON C DUP. & SNEDEKER R. S. (1971)
"A Study of Free Jet Impingement. Part 1, Mean Propertise of Free and Impinging Jets." *J. Fluid Mechanics*, Vol. 45 pt.2 pp 281-319

DUTOYA D. & MICHARD P. (1981)
"A Program for Calculating Boundary Layers along Compressor and Turbine Blades." *Numerical Methods of Heat Transfer*, Edited R. W. Lewis, John Wiley & Sons, New York.

ESKINAZI S. & ERIAN F. (1969)
"Energy Reversal in Turbulent Flows." *The Physics of Fluids*, Vol. 12, No. 10, pp 1988-1998.

FAN S., LAKSHMINARAYANA B & BARNETT M. (1993)
"Low-Reynolds-Number k-ε Model for Unsteady Turbulent Boundary Layer Flows." *AIAA Journal*, Vol. 31, No. 10, pp 1777-1784.

FINNIS M. V. (1993)
"Centrifugal Instability of a Laminar Boundary Layer on a Concave Surface." *PhD Thesis*, Thermo-Power Group, Cranfield Institute of Technology, Shrivenham, Wiltshire, UK.

GAUNTNER J. W. (1970)
"Survey of Literature on Flow Characteristics of a Single Turbulent Jet Impinging on a Flat Plate." *NASA TN* D-5652.

GEORGE W. K., BEUTHER P. D. & AHMAD M. (1981)
"Polynomial Calibration and Quasi-Linearization of Hot-wires." Turbulence Research Laboratory Report, Sunny Buffalo, USA.

GEORGE W. K., BEUTHER P. D. & SHABBIR A. (1989)
"Polynomial Calibrations for Hot-wires in Thermally Varying Flows." *Exp. Thermal and Fluid Sci.*, Vol. 2, pp 230-235.

GESSO J. & DAVIES T. W. (1977)
"Hot-wire Anemometery in a Two-dimensional Separated Flow." 1st Turbulent Shear Flow Conference, Penn. State University, USA.

GILMORE D. C. (1967)
"The Probe Intereference Effects of Hot-wire Anemometer" *Technical Note 67-3*, Mech. Eng. Dept., McGill University, Montreal, Canada.

GLAUERT M. (1956)
"The Wall Jet." *J. Fluid Mechanics*, Vol. 1, Pt. 6, pp 625-643.

GLYNN D. R. & JAL E. N. (1987)
"Numerical Prediction of Flow in Free and Impacting Jets." Report no. CHAM 3181/1, CHAM Limited, Wimbledon, London, UK.

GOLDSTEIN R. J. & FRANCHETT M. E. (1988)
"Heat Transfer from a Flat Surface to an Oblique Impinging Jet." *ASME Journal of Heat Transfer*, Vol. 110, pp 84-90.

GUITTON D. E. (1968)
"Correction of Hot-wire Data for High Intensity Turbulence, Logitudinal Cooling and Probe Interefernce" *Technical Note 68-6*, Mech. Eng. Dept., McGill University, Montreal, Canada.

GUTMARK E., SCHADOW K. C. & BICKER C. J. (1990)
"Near Acoustic Field and Shock Structure of Rectanglar Supersonic Jets." *AIAA Journal*, Vol. 28, July, pp 1163-1170.

GUTMARK E., WOLFSHTEIN M. & WYGNANSKI I. (1978)
"The Plane Turbulent Impinging Jet." *J. Fluid Mechanics*, Vol.88, pp 735-756.

HARLOW F. H. & NAKAYAMA P. I. (1968)
"Transport of Turbulence Energy Decay Rate." LA-3854, Los Alamos Science Lab., University of California, USA.

HARLOW F. H. & WELCH J. E. (1965)
"Numerical Calculation of Time Dependent Viscous Incompressible Flow of Fluid with Free Surfaces." *Physics of Fluids*, Vol.8, pp 2182.

HASSID S. & POREH M. (1978)
"A Turbulent Energy Model for Flows with Drag Reduction." *Trans. A.S.M.E. J. Fluid Engineering*, Vol. 100, pp 107-112.

HOFFMANN G. H. (1975)
"Improved form of the Low Reynolds Number k-e Turbulence Model." *Physics of Fluids*, Vol. 188, pp 309-312.

HOOLE B. J. & CALVERT J. R. (1967)
"The Use of a Hot-wire Anemometer in Turbulent Flow." *Journal of the Royal Aeronautical Society*, Vol. 71, pp 511

HRYCAK P., LEE D., GAUNTNER J & LIVINGOOD J. (1970)
"Experimental Flow Characteristics of a Single Turbulent Jet Impinging on a Flat Plate." *NASA* TN D-5690.

HWANG C. J. & LIU J. L. (1989)
"Numerical Studies of Two-dimensional Impinging Jet Flow-Fields." *AIAA Journal*, Vol. 27, No. 7, pp 841-842.

JAMBUNATHAN K., LAI E., MOSS M. A. & BUTTON B. L. (1992)
"A Review of Heat Transfer Data for Single Circular Jet Impingement." *International Journal of Heat and Mass Transfer*, Vol. 13, No.2, pp 106-115.

JEROME F. E. (1971)
"Experimental Study of the Thermal Wake Interference Between Closely Spaced Wires of a Cross-type Hot-wire Probe", Aero. Quarterly, pp 119.

JONES W. P. & MCGUIRK J. J. (1980)
"Computation of a Round Turbulent Jet Discharging into a Confined Cross-Flow." *Turbulent Shear Flows 2*, Edited by L. Bradbury, Springer-Verlag, Berlin.

JUSTESEN P & SPALART P. R. (1990)
"Two-Equation Turbulence Modelling of Oscillatory Boundary Layers." *AIAA Paper* 90-0496.

KATAOKA K. (1985)
"Optimal Nozzle-to-Plate Spacing for Convective Heat Transfer in Nonisothermal Variable-Density Impinging Jets." *Drying Technology*, Vol. 3, pp 235-254.

KING L. V. (1914)
"On the Convection of Heat from Small Cylinders in a Stream of Fluid : Determination of the Convection Constants of Small Platinum Wires with Applications to Hot-Wire Anemometry" *Phil. Trans. Roy. Soc.*, A214, pp 373-432.

KIRKHAM L. (1996)
"Coaxial Jet Flows for ASTOVL Applications." *MPhil Thesis*, Department of Aerospace and Guidance Systems, Cranfield University, Shrivenham, Wiltshire, UK..

KNOWLES K. & BRAY D. (1991)
"Recent Research into the Aerodynamics of ASTOVL Aircraft in Ground Effect." *Proceedings Instn. Mech. Engrs*, Vol 205, pp 123 - 131.

KNOWLES K., JUBRAN B. A. & BRAY D. (1993)
"Numerical Modelling of Impinging Jet Flow-Field using a Modified k-ε Turbulence Model." *Numerical Methods in Laminar and Turbulent Flows*, Vol. 8, pp 280-289, Edited C. Taylor, Pineridge Press.

KNOWLES K. (1996)
"Computational Studies of Impinging Jets Using k-e Turbulence Models." *International Journal of Numerical Methods in Fluids, Vol. 22, No. 8,* pp 799-810.

LAM C. K. G. AND BREMHORST K. A. (1981)
"Modified Form of the k-e Model for Predicting Wall Turbulence." *Trans. A.S.M.E. J. Fluids Engineering*, Vol. 103, pp 456-460.

LAU J. C., FISHER M. J & FUCHS H. V. (1972)
"The Intrinsic Structure of Turbulent Jets." *J. Sound Vibration*, Vol 22, pp 379-406.

LAUNDER B. E. (1975)
"Progress in the Modelling of Turbulent Transport." Lecture Series 76, von Kármán Institute for Fluid Dynamics, Rhode-Saint Genese, France.

LAUNDER B. E. & RODI W. (1983)
"The Turbulent Wall Jet - Measurements and Modeling." *Ann. Rev. Fluid Mech.*, Vol. 15, pp 429-459.

LAUNDER B. E. & SHARMA B. I. (1974)
"Application of the Energy Dissipation Model of Turbulence to the Calculation of Flow near a Spinning Disc." *Letters in Heat and Mass Transfer*, Vol.1, pp 131-138.

LESCHZINER M. A. (1996)
Comments made at *RAeS Aerodynamics Research Forum*, London, 4-5 January.

LESCHZINER M. A. & LAUNDER B. E. (1993)
"Round Normal Impinging Turbulent Jet & Turbulent Flow through Tube Bank Sub-Channel." *2nd ERCOFTAC-IAHR Workshop on Refined Flow Modelling*, UMIST, Manchester, UK.

LOMAS C. G. (1986)
"Fundamentals of Hot-wire Anemometry." Cambridge University Press, Cambridge.

MALIN M. R. (1988)
"Prediction of Radially Spreading Turbulent Jets." *AIAA Journal*, Vol. 26, No.6, pp 750-751.

MANKBADI R. R. & MOBARK A. (1991)
Quasi-Steady Turbulence Modelling of Unsteady Flows." *Int. J. Heat and Fluid Flow*, Vol. 12, No.2, pp 122-129.

MARGASON R. J. (1993)
"Fifty Years of Jet in Cross-flow Research" *AGARD* CP-534.

MARTIN H. (1977)
"Heat and Mass Transfer between Jets and Solid Surfaces." *Advances in Heat Transfer*, Vol. 13, pp 1-60, Academic Press, New York.

MATHIEU J. & CHARNAY G. (1981)
Structure and Development of Turbulent Jets." *Fluid Dynamics of Jets with Application to V/STOL*, AGARD CP-308.

MICHELASSI V., RODI W. & ZHU J. (1993)
"Testing a Low Reynolds Number k-ε Turbulence Model Based on Direct Simulation Data." *AIAA Journal*, Vol. 31, No.9, pp 1720-1723.

MILLER P. & WILSON M. (1993)
"Wall Jets Created by Single and Twin High Pressure Jet Impingement." *Aeronautical Journal*, March, pp 87-100.

MYSZKO M. (1993)
"Effect of Nozzle Height on Wall Jet Development Following Jet Impingement." *Mechanical Engineering Degree Project Report*, Aeromechanical Systems Group, Cranfield Institute of Technology, Shrivenham, Wiltshire, UK.

NEWLAND D. E. (1975)
"An Introduction to Random Vibrations and Spectral Analysis." Published by Logman Group Limited, London, U.K.

NORRIS L. H. & REYNOLDS W. C. (1975)
"Turbulent Channel Flow with a Moving Wave Boundary." Report No. FM-10, Mech. Eng. Dept., Stanford University, USA.

PADMANABHAM G. & LAKSHMANA GOWDA B. H. (1991)
"Mean and Turbulence Characteristics of a Class of Three Dimensional Wall Jets - Part 2: Turbulence Charcateristics." *Trans. A.S.M.E J. Fluids Engineering*, Vol. 113, pp 629-634.

PALMER M. D. & KEFFER J. F. (1972)
"An Experimental Investigation of an Asymmetrical Turbulent Wake." *J. Fluid Mechanics*, Vol. 53, Pt.4, pp 593-610.

PATANKAR S. V. (1981)
"A Calculation Procedure for Two-Dimensional Elliptic Problems." *Numerical Heat Transfer*, Vol. 4, pp 409-426.

PATANKAR S. V. (1980)
"Numerical Heat Transfer and Fluid Flow." Hemispher Publishing Corporation, London.

PATANKAR S. V. & SPALDING D. B. (1972)
"A Computational Procedure for Heat, Mass and Momentum Transfer In Three-Dimensional Parabolic Flows." *International Journal of Heat and Mass Transfer*, Vol. 15, pp 1787.

PATEL V. C., RODI W. & SCHEUERER G. (1985)
"Turbulence Models for Near-Wall And Low Reynolds Number Flows: A Review." *AIAA Journal*, Vol. 23, No. 9, pp 1308-1319.

POLAT S. (1993)
"Heat and Mass Transfer in Impingement Drying." *Drying Technology*, Vol. 11, Pt. 6, pp 1147-1176.

POLAT S. & DOUGLAS W. J. M. (1990)
"Heat Transfer Under Multiple Slot Jets Impinging on a Permeable Moving Surface." *AIChE Journal*, Vol.36, No. 9, pp 1370-1378 .

POLAT S. MUJUMDAR A. S. & DOUGLAS W. J. M. (1991)
"Impingement Heat Transfer Under a Confined Slot Jet, Part II : Effect of Surface Motion and Through Flow." *CJChe*, Vol. 69, pp 274-280.

POPIEL C. O. & TRASS O. (1982)
"The Effect of Ordered Structure of Turbulence on Momentum, Heat and Mass Transfer of Impinging Round Jets." *7th Heat Transfer Conf.*, Munchen, 6-10 Sept.

POREH M., TSEUI Y. G. & CERMAK J. E. (1967)
"Investigation into the Turbulent Wall Jet." *J. Appl. Mechanics*, Vol. 89, pp 437-463.

PRANDTL L. (1942)
"Bemerkungen zur Theorier der Turbulenz." *ZAMM*, Vol. 22, pp 241-243.

REYNOLDS W. C. (1976)
"Computation of Turbulent Flows." *Ann. Rev. Fluid Mech.*, Vol. 8, pp 183-208.

RODI W. (1980)
"Turbulence Models and their Application in Hydraulics - A State of the Art Review." *Book Publication of International Association for Hydraulic Research*, Delft, The Netherlands.

RODI W. (1991)
"Experience with Two-Layer Models Combining the k-ε Model with One-Equation Model Near the Wall." AIAA-91-0216, *29th Aerospace Sciences Meeting*, Reno, Nevada, USA, 7-10 June.

RODI W. & MANSOUR N. N. (1993)
"Low Reynolds Number k-ε Modelling with the Aid of Direct Simulation Data." *J. Fluid Mech.*, Vol. 250, pp 509-529.

SCHWANTES E. (1973)
"The Recirculating Flow Pattern of a VTOL Lifting Engine." *NASA* TT-F-14912.

SCHWARZ W. H. & COSART W. P. (1961)
"The Two Dimensional Turbulent Wall Jet." *J. Fluid Mech.*, Vol. 10, pp 481-495.

SIDDALL R. G. & DAVIES T. W. (1972)
" An Improved Respounce Equation for Hot-wire Anemometry" *Int. J. Heat and Mass Transfer*, Vol.15, pp 367-375.

SPEZIALE C. G. (1991)
"Analytical Methods for the Development of Reynolds-Stress Closures in Turbulence." *Ann. Rev. Fluid Mech.*, Vol. 23, pp 107-157.

SQUIRE H. B. (1950)
"Jet Flow and its Effect on Aircraft." *J. Aircraft Eng.*, Vol. 22.

STRYKOWSKI P. J., KROTHAPALLI A. & JENDOUBI S. (1996)
"The Effect of Counterflow on the Development of Compressible Shear Layers" *J. Fluid Mech.*, Vol. 308, pp 63-96.

SWAMINATHAN M. K., RANKIN G. W. AND SRIDHAR K. (1986)
" A Note on the Response Equations for Hot-wire Anemometry." *Trans. A.S.M.E. J. Fluids Eng.*, Vol. 108, pp 115-118.

TUTU N. K. & CHEVRAY R. (1975)
"Cross-wire Anemometry in High Intensity Turbulence" *Journal of Fluid Mechanics*, Vol. 71, No. 4, pp 785 - 800.

VAN DER HEGGE ZIJNEN B. G. (1924)
"Modified Correlation Formulae for the Heat Transfers by Natural and by Forced Convection from Horizontal Cylinders." *Appl. Sci. Res.*, A6, pp 129-140.

WILCOX D.C AND RUBESIN W. M. (1980)
"Progress in Turbulence Modelling for Complex Flow-Fields Including Effects of Compressibility." *NASA* Tech. Paper 1517.

WILLIAMS J. & WOOD M. (1966)
"Aerodynamic Interference Effects with Jet-Lift V/STOL Aircraft under Static and Forward Speed Conditions." *R. A. E.* Technical Report 66403.

WILSON M. J. (1995)
"Unsteady Aerodynamics of Impinging Jets for STOVL Aircraft." *MPhil Thesis*, Aeromechanical Systems Group, Cranfield University, Shrivenham, Wiltshire, UK..

YOKOBORI S. ET AL. (1979)
"Characteristic Behaviour of Turbulence and Transport Phenomena at the Stagnation Region of an Axisymmertic Impinging Jet." *2nd Turbulent Shear Flows Conf.*, London, U.K.,12-17 April.

Appendix A : Hot-wire Anemometry

This appendix describes the fundamentals and techniques for hot-wire anemometry used during the course of this project.

A.1 Constant Temperature Anemometry

The Dantec CTA hot-wire anemometer is of the constant temperature type, that is, it supplies a hot-wire probe heating current that varies with the fluid velocity over the probe to maintain a constant probe resistance and, thus, a constant probe temperature. The electronic heart of a CTA is a Wheatstone bridge circuit, where the hot-wire probe system (hot-wire, support arm and cable connecting it to the CTA) forms one arm of the bridge. Two fixed resistors and a variable resistor complete the circuit.

Before the system can be operated, the Wheatstone bridge has to be balanced, that is the resistance of the probe system has to be given to the CTA so that an initial value for the adjustable resistance can be set. Once started, a differential feedback amplifier senses if the bridge becomes unbalanced, that is, the resistance of the probe system changes from the initial set value, and adds current to hold the probe temperature constant. If the velocity over the probe increases, so cooling it, the probe resistance will decrease so causing the bridge to become unbalanced. The CTA reacts by increasing the current through the probe system until balance is restored. Since the feedback amplifier responds rapidly, the sensor temperature remains virtually constant as the velocity changes. The CTA then gives the voltage across the bridge as an output, as this is proportional to the fluid velocity.

A.2 Bridge Balance

The resistance of the probe system with the wire hot has to be given to the CTA as this sets the initial conditions for operation. This is firstly found by measuring the

resistance of the hot-wire element (the 5μm diameter wire between the prongs) when cold and then multiplying this by an overheat ratio which gives a resistance for the wire when hot and hence fixes the temperature at which the wire will operate.

The resistance of the wire when cold is found by measuring the resistance of the total probe system and then by measuring the resistance of the individual components of the system. The probe system comprises four main components: the hot-wire element, the prongs, the support arm and the cable. The resistance of the prongs (R_P) is given by the manufacturer of the probe and is usually 0.5 or 1.0Ω, the resistance of the cable and support arm (R_C) are measured together by placing a shorting probe in the end of the support arm, and the total resistance when cold (R_{Tc}) is measured with the hot-wire probe attached to the support arm. The resistance of the wire element is then given by:

$$R_{Wc} = R_{Tc} - R_P - R_C$$

Equation A.1

The resistance of the wire element when at operating temperature is then given by:

$$R_{Wh} = a * R_{Wc}$$

Equation A.2

and so the total resistance of the probe system when at operating temperature is given by:

$$R_{Th} = aR_{Tc} + (1-a)R_P + (1-a)R_C$$

Equation A.3

The value of a (the overheat ratio) is important as it fixes the operating temperature of the wire which influences both the operating life of the probe and its sensitivity to velocity and ambient temperature changes. For these tests, the value of a was set to 1.8 which gave a wire operating temperature of around 280°C.

A.3 Velocity - Voltage Relationship for a Hot-wire

This section describes a number of relationships for the CTA output voltage against velocity over the sensor.

A.3.1 King's Law

Following work by King (1914), the convective heat transfer from a circular cylinder in a fluid flow is often expressed as:

$$Nu=A+BR_e^{\frac{1}{2}}=A+\left(\frac{BD_w^{\frac{1}{2}}}{\nu^{\frac{1}{2}}}\right)u^{\frac{1}{2}}=\frac{hD_w}{k}$$

Equation A.4

where A and B are empirical constants for each fluid, u is the fluid velocity, h is the heat transfer coefficient, D_w is the diameter of the wire and k is the thermal conductivity of the fluid.

For the hot-wire element, the rate of heat loss from the wire is given by:

$$Q=h\times A_s\times(T_w-T_c)=\frac{V^2}{R_{wh}}$$

Equation A.5

where A_S is the wire surface area, T_w is the wire temperature, T_c is the fluid temperature and V is the voltage across the wire (CTA output voltage).

Combining A.4 and A.5 and rearranging gives:

$$V^2=\frac{AR_{wh}A_S(T_w-T_\infty)k}{D_w}+\left(\frac{BR_{wh}A_S(T_w-T_c)k}{(D_w\nu)^{\frac{1}{2}}}\right)u^{\frac{1}{2}}$$

$$V^2=a+bu^n$$

Equation A.6

where a, b are constants for each specific wire and CTA balance and n is theoretically equal to 0.5.

Therefore, as long as the ambient fluid temperature remains constant then the relationship between CTA output voltage and fluid velocity can be given by equation A.6 which is commonly known as King's law.

A.3.2 Extended Power Law

Van der Hegge Zijnen (1956) proposed that for high Reynolds number flows (up to 500,000), the non-dimensional heat transfer equation should be:

$$Nu=0.35+0.5R_e^{0.5}+0.001R_e$$

Equation A.7

which was applied to hot-wires by Davies and Patrick (1972) and Siddall and Davies (1972) to give:

$$V^2 = a + bu^{0.5} + cu$$

Equation A.8

the values of a, b and c being found by fitting a polynomial to the data using:

$$y = a + bx + cx^2$$

Equation A.9

where:

$$y = V^2 \text{ and } x = u^{0.5}$$

Equation A.10

This technique is commonly called the extended power law and is claimed to give a good curve fit over the range 0-160 ms^{-1}.

A.3.3 Universal-function Principle

Bruun (1971) suggested a relationship called the Universal-function principle which stated :

$$V^2 - V_0^2 = c\mathrm{F}(u)$$

Equation A.11

where V_0 was the output voltage at zero flow, F(u) is the universal function and c is a constant specific to each wire.

A.3.4 Polynomial Curve Fit

The methods stated above all have the problem that the equations have to be inverted to find velocity in terms of voltage. George et al. (1981, 1989) suggested that the relationship could be expressed as:

$$u = a + b\mathrm{V} + c\mathrm{V}^2 + d\mathrm{V}^3 + ...$$

Equation A.12

where a simple polynomial curve was fitted. However, it was found that the solution became unstable above the fourth order.

A.4 Calibration of a Hot-wire

It is obvious that the choice of equation for the velocity - voltage relationship will have an effect of the measured flow, albeit small. The Universal-function principal suggested by Bruun (1971) was no longer recommend by Bruun (1995) as the availability of cheap and accessible computing power removed the advantage of only needing to calibrate for one constant. The polynomial fit to the relationship was shown by Bruun (1995) to need to go to the fourth order to obtain accuracies similar to those of King's law. Considering the extra complexity of the solution, the advantage that it gives u in terms of V is outweighed.

The King's law relationship and its modification, the extended power law, seem to give the greatest accuracy. Bruun (1995) suggests the use of King's law for the medium velocity range of 5-50ms^{-1}, although work by Swaminathan et al. (1986) and Bruun et al. (1988) suggested that the extended power law did not give a greatly more accurate curve fit, even over the extended velocity range up to 160ms^{-1}. Bruun suggested that over a large velocity range, a spline of at least 6 intervals gives the most accurate fit to the relationship, giving errors around half those possible with King's law (velocity range 5-50ms^{-1}). However, he does concede the computationally time-consuming manner of this approach, and for that reason, together with the knowledge and computational routines provided by Dr M. V. Finnis, King's law was used for the solution of velocity from the CTA voltage.

From theory it can be shown that the value of n should be 0.5, but in practice a calibration of V against u will very rarely, if ever, give a value for n of 0.5. This is because the theory assumes the length of the wire to be infinite which is not the case (although the length to diameter ratio of the wires are large, typically ≈ 600) and that there is no interference from any surrounding support structure. For these reasons, the hot-wire probes used in these tests were calibrated for a, b and n.

The hot-wires were calibrated using Disa 55D90 calibration equipment, a schematic of which is shown in Figure A.1. Once set up, the nozzle gave a known velocity linearly proportional to the supply pressure, the constant being a function of the exit area of the nozzle used.

The CTA output voltage was recorded at given velocities and used to give the King's law coefficients using a routine written by Dr M. V. Finnis. This routine used a least-squares fit to evaluate a and b for a given n using:

$$\sum_{i=1}^{n} \delta_i^2 = \sum [a + bu_i^n - V_i^2]$$

Equation A.13

where:

$$\frac{\partial \sum_{i=1}^{n} \delta_i^2}{\partial a} = 0$$

Equation A.14

$$\frac{\partial \sum_{i=1}^{n} \delta_i^2}{\partial b} = 0$$

Equation A.15

The value of n was found using a secant iterative method, the tolerance on n being set to 1.0×10^{-5}.

A.4.1 Calibration Errors

The follow section discusses possible errors that could be encountered when calibrating a hot-wire.

A.4.1.1 Calibration Temperature

The coefficients for King's law obtained during the calibration of a hot-wire are only valid if the measured fluid is at the same temperature as the calibration fluid because of the effect of the fluid temperature on the rate of heat transfer from the wire. A variation in the fluid temperature, if uncorrected, would lead to an inaccurately calculated velocity from the returned wire voltage.

For Phase 1, no correction to the sampled anemometry voltage was applied as earlier work had indicated that there was very little temperature difference between the nozzle exit flow and that of ambient (Myszko 1993). As the calibration equipment used ambient air collected within a few metres of the rig, this error was considered small. For a typical calibration, a 1^0C difference between calibration and measured fluid temperature represents approximately a 2% error in calculated instantaneous velocity if uncorrected.

During Phase 2 of this research, a correction was applied to the King's law equations which compensated for a variation in the measured fluid temperature when compared with the calibration fluid temperature. This correction was as follows:

$$kE^2 = a + bu^n$$

Equation A.16

where

$$k = \frac{(T_w - T_c)}{(T_w - T)}$$

Equation A.17

T_c was the fluid flow temperature at the time of calibration, T was the fluid flow temperature at the time of the sample given by the mean of the settling chamber temperature and the fluid flow temperature at the end of the table and T_w was the operational temperature of the hot-wire given by:

$$R_{Wh} = R_{20}(1 + a_{20}(T_w - 20.0))$$

Equation A.18

where R_{wh} is the resistance of the wire when hot, R_{20} is the resistance at 20^0C and α_{20} is the temperature coefficient of resistivity of the wire. R_{20} and α_{20} are given by Dantec for each wire on the probe and were used to calculate T_w at the time of calibration.

A.4.1.2 Prong Interference

Probe interference can dramatically affect the accuracy of any measurements made using hot-wire anemometry. It was shown by Hoole and Calvert (1967) and Gilmore (1967) that the cooling effect experienced by a hot-wire probe when the flow is normal to the wire and in the plane of the prongs is lower than that when the flow is normal to both the wire and the plane of the prongs. This effect is attributed to the prongs and the stem of the probe forming a blockage for the flow when in the plane of the prongs and the reduced flow area causing acceleration of the flow when normal to the plane of the

prongs. A probe calibration is therefore only valid if the measured flow is in the same direction with respect to the wire / prongs as was the calibration fluid flow direction. This is not valid if the turbulence intensity of the flow *is high due to its rapidly changing* flow direction. During all phases of this work, great effect was made to keep the flow direction with respect to the prongs of the probe the same for both flow calibration and measuring.

A.4.1.3 Calibration Drift

The calibration of the hot-wire will drift over time due to damage to the wire by particles in the fluid flow and due to degradation of the wire surface. This effect can be reduced by efficient filtration of both the calibration and measured fluid and by reducing unnecessary periods of operation. Ideally, the wires should be calibrated before and after acquiring velocity profiles or time histories and these should only be accepted if the calibration drift were within acceptable levels. Errors associated with calibration drift are difficult to estimate but would increase dramatically with extended periods of use without re-calibration. During both Phases 1 and 2 of this work, the hot-wire was recalibrated, on avarege, once everly other day.

A.5 Cross Wire Anemometry

The voltage signals from the cross-wires were reduced to give the component velocities and turbulence intensities using the following method.

A.5.1 Hinze Yaw-angle Relationship

As the cross-wires have an aspect ratio (ratio of wire length to wire diameter) of less than 600, the standard cosine law for hot wires is not accurate. Therefore, the Hinze (see Lomas (1986), page 23) yaw-angle relationship is used which states:

$$U_{eff}^2 = U_x^2 + k^2 U_y^2$$

Equation A.19

where U_{eff} is the effective velocity measured by the hot-wire and k is the yaw factor which accounts for the additional cooling by the tangential component of the velocity. This equation can be rewritten as:

$$U_1^2 = U^2(\cos^2\theta_1 + k^2 \sin^2\theta_1)$$

Equation A.20

where θ is the angle the effective flow makes to the normal of the wire.

A.5.2 Solution for a Cross-wire

For a cross-wire, it is possible to obtain the above equation for each of the two wires, thus making a solution possible as we have two equations with two unknowns.

For wire one:

$$U_1^2 = U^2(\cos^2\theta_1 + k_1^2 \sin^2\theta_1)$$

Equation A.21

and for wire two:

$$U_2^2 = U^2(\cos^2\theta_2 + k_2^2 \sin^2\theta_2)$$

Equation A.22

where U_1 and U_2 are the velocities measured on each cross-wire.

Dividing A.21 by A.22:

$$\lambda = \frac{U_1^2}{U_2^2} = \left(\frac{\cos^2\theta_1 + k_1^2 \sin^2\theta_1}{\cos^2\theta_2 + k_2^2 \sin^2\theta_2} \right)$$

Equation A.23

There is a relationship between θ_1 and θ_2 (see Figure A.2):

$$\theta_2 = \alpha - \theta_1$$

Equation A.24

where α is the angle made by the intercept of the two wires.

Substituting this into A.23 gives:

$$\lambda = \left(\frac{\cos^2\theta_1 + k_1^2 \sin^2\theta_1}{\cos^2(a-\theta_1) + k_2^2 \sin^2(a-\theta_1)} \right)$$

Equation A.25

Unfortunately, this equation can only be rearranged to give θ_1 in terms of λ and k if we assume that $\alpha = 90^0$.

If $\alpha = 90^0$ then :

$$\cos^2(a-\theta_1) = \sin^2\theta_1 = 1 - \cos^2\theta_1$$

Equation A.26

and

$$\sin^2(a-\theta_1) = \cos^2\theta_1$$

Equation A.27

Substitution into equation A-25 gives:

$$\lambda = \left(\frac{\cos^2\theta_1 + k_1^2(1-\cos^2\theta_1)}{1-\cos^2\theta_1 + k_2^2\cos^2\theta_1} \right)$$

Equation A.28

which can be rearranged to give:

$$(\lambda - k_1^2) - \lambda\cos^2\theta_1 + \lambda k_2^2\cos^2\theta_1 = \cos^2\theta_1 - k_1^2\cos^2\theta_1$$

Equation A.29

Therefore:

$$\theta_1 = \arccos \sqrt{\frac{\lambda - k_1^2}{1 - k_1^2 + \lambda\left(1 - k_2^2\right)}}$$

Equation A.30

A.5.3 Solution Technique

The following two sections will briefly discuss the computer algorithm written to solve the above cross-wire equations, followed by a worked example.

A.5.3.1 Computer Algorithm

As it is unlikely that the angle between the cross-wires on an actual probe would be 90^0, a secant method of iteration is used to solve for each value of sampled λ to give a value for θ_1 and hence using equation A.25, a value for U. If the angle the cross-wires make with one of the component directions is known, it is then possible to give values for each component of the instantaneous velocity. The mean and rms value of the velocity can then be calculated in the usual manner.

The secant method works by repeated estimates, based on the difference between the last estimated value and the actual value, to iterate down to the correct answer. The value obtained from the method is defined to be correct when the answer using the guessed value is within a certain tolerance of the actual answer. In this case, the algorithm starts with an initial estimate for θ_1 which, using equation A.30, gives the corresponding value of λ. This is then compared with the actual value formed by the ratio of the effective velocity over the cross-wires to give a new estimate for θ_1. The speed at which convergence is reached will depend on how accurate the initial estimate is. Therefore it was decided to use a start value of θ_1 given when $\alpha = 90^0$ as this was explicit and so could be calculated from the actual value of λ (although at an error). Using this starting value, the algorithm was found to converge in around 6-7 iterative loops.

As the speed of the reduction process was very important, the solution procedure had to be done in real time otherwise each 30mm profile would require storage in excess of 10Mb. To decrease the solution time further, the algorithm ran on the computers maths co-processor, reducing the process time to around 15 seconds for each sample position.

A.5.3.2 Worked Example

The following is a worked example showing how a voltage sample of the two hot-wires in a cross-wire probe was converted into velocities in the correct co-ordinate system.

The wires were calibrated using the technique described in A.4 which gave the following coefficients:

Wire 1 : $A = 1.8872$ $B = 0.8281$ $n = 0.4786$

$T_c = 289.51\,K$ $T_w = 568.42\,K$

Wire 2 : $A = 1.8484$ $B = 0.8946$ $n = 0.4646$

$T_c = 289.23\,K$ $T_w = 568.28\,K$

The angle made by the intersection of the two wires, α, and the angle of the normal of wire 1 to the required co-ordinate system were measured (as described in Chapter 2) and the value of the yaw factor, *k*, set. For this example, the following values are used:

$\alpha = 91.4^0$ $\beta = 52.3^0$ $k = 0.21$

At a given probe position, *i* number of voltage sample of the hot-wires were taken. For each sample there were two voltages, one for each of the wires in the probe, recorded with a 20 μs decay between them. For this example, the voltage on each wire is:

Wire 1 = 2.434 V Wire 2 = 2.163 V

and the temperature of the measured fluid is T = 293.51 K

These were converted into effective velocities over each wire using King's law. If temperature compensation (Phase 2 only) was used, this was performed at this stage.

$$U_1 = 28.625 \text{ ms}^{-1}$$

$$U_2 = 12.597 \text{ ms}^{-1}$$

This gave two instantaneous effective velocities over the wires. These were used together with equation A.30 and the assumption that $\alpha = 90^0$ to give the angle which the measured instantaneous flow made to the normal of wire 1:

$$\theta_1 = 27.480^0$$

As the assumption of $\alpha = 90^0$ is incorrect, the above value of θ_1 was used as first guess in an iterative cycle involving equation A.25. After 6-7 iterative loops, using the values of U_1, U_2 and α, equation A.25 gives:

$$\theta_1 = 28.5439^0$$

Using equation A.24, the angle the instantaneous flow made to the normal of wire 2, θ_2, can be calculated:

$$\theta_2 = 62.8561^0$$

Using equation A.21, U, the magnitude of the instantaneous flow can be calculated:

$$U = 32.375 \text{ ms}^{-1}$$

The above procedure has give a value for the magnitude of the instantaneous velocity measured by the cross-wire probe, U, and the angle which the flow made to the normal of wire 1, θ_1. Using trigonometry and the angle the normal of wire 1 makes with the desired co-ordinate system, β, this can be converted into instantaneous components of U.

$$U_x = U \cos \beta \quad = 19.789 \text{ ms}^{-1}$$

$$U_y = U \sin \beta \quad = 25.616 \text{ ms}^{-1}$$

These are calculated using the above method for each voltage sample at a probe position to give *i* number of instantaneous component velocities. These were then averaged to give the mean flow for each component and the fluctuating value was then calculated.

A5.4 Cross-wire Measurement Errors

The following sections discuss possible errors associated with using cross-wire probes for measuring turbulent flow.

A.5.4.1 Thermal Wake Error

The voltage across a hot-wire, and so the calculated velocity over that wire, depends on the heat loss from the wire. With two hot-wires in close proximity, as in a cross-wire, the heat loss from one wire will be affected by the temperature of the second wire. Although this will be compensated for to some degree during calibration (as long as both wires are operational during calibration), the error will reappear whenever the mean flow direction deviates from that during calibration. This is very likely, especially for highly turbulent flow where the flow direction is constantly changing. Work by Jerome at al. (1971) indicated that the effect could cause an error as large as 5% for the normal stresses and 25% for the shear stress when a closely spaced cross-wire is used.

A.5.4.2 High Intensity Turbulent Flow

There are two potential problems that can arise when analysing hot-wire signals in high turbulence intensity flows.

Firstly, the non-linear response of the voltage-velocity equation can produce significant errors if mean and rms hot-wire voltages are used to calculate velocities via the time averaged King's law equations. Figure A.3 shows this voltage-velocity relationship diagrammatically when the heat loss from the hot-wire is governed by

King's law. If a fluid flow fluctuates between U_{min} and U_{max}, with a mean velocity of U, then the hot-wire signal will vary between E^2_{min} and E^2_{max} and have a mean voltage of E^2_{mean}. Figure A.3 shows that E^2_{mean} does not relate to U and if E^2_{mean} is used in King's law to calculate a mean velocity, it will be lower than the actual mean velocity. Guitton (1968) states that the error in the mean velocity is around 6% for a turbulence intensity of 40%.

This error is produced by ignoring higher order terms in the time-averaging of King's law which significantly reduces the complexity of the equation. Doing this is only valid for turbulence intensities below 20%.

The error produced by the magnitude of the fluctuations can be removed by the use of a linearizer with produces a linear relationship between voltage and velocity, or by removing the mean and rms voltage meters from the system. Here, the hot-wire needs to be sampled at a suitable frequency to capture the velocity fluctuations, individual voltage readings then being converted into velocities using King's law. These velocities are then time averaged to produce a mean and fluctuating velocity, this being the method used in Phases 1 and 2 of this report.

The second potential problem for measurements in high turbulence intensity flows is signal rectification, which occurs whenever the component of the flow normal to the wire crosses zero. For a wire held normal to the mean flow direction, it is obvious that this happens at times of flow reversal in the mean direction, but for a cross-wire, the wires are normal angled to the mean flow direction and so this effect occurs before flow reversal in the mean direction. Tutu and Chevray (1975) stated that for turbulence intensities greater than 30%, all turbulent properties measured with a cross-wire probe can have significantly large errors. They quoted an error of 28% for Reynolds shear stresses (over and above any calibration and set-up errors) when the turbulence intensity was around 35%.

A.5.4.3 Errors due to Cross-wire Angles

As section A.5.3.2 shows, the solution to the cross-wire equations depends on accurately knowing the angle of intersection of the two hot-wires, α, and the angle which the co-ordinate system used makes to the normal of one of the wires, β. Gesso and Davies (1977) quote errors of 1.5% in calculated mean velocity and 5% in calculated turbulence intensity for a 1^0 error in wire measurement or initial probe set-up.

A.6 The Fast Fourier Transform

The Fast Fourier Transform (FFT) is a rapid way of calculating the spectral content of a signal with a time history. The FFT computer algorithm used was based on that described in Newland (1975) and was written by Dr. M. V. Finnis.

The time history signal was broken down into a number of short data sequences (the length of which had to be a power of 2 as the algorithm used was based on the radix-2 FFT). A Discrete Fourier Transform (DFT) was then calculated for this data sub-sequence, sequences then being recombined to yield the full FFT of the signal. A tapered window was applied to each sub-sequence to smooth the data at each end and weight the data to the middle of the sequence. This was done to reduce the effect of the discontinuities in the signal.

BLANK IN ORIGINAL

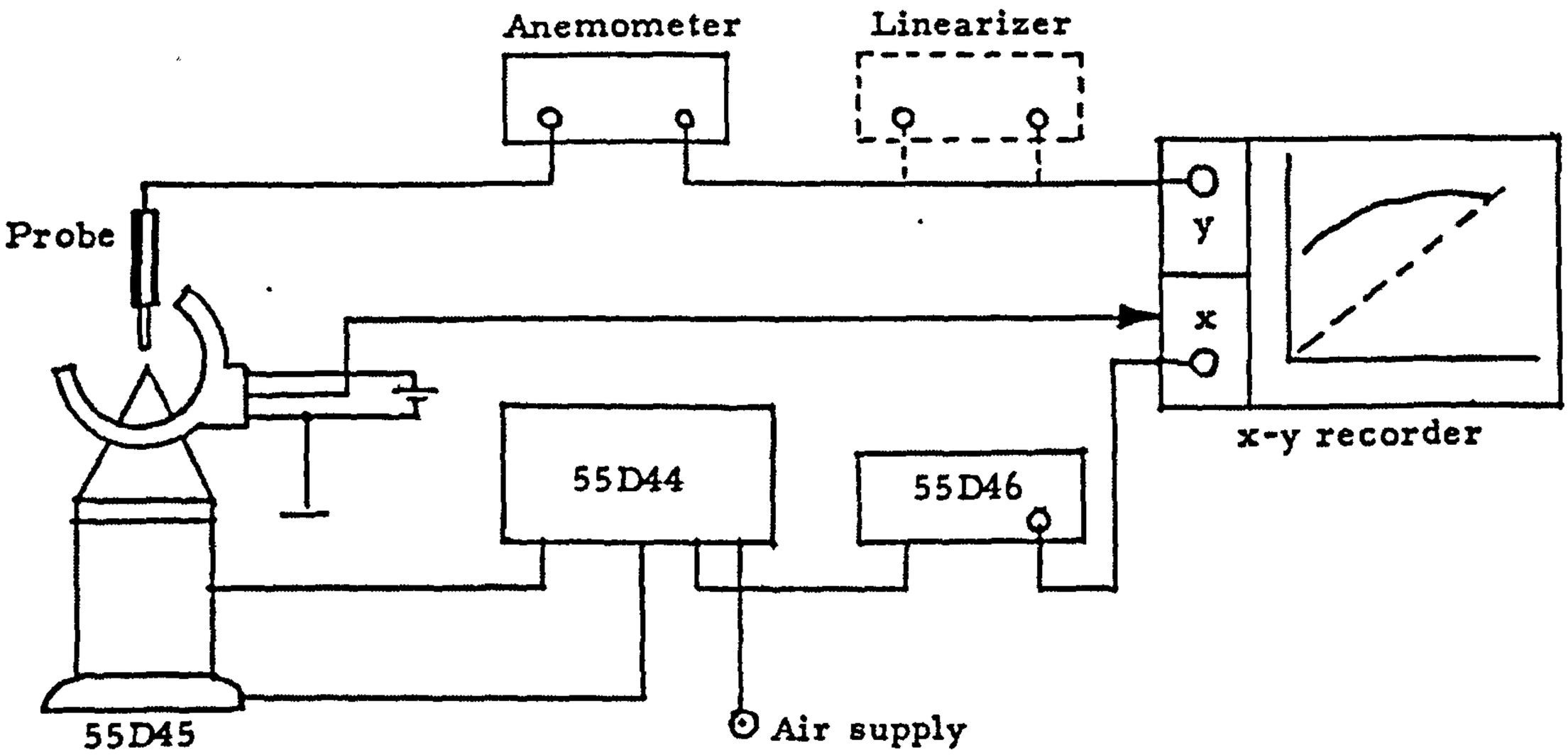

Figure A.1 : Schematic of Disa 55D90 Calibration Equipment

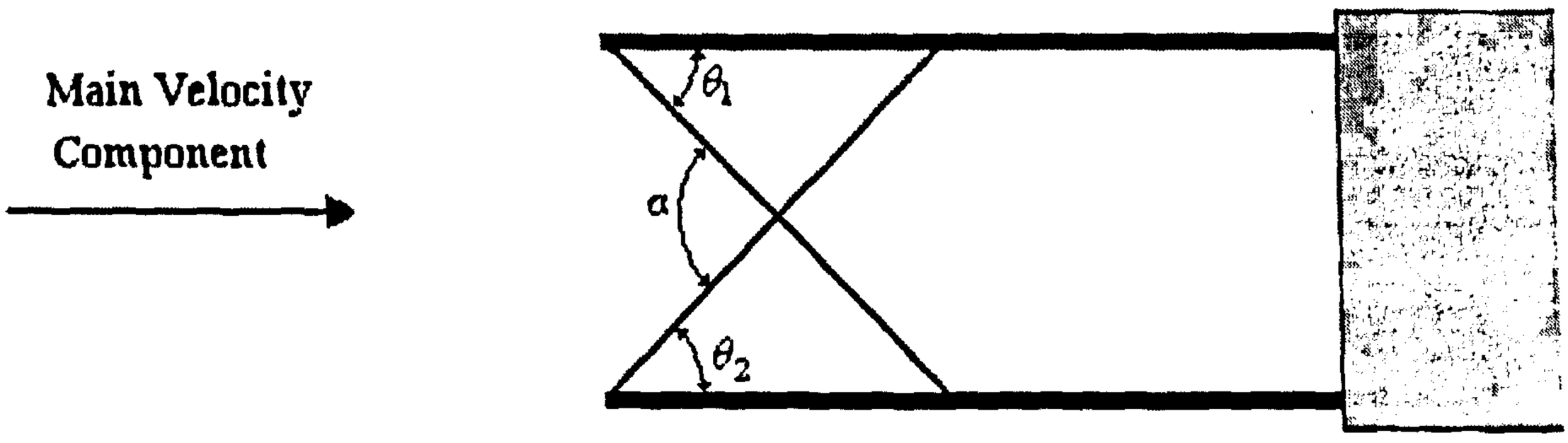

$$\alpha + (90 - \theta_1) + (90 - \theta_2) = 180^0$$

$$\therefore \theta_2 = \alpha - \theta_1$$

Figure A.2 : Relationship Between θ_1 and θ_2 for Cross-wire Probe

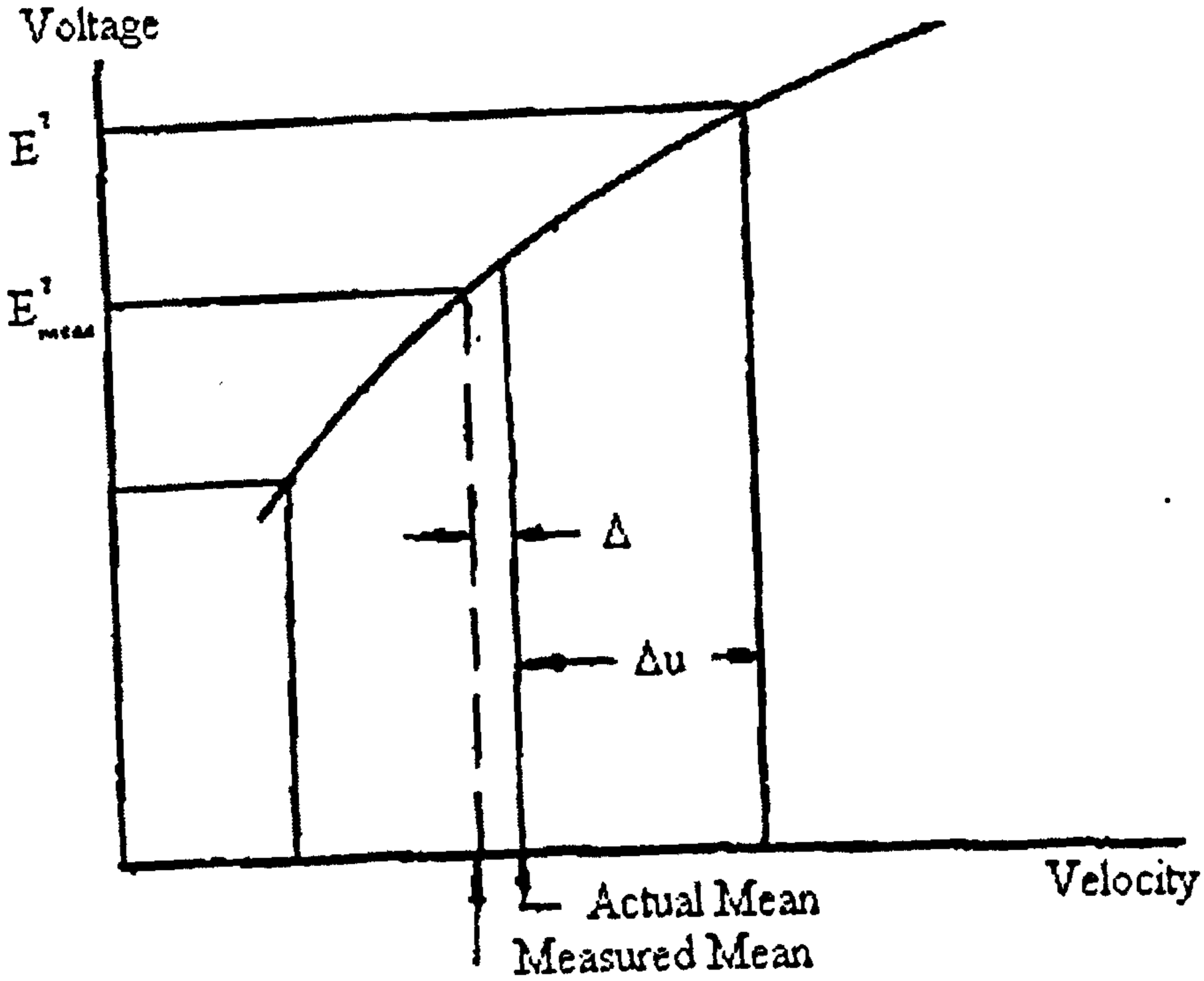

Figure A.3 : Non-linear Voltage-Velocity Response of a Hot-wire

Appendix B : Governing Equations for CFD

This appendix describes the fundamentals of Computational Fluid Dynamics (CFD) and the turbulence models used in this study.

B.1 Computational Fluid Dynamics

The origins of the mean flow equations used in CFD are as follows:

Mass conservation (Continuity Equation):

$$\frac{\partial U_i}{\partial x_i} = 0$$

Equation B.1

Momentum conservation (Navier-Stokes Equations):

$$\frac{\partial U_i}{\partial t} + U_j \frac{\partial U_i}{\partial x_j} = -\frac{1}{\rho}\frac{\partial P}{\partial x_i} + \nu \frac{\partial^2 U_i}{\partial x_i \, \partial x_j}$$

Equation B.2

Thermal energy conservation:

$$\frac{\partial \phi}{\partial t} + U_i \frac{\partial \phi}{\partial x_j} = \lambda \frac{\partial^2 \phi}{\partial x_i \, \partial x_j} + S_\phi$$

Equation B.3

where U_i is the instantaneous velocity component in the direction x_i, P is the instantaneous static pressure, ϕ is a scalar quantity (e.g. temperature), S_ϕ is a volumetric source term (e.g. heat generated) and ν and λ are the molecular (kinematic) viscosity and diffusivity (of ϕ) respectively.

Although these equations can be solved using Direct Numerical Simulation techniques, the computer power necessary is inhibitive and present studies have been

limited to flow in boxes. It will still be some time before these equations can be solved for turbulent flows of practical relevance.

In order to model turbulent flows mathematically, a statistical method is required. Osborne Reynolds suggested that the instantaneous quantity (U, P and ϕ) can be split into a mean and a fluctuating component:

$$U_i = \overline{U_i} + u_i \, , P = \overline{P} + p \, , \phi = \overline{\phi} +$$

Equation B.4

where the mean quantity is defined as :

$$\overline{\phi} = \frac{1}{t_2 - t_1} \int_{t_1}^{t_2} \phi \partial t$$

Equation B.5

When the Navier-Stokes equations are timed-averaged with the suggestion of Reynolds, we get:

$$\frac{\partial U_i}{\partial t} + U_j \frac{\partial U_i}{\partial x_j} = -\frac{1}{\rho} \frac{\partial P}{\partial x_i} + \frac{\partial}{\partial x_j} \left(\nu \frac{\partial U_i}{\partial x_j} - \overline{u_i u_j} \right)$$

Equation B.6

and the thermal energy equations give:

$$\frac{\partial \phi}{\partial t} + U_i \frac{\partial \phi}{\partial x_i} = \frac{\partial}{\partial x_i} \left(\lambda \frac{\partial \phi}{\partial x_i} - \overline{u_i \phi} \right) + S_\phi$$

Equation B.7

Because of the non-linearity of the terms in the original equations, when time averaged, a set of unknown turbulent variables, ($\overline{u_i u_j}$ or $\overline{u_i \phi}$), known as the *Reynolds Stresses* are introduced which render the equations unsolvable.

A *Turbulence Model* is a set of differential equations which allow the Reynolds Stresses to be determined and hence close the time-averaged equations for fluid motion. The role of the turbulence model is to provide an answer to the question: what is the numerical value of $u_i u_j$ at each point in the flow.

B.2 The Eddy Viscosity Turbulence Model

In order to close the time averaged equations, it is necessary to model the Reynolds Shear Stresses. Boussinesq (1877) hypothesised that in turbulent flow, the Reynolds Shear Stresses may be modelled as being proportional to the (mean) rates of strain, the proportionality coefficient defined as the turbulent (or eddy) viscosity thus:

$$-\overline{u_i u_j} = \nu_t\left(\frac{\partial U_i}{\partial x_j} + \frac{\partial U_j}{\partial x_i}\right) - \tfrac{2}{3}\delta_{ij}k$$

Equation B.8

where ν_t is the eddy viscosity, δ_{ij} is the Kronecker delta (=1 if i=j, otherwise =0) and k is the turbulent kinetic energy.

Unlike its molecular counterpart, ν_t is not a function of the fluid but rather of the flow and in turbulent flow will vary from point-to-point depending on the local level of turbulence activity.

Therefore an eddy viscosity turbulence model has to provide values for the eddy viscosity which will allow the evaluation of the turbulent stresses from Boussinesq's hypothesis. These stresses will then be substituted into the time averaged Navier-Stokes equations, enabling those to be solved numerically.

B.2.1 The k-ε Turbulence Model

The k-ε turbulence model is a two-equation model which evaluates the eddy viscosity from the solution of two differential equations, one for k, the turbulent kinetic energy and another for ε, the rate of dissipation of turbulent kinetic energy.

The complete k-ε model equations are as follows:

$$\nu_t = C_\mu \frac{k^2}{\varepsilon}$$

Equation B.9

$$P_k = -\overline{u_i u_j}\frac{\partial U_j}{\partial x_j}$$

Equation B.10

$$\frac{\partial k}{\partial t} + U_i\frac{\partial k}{\partial x_i} = \frac{\partial}{\partial x_i}\left(\frac{\nu_t}{\sigma_k}\frac{\partial k}{\partial x_i}\right) + P_k - \varepsilon$$

Equation B.11

$$\frac{\partial \varepsilon}{\partial t} + U_i\frac{\partial \varepsilon}{\partial x_i} = \frac{\partial}{\partial x_i}\left(\frac{\nu_t}{\sigma_\varepsilon}\frac{\partial \varepsilon}{\partial x_i}k\right) + C_{\varepsilon_1}\frac{\varepsilon}{k}P_k - C_{\varepsilon_2}\frac{\varepsilon^2}{k}$$

Equation B.12

where P_k is the production of turbulent kinetic energy.

The model contains five coefficients that have been determined from reference to experimental data and from computer optimisation. The most widely accepted set of values are

$$C_\mu = 0.09,\ C_{\varepsilon_1} = 1.44,\ C_{\varepsilon_2} = 1.92,\ \sigma_k = 1.0,\ \sigma_\varepsilon = 1.3$$

The result of these equations is that there is a fully coupled set of non-linear partial differential equations.

The ε equation represents a balance between the rate of transport of ε by the mean flow and the rates of its diffusion by the turbulent fluctuations, its generation by vortex stretching and, finally, its destruction by the action of viscosity.

The diffusion term is modelled using the gradient transport hypothesis as:

$$\text{Diffusion}\ (\varepsilon) = \frac{\partial}{\partial x_i}\left(\frac{\nu_t}{\sigma_\varepsilon}\frac{\partial \varepsilon}{\partial x_i}\right)$$

Equation B.13

The sources of ε (production and dissipation respectively) are modelled thus:

$$\text{Source}\ (\varepsilon) = C_{\varepsilon_1}\frac{\varepsilon}{k}P_k - C_{\varepsilon_2}\frac{\varepsilon^2}{k}$$

Equation B.14

The k equation is based on the same format, with a diffusion term (via the gradient -transport hypothesis), a production term (P_k) and a dissipation term (ε).

B.2.2 Boundary Conditions

A particularly problem that arises with solvers of these differential equations is what happens at a the edge of the grid, due to the reliance on the values in the cells before and after or above and below. This has been overcome by the addition of boundaries into the domain were different equations exist to model the flow and for a solid boundary, the most common is called 'The Wall Function'.

The k-ε model is only applicable in regions of high turbulent Reynolds number. As a wall is reached, the Reynolds number falls and viscous effects become more and more dominant, reducing the validity of some of the assumptions made in modelling the ε equation. The very steep velocity gradients encountered in the viscous sublayer would also require many grid points for accurate modelling and so is computational expensive.

To overcome this problem, the near-wall region is bridged with empirical relations based on the assumptions of a logarithmic velocity profile, local equilibrium of turbulence, and a constant near-wall stress layer. It works by carrying out the standard calculations down to a point p close to the wall but outside the viscous sublayer. Boundary conditions for U, k and ε are needed at point p and these are obtained using the following approach.

It is assumed that at point p, the velocity component parallel to the wall obeys the usual logarithmic law-of-the-wall:

$$\frac{U_p}{\mu_\tau} = \frac{1}{\kappa}\ln(EY^+)$$

Equation B.15

where U_p is the resultant velocity parallel to the wall, μ_τ is the resultant friction velocity given by:

$$\sqrt{\left(\frac{\tau_w}{\rho}\right)}$$

Equation B.16

κ is the von Kármán constant, E is the is the roughness parameter and Y^+ is a non-dimensional wall distance given by:

$$Y^+ = \frac{\mu_\tau y_p}{\nu}$$

Equation B.17

where y_p is the position above the wall and ν is the kinematic viscosity. This equation can then be solved iteratively to yield τ_w. Similar laws are available for temperature, relating the heat flux at the wall to the difference between the wall temperature and the temperature just outside the viscous sublayer.

In the near-wall region, it is assumed that the Reynold Stresses are nearly constant (i.e.. Couette-flow assumption), convection and diffusion of $\overline{u_i v_j}$ are negligible so that local equilibrium exists implying that $P_k = \varepsilon$ which, together with the fact that the Reynolds shear stress is approximately equal to the wall shear stress, allows us to write:

$$\frac{k_p}{U_\tau^2} = \frac{\mu_\tau^2}{\sqrt{C\mu C_D}}$$

Equation B.18

With $\varepsilon = P_k$ and $\partial U/\partial y$ coming from the differentiation of equation B-15, we can write:

$$\varepsilon_p = \frac{(C_\mu C_D)^{\frac{3}{4}} k_p^{\frac{3}{2}}}{\kappa y_p}$$

Equation B.19

This enables the values of k and ε to be fixed at point p.

This method has the restriction that the Y^+ for the first calculation point (cell centre for PHOENICS) should strictly be within the region $30.0 < Y^+ < 130$. Below $Y^+ = 30.0$, the flow no longer flows the logarithmic-law-of-the-wall due to effects of the laminar sublayer, and above $Y^+ = 100.0$, the flow increasingly deviates from the law due to the ever increasing effect of turbulence.

B.2.3 Chen-Kim Correction to the k-ε Turbulence Model

This modification to the standard high-Reynolds number k-ε turbulence model was introduced to remove the equations reliance on a single time scale to characterise the various dynamic processes occurring in turbulent flows. This is achieved by the addition of a volumetric production rate of k (P_k), V_k, which improves the dynamic response of the ε equations.

The Chen-Kim modified k-ε model differs in two ways from the standard form. Firstly, the following model constants were changed to:

$$\sigma_k = 0.75,\ \sigma_\varepsilon = 1.15,\ C_{\varepsilon_1} = 1.15,\ C_{\varepsilon_2} = 1.9$$

Equation B.20

and the following source term per unit volume added to the ε equation (B,12):

$$S_\varepsilon = \rho \times F_1 \times C_{\varepsilon_3} \times \frac{P_k^2}{\varepsilon}$$

Equation B.21

where $C_{\varepsilon 3} = 0.25$ and F_1 is the Lam and Bremhorst (1981) damping function (originally devised for a low Reynolds number k-ε turbulence model) which tends to unity at high turbulence Reynolds numbers (see the section on Low Reynolds Number k-ε Turbulence Model for further details).

B.2.4 Low Reynolds Number k-ε Turbulence Model

Several investigations have shown that simple wall functions based on the logarithmic law and the equilibrium turbulence assumption are not appropriate for unsteady turbulent boundary layers. It was shown that the accuracy of the model deteriorates with increasing level or rate of unsteadiness, due to its high Reynolds number dependence. A low Reynolds number model is necessary for accurate predictions where the near-wall physics is of interest.

The model is that suggested by Lam and Bremhorst (1981) and is basically the standard k-ε version with the addition of five new functions:

$$\nu_t = C_\mu F_\mu \frac{k^2}{\varepsilon}$$

Equation B.22

$$P_k = -\overline{u_i u_j}\frac{\partial U_i}{\partial x_j}$$

Equation B.23

$$\frac{\partial k}{\partial t} + U_i\frac{\partial k}{\partial x_i} = \frac{\partial}{\partial x_i}\left(\frac{\nu_t}{\sigma_k}\frac{\partial k}{\partial x_i}\right) + P_k - \varepsilon$$

Equation B.24

$$\frac{\partial \varepsilon}{\partial t} + U_i\frac{\partial \varepsilon}{\partial x_i} = \frac{\partial}{\partial x_i}\left(\frac{\nu_t}{\sigma_\varepsilon}\frac{\partial \varepsilon}{\partial x_i}k\right) + C_{\varepsilon_1}F_1\frac{\varepsilon}{k}P_k - C_{\varepsilon_2}F_2\frac{\varepsilon^2}{k} + E$$

Equation B.25

The new functions F_μ, F_1 and F_2 and the term E vary in magnitude and dependence depending on the type of flow under investigation (see Table 1, Patel et al. 1985).

The Lam and Bremhorst (1981) equations for the above functions are implemented in PHOENICS 2.0 and consequently were used in the low Reynolds number k-ε investigation.

These state:

$$F_\mu = [1 - \exp(-0.0165 \times REYN)]^2 \times \left(1 + \frac{20.5}{REYT}\right)$$

Equation B.26

$$F_1 = 1 + \left(\frac{0.05}{F\mu}\right)^3$$

Equation B.27

$$F_2 = 1 - \exp(-REYT^2)$$

Equation B.28

where

$$REYN = \sqrt{k} \times \frac{Y_n}{\mu}$$

Equation B.29

$$REYT = \frac{k\mu}{\varepsilon}$$

Equation B.30

where Y_n is the distance to the nearest wall. The functions F_μ, F_1 and F_2 tend to unity at high turbulence Reynolds numbers. At boundary's (i.e.. walls) the following conditions are applied:

$$k = 0.0, \frac{\partial \varepsilon}{\partial y} = 0.0$$

Equation B.31

The function, F_μ, is added to mimic the direct effect of molecular viscosity on the shear stress. Launder (1975) noted that pressure fluctuations near the wall also tended to reduce the shear stress via the pressure strain correlation. Thus, F_μ attempts to model both these effects, although it only properly correlates the former. The function F_2 is introduced primarily to incorporate low Reynolds number effects in the destruction term of ε, where as F_1 and E are empirical terms to introduce a quadratic growth of ε with distance from the wall.

BLANK IN ORIGINAL

Appendix C : PHOENICS

This appendix details the CFD package 'PHOENICS' and how the partial differential equations are solved.

C.1 Equations in PHOENICS

PHOENICS is an acronym for 'Parabolic, Hyperbolic or Elliptic Numerical Integration Code Series' and is a general-purpose code for simulating single and multi-phase flow, heat and mass transfer and chemical-reaction phenomena. It attempts to solve the equations detailed in Appendix B using finite-volume techniques for both steady and unsteady flows in 1, 2 and 3 dimensions.

C.2 The Grid

PHOENICS works by breaking the domain down into discrete small volumes (called cells) in which the appropriate variables are solved. These variables take a constant value over that cell, and for calculating gradients, are based at the cell centre or node point. Therefore, for flows with large gradient changes in variables, closely spaced cells are required to give accurate answers.

A problem can arrive when using a standard grid were all the variables are solved at the cell centres. When the continuity equation (B.1) is written in the discrete form using a truncated Taylor series form (see Patankar 1980 and Figure C.1), i.e.:

$$\frac{u_P + u_E}{2} - \frac{u_W + u_P}{2} = 0$$

Equation C.1

$$u_E - u_W = 0$$

Equation C.2

it demands that equality of velocities exists at alternative grid points and not adjacent ones. The consequence is that velocity fields shown in Figure C.2 can exist, although they are completely unrealistic.

These difficulties are resolved by realising that we do not have to calculate the variables at the same grid point. This form of grid is called a 'Staggered Grid' for the velocities (see Figure C.3) and was first used by Harlow and Welch (1965) and forms the basics of the Simple and Simpler computer algorithms. The velocity components are calculated for points that lie on the faces of the control volumes, thus for the x-direction, velocity, u is calculated at the faces that are normal to the x-direction. It is worth noting that the control volume face may not lie at the midway between grid points, but will depend on how the grid is defined.

The advantages of using this grid method are twofold. For a typical control volume, the discretized continuity equation would contain the differences of adjacent velocity components, not alternative grid components as with the normal grid, so preventing a wavy velocity field from satisfying the equation. Secondly, the pressure difference between adjacent grid points now becomes the natural driving force for the velocity components, so leading to pressure driven solutions which is an aid for convergence.

C.3 The Momentum Equations

The momentum equation can be written in is discrete form in a similar way as C.1:

$$a_n u_n = \sum a_{nb} + a_{nb} + b + \left(p_P - p_N\right)A_N$$

Equation C.3

where a_n is the diffusion coefficient for the velocity u in the n direction, a_{nb} is the diffusion coefficient for the neighbouring velocity u_{nb}, b is a source term, $(p_P - p_N)$ is the pressure difference across the cell face and A_n is the area of the cell face

These can be solved only when the pressure field is given or somehow estimated. Unless the pressure field is correctly guessed, the resulting velocity field will not satisfy the continuity equation. Imperfect velocity fields based on an estimated pressure field (p^*) are denoted as u^*, v^*, etc. Therefore:

$$a_n u_n^* = \sum a_{nb} u_{nb} + b + \left(p_P^* - p_N^*\right) A_N$$

Equation C.4

C.4 Velocity Correction Equations

In order to improve the satisfaction of the continuity equation, an improved guess of the pressure field, leading to an improved velocity field is required. If we assume the correct pressure (p) is given by:

$$p = p^* + p'$$

Equation C.5

where p' is a correction pressure. The corresponding velocity corrections are given by:

$$u = u^* + u'$$

Equation C.6

If we subtract C.5 and C.6 from C.4, we get:

$$a_n u_n' = \sum a_{nb} u_{nb}' + \left(p_P' - p_N'\right) A_N$$

Equation C.7

At this point we will drop the summation term from the equation. This term represents an indirect or implicit influence of the pressure correction on the velocity; pressure corrections at nearby locations can alter the neighbouring velocities and thus due to the linked nature of the equation, cause velocity corrections at the point under consideration. By not considering this term, the solution scheme is only partially implicit

(semi-implicit). The omission of the term also allows us to write p' in the general ϕ equation, enabling a sequential, one-variable at a time solution procedure.

This simplification does not effect the ultimate solution, as the corrected pressure is used to calculated the velocity field, and hence satisfy the continuity equation, although the corrected pressure may not equal the actual pressure field.

Therefore, the corrected velocity is given by:

$$u'_n = d_n\left(p'_P - p'_N\right)$$

Equation C.8

where

$$d_n \equiv \frac{A_n}{a_n}$$

Equation C.9

This gives the actual velocity as:

$$u_n = u^*_n + d_n\left(p'_P - p'_N\right)$$

Equation C.10

C.5 The Pressure Correction Equation

If the continuity equation (B.1) is integrated over the control volume or cell, the following equation can be obtained:

$$\frac{\left(p_P - p^0_P\right)\Delta x\Delta y\Delta z}{\Delta t} + \left[(\rho u)_e - (\rho u)_w\right]\Delta y\Delta z + \left[(\rho v)_n - (\rho v)_s\right]\Delta x\Delta z + \left[(\rho w)_h - (\rho w)_l\right]\Delta x\Delta y = 0$$

Equation C.11

If the velocity correction formulae (C.8) are now substituted for the velocity components, we obtain, after rearrangement, the following discretization equation (Finite Volume Equation) for p':

$$a_P p'_P = a_E P'_E + a_W P'_W + a_N P'_N + a_S P'_S + a_H P'_H + a_L P'_L + b$$

Equation C.12

where:

$$a_E = \rho_e d_e \Delta y \Delta z$$

Equation C.13

$$a_W = \rho_w d_w \Delta y \Delta z$$

Equation C.14

$$a_N = \rho_n d_n \Delta z \Delta x$$

Equation C.15

$$a_S = \rho_s d_s \Delta z \Delta x$$

Equation C.16

$$a_H = \rho_h d_h \Delta x \Delta y$$

Equation C.17

$$a_L = \rho_l d_l \Delta x \Delta y$$

Equation C.18

$$a_P = a_E + a_W + a_N + a_S + a_H + a_L$$

Equation C.19

$$b = \frac{\left(p_P^o - p_P\right)\Delta x \Delta y \Delta z}{\Delta t} + \left[\left(\rho u^*\right)_w - \left(\rho u^*\right)_e\right]\Delta y \Delta z$$

$$+\left[\left(\rho v^*\right)_s-\left(\rho v^*\right)_n\right]\Delta z\Delta x+\left[\left(\rho w^*\right)_l-\left(\rho w^*\right)_h\right]\Delta x\Delta y$$

Equation C.20

Since the density values are only available at the cell centres, a suitable interpolation technique is used to calculate the value at the cell edges. What ever the interpolation, it is very important that the value of the variable at the cell edge must be consistently used for the two control volumes to which the interface belongs.

C.6 The Computer Algorithm

The computer algorithm using by PHOENICS for solving the equations is called 'SIMPLER' and is based of the algorithm 'SIMPLE'

C.6.1 SIMPLE

SIMPLE stands for 'Semi-implict Method for Pressure Linked Equations' and was first suggested by Patanker and Spalding (1972). The important operations are:

1. Guess the pressure field p*
2. Solve the momentum equations (C.4) to give u*, v* and w*
3. Solve the pressure-corrected equation (C.12) to give p'
4. Calculate the actual pressure, p, by adding p* and p' (C.5), this becoming the new guessed pressure field, p*, in the next iteration
5. Calculate u, v and w from u*, v* , w* and p' using the velocity-correction equation (C.7)
6. Solve for any other variable ϕ
7. Repeat from step 2 until Convergence

C.6.2 SIMPLER

In an attempt to improve the rate of convergence, 'SIMPLER' was suggested by Patankar (1980), the name standing for SIMPLE Revised. The argument for this new method is based on the approximation introduced into the derivation of p' by the omission of the term $\sum a_{nb}u'_{nb}$, this omission leading to exaggerated pressure correction fields.

An example of this problem is given if we consider a simple one-dimension constant density flow with the velocity given at the inlet. The velocity is only governed by the continuity equation and hence, will be solved for after only a few iterations. The predicted pressure, p, will be far from the final answer due to the approximate nature of the p' equation and it would take many iterations before a converged pressure solution was obtained.

If we employ the pressure correction equation only to the task of solving the velocities and use some other method for the pressure field, we will obtain a more efficient algorithm. This is the essence of SIMPLER.

C.6.2.1 The Pressure Equation

We can rewrite equation C.7 to give:

$$u_e = \frac{\sum a_{nb}u_{nb} + b}{a_e} + d_e\left(p_P - p_E\right)$$

Equation C.21

If will define a pseudo velocity $\hat{u}_e$ as:

$$\hat{u}_e = \frac{\sum a_{nb}u_{nb} + b}{a_e}$$

Equation C.22

then we can say:

$$u_e = \hat{u}_e + d_e\left(p_P - p_E\right)$$

Equation C.23

Similarly, equations can be written for the other two velocities, u_n and u_h.

It then follows that a new discrete pressure equation can be written:

$$a_P p_P = a_E p_E + a_W p_W + a_N p_N + a_S p_S + a_H p_H + a_L p_L + b$$

Equation C.24

where the coefficients a_x are given by equations C.13 to C.19 and b is given by equation C.20 with u^* replaced with $\hat{u}$.

Although there are a great number of similarities with equation C.20, there have been no assumptions made in its derivation. Thus if a correct velocity field is used to calculate $\hat{u}$, then the pressure equation would at once give the correct pressure field.

C.6.2.2 The SIMPLER Algorithm

The algorithm works on the following basis:

1. Start with a guessed velocity field
2. Calculate the coefficients for the momentum equation and hence solve for $\hat{u}$, using the values of the neighbouring velocities u_{nb} (C.22)
3. Calculate the coefficients for the velocity field and solve for the correct pressure field (C.12)
4. Treat this pressure field as p^* and solve the momentum equations to give u^*, v^* and w^* (C.4)
5. Solve for the pressure corrected pressure p' (C.12)
6. Solve the actual velocity field (C.6)
7. Solve for other variables ϕ
8. Repeat from step 2 until convergence.

As can be seen, SIMPLER resembles SIMPLE in a number of ways, the two main differences being that the initial field required is velocity and not pressure, and the actual pressure field is solved for, not a calculated pressure field plus a correction.

Although SIMPLER has been found to converge faster than SIMPLE, it must be noted that one iteration of SIMPLER involves more computational effort. However, the additional effort per iteration is more than compensated by the overall saving on convergence time.

C.7 Elliptic, Parabolic and Hyperbolic

A parabolic problem (see Figure C.4) is one in which, although gradients in fluid properties do exist in the low-to-high direction, the higher slab values do not appear in the lower slab equations, hence a_H is zero for all points. This situation often occurs when the main fluid flow is in the z-direction and the Reynolds number is high (e.g. modelling of a free jet) as the influence of downstream conditions on upstream ones is very small. If this is the case, a single pass (sweep) through the domain (low-to-high) will suffice with the corresponding large reduction in computing power.

For simulations where conditions do effect upstream ones, the Elliptical method should be used, where a large number of passes through the domain (including the coefficient a_H in the equations) allow for some reversibility in the flow. This method is required when modelling an impinging jet.

The Hyperbolic method is a simplified Elliptical solver where the region of influence is restricted to the so-called 'Mach Cone'.

BLANK IN ORIGINAL

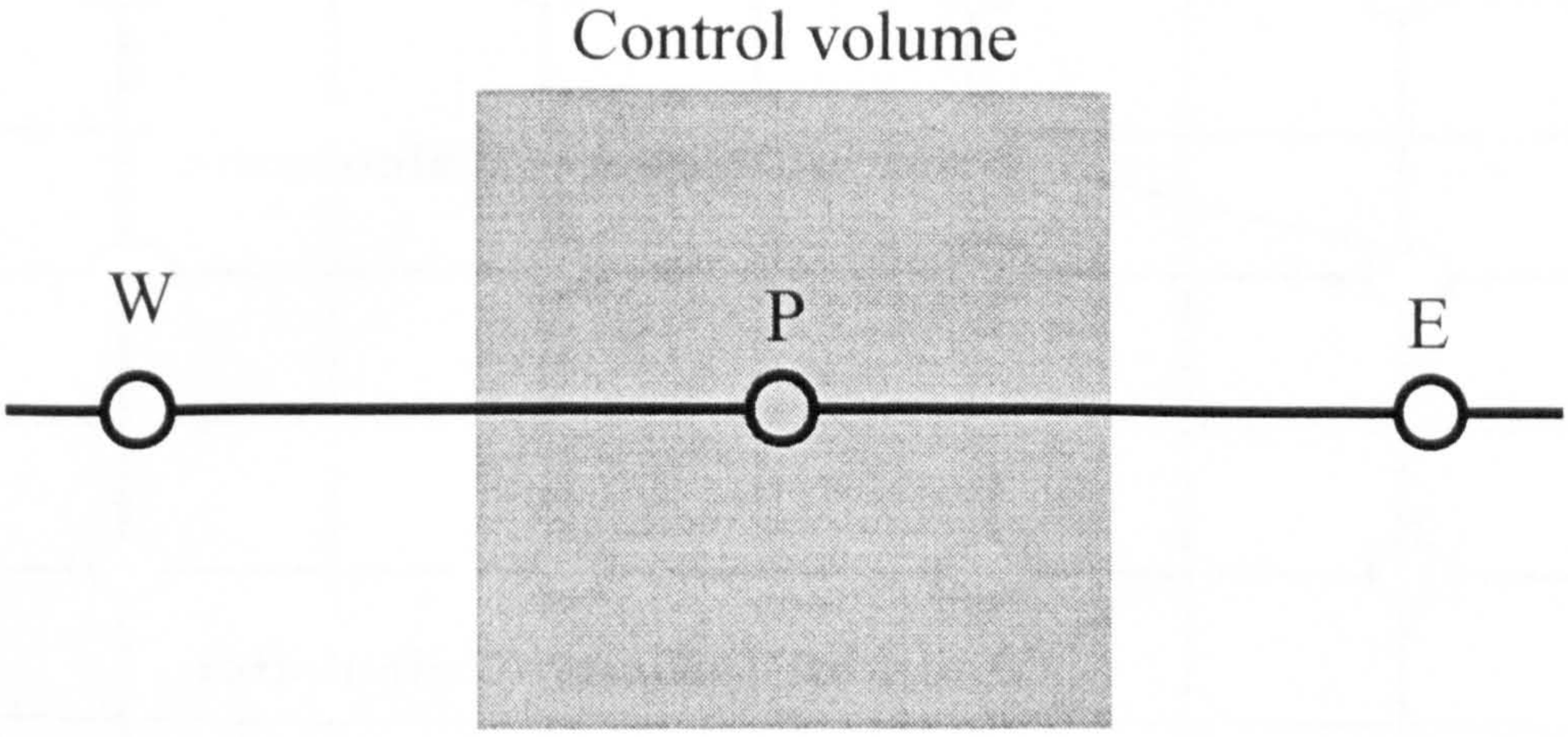

Figure C1 : Standard Grid

Figure C.2 : Alternating Velocity Field

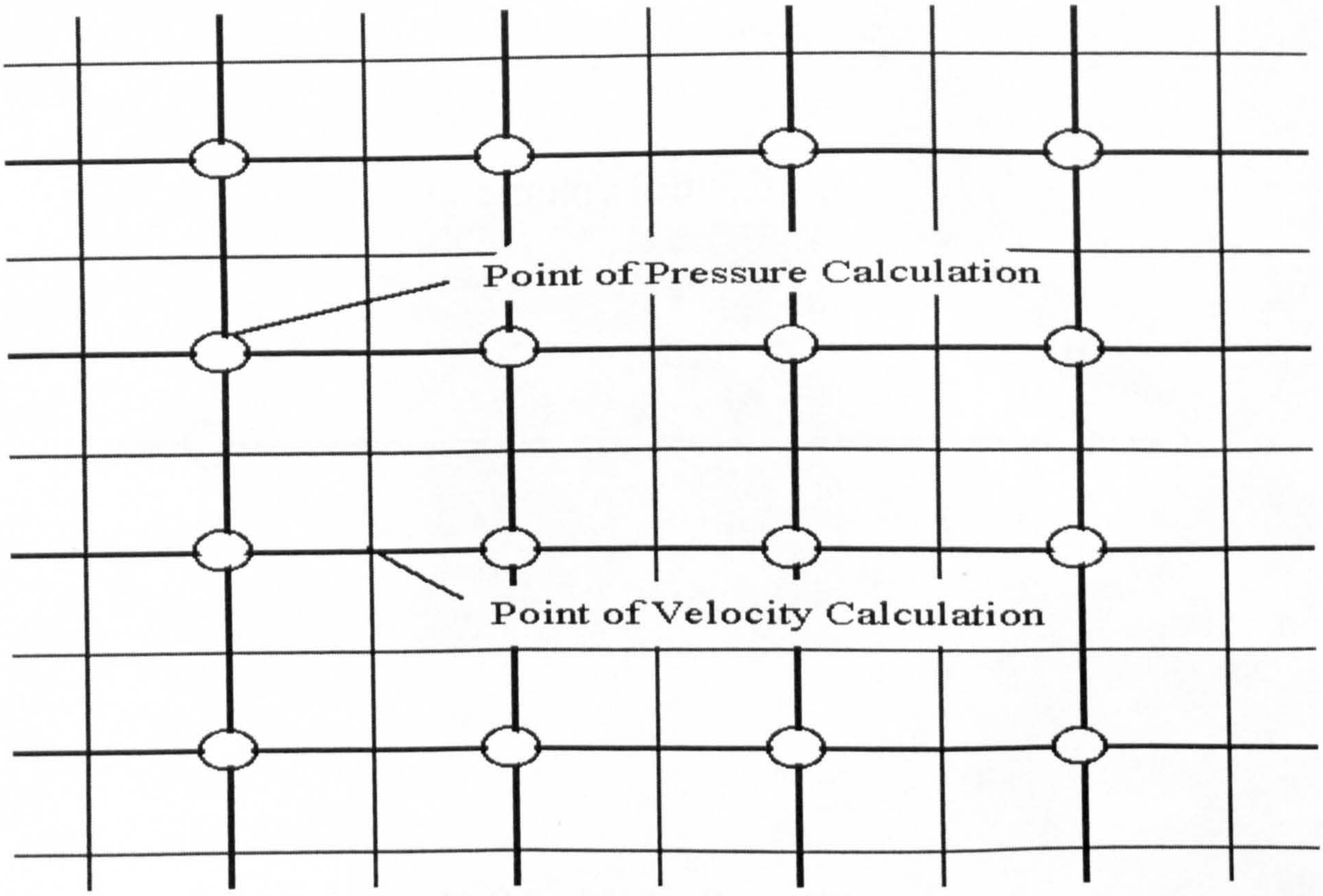

Figure C.3 : The Staggered Grid

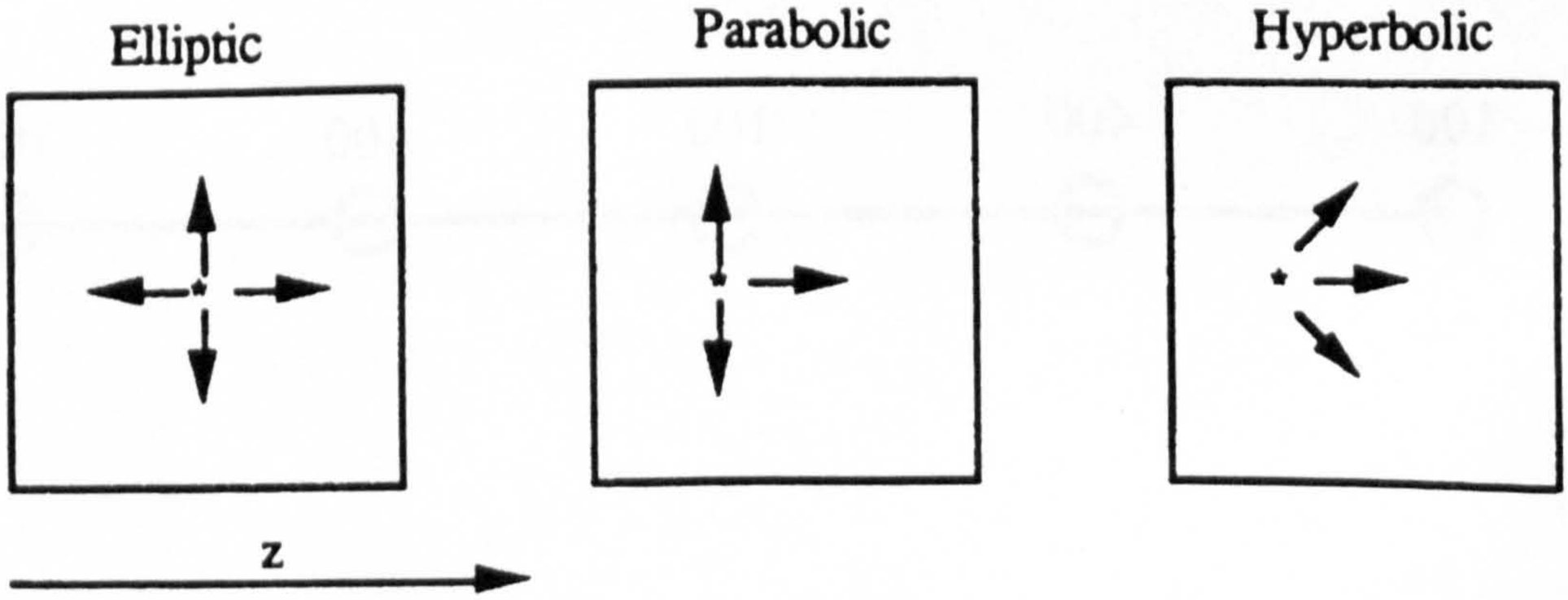

Figure C.4 : Elliptic, Parabolic and Hyperbolic Problems